

Nonthermal Plasma Chemistry and Physics

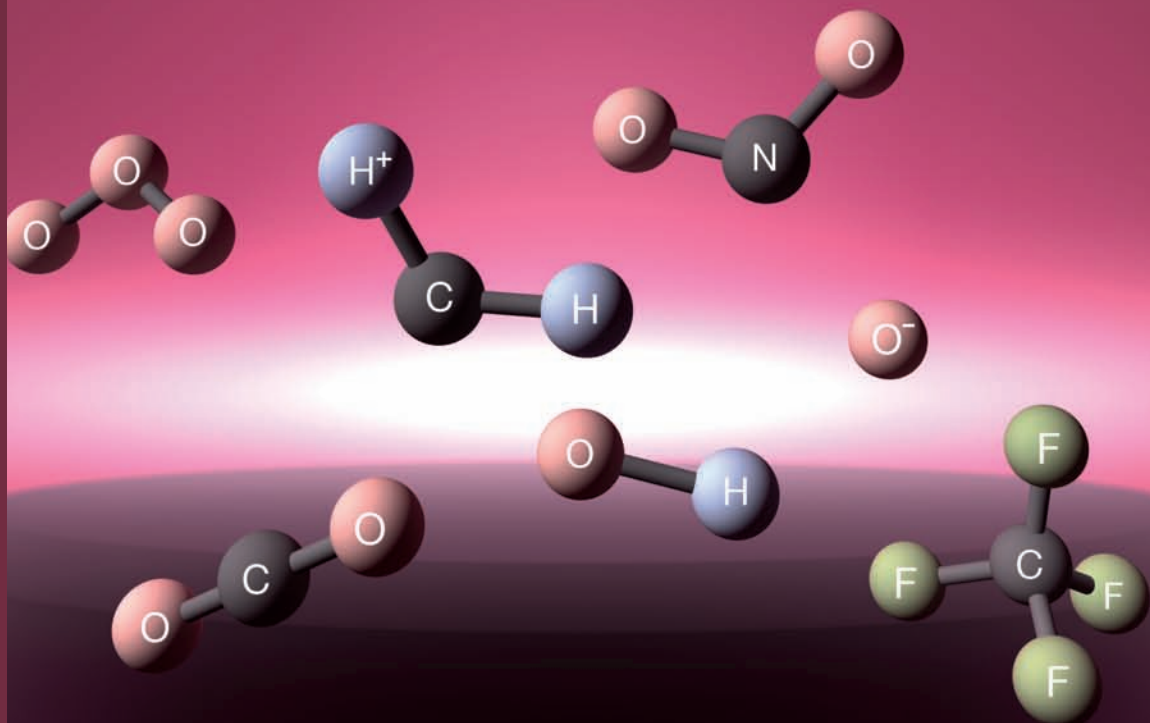
edited by

Jürgen Meichsner

Martin Schmidt

Ralf Schneider

Hans-Erich Wagner



CRC Press
Taylor & Francis Group

Nonthermal Plasma Chemistry and Physics

Nonthermal Plasma Chemistry and Physics

edited by

Jürgen Meichsner

Martin Schmidt

Ralf Schneider

Hans-Erich Wagner



CRC Press

Taylor & Francis Group

Boca Raton London New York

CRC Press is an imprint of the
Taylor & Francis Group, an **informa** business

Cover design by Sascha Meichsner and Carsten Desjardins.

CRC Press
Taylor & Francis Group
6000 Broken Sound Parkway NW, Suite 300
Boca Raton, FL 33487-2742

© 2013 by Taylor & Francis Group, LLC
CRC Press is an imprint of Taylor & Francis Group, an Informa business

No claim to original U.S. Government works
Version Date: 20121207

International Standard Book Number-13: 978-1-4200-5921-2 (eBook - PDF)

This book contains information obtained from authentic and highly regarded sources. Reasonable efforts have been made to publish reliable data and information, but the author and publisher cannot assume responsibility for the validity of all materials or the consequences of their use. The authors and publishers have attempted to trace the copyright holders of all material reproduced in this publication and apologize to copyright holders if permission to publish in this form has not been obtained. If any copyright material has not been acknowledged please write and let us know so we may rectify in any future reprint.

Except as permitted under U.S. Copyright Law, no part of this book may be reprinted, reproduced, transmitted, or utilized in any form by any electronic, mechanical, or other means, now known or hereafter invented, including photocopying, microfilming, and recording, or in any information storage or retrieval system, without written permission from the publishers.

For permission to photocopy or use material electronically from this work, please access www.copyright.com (<http://www.copyright.com/>) or contact the Copyright Clearance Center, Inc. (CCC), 222 Rosewood Drive, Danvers, MA 01923, 978-750-8400. CCC is a not-for-profit organization that provides licenses and registration for a variety of users. For organizations that have been granted a photocopy license by the CCC, a separate system of payment has been arranged.

Trademark Notice: Product or corporate names may be trademarks or registered trademarks, and are used only for identification and explanation without intent to infringe.

Visit the Taylor & Francis Web site at
<http://www.taylorandfrancis.com>

and the CRC Press Web site at
<http://www.crcpress.com>

Contents

Preface	vii
Acknowledgments	ix
Editors	xi
Contributors.....	xiii
Chapter 1 Introduction	1
Chapter 2 Nonthermal Plasma Chemical Processes of General Interest	7
Chapter 3 Physics of Nonthermal Plasmas.....	15
Chapter 4 Nonthermal Plasma Chemical Reactors	137
Chapter 5 Elementary Processes on Surfaces in Plasma–Wall Interaction.....	163
Chapter 6 Plasma Diagnostics	187
Chapter 7 Surface and Thin Film Analysis	255
Chapter 8 Selected Applications.....	285
Chapter 9 Modeling and Simulation	407
Chapter 10 Trends and New Concepts	469
References.....	473
Index.....	539

Preface

Plasma processing is one of the key technologies worldwide, especially using non-thermal, low-temperature plasmas. Recently, the situation is characterized by the fast-growing interest in the optimization of existing applications as well as the development of new ones.

This book provides a basic introduction to nonthermal plasma chemistry and physics for students of plasma physics, PhD students, and scientists. The fundamentals of plasma chemical reactions and its modeling, most importantly nonthermal plasma sources, relevant diagnostic techniques, as well as selected applications, are presented and discussed in a systematic manner. Interconnections are shown; trends and new concepts are illustrated. The chapters discuss the basic principles and provide exemplary illustrations of the wide field of applications. Therefore, it is not the aim of this book to give a complete overview of the state of the art in the research areas. For this, the readers can refer to already existing excellent monographs and topical reviews given in the references.

The book is based on contributions from internationally known experts in their research fields, using examples from their own scientific activities to illustrate the basic principles with applications.

After a short introduction to the field of nonthermal plasma chemistry with some historical notes and its specific characteristics, topics of general interest in this field are briefly presented, which illustrate the broad spectrum of applications. Dry air plasma chemistry with ozone generation or lacquer stripping and ashing reactions are briefly discussed. Plasma etching presents a key technology in integrated circuit production. Methane gas reformation as well as diamond deposition are important topics of hydrocarbon plasma chemistry. The formation of pre-biochemical compounds is also observed in nonthermal plasmas. Thin film generation of plasma polymers, of metallic compounds, and silicone-based cells are products of plasma chemical processes.

The fundamentals, sources, and diagnostics of nonthermal plasmas are discussed next. The basic concepts of plasma physics for thermal and nonthermal plasmas, including collisional processes, plasma kinetics, and macroscopic transport equations, are introduced. Due to the importance of surface processes in many applications, the plasma-wall boundary is also considered. The basic physics of different nonthermal plasmas of electric discharges and the realizations for technical plasma sources are presented at the end of this chapter.

Nonthermal plasma reactors are characterized in terms of the principles of chemical quasi-equilibria, macroscopic kinetics, and plasma chemical similarity.

Plasma–surface interaction is one of the fastest-growing branches in plasma physics and has got an important issue in the field of applied surface science. Its basic question concerns the mastering of an old problem: the contact of different states of matter. The investigation and application of plasma–surface interaction plays an essential role in low-temperature plasma processing such as etching, deposition, or modification of surfaces as well as in fusion research. Therefore, such elementary processes on surfaces in contact with plasmas are discussed. The particle and energy balance at the surface determine the importance of the different mechanisms.

According to the broad spectrum of plasma components, different tasks exist for the investigation of the plasma to understand the processes and to control chemical reactions characteristic of the various applications. Therefore, the fundamentals of probe measurements, microwave interferometry, emission and absorption spectroscopy, laser-induced fluorescence spectroscopy, and gas chromatography are discussed.

Complementary techniques needed for surface and thin film analysis are presented next.

The first part of the next chapter presents examples of applications of volume plasma chemistry. The reactions take place in the volume, as pure gas phase reactions, or in heterogeneous processes with participation of the surface of substrates, electrodes, or walls, sometimes assisted by catalytic effects. The second part concerns applications of surface chemistry. Here the plasma chemical reactions result in changes in surface properties. The reactions may involve volume processes, but the essential reactions take place at the surface. Etching and thin film deposition as well as surface functionalization up to plasma medical applications are presented.

Modeling and simulation provide an increasing number of tools to improve the basic understanding of nonthermal plasmas and allow predictive studies for optimization of processes. The hierarchy of plasma models is explained at the beginning of the next chapter, followed by a discussion of theoretical concepts for elementary volume and surface processes in gas discharges. The chapter concludes with an example of modeling, namely, the spatiotemporal dynamics in radio-frequency discharges of oxygen and its comparison with experimental results.

The book concludes with a discussion of trends and new concepts in this fascinating and dynamic research area.

Acknowledgments

We would like to express our deep gratitude to all coauthors. They are the fundament on which this work is based.

A very special thank you goes to Andrea Kleiber (Max-Planck-Institut für Plasmaphysik, Teilinstitut Greifswald, EURATOM Association, Greifswald) for her endless patience and amazing support. The book would never have been completed without her uncountable contributions and her careful attention. Bert Krames helped as emergency support in the final processing and transformed the impossible into reality.

We would also like to gratefully acknowledge the work of Marcel Beu (Leibniz-Institut für Plasmaforschung und Technologie e.V. (INP Greifswald)) for helping us with the drawings.

This work was partly supported by the Deutsche Forschungsgemeinschaft, Sonderforschungsbereich Transregio 24. One of the editors (M. S.) appreciates the support of the INP Greifswald.

Very special thanks go to Lance Wobus of Taylor & Francis Group for his valuable advice and his patience during the preparation of this book. We gave him a hard time with this project, but he was always giving us a backup whenever problems appeared.

Editors

Jürgen Meichsner

Institut für Physik der Ernst-Moritz-Arndt-Universität Greifswald, Felix-Hausdorff-Str. 6, D-17489 Greifswald, Germany

Martin Schmidt

Leibniz-Institut für Plasmaforschung und Technologie e.V. (INP Greifswald) Felix-Hausdorff-Str. 2, D-17489 Greifswald, Germany

Ralf Schneider

Recent address:

Institut für Physik der Ernst-Moritz-Arndt-Universität Greifswald, Felix-Hausdorff-Str. 6, D-17489 Greifswald, Germany

Max-Planck-Institut für Plasmaphysik, Teilinstitut Greifswald, EURATOM Association, Wendelsteinstr. 1, D-17491 Greifswald, Germany

Hans-Erich Wagner

Institut für Physik der Ernst-Moritz-Arndt-Universität Greifswald, Felix-Hausdorff-Str. 6, D-17489 Greifswald, Germany

Contributors

Name	Institute	Sections
Kurt H. Becker	PU Brooklyn ^a	Section 8.3
Ronny Brandenburg	INP Greifswald ^b	Section 8.2.2
Franz X. Bronold	IfP Greifswald ^c	Section 9.2
Paul B. Davies	DoC Cambridge ^d	Section 6.3
Andreas Dinklage	IPP Greifswald ^e	Section 6.4
Kristian Dittmann	IfP Greifswald ^c	Section 9.4
Jörg Ehlbeck	INP Greifswald ^b	Section 8.2.2
Holger Fehske	IfP Greifswald ^c	Section 9.2
Rüdiger Foest	INP Greifswald ^b	Sections 8.2.2 and 8.2.3.4
Mario Hannemann	INP Greifswald ^b	Section 6.1
Hans-Jürgen Hartfuß	IPP Greifswald ^e	Section 6.2
Rainer Hippler	IfP Greifswald ^c	Section 8.4
Holger Kersten	IEAP Kiel ^f	Sections 5 and 8.4
Kirill V. Kozlov	MSU Moscow ^g	Section 8.1.1
Boris P. Lavrov	FoP St.-Petersburg ^h	Section 6.3
Detlef Loffhagen	INP Greifswald ^b	Sections 8.1.3 and 9.1
Jürgen Meichsner	IfP Greifswald ^c	Chapters 1, 10, Sections 3.1 through 3.7, 7.1
Siegfried Müller	INP Greifswald ^b	Sections 8.1.2, 8.1.3, and 8.2.2.2
Andreas Ohl	INP Greifswald ^b	Section 8.2.3.4
Abha Rai	IPP Greifswald ^e	Sections 8.2.4.1.1 and 9.3
Jürgen Röpcke	INP Greifswald ^b	Section 6.3
Antoine Rousseau	LPT Palaiseau Cedex ⁱ	Section 6.3
Martin Schmidt	INP Greifswald ^b	Chapters 1, 6, 10, Sections 3.8, 6.5, 7.3, 8.1, and 8.2
Ralf Schneider	IfP Greifswald ^c	Chapters 1, 4, 10, Sections 8.2.3.1.1, 9.3, and 9.4
†Karsten Schröder	INP Greifswald ^b	Sections 7.2 and 8.2.3.4
Hartmut Steffen	INP Greifswald ^b	Sections 7.2 and 8.2.4.2
Dirk Uhrlandt	INP Greifswald ^b	Section 9.1
Achim von Keudell	RUB Bochum ^j	Chapter 5
Th. von Woedtke	INP Greifswald ^b	Section 8.2.3.5
Hans-Erich Wagner	IfP Greifswald ^c	Chapters 1, 4, 10, Section 6.6

(continued)

(continued)

Name	Institute	Sections
K.-D. Weltmann	INP Greifswald ^b	Section 8.2.3.5
Harm Wulff	IfB Greifswald ^k	Sections 7.3, 7.5, and 8.2.4.2
Rolf-Jürgen Zahn	INP Greifswald ^b	Sections 8.1.2 and 8.2.3.3

^a Polytechnic Institute of New York University, Brooklyn, NY 11201, USA.

^b Leibniz-Institut für Plasmaforschung und Technologie e.V. (INP Greifswald), Felix-Hausdorff-Str. 2, D-17489 Greifswald, Germany.

^c Institut für Physik der Ernst-Moritz-Arndt-Universität Greifswald, Felix-Hausdorff-Str. 6, D-17489 Greifswald, Germany.

^d Department of Chemistry, University of Cambridge, Lensfield Road, Cambridge CB2 1EW, U.K.

^e Max-Planck-Institut für Plasmaphysik, Teilinstitut Greifswald, EURATOM Association, Wendelsteinstr. 1, D-17491 Greifswald, Germany.

^f Institut für Experimentelle und Angewandte Physik der Christian-Albrechts-Universität zu Kiel, Leibnizstr. 19, D-24118 Kiel, Germany.

^g Moscow State University, Department of Chemistry, 119991 Moscow, Russia.

^h Faculty of Physics, St.-Petersburg State University, Ulianovskaya 2, 198904 St.-Petersburg, Russia.

ⁱ Laboratoire de Physique et Technologie des Plasmas, Ecole Polytechnique, Route de Saclay, F-91128 Palaiseau Cedex, France.

^j Ruhr-Universität Bochum, Universitätsstraße 150, D-44801 Bochum, Germany.

^k Institut für Biochemie der Ernst-Moritz-Arndt-Universität Greifswald, Felix-Hausdorff-Str. 4, D-17489 Greifswald, Germany.

† Deceased.

1 Introduction

CONTENTS

1.1	Plasma Chemistry	1
1.2	Historical Notes.....	1
1.3	Thermal and Nonthermal Plasma Chemistry	2
1.4	Specifics of Nonthermal Plasma Chemistry.....	3

1.1 PLASMA CHEMISTRY

The plasma state of matter (also named fourth state) is characterized by the existence of free electrons, positive and negative ions, as well as excited species and radicals in mixture with the other neutrals of gaseous systems (atoms, molecules) or liquids. Well-known examples for natural plasmas are the interstellar matter, stars, the ionosphere, lightnings, and flames.

Plasmas are generated by the input of thermal energy, electric field energy, radiation, or beams (lasers, UV photons, electrons, protons), respectively. The principles of plasma generation are summarized in Figure 1.1. *The focus of the book is on technical plasmas in gaseous systems* that are mostly initiated by applied electric fields. Examples of such electrical gas discharges are the corona and barrier discharge, sparks, arcs, and plasma torches, operating usually at atmospheric pressure. Technically important low-pressure plasmas are the different kinds of glow discharges driven by dc and rf voltages or microwaves.

Gas heating by thermal energy and/or collisions of neutrals with free electrons and photons of sufficiently high energy initiate the production of free radicals and further charged species. The generated particles are the source for various chemical reactions in the volume as well as on the plasma interfaces, forming new compounds, depositing layers, and modifying the properties of materials.

The science and application of chemical conversions in plasmas, including reactive processes at interfaces, is the subject of plasma chemistry.

1.2 HISTORICAL NOTES

The existence of chemical reactions in plasmas, initiated by the input of electrical energy in gaseous atmosphere, is a very old experience of mankind, with even Homer describing the *smell of sulfur** in the *Iliad* in air after lightning.

* Sulfur was later identified as nitrogen oxides.

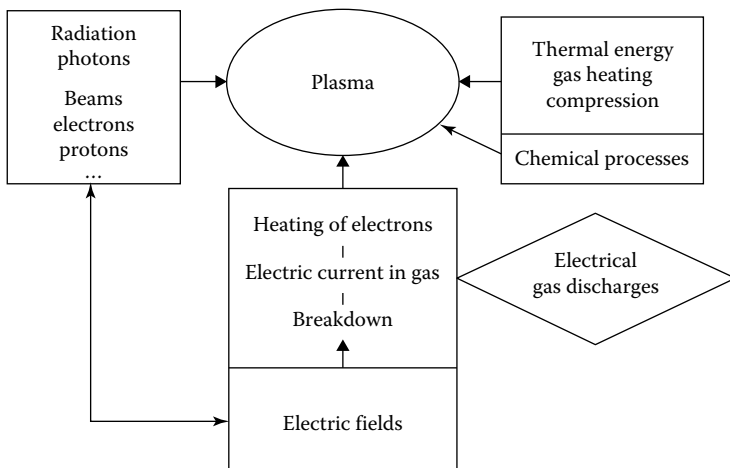


FIGURE 1.1 Principles of plasma generation.

Important historical milestones in the investigation and application of plasma chemical reactions are as follows:

- The synthesis of H_2O in spark discharges operating in H_2/O_2 mixtures (H. Cavendish 1781)
- The fixation of air nitrogen in spark discharges forming NO (H. Cavendish 1784, J. Priestley 1785)
- The discovery and application of the ozonizer (W. v. Siemens 1857)
- The conversion of organic compounds in silent discharges (M. Berthelot 1866)
- The industrial production of nitrogen oxides in the arc discharge (Birkeland-Eyde process 1905)
- The industrial production of acetylene in plasmatrons (Hüls process 1940)

1.3 THERMAL AND NONTHERMAL PLASMA CHEMISTRY

We have to distinguish two kinds of plasma chemical conversions, the thermal as well as the nonthermal plasma chemistry. In the case of *thermal plasma chemistry* the plasmas act primarily as generators of thermal energy. They operate typically in the kW to MW power range. At high temperatures (range 10^3 – 10^4 K) and high specific enthalpies, the chemical compounds are decomposed. This process is called plasma pyrolysis. The chemical reactions take place in/or nearby the thermal equilibrium, characterized by the common temperature (the gas temperature) of all species. The output of reaction products has to be optimized by a quenching procedure and their separation from the gas mixture.

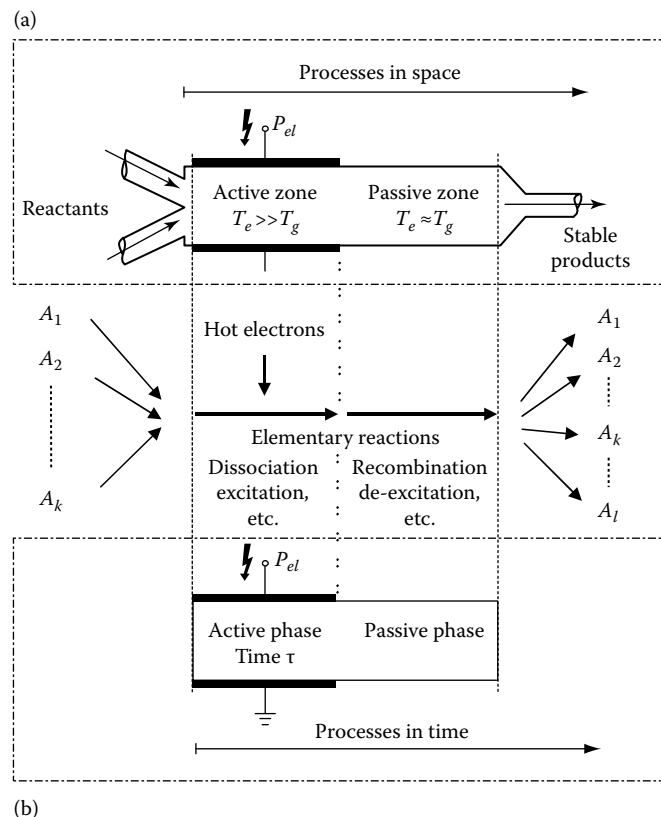


FIGURE 1.2 Operation scheme of a nonthermal plasma chemical flow reactor (a) and of a closed reactor (b), with P_{el} electrical power, T_e kinetic temperature of electrons, and T_g gas temperature.

The subject of this book is the *plasma chemistry in nonthermal plasmas*. In this case, the reaction mixture is far from the thermal equilibrium. The chemical conversions are initiated by the high temperature ($T_e \geq 10^4$ K) of free electrons at relative low gas temperature ($T_g \leq 10^3$ K) (plasma electrical conversion). The processes take place under highly nonequilibrium conditions of all plasma species. Hot electrons, energetic ions, cold excited species, free atoms, and radicals are produced in the so-called active zone (phase) of the different kinds of nonthermal (electrical) gas discharges. In the passive zone (phase), the electrons cool down fast. The unstable plasma components change to stable reaction products by volume and wall reactions. The operation scheme of nonthermal plasma chemical reactors is illustrated in Figure 1.2.

1.4 SPECIFICS OF NONTHERMAL PLASMA CHEMISTRY

Two important advantages of the application of nonthermal plasma chemistry have to be emphasized. First, because of the high electron temperature of 10^4 – 10^5 K

(about 1–10 eV mean energy), reactive processes that require an extremely high activation energy can be realized. Therefore, nearly all plasma chemical processes are practicable, including the synthesis of rare and new products. For example, the effective synthesis of ozone succeeds only under nonthermal plasma conditions. Second, as a result of the relative low gas temperature, there is no thermal dissociation of reaction products and no quenching needed. Connected with this, the thermal stress of the reactor walls as well as of the treated interfaces is minimal. Therefore, thermal-sensitive materials can only be modified under nonthermal plasma conditions. This fact was essentially important for the fabrication of microelectronic elements, and it opens the window for future technical applications, e.g., in plasma medicine.

On the other hand, the selectivity of nonthermal plasma processes, the output, and energetic efficiency of the reaction products is usually small, with the exception of ozone synthesis. Therefore, the applications of nonthermal plasma processing are dominated by reactive plasma-wall processes (modification, etching of targets, thin film deposition, etc.). Important applications are summarized in Figure 1.3.

Nonthermal plasma chemical flow reactors are often operated under low pressure conditions. This requires the installation of an expensive vacuum technique and limits the introduction of plasma processes in technological lines. To overcome these problems, the recent trend worldwide is to develop atmospheric pressure plasma methods. The focus is directed on the application of numerous types of microplasmas.

Nonthermal plasma processes take place under highly nonequilibrium conditions for all species. Therefore, microphysical modeling of the physics and chemistry in nonthermal plasmas requires the knowledge of the energy distribution function of the

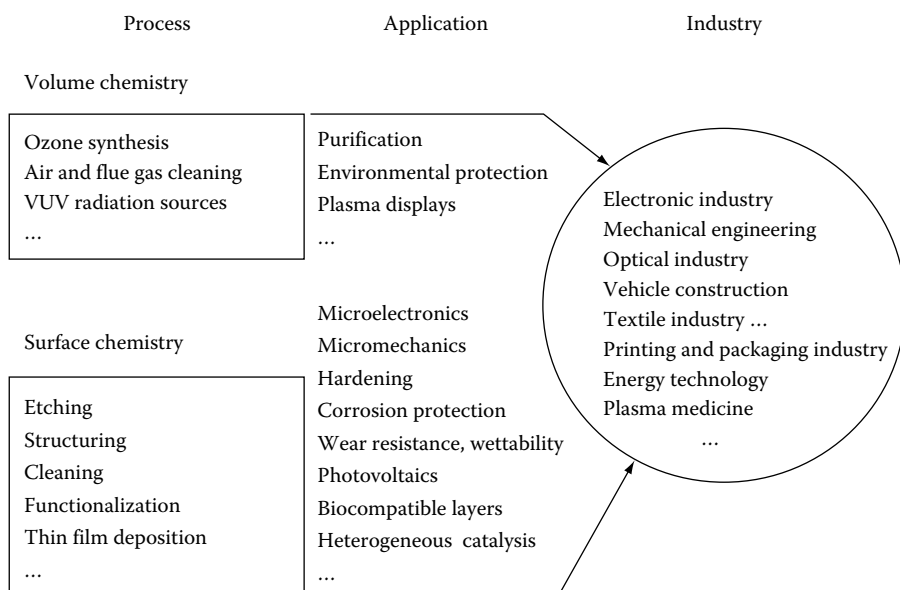


FIGURE 1.3 Important applications of nonthermal plasma chemistry.

electron gas in the active reactor zone. Its simulation has to be solved simultaneously with the complex system of master equations for heavy particles, including the reaction products. The mass action law of the equilibrium chemistry is not applicable. Generally, the solution of this complex problem is a challenge to computational physics.

The realization and optimization of plasma chemical processes starts with the selection of suitable plasma sources. Indispensable are a profound plasma diagnostics and process control. This requires the knowledge of the discharge operation parameters (power input, pressure, flow, gas mixture, etc.) and its interconnection with the most important plasma parameters (gas temperature, electron density, electron energy, electron distribution, etc.) and the plasma chemical process itself (particle densities, mass balance, surface properties, etc.).

To sum up, nonthermal plasma sources of technical relevance, important diagnostic methods, as well as the fundamentals of kinetic modeling of complex plasma processes are presented in this book.

2 Nonthermal Plasma Chemical Processes of General Interest

CONTENTS

2.1	Dry Air, Oxygen, and Nitrogen Plasma Chemistry	7
2.1.1	Ozone Generation.....	8
2.1.2	Plasma Ashing	9
2.2	Plasma Etching	9
2.3	Hydrocarbon Plasma Chemistry	9
2.3.1	Methane Gas Reformation	10
2.3.2	Diamond Deposition.....	12
2.3.3	Origin of Prebiochemical Compounds on Earth	12
2.3.4	Plasma Polymerization	13
2.3.5	Thin Film Deposition of Metal Compounds	13
2.4	Thin Film Silicon Solar Cells	14
2.5	Summary	14

In this chapter, typical topics of general interest are briefly presented, which illustrate the broad spectrum of applications. Dry air plasma chemistry with ozone generation or lacquer stripping and ashing reactions are briefly discussed. Plasma etching presents a key technology in integrated circuit production. Methane gas reformation as well as diamond deposition are important topics of hydrocarbon plasma chemistry. The formation of pre-biochemical compounds is observed in nonthermal plasmas, too. Thin film generation as plasma polymers, of metallic compounds and silicone-based cells are products of plasma chemical processes. Detailed discussions of selected topics are given in Chapter 8.

2.1 DRY AIR, OXYGEN, AND NITROGEN PLASMA CHEMISTRY

The main processes in nonthermal plasmas operating in oxygen, nitrogen, or dry air plasma are dissociative collisions of molecules, resulting in the generation of the reactive atoms (O, N) [1,2], the formation of excited atoms and molecules, as well as positive or negative ions. The formation of negative ions is essential mainly for electronegative gases such as oxygen. The dissociative attachment of electrons of excited O₂ molecules generates negative atomic ions as well as oxygen atoms. The threshold energy of this process is essentially lower than electron impact dissociation and dissociative ionization of ground state molecules [3]. The reaction probability of

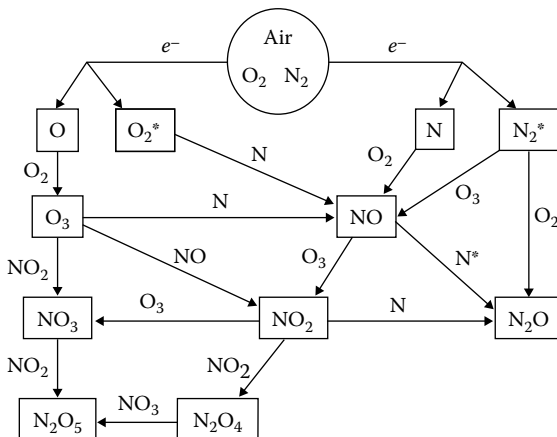


FIGURE 2.1 Diagram of primary chemical reactions in dry air plasma induced by electron impact. (According to Becker, K.H. et al., Air plasma chemistry, in Becker, K.H. et al. (eds), *Non-Equilibrium Air Plasmas at Atmospheric Pressure*, IoP, Bristol, U.K., pp. 124–182, 2005.)

heavy particle reactions of electronically excited species can exceed the probabilities of ground state reactions by orders of magnitude [4,5].

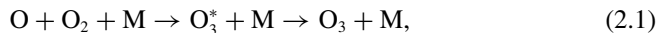
The air plasma chemistry, e.g., is responsible for producing N_xO_y compounds, which have a key role in global environmental problems like acid rain. The scheme in Figure 2.1 of dominant plasma chemical reactions in dry air demonstrates the complexity of the processes [6].

The plasma chemistry in oxygen is also of practical importance, namely, for the ozone generation and for plasma ashing. Augmented combustion is essentially influenced by air plasma chemistry [7].

2.1.1 OZONE GENERATION

Ozone is a powerful oxidizing agent which is non-chlorine alternative applied for water treatment, disinfection, and odor removal. The only economical method for ozone production is by dielectric barrier discharge in atmospheric pressure oxygen or air with its nonthermal plasma. Ozone is the sole substance which is generated in volume processes in nonthermal plasma in industrial dimensions.

Ozone results in three-body collision processes



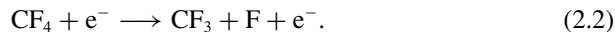
where M is a third collision partner as O_2 , O, also O_3 or N_2 . Oxygen atoms are generated by dissociative electron impact. The ozone formation is reduced by competitive reactions like recombination of two O atoms to O_2 or reactions of O atoms with ozone molecules $O + O_3 + M \rightarrow 2O_2 + M$ [8]. In Section 8.1.1 the ozone synthesis is discussed in more detail.

2.1.2 PLASMA ASHING

The interaction of an oxygen plasma with hydrocarbon compounds leads to CO₂ and H₂O. In microelectronic industry, e.g., the photoresist mask is removed (stripped) by an oxygen plasma. Damage of the semiconductor material by high-energy ions must be avoided by low ion energies and high fluxes of neutral radicals, i.e., oxygen atoms to the resist surface. The low-temperature plasma ashing procedure is used for preparation of samples for electron microscopy [9] and for quantitative analysis of lignite [10]. Oxygen plasmas are applicable to precision cleaning of metallic surfaces contaminated by organic substances such as grease or oil [11]. Hazardous gaseous organic molecules as volatile organic compounds (VOCs) may be destroyed by reactive species like O₂^{*} (a¹D_g), O(¹D), O(³P), H, OH, N₂^{*} (A₃S_u⁺), N₂^{*} (B₃P_g), and N best into CO₂ or H₂O [12].

2.2 PLASMA ETCHING

Plasma etching is the key technology for patterning in every chip production in the microelectronic industry. It enables nonisotropic etching in sub-μm range with significant increasing of packed density of electronic elements in integrated circuits applied in computer production. For this process a nonreactive gas is fed into the plasma where it is activated. The interaction of this activated gas with a solid substrate generates in a chemical reaction a volatile compound which contains atoms of the substrate. Exemplary is the silicon etching by a fluorine compound feed gas as CF₄. The plasma activation leads to generation of fluorine atoms by electron impact dissociation of the CF₄ molecule.



The fluorine atoms react with silicon and produce volatile SiF₄[↑]



The activation energy for desorption of the etch product SiF₄[↑] is transferred from the plasma to the surface by ion bombardment. Because of the existence of fluorocarbon radicals (CF_n) a polymer film is deposited on the silicon surface, also on sidewalls of trenches. The sidewall protection is important for the anisotropy of trench etching with high aspect ratio (ratio depth to width).

Fundamental starting processes of activating the etching gases are the electron–molecule collisions. A critical review of data of electron collision processes for a lot of fluorine and chlorine containing gases is given by Christophorou and Olthoff [13]. An extensive presentation of plasma etching can be found in Section 8.2.1.

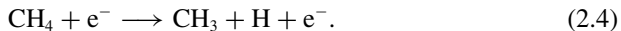
2.3 HYDROCARBON PLASMA CHEMISTRY

Important reaction channels in hydrocarbons are induced by collisions of hot electrons with gaseous molecules in a cold environment. It offers a broad spectrum of applications beyond standard organic chemistry. The spectrum covers from complicated

reactions of the formation of bio-organic compounds in the early earth atmosphere, natural gas reformation, thin polymeric film formation, and creation of higher hydrocarbons to deposition of diamond-like thin films and generation of pure carbon as soot or even diamond.

2.3.1 METHANE GAS REFORMATION

Methane is a dominant part of natural gas. Other sources are petroleum processing off-gas and biogas. It is an important energy carrier and initial compound of chemical industry but also a dangerous greenhouse gas. Electron impact dissociation leads to CH_3 radicals and H atoms [14]



Another pathway is the reaction of this molecule with hydrogen atoms (also generated by electron impact processes) [17]



The abstraction of further H atoms leading to CH_2 , CH , and C is possible by H atoms but also by electron collisions, especially in pure methane plasmas. The reverse reaction, the addition of H atom to CH_3 to form CH_4 occurs at low temperature [18]. H atoms may be generated by dissociative electron collisions of H_2 molecules; at higher gas temperatures thermal dissociation of hydrogen molecules becomes dominant as studied in thermal plasma chemistry. Here, some processes may be more effective, but the specific production sensitivity of nonthermal plasma chemistry is lost due to generation of new compounds in a cold gaseous environment.

A reaction scheme is presented in Figure 2.2 for dissociative electron collisions with CH_4 and H_2 molecules [15] as well as for the formation of CH_x and C_2H_y compounds controlled by collisions of hydrocarbon molecules with H atoms [16]. Concerning the variety of the processes in a H_2 – CH_4 plasma, including the electron impact-induced reactions, see also [15].

The principle process scheme (see Figure 2.2) shows the formation of ethane, ethylene, and acetylene. An investigation of methane conversion in a pulsed microwave discharge ($p = 30$ mbar) yields a selectivity of acetylene generation near 70% with an energy input of 10 eV/molecule. Here the methane dissociation is initiated by electron impact. The generated H atoms provide the source for further H atom abstraction from the methane molecule [19].

The conversion of a CH_4/CO_2 mixture into higher hydrocarbons or syngas (CO/H_2) in a hybrid catalytic plasma reactor is reviewed by Istadi [20]. The chemical reactions are initiated by electron impact dissociation of CO_2 and CH_4 generating CO and O as well as CH_3 and H, respectively. An important research topic is the direct conversion of methane and carbon dioxide to methanol [21,22]. The investigation of the reaction products of methane– CO_2 mixture in an atmospheric pressure dielectric barrier discharge shows a small concentration of methanol, but a lot of other pure

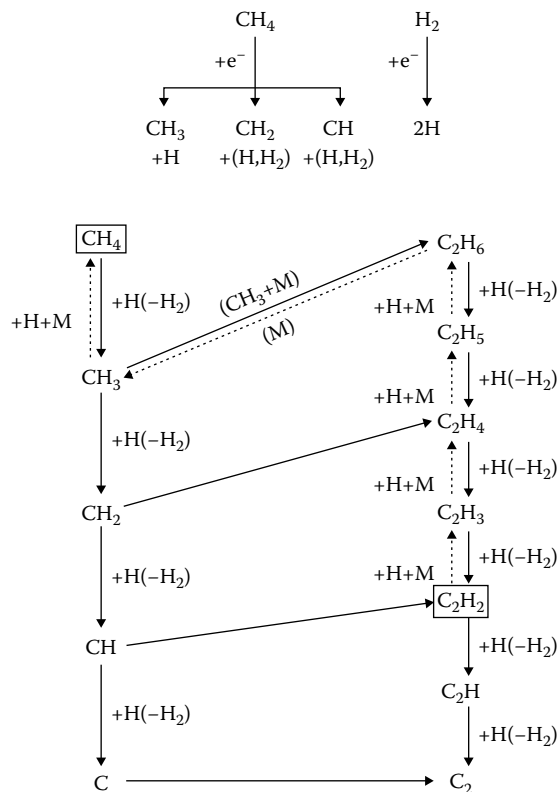
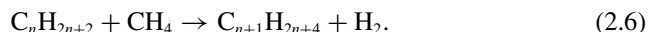


FIGURE 2.2 Reaction schemes for the electron collision of CH_4 induced CH_3 , CH_4 , and CH formation. (According to Röpcke, J. et al., *J. Phys. D: Appl. Phys.*, 34, 2336, 2001.) H_2 dissociation and of the transformation of C_1H_x and C_2H_y species by reactions with H atoms in diamond plasma CVD. (According to Ma, J. et al., Exploration of the gas phase chemistry in microwave activated diamond depositing plasmas by laser spectroscopy, in *ISPC 2007 Peking CD*, ISPC, Peaking University, Beijing, China, 2007.) M indicates the action of the wall.

and oxygenated hydrocarbons. A carbon chain growth is supposed to occur mainly by the reaction



According to the practical application an essential problem is the bad selectivity of the plasma process [22,23]. Products of the methane conversion include syngas, gaseous products as ethylene, acetylene, and propylene, liquid hydrocarbons, plasma polymers, and oxygenates. The complexity of hydrocarbon plasmas is demonstrated in [24] by review of plasma chemical reactions in low-pressure acetylene plasmas.

A spectacular example of application of nonequilibrium plasma chemistry is the deposition of diamond films.

2.3.2 DIAMOND DEPOSITION

Plasma-assisted chemical vapor deposition enables the formation of diamond at moderate temperature and low pressure with hydrocarbons as starting compounds on non-diamond substrates. This allows the extended industrial use of the outstanding properties of the diamond, such as extreme hardness, high thermal conductivity, broad optical transparency (deep UV to far IR), and wide band gap (5.4 eV). In gas phase chemistry of a CH₄/H₂ plasma the CH₄ molecule is activated which leads to carbon deposition with sp³ (diamond) or sp² (graphite) bonding. The hydrogen atoms generated in the plasma etch the deposited carbon producing volatile compounds CH_n ($n = 1 - 4$). Because the approximately 100 times higher etch rate of graphite [25] diamond remains on the substrate.

For the diamond synthesis the principle growth species are CH₃, C₂, and H [26]. In the conventional H₂ rich plasma in H₂/CH₄ mixtures the CH₃ radical is responsible for the diamond growth. In plasmas with lower H₂ concentration, as in Ar/H₂/CH₄ gas mixtures C₂ controls the diamond deposition.

The radicals C₂, CH, H, CH₃ are observed by tunable infrared diode laser absorption and emission spectroscopy, respectively [16,27].

The impact of the H atoms is manifold for the diamond deposition process. Besides the already mentioned etching of the graphite phase and the importance for CH₃ generation the H atoms act with bonded hydrogen and create reactive sites for the reaction of CH₃ radicals and serve for the addition of a C atom into the diamond lattice [26].

Hot filament chemical vapor deposition process and microwave plasma CVD with low or higher energy input were the most successfully applied methods for diamond deposition [25]. High substrate temperatures (typically >700°C) ensure good diamond quality. For various industrially important applications such as deposition on microelectronic substrates lower substrate temperatures are necessary. The decrease of the deposition rate with decreasing substrate temperature could be compensated using other starting gases such as halogenated compounds like C₂H₅Cl [28] or CO [29] and CO₂ [30] with H₂ admixtures.

The deposition of well-ordered nanostructures as nanotips and nanotubes, nanowalls, graphene, and ultra nanocrystalline diamond is also observed under plasma conditions using as source material mixtures of carbon-carrier gases such as hydrocarbons, fluorocarbons, etc. [31–35]. Fullerenes are generated successfully in thermal plasmas [31].

A more detailed discussion of the plasma-assisted deposition of a-CH films, diamond and erosion of graphite by H atoms is given in Section 8.2.4.1.1.

2.3.3 ORIGIN OF PREBIOCHEMICAL COMPOUNDS ON EARTH

One exciting and still not resolved question is the origin and the development of life on earth. The first step may be the formation of organic molecules, e.g., amino acids. Miller [36] investigated spark discharges in a mixture of methane, ammonia, hydrogen, water vapor, and liquid water. In particular, under the action of UV radiation the formation of various organic compounds were observed, e.g., hydrogen cyanide, amines, aldehydes, acrylonitrile. In the aqueous solution, amino acids were formed.

The products in the gas phase were generated by reactions between free radicals and ions.

The state of the early earth atmosphere is discussed by Abelson [37]. An N₂–CO–H₂ atmosphere is supposed and HCN and H₂O were the principal products of a gas discharge, beside small amounts of CO₂ and CH₄. HCN in aqueous solution can lead to other organic compounds.

Also the plasma chemistry in CH₂–H₂S [38] and CH₄–PH₃ [39] atmospheres is studied to detect prebiochemical substances.

These experiments show the formation of organic compounds in plasma chemical experiments, but the further reaction steps in the direction of formation of living structures are largely speculative.

2.3.4 PLASMA POLYMERIZATION

Plasma polymerization is a process of thin film deposition on electrodes, walls, or substrates under the action of plasmas in an organic molecules containing atmosphere.

The term “polymerization” is misleading because this product is not a polymer consisting of equal components. Plasma polymer films consist of highly cross-linked, brittle material with good dielectric properties. They are pinhole-free, have low solubility, pronounced chemical inertness, and good adhesion to the surface. A broad spectrum of organic compounds such as hydrocarbons, fluorocarbon, and silicon organics was applied for plasma polymerization. In contrary to chemical polymerization these starting compounds in the feed gas can be free of double or multiple bonds or cyclic structures. The starting gas is activated in the plasma by electron collisions or by collisions with other energetic plasma components as H atoms. Ionic or neutral radicals are created. The target surface is activated by ion bombardment. The radicals diffuse (neutral) or drift (ionic) to the surface where they are bonded to the surface. The starting material can also move directly to the surface where a plasma-induced polymerization is possible.

Section 8.2.4.1.2 gives more detailed information on plasma polymerization.

2.3.5 THIN FILM DEPOSITION OF METAL COMPOUNDS

A method of thin film deposition of simple metal compounds (e.g., oxides, nitrides) is the plasma-enhanced chemical vapor deposition with metal organic starting gases. The advantage of this method is the low substrate temperature and is therefore useful for deposition on temperature sensitive materials [40]. A study of deposition of TiN using Tetrakis(diethylamine)titanium (TDEAT) shows the importance of H-radicals in the H₂ plasma for the stripping of TDEAT. The formation of TiN requires N₂ addition to the process [41].

The deposition of thin films of pure metals or simple metal compounds is possible by sputtering in low-pressure discharges inert gas. An example of reactive sputtering is the deposition of TiN films. The nitride formation is a surface process of the freshly deposited Ti with plasma-activated nitrogen.

Plasma-enhanced atomic layer deposition (PEALD) of metals or metallic compounds is based on a sequential use of self-terminating plasma-enhanced gas solid

reactions which leads to a coverage of the target surface by monolayer films with good conformality [42].

2.4 THIN FILM SILICON SOLAR CELLS

The development of alternative energy sources to adverse fossil fuels is an important task for science and technology in the twenty first century. Photovoltaic is a promising candidate in future renewable energy technology. Thin Si-films are expected to be successful material for effective solar cells [43,44]. Beside other methods plasma-enhanced chemical vapor deposition is widely used for generation of amorphous silicon (a-Si:H) and microcrystalline (μ c-Si:H) films. Feed gas for plasma-assisted silicon deposition is mainly pure monosilane SiH_4 or SiH_4/H_2 mixtures. Inside the plasma silane is dissociated by electron impact into SiH_3 , SiH_2 , SiH , Si , H_2 and H , and H_2 in H atoms. Also SiH_x^+ , SiH_x^- , and H_x^+ ions are generated. Secondary ion molecule reactions and reactions between neutral species also have to be taken into account, too. Data on silane plasma chemistry are reviewed in [45].

SiH_3 reaching the surface reacts to SiH_4 with bonded hydrogen atoms and generates dangling bonds or recombines with another SiH_3 to Si_2H_6 . SiH_4 and Si_2H_6 are desorbed from the surface. The formation of a Si–Si bond occurs by reaction of SiH_3 radicals with dangling bonds, the Si film is growing [43]. The low-temperature plasma-enhanced deposition process (150°C–300°C) enables the deposition on temperature-sensitive substrates as polymer foils. The fabrication of homogenous large-area a-Si:H films with high deposition rate is important for applications from an economical viewpoint. Parallel plate rf-reactors operating at 13.56 MHz are usually used. Deposition rates of 0.2–0.3 nm/s are observed. Rates of 2 nm/s were achieved by higher operating frequency (70 MHz). The deposition rate of μ c-Si:H could be increased by application of a narrow gap discharge at higher pressures [46].

2.5 SUMMARY

Selected examples of the various possibilities of plasma chemical processes were presented. Most applications concern surface processes, such as thin film deposition, etching, and cleaning. Only one volume process for the generation of larger amounts of material has reached technical maturity and commercial importance, the ozone synthesis. Some processes and procedures are specific for plasma processing. Examples are the micropatterning in microelectronics, or the deposition of plasma polymers on various substrates.

The aim of future technical developments must be to enhance the selectivity and energy efficiency of plasma chemical processes, and research may lead to new materials with exciting properties.

3 Physics of Nonthermal Plasmas

CONTENTS

3.1	Basic Concepts of Plasma Physics	17
3.1.1	Introduction and Basic Items	17
3.1.1.1	Classification of Plasmas Concerning Their Energy Content	17
3.1.1.2	Ionization Degree	19
3.1.1.3	Quasi-Neutrality and Debye Shielding	19
3.1.2	Debye Shielding Length	20
3.1.3	Plasma Frequency.....	22
3.1.4	High-Frequency Conductivity and Permittivity of Plasmas	24
3.1.5	Ambipolar Diffusion of Charged Particles	27
3.1.6	Motion of Charged Single Particle in Homogeneous Magnetic Field	29
3.1.6.1	Cyclotron Motion	29
3.1.6.2	Drift Velocity Perpendicular to the Magnetic Field due to Additional External Forces	31
3.1.6.3	Influence of Collisions on Charged Particle Transport in Magnetized Plasmas	33
3.2	Thermal and Nonthermal Plasmas	33
3.2.1	Plasma in Thermodynamic Equilibrium	33
3.2.1.1	Complete Thermodynamic Equilibrium	33
3.2.1.2	Local Thermodynamic Equilibrium.....	35
3.2.2	Nonequilibrium Plasmas	36
3.3	Elementary Collision Processes and Cross Sections	38
3.3.1	Introduction and Overview	38
3.3.1.1	Dynamics of Elastic and Inelastic Collisions	39
3.3.2	Collision Processes in Nonthermal Plasmas and Their Classification	42
3.3.3	Collision Cross Section	48
3.3.3.1	Gas Kinetic Cross Section	48
3.3.3.2	Polarization Cross Section.....	49
3.3.3.3	Coulomb Scattering	53
3.3.3.4	Electron Attachment Cross Section	55
3.3.3.5	Electron Impact Excitation and Ionization Cross Section.....	55
3.3.3.6	Cross Section of the Neutral–Neutral Reaction at Thermal Velocity with Threshold Energy	59

3.4	Plasma Kinetics	60
3.4.1	The Boltzmann Equation	60
3.4.2	Electron Energy Distribution Function in Nonthermal Plasmas	62
3.5	Averaged Quantities, Transport Equations, and Rate Coefficients	64
3.5.1	Weighted Average of Physical Quantities	64
3.5.2	Macroscopic Transport Equations	65
3.5.3	Analytical Calculation of Rate Coefficients and Collision Frequencies	68
3.5.3.1	Gas Kinetic Neutral–Neutral Collision Frequency and Mean Free Path Length	68
3.5.3.2	Rate Coefficient for Ion–Molecule Reactions with the Langevin Capture Cross Section	69
3.5.3.3	Rate Coefficient for Neutral–Neutral Reactions with Threshold Energy	69
3.5.4	Rate Coefficient for Electron Impact Ionization	70
3.5.5	Rate Coefficient of Three-Particle Collisions	72
3.5.6	Reaction Rate Coefficient of Chemical Reactions	73
3.5.7	Order of Chemical Reactions	74
3.6	Boundary Plasma-Surface, Plasma Sheaths	76
3.6.1	Stationary Plasma Sheath and Bohm Sheath Criterion	77
3.6.1.1	Generalized Bohm Sheath Criterion	80
3.6.1.2	Plasma Sheath in Electronegative Gases	80
3.6.1.3	Multi-Species Plasmas	81
3.6.1.4	Plasma Sheath in Front of the Floating Surface	82
3.6.2	High-Voltage Plasma Sheaths	82
3.6.2.1	Matrix Sheath	83
3.6.2.2	Child–Langmuir Sheath	83
3.6.2.3	Plasma Sheath with Ion Collisions	84
3.6.2.4	Ion Energy Distribution at the Surface	86
3.6.3	Nonstationary Plasma Sheaths	86
3.6.3.1	Collisionless Sheath in Capacitively Coupled RF Plasma ($e \cdot \Delta\phi_{sh} \gg k_B \cdot T_e$)	87
3.6.3.2	Strongly Asymmetric Capacitively Coupled RF Plasma	89
3.7	Nonthermal Plasmas of Electric Gas Discharges	91
3.7.1	Introduction and Overview	91
3.7.2	Electric Breakdown in Gases and Townsend Discharge	93
3.7.2.1	Townsend Discharge	98
3.7.3	Glow Discharges	100
3.7.3.1	Transition from the Townsend Discharge to the Glow Discharge	100
3.7.3.2	Glow Discharges	101
3.7.3.3	Cathode Sheath and Negative Glow in Strongly Anomalous Glow Discharges	102
3.7.3.4	Stable Positive Column	105
3.7.4	Arc Discharges	107

3.7.5	High Voltage Breakdown at Atmospheric Pressure, Corona and Barrier Discharge	107
3.7.5.1	Barrier Discharge	109
3.7.6	Glow Discharges at Alternating Electric Field, RF and Microwave Plasmas	110
3.7.6.1	Heating of Electrons in the Bulk Plasma by the High-Frequency Electric Field	112
3.7.6.2	Radio Frequency Plasmas	113
3.8	Technical Plasma Sources	115
3.8.1	Introduction	115
3.8.2	Plasma Generation by Electric Fields.....	115
3.8.3	Low-Pressure Plasma	116
3.8.4	Direct Current Discharges.....	116
3.8.5	Radio Frequency Discharges	117
3.8.6	Capacitively Coupled Discharges	118
3.8.7	Inductively Coupled Discharges	120
3.8.8	Microwave Discharges	121
3.8.9	Atmospheric Pressure Discharges.....	125
3.8.10	Dielectric Barrier Discharge.....	125
3.8.11	Microdischarge.....	128
3.8.12	Cold Plasma Jets	130
3.8.13	Beam-Generated Plasmas	132
3.8.14	Properties of Plasma Sources for Plasma Chemistry	133
3.8.15	Conclusions	135

3.1 BASIC CONCEPTS OF PLASMA PHYSICS

3.1.1 INTRODUCTION AND BASIC ITEMS

The name *plasma* defines a quasi-neutral many-particle system (total charge zero) consisting of sufficient high concentration of free positive (q_+) and negative (q_-) charged species, e.g., positive ions, negative ions, and electrons. The system may contain additionally neutral atoms, molecules, radicals, and excited species. The classical plasma is characterized by higher mean kinetic energy of electrons or other plasma species (1– 10^5 eV) compared to usual matter, and exceptional electromagnetic phenomena like the shielding of the far-ranging Coulomb interaction and collective oscillations of the electron or ion ensemble. Due to the presence of free charged particles the plasma is electrically conductive. Furthermore, plasmas reveal nonlinear behavior and have specific dielectric properties, and in interaction of charged plasma particles with an external magnetic field the plasma shows an anisotropic behavior concerning the charged particle transport and electromagnetic wave propagation.

3.1.1.1 Classification of Plasmas Concerning Their Energy Content

The plasma state of matter in astrophysics, terrestrial environment, and under artificial conditions in laboratory stretches over wide ranges in electron concentration and mean kinetic energy or temperature of charged species. Therefore, the plasma

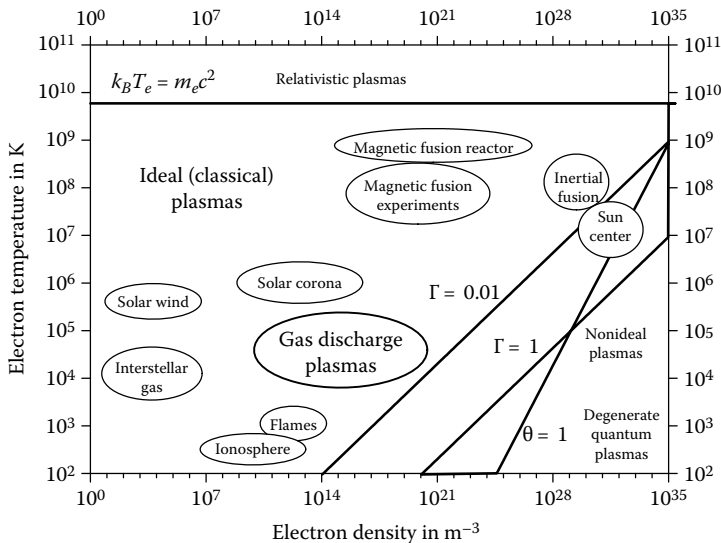


FIGURE 3.1 Temperature–density plot of the plasma world. (With courtesy to A. Könies.)

state is classified with respect to their energy content and physical-based collective interactions of the charged particles into

- Ideal or classical plasmas
- Nonideal and degenerate plasmas
- Relativistic plasmas

Whereas *relativistic plasmas* are characterized by the mean electron energy $k_B \cdot T_e > 0.5 \text{ MeV}$ which corresponds to the electron rest mass, the *ideal plasmas* are defined for the case that the mean translational energy exceeds the electrostatic interaction energy between two charged species (e.g., positive ion with charge number z and electron, Figure 3.1). By use of the coupling parameter (Γ) the ideal (classical) plasmas are distinguished from nonideal plasmas

$$\Gamma = \frac{z \cdot e^2}{4\pi\epsilon_0 \langle r \rangle k_B T_e} \approx 2 \cdot 10^{-5} \frac{z \cdot n_e^{1/3} [\text{m}^{-3}]}{T_e [\text{K}]}, \quad (3.1)$$

where

- $\Gamma \ll 1$ (ideal plasma), $\Gamma < 1$ (weakly ideal plasma)
- $\Gamma > 1$ (strongly nonideal plasma)
- $\langle r \rangle \propto n_e^{-1/3}$ is the mean particle distance
- n_e is the electron density
- z is the ion charge number

In the special case that the mean particle distance is lower than the thermal *de Broglie wave length* the quantum effects have to be considered in the field of nonideal

plasmas, and the quantum or degenerate plasmas have to be distinguished. The degenerate quantum plasma is defined if the Fermi energy exceeds the translational energy of the electrons according to the degeneration parameter $\Theta > 1$

$$\Theta = \frac{h^2}{2 \cdot m_e \cdot k_B \cdot T_e} \cdot \left(\frac{3 \cdot n}{8 \cdot \pi} \right)^{2/3} \approx 4 \cdot 10^{-15} \cdot \frac{n^{2/3} [\text{m}^{-3}]}{T_e [\text{K}]} . \quad (3.2)$$

The dense or strongly nonideal plasmas are observed in astrophysics, e.g., in the white dwarfs or warm dense matter in giant planets and in laboratory due to the interaction of high-intense laser pulse with solids as well as in semiconductors as electron-hole plasma.

The *ideal* or *classical plasmas* are defined when the translational energy of charged particles is the dominant energy ($\Gamma \ll 1$) like in the ideal gas approximation. Within the region of ideal plasmas the *nonequilibrium* and *nonthermal plasmas*, respectively, of electric gas discharges will be the focus and of interest.

3.1.1.2 Ionization Degree

The degree of ionization χ gives information about the content of charged particles in relation to the total particle concentrations. In the simplest case, considering the plasma of single charged positive ions, electrons, and neutrals, the *degree of ionization* χ is defined as

$$\chi = \frac{n_e}{n_e + n_n}, \quad (3.3)$$

where n_e, n_n are the particle concentrations of electrons and neutrals.

The degree of ionization in plasmas observed in nature and laboratory varies over a wide range between 10^{-8} and 1. From that point of view two important types of plasmas can be distinguished:

1. Partially or weakly ionized plasmas with $\chi \ll 1$
2. Completely or strongly ionized plasmas with $\chi \sim 1$

The considered *nonthermal plasmas* are exclusively associated to partially or weakly ionized plasmas ($n_e \ll n_n$) with ionization degrees of $\chi \approx n_e/n_n = 10^{-4}-10^{-6}$.

3.1.1.3 Quasi-Neutrality and Debye Shielding

The demand of quasi-neutrality (3.4) in plasmas has to be fulfilled over the *macroscopic length scale* L of plasma dimension

$$q_+ - q_- = \sum_z z \cdot e \cdot n_{z+} - e \cdot n_e - e \cdot n_- = 0 \quad \text{for } L > \lambda_D, \quad (3.4)$$

where

z is the charge number of positive ions

n_{z+}, n_-, n_e are the particle concentrations of positive ions with charge number z , single charged negative ions and electrons

The electromagnetic interaction between charged species in the plasma and their response to internal and external impacts lead to following deviations from the quasi-neutrality:

1. Debye shielding (charge shielding length): On the microscopic scale the statistical deviations from the quasi-neutrality in the electron and ion ensemble result in the shielding of the far-ranging Coulomb interaction over a characteristic length scale, the Debye length λ_D , see Section 3.1.2. In other words, within regions with a dimension smaller than the Debye length the quasi-neutrality is fulfilled time-averaged, only. Therefore, the plasma is defined if the deviation from the quasi-neutrality in relation to the characteristic length scales L of the plasma dimension is in the limit:

$$\frac{|q_+ - q_-|}{q_+} \leq \frac{\lambda_D}{L}. \quad (3.5)$$

2. Polarization drift: Deviations from the quasi-neutrality are also observed during the interaction of the plasma particles with fast fluctuating external electric fields due to the *polarization drift* of charged species. In particular, the electrons are shifted out of the mean equilibrium position because of their lower inertia in respect to the heavy positive ions, see Section 3.1.4.
3. Ambipolar diffusion: In spatially inhomogeneous plasmas with plasma density gradients over the length scale $L \gg \lambda_D$ space charges are generated due to higher mobility and diffusion coefficient of electrons against the heavy ions. The transport of positive ions and electrons is determined by the ambipolar electric field and described by the ambipolar diffusion coefficient, see Section 3.1.5.
4. Plasma boundary sheath: Plasmas in contact to condensed matter such as discharge electrodes, surrounding solid walls or liquids, immersed probes for plasma diagnostics and materials for surface processing are characterized by a transition between the quasi-neutral plasma bulk and the interface to the condensed matter: the *plasma boundary sheath or plasma sheath*. The electric potential and the charge of the interface are shielded against the plasma potential due to the self-consistent electric field of macroscopic space charges in the plasma sheath, i.e., an electric double layer is formed, see Section 3.6.

3.1.2 DEBYE SHIELDING LENGTH

Considering the plasma as a continuum, the plasma can be described by macroscopic quantities. In that way the *Debye shielding length* can be calculated by taking into account the polarization effect around a selected positive and negative charged particle as reference point, respectively. The distribution of electrons (n_e), respectively, positive ions with state of charge z around the reference point is given by the Boltzmann distribution with electron temperature (T_e) and ion temperature (T_+), respectively:

$$n_e(r) = n_{e0} \cdot \exp\left(\frac{e \cdot \varphi(r)}{k_B \cdot T_e}\right), \quad (3.6)$$

$$n_e(r) = n_{+0} \cdot \exp\left(\frac{-z \cdot e \cdot \varphi(r)}{k_B \cdot T_+}\right), \quad (3.7)$$

where

$n_{e0} = n_{+0}$ is the charged particle concentration without polarization
 $\varphi(r)$ is the macroscopic electric potential

By use of the space charge density ρ and the linear approximation of the exponential function for the condition $e \cdot \varphi / k_B \cdot T_{e,+} \ll 1$, the Poisson equation (3.8) can be solved in spherical symmetry.

$$\varepsilon_0 \cdot \nabla_r^2 \varphi(r) = -\varrho = e \cdot (n_e - z \cdot n_+) \approx \frac{e^2 \cdot n_{e0}}{k_B} \cdot \left(\frac{1 + z \cdot T_e / T_+}{T_e} \right) \cdot \varphi(r). \quad (3.8)$$

The result is the well-known Debye–Hueckel potential with characteristic length parameter, the Debye length λ_D , for the shielding of the Coulomb potential, see Figure 3.2 and (3.9)–(3.11).

$$\varphi(r) = \frac{z \cdot e}{4\pi \cdot \varepsilon_0} \cdot \frac{1}{r} \cdot \exp\left(\frac{-r}{\lambda_D}\right), \quad (3.9)$$

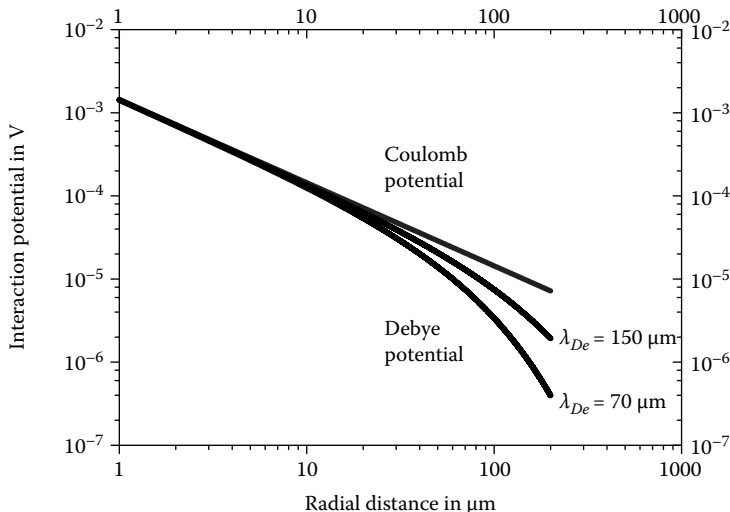


FIGURE 3.2 Coulomb potential in comparison with the Debye shielding potential $\varphi(r)$, see (3.9), for two selected electron Debye lengths λ_{De} , see (3.12).

$$\lambda_D = \left(\frac{\varepsilon_0 \cdot k_B \cdot T_e}{e^2 \cdot n_{e0} \cdot \left(1 + \frac{z \cdot T_e}{T_+} \right)} \right)^{1/2}, \quad (3.10)$$

$$1/\lambda_D^2 = 1/\lambda_{De}^2 + 1/\lambda_{D+}^2. \quad (3.11)$$

In the case of *nonthermal plasmas* ($T_e \gg T_+$) the positive ion ensemble may be assumed as static background, and the electron Debye length λ_{De} is applied

$$\lambda_{De} = \left(\frac{\varepsilon_0 \cdot k_B \cdot T_e}{e^2 \cdot n_{e0}} \right)^{1/2} \quad (3.12)$$

$$\lambda_{De} [\mu\text{m}] = 6.9 \cdot 10^4 \left(\frac{T_e [\text{K}]}{n_{e0} [\text{cm}^{-3}]} \right)^{1/2}. \quad (3.13)$$

In laboratory plasmas the Debye length scales typically in the range of between 10 and 200 μm .

Taking into consideration the total number of electrons N_e in a sphere with radius of the Debye length, it follows

$$N_e = \frac{4}{3} \cdot \pi \cdot \lambda_{De}^3 \cdot n_e. \quad (3.14)$$

The used description of plasmas by means of averaged and macroscopic quantities with dominance of the translational energy of the electrons is only valid in case of large number of electrons within the Debye sphere, which corresponds with the classification of an ideal plasma, according to

$$\lambda_{De}^3 \cdot n_e \gg 1. \quad (3.15)$$

Furthermore, the Debye length is an important scaling parameter for the plasma boundary sheath thickness, see Section 3.6.

3.1.3 PLASMA FREQUENCY

The temporal deviation from the quasineutrality in nonthermal plasmas is mainly determined by the oscillation frequency of the electron ensemble—the *electron plasma frequency* ω_{pe} . The collective shift of the plasma electrons out of their equilibrium position relative to the positive ion leads to the formation of macroscopic space charges. The resulting electric space charge field initiates an opposite electron movement and vice versa: The electron ensemble performs collective oscillations. Considering the plasma as a continuum again the frequency of electron oscillations can be calculated by the

$$\text{Equation of motion} \quad m_e \cdot \frac{d\vec{v}}{dt} = -e \cdot \vec{E} \quad (3.16)$$

$$\text{Source equation} \quad \text{div} \vec{E} = \frac{\rho}{\varepsilon_0} \quad (3.17)$$

$$\text{Particle balance equation} \quad \frac{\partial \rho}{\partial t} + \text{div} \vec{j}_e = 0 \quad (3.18)$$

$$\text{Electron current density} \quad \vec{j}_e = -e \cdot n_e \cdot \vec{v} \quad (3.19)$$

The calculation of the divergence of (3.16) and its time derivative results in

$$\text{div} \left(m_e \cdot \frac{d\vec{v}}{dt} \right) = -e \cdot \text{div} \vec{E} = -e \cdot \frac{\varrho}{\epsilon_0} \quad (3.20)$$

and

$$m_e \cdot \frac{\partial^2}{\partial t^2} (\text{div} \vec{v}) = -\frac{e}{\epsilon_0} \cdot \frac{\partial \varrho}{\partial t} = \frac{e}{\epsilon_0} \cdot \text{div} \vec{j}_e = -\frac{e^2 \cdot n_e}{\epsilon_0} (\text{div} \vec{v}), \quad (3.21)$$

respectively. With the replacement of the scalar velocity source term by $\text{div} \vec{v} = \delta$ in (3.21) it follows

$$\frac{\partial^2 \delta}{\partial t^2} + \frac{e^2 \cdot n_e}{m_e \cdot \epsilon_0} \cdot \delta = 0. \quad (3.22)$$

This expression represents the differential equation of the free undamped harmonic oscillator with a solution

$$\delta(t) = \delta_0 \cdot \exp [-i \cdot (\omega_{pe} \cdot t + \varphi_0)] \quad (3.23)$$

and the electron plasma frequency

$$\omega_{pe}^2 = \frac{e^2 \cdot n_e}{m_e \cdot \epsilon_0} \quad (3.24)$$

$$\omega_{pe} [\text{GHz}] = 5.64 \cdot 10^{-8} \cdot (n_e [\text{m}^{-3}])^{1/2}. \quad (3.25)$$

In a similar procedure the ion plasma frequency ω_{p+} of the collective oscillation of positive ions with charge number z can be found according to

$$\omega_{p+}^2 = \frac{e^2 \cdot z^2 \cdot n_+}{m_+ \cdot \epsilon_0} \quad (3.26)$$

$$\omega_{p+} [\text{MHz}] = 1.32 \cdot 10^{-6} \cdot z \cdot \left(\frac{n_+ [\text{m}^{-3}]}{A_+[u]} \right)^{1/2}, \quad (3.27)$$

where $A_+[u]$ is the ion mass in unified atomic mass units with $1u = 1.66538921(73) \cdot 10^{-27} \text{ kg}$. It follows for the ratio between both plasma frequencies

$$\frac{\omega_{pe}}{\omega_{p+}} = \frac{1}{z} \cdot \sqrt{\frac{m_+}{m_e}} \approx 10^2. \quad (3.28)$$

For example, the electron plasma frequency of a *weakly ionized low-pressure plasma* with an electron density $n_e = 10^{16} \text{ m}^{-3}$ is about $\omega_{pe} \sim 5.64 \text{ GHz}$ (microwave range), whereas the ion plasma frequency for Ar^+ ions ($u=40$) has a much lower value of about $\omega_{p+} \sim 20.9 \text{ MHz}$ (radio frequency range).

3.1.4 HIGH-FREQUENCY CONDUCTIVITY AND PERMITTIVITY OF PLASMAS

In this section the forced oscillation of electrons in a high frequency harmonic electric field $E(t) = E_0 \cdot \exp(-i\omega t)$ is described to understand the basic physics concerning the electric conductivity and electromagnetic wave propagation in ideal and cold plasmas without external magnetic field. Concerning the behavior of the electrons in interaction with high-frequency electric field of an electromagnetic wave, the quasi-homogeneous field approximation is used. That means the amplitude of electron oscillation is small compared with the wavelength [1]. Taking into calculation the electric field force and the Langevin term for considering the elastic collisions of electrons with neutrals by use of the mean collision frequency ν_e , the 1D equation of motion in z -direction for the electrons can be written as

$$m_e \cdot \frac{dv_{ez}}{dt} = -e \cdot E_0 \cdot \exp(-i\omega t) - m_e \cdot \nu_e \cdot v_{ez}. \quad (3.29)$$

The integration of (3.29) provides the complex solutions for the electron velocity $v_{ez}(t)$

$$v_{ez}(t) = \frac{-e \cdot (\nu_e + i\omega)}{m_e \cdot (\omega^2 + \nu_e^2)} \cdot E_0 \cdot \exp(-i\omega t) \quad (3.30)$$

and the corresponding electron shift z

$$z(t) = \frac{e \cdot (\omega - i\nu_e)}{m_e \cdot \omega \cdot (\omega^2 + \nu_e^2)} \cdot E_0 \cdot \exp(-i\omega t). \quad (3.31)$$

Following, the electron current density j_{ez} is expressed by

$$j_{ez} = -e \cdot n_e \cdot v_{ez} = \frac{n_e \cdot e^2 \cdot (\nu_e + i\omega)}{m_e \cdot (\omega^2 + \nu_e^2)} \cdot E_0 \cdot \exp(-i\omega t). \quad (3.32)$$

Using the electric power $P_e = j_e \cdot E$, the real part $\text{Re}\{P_e = j_e \cdot E\}$ corresponds to the absorbed power of the electrons from the electric high-frequency field

$$\text{Re}\{P_e\} = \frac{n_e \cdot e^2 \cdot \nu_e}{m_e \cdot (\omega^2 + \nu_e^2)} \cdot E_{\text{eff}}^2 = \sigma(\omega) \cdot E_{\text{eff}}^2 = \sigma_{DC} \cdot \frac{1}{1 + (\omega/\nu_e)^2} \cdot E_{\text{eff}}^2. \quad (3.33)$$

In the case of no collisions $\nu_e = 0$ the electron current density consists of a pure imaginary part, which means no power from the electric field is absorbed by electrons.

If $\omega = 0$, we have the DC case and the electrical conductivity σ_{DC} corresponds to the Drude model of quasi-free electrons. The electric conductivity is proportional to the electron concentration n_e , and taking into account that the mean free path length for elastic electron collisions with the neutrals scales with $\nu_e \sim 1/\lambda \sim p$, the electron current density increases with rising E_0/p

$$j_{ez} \sim \frac{e^2}{m_e} \cdot n_e \frac{E_0}{p}. \quad (3.34)$$

Considering the resulting polarization P_{pol} due to the shift of electrons in the high-frequency electric field by the distance z against the static positive ion ensemble, it follows

$$P_{pol}(t) = -e \cdot n_e \cdot z(t). \quad (3.35)$$

Finally, the complex permittivity of such plasma is found from $D = \varepsilon \varepsilon_0 E = \varepsilon_0 E + P_{pol}$

$$\varepsilon = 1 + \frac{P_{pol}(t)}{\varepsilon_0 \cdot E(t)} \quad (3.36)$$

$$\varepsilon = 1 - \frac{e^2 \cdot n_e}{\varepsilon_0 \cdot m_e} \cdot \frac{(\omega - i\nu_e)}{\omega \cdot (\omega^2 + \nu_e^2)} = 1 - \frac{\omega_{pe}^2}{\omega} \cdot \frac{(\omega - i\nu_e)}{(\omega^2 + \nu_e^2)} \quad (3.37)$$

$$= \left(1 - \frac{\omega_{pe}^2}{\omega^2 + \nu_e^2} \right) + i \frac{\sigma(\omega)}{\varepsilon_0 \cdot \omega} = \varepsilon'(\omega) + i\varepsilon''(\omega). \quad (3.38)$$

With the relations for the refractive index n_r , the attenuation of the wave κ , and the absorption coefficient μ , it can be written

$$n_r^2 - \kappa^2 = \varepsilon'(\omega), \quad 2 \cdot n_r \cdot \kappa = \varepsilon''(\omega) = \frac{\sigma}{\varepsilon_0 \cdot \omega}, \quad \mu = \frac{2 \cdot \kappa \cdot \omega}{c_0} = \frac{\sigma(\omega)}{\varepsilon_0 \cdot n_r \cdot c_0}. \quad (3.39)$$

By use of the Maxwell relation (3.40) the dispersion function $k(\omega)$ of the electromagnetic wave can be obtained without exact solution of the Maxwell equations in that special case

$$\varepsilon = \left(\frac{c_0}{c_{ph}} \right)^2 = c_0^2 \cdot \frac{k^2}{\omega^2}, \quad (3.40)$$

where

ε is the complex permittivity

c_0 is the speed of light

c_{ph} is the phase velocity, and k is the wavenumber

According to this simplified calculation it follows for the dispersion function $k(\omega)$,

$$k^2 = \left(\frac{\omega}{c_0} \right)^2 \cdot \left(1 - \frac{\omega_{pe}^2}{\omega} \cdot \frac{(\omega - i\nu_e)}{(\omega^2 + \nu_e^2)} \right). \quad (3.41)$$

Generally, the dispersion function $k(\omega)$ contains all information about the wave properties, e.g.,

- Stability of waves
- Temporal and spatial change of wave amplitude
- Strong absorption \rightarrow resonances in dispersion function, $k(\omega) \rightarrow \infty, c_{ph} = 0$
- Reflection \rightarrow zero points in the dispersion function, $k(\omega) = 0, c_{ph} \rightarrow \infty$

TABLE 3.1

Phase and Group Velocity for Different Electric Field Frequencies in Comparison with Electron Plasma Frequency (Collision-Free Case)

Angular Frequency ω	Phase Velocity c_{ph}	Group Velocity c_{gr}	Comment
$\omega < \omega_{pe}$	Not defined ($\varepsilon < 0$)	Not defined ($\varepsilon < 0$)	No wave propagation Total reflection
	$c_{ph} \rightarrow \infty$ ($\varepsilon = 0$)	$c_{gr} = 0$ ($\varepsilon = 0$)	No wave propagation Total reflection
$\omega = \omega_{pe}$	$c_{ph} > c_0$	$c_{gr} < c_0$	Wave propagation
	($0 < \varepsilon < 1$)	($0 < \varepsilon < 1$)	

In the following, we will discuss the dispersion function (3.41) without collisions ($\nu_e = 0$) as the simplest case

$$k(\omega) = \frac{1}{c_0} \cdot \sqrt{\omega^2 - \omega_{pe}^2}. \quad (3.42)$$

The phase and group velocity (c_{ph} and c_{gr}) are defined to (Table 3.1)

$$c_{ph} = \frac{\omega}{k} = c_0 \cdot \left(1 - \left(\frac{\omega_{pe}}{\omega}\right)^2\right)^{-1/2}, \quad (3.43)$$

$$c_{gr} = \frac{d\omega}{dk} = c_0 \cdot \left(1 - \left(\frac{\omega_{pe}}{\omega}\right)^2\right)^{1/2}. \quad (3.44)$$

A characteristic cutoff is observed in the dispersion function $k(\omega)$ at the electron plasma frequency (see Figure 3.3). That means without external magnetic field no electromagnetic wave propagation takes place below the electron plasma frequency ω_{pe} , or above the critical electron concentration n_{ec}

$$n_{ec} = \frac{m_e \cdot \varepsilon_0}{e^2} \cdot \omega_{pe}^2 \quad (3.45)$$

$$n_{ec} [\text{cm}^{-3}] = 1.24 \cdot 10^{10} \cdot (\nu [\text{GHz}])^2. \quad (3.46)$$

In the case of total reflection ($\omega \leq \omega_{pe}$ or $n_e \geq n_{ec}$), the penetration depth of the electromagnetic wave δ can be estimated by

$$\delta \approx \frac{c_0}{\omega_{pe}}. \quad (3.47)$$

In a plasma with collisions ($\nu_e \neq 0$) and high conductivity $\sigma(\omega)$, a damping of the wave is observed. At frequencies below the electron plasma frequency the wave is

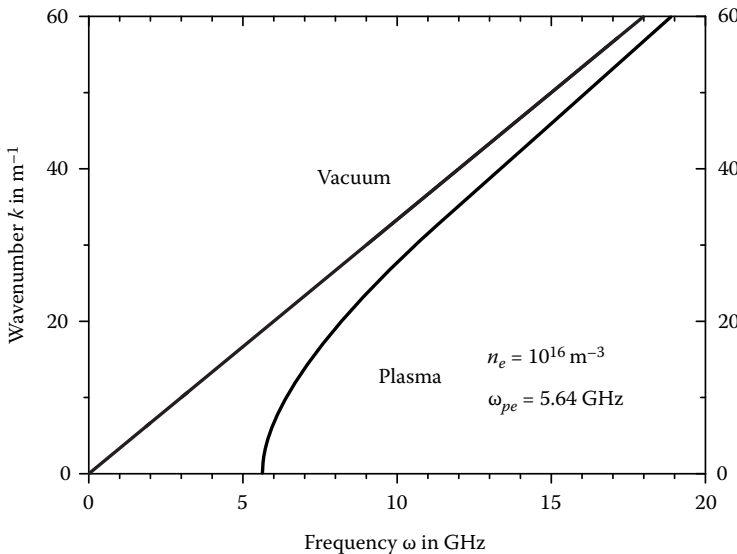


FIGURE 3.3 Real part or the dispersion function (3.41) for electromagnetic wave propagation in nonmagnetized plasma (collision-free case $\gamma_e = 0$) with the cutoff frequency $\omega_{pe} = 5.64 \text{ GHz}$, in comparison with the propagation in vacuum.

reflected whereas the wave penetrates into the plasma over the skin depth δ_s and dissipates wave energy

$$\delta_s = \frac{c_0}{\omega \cdot \kappa} = \sqrt{\frac{2}{\sigma \cdot \omega \cdot \mu_0}}. \quad (3.48)$$

Furthermore, the cutoff at the electron plasma frequency spreads in lower frequency ranges and the resonances are finite. But, normalized collision frequencies with γ_e/ω lower than 10^{-3} have only little influence on the dispersion function. More detailed information about the propagation of manifold waves in plasmas, in particular their anisotropic behavior in presence of external magnetic fields, can be found in the literature [2].

3.1.5 AMBIPOLAR DIFFUSION OF CHARGED PARTICLES

The ambipolar diffusion describes the transport of charged species in quasi-neutral plasmas in the case of gradients in the charged species concentration and without external fields. Considering a spatially inhomogeneous quasi-neutral plasma region over a distance $L \gg \lambda_D$ and the separated movement of single charged positive ions and electrons, the free diffusion of the electron ensemble takes place much faster with respect to the heavy ions due to their lower mass and therefore the higher mobility. The fast electron diffusion causes space charges and corresponding electric fields. Following, the positive ions are accelerated and electrons decelerated in the

self-consistent ambipolar electric space charge field. In steady state, both kinds of charged plasma particles, the positive ions and the electrons, are moving with the same current density determined by the ambipolar diffusion coefficient and the plasma density gradient. The calculation of the ambipolar diffusion coefficient can be done taking into calculation the free diffusion of electrons and ions as well as their electric field drift [3].

We consider the current density

$$\vec{j}_{+,e} = \pm e \cdot n_{+,e} \cdot b_{+,e} \cdot \vec{E}_a - e \cdot D_{+,e} \cdot \text{grad}(n_{+,e}) \quad (3.49)$$

for the single charged positive ions and the electrons, respectively, with the corresponding diffusion constant D and mobility b of charged particles, as well as the source equation of the ambipolar electric field \vec{E}_a

$$\text{div} \vec{E}_a = \frac{e \cdot (n_+ - n_e)}{\varepsilon_0}. \quad (3.50)$$

With the assumption that the charge separation is sufficiently small, according to $|n_+ - n_e| \ll n_e \approx n_+ \approx n$, it follows for the current density $\vec{j}_+ \approx \vec{j}_e$.

$$e \cdot n \cdot b_+ \cdot \vec{E}_a - e \cdot D_+ \cdot \text{grad}(n) \approx -e \cdot n \cdot b_e \cdot \vec{E}_a - e \cdot D_e \cdot \text{grad}(n). \quad (3.51)$$

From (3.51) we calculate the ambipolar electric field \vec{E}_a and insert the result in one of the equations of the current density (electrons or ions) in (3.51), e.g.,

$$\vec{j}_a = -e \cdot \left[\frac{b_+ \cdot D_e + b_e \cdot D_+}{b_e + b_+} \right] \cdot \text{grad}(n) = -e \cdot D_a \cdot \text{grad}(n), \quad (3.52)$$

where

\vec{j}_a is the ambipolar current density

D_a is the ambipolar diffusion coefficient

In nonthermal plasmas with $T_e \gg T_+$ as well as $b_e \gg b_+$, and by use of the Einstein relation $D/b = k_B \cdot T/e$ it follows the often applied approximation for the ambipolar diffusion coefficient

$$D_a \approx \frac{b_+ \cdot D_e}{b_e} = \frac{k_B \cdot T_e}{e} \cdot b_+ = \frac{2}{3} \cdot b_+ \cdot \langle \varepsilon_{kin}[eV] \rangle. \quad (3.53)$$

For example, in *non-thermal nitrogen plasma* with $T_e = 10^4$ K, the ambipolar diffusion coefficient gets $p \cdot D_a \approx 1.7 \cdot 10^5$ cm² Pa s⁻¹. Taking into account the mobilities for N₂⁺-ions in N₂ $p \cdot b_+ \approx 2 \cdot 10^5$ cm² PaV⁻¹s⁻¹ and electrons $p \cdot b_e \approx 5.6 \cdot 10^7$ cm² PaV⁻¹s⁻¹, respectively, the estimation of the typical diffusion time constant can be performed at the given total pressure p by means of the characteristic diffusion length Λ which is in the order of the minimum length of the given geometry, see Table 3.2,

$$\tau_{Diff} = \frac{\Lambda^2}{D_a}. \quad (3.54)$$

TABLE 3.2
Diffusion Lengths for Different Geometries of the Diffusion Problem

Symmetry of the Problem	$(1/\Lambda)^2$
Cylinder (radius R , length L)	$(2.4/R)^2 + (\pi/L)^2$
Sphere (radius R)	$(\pi/R)^2$
Parallelepiped (side lengths L_1, L_2, L_3)	$(\pi/L_1)^2 + (\pi/L_2)^2 + (\pi/L_3)^2$

Source: Raizer, Y.P., *Gas Discharge Physics*, Springer-Verlag, Berlin, Germany, 1991.

By use of the ambipolar diffusion coefficient for a nitrogen plasma, discussed above the typical diffusion time constant at a total pressure of 100 Pa (1 mbar) in a spherical geometry with radius $R = 20$ cm of the plasma vessel gets about $2.4 \cdot 10^{-2}$ s.

In the case of three-component plasmas, consisting of positive and negative ions as well as electrons, three ambipolar diffusion coefficients D_{a+} , D_{a-} , and D_{ae} are defined by use of the condition for quasi-neutrality $n_+ = n_e + n_-$ and the electronegativity $\alpha = n_- / n_e$ [4]

$$D_{a+} = \frac{b_e D_+ + b_+ D_e (1 + \alpha) (\nabla n_e / \nabla n_+) + b_- D_+ \alpha + b_+ D_- (1 + \alpha) (\nabla n_- / \nabla n_+)}{b_e + b_- \alpha + b_+ (1 + \alpha)}, \quad (3.55)$$

$$D_{ae} = \frac{b_+ D_e (1 + \alpha) + b_e D_+ (\nabla n_+ / \nabla n_e) + b_- D_e \alpha - b_e D_- (\nabla n_- / \nabla n_e)}{b_e + b_- \alpha + b_+ (1 + \alpha)}, \quad (3.56)$$

$$D_{a-} = \frac{b_+ D_- (1 + \alpha) + b_- D_+ (\nabla n_+ / \nabla n_-) + b_e D_- - b_- D_e \alpha (\nabla n_e / \nabla n_-)}{b_e + b_- \alpha + b_+ (1 + \alpha)}. \quad (3.57)$$

These equations for the ambipolar diffusion coefficient can be approximated to specific cases, e.g., for weak, strong, or very strong electronegativity α .

3.1.6 MOTION OF CHARGED SINGLE PARTICLE IN HOMOGENEOUS MAGNETIC FIELD

3.1.6.1 Cyclotron Motion

Firstly, we consider the motion of a single particle (charge q and mass m) with a component of velocity perpendicular to a homogeneous magnetic field $\vec{B} = B \cdot \hat{e}_z = \text{const.}$

$$m \cdot \begin{pmatrix} \dot{v}_x \\ \dot{v}_y \\ \dot{v}_z \end{pmatrix} = q \cdot \begin{pmatrix} v_x \\ v_y \\ v_z \end{pmatrix} \times \begin{pmatrix} 0 \\ 0 \\ B \end{pmatrix} = q \cdot \begin{pmatrix} +v_y \cdot B \\ -v_x \cdot B \\ 0 \end{pmatrix}. \quad (3.58)$$

The decoupling of (3.58) for the particle motion in x - and y -direction results in

$$\ddot{v}_{x,y} + \left(\frac{q \cdot B}{m} \right)^2 \cdot v_{x,y} = 0. \quad (3.59)$$

It follows directly the cyclotron frequency $\omega_c = qB/m$. Further, the velocity perpendicular $v_\perp^2 = v_x^2 + v_y^2$ and parallel $v_\parallel = v_z$ to the magnetic field lines, the cyclotron radius $r_c = v_\perp/\omega_c = m \cdot v_\perp/(q \cdot B)$, and the solution for velocity and spatial coordinates are found which describe the circular motion in the x - y -plane perpendicular, and the particle movement in z -direction parallel to the magnetic field lines

$$\vec{v}(t) = \begin{pmatrix} v_\perp \cdot \sin(\omega \cdot t) \\ v_\perp \cdot \cos(\omega \cdot t) \\ v_\parallel = \text{const.} \end{pmatrix} \quad \vec{r}(t) = \begin{pmatrix} x_0 - r_c \cdot \cos(\omega \cdot t) \\ y_0 + r_c \cdot \sin(\omega \cdot t) \\ z_0 + v_\parallel \cdot t \end{pmatrix}. \quad (3.60)$$

The circular cyclotron motion in the x - y -plane is clockwise for positive charged and counter-clockwise for negative charged species, see Figures 3.4 and 3.5.

Some useful formulas are given for the characterization of the cyclotron motion ($\omega_{ce/c+} = 2\pi \cdot \nu_{ce/c+}$) in nonthermal plasmas

$$\nu_{ce} [\text{GHz}] = 28 \cdot B[\text{T}] \quad \frac{\nu_{c+}}{\nu_{ce}} = \frac{z}{1836.1 \cdot A_+[u]} \quad (3.61)$$

$$r_{ce} [\text{mm}] = 3.129 \cdot 10^{-5} \cdot \frac{\sqrt{T_e[\text{K}]}}{B[\text{T}]} \quad \frac{r_{c+}}{r_{ce}} = 43 \cdot \frac{\sqrt{A_+[u]}}{z} \cdot \sqrt{\frac{T_+}{T_e}}, \quad (3.62)$$

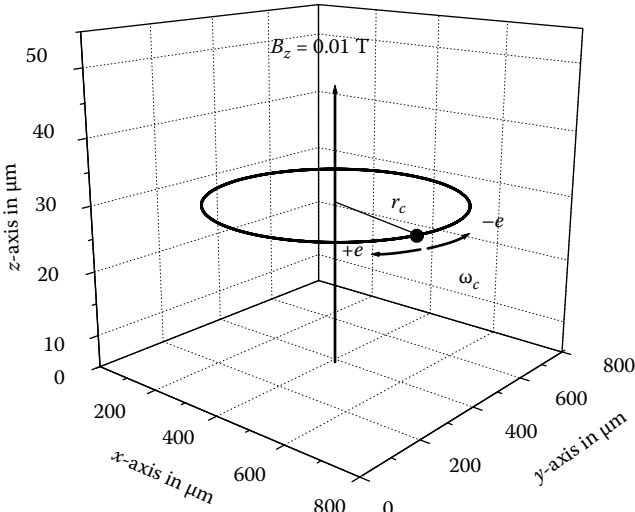


FIGURE 3.4 Cyclotron motion of a positive and negative charged particle in magnetized plasma with $B_z = 0.01 \text{ T}$, $\omega_c = 1.76 \text{ GHz}$, and $r_c = 300 \mu\text{m}$.

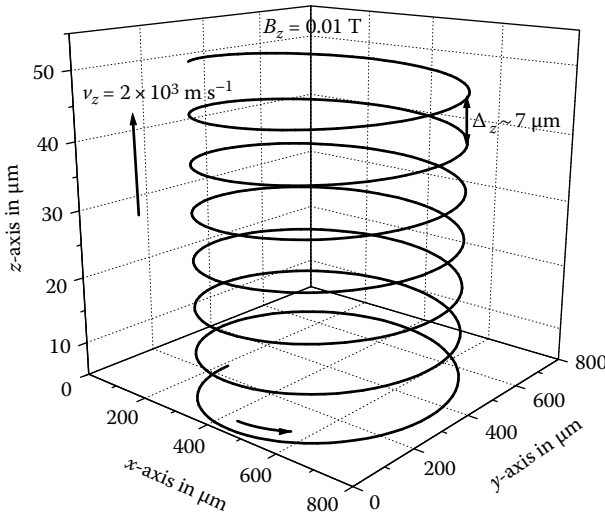


FIGURE 3.5 Electron cyclotron motion in magnetized plasma with additional parallel velocity $v_z = 2 \cdot 10^3 \text{ m s}^{-1}$ to the magnetic field $B_z = 0.01 \text{ T}$, $\omega_c = 1.76 \text{ GHz}$.

where

B is the magnetic field in Tesla

$A_+[u]$ is the ion mass in unified atomic mass units, $1u = 1.66538921(73)10^{-27} \text{ kg}$

z is the charge number of the ion

$T_{e/+}$ is the translational temperature in Kelvin for electrons and ions, respectively

At the conditions $B = 0.1 \text{ T}$, $T_e = 10 \cdot T_+ = 10^4 \text{ K}$, the cyclotron motion of electrons and single charged positive argon ions is characterized by

$$\text{Electrons: } \nu_{ce} = 2.8 \text{ GHz}, r_{ce} = 31 \mu\text{m};$$

$$\text{Ions (Ar}^+, u = 40\text{:)} \nu_{c+} = 38.1 \text{ kHz}, r_{c+} = 2.7 \text{ mm.}$$

3.1.6.2 Drift Velocity Perpendicular to the Magnetic Field due to Additional External Forces

We consider an additionally external force \vec{F} on the charged particle to investigate the mean drift velocity \vec{v}_D of the guiding center perpendicular to the magnetic field. That means the fast cyclotron motion is time-averaged and the movement of the cyclotron centre is considered by the drift approximation

$$m \frac{d\vec{v}_D}{dt} = \vec{F} + q(\vec{v}_D \times \vec{B}). \quad (3.63)$$

For the steady state and after some mathematical operations it follows

$$\vec{v}_{D,\perp} = \frac{\vec{F} \times \vec{B}}{q \cdot B^2}. \quad (3.64)$$

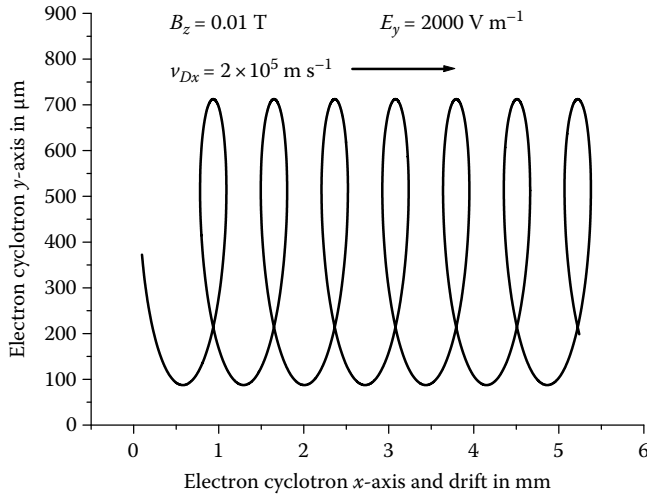


FIGURE 3.6 Electron drift velocity due to the $E \times B$ drift ($B_z = 0.01$ T, $E_y = 2000$ V m $^{-1}$, $v_{Dx} = 2 \cdot 10^5$ m s $^{-1}$).

In the special case of $\vec{F} = q \cdot \vec{E}$, it follows the expression for the well-known $\vec{E} \times \vec{B}$ -drift (Figure 3.6)

$$\vec{v}_{D,\perp} = \frac{\vec{E} \times \vec{B}}{B^2}. \quad (3.65)$$

The drift velocity of charged particles perpendicular to the electric and magnetic field is independent of charge and mass. In magnetron discharges (see Section 3.8) the electrons with low cyclotron radius are trapped in regions in front of the cathode due to the $\vec{E} \times \vec{B}$ -drift with the consequence of efficient electron impact ionization and increasing plasma density in that region, see Figure 3.6.

Taking additionally into account an external harmonic electric field with direction in the $x-z$ -plane and with the circular frequency ω , the resulting additional velocity perpendicular to the magnetic field $\omega_c \neq \omega$ can be estimated for two limits [2]

1. Low electric field frequency ($\omega \rightarrow 0$) results in a modified $\vec{E} \times \vec{B}$ -drift

$$\Delta \vec{v}_E(t) = \Delta \vec{v}_y = \frac{\omega_c^2}{\omega_c^2 - \omega^2} \cdot \frac{\vec{E}(t) \times \vec{B}}{B^2}. \quad (3.66)$$

2. Low cyclotron frequency ($\omega_c \rightarrow 0$) results in a modified polarization drift

$$\Delta \vec{v}_{pol}(t) = \Delta \vec{v}_x = \frac{q}{m} \cdot \frac{1}{\omega_c^2 - \omega^2} \cdot \frac{\vec{B} \times \left[\left(d\vec{E}(t)/(dt) \right) \times \vec{B} \right]}{B^2}. \quad (3.67)$$

The special situation $\omega_c = \omega$ describes the *cyclotron resonance* either for electrons or positive ions. In the case of electrons, the electron cyclotron motion is in phase

with the electric field vector of a right-hand circularly polarized electromagnetic wave (*R*-wave) with the consequence of permanent electron acceleration and the absorption of energy from the electromagnetic wave. This phenomenon is mainly applied for *electron cyclotron resonance heating* (ECRH), e.g., in magnetized low-pressure microwave plasmas. For example, the electron cyclotron resonance in a 2.45 GHz microwave plasma is achieved at a magnetic field of $B = 0.0875$ T.

3.1.6.3 Influence of Collisions on Charged Particle Transport in Magnetized Plasmas

Any collision during the cyclotron motion weakens the strong binding to the circular motion around the B -field lines. The equation of motion for electrons in drift approximation is given by the expression

$$m_e \cdot \frac{d\vec{v}_D}{dt} = -e \cdot (\vec{E} + \vec{v}_D \times \vec{B}) - m_e \cdot \nu_e \cdot \vec{v}_D \quad (3.68)$$

with ν_e the mean elastic electron collision frequency, $\vec{v}_D = -b_e \cdot \vec{E}$ and $\vec{j} = -e \cdot n \cdot \vec{v}_D$.

Taking into account the homogeneous magnetic field in z -direction (B_z) and a homogeneous electric field within the x - z -plane, the steady-state solution results in anisotropic electron transport described by different mobilities perpendicular to the magnetic field in x - and y -direction as well as parallel to the magnetic field lines in z -direction. The last one is not influenced by the magnetic field

$$b_{e,\perp,x} = \frac{1}{1 + (\omega_{ce}/\nu_e)^2} \cdot b_{e,\parallel,z} \quad b_{e,\perp,y} = \frac{\omega_{ce}/\nu_e}{1 + (\omega_{ce}/\nu_e)^2} \cdot b_{e,\parallel,z} \quad b_{e,\parallel,x} = \frac{e}{m_e \cdot \nu_e}. \quad (3.69)$$

By use of the Einstein relation, the electron diffusion coefficient in *magnetized nonthermal plasmas* is given by the expression

$$D_{e,\parallel/\perp} = \frac{k_B \cdot T_e}{e} \cdot b_{e,\parallel/\perp}. \quad (3.70)$$

Whereas the magnetic fields have strong influence on electron movement and sampling in electric probe diagnostics (see Section 6.1), the influence of magnetic fields on heavy ions in nonthermal plasmas can be mostly neglected because of the larger cyclotron radius and lower cyclotron frequency.

3.2 THERMAL AND NONTHERMAL PLASMAS

3.2.1 PLASMA IN THERMODYNAMIC EQUILIBRIUM

3.2.1.1 Complete Thermodynamic Equilibrium

For better understanding of the specifics of nonthermal plasmas we consider at first the ideal plasma in the thermodynamic equilibrium state [1]. Only two parameters, the temperature and pressure, are sufficient for quantitative description of homogeneous plasmas in thermodynamic equilibrium. In the *complete thermodynamic equilibrium* (CTE) state, the plasma is characterized by the same temperature for

translational energy of all plasma particles and energies of internal degrees of freedom like electronic, vibrational, and rotational excitation of atoms and molecules for each ionization level, respectively.

The distribution of the translational energy ε_T of plasma particles is given by the Maxwellian energy distribution function

$$f(\varepsilon_T) = \frac{dn}{n \cdot d\varepsilon_T} = \frac{2\pi}{(\pi \cdot k_B \cdot T)^{3/2}} \cdot \sqrt{\varepsilon_T} \cdot \exp\left(-\frac{\varepsilon_T}{k_B \cdot T}\right), \quad (3.71)$$

with $\varepsilon_T = m/2 \cdot v^2$ and $f(\varepsilon_T) \cdot d\varepsilon_T = f(v) \cdot dv$.

The distribution of the internal energy in excited states (electronic, vibrational, rotational) for selected species at the same ionization level ($z=0, 1, \dots$) is given by the Boltzmann distribution

$$\frac{n_{zj}}{n_z} = \frac{g_{zj}}{g_{z0}} \cdot \exp\left(-\frac{\varepsilon_{zj}}{k_B \cdot T}\right), \quad (3.72)$$

when g_{zj} and g_{z0} represent the statistical weights of the level j at the excitation energy ε_{zj} and the ground state (0), as well as n_{zj} and n_{z0} the particle concentrations, respectively.

Furthermore, the plasma is in equilibrium with the radiation field described by Planck's law of the black body radiation. The Kirchhoff's law provides the ratio between the spectral emissivity $E_\nu(\nu)$ and the absorption coefficient A_ν

$$\begin{aligned} \frac{E_\nu}{A_\nu} &= B_\nu(T) = \frac{c_0}{4\pi} \cdot \frac{8\pi \cdot h}{c_0^3} \cdot \frac{\nu^3}{\exp(h\nu/(k_B T)) - 1} \\ &= \frac{2h}{c_0^2} \cdot \frac{\nu^3}{\exp(h\nu/(k_B \cdot T)) - 1}. \end{aligned} \quad (3.73)$$

The quantity $E_\nu \cdot d\nu = B_\nu(T) \cdot d\nu$ represents the emitted radiation energy of the plasma as a black body ($A_\nu = 1$) at the temperature T per unit of area and time into the solid angle $d\Omega$ in the frequency interval of between ν and $\nu + d\nu$.

In the CTE the *general principle of detailed equilibrium* describes for each elementary reaction at the given temperature T that the forward and backward reaction takes place at the same probability, which means with the same reaction velocity, e.g., see Table 3.3.

In that way, the *ionization-recombination equilibrium* is determined by the Eggert-Saha-equation (3.75) which describes the constant ratio between charged and neutral particles for a given temperature.

For electron impact ionization and three-body recombination in thermodynamic equilibrium,



follows the *Eggert-Saha-equation*

$$\frac{[A^+] \cdot [e]^2}{[A] \cdot [e]} = K_{ion}(T) = \text{const. } [\exp(-\varepsilon_{ion}/(k_B T))]. \quad (3.75)$$

TABLE 3.3
Selection of Equilibrium Reactions in Plasmas at CTE

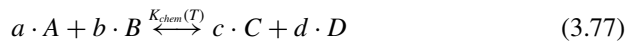
1.	Electron impact ionization →	← three-body recombination
	$\text{Ar} + e \leftrightarrow \text{Ar}^+ + 2e$	
2.	Electron impact excitation →	← de-excitation by collisions
	$\text{Ar} + e \leftrightarrow \text{Ar}^* + e$	
3.	Photo ionization →	← radiative recombination
	$\text{Ar} + h\nu \leftrightarrow \text{Ar}^+ + e$	
4.	Photo absorption →	← spontaneous emission
	$\text{Ar} + h\nu \leftrightarrow \text{Ar}^*$	

For the ionization degree χ of the plasma in CTE at the gas pressure p follows

$$\frac{\chi^2}{1 - \chi^2} \cdot p [\text{Pa}] = 5.56 \cdot 10^{-5} \cdot T^{5/2} \cdot \exp \left[-\frac{1.16 \cdot 10^4 \cdot U_{ion} [\text{V}]}{T [\text{K}]} \right]. \quad (3.76)$$

In the case of chemical reactions in plasmas the thermodynamic equilibrium provides the ratio between the concentrations of reaction products (e.g., $[C]$ and $[D]$) and the concentrations of the chemical reactants (e.g., $[A]$ and $[B]$) expressed by the mass action law [5]. At constant external conditions, the ratio only depends on one parameter, the temperature T .

For chemical reactions in thermodynamic equilibrium



follows the mass action law in thermochemistry

$$\frac{[C]^c \cdot [D]^d}{[A]^a \cdot [B]^b} = K_{chem}(T) = \text{const. } [T]. \quad (3.78)$$

$[A]$, $[B]$, $[C]$, and $[D]$ are the particle concentrations of the reactants and products with the stoichiometric coefficients a , b , c , and d , respectively.

One has to note that a *complete thermodynamic equilibrium* (CTE) in dissipative systems, like laboratory plasmas, is not realized. That means, under real conditions the transport processes of mass, charge, momentum, and energy are observed in plasmas, and, for example, the ionization and recombination as well as the emission and absorption processes are not balanced at any local point in the plasma.

3.2.1.2 Local Thermodynamic Equilibrium

Nevertheless, the approximation of a *local thermodynamic equilibrium state* (LTE) can be applied if in a local region the gradients of a function $\varphi(T, n, v)$ as well as the resulting fluxes are not significant. In other words the particle distribution function

deviates only weakly from the Maxwellian type. Following a high particle collision frequency is necessary to achieve the LTE, which can satisfy the condition [5]

$$\frac{\lambda \cdot |\nabla \varphi|}{\varphi} \ll 1 \quad (3.79)$$

with λ the mean free path length and $\varphi = \varphi(T, n, v)$.

It follows for the existence of the LTE

1. The electrons, heated in the electric field, transfer sufficient kinetic energy by elastic collisions into the heavy particle system.
2. The electron impact ionization process is mostly balanced by three-particle recombination, and the loss by diffusion processes is weak.
3. A sufficient number of inelastic collisions transfer the internal energy of excited particles.
4. The energy transfer between particles exceeds the rate of processes in which energy in the plasma increases or decreases significantly.

Usually, the loss of energy due to radiation out of the plasma is mostly not significant compared with other loss processes.

3.2.2 NONEQUILIBRIUM PLASMAS

The *nonthermal plasmas* within the field of ideal plasmas represent the plasma state of matter under nonequilibrium conditions. That means *no thermodynamic equilibrium state* between translational energy of plasma particles, their internal energies, and the plasma radiation exists, and the parameter *temperature* for characterizing the total many-particle system is not valid.

The following physical reasons may inhibit the existence of a thermal equilibrium [1,3]

1. In the electric field the mobile electrons are strongly accelerated and they gain much more translational energy per time unit in comparison with heavy ions. The heavy ions cannot absorb a high amount of electric field energy per time unit due to their considerable inertia. In weakly ionized and collision-dominated plasmas, the power absorption of electrons per volume in electric field is given by Joules heating, expressed by

$$P_{abs}^e = \text{Re} \left\{ \vec{j}_e \cdot \vec{E} \right\} = \sigma_{eff} \cdot E_{eff}^2 = \frac{n_e \cdot e^2 \cdot v_e}{m_e \cdot (\omega^2 + \nu_e^2)} \cdot E_{eff}^2. \quad (3.80)$$

2. An efficient kinetic energy transfer is necessary into the heavy particle system (ions, neutrals) to achieve the thermal equilibrium with uniform temperature in translational and internal energy distribution. According to the conservation of kinetic energy and momentum in elastic collisions, the kinetic energy transfer depends on the mass ratio of the interacting particle. In elastic electron-neutral collisions the momentum gain of the

neutral particle is easily expressed by $\Delta p_n = m_e \cdot \Delta v_e$ which results in increase of the kinetic energy of heavy particles m

$$\frac{\Delta p_n^2}{2m} = \frac{(m_e \cdot \Delta v_e)^2}{2m} = \frac{m_e}{m} \cdot \left(\frac{m_e}{2 \cdot \Delta v_e^2} \right) = \frac{m_e}{m} \cdot \Delta \varepsilon_T^e. \quad (3.81)$$

An efficient energy transfer is achieved at nearly the same mass of collision partners. In the case of electron–heavy particles collisions the mass ratio amounts to about 10^{-5} which is connected with corresponding low kinetic energy transfer.

The total rate of kinetic electron energy variation can be expressed by [1]

$$\begin{aligned} n_e \cdot \nu_e \cdot \frac{m_e}{m} \cdot \Delta \varepsilon_T^e &= n_e \cdot \nu_e \cdot \frac{m_e}{m} \cdot 3 \cdot k_B(T_e - T) \\ &= P_{abs}^e = \frac{e^2 \cdot n_e \cdot \nu_e}{m_e \cdot (\omega^2 + \nu_e^2)} \cdot E_{eff}^2. \end{aligned} \quad (3.82)$$

The maximum difference between the electron and heavy particles (gas) temperature can be estimated

$$\begin{aligned} T_e - T &= \frac{\sigma_{eff} \cdot m \cdot E_{eff}^2}{3 \cdot k_B \cdot m_e \cdot n_e \cdot \nu_e} = \frac{e^2 \cdot m \cdot E_{eff}^2}{3 \cdot k_B \cdot m_e^2 \cdot (\omega^2 + \nu_e^2)} \\ &\sim \frac{E_{eff}^2}{(\omega^2 + \nu_e^2)} \sim \frac{E_{eff}^2}{(\omega^2 + c_1 \cdot p^2)}. \end{aligned} \quad (3.83)$$

That means, the temperature difference increases with decreasing total pressure and electric field frequency and consequently stronger nonthermal conditions are observed.

3. The existence of gradients in particle concentration and temperature as well as the presence of external electric and magnetic forces cause energy fluxes out of the active plasma region to electrodes and walls which is connected with extraction or recombination of charged particles at the plasma boundary.

Furthermore, the energy loss by electromagnetic radiation out of the plasma contributes to the formation of nonthermal plasma.

All the loss processes reduce the energy confinement time $\tau_E = W/P_{loss}$ in the plasma.

In the consequence, no thermal equilibrium is achieved in stationary and weakly ionized low pressure plasmas because of the low electron concentration ($< 10^{18} \text{ m}^{-3}$) and the corresponding low collision frequency between electrons and heavy particles. The low heavy particle confinement time compared with the translational energy relaxation time results in the formation of plasmas in nonthermal equilibrium state.

Further, no thermal equilibrium is achieved in electric discharges of short duration, e.g., microdischarge channels in barrier discharges or streamers in corona discharges (duration $< 100 \text{ ns}$) in spite of higher local electron concentration ($> 10^{20} \text{ m}^{-3}$) and increasing collision frequency at higher gas pressure. The duration

of that discharge phenomena is much lower than the characteristic energy relaxation times.

In some restricted cases the approximation of a local *partial thermodynamic equilibrium state* (PTE) can be applied for nonequilibrium plasmas which implies the definition of separate temperatures for

1. Translational energy of electrons T_e , ions T_+ and neutrals T_n
2. Internal energy distribution in excited electronic T_{exc} , vibrational T_{vib} and rotational T_{rot} states

As an example, the *nonthermal plasma of the positive column in low-pressure DC glow discharge* represents a weakly ionized nonthermal plasma characterized by total pressure $p < 10^3$ Pa, degree of ionization $\chi = 10^{-6} - 10^{-4}$, and electron density $n_e < 10^{18} \text{ m}^{-3}$.

The electron temperature is much higher than the ion and neutral gas temperature, typically $T_e \sim 10^4 \text{ K} \gg T_+ \sim T_n \sim 300 \text{ K}$. In such plasmas, also indicated as *cold plasmas*, the electrons represent the main energetic particles with mean kinetic energy of few electron volts (1 eV corresponds to 11,600 K).

3.3 ELEMENTARY COLLISION PROCESSES AND CROSS SECTIONS

3.3.1 INTRODUCTION AND OVERVIEW

Elastic and inelastic collisions between electrons, ions, and neutral atoms and molecules represent key processes in nonthermal plasmas for the dissipation of translational and internal energy. In particular, the inelastic collisions of the hot electrons with heavy particles are of great importance as the main source in the generation of charged, excited, and/or highly reactive radicals. The elementary collisions processes between plasma particles have to be described by conservation laws such as the total momentum and energy of the participating particles under consideration of the quantum states of the atomic or molecular collision partners and their selection rules for electronic transitions as well as the vibrational and rotational transitions in the case of molecules, respectively. Collisions in nonthermal plasmas at low pressure are dominated by binary collisions. Generally, the result of the collision between two particles A and B depends on their specific physical interaction determined by the energy, mass, and charge of the particles, and their specific collision cross section σ_{AB} , as exemplarily demonstrated in Figure 3.7.

With increasing particle density, e.g., in nonthermal plasmas at atmospheric or higher pressure, the collisions involving three particles must be taken into account, too.

The collision of charged, metastable excited and reactive plasma particles as well as the VUV/UV photons with surfaces at the plasma boundaries has to be additionally considered, such as on discharge electrodes, immersed probes for diagnostics, material surfaces for plasma processing, and the wall of the plasma vessel. The plasma–surface interactions may result in emission of secondary species, or the plasma boundary acts as a third collision partner, see Figure 3.8. Therefore, many

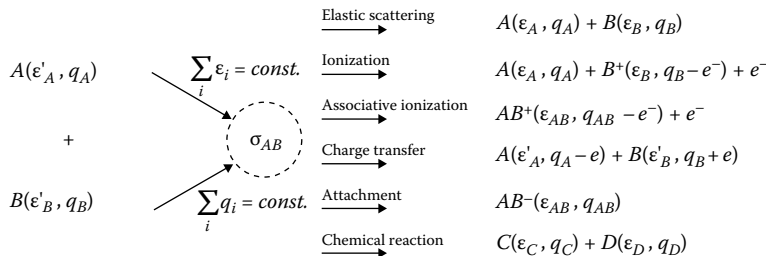


FIGURE 3.7 Important elementary collision processes between particles in the plasma volume with collision cross section $\sigma_{AB}(\varepsilon)$ (A, B : particles with total energy ε and charge q ; e : elementary charge).

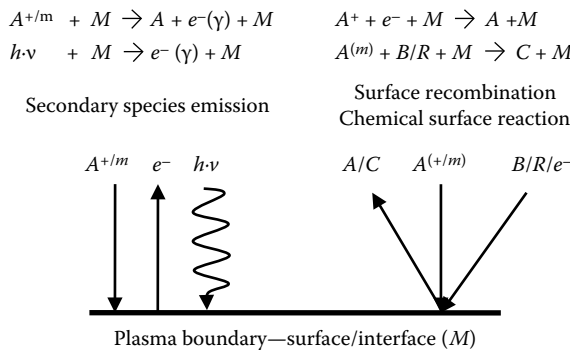


FIGURE 3.8 Important elementary collision processes on the surface, $A^{+/m}$: ion/metastable; R : radical; $h \cdot v$: photon; e^- : electron; A, B, C : atom or molecule; M : surface.

chemical reactions and recombination processes take place on the plasma boundary in nonthermal plasmas, see Sections 3.5 and 3.6.

The transport of charged species from the plasma bulk to the plasma boundary in low-pressure plasmas is driven by the ambipolar diffusion and the electric field drift due to the external electric field or the self-consistent electric field of space charges inside the plasma sheath in front of any surface in contact with the plasma such as discharge electrodes, walls, or immersed samples/probes. In dependence on the total pressure and gas flow rate of neutral particles through the plasma reactor, the neutral particle transport by diffusion and/or convection has to be taken into account, see Section 3.4.

3.3.1.1 Dynamics of Elastic and Inelastic Collisions

In the simplest case, the dynamics of a binary collision between neutral particles in the volume is illustrated in Figure 3.9 by use of the hard sphere model. An interaction takes place for the impact parameter $b < (a_1 + a_2) = b_{HS} = b_{max}$, with the radius a_1 and a_2 of the particle 1 and 2, respectively. Indeed, the interaction is based on internal

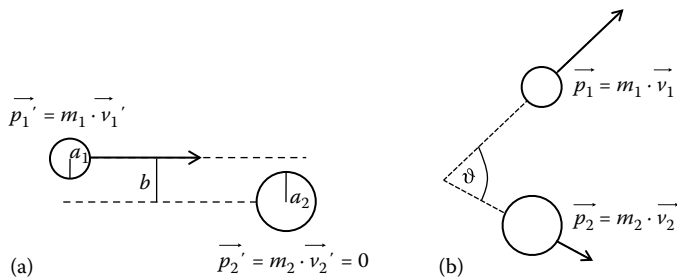


FIGURE 3.9 Scheme of a binary collision in the laboratory system, before (a) and after (b) the collision. It is shown the particle momentums and the angle ϑ after the scattering for two hard spheres with different mass and atomic radius.

forces (Coulomb interaction) of short lengths scale, only, and the total momentum is invariant in the collision process.

The *elastic collisions* are characterized by the conservation of the total translational energy of the collision partners. The conservation of the total momentum (3.84) and translational energy (3.85) results in (3.86), which describes all possible momentums \vec{p}_1' and \vec{p}_2' of the two particles after the elastic collision. Equation 3.86 can be visualized by the momentum sphere, see Figure 3.10.

Conservation of the total momentum:

$$\vec{p}_1' = \vec{p}_1 + \vec{p}_2' = \text{const.} \quad (3.84)$$

Conservation of the total translational energy:

$$\varepsilon_T = \frac{(p_1')^2}{2m_1} = \frac{p_1^2}{2m_1} + \frac{p_2^2}{2m_2} = \text{const.} \quad (3.85)$$

Momentum sphere:

$$\left(\frac{m_2}{m_1 + m_2} \cdot \vec{p}_1' \right)^2 = \left(\vec{p}_1 - \frac{m_1}{m_1 + m_2} \cdot \vec{p}_1' \right)^2. \quad (3.86)$$

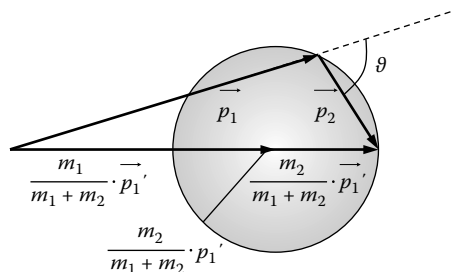


FIGURE 3.10 The momentum sphere illustrates the elastic collisions between two particles for the condition $m_1 > m_2$.

For collinear momentums, one solution exists for \vec{p}'_1 in Figure 3.10 on the momentum sphere and the gain of translational energy of the target particle, $\varepsilon_T^{gain}(m_2)$ can be easily calculated

$$\varepsilon_T^{gain}(m_2) = \varepsilon'_T(m_1) \cdot \frac{4 \cdot m_1 \cdot m_2}{(m_1 + m_2)^2}. \quad (3.87)$$

The maximum gain of translational energy of the target particle is achieved for equal mass of the collision partners ($m_1 = m_2 = m$).

The *inelastic collisions* are characterized by the loss of translational energy and its transfer into internal energy of the target particle. In the total translational energy balance equation (3.88) this loss of translational energy has to be compensated by the factor $\alpha^2 < 1$. Together with the total momentum conservation (3.84) the derived momentum sphere (3.89) is characterized by a reduced radius of the sphere ($\gamma^2 < 1$), see Figure 3.11.

Translational energy balance equation:

$$\alpha^2 \cdot \frac{(p'_1)^2}{2m_1} = \frac{p_1^2}{2m_1} + \frac{p_2^2}{2m_2}. \quad (3.88)$$

Momentum sphere:

$$\gamma^2 \cdot \left(\frac{m_2}{m_1 + m_2} \cdot \vec{p}_1' \right)^2 = \left(\vec{p}_1 - \frac{m_1}{m_1 + m_2} \cdot \vec{p}_1' \right)^2 \quad (3.89)$$

$$\text{with } \gamma^2 = \left[\alpha^2 \cdot \left(1 + \frac{m_1}{m_2} \right) - \frac{m_1}{m_2} \right]. \quad (3.90)$$

The strongest loss of translational energy of the impinging particle, $\Delta\varepsilon_T^{loss}(m_1)$, is achieved for collinear momentums, which provides $\gamma = 0$ and $\alpha_{min}^2 = m_1/(m_1 + m_2)$, respectively

$$\Delta\varepsilon_T^{loss}(m_1) = \varepsilon'_T(m_1) \cdot \frac{m_2}{m_1 + m_2}. \quad (3.91)$$

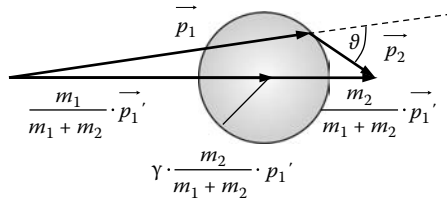


FIGURE 3.11 The momentum sphere illustrates the inelastic collisions ($\gamma^2 < 1$) between two particles for the condition $m_1 > m_2$.

In that case both particles have the same velocity after the collision. The optimal transfer of translational into internal energy is observed if the mass of the impinging particle is small compared with the mass of the target particle ($m_1 \ll m_2$), with the consequence of nearly complete transfer of the translational energy from the impinging particle into the internal energy of the target particle.

3.3.2 COLLISION PROCESSES IN NONTHERMAL PLASMAS AND THEIR CLASSIFICATION

The *elastic collisions* in plasmas can be classified in collisions between neutral atoms/molecules, between neutral atom/molecule and an electron or positive/negative ion, and between charged atoms/molecules such as ion–ion, ion–electron, and electron–electron as well.

Gas kinetic scattering: $A \leftrightarrow B$

Polarization scattering: $e^- \leftrightarrow B$ or $A^{+/-} \leftrightarrow B$

Coulomb scattering: $A^{+/-} \leftrightarrow B^+$ or $e^- \leftrightarrow B^{+/-}$ or $e^- \leftrightarrow e^-$

The elastic collisions are of great importance for the exchange of translational energy and the development of the velocity or energy distribution function of the plasma particles, such as the energy distributions function of electrons, ions, and neutral particles in nonthermal plasmas.

Some specific collisions processes are observed in plasmas which are classified as elastic collisions such as the super elastic collisions and the elastic electron–neutral interaction due to the “Ramsauer effect.” In *super elastic collisions* the internal energy of an excited particle is transferred in additional translational energy of the collision partner during the collision, which may be interpreted as a reversal process of the inelastic collision. Further, the interaction between an electron and neutral particle at low electron energy around 1 eV provides for many atoms/molecules an extremely low collision probability. This resonance phenomenon is called the “Ramsauer effect” [6] and is described by the quantum mechanical scattering theory. A simplified explanation is based on the appropriate de Broglie wavelength of the electron in the range of the atomic/molecular diameter which strongly reduces the interaction with the neutral atom or molecule.

The *inelastic collisions* in nonthermal plasmas are characterized by the transfer of translational energy into internal energy of the neutral/charged atomic or molecular target particle under consideration of the quantum states (electronic, vibration, rotation) and the selection rules for transitions between the quantum states. In contrast to the elastic collisions the inelastic collisions are usually characterized by a specific threshold energy (ε_{thres}) or activation energy (ε_{act}). The inelastic collisions of electrons are of great significance in plasmas for the production and recombination of charge carriers in the plasma volume and therefore for the sustainment of the plasma state. Furthermore, the inelastic electron collisions are the source of excited and chemically reactive particles.

Inelastic collisions between electrons and neutrals with relative translational energy lower than the ionization threshold may produce electronic excited neutral atoms in resonant or metastable levels, and, in the case of molecules the electronic

excitation is combined with change of the vibrational and rotational quantum states, or the dissociation of the molecule if the excited electronic molecular state is described by a repulsive potential energy.

For the designation of the electronic energy levels of atoms and diatomic molecules the following spectroscopic notation is used

$$\text{Atom: } nl^w \ 2S+1 L_j \quad \text{Diatom: } nl^w \ 2S+1 \Lambda_\Omega$$

with the main quantum number n , the angular momentum l , the number of electrons in the shell w , the resulting spin S , the multiplicity $2S + 1$, the resulting angular momentum L ($L = 0, 1, 2, \dots$ corresponding to energy levels indicating the S, P, D, \dots states), the total angular momentum $J = L + S$ which represents the LS coupling in the case of light atoms, and in the case of diatomic molecules $\Omega = \Lambda + \sum_{g,u}^{+, -}$ represents the projection of the corresponding momentum vectors onto the internuclear axis in Greek letters with the addition + or - as well as g or u describing the symmetry properties of the electronic wave function. The convention for the state assignment in molecules are X for the ground state, A, B, \dots for excited states of the same multiplicity as the ground state X , and a, b, \dots for excited states of different multiplicity as X .

An electric dipole transition $\nu(E_H - E_L)/h$ with $\lambda = c/\nu$ is permitted if the following selection rules are complied: $\Delta L = 0, \pm 1$, $\Delta J = 0, \pm 1$ and $\Delta S = 0$ for atoms, and $\Delta \sum = 0, u \leftrightarrow g$ for the molecules. It is to be noted that $\Delta L = 0$ and $\Delta J = 0$ is not allowed if the angular momentums of both states involved are zero.

The total energy of the molecule expressed in terms of the wavenumber [cm^{-1}] is given by $T_{\text{tot}} = T_E + G(v) + F(J)$ involving the electronic term T_E as well as the terms for vibrational G and rotational F excitation with corresponding quantum numbers v and J , respectively. The selection rules are $\Delta v = \pm 1$ (heteronuclear), $\pm 2, 3, \dots$ and $\Delta J = 0, \pm 1$, $(+ \leftrightarrow -)$ assigned to the P, Q , and R branch of the rotational spectrum. If $\Lambda = 0$ for both states then the Q -branch is forbidden. The probability of the electronic molecule transitions with a corresponding change of rotational and vibrational quantum states is determined by the Franck-Condon $q_{v,v}$ and the Hön-London $S_{nJ,nJ}$ factors, respectively [7–9].

An overview about the energy levels and transitions in atoms provide the Grotrian diagram, as shown exemplarily for atomic hydrogen in Figure 3.12.

The Table 3.4 presents some well-known permitted radiative transitions in neutral atoms which are often used in plasma diagnostics by optical emission spectroscopy.

Figure 3.13 shows exemplarily the potential energy curves of the hydrogen molecule for selected electronic excited molecular states.

Furthermore, the production of long-lived metastable excited atoms or molecules plays an important role in nonthermal plasmas because of the storage of internal energy. For atoms or molecules excited in metastable energy levels the radiative electric dipole transition in lower energy levels is forbidden. Table 3.5 represents a selection of relevant atoms and molecules and their metastable energy levels.

The *electron impact ionization* of neutral gas atoms and molecules in nonthermal plasmas is the main channel to generate free charged particles like electrons and positive ions, e.g., the electron impact ionization of ground state argon atom with threshold (ionization) energy of 15.76 eV, see also Table 3.6.

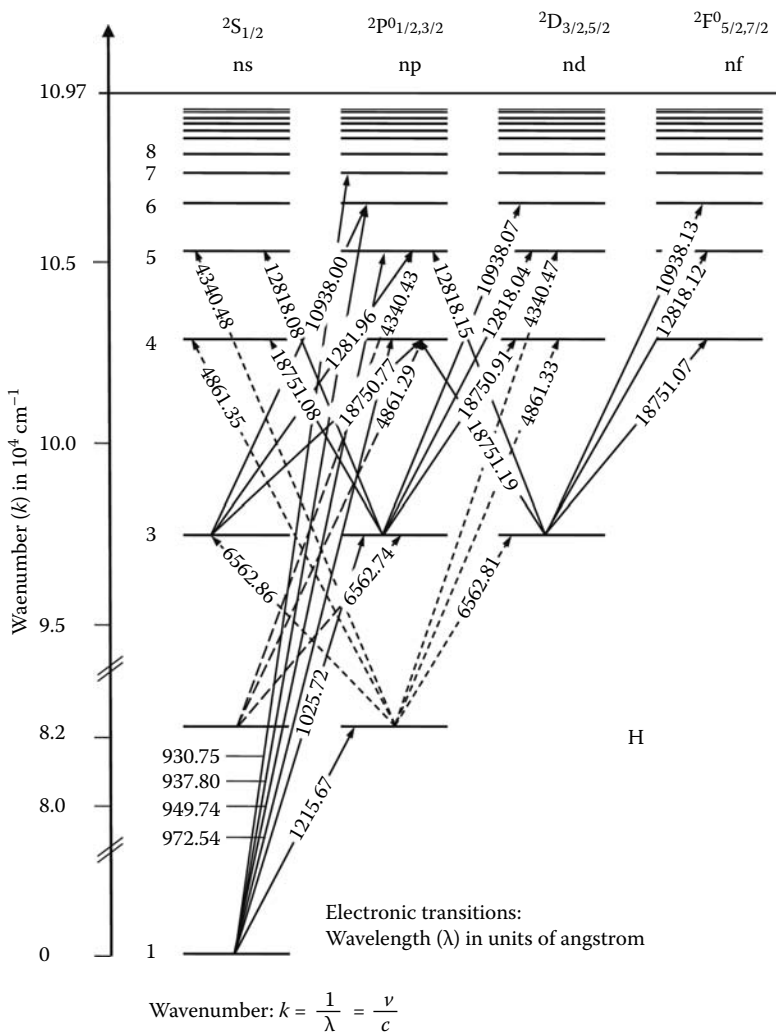


FIGURE 3.12 Combined partial energy levels Grotian diagram for the hydrogen atom. (From Radzig, A.A. and Smirnov, B.M., *Reference Data on Atomic, Molecules and Ions*, Springer Series Chemical Physics, Vol. 31, Springer Verlag, Berlin, Germany, 1985.)



Furthermore, in the case of electronegative gases, the electron may be captured and a stable negative ion is produced, e.g., the *dissociative electron attachment* reaction for oxygen molecule.

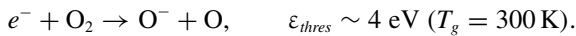


TABLE 3.4
Selected Atomic Transitions in Helium, Argon, Hydrogen, and Oxygen

Atom	λ [Å]	Intensity [a.u.]	E_L [eV]	E_H [eV]	Transition	J	A [10^8 s^{-1}]
He	3888.648	5.000	19.82	23.01	$2s^3S-3p^3P^0$	1-2, 1, 0	$0.09478 \pm 1\%$
Ar	7503.8685	700	11.83	13.48	$4s^1P_1-4p^1S^0$	1-0	$0.472 \pm 25\%$
Ar	7635.1056	500	11.55	13.17	$4s^3P_2^0-4p^1D_2$	2-2	$0.274 \pm 25\%$
H_α	6562.86				$2p^2P_{1/2,3/2}^0-3s^2S_{1/2}$		
H_α	6562.81				$2p^2P_{1/2,3/2}^0-3pD_{3/2,5/2}$		
H_α	6562.74				$2s^2S_{1/2,3/2}-3pP_{1/2,3/2}^0$		
O	7775.388	26				2-1	
O	7774.166	27	9.14	10.47	$3s^5S^0-3p^3P$	2-2	$0.34 \pm 10\%$
O	7771.934	28				2-3	
O	8446.758	29				1-1	
O	8446.359	30	9.52	10.99	s^3S-3p^3P	1-2	
O	8446.250	27				1-0	

Source: Striganov, A.R. and Sventitskii, N.S., *Tables of Spectral Lines of Neutral and Ionized Atoms*, IFI/Plenum, New York, 1968.

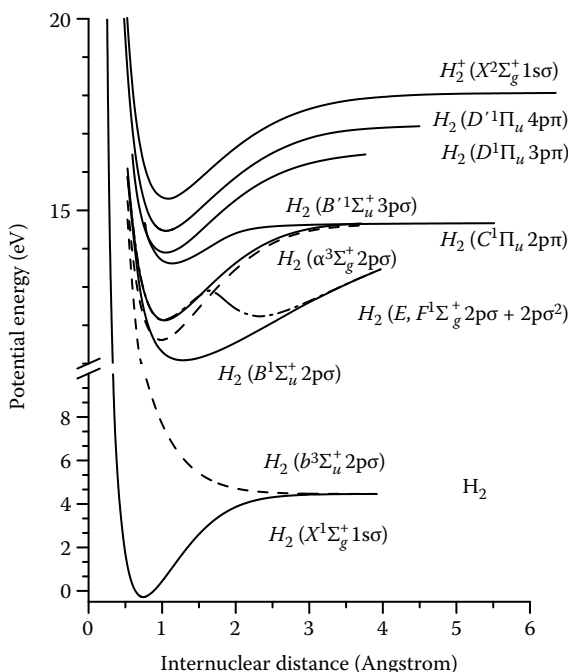


FIGURE 3.13 Energy level diagram of the hydrogen molecule. (Data from Schmoranz, H. and Zietz, R., *Phys. Rev. A*, 18, 1472, 1978.)

TABLE 3.5**Examples of Metastable Excited States of Rare Gas Atoms and Molecules**

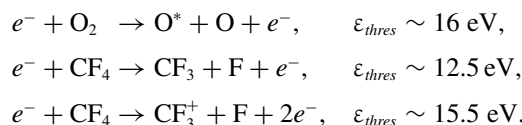
Atom/Molecule	Atomic/Molecular State	Internal Energy [eV]	Lifetime [s]
He	1S	20.6	$2 \cdot 10^{-2}$ [13]
He	3S	19.82	$6 \cdot 10^{-5}$
Ne	3P_0	16.7	
Ne	3P_2	16.62	
Ar	3P_0	11.72	44.9
Ar	3P_2	11.55	55.9
N ₂	$A^3\Sigma_u^+$	6.17	2
O ₂	a ¹ Δ	0.98	

TABLE 3.6**Ionization Energy and Electron Affinity of Selected Atoms and Molecules**

Atom/Molecule	Ionization Energy		Electron Affinity	
	ε_{ion} [eV]	Atom/Molecule	ε_{aff} [eV]	Atom/Molecule
He	24.59	H	0.754	
Ar	15.76	C	1.263	
H	13.60	O	1.461	
H ₂	15.43	F	3.401	
N	14.53	F ₂	3.080	
N ₂	15.58	Cl	3.610	
O	13.61	Cl ₂	2.380	
O ₂	12.07	CH	1.238	
CH ₂	10.39	CH ₂	0.652	
CF ₂	11.44	CF ₂	0.165	

Source: Lide, D.R., ed., *CRC Handbook of Chemistry and Physics*, CRC Press, Boca Raton, FL, 2001.

Besides the ionization of neutral gas atoms and molecules or the formation of negative ions, the inelastic electron–molecule collisions also represent an important channel for production of *chemical reactive species* due to excitation of particles and/or dissociation of molecules in atomic and molecular radicals, e.g.,



The produced atomic and molecular radicals may initiate manifold plasma chemical reactions in further collision processes in the plasma volume or at plasma boundaries.

More in detail, the inelastic electron–molecule interaction results in a highly excited intermediate molecule complex. The electronic transitions in molecules takes place at constant internuclear distance and the transition probability is determined by the Franck-Condon factors which imply the optimum overlapping of the wave functions of the considered electronic states. The relaxation of the excited molecule complex may result in the stabilization of the complex if a binding molecular state exists and the excess energy can be distributed in internal degrees of freedom or transferred in collisions with the background gas at higher gas pressure like that in swarm experiments. In the case of a repulsive potential curve the relaxation of the molecule complex results in dissociation and the products are excited or they have excess in translational energy, $A^* + B^+ (+\varepsilon_T)$, see Figure 3.14.

The *charge transfer collisions* between positive ions and neutrals are characterized by the transfer of an electron from the neutral to the positive ion without exchange of translational energy. Charge transfer collisions are classified in *resonant* or *nonresonant* collisions concerning the same or different ionization energy of the collision partners, and in *symmetric* or *asymmetric* collisions concerning the same or different nature of the collision partners. As an example, the symmetric and resonant charge transfer collision is observed between a single charged positive argon ion and the neutral argon atom in ground state

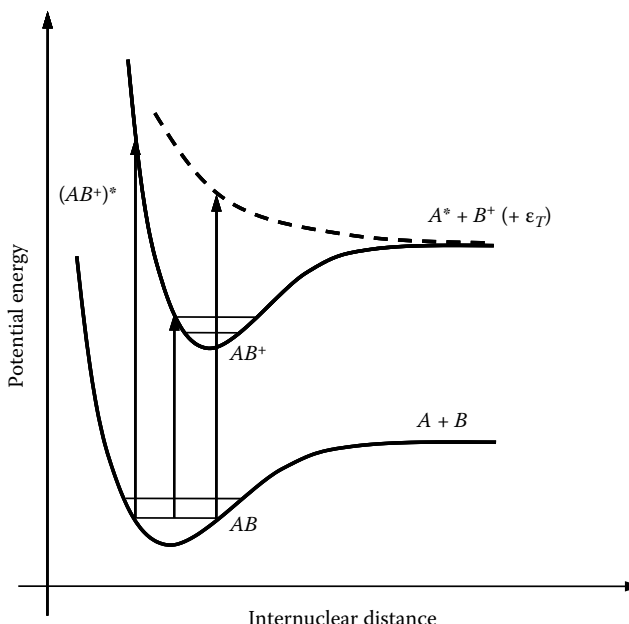
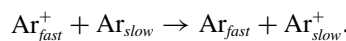
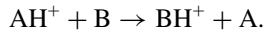


FIGURE 3.14 Principle of direct electron impact ionization of a diatomic molecule. At higher electron energy the highly excited ionized molecule complex results in dissociative ionization.

In the plasma boundary sheath the positive ions gain translational energy in the electric space charge field and the charge transfer collisions in the sheath represent a source of fast neutrals.

Further important inelastic collisions in nonthermal plasmas are the *ion–molecule reactions*, which are based on the polarization interaction and the capture of the charged particle. In dependence on the nature of the collision partners this interaction on short length scale results in the formation of new chemical compounds, e.g., due to the proton exchange reaction



An overview and the classification of the different elementary collision processes in the plasma volume are given in Tables 3.7 and 3.8 including electrons, ions, neutrals, and photons.

3.3.3 COLLISION CROSS SECTION

Any interaction between particles on short length scale in nonthermal plasmas is characterized by their specific collision cross section σ . The knowledge about the cross section for each elementary collision process and its dependence on the translational energy, the internal quantum states of the collision partners, and the scattering angle is of fundamental interest in nonthermal plasma chemistry and physics. For example, the set of collision cross sections is one of the necessary input data in any kinetic modeling of nonthermal plasmas (see Section 3.9), and in the calculation of the macroscopic rate coefficient of elementary collision processes in the fluid modeling, see Sections 3.5 and 3.9.

Simplified, a collision cross section σ may be interpreted as a virtual target area of the particle for a specific interaction with the impinging particle. The total collision cross section can be expressed by the ratio between the number of specific interactions with target particles per unit of time in the infinite volume dV given by the collision frequency $d\nu$ and the current density of the impinging particles ($dj = dn \cdot v$) given by their particle density dn with velocity v .

Total collision cross section:

$$\sigma [\text{m}^2] = \frac{d\nu [\text{s}^{-1}]}{dn \cdot v [\text{s}^{-1} \cdot \text{m}^{-2}]} \quad (3.92)$$

Following, the collision cross section is illustrated and derived for specific interactions between two particles.

3.3.3.1 Gas Kinetic Cross Section

The elastic neutral–neutral collision can be illustrated by use of the hard sphere model and the construction of a geometric target area, see Figure 3.15. The hard sphere cross

TABLE 3.7
Overview and the Classification of the Different Elementary Collision Processes of Electrons in the Plasma Volume

With atoms

$e^- + A \rightarrow A + e^-$	Elastic electron scattering	1
$e^- + A \rightarrow A^{*/m} + e^-$	Excitation of atoms, inelastic electron scattering	2
$A^{*/m} \rightarrow A + h\nu$	Spontaneous de-excitation	3
$e^- + A^{*/m} \rightarrow A^{**} + e^-$	Stepwise excitation	4
$e^- + A^{*/m} \rightarrow A + h\nu + e^-$	Collisional induced de-excitation	5
$e^- + A^{*/m} \rightarrow A + e^- + \varepsilon_T$	Super elastic collisions	6
$e^- + A \rightarrow A^+ + 2e^-$	Ionization of atoms	7
$2e^- + A^{*/m} \rightarrow A^+ + 2e^-$	Stepwise ionization	8
$e^- + A \rightarrow A^-$	Attachment	9
$e^- + A^- \rightarrow A + 2e^-$	Detachment	10
$e^- + A^+ \rightarrow A$	Recombination	11
$e^- + A^+ + M \rightarrow A + M$	Three-body collision recombination	12

With molecules

$e^- + AB \rightarrow AB^{*/m} + e^-$	Excitation of molecules	13
$AB^{*/m} \rightarrow AB + h\nu$	Spontaneous de-excitation	14
$e^- + AB^* \rightarrow AB + h\nu + e^-$	Collisional induced de-excitation	15
$e^- + AB \rightarrow A^{(*)} + B + e^-$	Dissociation of molecules	16
$e^- + AB \rightarrow AB^+ + 2e^-$	Ionization of molecules (parent ion)	17
$e^- + AB \rightarrow A + B^+ + 2e^-$	Dissociative ionization	18
$e^- + AB \rightarrow A^* + B^+ + 2e^-$	Dissociative ionization with excitation	19
$e^- + AB \rightarrow A^- + B^+ + e^-$	Ion-pair formation	20
$e^- + AB \rightarrow AB^-$	Parent negative ion formation	21
$e^- + AB \rightarrow A^- + B$	Dissociative attachment	22
$e^- + AB^- \rightarrow AB + 2e^-$	Detachment	23
$e^- + AB^+ \rightarrow AB$	Recombination	24
$e^- + AB^+ + M \rightarrow AB + M$	Three-body collision recombination	25

section (3.93) is calculated using the gas kinetic radius of each atom or molecule, a_1 and a_2 , or the corresponding impact parameter b_{HS}

$$\sigma_{HS} = \pi (a_1 + a_2)^2 = \pi \cdot b_{HS}^2. \quad (3.93)$$

More in detail, the physical nature of the interaction between neutral particles is based on the Coulomb interaction, e.g., due to the short-range Van der Waals potential. Therefore, the impact parameter is in the order of the gas kinetic atom/molecule radius.

3.3.3.2 Polarization Cross Section

In weakly ionized plasmas the collisions of charged particles (electrons, ions) with neutral particles dominate. At low relative translational energy the elementary collision process between a charged particle and a neutral is determined by the short-range

TABLE 3.8
Overview and the Classification of the Different Elementary Collision Processes of Heavy Particles in the Plasma Volume
Ion processes

$A^+ + B \rightarrow A + B^+$	Charge transfer (asymmetric, nonresonant)	26
$A^+ + A \rightarrow A + A^+$	Charge transfer (symmetric, resonant)	27
$A^m + B \rightarrow A + B^+ + e^-$ → $AB^+ + e^-$	Penning ionization	28
$A^m + A^m \rightarrow A + A^+ + e^-$	Pair ionization	29
$A^* + A \rightarrow A_2^+ + e^-$	Hornbeck-Molnar (associative) ionization	30
$A^+ + BC \rightarrow AC^+ + B$	Ion–molecule reaction	31
$A^+ + B^- \rightarrow A + B$ → AB	Ion–ion recombination	32
$A^- + B \rightarrow A + B + e^-$	Collisional detachment	33
$A^- + B \rightarrow AB + e^-$	Associative detachment	34
<i>Neutral processes</i>		
$A^* + B \rightarrow A + B^*$	Excitation transfer	35
$AB^* + C \rightarrow A + B + C$	Dissociation	36
$A + BC \rightarrow AC + B$	Chemical reactions	37
$AB + CD \rightarrow AC + BD$	Two-body molecule reaction	
$AB + CD \rightarrow ABC + D$		
$R + BC \rightarrow RC + B$	Chemical reactions with radical R in the plasma	38
$A^* + BC \rightarrow AC + B$	Chemical reactions with excited atom or molecule	39
$A^+ BC + M \rightarrow AB + C + M$	Three-body reaction (or wall as third partner)	40
<i>Photon processes</i>		
$A + h\nu \rightarrow A^*$	Photoexcitation	41
$A + h\nu \rightarrow A^+ + e^-$	Photoionization	42
$AB + h\nu \rightarrow A + B$	Photodissociation	43
$A^* + h\nu \rightarrow A + h\nu + h\nu$	Induced emission	44

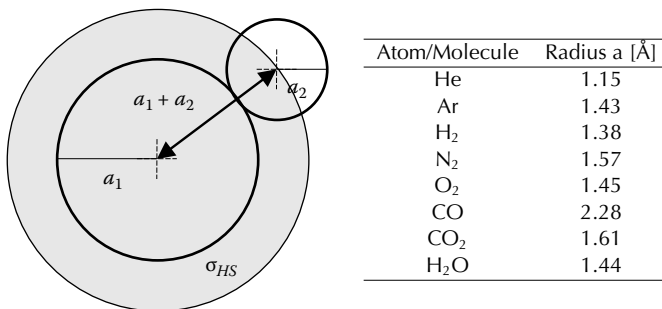

FIGURE 3.15 Scheme of the hard sphere collision cross section and examples of gas kinetic atom/molecule radius. (From Heinze, W., *Einführung in die Vakuumtechnik, Vol. I: Physikalische Grundlagen der Vakuumtechnik*, Verlag Technik, Berlin, Germany, 1955.)

TABLE 3.9
Polarizabilities of Selected Atoms and Molecules

Atom/Molecule	Averaged Polarizability	
	$\alpha_{cgs} [10^{-24} \text{ cm}^3]$	$\alpha_{SI} = [\text{A V}^{-1} \text{s m}^2] = 4\pi\epsilon_0 \cdot 10^{-6} \cdot \alpha_{cgs} [\text{cm}^{-3}]$
He	0.18	0.21
Ar	1.64	1.82
H	0.67	0.74
H ₂	0.81	0.90
N	1.10	1.22
N ₂	1.74	1.94
O	0.80	0.89
O ₂	1.58	1.76
CF ₄	3.84	4.27
CO ₂	2.91	3.24
CH ₄	2.60	2.89
NH ₃	2.81	3.13

Source: Lide, D.R., ed., *CRC Handbook of Chemistry and Physics*, CRC Press, Boca Raton, FL, 2001.

polarization scattering due to the interaction between a permanent or induced dipole moment of the neutral and the electric Coulomb field of the charged particle. For higher relative energy the interaction time is much lower compared with the characteristic time constant for polarization of the neutral particle. In that case the interaction is similar to the Coulomb interaction but with maximum impact parameter in the order of the atomic radius.

Neglecting a permanent dipole moment, an induced dipole moment \vec{p}_{ind} of the neutral particle in an external electric field is determined by the atomic or molecular polarizability α of the neutral particle, see Table 3.9. Equation 3.94 describes a linear and isotropic relation between the polarizability and the local electric field \vec{E}

$$\vec{p}_{ind} = \alpha \cdot \vec{E}. \quad (3.94)$$

Generally, the polarizability α represents a tensor quantity which considers the anisotropic polarization of the atom or molecule in the electric field, and the electric dipole moment may be determined by a further additive term with quadratic electric field in the case of strong field strength. The static polarizability can be applied if the temporal change of the electric field strength is much lower than the electron orbit frequencies in the atom, otherwise the averaged polarizability can be used in calculations.

The force on the electric dipole moment in the inhomogeneous electric field (3.95) is used to calculate the change of the potential energy (3.96) of the point charge with distance r to the polarized neutral target particle, and the attracting polarization potential (3.97).

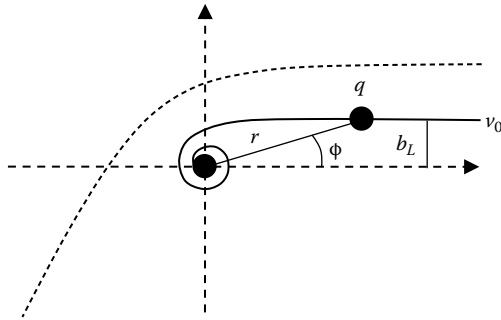


FIGURE 3.16 Polarization interaction between the charged particle (point charge q) and polarized neutral particle in the center of the laboratory system. At the impact parameter $b \leq b_L$ the charged particle is captured in the attractive potential.

$$\vec{F}_{pol} = (\vec{p}_{ind} \cdot \text{grad}) \vec{E} = (\alpha \vec{E} \cdot \text{grad}) \vec{E}. \quad (3.95)$$

$$\begin{aligned} \Delta \varepsilon_{pot} &= - \int \vec{F}(\vec{r}) \cdot d\vec{r} = - \int \alpha \cdot E(r) \cdot \frac{dE}{dr} dr \\ &= - \int \alpha \cdot E \cdot dE = -\alpha \frac{E^2}{2}. \end{aligned} \quad (3.96)$$

$$\varepsilon_{pot}(r) = \varepsilon_{pol}(r) = -\frac{\alpha_{SI} \cdot q^2}{2 \cdot (4\pi\varepsilon_0)^2 \cdot r^4}. \quad (3.97)$$

The scattering of the charged particle in the polarization potential is described by the conservation of the mechanical energy (3.98) and the angular momentum (3.99) in the laboratory system for polar coordinates, see Figure 3.16. The elimination of the angular velocity and the condition of vanishing radial velocity at the minimal radial distance r_0 results in a quadratic equation (3.100) for the determination of r_0 .

$$\varepsilon = \frac{m}{2} \cdot v_0^2 = \frac{m}{2} \cdot \left[\left(\frac{dr}{dt} \right)^2 + r^2 \left(\frac{d\phi}{dt} \right)^2 \right] - \frac{\alpha_{SI} \cdot q^2}{2 \cdot (4\pi\varepsilon_0)^2 \cdot r^4}. \quad (3.98)$$

$$m \cdot v_0 \cdot b = m \cdot r^2 \cdot \frac{d\phi}{dt} \rightarrow \frac{d\phi}{dt} = \frac{b \cdot v_0}{r^2}. \quad (3.99)$$

A real solution of (3.100) exists for the case that the impact parameter satisfies the relation (3.101).

$$(r_0^2)^2 - b^2 \cdot r_0^2 + \frac{\alpha_{SI} \cdot q^2}{(4\pi\varepsilon_0)^2 \cdot v_0^2 \cdot m} = 0. \quad (3.100)$$

$$\frac{b^4}{4} - \frac{\alpha_{SI} \cdot q^2}{(4\pi\varepsilon_0)^2 \cdot v_0^2 \cdot m} \geq 0. \quad (3.101)$$

Solving (3.101) for the minimum impact parameter $b_{min} = b_L$ and taking into account the relative velocity v_r of the particles and the reduced mass m_{red} in the center of mass

system the *Langevin capture cross section* σ_L (3.102) is found

$$\sigma_L = \pi \cdot b_L^2 = \left(\frac{\alpha_{SI} \cdot q^2}{\varepsilon_0^2 \cdot m_{red} \cdot v_r^2} \right)^{1/2} \sim \frac{1}{v_r} \quad (3.102)$$

with $v_r = |\vec{v}_1 - \vec{v}_2|$ and $m_{red} = m_1 \cdot m_2 / (m_1 + m_2)$. The capture cross section depends reciprocally on the relative velocity.

In the case of polar molecules with permanent electric dipole moment the additional interaction potential has to be considered and the capture cross section has to be extended by a supplemental term depending on the temperature. The capture of the charged particles by neutrals in nonthermal plasmas has importance for negative ion formation due to electron attachment, and for ion–molecule reactions. The elastic scattering in the attractive polarization potential with impact parameter $b > b_L$ has to be described by a similar way as the scattering of a point charge in the Coulomb potential to find the scattering angle and particle trajectories, see Section 3.3.3.3.

3.3.3.3 Coulomb Scattering

The interaction between two charged particles is described by the classical Coulomb scattering and is illustrated in Figure 3.17 for the case of the repulsive Coulomb potential in the laboratory system.

It is useful to introduce the differential scattering cross section (3.103) which provides the scattering of charged particles in the angle ϑ at the given impact parameter $b(\vartheta)$.

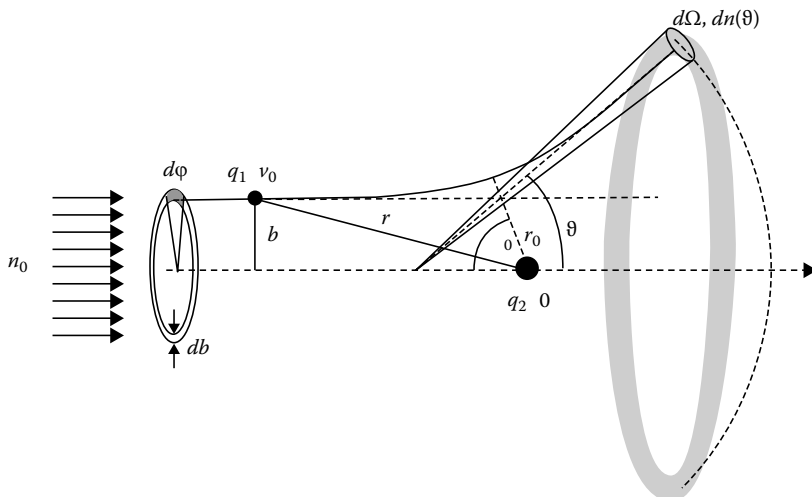


FIGURE 3.17 Illustration of the differential scattering of charged particles in the repulsive Coulomb potential with the impact parameter b from $b \cdot d\varphi \cdot db$ into the solid angle $d\Omega = \sin \vartheta \cdot d\vartheta \cdot d\varphi$ in the laboratory system.

$$\sigma_{diff}(\vartheta) \equiv \left(\frac{d\sigma}{d\Omega} \right) = \frac{1}{n_0} \cdot \frac{2\pi \cdot b \cdot db \cdot n_0}{2\pi \cdot \sin \vartheta \cdot d\vartheta} = \frac{b}{\sin \vartheta} \cdot \frac{db}{d\vartheta}. \quad (3.103)$$

The factor 2π in (3.103) results from the symmetry of the scattering problem and the integration over the complete angle φ , see Figure 3.17.

The integration over the solid angle provides the total scattering cross section.

$$\sigma_{total} = \int \frac{\partial \sigma(\Omega)}{\partial \Omega} \cdot d\Omega = \int \sigma_{diff} \cdot d\Omega. \quad (3.104)$$

The impact parameter for the Coulomb scattering $b_{Coul}(\vartheta)$ can be found by use of the invariance of the mechanical energy (3.105) and angular momentum (3.106) of the charged projectile particle with charge q_1 and the mass m in the electric Coulomb field of the point charge q_2 in the center of the laboratory system, similar to the polarization scattering discussed above.

$$\varepsilon = \frac{m}{2} \cdot v_0^2 = \frac{m}{2} \cdot \left[\left(\frac{dr}{dt} \right)^2 + r^2 \left(\frac{d\phi}{dt} \right)^2 \right] + \varepsilon_{Coul}(r) \quad (3.105)$$

$$\varepsilon_{Coul}(r) = \frac{q_1 \cdot q_2}{4\pi \varepsilon_0 \cdot r}.$$

$$m \cdot v_0 \cdot b = m \cdot r^2 \cdot \frac{d\phi}{dt} \quad \rightarrow \quad \frac{d\phi}{dt} = \frac{v_0 b}{r^2}. \quad (3.106)$$

The rearrangement of Equations 3.105 and 3.106 for the radial and angular velocity, respectively, and following the ratio of both quantities results in

$$\frac{d\phi/dt}{dr/dt} = \frac{d\phi}{dr} = \frac{v_0 \cdot b/r^2}{\sqrt{v_0^2 - v_0^2 \cdot b^2/r^2 - 2 \cdot \varepsilon_{Coul}(r)/mv_r^2}}. \quad (3.107)$$

Replacing the velocity and mass in the laboratory system by the relative velocity and the reduced mass in the center of mass system, the integral (3.108) has to be solved, see detailed calculation in [36]

$$\int_0^{\phi_0} d\phi = \phi_0 = \int_{r_0}^{\infty} \frac{b \cdot dr}{r^2 \cdot (1 - b^2/r^2 - 2\varepsilon_{Coul}/m_{red}v_r^2)^{1/2}}. \quad (3.108)$$

Taking into account the scattering angle $\vartheta = \pi - 2\phi_0$, the impact parameter b_{Coul} (3.109) in dependence on the scattering angle ϑ is found, see [36]

$$b_{Coul} = \frac{q_1 q_2}{4\pi \cdot \varepsilon_0} \cdot \frac{1}{m_{red} \cdot v_r^2} \cdot \cot \frac{\vartheta}{2}. \quad (3.109)$$

Further, with the known impact parameter b_{Coul} , the differential collision cross section of the Coulomb scattering is achieved

$$\sigma_{diff}(\vartheta, v_r) = \left(\frac{q_1 q_2}{8\pi \cdot \varepsilon_0 \cdot m_{red} \cdot v_r^2} \right)^2 \frac{1}{\sin^4 \vartheta/2} \sim \frac{1}{v_r^4}. \quad (3.110)$$

The total Coulomb collision cross section (3.111) from the integral (3.104) is calculated by use of the minimum and maximum impact parameter in plasmas given by the Landau (l_L) and the Debye (λ_D) length, and their corresponding scattering angles ϑ_{max} and ϑ_{min} from (3.109)

$$\sigma_{total}^{Coul} = \int_{\vartheta_{min}}^{\vartheta_{max}} \sigma_{diff} \vartheta \cdot 2\pi \cdot \sin \vartheta \cdot d\vartheta = \frac{(q_1 q_2)^2}{4\pi \cdot \varepsilon_0^2} \cdot \frac{\ln(\lambda_D/l_L)}{m_{red}^2 \cdot v_r^4}. \quad (3.111)$$

In non-thermal plasmas the collisions of charged particles (electrons or ions) with neutral particles dominate. Nevertheless, the elastic Coulomb scattering between electrons is important for the efficient exchange of their translational energy and the formation of the electron energy distribution function. An estimation of the total electron–electron scattering cross section, using $T_e = 10^4$ K and $m_{red} \cdot v_r^2 \sim k_B T_e$, results in $\sigma_{total}^{ee} \sim 3 \cdot 10^{-12}$ cm² which is significantly larger than the gas kinetic cross section $\sigma_{gas} \sim 10^{-15}$ cm² of an electron–neutral collision.

3.3.3.4 Electron Attachment Cross Section

The interaction between an electron and atom or molecule with an electron affinity ε_{aff} and a polarizability α , see Tables 3.6 and 3.9, can result in the electron capture and the formation of a negative ion by direct or dissociative electron attachment [16]. Under consideration of the specific atomic or molecular energy levels and electronic transition probabilities, a stable negative ion may be produced if the excess of energy (electron affinity and electron translational energy) is distributed into internal degrees of freedom or into translational energy of the molecule fragments in the case of dissociation. For example, the negative ions in CF₄ are produced by dissociative electron attachment, only, such as CF₃⁻ and F⁻, see Figures 3.18 and 3.19.

The characteristic resonance-like shape of the attachment cross sections is seen exemplarily for CF₄ in Figure 3.19, resulting from the polarization interaction and the specific potential energy curves of the molecule in Figure 3.18.

3.3.3.5 Electron Impact Excitation and Ionization Cross Section

The electron impact cross section for electronic excitation or ionization of atoms and molecules in dependence on the electron energy can be determined by extensive quantum physical calculation involving different approximations [19]. Nevertheless, the cross sections are often experimentally determined in specially designed electron beam experiments, e.g., [20,21].

In particular, the electronic excitation of atoms and molecules by electron impact and their radiation (VUV-vis-NIR) due to spontaneous de-excitations are important elementary processes in nonthermal plasmas. The emitted radiation is often analyzed

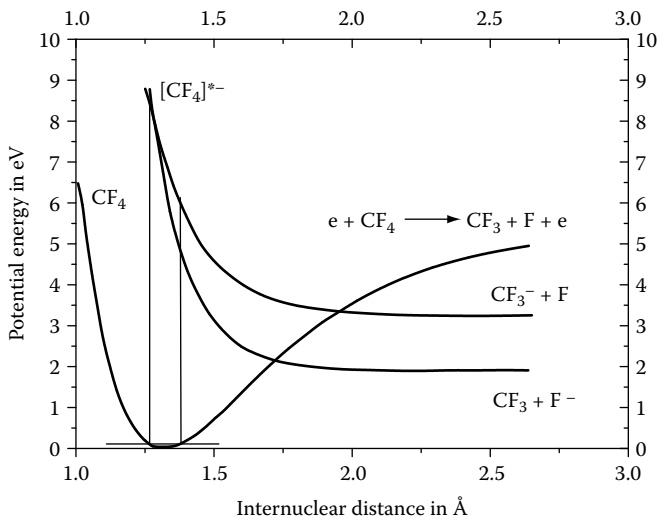


FIGURE 3.18 $\text{CF}_3\text{-F}$ potential energy and dissociative electron attachment in CF_4 . (Data from Spyrou, S.M. et al., *J. Chem. Phys.*, 78, 7200, 1983.)

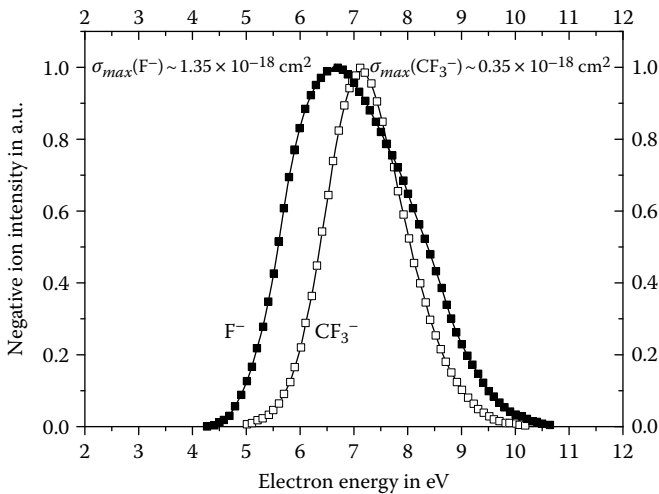


FIGURE 3.19 Negative ion production F^- (maximum at 6.7 eV) and CF_3^- (maximum at 7.1 eV) due to dissociative electron attachment of CF_4 [17], and their maximum cross sections [18]. (Data from Spyrou, S.M. et al., *J. Chem. Phys.*, 78, 7200, 1983; Iga, I., *Z. Phys. D Atoms, Mol. Clus.*, 24, 111, 1992.)

in plasma diagnostics by optical emission spectroscopy. The measured emission intensity of characteristic atomic lines and molecular bands provide immediately qualitative information about the plasma composition. The quantitative analysis is much more complicated to determine particle densities, temperatures, or electric field strength, line shape or shift from the emission intensity. The intensity of the emission

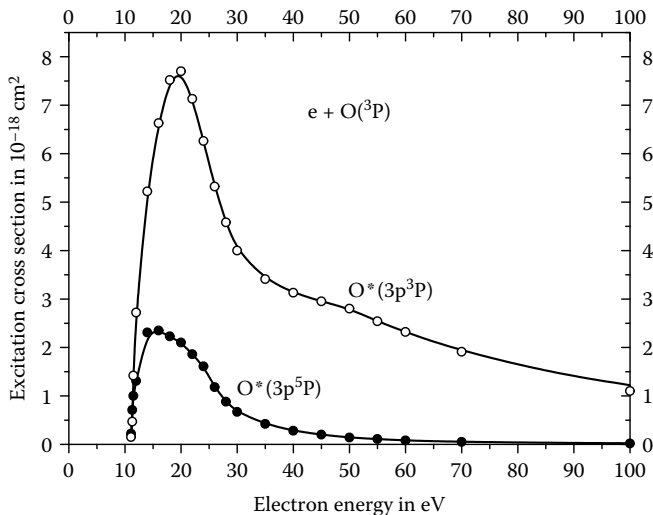


FIGURE 3.20 Electron excitation cross section of ground state atomic oxygen $\text{O}(^3\text{P})$ into the levels $\text{O}(3\text{p}^3\text{P})$ and $\text{O}(3\text{p}^5\text{P})$ in dependence on the electron energy according to the listed data in [22]. (Data from Laher, R.R. and Gilmore, F.R., Updated excitation and ionization cross section for electron and impact on atomic oxygen, Technical Report, R & D Associates Marina Del Rey, CA, 1988.)

spectrum is influenced by many factors, e.g., the electron energy distribution function, the direct or dissociative excitation, the cascade processes, the branching, the radiation transport, and the collision of excited particle which may result in de-excitation without radiation. All these factors have influence on the emission intensity, the line broadening, or the ro-vibrational band structures of electronic transitions in molecules. Generally, the quantum physics of the elementary excitation and de-excitation processes and the collision-radiation model have to be involved to achieve exactly the appropriate information from the measured emission spectrum for further analysis.

As an example, the electron impact excitation cross section of atomic oxygen from the ground state $\text{O}(^3\text{P})$ into the levels $\text{O}(3\text{p}^5\text{P})$ and $\text{O}(3\text{p}^3\text{P})$ is shown in Figure 3.20 [22]. These states are the upper levels of the intensive optical transitions at 777 and 844 nm into the $\text{O}(3s^1\text{S})$ and $\text{O}(3s^3\text{S})$ state, respectively.

The optical emission cross section σ_{opt} can be directly determined from measured data in electron beam experiments according to (3.112) [20,23].

$$\sigma_{opt}(i \rightarrow j) = \frac{e}{n_{\text{gas}} \cdot L \cdot I_e} \cdot \left[4\pi \cdot A_s \cdot F(\lambda, T) \cdot \Delta\lambda \cdot \frac{\Omega_s \cdot \gamma_s(\lambda) \cdot R_c}{\Omega_c \cdot \gamma_c(\lambda) \cdot R_s} \right] \quad (3.112)$$

with I_e the electron current, L path length of the electron beam, and n gas number density.

The terms in the bracket describe the measured total photon flux per second for the atomic transition $i \rightarrow j$, with an effective radiation area of the standard

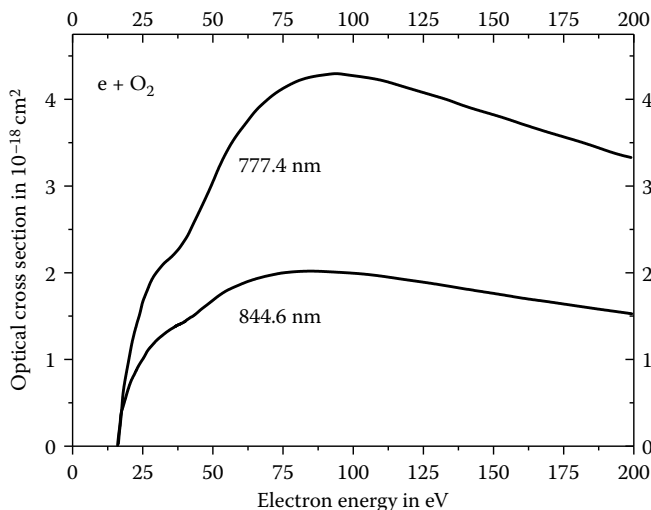


FIGURE 3.21 Optical emission excitation cross section for atomic oxygen multiplet radiation at 777.4 and 844.6 nm from dissociative excitation of oxygen molecule. (Data from Schulman, M.B. et al., *Phys. Rev. A*, 32, 2100, 1985.)

lamp A_s , the solid angle of observation Ω , the spectral transmittance of the light path $\gamma(\lambda)$, the measured photomultiplier signal R without background and dark current with the index s for the reference measurements with the standard lamp. The function $F(\lambda, T) \cdot \Delta\lambda$ is the photon emission rate of the standard lamp at the operating temperature T in the interval between λ and $\lambda + \Delta\lambda$, whereas $\Delta\lambda$ is the spectral passband by the monochromator. The experimentally determined optical emission excitation cross sections of the two prominent multiplet transition of atomic oxygen at 777 and 844 nm from the dissociative electron impact excitation of molecular oxygen are shown in Figure 3.21. The shoulder observed at about 35 eV has its origin from additional contribution of the dissociative excitation of atomic oxygen from the molecular oxygen ion [20].

The *electron impact ionization* is the most prominent elementary collision process for charged species generation in the volume of nonthermal plasmas. The ionization of a neutral atom or molecule due to the collision with an electron has to be described exactly by quantum physics and needs extensive calculations. Already the single ionization of a neutral atom represents a three-body problem. For the calculation of the ionization cross section, mostly methods of the perturbation theory are applied using the Born approximation. Here, the wave function of the free electron is expressed by partial wave development. This can be used if the scattering potential of the neutral is small compared with the energy of the impinging electron. In result the ionization cross section at higher energy is proportional to $\ln E/E$. Taking into account specific interaction potentials, the different quantum mechanical approximations, such as *Coulomb-Born-approximation* and the *distorted plane wave approximation*, provide reliable results in special cases. Therefore, semiclassical

formalisms are applied for the estimation of ionization cross sections, for example, the formalism of Lotz [24], Gryzinski [25], Born-Bethe [26], Deutsch-Märk [27], or Kim [28,29].

For example, the formalism by Gryzinski provides for the ionization cross section the formula

$$\sigma_{nl} = 4\pi \cdot a_0^2 \cdot \xi_{nl} \cdot \left(\frac{\varepsilon_{ion}^H}{\varepsilon_{nl}} \right) \cdot \frac{1}{U} \cdot \left(\frac{U-1}{U+1} \right)^{3/2} \cdot \left[1 + \frac{2}{3} \cdot \left(1 - \frac{1}{2U} \right) \cdot \ln (2.7 + (U-1)^{1/2}) \right] \quad (3.113)$$

with $U \equiv \varepsilon / \varepsilon_{nl}$, σ_{nl} the ionization cross section of the nl sub-shell which emit the electron, ε the energy of the impinging electron, ε_{nl} the electron bond energy in the nl sub-shell, ξ_{nl} the number of equivalent electrons in the nl sub-shell, a_0 the Bohr radius ($5.29 \cdot 10^{-11}$ m), ε_{ion}^H the ionization energy of the hydrogen atom (13.6 eV).

In particular, the electron impact ionization of molecules provides different ionization channels due to the dissociative ionization of the parent molecule. In the case of the dissociative ionization of molecules, the partial ionization cross section $\sigma_n^{ion}(\varepsilon)$ for each positive fragment ion (n) is introduced. The summation over all partial ionization cross sections provides the total ionization cross section $\sigma_{total}^{ion}(\varepsilon)$ of the molecule

$$\sigma_{total}^{ion}(\varepsilon) = \sum_n \sigma_n^{ion}(\varepsilon). \quad (3.114)$$

According to the difficulty in the cross section calculation the measurement of ionization cross sections is unavoidable in many cases. For example, the electron impact ionization of the CF_4 molecule produce no stable ionized parent molecule, but all single charged fragment ions are observed, such as CF_3^+ , CF_2^+ , CF^+ , C^+ , and F^+ , see Figure 3.22.

3.3.3.6 Cross Section of the Neutral–Neutral Reaction at Thermal Velocity with Threshold Energy

The energy dependence of the collision cross section in reaction between neutral particles near the threshold energy can be estimated using the conservation of the angular momentum (3.115) and energy (3.116) for the case of neglecting interaction potential, see also [36].

$$v_{th} \cdot b = v_\phi \cdot b_{eff}. \quad (3.115)$$

Here v_{th} is the thermal velocity and v_ϕ the angular component of the velocity at the effective impact parameter b_{eff} for the reaction:

$$\frac{m_{red}}{2} \cdot v_{th}^2 = \varepsilon = \frac{m_{red}}{2} \cdot v_\phi^2 + \varepsilon_{thres}. \quad (3.116)$$

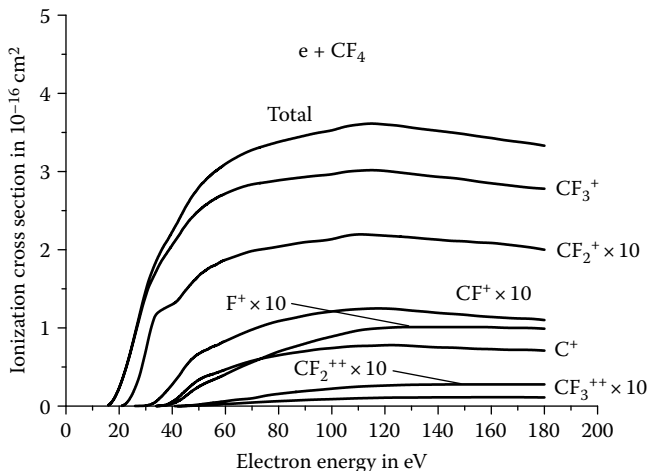


FIGURE 3.22 Partial and total electron impact ionization cross section of CF_4 . (Data from Stephan, K. et al., *J. Chem. Phys.*, 83, 5712, 1985.)

The combination of the equations (3.115) and (3.116) results in (3.117)

$$\varepsilon = \frac{m_{red}}{2} \cdot v_\Phi^2 + \varepsilon_{thres} = \frac{m_{red}}{2} \cdot v_{th}^2 \cdot \frac{\pi \cdot b^2}{\pi \cdot b_{eff}^2} + \varepsilon_{thres} = \varepsilon \cdot \frac{\sigma}{\sigma_{eff}} + \varepsilon_{thres} \quad (3.117)$$

and provides the cross section for $\varepsilon > \varepsilon_{thres}$:

$$\sigma = \sigma_{eff} \cdot \left(1 - \frac{\varepsilon_{thres}}{\varepsilon}\right). \quad (3.118)$$

3.4 PLASMA KINETICS

3.4.1 THE BOLTZMANN EQUATION

Besides the microphysics of elementary collision processes the collective behavior of the plasma particles needs a statistical treatment to determine their movement in the six-dimensional phase space (\vec{r}, \vec{v}) , the production and recombination of charged particles as well as the chemical reactions under nonequilibrium conditions. Here, the knowledge of the single particle velocity distribution function of the different plasma particles (electrons, ions, neutrals) is of fundamental interest to describe the nonthermal plasma as many-particle system. In particular, the knowledge of velocity distribution functions is a precondition for

1. The calculation of the weighted average of local physical quantities which can be directly compared with experimental data
2. The fluid modeling of nonthermal plasmas using conservation quantities and macroscopic transport equations

The most important kinetic equation to calculate velocity distribution functions in nonthermal plasmas at low pressure is the Boltzmann equation (BLME) which describes the evolution of the single particle distribution function $f_i(t, \vec{r}_i, \vec{v}_i)$ in the phase space [5,30]

$$\frac{df_i}{dt} = L(f_i) = \left[\frac{\partial}{\partial t} + \vec{v}_i \cdot \frac{\partial}{\partial \vec{r}} + \frac{\vec{F}}{m_i} \cdot \frac{\partial}{\partial \vec{v}} \right] \cdot f_i = \left(\frac{\partial f_i}{\partial t} \right)_{coll}. \quad (3.119)$$

The function $f_i(\vec{r}_i, \vec{v}_i, t)$ describes the number of particles i in the phase space unit $d^3 r_i \cdot d^3 v_i$ at (\vec{r}_i, \vec{v}_i) and the time t .

The Boltzmann equation consists of two terms:

1. The *flow term* on the left side describes the explicit time dependence, and the particle movement due to macroscopic forces along trajectories in the six-dimensional phase space represented by the Liouville differential operator $L(f_i)$.
2. The *collision term* considers the velocity variation of the particles i as well as the change of the particle identity due to binary collisions in the phase space unit by an integral operator $(\partial f_i / \partial t)_{coll}$ on the right side.

In detail, the *differential operator* describes the explicit time dependence due to relaxation or other time-depending processes, and the particle flow in the phase space controlled by the averaged macroscopic forces F . In the case of nonthermal plasmas the forces have to be considered originating from external electric and magnetic fields as well as the self-consistent electric space charge fields. The *integral operator* includes all essential binary elastic and inelastic particle collisions which are controlled by micro fields and the quantum physics of atomic or molecular interactions at short distances. During the collision the macroscopic forces are neglected.

Generally, any binary collision



may change the translational velocity of the selected species i , their internal energy, or their identity due to ionization, recombination, dissociation, or chemical reactions (see also Figure 3.23). Following, a set of Boltzmann equations has to be taken into account considering the different kind of plasma particles such as electrons, ions, and neutrals.

$$\begin{aligned} \frac{\partial f_i}{\partial t} + \vec{v}_i \cdot \frac{\partial f_i}{\partial \vec{r}} + \frac{\vec{F}}{m_i} \cdot \frac{\partial f_i}{\partial \vec{v}} &= \left(\frac{\partial f_i}{\partial t} \right)_{coll} \\ &= \sum_{\substack{k l m n \\ i \ni k l m n}} \left[\iint d\Omega \cdot d^3 v_k \cdot |\vec{v}_{kl}| \cdot \sigma_{klmn}(|\vec{v}_{kl}|, \Omega) \cdot (f_k \cdot f_l - f_m \cdot f_n) \right]^{(i)}. \end{aligned} \quad (3.121)$$

The summation of the collision integrals in (3.121) involves all gains or losses of the velocity \vec{v}_i in the phase space volume $d^3 \vec{r} \cdot d^3 \vec{v}$ as well as the production or

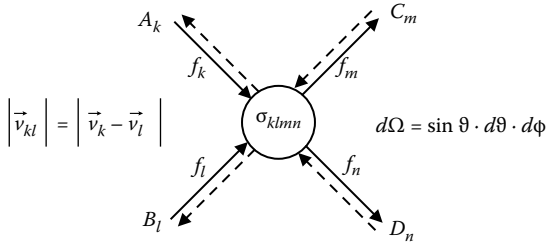


FIGURE 3.23 Scheme of the binary collision process between particles A_k and B_l with velocity distribution function f_k and f_l , the relative velocity v_{kl} , and the collision cross section σ_{klmn} .

consumption of particles i in collisions. Thereby, the different velocity distribution functions f_k, f_l and f_m, f_n in (3.121) consider all binary collisions which are related to the particle i ($i \ni klmn$) with the relative velocity $v_r = v_{kl} = |\vec{v}_k - \vec{v}_l|$ and collision cross section σ_{klmn} (v_r, Ω) depending on the relative velocity and the solid angle.

In the case of elementary processes which involve a third collision partner, e.g., in the case of the three-body recombination or the chemical reaction of third order at higher gas pressure, the collision term contains a triple collision integral, respectively.

A lot of knowledge about the manifold elementary collision processes is necessary, in particular, the collision cross sections in dependence on the translational energy of the collision partners and their internal quantum states to solve the BLME for selected kind of plasma species i .

3.4.2 ELECTRON ENERGY DISTRIBUTION FUNCTION IN NONTHERMAL PLASMAS

In nonthermal plasma physics and chemistry the calculation of the *electron velocity distribution function* is the fundamental task

$$\begin{aligned} \frac{df_e}{dt} &= \frac{\partial f_e}{\partial t} + \vec{v}_e \cdot \frac{\partial f_e}{\partial \vec{r}} - e \frac{(\vec{E}_{ext} + \vec{E}_\rho + \vec{v}_e \times \vec{B})}{m_e} \cdot \frac{\partial f_e}{\partial \vec{v}} \\ &= \left(\frac{\partial f_e}{\partial t} \right)_{coll} = C^{el} + \sum_n C_n^{inel} \end{aligned} \quad (3.122)$$

considering electric and magnetic fields and the terms for elastic electron collisions and the summation over all inelastic collisions involving electrons [31].

Neglecting the magnetic field, the electric field $\vec{E} = \vec{E}_{ext} + \vec{E}_\rho$ from external sources and the electric space charges

$$\epsilon_0 \cdot \text{div} \vec{E}_\rho = \rho = e \int (f_{ion} - f_e) \cdot d^3 v \quad (3.123)$$

has to be considered for the macroscopic force in gas discharges.

Assuming elastic electron–electron collisions, only, and no macroscopic forces, the stationary solution of the BLME provides the well-known isotropic Maxwellian velocity distribution function

$$f_e^0(\vec{v}_e) \cdot d\vec{v}_e \sim \exp\left(-\frac{m_e \cdot v_e^2}{2 \cdot k_B T_e}\right) \cdot d^3 v_e \quad (3.124)$$

and the normalized distribution function $f_e^0(v_e)$, respectively, for the absolute value of the electron velocity

$$\frac{dn_e}{n_e \cdot dv_e} = f_e^0(v_e) = 4\pi \cdot \left(\frac{m_e}{2\pi \cdot k_B T}\right)^{3/2} \cdot v_e^2 \cdot \exp\left(-\frac{m_e \cdot v_e^2}{2 \cdot k_B T_e}\right), \quad (3.125)$$

with $\int_0^\infty f_e^0(v_e) \cdot dv_e = 1$, $f_e^0(v_e) \cdot dv_e = f_e^0(\varepsilon_T) \cdot d\varepsilon_T$, $\varepsilon_T = m_e/2 \cdot v_e^2$ and $dv_e = (2 \cdot m_e \cdot \varepsilon_T)^{-1/2} \cdot d\varepsilon_T$. The electron velocity distribution can be easily converted into the electron energy distribution function (EEDF)

$$\frac{dn_e}{n_e \cdot d\varepsilon_T} = f_e^0(\varepsilon_T) = 2 \cdot \pi^{-1/2} \cdot (k_B \cdot T_e)^{-3/2} \cdot \sqrt{\varepsilon_T} \cdot \exp\left(-\frac{\varepsilon_T}{k_B T_e}\right) \quad (3.126)$$

replacing the electron velocity v_e by the translational energy ε_T .

The electrons in the high energetic tail of the distribution function ($\varepsilon_T > \varepsilon_{thres}$) are able for *excitation* and *ionization* of atoms and molecules and/or *dissociation* of molecules. These inelastic collisions and the charged particle transport in gas discharges due to electric field drift and diffusion cause deviations from the Maxwellian distribution function. Consequently, the statistical description of the electron ensemble in nonthermal plasma by means of the Maxwellian velocity distribution function with the electron temperature T_e is strongly restricted. Nevertheless, the quantity electron temperature is often applied to describe the nonthermal properties and to determine the transport and rate coefficients in dependence on T_e .

In gas discharge physics it is often applied the EEDF in terms of voltage due to the replacement of the translational energy by $\varepsilon_T = e \cdot U$, $d\varepsilon_T = e \cdot dU$, and $k_B \cdot T_e = e \cdot U_e$, respectively

$$\frac{dn_e}{n_e \cdot dU} = f_e^0(U) = 2 \cdot \pi^{-1/2} \cdot U_e^{-3/2} \cdot \sqrt{U} \cdot \exp\left(-\frac{U}{U_e}\right). \quad (3.127)$$

Taking into account the influence of the macroscopic electric field, only, the calculation of the electron velocity distribution function using the BLME may be performed by different approximations concerning the electric field strength in gas discharges. For example, it is applied

1. The *two-term approximation* for weak electric field strength with the isotropic Maxwellian f_e^0 and the small anisotropic f_e^1 term

$$f_e(\vec{v}_e) = f_e^0(v_e) + \frac{\vec{v}_e}{v_e} \cdot f_e^1. \quad (3.128)$$

2. The *multi-term approximation* for stronger electric fields by use of surface spherical harmonics with Legendre polynomials P_j

$$f_e(\vec{v}_e) = \sum_j f_e^j(\vec{v}_e) \cdot P_j(\cos \vartheta). \quad (3.129)$$

3. The *electron beam approximation* for runaway electrons in the case of very strong electric field strength, only. All the electrons have nearly the same velocity \vec{v}_e due to the strong acceleration within the potential drop ΔU , low cross section and the dominating forward scattering in collisions with the background gas. The high anisotropic electron velocity distribution can be approximated by the Dirac delta function

$$f_e(\vec{v}_e) \sim \vec{v}_e(\Delta U) \cdot a \cdot \delta(\vec{v}_0 - \vec{v}_e) \quad (3.130)$$

with the mean energy loss factor a due to the scattering.

Beside the different amount of the electric field strength which influences the anisotropy of the electron velocity distribution function, the consideration of all the relevant inelastic electron collisions with their specific collision cross section is a great challenge in modeling of molecular nonthermal plasmas.

On the other hand, the *velocity distribution function of heavy species* in the quasi-neutral plasma can be well described by a Maxwellian velocity distribution function with separate temperatures for the neutrals and ions, e.g., $T_n = T_{gas}$ and T_+ . Usually the temperature of the ions exceeds the neutral gas temperature due to heating in the external electric field. The difference in the heavy particle temperature may be expressed by the approximation

$$T_+ = T_{gas} + \frac{m_n \cdot v_{D,A^+}^2}{3 \cdot k_B}. \quad (3.131)$$

This formula estimates the result of collisions between neutral gas particles with the mass m_n and positive ions A^+ with the drift velocity v_{D,A^+} .

3.5 AVERAGED QUANTITIES, TRANSPORT EQUATIONS, AND RATE COEFFICIENTS

3.5.1 WEIGHTED AVERAGE OF PHYSICAL QUANTITIES

At known velocity distribution function f_A the weighted average of a physical quantity $A(\vec{v})$

$$\langle A \rangle = \frac{1}{n} \cdot \int A(\vec{v}) \cdot f_A(\vec{v}) \cdot d^3 v \quad (3.132)$$

is achieved by integration over all velocities providing the local averaged value $\langle A \rangle$.

Exemplarily, it is concerned the average quantities particle density n

$$n(\vec{r}, t) = \int f_A(\vec{v}) \cdot d^3 v \quad (3.133)$$

the particle flux density \vec{j}

$$\vec{j}(\vec{r}, t) = n \cdot \langle \vec{v} \rangle = n \cdot \vec{u} = \int \vec{v} \cdot f_A(\vec{v}) \cdot d^3 v \quad (3.134)$$

and the particle translational energy density w

$$w = n \cdot \frac{3}{2} k_B T + n \cdot \frac{1}{2} m \cdot u^2 = \frac{1}{2} \cdot m \cdot \int v^2 \cdot f_A(\vec{v}) \cdot d^3 v \quad (3.135)$$

using the separation of the isotropic and the flow energy density.

In the simple case of a neutral gas consisting of identical atoms A with mass m , the (isotropic) mean thermal velocity

$$v_{th} = \langle v \rangle = \int_0^\infty v \cdot f_A^0(v) \cdot dv = \sqrt{\frac{8 \cdot k_B T}{\pi \cdot m}} \quad (3.136)$$

can be easily calculated by use of the Maxwellian velocity distribution function at the gas temperature T .

Using the Maxwellian electron energy distribution function $f_e^0(U)$ for the electron ensemble, the mean electron energy $\langle U \rangle$ in terms of Volt can be calculated

$$\begin{aligned} \langle U \rangle &= \int_0^\infty U \cdot f_e^0(U) \cdot dU = 2 \cdot \pi^{-1/2} \cdot U_e^{-3/2} \\ &\cdot \int_0^\infty U^{3/2} \cdot \exp\left(-\frac{U}{U_e}\right) \cdot dU = \frac{3}{2} \cdot U_e = \frac{3}{2} \cdot \frac{k_B T_e}{e} \end{aligned} \quad (3.137)$$

with $k_B T_e = e \cdot U_e$ (T_e [K] = 11,604 · U_e [V]).

In most cases the approximation $1 \text{ V} \sim 10^4 \text{ K}$ is applied.

3.5.2 MACROSCOPIC TRANSPORT EQUATIONS

The macroscopic or hydrodynamic description of nonthermal plasmas can be applied if the mean free path length λ of the plasma particles is much lower than the characteristic length scale l in which the velocity distribution function significantly varies $\lambda \ll l$.

The macroscopic transport equation in position space can be obtained by multiplying the BLME equation with a conservation quantity ξ and the following integration over all velocities

$$\int \left[\frac{\partial f}{\partial t} + \vec{v} \cdot \frac{\partial f}{\partial \vec{r}} + \vec{a} \cdot \frac{\partial f}{\partial \vec{v}} \right] \cdot \xi \cdot d^3 v = \int \left(\frac{\partial f_e}{\partial t} \right)_{coll} \cdot \xi \cdot d^3 v \quad (3.138)$$

with $\xi \equiv M \cdot \vec{v}^\beta$.

This integration results in

$$\begin{aligned} \frac{\partial}{\partial t} (n \cdot \langle \xi \rangle) - n \cdot \left\langle \frac{\partial \xi}{\partial t} \right\rangle + \frac{\partial}{\partial \vec{r}} (n \cdot \vec{v} \cdot \langle \xi \rangle) - n \cdot \left\langle n \cdot \xi \frac{\partial \vec{v}}{\partial \vec{r}} \right\rangle - n \cdot \left\langle \frac{\partial}{\partial \vec{v}} (\vec{a} \cdot \xi) \right\rangle \\ = \int \left(\frac{\partial f}{\partial t} \right)_{coll} \cdot \xi \cdot d^3 v \end{aligned} \quad (3.139)$$

and has to be discussed for the different physical conservation quantities.

With $\langle \xi \rangle = \frac{1}{n} \int \xi \cdot f \cdot d^3 v$, $n = \int f \cdot d^3 v$, $\vec{a} = \vec{F}/m$, $\vec{v} = \vec{v}_{iso} + \vec{u}$.

Depending on the physical quantity M and the considered exponent β , the different orders of macroscopic transport equations are deduced. The most important transport equations of first, second, and third order correspond to the balance equations for the particle number density, the momentum and translational energy of the particles, respectively (see Table 3.10).

In particular, the *particle balance equation*

$$\frac{\partial n_i}{\partial t} + \frac{\partial}{\partial \vec{r}} (n_i \cdot \vec{u}) = \frac{\partial n_i}{\partial t} + \text{div} \vec{j}_i = S_i = G_i - L_i \quad (3.140)$$

is of interest in nonthermal reactive plasmas, which balances the temporal change of the particle concentration n_i and the particle transport $\text{div} \vec{j}_i$ on the left side with that of the production and consumption of the particles i in elementary collision processes by the effective source term S_i consisting of gain G_i and loss L_i term on the right side of (3.140).

Besides the consideration of the particle transport, due to diffusion and convection, the macroscopic production (gain) or consumption (loss) rates have to be calculated for the considered kind of particles n_i . The calculation of the source term S_i needs the corresponding velocity distributions functions and the collision cross sections

TABLE 3.10

The Most Important Transport Equations of First, Second, and Third Order Correspond to the Balance Equations for the Particle Number Density, the Momentum and Translational Energy of the Particles

Particle conservation	$M = 1,$	$b = 0 \rightarrow \xi = 1$
Momentum conservation	$M = m,$	$b = 1 \rightarrow \xi = m \cdot \vec{v}$
Translational energy conservation	$M = m/2,$	$b = 2 \rightarrow \xi = \frac{m}{2} \cdot \vec{v}^2$

$$\begin{aligned}
S_i &= \int \left(\frac{\partial f_i}{\partial t} \right)_{\text{coll}} d^3 v_i \\
&= \sum_{\substack{k l m n \\ i \ni k l m n}} \left[\iiint d\Omega d^3 v_l d^3 v_k \cdot |\vec{v}_l - \vec{v}_k| \cdot \sigma_{klmn} (|\vec{v}_l - \vec{v}_k|, \Omega) \cdot (f_k \cdot f_l - f_m \cdot f_n) \right]^i
\end{aligned} \quad (3.141)$$

too.

In most cases the gain and loss terms are expressed by means of the rate coefficient k

$$\begin{aligned}
S_i &= \sum_{klmn} \pm k_{klmn}^i \cdot n_k \cdot n_l \\
&= \sum_{klmn} \pm \left(\iint d^3 v_k \cdot d^3 v_l \cdot |\vec{v}_l - \vec{v}_k| \cdot \sigma_{klmn}^i (|\vec{v}_l - \vec{v}_k|) \cdot f_k \cdot f_l \right) \cdot n_k \cdot n_l
\end{aligned} \quad (3.142)$$

of the binary collision with $[k_{klmn}^i] = \text{m}^3 \cdot \text{s}^{-1}$.

As an example, we assume collisions between two particles with mass m_1 and m_2 . The Maxwellian velocity distribution at the same temperature T does not depend on the internal energy states of the particles. The transformation in the center of mass system using the reduced mass m_{red} and the integration over the relative velocity v_r results in following analytical expression of the rate coefficient $k(T)$

$$\begin{aligned}
k(T) &= \langle v_r \cdot \sigma(v_r) \rangle = \int f(v_r) \cdot v_r \cdot \sigma(v_r) \cdot dv_r \\
&= 4\pi \cdot \left(\frac{m_{\text{red}}}{2\pi \cdot k_B T} \right)^{3/2} \cdot \int_0^\infty \sigma(v_r) \cdot v_r^3 \cdot \exp \left(-\frac{m_{\text{red}} \cdot v_r^2}{2 \cdot k_B T} \right) \cdot dv_r
\end{aligned} \quad (3.143)$$

with the reduced mass $m_{\text{red}} = (m_1 \cdot m_2) / (m_1 + m_2)$ and the relative velocity $v_r = |\vec{v}_1 - \vec{v}_2|$.

In similar way the corresponding rate coefficient $k(T)$ is achieved using the relative translational energy

$$k(T) = \frac{1}{k_B T} \cdot \left(\frac{8}{\pi \cdot m_{\text{red}} \cdot k_B T} \right)^{1/2} \cdot \int_0^\infty \sigma(\varepsilon_r) \cdot \varepsilon_r \cdot \exp \left(-\frac{\varepsilon_r}{k_B T} \right) d\varepsilon_r \quad (3.144)$$

with the relative energy $\varepsilon_r = m_{\text{red}} / 2 \cdot v_r^2$.

Another simple case considers two different temperatures T_1 and T_2 of the particles with masses m_1 and m_2 , respectively. An effective temperature can be defined in the expression of the rate coefficient $k(T_{\text{eff}})$.

$$k(T_{\text{eff}}) = 4\pi \cdot \left(\frac{m_{\text{red}}}{2\pi \cdot k_B T_{\text{eff}}} \right)^{3/2} \cdot \int_0^\infty \sigma(v_r) \cdot v_r^3 \cdot \exp \left(-\frac{m_{\text{red}} \cdot v_r^2}{2 \cdot k_B T_{\text{eff}}} \right) \cdot dv_r \quad (3.145)$$

$$T_{\text{eff}} = (m_1 T_2 + m_2 T_1) / (m_1 + m_2) \quad \text{and} \quad m_{\text{red}} = (m_1 \cdot m_2) / (m_1 + m_2).$$

The special case for $T_1 \ll T_2$, and $m_1 \ll m_2$ results in $T_{\text{eff}} \sim T_1$ and $m_{\text{red}} \sim m_1$, which is relevant for the nonthermal plasma in partial thermodynamic equilibrium ($T_e \gg T_{\text{ion}} \sim T_{\text{neutral}}$, $m_e \gg m_{\text{ion}}$, m_{neutral}).

3.5.3 ANALYTICAL CALCULATION OF RATE COEFFICIENTS AND COLLISION FREQUENCIES

Following, several simple examples for the analytical calculation of rate coefficients or the corresponding collision frequencies are given taking into account the Maxwellian distribution function and the cross sections of binary collisions discussed in Section 3.8, concerning the

1. Gas kinetic hard sphere cross section
2. Langevin capture cross section for ion–molecule reactions
3. Cross section of neutral–neutral reactions with threshold energy

3.5.3.1 Gas Kinetic Neutral–Neutral Collision Frequency and Mean Free Path Length

Taking into account a neutral gas with the Maxwellian velocity distribution function at the temperature T (3.146) with the relative velocity v_r and the reduced mass m_{red} , as well as the hard sphere cross section σ_{HS} , the mean collision frequency (3.147) of neutrals can be calculated by use of the relation $d\nu = dn_{v_r} \cdot v_r \cdot \sigma_{\text{HS}}$.

$$dn_{v_r} = n \cdot 4\pi \cdot \left(\frac{m_{\text{red}}}{2\pi \cdot k_B T} \right)^{3/2} \cdot \exp \left(-\frac{m_{\text{red}} \cdot v_r^2}{2 \cdot k_B T} \right) v_r^2 \cdot dv_r. \quad (3.146)$$

$$\nu = n \cdot 4\pi \cdot \left(\frac{m_{\text{red}}}{2\pi \cdot k_B T} \right)^{3/2} \cdot \sigma_{\text{HS}} \cdot \int_0^\infty \exp \left(-\frac{m_{\text{red}} \cdot v_r^2}{2 \cdot k_B T} \right) v_r^3 \cdot dv_r. \quad (3.147)$$

The integral in (3.147) provides the mean collision frequency, which is connected with the quantities mean thermal velocity $\langle v_r \rangle$, mean collision time τ , and mean free path length λ_r :

$$\nu = n \cdot \sigma_{\text{HS}} \cdot \langle v_r \rangle = \frac{1}{\tau} = \frac{\langle v_r \rangle}{\lambda_r} \quad \langle v_r \rangle = \sqrt{\frac{8 \cdot k_B T}{\pi \cdot m_{\text{red}}}} \quad \lambda_r = \frac{1}{n \cdot \sigma_{\text{HS}}}.$$

In the case of a chemical reaction between the neutral atom A and the molecule BC



without threshold energy the reaction rate is given by

$$\left[\frac{dn_{\text{A}}}{dt} \right]_{\text{HS}} = \left[\frac{dn_{\text{BC}}}{dt} \right]_{\text{HS}} = -k_{\text{HS}}^{\text{ABC}} \cdot n_{\text{A}} \cdot n_{\text{BC}} = -\nu_{\text{A}} \cdot n_{\text{BC}} = -\frac{n_{\text{BC}}}{\tau_{\text{A}}} \quad (3.149)$$

with rate coefficient k_{ABC} depending on the square root of the gas temperature.

$$k_{ABC} = \sigma_{HS}^{ABC} \cdot \langle v_r \rangle = \sigma_{HS}^{ABC} \cdot \sqrt{\frac{8 \cdot k_B T}{\pi \cdot m_{red}}} \sim \sqrt{T}. \quad (3.150)$$

3.5.3.2 Rate Coefficient for Ion–Molecule Reactions with the Langevin Capture Cross Section

Considering the ion–molecule reaction



the reaction rate

$$\begin{aligned} \left[\frac{dn_A^+}{dt} \right]_L &= \left[\frac{dn_{BC}}{dt} \right]_L = - \langle v_r \cdot \sigma_L^{A^+BC} (v_r) \rangle \cdot n_{A^+} \cdot n_{BC} \\ &= -k_L^{A^+BC} \cdot n_{A^+} \cdot n_{BC} = -\nu_{A^+} \cdot n_{BC} = -\frac{n_{BC}}{\tau_{A^+}} \end{aligned} \quad (3.152)$$

can be calculated by use of the Langevin capture cross section

$$\sigma_L^{A^+BC} (v_r) = \left(\frac{\alpha_{BC} \cdot q_A^2}{\varepsilon_0^2 \cdot m_{red} \cdot v_r^2} \right)^{1/2} \sim \frac{1}{v_r} \quad (3.153)$$

and the Maxwellian velocity distribution with the same temperature for the neutral gas and the ions $T_{gas} = T_+ = T$. The corresponding rate coefficient $k_L^{A^+BC}$ is calculated for the particle capture, which may be an estimation for the rate coefficient for ion–molecule reactions at low relative velocity in nonthermal plasmas. This capture rate coefficient $k_L^{A^+BC}$ depends not on the temperature and particle velocity.

$$k_L^{A^+BC} = \langle \sigma_L^{A^+BC} (v_r) \cdot v_r \rangle = \frac{q_A}{\varepsilon_0} \cdot \sqrt{\frac{\alpha_{BC}}{m_{red}}} \cdot \int_0^\infty f(v_r) \cdot dv_r = \frac{q_A}{\varepsilon_0} \cdot \sqrt{\frac{\alpha_{BC}}{m_{red}}}. \quad (3.154)$$

3.5.3.3 Rate Coefficient for Neutral–Neutral Reactions with Threshold Energy

The reaction



and the corresponding reaction rate

$$\begin{aligned} \left[\frac{dn_{CD}}{dt} \right]_{thres} &= -\frac{dn_C}{dt} = -\frac{dn_{DE}}{dt} = \langle v_r \cdot \sigma_{thres}^{CDE} (v_r) \rangle \cdot n_C \cdot n_{DE} \\ &= k_{thres}^{CDE} \cdot n_C \cdot n_{DE} = \nu_C \cdot n_{DE} = \frac{n_{DE}}{\tau_C} \end{aligned} \quad (3.156)$$

describe the reaction between the neutral particle C and the molecule DE with threshold energy ε_{thres}^{CD} to produce the particle CD. By use of the cross section σ_{thres}^{CD}

$$\sigma_{thres}^{CDE} = \sigma_{eff}^{CDE} \cdot \left(1 - \frac{\varepsilon_{thres}^{CDE}}{\varepsilon} \right) \quad (3.157)$$

for $\varepsilon \geq \varepsilon_{thres}^{CDE}$ and $\sigma_{thres}^{CDE} = 0$ for $\varepsilon < \varepsilon_{thres}^{CDE}$, the calculation of the reaction rate coefficient k_{thres}^{CD} results in

$$\begin{aligned} k_{thres}^{CDE} &= \frac{\pi}{2} \cdot \left(\frac{2 \cdot m_{red}}{\pi \cdot k_B T} \right)^{3/2} \cdot \sigma_{eff}^{CDE} \cdot \int_{\varepsilon_{thres}^{CDE}}^{\infty} \exp \left(-\frac{\varepsilon_T}{k_B T} \right) \cdot \frac{2 \cdot \varepsilon_T}{m_{red}^2} \cdot \left(1 - \frac{\varepsilon_{thres}^{CDE}}{\varepsilon_T} \right) \cdot d\varepsilon_T \\ &= \sigma_{eff}^{CDE} \cdot \sqrt{\frac{8 \cdot k_B T}{\pi \cdot m_{red}}} \cdot \exp \left(-\frac{\varepsilon_{thres}^{CDE}}{k_B T} \right) \sim \sqrt{T} \cdot \exp \left(-\frac{\varepsilon_{thres}^{CDE}}{k_B T} \right). \end{aligned} \quad (3.158)$$

This corresponds to an expression like the Arrhenius function typically for many chemical reactions with activation energy in thermochemistry.

3.5.4 RATE COEFFICIENT FOR ELECTRON IMPACT IONIZATION

The production rate of single charged positive ions due to direct electron impact ionization of neutral atoms A in ground state



is calculated by use of the specific electron impact ionization cross section and the electron velocity distribution function (nonthermal plasma conditions), and the particle densities of electrons n_e and neutrals n_A .

$$\left[\frac{dn_e}{dt} \right]_+ = \left[\frac{dn_A^{A+}}{dt} \right]_+ = \langle \sigma_A^{A+} \cdot v_r \rangle \cdot n_e \cdot n_A = k_A^{A+} \cdot n_e \cdot n_A = \gamma_{eA} \cdot n_A = \frac{n_A}{\tau_{eA}}. \quad (3.160)$$

The corresponding electron ionization rate coefficient k_A^{A+} results in:

$$k_A^{A+} = \langle \sigma_A^{A+} \cdot v_r \rangle = \int_{thres}^{\infty} f_e(v_r) \cdot v_r \cdot \sigma_A^{A+}(v_r) \cdot dv_r. \quad (3.161)$$

Generally, the electron velocity distribution function in (3.161) has to be calculated by a kinetic equation (Boltzmann equation). The necessary collision cross section in dependence on the relative velocity is mostly taken from experimental data approximated by analytical functions, or if available by quantum mechanical calculation or semiclassical formulas, see Section 3.8.

For example, in homogeneous nonthermal plasmas with mean electron energy of few electron volts the raising electron impact ionization cross section above the ionization threshold is often approximated by a linear fit function

$$\sigma_e^{ion}(\varepsilon_r) = a \cdot (\varepsilon_r - \varepsilon_{thres}^{ion}) \quad \text{for } \varepsilon_r \geq \varepsilon_{thres}^{ion} \quad (3.162)$$

limited for a specific range of the reduced electric field strength in dependence on the kind of gas. For the Maxwellian distribution of the electron energy, it follows

$$k(T_e) = 2a \cdot \left(\frac{2k_B T_e}{m_{red}} \right)^{1/2} \cdot \varepsilon_{thres}^{ion} \cdot \exp \left[-\frac{\varepsilon_{thres}^{ion}}{k_B T_e} \right]. \quad (3.163)$$

The total production rate of single charged positive ions and electrons due to electron impact ionization of atoms A in ground state may also determined by the step-like ionization from metastable excited levels of A, in particular for rare gases as shown for argon as an example

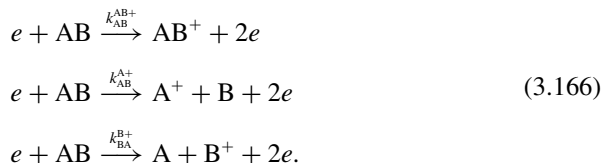
$$\left[\frac{dn_e}{dt} \right]_+ = \left[\frac{dn_{Ar}^{Ar+}}{dt} \right]_+ = k_{Ar}^{Ar+} \cdot n_{Ar,0} \cdot n_e + k_{Ar,ex}^{Ar+} \cdot n_{Ar,ex} \cdot n_e, \quad (3.164)$$

with

$$\begin{aligned} k_{Ar,0}^{Ar+} &= \int_{15.76 \text{ eV}}^{\infty} f_e(v_r) \cdot v_r \cdot \sigma_{Ar,0}^{Ar+}(v_r) \cdot dv_r \\ k_{Ar,ex}^{Ar+} &= \int_{11.2 \text{ eV}}^{\infty} f_e(v_r) \cdot v_r \cdot \sigma_{Ar,ex}^{Ar+}(v_r) \cdot dv_r. \end{aligned} \quad (3.165)$$

In the case of electron impact ionization of molecules the dissociative ionization or/and the ionization of molecules from highly excited vibrational states have to be considered, too.

For a heterogeneous diatomic molecule the following three ionization channels may exist.



The corresponding ionization rates consider the different rate coefficients, which are determined by the various threshold energies and cross sections for the positive ions

$$\left[\frac{dn_{AB}^{AB+}}{dt} \right]_+ = k_{AB}^{AB+} \cdot n_e \cdot n_{AB}, \quad \left[\frac{dn_{AB}^{A+}}{dt} \right]_+ = k_{AB}^{A+} \cdot n_e \cdot n_{AB}, \quad \left[\frac{dn_{AB}^{B+}}{dt} \right]_+ = k_{AB}^{B+} \cdot n_e \cdot n_{AB} \quad (3.167)$$

and the electrons, respectively.

$$\left[\frac{dn_e}{dt} \right]_+ = (k_{AB}^{AB+} + k_{AB}^{A+} + k_{AB}^{B+}) \cdot n_e \cdot n_{AB} = k_{total}^+ \cdot n_e \cdot n_{AB}. \quad (3.168)$$

3.5.5 RATE COEFFICIENT OF THREE-PARTICLE COLLISIONS

The collision of two particles A and B with a third target particle C at short distances within the interaction time τ depends on the particle current densities $n_A v_A$ and $n_B v_B$ and their collision cross sections σ_{AC} and σ_{BC} in the simultaneous interaction with target particles C, see scheme in Figure 3.24.

According to the scheme in Figure 3.24 the collision rate and the three-particle rate coefficient k_{ABC} can be estimated.

$$\begin{aligned} \frac{dn_{ABC}}{dt} &\sim n_A \cdot v_A \cdot \sigma_{AC} \cdot n_B \cdot v_B \cdot \sigma_{BC} \cdot \tau \cdot n_C = k_{ABC} \cdot n_A \cdot n_B \cdot n_C \\ k_{ABC} &\sim \sigma_{AC} \cdot \sigma_{BC} \cdot v_A \cdot v_B \cdot \tau \quad [k_{ABC}] = \text{m}^6 \cdot \text{s}^{-1}. \end{aligned} \quad (3.169)$$

By use of 10^{-20} m^2 for the collision cross section, 10^6 m s^{-1} for the thermal velocity, and 10^{-16} s for the typical interaction time the three-particle rate coefficient is estimated in the order of about $10^{-44} \text{ m}^6 \text{s}^{-1}$.

A sufficient high probability of a three-particle collisions can be expected at higher particle concentrations or total pressure, only. The macroscopic production rate of molecules AB in the reaction



is described by the three-particle rate coefficient k_{ABC}^{AB} and the concentrations of all participating particles

$$\frac{dn_{AB}}{dt} = k_{ABC}^{AB} \cdot n_A \cdot n_B \cdot n_C. \quad (3.171)$$

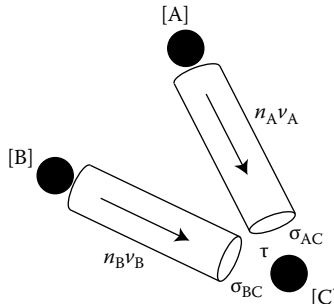


FIGURE 3.24 Scheme of the three-particle collision process.

In the special case that the particle concentration n_C is sufficient high against the concentration of the other participating particles, e.g., the particle concentration n_C represents the neutral background gas in nonthermal atmospheric pressure plasmas, the production rate

$$\frac{dn_{AB}}{dt} = k_{ABC}^{AB} \cdot n_A \cdot n_B \cdot n_C = (k_{ABC}^{AB} \cdot n_C) \cdot n_A \cdot n_B = \tilde{k}_{ABC}^{AB} \cdot n_A \cdot n_B \quad (3.172)$$

can be described as a quasi-binary collision with an effective rate coefficient \tilde{k}_{ABC}^{AB} involving the constant concentration n_C . Following, the effective rate coefficient is a function of the neutral gas concentration or pressure at constant temperature.

Taking into consideration the backward reaction of the electron impact ionization (3.156) the following three-particle recombination reaction has to be considered

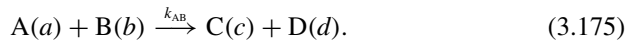


$$\frac{dn_A}{dt} = -\frac{dn_{A+}}{dt} = -\frac{dn_e}{dt} = k_{eeA+}^A \cdot n_e^2 \cdot n_{A+}. \quad (3.174)$$

Contrary to the detailed equilibrium in CTE, in the nonequilibrium plasma the rate coefficients for forward and backward reactions, e.g., electron impact ionization k_{eA}^{A+} and three-body recombination k_{eeA+}^A , and the corresponding reaction velocities are quite different, see Section 3.2.1.

3.5.6 REACTION RATE COEFFICIENT OF CHEMICAL REACTIONS

In the general case of chemical reactions in nonthermal plasmas the rate coefficient k_{AB} of a reaction between two particles A and B represents the reaction rate coefficient.



Taking into consideration the binary collisions of particles at different states of internal energy (a, b, c, d) the reaction rate of the product concentration n_C depends on the concentration of the reagents n_A and n_B as well as the reaction rate coefficient k_{AB} characterizing the probability of this chemical reaction [30].

$$\frac{dn_C(c, d | a, b)}{dt} = k_{AB} (C, D; c, d | A, B; a, b) \cdot n_A(a) \cdot n_B(b). \quad (3.176)$$

The averaging $\langle v_{AB} \cdot \sigma_{AB} \rangle$ over the distribution function f_{AB} , and the sum over all internal energy states of the reaction partners provide the total reaction rate coefficient of the chemical reaction between the particles A and B which produce the particles C and D.

$$k(C, D | A, B) = \sum_{abcd} x_A(a) \cdot x_B(b) \cdot k(C, D; c, d | A, B; a, b). \quad (3.177)$$

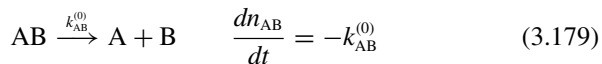
The relative contribution of the different internal states of the reagents A and B in the formation of the product C is considered by the two factors

$$x_A(a) = \frac{n_A(a)}{\sum an_A(a)} \quad \text{and} \quad x_B(b) = \frac{n_B(b)}{\sum bn_B(b)}. \quad (3.178)$$

3.5.7 ORDER OF CHEMICAL REACTIONS

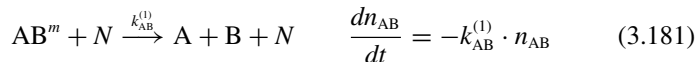
The type of chemical reactions is usually classified by the reaction order which depends on the number of simultaneous interacting particles in a collision process. In nonthermal plasmas the reactions of zero, first, second, and third order may be considered characterized by the following rate equations and corresponding rate coefficients.

1. *Zero-order chemical reaction:* For example, spontaneous dissociation of the molecule AB:



$$n_{\text{AB}}(t) = -k_{\text{AB}}^{(0)} \cdot t + n_{\text{AB}}(0) \quad [k^{(0)}] = \text{m}^{-3} \cdot \text{s}^{-1}. \quad (3.180)$$

2. *First-order chemical reaction:* For example, dissociation of metastable molecules by collision with background gas $n_N \gg n_{\text{AB}}$:



$$n_{\text{AB}}(t) = n_{\text{AB}}(0) \cdot \exp(-k_{\text{AB}}^{(1)} \cdot t) \quad [k^{(1)}] = \text{s}^{-1}. \quad (3.182)$$

The neutral density ($n_N \gg n_{\text{AB}}$) is considered as a constant and included in the rate coefficient.

Here, the special case of the consecutive reactions is exemplarily discussed starting with concentration n_A and the formation of an intermediate product n_B which is consumed to form the end product n_C (see Figure 3.25).



$$\frac{dn_A}{dt} = -k_A^{(1)} \cdot n_A. \quad (3.184)$$

$$\frac{dn_B}{dt} = k_A^{(1)} \cdot n_A - k_B^{(1)} \cdot n_B. \quad (3.185)$$

$$\frac{dn_C}{dt} = k_B^{(1)} \cdot n_B. \quad (3.186)$$

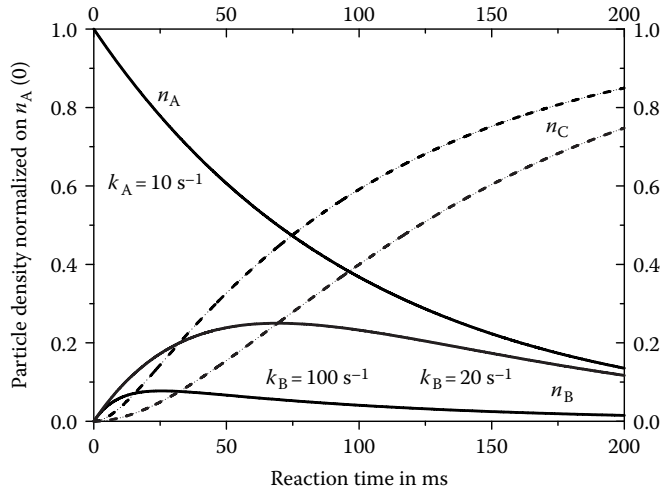


FIGURE 3.25 Example of consecutive chemical reactions of first order. Shown is the consumption of the particles A with $k_A = 10 \text{ s}^{-1}$, and the formation the final product C via the intermediate product B for two selected reaction coefficients, $k_B = 100 \text{ s}^{-1}$ and $k_B = 20 \text{ s}^{-1}$.

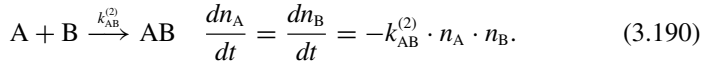
The rate equations are solved elementary with initial conditions $n_A(0)$ and $n_B(0) = n_C(0) = 0$.

$$n_A(t) = n_A(0) \cdot \exp(-k_A^{(1)} \cdot t). \quad (3.187)$$

$$n_B(t) = n_A(0) \cdot \frac{k_A^{(1)}}{k_B^{(1)} - k_A^{(1)}} \cdot [\exp(-k_A^{(1)} \cdot t) - \exp(-k_B^{(1)} \cdot t)]. \quad (3.188)$$

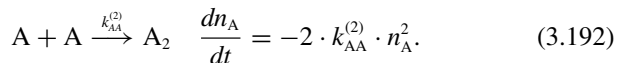
$$n_C(t) = n_A(0) \cdot \left[1 + \frac{1}{k_A^{(1)} - k_B^{(1)}} \cdot (k_B^{(1)} \cdot \exp(-k_A^{(1)} \cdot t) - k_A^{(1)} \exp(-k_B^{(1)} \cdot t)) \right]. \quad (3.189)$$

3. Second-order chemical reaction: The product formation depends on two reactant concentrations.

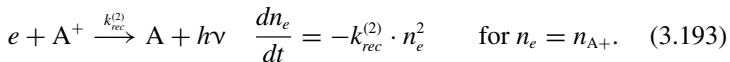


$$n_A(t) = n_A(0) \cdot \frac{(n_A(0) - n_B(0)) \cdot \exp([(n_A(0) - n_B(0)) \cdot k_{AB}^{(2)} \cdot t]}{[n_A(0) \cdot \exp([(n_A(0) - n_B(0)) \cdot k_{AB}^{(2)} \cdot t] - n_B(0)]}. \quad (3.191)$$

In the case of the reaction between identical particles it follows:

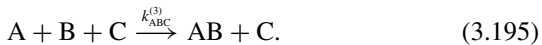


As an example the radiative recombination is considered:



$$n_e(t) = \frac{1}{k_{rec}^{(2)} \cdot t + 1/n_e(0)} \quad [k^{(2)}] = \text{m}^3 \text{ s}^{-1}. \quad (3.194)$$

4. *Third-order chemical reaction:* Product formation depends on three reactant concentrations.



$$\frac{dn_{AB}}{dt} = k_{ABC}^{(3)} \cdot n_A \cdot n_B \cdot n_C \quad [k^{(3)}] = \text{m}^6 \text{ s}^{-1}. \quad (3.196)$$

3.6 BOUNDARY PLASMA-SURFACE, PLASMA SHEATHS

The contact of the plasma with condensed matter, such as gas discharge electrodes, surrounding solid walls or liquids, immersed probes for the plasma diagnostics or materials in the plasma surface processing, is one of the most important phenomena in the plasma physics and chemistry. The transition zone between the plasma and phase boundary of condensed matter represents a general and complex problem.

In more general sense, the plasma surface interaction describes all phenomena which are connected with the interaction of charged and neutral plasma particles as well as photons with solid or liquid phase boundaries, their physical and chemical processes in the interface of the condensed matter, as well as their influence back to the plasma properties due to surface recombination of charged and neutral plasma particles, secondary particles emission, erosion of surface material, and formation of new compounds by means of heterogeneous chemical reactions. Therefore, the plasma surface interaction includes collective and synergistic processes involving charged particles, fast neutrals and meta-stable excited particles, energetic photons, and chemical reactive atoms and molecules. The particle flux to the surface and the plasma radiation may initiate manifold elementary processes in the phase boundary due to exchange of charge, energy, momentum, and mass. In dependence on the surface material at the phase boundary as well as their physical and chemical modification during interaction with the plasma it is observed a characteristic penetration depth of each kind of plasma particles. The complex surface processes may include secondary electron or negative ion emission, charge carrier recombination, (adsorbate) sputtering of surface material, chemical modification of a thin surface layer, desorption of chemical reaction products (cleaning, plasma etching) or thin film formation, see Figure 3.26. In molecular plasmas the chemical surface functionalization, the plasma etching, and thin film deposition take place simultaneously. The surface processes can be controlled by the plasma parameters and the kinetic energy of impinging positive ions (reactive ion etching, chemical sputtering, ion-assisted thin film deposition) as well as the surface temperature.

From the plasma physics point of view the transport of charged particles to or from the surface is in the focus of interest. This transport is controlled by the

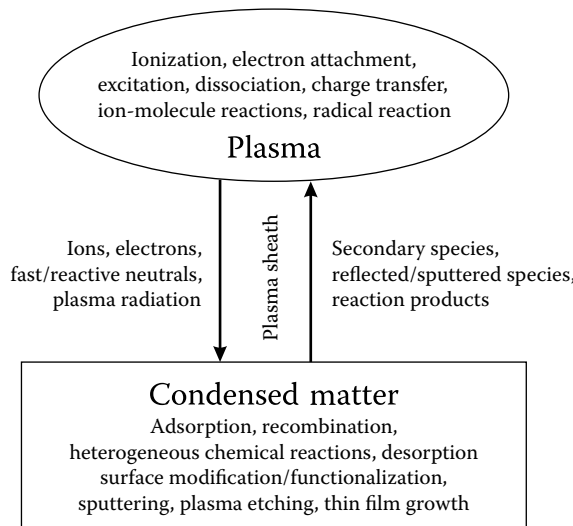


FIGURE 3.26 Complex plasma surface interaction.

self-consistent electric field of space charges in the plasma sheath immediately in front of the surface. The plasma sheath properties are mainly influenced by the energy distribution function of the plasma electrons, the plasma and neutral gas density, as well as the specific surface conditions, e.g., surface potential/electric conductivity, temperature/heat conductivity, secondary particles emission, and surface recombination. In particular, many electric gas discharges are sustained by means of secondary electron emission at discharge electrodes, such as the cathode processes in glow or arc discharges.

Following, an analytical description of the plasma surface interaction is given with useful approximations for the transport of charge carriers in the plasma sheath to understand the basic physics and to receive estimations about the current density and kinetic energy of positive ions at the phase boundary.

3.6.1 STATIONARY PLASMA SHEATH AND BOHM SHEATH CRITERION

We consider a stationary, uniform, and ideal nonthermal plasma consisting of electrons and the same kind of single charged positive ions with Maxwellian energy distribution $T_e \sim 10^4$ K $\gg T_+$ in contact with a surface. The immersed chemically inert and totally absorbing material surface will be negatively charged in relation to the plasma potential φ_p because of the higher thermal velocity of electrons compared with the heavy ions:

$$\sim \sqrt{\frac{m_+ \cdot T_e}{m_e \cdot T_+}}. \quad (3.197)$$

The negatively charged surface at the potential $-\varphi_s$ is shielded by a positive space charge sheath in front of the surface, see Figure 3.27.

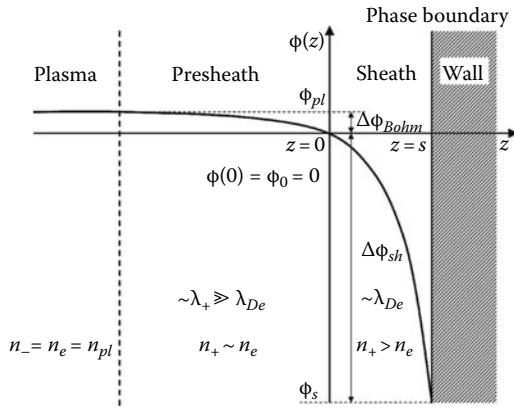


FIGURE 3.27 Qualitative behavior of the electric potential for the transition region from the bulk plasma over the presheath and space charge sheath to the phase boundary of condensed matter.

The resulting self-consistent electric field of the space charges determines the charge carrier transport to the surface.

Taking additionally into account no collisions and in the sheath ($\lambda_+ \gg s$) and cold plasma ions, the transport of ions can be simplified described by use of z as the distance normally toward the surface and the boundary condition for the potential $\varphi(z=0)=0$ at the sheath edge. The equations for continuity of the ion flux and conservation of the ion energy in the space charge sheath are given by (3.198) and (3.199), respectively.

$$n_+(z) \cdot v_+(z) = n_+(0) \cdot v_+(0) + const., \quad (3.198)$$

$$\frac{1}{2} m_+ \cdot v_+^2(z) = \frac{1}{2} m_+ \cdot v_+^2(0) - e \cdot \varphi(z) \quad \varphi(z > 0) < 0. \quad (3.199)$$

The combination of both equations provides the positive ion density $n_+(z)$ inside the sheath

$$n_+(z) = n_+(0) \cdot \left(1 - \frac{2e \cdot \varphi(z)}{m_+ \cdot v_+^2(0)} \right)^{-1/2}. \quad (3.200)$$

The corresponding electron density in the sheath region is described by the Boltzmann distribution in the repulsive sheath potential.

$$n_e(z) = n_e(0) \cdot \exp \left[\frac{e \cdot \varphi(z)}{k_B \cdot T_e} \right]. \quad (3.201)$$

With the assumed quasi-neutrality at the sheath edge $n_e(0) = n_+(0) = n(0)$ the Poisson equation results in

$$\begin{aligned} \frac{d^2\varphi(z)}{dz^2} &= \frac{e}{\varepsilon_0} \cdot [n_e(z) - n_+(z)] \\ &= \frac{e \cdot n(0)}{\varepsilon_0} \cdot \left[\exp\left(\frac{e \cdot \varphi(z)}{k_B \cdot T_e}\right) - \left(1 - \frac{2 \cdot e \cdot \varphi(z)}{m_+ \cdot v_+^2(0)}\right)^{-1/2} \right]. \end{aligned} \quad (3.202)$$

Multiplying (3.202) with $d\varphi/dz$ and integration over z we obtain

$$\begin{aligned} \int_0^\varphi \frac{d\varphi}{dz} \cdot \frac{d}{dz} \left(\frac{d\varphi}{dz} \right) \cdot dz &= \frac{1}{2} \cdot \left(\frac{d\varphi}{dz} \right)^2 \\ &= \frac{e \cdot n(0)}{\varepsilon_0} \cdot \int_0^\varphi \frac{d\varphi}{dz} \cdot \left[\exp\left(\frac{e \cdot \varphi(z)}{k_B \cdot T_e}\right) - \left(1 - \frac{2 \cdot e \cdot \varphi(z)}{m_+ \cdot v_+^2(0)}\right)^{-1/2} \right] \cdot dz. \end{aligned} \quad (3.203)$$

After the canceling of dz and integration over $d\varphi$, the received expression is developed in a Taylor series at the sheath edge in second order with the boundary conditions $\varphi(z)|_0 = 0$ and $d\varphi/dz|_0 = 0$ [36].

$$\frac{1}{2} \cdot \left(\frac{d\varphi}{dz} \right)^2 \sim \frac{e \cdot n(0)}{\varepsilon_0} \cdot \left[\frac{1}{2 \cdot k_B \cdot T_e} - \frac{1}{2 \cdot m_+ \cdot v_+^2(0)} \right] \cdot e \cdot \varphi^2. \quad (3.204)$$

The term in square bracket has to be *positive* and demands a minimum ion velocity at the sheath edge, which is referred to as the Bohm velocity or the *Bohm sheath criterion*.

$$\left[\frac{1}{2 \cdot k_B \cdot T_e} - \frac{1}{2 \cdot m_+ \cdot v_+^2(0)} \right] > 0 \quad \rightarrow \quad v_+(0) \geq v_{Bohm} := \sqrt{k_B \cdot \frac{T_e}{m_+}}. \quad (3.205)$$

The *Bohm sheath criterion* demands the acceleration of positive ions from the bulk plasma side toward the sheath edge in the *presheath*. Therefore, the presheath is defined by the necessary potential drop $\Delta\varphi_{Bohm}$ between the plasma potential φ_{pl} and the potential at the sheath edge φ_0

$$\frac{m_+}{2} \cdot v_{Bohm}^2 = \frac{1}{2} \cdot k_B \cdot T_e = e \cdot \Delta\varphi_{Bohm} = e \cdot (\varphi_{pl} - \varphi_0). \quad (3.206)$$

Summarized, the presheath is characterized by approximately quasi-neutrality and a weakly decreasing plasma density due to the repelling of electrons in the necessary small potential drop for ion acceleration on the Bohm velocity.

3.6.1.1 Generalized Bohm Sheath Criterion

A generalized Bohm sheath criterions was derived by [32] for the limit $\lambda_{De} \rightarrow 0$, including electrons and negative ions as well as the 1D velocity distribution functions of positive ions $f(v_+)$

$$\frac{1}{m_+} \int_0^\infty \frac{1}{v_+^2} \cdot f(v_+) \cdot dv_+ = \frac{1}{m_+} \cdot \left\langle \frac{1}{v_+^2} \right\rangle \leq \frac{1}{e \cdot n_+(0)} \cdot \frac{d(n_e + n_-)}{d\varphi} \Big|_{\varphi=0}. \quad (3.207)$$

By use of Dirac δ function for the ion energy distribution function as well as Maxwellian electrons, only, the Bohm sheath criterion (3.205) is reproduced.

$$\begin{aligned} \frac{1}{m_+} \int_{-\infty}^\infty \frac{1}{v_+^2} \delta[v_+ - v_+(0)] \cdot dv_+ &= \frac{1}{m_+ \cdot v_+^2(0)} \\ &\leq \frac{1}{e} \cdot \frac{d}{d\varphi} \exp\left(\frac{e \cdot \varphi}{k_B \cdot T_e}\right) \Big|_{\varphi=0} = \frac{1}{k_B \cdot T_e}. \end{aligned} \quad (3.208)$$

Another generalized Bohm sheath criterion is given by [33] taking into account the electron velocity distribution function $f(v_e)$

$$\frac{1}{m_+} \cdot \left\langle \frac{1}{v_+^2} \right\rangle \leq -\frac{1}{m_e} \int_{-\infty}^\infty \frac{1}{v_e} \cdot \frac{df_e}{dv_e} \cdot dv_e. \quad (3.209)$$

3.6.1.2 Plasma Sheath in Electronegative Gases

Equation 3.207 can be applied for electronegative plasmas with the approximation for cold positive ions and Maxwellian electrons and negative ions. Taking into account the quantities $\alpha = n_- / n_e$ defined as ratio of negative ion to electron density and $\gamma = T_e / T_-$ defined as ratio of the electron to negative ion temperature, it follows for quasi-neutrality at the sheath edge:

$$n_+(0) = (1 + \alpha_0) \cdot n_e(0), \quad (3.210)$$

$$n_e + n_- = n_e(0) \cdot \left[\exp\left(\frac{e \cdot \varphi}{k_B \cdot T_e}\right) + \alpha_0 \cdot \exp\left(\frac{\gamma \cdot e \cdot \varphi}{k_B \cdot T_e}\right) \right]. \quad (3.211)$$

Inserting the electron and negative ion density (3.211) into (3.207) and using monoenergetic positive ions at the sheath edge it follows

$$\frac{1}{m_+ \cdot v_+^2(0)} \leq \frac{1}{e \cdot n_+(0)} \cdot \frac{d(n_e + n_-)}{d\varphi} \Big|_{\varphi=0} = \frac{1 + \alpha_0 \cdot \gamma}{1 + \alpha_0} \cdot \frac{1}{k_B \cdot T_e} \quad (3.212)$$

and the Bohm criterion for electronegative plasmas is achieved:

$$\frac{k_B \cdot T_e}{m_+ \cdot v_+^2(0)} \leq \frac{1 + \alpha_0 \cdot \gamma}{1 + \alpha_0}. \quad (3.213)$$

But, for the condition $T_e \gg T_-$, the defined *electronegativity* α_0 at the sheath edge will not be the same compared with the bulk plasma α_{pl} . In the presheath the negative ions are much more repelled than the electrons. By use of the Boltzmann relation for electrons and negative ions in the presheath

$$n_e(0) = n_{e,pl} \cdot \exp\left(\frac{-e \cdot \varphi_{pl}}{k_B \cdot T_e}\right) \quad n_-(0) = n_{-,pl} \cdot \exp\left(\frac{-\gamma \cdot e \cdot \varphi_{pl}}{k_b \cdot T_e}\right) \quad (3.214)$$

it follows the expression for α_0 at the sheath edge in relation the α_{pl} in the plasma bulk

$$\alpha_0 = \alpha_{pl} \cdot \exp\left[e \cdot (1 - \gamma) \cdot \frac{\varphi_{pl}}{k_B \cdot T_e}\right]. \quad (3.215)$$

Further, taking into the consideration the energy conservation of negative ions, we obtain

$$\frac{e \cdot \varphi_{pl}}{k_B \cdot T_e} = \frac{1}{2} \cdot \frac{1 + \alpha_0}{1 + \gamma \cdot \alpha_0}. \quad (3.216)$$

Inserting (3.216) in (3.215) an expression for the bulk plasma electronegativity is obtained

$$\alpha_{pl} = \alpha_0 \cdot \exp\left[\frac{(1 + \alpha_0) \cdot (\gamma - 1)}{2 \cdot (1 + \gamma \cdot \alpha_0)}\right]. \quad (3.217)$$

From (3.215) and (3.217) the electronegativity α_0 at the sheath edge and $e\varphi_{pl}/k_B T_e$ can be calculated numerically if the bulk electronegativity α_{pl} is known. The ratio α_0/α_{pl} and $e\varphi_{pl}/k_B T_e$ over α_{pl} was firstly calculated by Boyd and Thomson [34]. For the conditions $\alpha_{pl} < 2$ and $\gamma > 30$ the plasma sheath can be treated similar to electro-positive plasmas which is relevant for most of the used nonthermal plasmas. Further investigations by Braithwhite and Allen have also shown the additional formation of a double layer at conditions with $\gamma > (5 + 24^{1/2})$, see [35].

3.6.1.3 Multi-Species Plasmas

Generally, the nonthermal molecular plasmas may contain several kinds of positive and negative ions, electrons, and neutral species. Some approximations are given in the literature concerning the Bohm sheath criterion for multi-species plasma, by a summation over several kinds of positive ions [33,36]

$$\sum_k \frac{z_k^2 \cdot n_{+k}}{n_e \cdot v_{+k}^2 \cdot m_{+k}} \leq \frac{1}{k_B \cdot T_e} \quad (3.218)$$

with z the charge number of the positive ion.

3.6.1.4 Plasma Sheath in Front of the Floating Surface

Taking into consideration an electric insulating surface immersed in a quasi-neutral plasma consisting of cold ions and Maxwellian electrons, the net charge flow will be zero under steady-state conditions

$$j_{+,sf} + j_{e,sf} = 0|_{surface}. \quad (3.219)$$

From (3.219) the potential drop over the plasma sheath $\Delta\varphi_{sh}$, see (3.222), is calculated taking into account the current density for ions $j_{+,sf}$, see (3.220), corresponding to the Bohm current density, and for electrons $j_{e,sf}$, see (3.221). Thereby, the electron density is reduced in the repulsive potential in the space charge sheath according to the Boltzmann distribution.

$$j_{+,sf} = e \cdot n_{pl} \cdot \exp\left(-\frac{1}{2}\right) \cdot \left(\frac{k_B \cdot T_e}{m_+}\right)^{1/2}, \quad (3.220)$$

$$j_{e,sf} = e \cdot n_{pl} \cdot \exp\left(-\frac{1}{2}\right) \cdot \left(\frac{k_B \cdot T_e}{2 \cdot \pi \cdot m_e}\right)^{1/2} \cdot \exp\left(\frac{-e \cdot \Delta\varphi_{sh}}{k_B \cdot T_e}\right). \quad (3.221)$$

The term $n_{pl} \cdot \exp(-1/2)$ is the reduced plasma density at the sheath edge. The solution for the potential drop over the sheath provides

$$\Delta\varphi_{sh} = \varphi_0 - \varphi_{sf} = \frac{1}{2} \cdot \frac{k_B \cdot T_e}{e} \cdot \ln\left(\frac{m_+}{2 \cdot \pi \cdot m_e}\right) \approx 3 \dots 4 \cdot \frac{k_B \cdot T_e}{e}. \quad (3.222)$$

Finally, the total potential drop between the plasma potential φ_{pl} and the floating surface potential $\varphi_{sf} < 0$ results in

$$\begin{aligned} \varphi_{pl} - \varphi_{sf} &= \Delta\varphi_{Bohm} + \Delta\varphi_{sh} = \varphi_{pl} - \varphi_0 + \varphi_0 - \varphi_{sf} \\ &= \frac{1}{2} \cdot \frac{k_B \cdot T_e}{e} \cdot \left[1 + \ln\left(\frac{m_+}{2 \cdot \pi \cdot m_e}\right) \right], \end{aligned} \quad (3.223)$$

$$\varphi_{pl} - \varphi_{sf} \approx \frac{1}{2} \cdot \frac{k_B \cdot T_e}{e} \cdot \ln\left(0.43 \cdot \frac{m_+}{m_e}\right) \approx 4.3 \cdot 10^{-5} \cdot T_e [\text{K}] \cdot (6.7 + \ln(A_+[u]))$$

with A_+ is the mass number of the positive ion.

For example, the floating surface potential for the electron temperature of $2 \cdot 10^4 \text{ K}$ and argon ion ($u = 40$) amounts to about 9 V negative compared with the plasma potential.

3.6.2 HIGH-VOLTAGE PLASMA SHEATHS

The high-voltage plasma sheath is defined for the case of high potential drop between the plasma and an external or self-biased surface potential characterized by the condition $e \cdot |\Delta\varphi_{sh}| \gg k_B \cdot T_e$. Two approximations are usually applied to describe

the space charge sheath in the collision-free regime, the matrix sheath, and the Child–Langmuir sheath, respectively.

3.6.2.1 Matrix Sheath

In the matrix sheath model the space charge density is defined as constant positive ion density. The electrons are neglected due to the strong repulsive potential in front of the surface.

With the boundary conditions for the electric field $E(z=0) = 0$ at the sheath edge and the surface potential $\varphi(z=s) = -\varphi_{sf}$ the solution of the source equation for the electric field provides the linear electric field profile, and consequently the parabolic potential in dependence on the distance z from the sheath edge normally toward the surface

$$E = \frac{e \cdot n_+}{\varepsilon_0} \cdot z \quad 0 \leq z \leq s_{matrix} \quad (3.224)$$

$$\varphi = -\frac{e \cdot n_+}{\varepsilon_0} \cdot \frac{z^2}{2}. \quad (3.225)$$

The matrix sheath thickness, scaled by the electron Debye length, is obtained from Equation 3.225 for $\Delta\varphi_{sh} = -\varphi_s$ and $z = s_{matrix}$

$$s_{matrix} = \lambda_{De} \cdot \left(\frac{2 \cdot e \cdot \varphi_s}{k_B \cdot T_e} \right)^2. \quad (3.226)$$

The matrix sheath model plays an important role in the plasma-ion-immersion-implantation (PIII) of material surfaces.

3.6.2.2 Child–Langmuir Sheath

The Child–Langmuir sheath model is based on the conservation of the ion flux and energy in the space charge sheath similar to (3.198) and (3.199), but neglecting the initial ion energy at the sheath edge ($v_+(0) = 0$) due to $e \cdot |\Delta\varphi_{sh}| \gg k_B \cdot T_e$

$$\frac{1}{2} \cdot m_+ \cdot v_+^2(z) = -e \cdot \varphi(z) \quad (3.227)$$

$$j_+ = e \cdot n_+(z) \cdot v_+(z) = const. \quad (3.228)$$

The combination of both equations provides the positive space charge in the sheath

$$n_+(z) = \frac{j_+}{e} \cdot \left(-\frac{2 \cdot e \cdot \varphi}{m_+} \right)^{-1/2} \quad (3.229)$$

and the 1D Poisson equation can be written as follows:

$$\frac{d^2\varphi}{dz^2} = -\frac{j_+}{\varepsilon_0} \cdot \left(-\frac{2 \cdot e \cdot \varphi}{m_+} \right)^{-1/2}. \quad (3.230)$$

With the boundary conditions $\varphi(z = s) = -\varphi_s$ and $\varphi(z = 0) = 0$ the integration of (3.230) results in the well-known solution for the space charge limited ion current, the Child–Langmuir $\Delta\varphi^{3/2}$ law

$$j_{+,s} = \frac{4}{9} \cdot \varepsilon_0 \cdot \left(\frac{2 \cdot e}{m_+} \right)^{1/2} \cdot \frac{\varphi_s^{3/2}}{s^2}. \quad (3.231)$$

By usage of the Bohm current density at the sheath edge ($j_{+,s} = j_{Bohm}$), it follows an expression for the thickness of the space charge sheath, scaled with the electron Debye length

$$s_{Child} = \frac{2^{1/2}}{3} \cdot \lambda_{De} \cdot \left(\frac{2 \cdot e \cdot \varphi_s}{k_B \cdot T_e} \right)^{3/4}. \quad (3.232)$$

In comparison with the matrix sheath thickness, the Child–Langmuir sheath thickness has a larger extension as shown by the following ratio

$$\frac{s_{Child}}{s_{matrix}} = \frac{\sqrt{2}}{3} \cdot \left(\frac{2 \cdot e \cdot \varphi_s}{k_B \cdot T_e} \right)^{1/4} \approx 5.8 \cdot \left(\frac{\varphi_s [\text{V}]}{T_e [\text{K}]} \right)^{1/4}. \quad (3.233)$$

For example, at $\varphi_s = 1000 \text{ V}$, $T_e = 10^4 \text{ K}$ and $n_e = 10^{16} \text{ m}^{-3}$, the ratio amounts to about 3.26 with a Child–Langmuir sheath thickness of about 11 mm compared with about 3 mm for the matrix thickness. For the potential, the electric field and the ion density in the sheath it is obtained

$$\varphi(z) = -\varphi_s \cdot \left(\frac{z}{s_{Child}} \right)^{4/3}, \quad (3.234)$$

$$E(z) = \frac{4}{3} \cdot \frac{\varphi_s}{s_{Child}} \cdot \left(\frac{z}{s_{Child}} \right)^{1/3}, \quad (3.235)$$

$$n_+(z) = \frac{4}{9} \cdot \frac{\varepsilon_0}{e} \cdot \frac{\varphi_s}{s_{Child}} \cdot \left(\frac{z}{s_{Child}} \right)^{-2/3}. \quad (3.236)$$

3.6.2.3 Plasma Sheath with Ion Collisions

The description of the plasma sheath with ion collisions represents a challenge because of several reasons:

1. Most of the nonthermal plasmas are characterized by a transition regime $\lambda_+ \approx s$.
2. The usual definition of the macroscopic quantity for the ion mobility (b_+) in strong inhomogeneous electric fields of the plasma sheath is a critical point.
3. On the microscopic scale the different elementary collision processes of ions with the neutrals have to be included, for example elastic collisions, charge transfer collisions and in molecular plasmas further ion–molecule reactions.

In the case of the mobility-dominated ion transport in the space charge sheath we use for the ion current density

$$j_+ = e \cdot n_+ \cdot v_+ = e \cdot n_+ \cdot \left(-b_+ \cdot \frac{d\varphi}{dz} \right) \quad (3.237)$$

with the ion mobility $b_+ \cdot p = b_{+0} = \text{const}$. The problem is the appropriate definition of the ion mobility. Using the ion mobility defined above and the special condition $\lambda_+ \ll s$, which may be realized in high-pressure plasmas as well as neglecting the electron density in the sheath, we can insert the ion density from (3.237) into the Poisson equation for a plane geometry. The integration over z with the boundary condition at the surface $\varphi(z=s_{\text{coll}}) = -\varphi_s$ results in the following ion current density at the surface

$$j_{+,s} = \frac{9}{8} \cdot \varepsilon_0 \cdot b_+ \cdot \frac{\varphi_s^2}{s_{\text{coll}}^3}. \quad (3.238)$$

Using the Bohm current density as an approximation of the ion current density in (3.238), the sheath thickness can be estimated

$$s_{\text{coll}} \propto \left(\frac{9}{8} \cdot \frac{\varepsilon_0 \cdot b_+}{e \cdot 0.61 \cdot n_{pl}} \cdot \left(\frac{m_+}{k_B \cdot T_e} \right)^{1/2} \right)^{1/3} \cdot \varphi_s^{2/3} \sim \varphi_s^{2/3} \cdot p^{-1/3}. \quad (3.239)$$

The more interesting case is the definition of the ion mobility in the transition regime in nonthermal plasmas at lower pressure for the condition $\lambda_+ \leq s$.

Without ionization processes in the sheath the continuity of the current density in the sheath is given by (3.198)

$$n_+(z) \cdot v_+(z) = n_+(0) \cdot v_+(0) \quad (3.240)$$

with $v_+(z) = b_+(v_+) \cdot E(z) \approx 2 \cdot e \cdot \lambda_+ / (\pi \cdot m_+ |v_+|) \cdot E(z)$.

Taking into calculation a mean free path length of ions independent on the ion velocity and $v_+(z) > 0$, the solutions for the electric field, potential, and current density at the surface follows according to Lieberman [36]

$$E(z) = \left(\frac{3 \cdot e \cdot n_+(0) \cdot v_+(0)}{2 \cdot \varepsilon_0 \cdot (2 \cdot e \cdot \lambda_+ / \pi \cdot m_+)^{1/2}} \right)^{2/3} \cdot z^{2/3}, \quad (3.241)$$

$$\varphi(z) = -\frac{3}{5} \cdot \left(\frac{3}{2 \cdot \varepsilon_0} \right)^{2/3} \cdot \frac{(e \cdot n_+(0) \cdot v_+(0))^{2/3}}{(2 \cdot e \cdot \lambda_+ / \pi \cdot m_+)^{1/3}} \cdot z^{5/3}, \quad (3.242)$$

$$j_{+,sf} = \frac{2}{3} \cdot \left(\frac{5}{3} \right)^{3/2} \cdot \varepsilon_0 \cdot \left(\frac{2 \cdot e \cdot \lambda_+}{\pi \cdot m_+} \right)^{1/2} \cdot \frac{\varphi_{sf}^{3/2}}{s^{5/2}}. \quad (3.243)$$

For the sheath thickness follows

$$s_{coll,\lambda} \propto \varphi_{sf}^{3/5} \cdot \lambda_+^{1/5} \sim \varphi_{sf}^{3/5} \cdot p^{-1/5}. \quad (3.244)$$

3.6.2.4 Ion Energy Distribution at the Surface

In the collisionless sheath the kinetic energy of positive ions is determined by the potential drop over the sheath, which means the energy distribution function is characterized by single peak at the position corresponding to $e \cdot |\Delta\varphi_{sheath}|$. Taking into account ion collisions the energy losses by elastic and charge transfer collisions have to be considered. Davis and Vanderslice [37] have firstly presented an analytical expression for the ion energy distribution function at the cathode of a DC low-pressure discharge. Rickards [38] has modified this model including the linear increasing electric field strength toward the cathode surface, the charge transfer collisions of ions with constant cross section, and no ionization in the cathode layer

$$F(\varepsilon^*) = \frac{dN_+}{d\varepsilon^*} = \frac{N_{+0}}{2} \cdot \frac{s_{DC}}{\lambda_{ex}} \cdot (1 - \varepsilon^*)^{-1/2} \cdot \exp \left[-\frac{s_{DC}}{\lambda_{ex}} + \frac{s_{DC}}{\lambda_{ex}} \cdot (1 - \varepsilon^*)^{1/2} \right], \quad (3.245)$$

where

λ_{ex} is the mean free path length for charge transfer collision

s_{DC} is the thickness of the cathode layer

$\varepsilon^* = (\varepsilon/e\varphi_c)$ is the ion energy relative to the maximal ion energy for collision free transport in the cathode layer with ($\varepsilon^* = 0 \dots 1$)

3.6.3 NONSTATIONARY PLASMA SHEATHS

More complicated is the situation at the electrodes or immersed probes and material surfaces in gas discharge plasmas at non-stationary plasma conditions. The plasma parameters, such as the energy distributions functions, charge carrier densities, plasma potential as well as surface potential may depend on time due to intrinsic or transient processes in electric gas discharges or time-dependent energy input by external power supplies. In connection with characteristic relaxations processes and response times the plasma sheath will show a nonstationary behavior.

It needs a detailed kinetic description, by means of kinetic equations or PIC-MCC simulations, to provide all information about the space charges, the self-consistent electric fields, the electric potentials, as well as the energy or velocity distribution functions of the considered plasma species in their spatiotemporal behavior at the given boundary conditions including the external electric circuit, see Section 9.4.

Taking into consideration nonthermal plasmas produced by power supplies with harmonic voltage of the circular frequency ω , we can separate the quasi-stationary case if $\omega \ll \omega_{p+}$ or $\omega \gg \omega_{pe}$. The first condition describes the situation similar to the DC case. The plasma sheath is formed for each phase position of the applied voltage. The second condition describes the high-frequency situation, if the electrons cannot more follow the external electric field instantaneously.

This section discusses the practical case of capacitive sheath in radio frequency (RF) plasmas, characterized by the condition

$$\omega_{p+} < \omega < \omega_{pe}. \quad (3.246)$$

3.6.3.1 Collisionless Sheath in Capacitively Coupled RF Plasma ($e \cdot |\overline{\Delta\varphi}_{sh}| \gg k_B \cdot T_e$)

The dynamics of the RF sheath is mainly determined by the electron dynamics in the sheath, which means the electron front oscillates in dependence on the variation of the electrode and plasma potential. This results in strong modulation of the space charges, the self-consistent electric field, the sheath potential, as well as the sheath thickness. In rough approximation the heavy positive ions follow the mean electric field. In this model the ion transport can be described by means of the time-averaged electric potential involving current continuity and energy conservation similar to the DC case

$$n_+(z) \cdot v_+(z) = n_+(0) \cdot v_+(0), \quad (3.247)$$

$$\frac{1}{2}m_+ \cdot v_+^2(z) = \frac{1}{2}m_+ \cdot v_+^2(0) - e \cdot \overline{\varphi(z)}. \quad (3.248)$$

The corresponding source equation for the instantaneous electric field is given by

$$\begin{aligned} \frac{\partial E(z, t)}{\partial z} &= \frac{e}{\varepsilon_0} \cdot n_+(z) && \text{for } z > s(t), \\ \frac{\partial E(z, t)}{\partial z} &= 0 && \text{for } z < s(t) \end{aligned} \quad (3.249)$$

with z is the distance from the ion sheath boundary ($z = 0$) to the electron sheath edge $s(t)$, see Figure 3.28.

The time averaging over the RF cycle provides the time-averaged quantities for the electric field strength, electron density in the sheath, and the electric sheath potential

$$\frac{\partial \bar{E}}{\partial z} = \frac{e}{\varepsilon_0} \cdot [n_+(z) - \bar{n}_e(z)], \quad (3.250)$$

$$\frac{d\bar{\varphi}}{dz} = -\bar{E} \quad (3.251)$$

with $\bar{n}_e(z) = (1 - 2 \cdot \phi/(2 \cdot \pi)) \cdot n_+(z)$.

The quantity $2 \cdot \phi(z) = 2 \cdot \omega \cdot t$ describes the RF phase interval for the condition $s(t) < z$ on \bar{n}_e . For small values of z , ϕ will be near zero for short time of the RF phase, only, which means $2\phi \approx 0$ and $\bar{n}_e \approx n_+$. On the other hand, for z near the maximum sheath thickness s_{max} , which is approximately for the most part of the RF cycle, the quantity 2ϕ can be set 2π and $\bar{n}_e \approx 0$ [36].

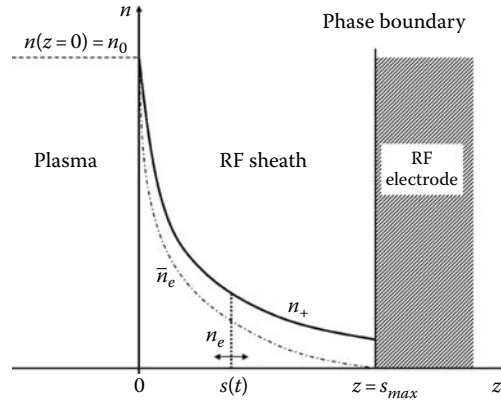


FIGURE 3.28 High-voltage RF sheath, density profiles, and moving electron sheath edge.

With the assumption of a sinusoidal RF current density in the sheath which is equal the conducting electron current density at the sheath edge, the movement of the electron sheath edge $s(t)$ is described by

$$-e \cdot n_+(s) \cdot \frac{ds(t)}{dt} = -j_c \cdot \sin(\omega \cdot t). \quad (3.252)$$

Some solutions from the equations above are given by Lieberman [36], see below

$$\frac{z}{s_0} = (1 - \cos \phi) + \frac{H}{8} \cdot \left(\frac{3}{8} \cdot \sin \phi + \frac{11}{18} \sin 2\phi - 3\varphi \cos \phi - \frac{1}{3} \cdot \varphi \cdot \cos 2\phi \right). \quad (3.253)$$

Ion density at the sheath edge

$$\frac{n_+(z)}{n_0} = \left[1 - H \left(\frac{3}{8} \cdot \sin 2\phi - \frac{1}{4} \varphi \cos 2\phi - \frac{1}{2} \cdot \phi \right) \right]^{-1} \quad (3.254)$$

with effective oscillation amplitude

$$s_{\text{eff}} = \frac{j_c}{e \cdot \omega \cdot n_0} \quad \text{and} \quad (3.255)$$

$$H = \frac{j_c^2}{\pi \cdot e \cdot \varepsilon_0 \cdot T_e \cdot \omega^2 \cdot n_0} = \frac{1}{\pi} \cdot \frac{s_{\text{eff}}^2}{\pi \cdot \lambda_{D0}^2}. \quad (3.256)$$

The integration of (3.250) results in a modified Child–Langmuir law for the self-consistent ion sheath

$$\frac{e \cdot \bar{\Phi}}{k_B \cdot T_e} = \frac{1}{2} - \frac{1}{2} \cdot \left[1 - H \left(\frac{3}{8} \cdot \sin(2\phi) - \frac{1}{4} \cdot \varphi \cdot \cos(2\phi) - \frac{1}{2} \cdot \phi \right) \right]^2. \quad (3.257)$$

At $\phi = \pi$ and for $H \gg 1$ it follows for the ion sheath voltage

$$\Delta\bar{\varphi}_{sh} = -\bar{\varphi}_s \quad \frac{e \cdot \bar{\varphi}_s}{k_B \cdot T_e} = \frac{9}{32} \cdot \pi^2 \cdot H^2 \quad (3.258)$$

and for the sheath thickness

$$z = s_{max} \quad \frac{s_{max}}{s_{eff}} = \frac{5}{12} \cdot \pi \cdot H \quad (3.259)$$

respectively.

Finally, we obtain with the Bohm current density an expression similar to the Child–Langmuir law

$$\bar{j}_+ = e \cdot n_0 \cdot v_{Bohm} = C_+ \cdot \varepsilon_0 \cdot \left(\frac{2 \cdot e}{m_+} \right)^{1/2} \cdot \frac{\bar{\varphi}_s^{3/2}}{s_{max}^2} \quad (3.260)$$

with $C_+ = 200/243$ (in the DC Child–Langmuir law $C_+ = 4/9$) and $s_{max} = \sqrt{50/27} \cdot s_{child}$.

In the case of collisional sheath a corresponding formula to (3.243) is derived [36]

$$\bar{j}_+ = e \cdot n_0 \cdot v_{Bohm} \approx 1.68 \cdot \varepsilon_0 \cdot \left(\frac{2 \cdot e}{m_+} \right)^{1/2} \cdot \frac{\bar{\varphi}_s^{3/2} \cdot \lambda_+^{1/2}}{s_{max}^{5/2}}. \quad (3.261)$$

3.6.3.2 Strongly Asymmetric Capacitively Coupled RF Plasma

In a capacitively coupled, unconfined, and for that reason asymmetrical RF discharge, a negative self-bias voltage (φ_{SB}) appears at the powered electrode which is little less than half the peak-to-peak RF voltage ($\Delta\varphi_{pp}$). Assuming capacitive sheath model and strong asymmetry, the idealized potentials over the RF cycle is represented in Figure 3.29.

$$\varphi_{RF}(t) = -\varphi_{SB} + \varphi_0 \cdot \sin(\omega \cdot t), \quad (3.262)$$

$$\varphi_{pl}(t) = \varphi_{sf} + \frac{1}{2} \cdot (-\varphi_{SB} + \varphi_0) \cdot [1 + \sin(\omega \cdot t)] \quad (3.263)$$

with $|\varphi_{SB}| \leq 1/2 \cdot \Delta\varphi_{pp} = \varphi_0$.

The negative self-bias potential results from the fact that no net DC current can flow over one RF cycle due to the capacitive coupling, and that the surface ratio between the powered and grounded electrode is significantly different ($A_{rf} \ll A_{grounded}$).

The electrons can follow the alternating electric field and leads to a moving electron edge which modulates the positive space charge region, the sheath potential, and the thickness, see Figures 3.28 and 3.29. Increasing RF voltage amplitudes mainly affect the self-bias voltage and sheath properties at the powered electrode. It has only little influence on the plasma potential in strongly asymmetric RF discharges. As the result, the self-bias voltage at the powered electrode increases with the applied RF

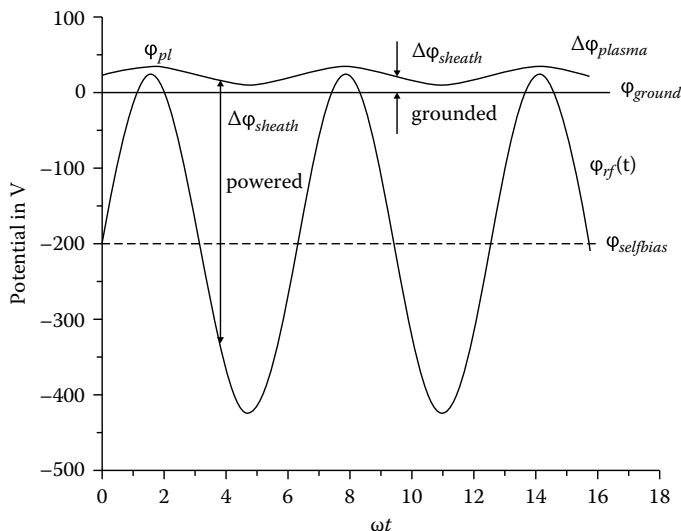


FIGURE 3.29 Electric potentials idealized for an asymmetric capacitively coupled RF plasma (CCP). The differences between the plasma potentials φ_{pl} and φ_{RF} , as well as the ground potential ($\varphi = 0$) represents the sheath voltage at the powered and grounded electrode, respectively. RF amplitude: 125 V, self-bias potential: -200 V, floating potential: 10 V.

voltage, whereas no significant influence can be observed at the grounded electrode. Due to the weak plasma potential modulation, the sheath properties at the grounded electrode are comparable with a DC plasma sheath.

The transport of positive ions to the RF powered electrode is strongly influenced by the oscillating plasma sheath voltage. Therefore, the flux of positive ions at the RF electrode depends on the ratio between the ion transit time over the RF sheath region and the RF-cycle. Furthermore, charge transfer collisions and elastic collisions in dependence on the nature of the positive ions and the total pressure affects the ion energy distribution in the sheath and at the electrode surface. Direct ion extraction at the discharge electrode and energy selective mass spectrometry was used to measure the flux of positive ions depending on their kinetic energy. Figure 3.30 shows the time-averaged Ar^+ energy distributions at the driven and grounded electrode of an RF-discharge in argon. As expected from the sheath potential, the maximum ion energy at the powered electrode is strongly coupled to the RF voltage due to the increasing self-bias voltage. The maximum ion energy is of the order of several hundred eV, whereas the maximal energy of positive ions at the grounded electrode is lower than about 20 eV.

Significant differences in the shape of the ion energy distribution at the two electrodes are observed. Ions coming from the bulk plasma need several RF cycles for transition to the powered electrode. In Figure 3.30a the arrows identify the situation for entering the ions from the bulk plasma into the sheath at the low and high sheath voltage, respectively. In result a saddle-shaped structure in the ion energy distribution is found. The observed multiple peak structure in the low energetic part results from charge transfer collisions in the sheath region. In the time-averaged ion energy

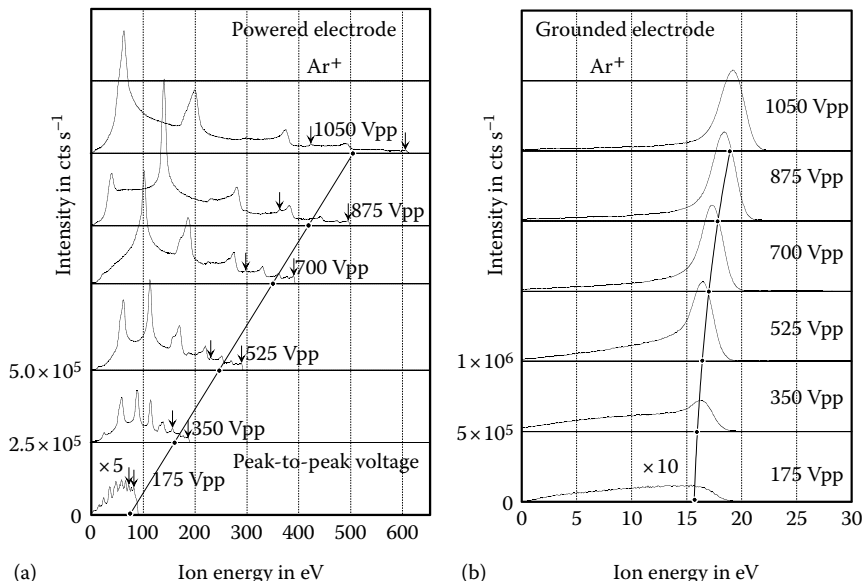


FIGURE 3.30 Ion energy distribution function (Ar⁺) at the RF electrode (a) and grounded electrode (b). 13.56 MHz-discharge in argon at 5 Pa, parameter: peak-to-peak voltage. (From Zeuner, M. et al., *J. Appl. Phys.*, 81, 2985, 1997.)

distribution the saddle-shaped structures overlap from ions directly from bulk plasma and ions from charge transfer collisions.

At the grounded electrode the single peak at the high energy end is seen, only, Figure 3.30b.

With increasing pressure the elastic collisions will have more influence. This is connected with increasing ion intensity at the low energy part and disappearing (multiple) peak structure.

3.7 NONTHERMAL PLASMAS OF ELECTRIC GAS DISCHARGES

3.7.1 INTRODUCTION AND OVERVIEW

Nonthermal plasmas are usually generated by electric gas discharges due to the heating of electrons in the electric field and the ionization of the neutral gas atoms or molecules by electron impact ionization. In this section the heating of electrons in the electric field is discussed in connection with the dissipation and confinement of energy. Thereby the evolution and re-distribution of the electron energy distribution function (EEDF) plays a significant role in electrical gas discharges. It depends on elementary plasma processes with characteristic time constants, for

- Production and recombination of charged species
- Dissociation of molecules and chemical reactions
- Excitation and de-excitation of neutral and charged atoms/molecules

- Energy relaxation, e.g., translation-translation τ_{TT} , vibration-vibration τ_{VV} , rotation-rotation τ_{RR} , translation-rotation τ_{TR} , translation-vibration τ_{TV} , vibration-rotation τ_{VR}
- Recombination/extraction and heterogeneous chemical reactions of plasma particles at plasma boundaries (electrodes, walls) due to field drift and/or diffusion

Different electrical gas discharge plasmas can be generated in dependence on the *neutral gas pressure*, from low pressure to atmospheric or higher pressure, the *specific boundary conditions* at discharge electrodes and walls, and the applied *electric power supplies* running over wide frequency range in continuous or pulsed mode operation, e.g.,

- Direct current (DC)
- Standard line frequency ($\nu = 50$ Hz)
 $\omega = 2 \cdot \pi \cdot \nu \ll \omega_{p+}, \omega_{pe}$
- Middle frequency ($\nu = 50$ kHz ... 500 kHz)
 $\omega = 2\pi\nu < \omega_{p+}, \ll \omega_{pe}$
- Radio frequency ($\nu = 10$ MHz ... 100 MHz ...)
 $\omega_{p+} < \omega = 2 \cdot \pi \cdot \nu < \omega_{pe}$
- Microwave frequency ($\nu = 2$ GHz ... 10 GHz ...)
 $\omega = 2 \cdot \pi \cdot \nu \gg \omega_{p+}, \geq \omega_{pe}$

Additionally, the external magnetic field may be applied for electron confinement in DC or RF magnetron discharges as well as for the wave heating of electrons like electron cyclotron resonance heating (ECRH) in microwave plasmas or helicon waves in RF plasmas.

The different kinds of gas discharges can be classified according to their current–voltage characteristics, the specific coupling to the electric power supply, and transfer of energy into the plasma as well as the elementary processes for production of charged particles in the gas volume and/or at the electrodes/walls. Thereby, the most important internal parameters of nonthermal plasmas are the electron density n_e , electron temperature T_e , or the electron energy distribution function (EEDF).

In connection to the characteristic time behavior of internal parameters the electric gas discharges can be classified in stationary and nonstationary or transient discharges. The nonstationarity of the plasma may have their origin from intrinsic plasma instabilities and relaxations processes or from the time-depending energy input by the external electric power supply.

Firstly, the *electric breakdown* in a gas is described as an initial process for the discharge ignition. Secondly, the generation of *nonthermal plasmas* is discussed from the plasma physics point of view taking into consideration the electric power supplies running from DC to microwave frequencies. In that way the different gas discharges or plasmas are classified and characterized, such as the Townsend discharge, the glow discharge, the arc discharge, the corona discharge, the spark discharge, the barrier discharge, the radio frequency, and microwave plasmas, see the overview in Figure 3.31.

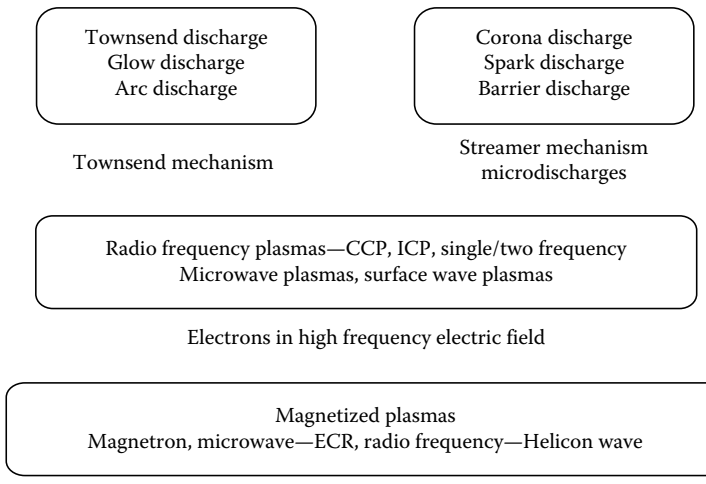


FIGURE 3.31 Overview and classification of electric gas discharges (CCP/ICP: Capacitively/inductively coupled plasma; ECR: electron cyclotron resonance).

3.7.2 ELECTRIC BREAKDOWN IN GASES AND TOWNSEND DISCHARGE

The classical Townsend mechanism describes the electric breakdown in a gas by electron avalanches without space charge effects. The electric breakdown means the transition of the gas from the insulator into the conductor which depends on the pressure and the external electric field strength. We consider a discharge gap consisting of two parallel metal plates as electrodes (cathode and anode) with the diameter R and separation d_E ($R \gg d_E$) filled with neutral gas at the pressure p , see Figure 3.32.

The uniform electric field strength $|\vec{E}| = U_E/d_E$ is generated by the applied voltage U_E from the external DC power supply over the electrode distance d_E . The starting point is the production of free electrons at the cathode surface by energetic photons resulting from an external source (e.g., cosmic radiation or natural radioactivity). These electrons are accelerated in the uniform electric field toward the anode. Thereby, they ionize neutral gas atoms in the gap due to electron impact ionization if their kinetic energy is above the threshold for ionization.

The first Townsend coefficient $\alpha = 1/n_e \cdot dn_e/dz$ describes the number of produced electron-ion pairs per length unit in z -direction by electrons moving from the cathode to the anode.

For a given gas, the total number of produced electron-ion pairs depends on the electrode separation d_E and the total gas pressure p . The ionization probability P_{ion} of electrons can be calculated taking into account the distribution law of the mean free path length of electrons for ionizing collisions λ_{ion} and the ionization length z_{ion} which corresponds to the path length of electrons in the electric field to achieve the

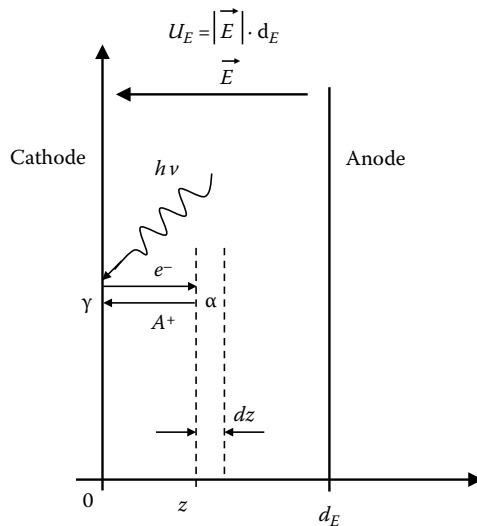


FIGURE 3.32 Charge carrier production in the discharge gap due to α and γ processes.

necessary kinetic energy for ionization.

$$P_{ion} = \frac{n_e(z)}{n_{eo}} = \exp\left(\frac{-z_{ion}}{\lambda_{ion}}\right). \quad (3.264)$$

This equation gives the probability that an electron has an ionization length greater than z_{ion} .

The first Townsend coefficient α , which means the number of ionizing electron collisions per length unit, can be achieved after division of (3.264) by λ_{ion} .

Then, we replace z_{ion} and λ_{ion} in

$$\alpha = \frac{1}{\lambda_{ion}} \exp\left(\frac{-z_{ion}}{\lambda_{ion}}\right) \quad (3.265)$$

by use of the electron energy gain in the electric field over z_{ion}

$$\Delta \varepsilon_{ion} = e \cdot E \cdot z_{ion} \quad (3.266)$$

and the pressure depending mean ionization path length

$$\lambda_{ion} \cdot n_{gas} = \lambda_{ion} \cdot \frac{p}{k_B \cdot T_{gas}} = \frac{\langle v_e \rangle}{\langle \sigma_{ion} \cdot v_e \rangle} = C_{ion} \quad (3.267)$$

to achieve the α coefficient

$$\alpha = \frac{\exp(-z_{ion}/\lambda_{ion})}{\lambda_{ion}} = \frac{p}{k_B \cdot T_{gas} \cdot C_{ion}} \cdot \exp\left(-\frac{\Delta\varepsilon_{ion}}{e \cdot C_{ion} \cdot k_B \cdot T_{gas} \cdot E/p}\right). \quad (3.268)$$

The constant C_{ion} depends on the ionization cross section of the used gas and the electron velocity distribution function.

Finally, the pressure reduced first Townsend coefficient

$$\frac{\alpha}{p} = C_1 \cdot \exp\left(-\frac{C_2}{E/p}\right) = f\left(\frac{E}{p}\right) \quad (3.269)$$

with $C_1 = (k_B \cdot T_{gas} \cdot C_{ion})^{-1}$ and $C_2 = \Delta\varepsilon_{ion}/(e \cdot k_B \cdot T_{gas} \cdot C_{ion})$ is found as a function of the reduced electric field strength E/p , only, firstly derived by Townsend.

The reduced electric field strength E/p expressed by E/n_{gas} is mostly given in units of Townsend which is defined as

$$\frac{E}{n_{gas}} = 1 \text{ Townsend} = 1 \text{ Td} = 10^{-17} \text{ V} \cdot \text{cm}^2.$$

The constants C_1 and C_2 in Equation 3.269 have to be determined experimentally and they are available for a special kind of gas at constant temperature in a limited range of the reduced electric field strength E/p , see Figure 3.33, [3]. Thereby the range of validity of the constant C_2 is in the limit between about $C_2/2 \leq E/p \leq 3C_2$ [40].

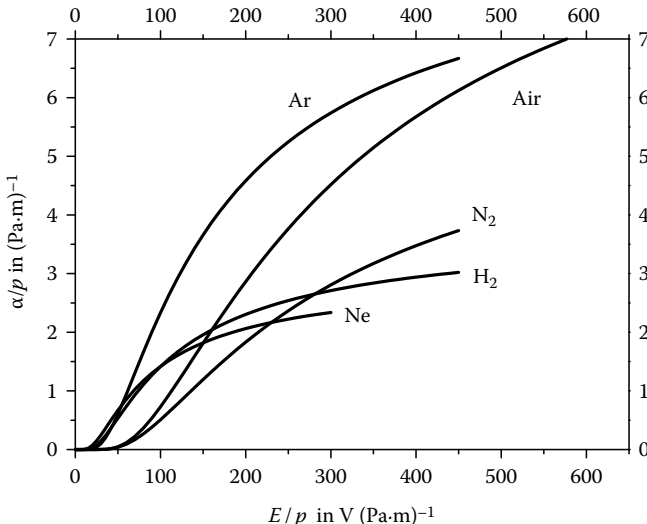


FIGURE 3.33 Analytical calculation (3.269) of the pressure reduced first Townsend coefficient α/p in dependence on E/p for different gases, using the corresponding values for C_1 and C_2 from literature.

With the known α coefficient the rising electron current density at the position z within dz in Figure 3.32 is given by the 1D stationary balance equation for electrons

$$\frac{dj_e}{dz} = \alpha \cdot j_e = \alpha \cdot e \cdot n_e \cdot v_{eD} = \nu_{ion} \cdot e \cdot n_e = \langle \sigma_{ion} \cdot v_e \rangle \cdot e \cdot n_e \cdot n_{gas} \quad (3.270)$$

where

α is the first Townsend coefficient

v_{eD} is the electron drift velocity in z -direction

ν_{ion} is the ionization frequency

σ_{ion} is the electron impact ionization cross section

The total electron current density and the electron density at the position z is achieved after integration of (3.270) for constant α

$$j_e(z) = j_{e0}(0) \cdot \exp(\alpha \cdot z), \quad (3.271)$$

$$n_e(z) = n_{e0}(0) \cdot \exp(\alpha \cdot z) \quad (3.272)$$

with $j_{e0}(0)$ and $n_{e0}(0)$ as the electron current density and the electron density at the cathode from the external source, respectively.

In other words, starting with one electron at the cathode the number of electrons rises on exponentially to N_{ez} with increasing path length z of the electron drift toward the anode

$$N_{ez} = 1 \cdot \exp(\alpha \cdot z) \quad (3.273)$$

and describes the *first electron avalanche*.

On the other hand, the produced positive ions in the gap will be accelerated in opposite direction toward the cathode. Thereby, the ionization of neutral gas atoms by collision with positive ions, described by the second Townsend coefficient β in the original theory of Townsend, is neglected. The cross section of ion-impact ionization is much lower in comparison with that of the electrons in the considered range of kinetic energy. Impinging positive ions at the cathode surface have sufficient high kinetic energy to produce secondary electrons, described by the *third Townsend coefficient* γ . From the macroscopic point of view the coefficient γ describes the number of emitted secondary electrons per impinging positive ion expressed by the corresponding current densities at the cathode

$$\gamma \equiv \frac{j_{es}}{j_+} |_{cathode}. \quad (3.274)$$

The coefficient γ depends on the kind of gas, the kinetic energy of ions, and the cathode material [41]. Typical values for γ in electric gas discharges are in the order of magnitude of between 0.01 and 0.1.

The total number of positive ions N_+ , generated from one electron moving from the cathode to the anode

$$N_+ = \exp(\alpha \cdot d_E) - 1 \quad (3.275)$$

produces N_{es} secondary electrons at the cathode surface

$$N_{es} = \gamma \cdot [\exp(\alpha \cdot d_E) - 1]. \quad (3.276)$$

These secondary electrons are accelerated in the electric field and produce new electron-ion pairs due to ionizing collisions with neutral gas atoms (α -process) as discussed above and a *second electron avalanche* is observed. That means the charge carrier multiplication is achieved.

In the *steady state*, we obtain for the secondary electron density $n_{es}(0)$, at the cathode

$$\begin{aligned} n_{es}(0) &= n_{e0}(0) + n_{es}(0) \cdot \gamma \cdot [\exp(\alpha \cdot d_E) - 1] \\ n_{es}(0) &= \frac{n_{e0}(0)}{1 - \gamma \cdot [\exp(\alpha \cdot d_E) - 1]}. \end{aligned} \quad (3.277)$$

The term $n_{e0}(0)$ in (3.277) describes the secondary electrons generated by the external source, again, and the second term by the ion bombardment in steady state, respectively. With the electron density at the cathode in steady state $n_{es}(0)$, the electron density at the anode $n_{eA} = n_e (z = d_E)$ and the electron current density j_{eA} were found. The electron current density j_{eA} corresponds to the total discharge current density.

$$\begin{aligned} n_{eA} &= n_{e0} \cdot \frac{\exp(\alpha \cdot d_E)}{1 - \gamma \cdot [\exp(\alpha \cdot d_E) - 1]}, \\ j_{eA} &= j_{e0} \cdot \frac{\exp(\alpha \cdot d_E)}{1 - \gamma \cdot [\exp(\alpha \cdot d_E) - 1]}. \end{aligned} \quad (3.278)$$

Here, n_{e0} and j_{e0} are the electron density and current density at the cathode due to an external source.

If the denominator of (3.278) becomes zero the current density tends to infinity and leads to the electrical breakdown in the gas.

The *Townsend criterion for electric gas breakdown*

$$\gamma [\exp(\alpha \cdot d_E) - 1] = 1 \quad (3.279)$$

reflects the reproduction of one electron by gas ionization and the secondary electron emission at the cathode.

Furthermore, the Townsend criterion for the electric breakdown in gases defines the transition to a self-sustaining gas discharge. That means no additional external source is necessary to generate secondary electrons at the cathode.

In the case of strongly electronegative gases the production of negative ions is taken into account by an effective attachment coefficient η in the electron current density.

$$j_{eA} = j_{e0} \cdot \frac{\frac{\alpha}{(\alpha - \eta)} \cdot \exp(\alpha \cdot d_E) - \frac{\eta}{(\alpha - \eta)}}{1 - \frac{\gamma \cdot \alpha}{(\alpha - \eta)} \cdot [\exp(\alpha \cdot d_E) - 1]}. \quad (3.280)$$

The attachment coefficient implies the number of produced negative ions per electron path length z . The Townsend criterion for electronegative gases is found [42]:

$$\frac{\gamma \cdot \alpha}{(\alpha - \eta)} \cdot [\exp(\alpha \cdot d_E) - 1] = 1. \quad (3.281)$$

The strong increase of the electron current density in (3.278) and (3.280) at the breakdown is limited by the external circuit and the capacity of the applied power supply. The characteristic time needed for the complex electric breakdown process and formation of steady state discharge conditions is in the limit of between 1 and 100 μs depending on the geometry, pressure, and charge carrier production in the used gas.

In the case of electropositive gases the necessary breakdown voltage for the discharge ignition is derived by use of (3.269) and the replacement of α by the breakdown condition (3.279) which results in the Paschen law:

$$U_B = E_B \cdot d_E = \frac{C_2 \cdot (p \cdot d_E)}{\ln [C_1 \cdot (p \cdot d_E) / \ln(1 + 1/\gamma)]}. \quad (3.282)$$

The breakdown voltage U_B in terms of the product $p \cdot d_E$ provides the well-known *Paschen-curves* in gas discharge physics with the characteristic *Paschen minimum* of the breakdown voltage, see Figure 3.34 and (3.283). That means the optimal relation between α/p and E/p for the gas breakdown and the ignition of the gas discharge can be found.

$$U_B^{\min} = \frac{2,72 \cdot C_2}{C_1} \cdot \ln(1/\gamma + 1) \quad (3.283)$$

with $(p \cdot d_E)_{\min} = \frac{2,72}{C_1} \cdot \ln(1/\gamma + 1)$ and $\left(\frac{E}{p}\right)_{\min} = C_2$.

3.7.2.1 Townsend Discharge

The first self-sustaining and stationary gas discharge at low pressure, the *Townsend* or *dark discharge*, is characterized by low discharge current densities ($\leq 10^{-6} \text{ Acm}^{-2}$). Due to the low discharge current and the corresponding low charge carrier density in the gap the contribution of space charges to the electric field is neglected. The uniform electric field is defined by the applied voltage over the discharge gap. The current density and charge carrier density of electrons and positive ions between the discharge gap can be easily calculated taking into account the transport of charge carriers by the electric field drift, only. By use of the stationary balance equation for electrons $dj_e/dz = \alpha \cdot j_e$ with $\alpha = \text{const.}$, the total discharge current density $j = j_e(z) + j_+(z) = \text{const.}$ and the boundary conditions at the cathode

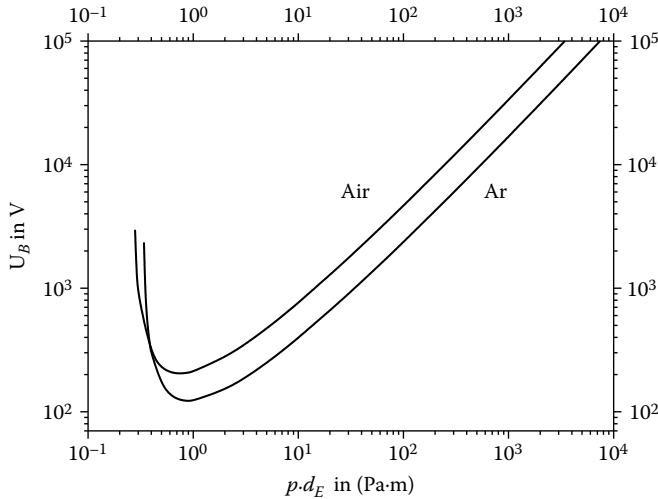


FIGURE 3.34 Breakdown voltage in dependence on $p \cdot d_E$ with the Paschen minimum calculated by (3.282) with $\gamma = 0.05$ in Ar ($C_1 = 9 \text{ (Pa}\cdot\text{m)}^{-1}$, $C_2 = 135 \text{ V(Pa}\cdot\text{m)}^{-1}$) and air ($C_1 = 11.3 \text{ (Pa}\cdot\text{m)}^{-1}$, $C_2 = 275 \text{ V(Pa}\cdot\text{m)}^{-1}$).

$j = j_{eC}(0) + j_{+C}(0) = j_{eC}(0) + 1/\gamma \cdot j_{eC}(0)$ and anode $j = j_{eA}(d_E)$, we obtain after integration over z for the electron and ion current density

$$\begin{aligned} j_e(z) &= j_{eC} \cdot \exp(\alpha \cdot z) = j \cdot \frac{\gamma}{1 + \gamma} \cdot \exp(\alpha \cdot z) \\ j_+(z) &= j \cdot \left[1 - \frac{\gamma}{1 + \gamma} \cdot \exp(\alpha \cdot z) \right]. \end{aligned} \quad (3.284)$$

Replacing γ in (3.284) with the breakdown condition (3.279) permits the rearrangement of the current densities

$$\begin{aligned} j_e(z) &= j \cdot \exp[\alpha(z - d_E)] = e \cdot n_e \cdot b_e \cdot E \\ j_+(z) &= j \cdot [1 - \exp[\alpha(z - d_E)]] = e \cdot n_+ \cdot b_+ \cdot E \end{aligned} \quad (3.285)$$

and the calculation of electron and positive ion density

$$\begin{aligned} n_e(z) &= \frac{j}{e \cdot E} \cdot \frac{1}{b_e} \cdot \exp[\alpha(z - d_E)] = \frac{j}{e \cdot C_{be}} \cdot \left(\frac{E}{p} \right)^{-1} \cdot \exp[\alpha(z - d_E)] \\ n_+(z) &= \frac{j}{e \cdot E} \cdot \frac{1}{b_+} \cdot [1 - \exp[\alpha(z - d_E)]] = \frac{j}{e \cdot C_{b+}} \cdot \left(\frac{E}{p} \right)^{-1} \cdot [1 - \exp[\alpha(z - d_E)]] \end{aligned} \quad (3.286)$$

with $0 \leq z \leq d_E$ and $b \cdot p = C_b = \text{const.}$ in the discharge gap, see Figure 3.35.

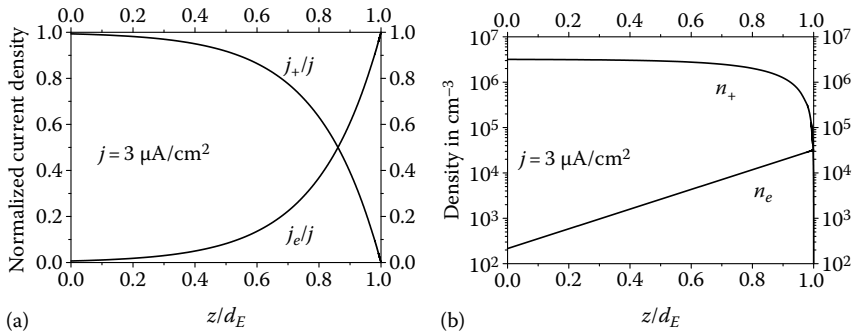


FIGURE 3.35 Characteristic axial profiles for the current density (a), and charge carrier density (b) between the discharge gap for a Townsend discharge ($E/p = 100 \text{ V} (\text{cm Pa})^{-1}$, $\alpha \cdot d_E = 5$, $b_+ \cdot p = 2 \cdot 10^5 \text{ cm}^2 \cdot \text{Pa V}^{-1} \text{s}^{-1}$, $b_e/b_+ = 100$).

It is to note the essential contribution of the ion current to the total current in the most part of the gap. Furthermore, no quasi-neutral region and therefore no plasma is observed because of the dominant positive ion density in the discharge gap, with the exception directly in front of the anode, see Figure 3.35b.

3.7.3 GLOW DISCHARGES

3.7.3.1 Transition from the Townsend Discharge to the Glow Discharge

With increasing discharge current the raising positive space charge density determines more and more the electric field strength in the discharge gap. At constant gap width and neutral gas pressure, the transition from the Townsend to the glow discharge regime may be defined for the special case that the electric field strength decreases from the maximum value at the cathode ($z = 0$) to the value zero at the anode position ($z = d_E$), see [43].

With the approximations $n_+ \gg n_e$ and $j \approx |j_+| = e \cdot n_+ \cdot v_{+D} = e \cdot n_+ \cdot b_+ \cdot E \gg |j_e|$, the 1D source equation for the electric space charge field is solved with the boundary conditions $E(z = 0) = E_0$ and $E(z = d_E) = 0$

$$E(z) = E_0 \cdot \left(1 - \frac{z}{d_E}\right)^{1/2} \quad (3.287)$$

with $E_0 = ((2 \cdot j \cdot d_E) / (\epsilon_0 \cdot b_+))^{1/2}$.

From the rearrangement of the expression for E_0 in (3.287) to the total discharge current density j and the multiplication with $1/p^2$ it follows

$$\frac{j}{p^2} = \frac{b_+ \cdot \epsilon_0 \cdot E_0^2}{2 \cdot d_E \cdot p^2} \cdot \frac{p}{p} = \frac{\epsilon_0}{2} \cdot \frac{(p \cdot b_+)}{(p \cdot d_E)} \cdot \left(\frac{E_0}{p}\right)^2. \quad (3.288)$$

The relation j/p^2 in terms of $(p \cdot d_E)$, (E_0/p) , and $(p \cdot b_+)$ provides a further similarity parameter in gas discharge physics.

TABLE 3.11
Important Similarity Parameters
in Gas Discharge Physics

$$\begin{array}{lll} \alpha/p & = & \text{Const.} \\ p \cdot d_E & = & \text{Const.} \end{array} \quad \begin{array}{lll} E/p & = & \text{Const.} \\ j/p^2 & = & \text{Const.} \end{array}$$

Summarized, the simple analytical description of the electric breakdown and the transition to stationary gas discharges provide important similarity parameters, see Table 3.11, which have *general importance* for comparison of gas discharges running at different processing parameters and geometry.

3.7.3.2 Glow Discharges

The glow discharges at low pressure ($1\text{--}10^4$ Pa) are characterized by typical discharge currents between 1 mA and a few 100 mA at voltages between 100 V and few kV. According to the U/I discharge characteristics the glow discharges are distinguished between *subnormal*, *normal*, and *anomalous glow discharges*. The *subnormal glow discharge* with negative U/I-characteristics represents a transition regime from the Townsend discharge to the normal glow discharge mode. The *normal glow discharge* mode is achieved if the voltage and current density at the cathode remains constant, even if the discharge current is varied. That means the cathode surface area contributes partially as discharge electrode, only. The effective cathode area increases or decreases corresponding to the total discharge current. The normal glow discharge is well characterized by the corresponding values for the normal cathode sheath voltage U_N and thickness for the considered kind of gas and pressure $p \cdot d_{CN}$. If the complete cathode surface is involved the normal glow discharge changes in the *anomalous glow discharge* mode which is characterized by a positive U/I-characteristics.

In a glow discharge the well separated discharge regions in axial direction between the cathode and anode are observed concerning the light emission, electric potential and field strength, as well as current and charge carrier densities. The following discharge regions are distinguished, well known described in many textbooks [3,36, 40,44]:

1. The *cathode sheath* with Aston dark space, the cathode glow, and Crookes dark space
2. The *negative glow region*
3. The *Faraday dark space*
4. The *positive column*
5. The *anode sheath* with anode dark space and anode glow

The external applied discharge voltage drops mainly over the cathode sheaths which is characterized by an inhomogeneous axial electric field strength of positive space

charges, decreasing from maximum fields strength at the cathode toward about zero at the cathode sheath edge at the axial position $z = d_C$.

In the *negative glow* region the electric field tends to zero. Only little negative space charges are present due to energetic electrons entering from the cathode sheath into the negative glow. A significant light emission in the negative glow is observed which results from excitation processes of the relaxing hot electrons from the cathode sheath and charge carrier recombination. Both, the cathode sheath and the negative glow, are the essential discharge regions for the maintenance of the glow discharge.

Toward the anode the following *Faraday dark space* represents a transition region between the negative glow and the positive column and is characterized by the increasing axial electric field strength.

The *positive column* represents a quasi-neutral region with constant and low axial electric field strength usually in the range of between 1 and 10 V/cm depending on the kind of gas, pressure, and tube radius [50]. In particular, the cylindrical positive column in discharge tubes has been widely used as a model system for weakly ionized nonthermal plasmas [45,46]. In dependence on the total pressure and discharge current, the diffuse and contracted positive column is observed. Furthermore, instabilities and nonlinear effects generate ionization waves which result in moving or standing striations of the positive column [47].

The nonthermal plasma of the positive column is mostly applied for low-pressure plasma light sources, such as fluorescent lamps.

The Faraday dark space and the positive column are only observed at sufficient high electrode separation and/or higher pressure, and they serve mainly to satisfy the current continuity in larger discharge gaps.

3.7.3.3 Cathode Sheath and Negative Glow in Strongly Anomalous Glow Discharges

In strong anomalous glow discharges at low pressure and high discharge voltage the basic physics and discharge mechanisms in the cathode sheath and negative glow will be discussed using the simple analytical description by means of drift/diffusion approximation. The boundary between the cathode sheath and the negative glow at the position $z = d_C$ is defined if the electric field strength of the cathode layer tends to zero. In accordance with experimental investigations the cathode sheath can be approximated by a matrix sheath (constant positive space charge density) which means that the electric field strength decreases linearly from the maximum value at cathode surface ($z = 0$) to zero at the cathode sheath edge ($z = d_C$). The glow discharge is sustained by physical processes in both the cathode sheath and the negative glow. At the cathode, the secondary electron emission (γ -process) by impinging energetic positive ions is essential, similar to the Townsend mechanism of the gas breakdown. The transport of the secondary electrons is determined by their drift in the inhomogeneous electric field of the cathode layer and the elastic and inelastic collisions with neutral gas atoms/molecules. At low gas pressure and strong electric field strength near the cathode, the secondary electrons gain quickly high kinetic energy which is combined with the decreasing collision cross section of the electrons (runaway electrons). The electron energy distributions function $f_e(\varepsilon, z)$

can be approximated by the Dirac δ -function for the beam-like electrons

$$f_e(\varepsilon, z) = \delta [a \cdot e \cdot \Delta\varphi(z) - \varepsilon] \text{ with } \int_0^\infty f_e(\varepsilon, z) \cdot d\varepsilon = 1 \quad (3.289)$$

with a the mean energy loss factor of the electrons in the cathode sheath.

Using the stationary 1D balance equation for electrons and the boundary condition at the cathode $j_{e0}(z=0)$ it follows

$$\frac{d(j_e \cdot f_e)}{dz} = j_e \cdot f_e \cdot n_{gas} \cdot \sigma_{ion}(\varepsilon) \quad (3.290)$$

and after integration the electron beam current density

$$j_e(z) = j_{e0}(0) \cdot \exp \left[\int_0^z n_{gas} \cdot \alpha_{ion}(a \cdot |e| \cdot \Delta\varphi(z') \cdot dz') \right] = j_{e0}(0) \cdot \exp \left[\int_0^z \alpha(z') \cdot dz' \right]. \quad (3.291)$$

Further, the electron multiplication factor M_e in the cathode sheath is defined as

$$M_e = \frac{j_e(d_c)}{j_{e0}(0)} = \exp \left[\int_0^{d_c} \alpha(z') \cdot dz' \right]. \quad (3.292)$$

It is to note, that in strongly anomalous glow discharges the multiplication factor is rather low, and amounts to between 1 and 2, only. Therefore, the ionizing electron collisions in the cathode sheath are mostly neglected in the analytical description of strongly anomalous glow discharges.

The beam electrons enter at the cathode sheath edge ($z=d_c$) in the approximated electric field free region of the negative glow. These electrons dissipate their kinetic energy in elastic scattering and inelastic collisions such as excitation and ionization of neutral gas atoms/molecules. The current density of the beam electrons in the negative glow can be approximated by an absorption law according to

$$j_e(z) = j_e(d_c) \cdot \exp [-\beta \cdot (z - d_c)] \quad (3.293)$$

with $z \geq d_c$ and β the effective absorption coefficient.

Usually, the scattering part dominates which is in the order of magnitude at about $\beta_{scatt} = n_{gas} \cdot \sigma_{scatt}/p \approx 0.2 \cdot (\text{Pa} \cdot \text{cm})^{-1}$.

Due to the very low space charge density and electric field strength in the negative glow, the charge carrier transport in axial direction is determined by the ambipolar diffusion. In a parallel plate glow discharge with $d_C, d_F \ll R$ the axial plasma density ($n = n_e = n_+$) profile in the negative glow can be estimated by use of the 1D diffusion equation

$$-D_a \cdot \frac{d^2 n}{dz^2} \propto \alpha(z) \cdot j_e(z) - r \cdot n. \quad (3.294)$$

The source and loss processes are assumed by the α -process of the beam electrons and the effective linear loss rate coefficient r which may include a weak loss by the radial ambipolar diffusion, respectively. The second order loss term is neglected. The boundary conditions for the plasma density can be set $n(d_C) = 0$ at the cathode sheath edge and $n(d_F) = n_F$ at the edge to the Faraday dark space characterized by increasing electric field strength.

Following, the negative glow region is characterized by the axially inhomogeneous plasma density with a dominant maximum ($\sim 10^{16}\text{--}10^{17} \text{ m}^{-3}$) nearby the cathode sheath edge and the low mean kinetic energy of the produced plasma electrons (few 0.1 eV).

The produced positive ions in the negative glow near to the cathode sheath edge can enter into the cathode sheath. Their current density at the cathode sheath edge may be approximated by the ambipolar diffusion current density $j_+(d_C) \propto -D_a \cdot (dn/dz)|_{dc}$. These ions, together with ions directly produced in the cathode sheath, drift in the inhomogeneous electric field towards the cathode. At the cathode surface, the kinetic energy of the ions is high enough for secondary electron emission (γ -process). Here, it is to note that in stationary glow discharges, the coefficient γ implies rather an effective secondary electron emission coefficient. The interaction of VUV/UV photons of the plasma radiation and/or metastable excited particles with the cathode surface may also contribute to the secondary electron emission.

The energy distribution function of positive ions in the cathode sheath is mainly influenced by charge transfer collisions and elastic collisions during their movement toward the cathode surface, and depends on total pressure and the kind of gas. In the collision-free case, the ion kinetic energy at the cathode surface corresponds directly to the voltage drop over the cathode sheath, see Section 3.6.2.

Furthermore special geometry and design of the cathode (e.g., cylindrical hollow cathode or double cathode) is applied to use the *hollow cathode effect*. Thereby, an effective overlapping of opposite negative glows results in more efficient ionization and excitation of gas atoms and molecules in the negative glow. A phenomenological explanation is based on the so-called pendulum electrons, which means the beam-like electrons entering from the cathode sheath into the negative glow are reflected at the opposite cathode sheath and so on. This increases the effective path length of energetic electrons and acts like an electron cavity. The inelastic electron neutral collisions result in significantly higher density of excited and ionized particles. The effective overlapping of the negative glows for a given gas needs suitable adjustment of the gas pressure in relation to the diameter of the cathode cylinder or the distance between the plane cathodes in the double cathode arrangement.

3.7.3.4 Stable Positive Column

At sufficient high distance between cathode and anode, the Faraday dark space and the positive column is observed. Due to the dissipation of the kinetic energy of the electrons as well as the loss of charge carriers due to recombination and ambipolar diffusion in the negative glow the loss processes have to be balanced by electron heating in the electric field and further gas ionization to satisfy the continuity of the total discharge current. Therefore, the electric field strength is slightly increasing in the Faraday dark space toward the positive column. The positive column is characterized by a constant electric field strength in axial direction and corresponding weak potential gradient, which is sufficiently high to heat the electrons for further electron impact ionization. The electron energy distribution function in the positive column is mostly approximated by the Maxwellian or Dryvesteyn distribution function. Thereby, sufficient electrons of the high energetic tail of the electron energy distribution function have kinetic energies above the threshold for inelastic collisions such as ionization, excitation, or dissociation of gas atoms/molecules.

In cylindrical discharge tubes (radius R) a simple model describes the diffusion-dominated stationary positive column ($\lambda_e, \lambda_+ \ll R$), taking into account

- Constant axial electric field strength E_z
- Ionization by electron impact from ground state with $\alpha = const.$
- No volume recombination
- Axially constant plasma density
- Radial ambipolar diffusion to the tube wall, ($n = n(r)$, $T_e \gg T_+, T_n$)
- Neglecting of plasma sheaths
- Totally absorbing wall

With the stationary particle balance equation for electrons $div \vec{j} = \nu_{ion} \cdot n$ and the diffusion current density $\vec{j} = -D_a \cdot grad n$ it follows for the radial part in cylinder symmetry

$$-D_a \cdot \left[\frac{d^2 n}{dr^2} + \frac{1}{r} \cdot \frac{dn}{dr} \right] = \nu_{ion} \cdot n. \quad (3.295)$$

The solution of this equation with the ionization frequency $\nu_{ion} = \alpha \cdot b_e \cdot E_z = \alpha \cdot v_{eD}$ results in Bessel function of zero order (J_0) for the radial plasma density distribution. By use of the boundary conditions, $n(0) = n_0$ and $n(R) = 0$, the radial plasma density profile

$$n(r) = n_0 \cdot J_0 \left(2.405 \cdot \frac{r}{R} \right) \quad (3.296)$$

follows.

Additionally, a useful equation was derived to estimate the electron temperature in the diffusion dominated positive column of a stable glow discharge, taking into calculation the equality of the ionization collision frequency and the loss frequency

due to the radial ambipolar diffusion for the charged particles balance in the positive column [3,50]

$$\nu_{ion}(E_z) = \nu_{diff} = D_a \cdot \left(\frac{2.4}{R} \right)^2 = \frac{k_B T_e}{e} \cdot b_+ \cdot \left(\frac{2.4}{R} \right)^2. \quad (3.297)$$

Thereby, the ionization frequency is calculated by the linear approximation of the electron impact ionization cross section above the threshold energy $e \cdot U_{ion}$ according to $\sigma_{ion}(U) \sim e \cdot (U - U_{ion})$ and the Maxwellian electron energy distribution function,

$$\nu_{ion} = \int_{U_{ion}}^{\infty} a^* \cdot p \cdot (U - U_{ion}) \cdot \sqrt{U} \cdot f(U) \cdot dU = V_{diff} = \frac{k_B T_e}{b_+} \cdot \left(\frac{2.4}{R} \right)^2. \quad (3.298)$$

The derived equation

$$\left(\frac{k_B \cdot T_e}{e \cdot U_{ion}} \right)^{1/2} \cdot \exp \left[\frac{e \cdot U_{ion}}{k_B \cdot T_e} \right] = 1.16 \cdot 10^7 \cdot (c \cdot p \cdot R)^2 \quad (3.299)$$

with $c^2 = (a \cdot (U_{ion})^{1/2}) / (b_+ \cdot p)$ combines the ratio between the mean electron energy and the ionization threshold energy ($k_B \cdot T_e / e \cdot U_{ion}$) with the product ($c \cdot p \cdot R$) where c is a constant, depending on the kind of gas, p is the total pressure in Torr, and R is the tube radius in cm, see Figure 3.36, [3].

The constant c amounts to He: $4 \cdot 10^{-3}$, Ne: $6 \cdot 10^{-3}$, Ar: $4 \cdot 10^{-2}$, H₂: $1 \cdot 10^{-2}$, N₂: $4 \cdot 10^{-2}$.

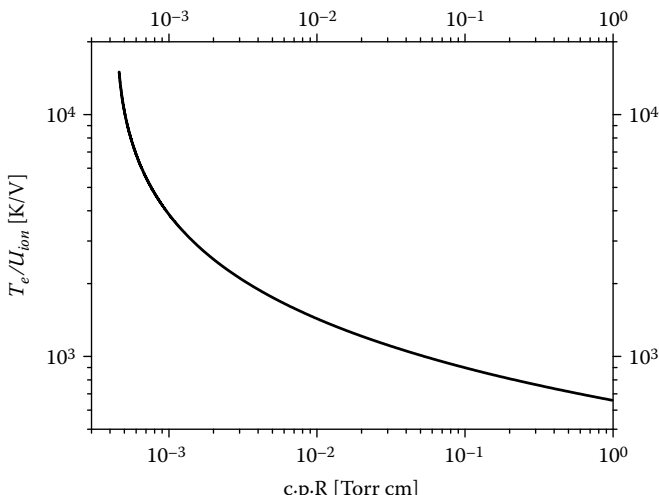


FIGURE 3.36 Universal graph from Equation (3.299) for the estimation of the electron temperature in the positive column in dependence on the product ($c \cdot p \cdot R$) calculated from the tube radius R as well as ionization potential U_{ion} and the gas specific constant c .

The plasma density and the mean kinetic electron energy is constant in axial direction for stable glow discharge mode. At the discharge axis the plasma density reach values in the order of between 10^{15} and 10^{17} m^{-3} at mean electron energies of few eV or electron temperatures of few 10^4 K .

The physics of the stable and striated positive column was extensively investigated over several decades in close interaction between experiments and numerical calculation involving kinetic calculations by the Boltzmann equation and particle-in-cell (PIC) simulations as well as drift/diffusions equations, see [45–49].

3.7.4 ARC DISCHARGES

With increasing discharge current the ion bombardment results usually in the strong heating of the cathode surface and the thermal electron emission becomes significant. The glow discharge changes in an arc discharge. In that case the *thermal arc discharge* is generated which is characterized by high discharge current in the order of few 10 A and discharge voltage much lower than 100 V . Beside the thermal electron emission, the electric field emission may be also important for secondary electrons. Here, the voltage drop over the thin cathode sheath at higher pressure is connected with strong electric field in front of the cathode surface and the secondary electrons may be emitted by the quantum mechanical tunneling of electrons over the thin potential barrier at the cathode surface. In that case the electric field arc is distinguished from the thermal arc.

The arc discharges at atmospheric or higher pressure produce a plasma in local thermodynamic equilibrium, see Section 3.2.1. That means in a local region of the plasma the transport processes represents a small disturbance only, and the plasma is described by the same translational temperature of the plasmas particles $T_e = T_+ = T_{\text{gas}} = T \sim 5 - 10^4 \text{ K}$, but this temperature and the plasma density vary in the position space.

Because of the focus on nonthermal plasmas the thermal plasma of arc discharges will not be discussed in detail.

3.7.5 HIGH VOLTAGE BREAKDOWN AT ATMOSPHERIC PRESSURE, CORONA AND BARRIER DISCHARGE

Generally, these types of discharges operate nonstationary despite of the application of DC power supply in the case of a corona discharge. They need high voltages (high electric field strength) and they appear typically at higher (atmospheric) pressure. The classical Townsend breakdown mechanism by charge carrier multiplication due to electron avalanches and secondary electron emission at the cathode for about $p \cdot d_E < 10^4 - 10^5 \text{ Pa} \cdot \text{cm}$ is not more valid. At higher pressure the electric breakdown and discharge development have to be partially replaced and extended by more complicated processes which involve the formation of thin short-lived *discharge filaments* or *streamers*.

The streamer can grow in one or both directions toward the electrodes (cathode directed, anode directed streamers). Similar to the electrical breakdown at low pressure the starting point is a free electron and the formation of a primary electron avalanche and the amplification of the external electric field E_{ext} due to the electric

space charge field. The avalanche-to-streamer transition was firstly predicted by the Raether-Meek breakdown criterion [51,52] taking into account the electric space charge field E_a in the avalanche front by assumption of a spherical charge distribution with r_A as the radius of the sphere and z as the location along the gap (3.300).

$$E_a = \frac{e}{4\pi\epsilon_0 \cdot r_A^2} \cdot \exp(\alpha \cdot z) \sim E_{ext}. \quad (3.300)$$

The breakdown criterion $\alpha \cdot d \geq 20$ (d : gap width) has to be fulfilled which corresponds to an electron multiplication $\exp(\alpha \cdot d) \geq 10^8$ by one starting electron. Thereby, no photoionization processes were considered.

Because of the high electric field and the high pressure it is produced a local plasma, which emits energetic photons. The re-absorption of the photons produces new electrons and ions by photoionization which contributes essentially to the growing of the streamer, the streamer branching, and the creation of secondary streamers. The streamer can grow in one or both directions towards the electrodes (cathode directed, anode directed streamer). Usually the cathode-directed streamer is observed if the discharge gap is small and the primary electron avalanche reaches the anode, whereas the anode-directed streamer is observed for larger gaps where the streamer formation is observed far from the anode. In that case the streamer may grow in both directions [53].

Recent modeling of the streamer evaluation reveals also nonlinear processes for streamer branching [53]. The generation rate of electrons is proportional to the electron density, but also depends on the local electric field strength in a nonlinear way. It becomes substantial if both the electron density is nonvanishing and the local electric field is sufficiently strong. Since the motion of the free electrons and ions is damped by collisions with the gas atoms, the current is composed of a drift and a diffusive term. The proposed simple but realistic model can exhibit already spontaneous spark branching, in contrast to previous expectations.

The high-voltage breakdown between discharge electrodes may be performed within few 10 ns.

The *corona discharge* (positive or negative corona) can be observed in regions with large electric field strength nearby a strong curved surface, like that of a needle, thin wire, or cutting edge. In the region of high electric field strength the condition for a high voltage gas breakdown is fulfilled.

The corona discharge is characterized by low discharge current and weak light emission similar to the Townsend or dark discharge.

The *negative corona* (wire on negative potential, see Figure 3.37a) may also assisted by a cathode mechanism similar to that of the glow discharge. Away from the wire the electric field strength goes down rapidly. In this drift region the low energetic electrons may be attached by neutral gas atoms or dust particles and form negative ions as well as negatively charged dust particles, respectively. The *positive corona* (wire at positive potential, see Figure 3.37b) starts by a streamer mechanism nearby the wire but no cathode mechanism assists the discharge. In the low field region away from the wire mainly positive ions are present.

The application of a high-energy power supply results in the development of the *spark discharge*, which means a short-lived high current arc (10^4 – 10^5 A).

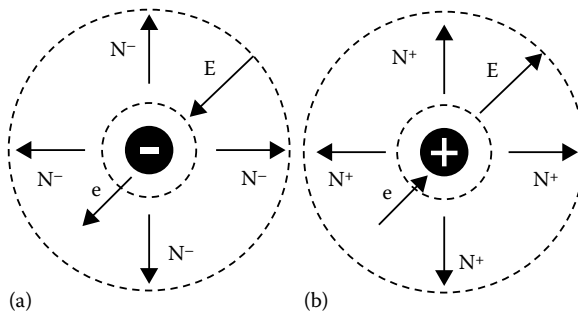


FIGURE 3.37 (a) Negative corona discharge around a thin wire with negative ions outside of the active discharge region at low electric field strength. (b) Positive corona discharge around a thin wire with positive ions outside of the active discharge region at low electric field strength.

3.7.5.1 Barrier Discharge

The barrier discharges (BDs) are observed between small discharge gaps (few mm) consisting of two electrodes whereas one of them or both are covered by an insulator (dielectric or ferroelectric barrier). Due to the insulating material on the electrode no DC power supply can be used. Therefore, the AC power supply at frequencies in the range of between standard line frequency and about 1 MHz are applied with typical peak-to-peak voltages from 5 to 100 kV.

The barrier discharge may appear in the filamentary or the diffuse mode. In the filamentary barrier discharge in each half cycle of the discharge voltage thin single discharge filaments are observed which can be seen in sharp current spikes over the displacement current. During the discharge operation in the filamentary mode many statistical distributed short-lived filaments are observed in the discharge gap. The analysis of the temporal development of a single discharge filament in the nanosecond scale reveals different discharge phases like a Townsend pre-phase followed by an ionization wave from the anode to the cathode, and the formation of high electric field region near the cathode (glow mode).

During the electric breakdown the charges will be accumulated on the insulator surface which may be combined with a surface discharge. The effective electric field strength in the gap is reduced and the discharge filament will be quenched. The remaining surface charges may have influence on the development of further discharge filaments.

A single discharge filament is characterized by a lifetime of few 10 ns, the diameter of about 100 μm , and the current density of between 10^2 and 10^3 A cm^{-2} . The plasma in the filament represents a nonthermal plasma which is characterized by a high electron density $n_e \sim 10^{20} - 10^{21} \text{ m}^{-3}$ and an electron temperature $T_e \sim 1 - 10 \text{ eV}$.

In the diffuse barrier discharge a quasi-homogeneous optical emission over the discharge gap is visible. In the discharge current a temporally extended current pulse (e.g., 1–10 μs) over the displacement current can be seen. Thereby, the diffuse barrier discharge can operate in the Townsend mode or the glow mode in analogy to the Townsend and glow discharge concerning the electric field and charged particle

distribution in the gap. Particularly in the glow mode the production and presence of metastable excited particles is essential. Therefore, these discharges operate mostly with helium. The metastables represent a reservoir of internal energy and have influence on the charged particle production (Penning ionization, step-like ionization) and/or on the secondary electron emission at the cathode (exoemission) which may contribute to the discharge sustaining.

The corona and barrier discharges have found increasing technical interest again for plasma chemical gas cleaning and surface treatment because of their operation at atmospheric pressure (no vacuum equipment is necessary) and their good upscaling from laboratory to industrial devices. Furthermore, the barrier discharges are applied for efficient UV and VUV radiation sources, e.g., excimer lamps [54] and plasma display panels [55].

3.7.6 GLOW DISCHARGES AT ALTERNATING ELECTRIC FIELD, RF AND MICROWAVE PLASMAS

By use of a harmonic electric field (circular frequency $\omega = 2\pi\nu$) over the discharge gap, the charged particles start to oscillate (polarization drift). Taking into account the solution for the polarization drift

$$z(t) = \frac{e \cdot (\omega - i\nu_{e,+})}{m_{e,+} \cdot \omega \cdot (\omega^2 + \nu_{e,+}^2)} \cdot E_0 \cdot \exp(-i\omega t) \quad (3.301)$$

of charged species in an electric field with constant amplitude E_0 and the elastic collision frequency $\nu_{e,+}$ of electrons and positive ions with neutrals see Section 3.1.4, the corresponding oscillation amplitude z_A results in

$$\begin{aligned} z_A &= E_0 \cdot \frac{e}{m_e \cdot \omega} \cdot \frac{1}{\sqrt{\omega^2 + \nu_e^2}} = \frac{E_0 \cdot b_{e,+}}{\omega} \cdot \frac{1}{\sqrt{1 + (\omega/\nu_e)^2}} \\ &= \frac{E_0}{p} \cdot \frac{C_{e,+}}{\omega} \cdot \frac{1}{\sqrt{1 + (\omega/\nu_e)^2}} \end{aligned} \quad (3.302)$$

with $b_{e,+} = e/(m_{e,+} \cdot \nu_{e,+})$ and $b_{e,+} \cdot p = C_{e,+} = \text{const.}$

Assuming $(\omega/\nu_{e,+})^2 \ll 1$, the charged particles (electrons or positive ions) from the discharge centre can arrive the electrode at the condition $z_A = d_E/2$.

$$d_E \cdot \omega \propto 2 \cdot C_{e,+} \cdot \frac{E_0}{p}. \quad (3.303)$$

For example, at the discharge gap of $d_E = 2.5$ cm and the reduced electric field strength of $E/p = 10$ V/(Pa·cm) in Figure 3.38 the limit for ion and electron trapping in the gap center corresponds to frequencies $\nu \geq 250$ kHz and $\nu \geq 25.5$ MHz, respectively.

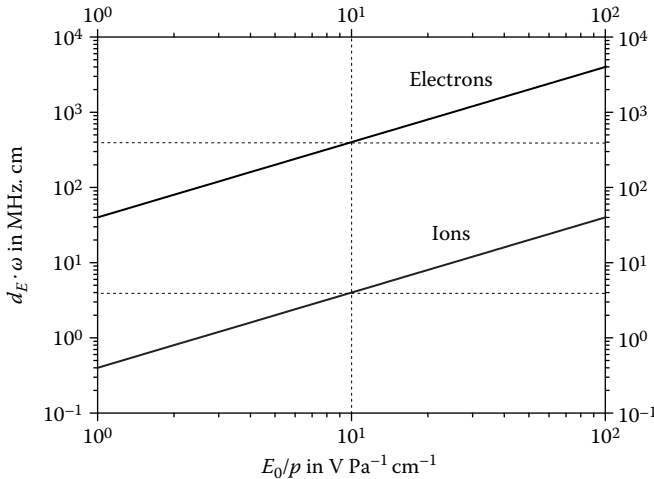


FIGURE 3.38 Ions and electrons arriving the electrode from the discharge center represented by the product $d_E \cdot \omega$ in dependence on the reduced electric field strength E/p according to (3.303) with $b_+ \cdot p = C_+ = 2 \cdot 10^5 \text{ cm}^2 \text{ Pa(V s)}^{-1}$ and $b_e/b_+ = 100$.

Furthermore, the transit time

$$\tau_+ = \frac{3 \cdot s_{\text{Child}}}{v_0} \quad (3.304)$$

(with $v_0 = (2 \cdot e \cdot \Delta\varphi_{\text{Child}}/m_+)^{1/2}$) of the ions through the plasma sheath is important which is estimated by use of the Child–Langmuir sheath model and time-averaged sheath thickness and potential.

As the consequence, at higher electric field frequencies the breakdown voltage depends on both, the product $p \cdot d_E$ and $\omega \cdot d_E$.

Firstly, a qualitative overview is given about the characteristic changes in the discharge mechanisms with increasing electric field frequency.

Standard line frequency $50 \text{ Hz} \ll \omega_{pe}, \omega_+$: At very low frequency case the discharge processes are considered to be similar to the static electric field (quasi-stationary conditions). For example, at the standard line frequency of 50 Hz , the low-pressure discharge represents an alternating DC glow discharge. For each half cycle an electric breakdown (ignition) and the development of the discharge regions (e.g., cathode sheath, negative glow) is observed. If the voltage goes down the discharge disappears. At the zero point of the cycle no charged particles are present due to ambipolar diffusion to the electrodes/walls and recombination. With increasing voltage at the next half cycle the discharge starts at the breakdown voltage completely new.

Mid-frequency range 10^4 – $10^5 \text{ Hz} \ll \omega_{pe}, \omega_+$: At mid-frequencies the loss of charged particles by ambipolar diffusion and recombination per time unit is in the order with the electric field frequency. No complete new ignition is necessary for

each half cycle because of the pre-ionization by the remaining charged particles in the discharge center between the electrodes. The charged particles can instantaneously follow the alternating electric field. The cathode sheath and negative glow alternate between the two electrodes according to the frequency of the applied voltage.

Radio frequency range $\omega_{p+} < 10^6 - 10^8 \text{ Hz} < \omega_{pe}$: At radio frequencies the heavy ions are not able to follow instantaneously the change in electric field. Depending on the discharge geometry, the coupling of the electric power supply, and the plasma processing parameters, the capacitively and inductively coupled radio frequency plasmas is distinguished. With exception of the γ -mode in capacitively coupled radio frequency plasmas the secondary cathode processes like that in DC glow discharges are not necessary for the discharge sustaining.

Microwave range $10^9 - 10^{11} \text{ Hz} \geq \omega_{pe} \gg \omega_{p+}$: At microwave frequencies the electrons are heated in the plasma bulk due to absorption of electric energy from the microwave electric field. If the plasma density exceeds the critical electron density n_{ec} the microwave penetration in the plasma is limited by the skin depth, and the microwave will be reflected. At the considered frequency range the critical electron density is in the range between about 10^{16} and 10^{18} m^{-3} .

3.7.6.1 Heating of Electrons in the Bulk Plasma by the High-Frequency Electric Field

The input of electrical power to plasma electrons in the bulk ($n_e = \text{const.}$) can be simplified described using the result for the electron current density (3.291) in calculation of the polarization drift in Section 3.1.4 and the electric power

$$j_{ez} = -e \cdot n_e \cdot v_{ez} = \frac{n_e \cdot e^2}{m_e \cdot (\omega^2 + \nu_e^2)} \cdot (\nu_e + i\omega) \cdot E_0 \cdot \exp(-i\omega t) \quad (3.305)$$

and

$$P = \bar{j} \cdot \bar{E} = \sigma \cdot E^2. \quad (3.306)$$

The cycle-averaged real part of the electric power provides the absorbed electric power

$$\text{Re}\{P\} = P_{abs} = \frac{n_e \cdot e^2}{m_e \cdot \omega} \cdot \frac{(\nu_e/\omega)}{1 + (\nu_e/\omega)^2} \cdot E_{eff}^2 = \sigma_{DC} \cdot \frac{(\nu_e/\omega)^2}{1 + (\nu_e/\omega)^2} \cdot E_{eff}^2 \quad (3.307)$$

per volume unit which is referred to as the ohmic heating of the electrons in the high-frequency electric field.

It is clearly seen that without elastic electron neutral collisions $nu_e = 0$ no electric power absorption takes place. Here, the imaginary part exists only, and the phase shift of the electron motion related to the electric field can be interpreted by a nonmagnetic inductivity. If the excitation frequency $\omega = 0$ we have the DC case $P_{abs} = P_{DC}$. At a given electron density n_e and effective electric field strength E_{eff} , the maximum absorbed power by electrons is achieved in the case $\omega = \nu_e$

$$P_{abs}^{max} = \frac{1}{2} \cdot \frac{n_e \cdot e^2}{m_e \cdot \omega} \cdot E_{eff}^2. \quad (3.308)$$

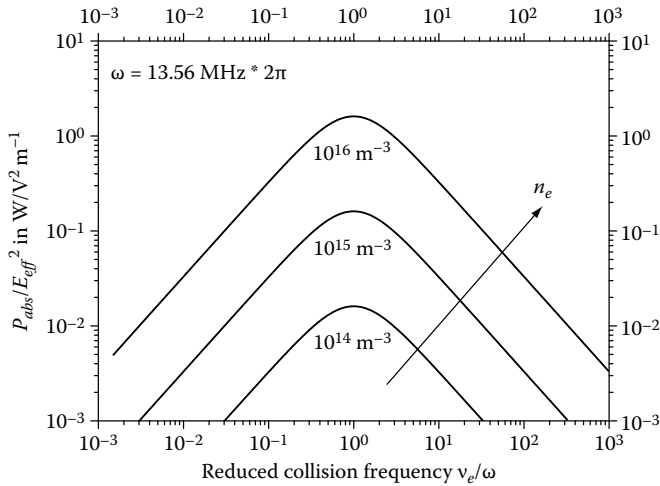


FIGURE 3.39 Absorbed electric power P_{abs} for electric field frequency of 13.56 MHz with the electron density as parameter.

Figure 3.39 shows the power absorption in the high-frequency electric field in dependence on the reduced collision frequency v_e/ω at the radio frequency of 13.56 MHz. The generation of dense nonthermal plasma can be reached by heating of the electrons by microwaves, for example at 2.45 GHz. The microwaves produce much larger electric fields in the plasma bulk. Furthermore, microwave plasmas are of special interest in combination with external magnetic fields. If the electron cyclotron motion ω_{ce} is in phase with the rotating electric field vector of the R-wave ω , and the electron neutral collision frequency is low enough the electrons absorb efficiently wave energy [56]. Then the absorbed power depends additionally on the electron cyclotron frequency

$$P_{abs} = \frac{n_e \cdot e^2}{m_e \cdot \omega} \cdot \frac{(\nu_e/\omega)}{[1 - (\omega_{ce}/\omega)]^2 + (\nu_e/\omega)^2} \cdot E_{eff}^2 \quad (3.309)$$

see Figure 3.40.

3.7.6.2 Radio Frequency Plasmas

Radio frequency (rf) plasmas at excitation frequencies between the ion and electron plasma frequency, e.g., 13.56 or 27.12 MHz, are widely used in plasma technologies for material surface treatment and thin film deposition. The RF discharges may be operate by means of internal or external electrodes and they are classified into two types according to the coupling the high frequency power

- Capacitively coupled plasma (CCP)
- Inductively coupled plasma (ICP)

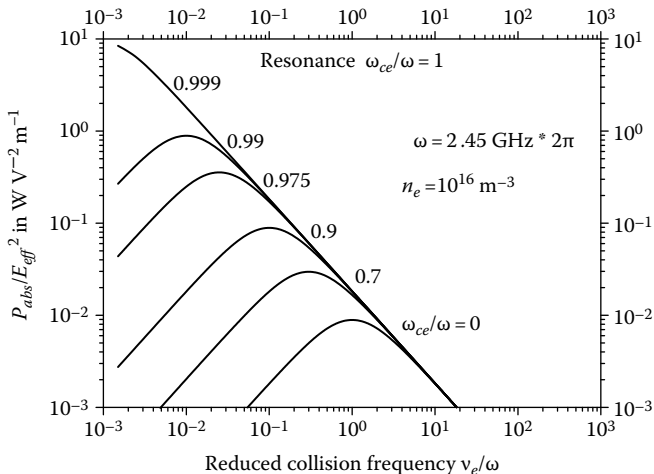


FIGURE 3.40 Power absorption of electrons per volume unit at 2.45 GHz microwave in dependence on the reduced collisions frequency for an electron density of 10^{16} m^{-3} . The influence of the magnetic field ω_{ce} on the power absorption is shown.

In many applications of RF plasmas in treatment of surfaces the coupling is capacitively due to the power absorption of electrons in the electric field from the applied RF-voltage between two parallel plate discharge electrodes (CCP). In that case high-voltage plasma sheaths in front of the RF electrodes becomes important concerning their sheath dynamics and contribution in the heating of electrons at the sheath edge during the sheath expansion phase (α -mode). In particular, the asymmetric capacitively coupled discharge arrangement is often applied by use of different areas of the powered and grounded electrode. The additional formation of negative DC voltage, the *self-bias voltage*, at the smaller electrode shifts the RF voltage which is combined with strong modulation the RF sheath voltage, and a maximum sheath voltage up to the peak-to-peak RF voltage, see Section 3.6.3. The self-bias voltage is the result of the current continuity in the discharge at capacitively coupling and the fact that no resulting DC current can flow over one RF cycle. Asymmetric RF discharges are even observed in unconfined discharge configuration of symmetric electrode geometry because of a larger effective grounded electrode area due to grounded shielding of the RF-electrode and/or the grounded walls of the vacuum vessel. Beside the α -mode the discharge can be also driven in the γ -mode which means the heating of secondary electrons due to strong acceleration of the electrons over the expanded RF sheath into the plasma bulk. Because of the low collision cross section of electrons at high kinetic energy the electrons can considerable penetrate into the plasma bulk. According to their kinetic energy in the plasma bulk in relation to the specific collision cross section (excitation, ionization) they can significantly contribute to the discharge sustainment. Besides the electric power absorption due to electron neutral collisions (ohmic heating in α - and γ -mode), a collision-free or *stochastic heating* can be observed in capacitively coupled RF discharges at low pressure. The electrons

are heated due to the interaction of electrons with the RF sheath edge, which means electrons move randomly towards the RF electrode during the sheath expansion phase [36].

Considering capacitively coupled plasmas in electronegative gases an additional electron heating due to the electric field reversal in front of the powered electrode is observed during the sheath collapse phase [138], as well as in the special case of strongly electronegative plasmas in CF_4 and symmetric rf discharge a new electron heating mode in the bulk plasma exists due to drift and ambipolar electric fields [139].

In the case of the *inductive coupling* the high-frequency current passes through a planar or solenoid coil and generates an oscillating magnetic field which induces the electric field. The electrons can absorb electric power from the induced high-frequency electric field similar to the power absorption discussed above. As already discussed in case of electron heating in the microwave field, the inductively coupled plasma may also run at higher plasma density at about 10^{17} m^{-3} which can limit the radio frequency penetration into the plasma by the corresponding skin depth.

3.8 TECHNICAL PLASMA SOURCES

3.8.1 INTRODUCTION

Plasmas are generated by input of energy into the gas phase for producing sufficient number of charge carriers that means namely free electrons and positive ions. Electric energy is applied usually by electrical fields as discussed in Section 3.7, but also energy input is possible by beams of energetic particles like electrons or UV or laser radiation. Plasma sources can be classified according to the energy input source, the geometry of the vessel including configuration of electrodes and the gas pressure. Another criterion may be the coupling of the plasma to the substrate [57]. Plasma chemical reactors often operate with gas flows. The topic of this chapter is a short description of plasma sources applied for plasma chemical processes. A detailed discussion can be found in various textbooks as [36,44,58–61]. The chapter is organized as follows. In the first part a characterization of typical plasma sources is given classified according to the energy input and the gas pressure. Thereafter, demands on plasma sources for plasma chemistry are listed.

3.8.2 PLASMA GENERATION BY ELECTRIC FIELDS

Technical plasmas are mostly generated by electrical discharges in a gas. Depending on the temporal behavior of the sustaining electric field direct current (DC) and alternating current (AC) discharges are distinguished, working in continuous (cw) or pulsed mode. The frequency range of the sustaining voltage of the AC discharges is very broad, reaching from line frequency (50 Hz), low frequency (some kHz), radio frequency (1–100 MHz)—technically preferred frequencies are 13.56 and 27.12 MHz—up to microwaves. Here, 2.45 GHz is the mostly used frequency.

Plasma sources operate at very low pressures ($p \sim 10^{-2} \text{ mbar}$), in the low pressure range ($p \sim 1 \text{ mbar}$) up to atmospheric pressure ($p \sim 1 \text{ bar}$). The discharge current varies for low current discharges from $<10^{-3}$ up to $>10 \text{ A}$ in high current discharges. The configurations of the electrodes are very different: inner and outer electrodes

(this is named electrodeless), plane, hollow, cold, and heated electrodes, to mention only some.

In a plasma the power absorption P_{abs} per volume unit V is given by (see also Section 3.7.6.1 (3.309))

$$P_{abs} = \frac{e^2 n_e}{m_e \nu_e} \frac{(\nu_e/\omega)^2}{[1 - (\omega_{ce}/\omega)]^2 + (\nu_e/\omega)^2} \cdot E_{eff}^2, \quad (3.310)$$

where

e , n_e , m_e are the electron charge, density, and mass, respectively

ν_e is the electron-neutral collision frequency

ω and ω_{ec} are the angular frequency of an external electromagnetic field

$E = E_0 \cos \omega t$ and the electron cyclotron frequency $\omega_{ec} = eB/m_e$ in a magnetic field B , respectively

The power absorption in an RF discharge is maximum for $\omega = \nu$. Therefore, discharges at higher pressures operate more effectively by microwave excitation, because the power deposition criterion is better matched. For a static electric field and $B = 0$ the frequencies ω and ω_{ec} are zero, respectively. The power absorption per volume is

$$P_{abs} = jE = \sigma \cdot E^2 = \frac{n_e e^2 E^2}{m_e \nu_e}, \quad (3.311)$$

E equals the external electric field. The generation of charge carriers (electrons and positive ions) is essential for sustaining an electrical discharge to compensate the losses at the walls, the electrodes, and sometimes also in the volume. Typical processes of charge carrier generation in nonthermal plasmas are electron impact ionization of neutral atoms/molecules (α -process) and secondary emission of electrons by collisions of energetic ions, photons or metastable neutrals, e.g., with the electrode surface (γ -process), see Section 3.7.2. Typical arc discharges with large currents and thermal plasmas are characterized by hot cathodes with thermo-emission of electrons.

3.8.3 LOW-PRESSURE PLASMA

Low-pressure plasmas operating at gas pressures in the range of 10^{-1} – 10^2 Pa are characterized by a large mean free path of the plasma particles. Therefore, these plasmas are suited for the generation of directed ion currents to the target surface, whereas the formation rate of higher radical densities and reaction products resulting from two body or even three body collisions of heavy particles is small. The development of plasma sources operating with low pressure was strongly linked with the requirements of the microelectronic industry.

3.8.4 DIRECT CURRENT DISCHARGES

DC plasma is generated in the low-pressure glow discharge burning in a closed discharge vessel between inner electrodes, the negative cathode, and the positive

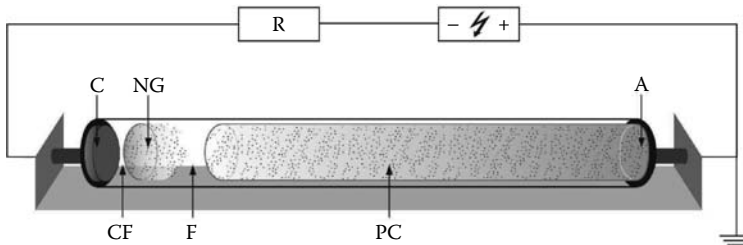


FIGURE 3.41 Low pressure DC glow discharge. C, cathode; A, anode; CF, cathode fall; NG, negative glow; F, Faraday dark space; PC, positive column; R, resistance.

anode. The discharge in a long cylindrical vessel with dielectric walls shows different characteristic regions: cathode fall, negative glow, Faraday dark space, positive column with charge carrier generation by electron impact ionization of the molecules/atoms is applied as model plasma for fundamental investigations of plasma chemical processes [62–64].

The transition of the glow into an arc discharge is prevented by a current limiting resistor in series with the discharge. Another method is the pulsed operation, where the cathode heating is limited and the time for the development of an arc discharge is too short.

The generation of a positive column with higher current is possible by changing the cathode to a hollow cathode (using a hollow cylinder) or externally heated cathode. The hollow cathode itself is an important reactor also for plasma chemical applications with its high concentration of charge carriers, radicals and intensive photon emission. The generation of charge carriers in hollow cathodes is supported by pendulum electrons (electrons traveling forward/backward within the system) as well as by additional electron emission by the impact of photons and metastables on the inner cathode surface, see [65,66] and references cited therein. Such a discharge operates with lower sustaining voltage and higher currents.

The magnetron discharge mainly applied in sputter devices is characterized by the application of an external magnetic field approximately parallel to the cathode surface (Figure 3.42). For sufficient low pressures (1 Pa) the electrons are trapped by their gyration, because they are magnetized. This prolonged mean free path length enables a satisfactory ionization rate at very low gas pressures. The ions are not magnetized due to their larger mass and therefore not trapped. They collide with sufficient energy for sputtering at the cathode surface. Magnetrons can operate with medium-frequency (~ 10 kHz) and RF (13.56 and 27.12 MHz) [67].

Table 3.12 shows some examples of DC discharges, parameters, and applications.

3.8.5 RADIO FREQUENCY DISCHARGES

Radio frequency discharges usually operate in the frequency range $f = 1\text{--}100$ MHz. The wavelengths ($\lambda = 3\text{--}300$ m) are large in comparison to the reactor dimensions. At lower frequencies the ions collide with the electrode surface and generate secondary

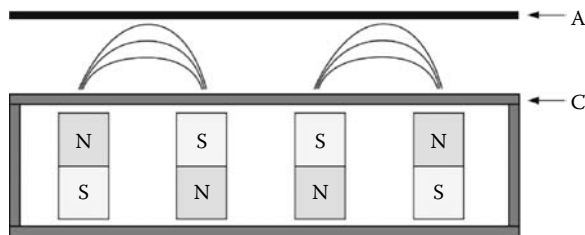


FIGURE 3.42 DC magnetron discharge. NS, permanent magnets with N north and S south pole; C, cathode; and A, anode. Magnetic field lines are sketched near the cathode.

TABLE 3.12
Examples of DC Discharges

Type	Pressure [Pa]	n_e [cm^{-3}]	T_e [eV]	Applications
DC glow discharge				
Cathode region	$10^{-1}\text{--}10^4$	$10^5\text{--}10^9$	10^2	High ion energy, sputtering, deposition, surface analysis
Negative glow	$10^{-1}\text{--}10^4$	10^{12}	0.5	Chemistry, radiation
Positive column	$1\text{--}10^4$	10^{10}	1–10	Radiation, chemistry, deposition
Hollow cathode	$1\text{--}10^5$	$10^{12}\text{--}10^{15}$	0.5	Radiation, chemistry
Magnetron	0.1–10	10^{10}		Sputtering

electrons, see Section 3.7.6. For higher frequencies neither the ions nor the electrons can reach the electrode surface during the acceleration phase of the external electric field, the charge carriers are produced by electron impact ionization of heavy particles in the volume. The power supply must be connected with the reactor by an impedance matching network. In this way the power transfer is maximized and the reflected RF power is minimized [68]. Two different ways are used for coupling of the high-frequency electromagnetic energy into the reactor: capacitive and inductive.

3.8.6 CAPACITIVELY COUPLED DISCHARGES

Capacitive plasma reactors often operate with inner plane electrodes (Figure 3.43). It generates the RF plasma between these two electrodes with electron densities up to 10^{10} cm^{-3} . Also, configurations of a cylindrical discharge tube with dielectric walls (usual glass or quartz) and two ring-shaped or other hemi-cylindrical outer electrodes are possible. The electrodeless operation has the advantage that there is no erosion or contamination of the electrode surface in chemical active gases. These discharges are generated in gas pressures between 10^{-1} up to 10^3 Pa .

The asymmetric capacitively coupled discharge with inner electrodes offers the possibility for the generation of a negative self-bias of the blocked powered electrode. In a asymmetric reactor the currents at the two electrodes can be equal only for a higher voltage across the sheath in front of the smaller electrode what is achieved by a negative bias potential of the small blocked electrode. The negative biases V_1 and

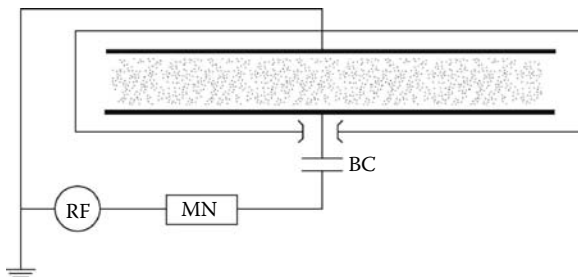


FIGURE 3.43 Scheme of a capacitive coupled RF discharge with plane electrodes and coupling capacitor. RF, generator; MN, matching network; BC, coupling capacitor.

V_2 on the two electrodes depend on the electrode areas A_1, A_2 as

$$\frac{V_1}{V_2} = \left(\frac{A_2}{A_1} \right)^n, \quad (3.312)$$

where n varies in the range from ~ 1 to 4 for different conditions [36,69,70]. Ion energies at the powered electrode can reach values up to some hundred electron volts due to the self-bias.

The application of two different frequencies for plasma excitation allows an approximate control of the plasma density and therefore of the ion flux to the electrode by the higher frequency (e.g., 27.12 MHz) as well as the ion energy by the low frequency (e.g., 1.94 MHz) [77]. In a simplified picture this behavior can be explained by the low impedance of the sheath capacitance for the high frequency and therefore high power absorption and effective electron heating inside the plasma bulk. This increases the ionization and the ion flux. The low frequency acts across the sheath and controls the ion energy [3,72].

For the capacitively coupled discharges two different modes are observed, the α and γ mode [3,72].

Various types of capacitively coupled reactors are used in applications. The barrel reactor is cylindrical with outer electrodes fixed onto the dielectric wall. This reactor was used in microelectronic industry to remove the photoresist by plasma etching or plasma stripping in an oxygen plasma. The targets are floating at a potential against the plasma of about 10–20 eV. Therefore the etch process occurs by neutral activated species and a damage of the target material by energetic ions is avoided. This etching is a purely chemical process. The action of the ions is utilized in the planar and cylindrical diode reactors. Planar reactors consists of a planar electrode, the second electrode is the reactor wall or a second planar electrode in front of the first one. In a triode system the two planar electrodes are insulated with respect to the reactor wall, which serves as a third electrode. A coaxial cylindrical diode system consists of a centrally mounted hexagonal electrode which supports the six substrates, e.g., wafers. This electrode is powered, the reactor wall grounded. Today, the development in microelectronic industry leaves the simultaneously treatment of several wafers and goes in the direction of processing of larger wafers (300 mm).

An example of generation of a large planar RF plasma in the frequency range 13.56–200 MHz for gas pressures near 5 Pa is reported by Kawai [73] using a ladder-shaped antenna (422 mm × 422 mm with 17 rods) for preparing a-Si:H films for solar cells.

The capacitive coupling has the advantage of plasma generation including an energetic ion current (100–1 000 eV) in direction of the powered electrode. This method allows charge carrier densities of 10^9 – 10^{10} cm $^{-3}$. Higher plasma densities require excitation mechanisms with higher ionization efficiency as well as minimized diffusion losses by improved confinement and application of resonant effects in an externally generated static magnetic field.

3.8.7 INDUCTIVELY COUPLED DISCHARGES

Inductive coupled discharges are excited by an RF electric field of a helical coil surrounding the plasma volume or of a spiral coil in front of the plasma [74,75] (Figure 3.44a and b). The last planar configuration is similar to a capacitively coupled plasma reactor. The plasma generating voltage is induced by the varying magnetic field generated by the RF current in the exciting coil. The coupling between the coil and the plasma can be understood as a transformer with many primary windings of the coil and the plasma as one winding. The inductive excited plasma has typical high electron densities (10^{11} – 10^{12} cm $^{-3}$) and low electric fields. The inductive coupled plasma builds up, in contrast to the capacitively coupled one, only a small sheath voltage in front of the wall or of the substrate (20–40 V), which results in low ion energies. The low kinetic energy of the positive ions makes such plasmas suitable for material

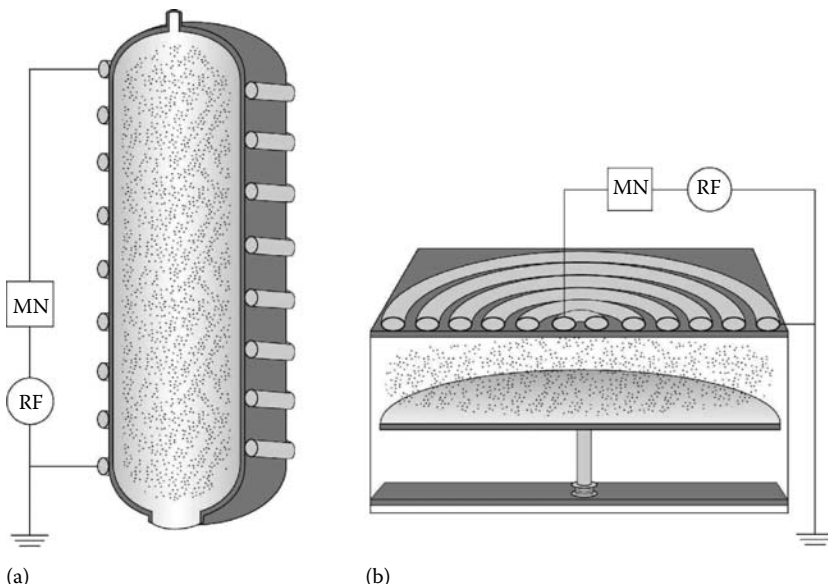


FIGURE 3.44 Scheme of an inductively coupled RF discharge with helical (a) and plane spiral (b) coupler. RF, generator; MN, matching network.

TABLE 3.13
Selected Radio Frequency Plasma Reactors

Type	Pressure [Pa]	n_e [cm^{-3}]	T_e [eV]	Applications
Capacitive				
Low pressure	0.1–10	10^{10}	1–10	Sputtering
Moderate pressure	10–1000	10^{10}	1–10	Deposition
Dual frequency	1	10^{10}		Etching, separate control ion density (ion flux) and ion energy
Inductive	0.1–1000	10^{12}	1	Etching
Neutral loop discharge	0.01–1	10^{11}	5	Etching
Helicon discharge	0.01–1	10^{13}	1	Etching

treatment with reduced surface damage in semiconductor industry and surface treatment of various heat sensitive materials. The application of a spiral coil in front of the plasma volume generate plasmas for homogeneous treatment of a planar object. For the treatment of 3D objects double inductively coupled plasma reactors with two flat RF-coils are developed, one on the top and another on the bottom of the reactor vessel [76]. The plasma is of reasonable homogeneity in radial and axial direction.

An interesting variant of inductively coupled plasma sources for low processing pressures (~ 0.1 Pa) is the neutral loop discharge source [77,78]. The plasma is generated along a magnetic neutral loop ($B = 0$) by an RF electric field excited by an one turn antenna. The magnetic neutral loop is produced by a set of three DC magnetic coils, in which the inner coil produces a magnetic field in opposite direction to the outer coils. In this configuration plasma is generated with high electron density and relatively low electron temperature. The position of the plasma can be controlled by the magnetic field and therefore a uniform processing can be achieved over large wafers.

The helicon plasma source operates usually with a static longitudinal homogeneous magnetic field (0.005–0.03 T) in a cylindrical vacuum vessel ($1 \cdot 10^{-2}$ –10 Pa). Helicon waves are generated by specially shaped antennas in the frequency range between 1 and 50 MHz, usually 13.56 MHz for processing plasmas. In Ar peak electron densities of 10^{12} – 10^{13} cm^{-3} are achieved [79,80]. The high plasma density is promoted by the (collision-free) Landau damping of the helicon waves.

Capacitively and inductively coupled radio frequency plasma reactors are especially improved in microelectronic industry for wafer manufacturing with its broad application spectrum for thin film deposition and plasma etching. Some examples of RF plasma reactors with typical data of plasma parameters and applications are shown in Table 3.13.

3.8.8 MICROWAVE DISCHARGES

The plasma generation by microwaves has the advantage of an electrodeless discharge with an effective power absorption in a broad pressure range (1– 10^5 Pa), with high electron densities (up to 10^{13} cm^{-3}) and low sheath potentials and therefore low ion

energies at the wall or the target surface. The density of chemically active free radicals and dissociation products is comparatively high caused by the shape of the electron energy distribution function (EEDF) with a high concentration of electrons in the higher energy range. The EEDF is more a Maxwellian than the EEDF in a low-frequency plasma [81–83]. Microwave discharges can be generated in closed or open structures or on a plasma resonance [84]. In the low-pressure regime the ignition and sustaining of a microwave discharge can be supported by magnetic fields.

A simple kind of plasma generation by microwaves is achieved by the coupling of the discharge tube with a rectangular waveguide (Figure 3.45). An example for plasma generation in open configurations is the slow wave structure (Figure 3.46),

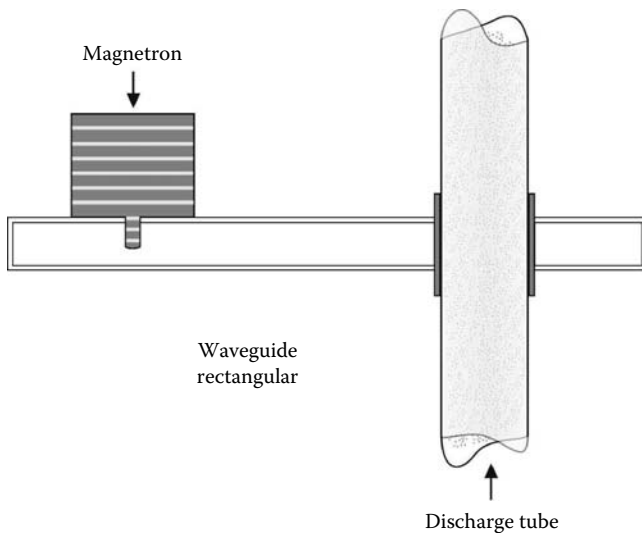


FIGURE 3.45 Coupling of discharge tube with a rectangular wave guide.

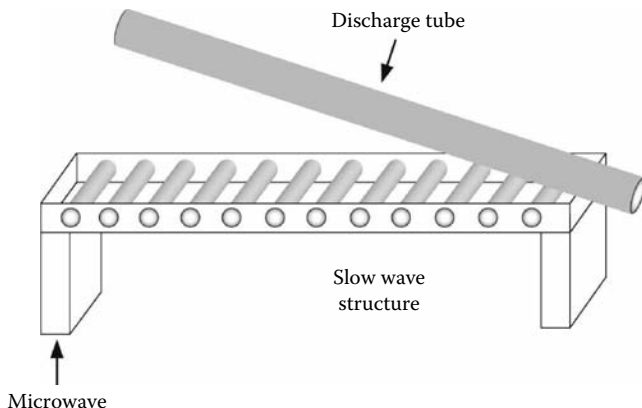


FIGURE 3.46 Microwave plasma generation by a slow wave structure. (From Bosisio, R.G. et al., *J. Phys. E Sci. Instrum.*, 6, 628, 1973.)

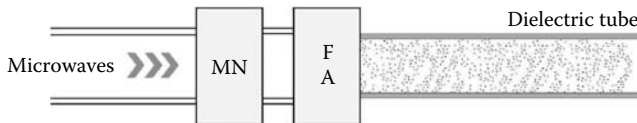


FIGURE 3.47 Microwave plasma generation by a surfatron. MN, impedance matching network; FA, field applicator. (From Moisan, M. et al., Surface wave plasma sources, in Popov, O. ed., *High Density Plasma*, p. 191, Noyes Publications, Park Ridge, NY, 1995.)

where the constant excitation is achieved by the varying distance between exciting antenna and plasma tube [85]. The Surfatron is an other example which operates by energy absorption of traveling waves on the surface of a plasma column (Figure 3.47). This plasma can be sustained in some distance from the field applicator in a broad gas pressure range, with density between 10^8 – 10^{15} cm $^{-3}$ and also various excitation frequencies (200 kHz and 10 GHZ) [86,87].

Linear extended plasmas were generated by the Duo-Plasmaline [88]. A copper rod coupled to magnetrons at both ends is central in a quartz tube within a vacuum vessel. In the low-pressure region (5–500 Pa) outside the tube a plasma is formed and the microwaves propagate in this coaxial waveguide. In the vacuum vessel a linear extended homogeneous plasma is generated by feeding microwaves from both sides.

A large area planar microwave plasma can be generated by a plasma source shown in Figure 3.48 [89,90]. The microwave applicator consists of two rectangular waveguides connected by adjustable coupling hooks. The first waveguide is linked with a microwave power source and closed by a matched load. Matched loads close the second waveguide on both ends. The fourth wall of this waveguide is the plasma in the vacuum vessel (2 Pa–2 kPa) behind a quartz window. Microwave energy is coupled across the adjustable coupling hooks whereby a homogeneous plasma can be generated in the vacuum vessel. A planar plasma of 30×30 cm 2 was created with an array of such applicators.

Large-size plasmas can also be produced by single microwave plasma sources in a matrix configuration in the sub-100 Pa range [91].

An interesting solution for the microwave excitation of a large volume plasma in a broad pressure range (10^{-3} – 10^5 Pa) are the slot antenna plasma sources (SLAN) (Figure 3.49). The microwave energy is transferred from a ring cavity through equidistantly positioned slot antennas into the quartz plasma chamber [81,92,93]. The homogeneity of the plasma density at higher pressures could be improved in the CYRANNUS-I source operating also on the slot antenna principle [94].

The treatment of heat-sensitive materials by an atmospheric pressure microwave discharge is possible by a moving plasma (Figure 3.50). The application of a microwave field generates a ball-like plasma zone, which moves along the discharge chamber and interacts with the installed target. A treatment of inner surfaces of tubes or bottles is possible [95].

Typical examples for plasma excitation by plasma resonance are electron cyclotron resonance reactors. The microwaves are launched through a window into the

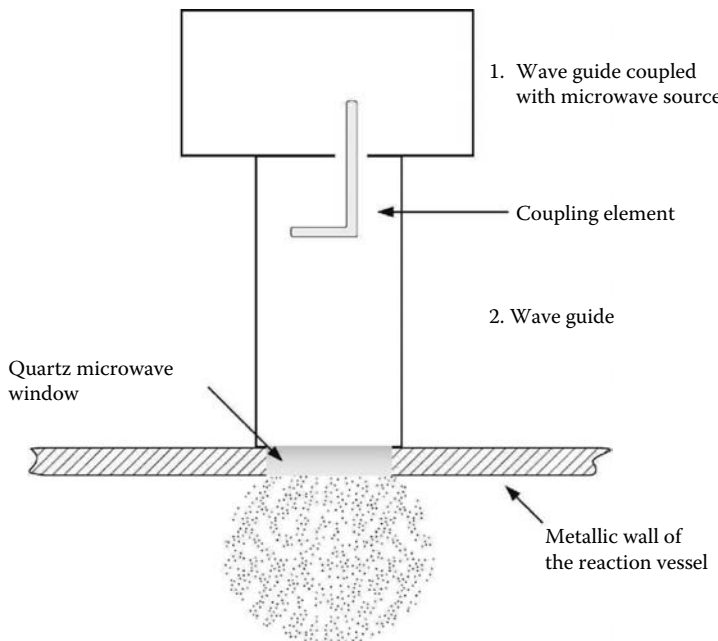


FIGURE 3.48 Field applicator for generation of an extended microwave plasma (1) R22 rectangular wave guide coupled with microwave source, (2) second R22 wave guide. (From Ohl, A., Large area planar microwave plasmas, in C.M. Ferreira and M. Moisan, eds., *Microwave Discharges Fundamentals and Applications*, pp. 205–214, Plenum Press, New York, 1993.)

vacuum vessel with outer magnet coils which generate an axial symmetric magnetic field. For a magnetic field of 0.0875 T the electron cyclotron frequency becomes 2.45 GHz. Here the microwave energy is absorbed by the electron cyclotron resonance. The mean free path of the electrons should exceed their gyration radius in the magnetic field. Therefore, the pressure is limited to a range from 10^{-3} to 1 Pa [96].

In a distributed electron cyclotron resonance (DECR) plasma reactor the arrangement of permanent magnets in a multipolar array enables the generation of plasmas of high density and high homogeneity up to square meters [97–100].

Microwave plasma sources operate in a broad pressure range with high electron densities and low ion energies. Data of selected sources are shown in Table 3.14. In practice the microwaves are usually transferred from the power source by waveguides to the microwave plasma applicator. A circulator protects the power source from reflected microwave power. The transferred and reflected energy is measured using directional couplers and power meters. A stub tuner as a tuning device provides the matching to the applicator. The reflected power is minimized, whereas the forward power is maximized. The adaptation of a rectangular to a cylindrical waveguide occurs by a mode converter [58].

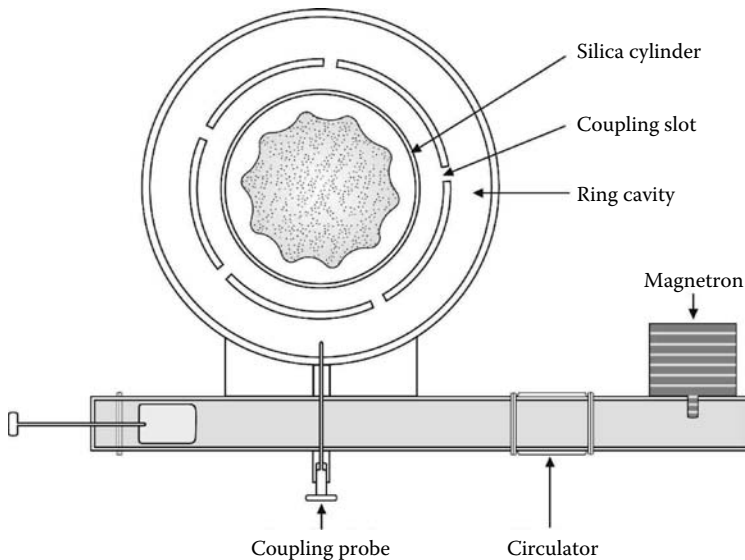


FIGURE 3.49 Scheme of the slot antenna plasma source (SLAN), plasma inside the silica cylinder. (From Werner, F. et al., *Plasma Source Sci. Technol.*, 3, 473, 1994.)

3.8.9 ATMOSPHERIC PRESSURE DISCHARGES

The application of nonthermal plasmas at atmospheric pressure offers some advantages, as investment costs are reduced, and higher density of neutral particles enables higher reaction rates for certain gas phase processes [101]. Sometimes batch processes can be replaced by continuous processing. Plasma processing can be applied to low value items also [102].

Atmospheric pressure nonthermal plasmas are subject of some reviews in the last time, as [103–107,129], see also [108]. Nonthermal atmospheric pressure plasmas are generated by corona discharges (negative and positive corona), RF plasma torches, gliding arcs and by some kinds of micro wave discharges. Of special interest concerning the scientific aspects as well as the applications are the dielectric barrier discharges, the microdischarges and the arc-free atmospheric pressure plasma jets.

3.8.10 DIELECTRIC BARRIER DISCHARGE

The dielectric barrier discharge (DBD) is characterized by a small gap (~ 1 mm) between two electrodes filled with a gas at atmospheric pressure and the discharge path is hindered by at least one dielectric barrier which prevents the transfer of the barrier discharge with its nonthermal plasma to an arc discharge. Planar configurations with one or two dielectric barriers between the plane electrodes, cylindrical reactors with a coaxial arrangement of the electrodes with the barrier in between, and surface discharges in coplanar configurations are known (Figure 3.51).

The DBD generates nonthermal plasma at higher gas pressures, typically atmospheric, and is very flexible with respect to the working gas mixture and a broad

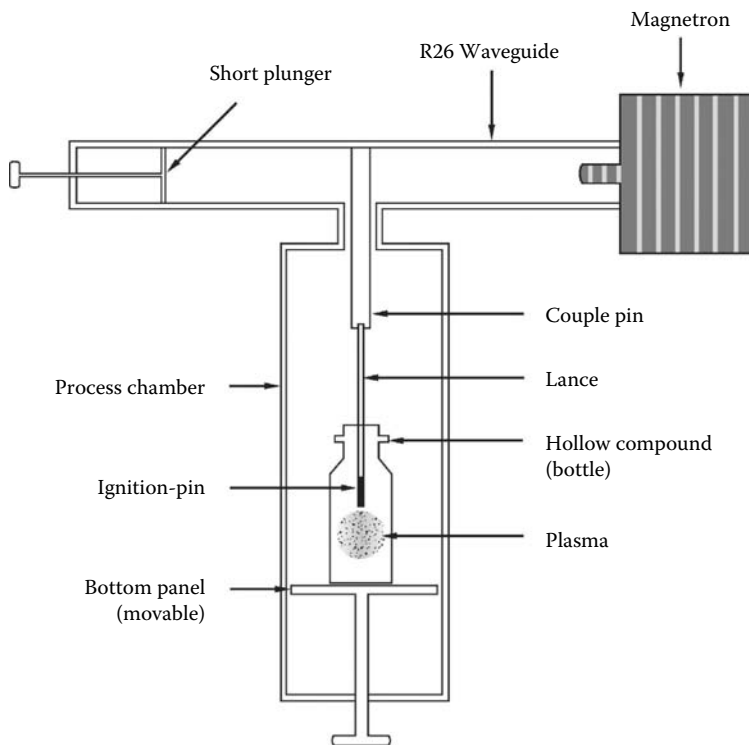


FIGURE 3.50 Scheme of source with moving plasma. (From Ehlbeck, J. et al., *Surf. Coat. Technol.*, 174–175, 493, 2003.)

TABLE 3.14
Examples of Microwave Plasma Sources

Source	Pressure [Pa]	n_e [cm^{-3}]	T_e [eV]	Application
Closed structure				
SLAN [81]	10^{-3} – 10^5	10^{11}	5	PACVD
Open structure				
Surfatron [86]	10^5	10^{12} – 10^{15}	5	Etching, coating
Planar Source [89]	10 – 10^5	10^{11}	2	Coating, cleaning
ECR [97]	10^{-2} –1	10^{12}	5	Coating

range of operating parameters as power input, sustaining frequency, and gas flow. The scaling also to industrial dimensions is without essential problems [105,109]. The DBD operates in a filamentary mode and a diffuse mode existing under special conditions is known as the atmospheric pressure glow discharge (APGD) [110].

Typical operation conditions of dielectric barrier discharges in air are presented in Table 3.15.

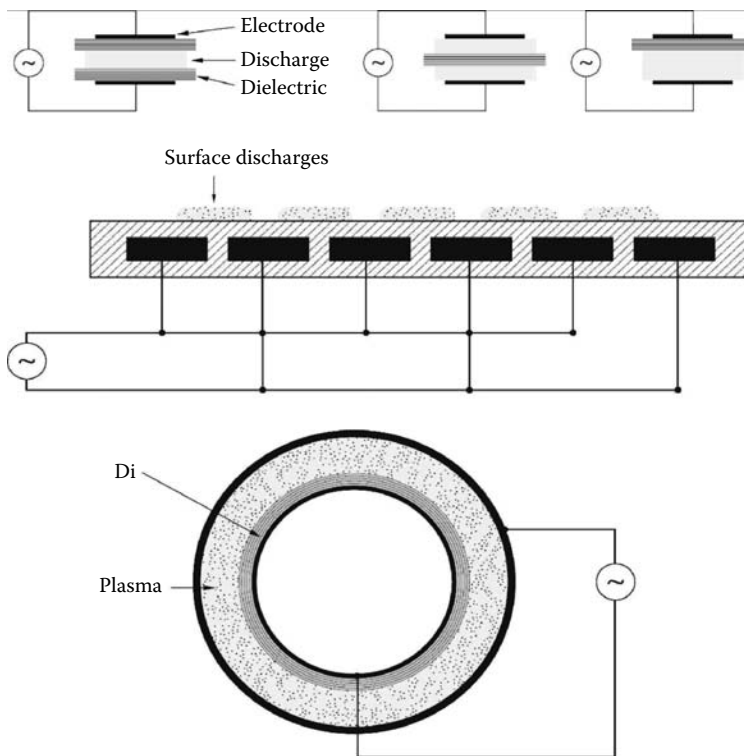


FIGURE 3.51 Dielectric barrier discharge configurations (Di, dielectric). (From Kogelschatz, U. et al., History of non-equilibrium air discharges, in K.H. Becker, U. Kogelschatz, K.-H. Schoenbach, and R.J. Barker, eds., *Non-Equilibrium Air Plasmas at Atmospheric Pressure*, pp. 17–75, IoP, Bristol, U.K., 2005.)

TABLE 3.15
Typical Operation Conditions of DBD
in Air

Voltage V_{pp}	3–20 kV
Repetition frequency f	50 Hz–1 MHz
Pressure	1–3 bar
Gap distance	0.2–5 mm
Dielectric material	Glass, Al_2O_3 , ferroelectrics

Characteristic properties of one filament of a DBD in air at atmospheric pressure with a gap of 1 mm are listed in Table 3.16 [111].

The nonthermal plasma of the DBD with its energetic electrons generates in suitable feed gases reactive radicals as precursors for various chemical reactions on surfaces as cleaning of work pieces or activation of foils to improve printability, and

TABLE 3.16
Characteristic Properties of One Filament DBD in Air at Atmospheric Pressure and a Gap of 1 mm

Duration	1–10 ns	Total charge	0.1–1 nC
Filament radius	~0.1 mm	Electron density	10^{14} – 10^{15} cm $^{-3}$
Peak current	0.1 mA	Electron energy	1–10 eV
Current density	10^2 – 10^3 A cm $^{-2}$	Gas temperature	Close to average gap temperature

Source: Kogelschatz, V. et al., DC and low frequency air plasma sources, in K.H. Becker, U. Kogelschatz, K.-H. Schoenbach, and R.J. Barker, eds., *Non-Equilibrium Air Plasmas at Atmospheric Pressure*, pp. 276–361, IoP, Bristol, U.K., 2005.

in the volume for ozone formation or gas cleaning, for excimer creation as sources of VUV radiation.

3.8.11 MICRODISCHARGE

Microdischarges are a fast developing field of the generation of nonthermal plasmas with interesting application aspects [106,111–114]. Unbounded microdischarges are the single filaments in a dielectric barrier discharge or the corona discharge near the sharp tip electrode. The size of bounded microdischarges is determined by the dimensions of the spatial cavity in which the discharge is generated. Various configurations of microplasma devices are described in the past, as coaxial cathode and anode micro cavities, cathode boundary layer discharge and capillary plasma electrode configurations, plasma needle, RF driven plasma jets. For dimensions of microcavity plasmas of 30–100 μm which operates stable for gas pressures up to one atmosphere [112] electron densities in the range of 10^{13} – 10^{16} cm $^{-3}$ were determined.

Schoenbach et al. [65,66] first reported the stable atmospheric pressure operation of a microdischarge in a cylindrical hollow cathode geometry with a cathode diameter of 200 μm . Various discharge systems were developed for operation in small volumes at high-near atmospheric pressures (Figure 3.52) [129], see also [115]. Stable glow discharges with a small gap down to 20 μm between metallic electrodes were studied in [116]. Cathode boundary layer discharges are high-pressure glow discharges operating between a planar cathode and a ring-shaped anode with a diameter below 1 mm up to some mm. The electrodes are separated by a dielectric with a thickness in the order of 100 μm (Figure 3.53). The discharge consists of the cathode fall and the negative glow, which acts as a virtual anode. The positive V – I characteristic and the parallel operation without individual ballast resistors enable the construction of arrays of such microdischarges [117].

The capillary plasma electrode (CPE) discharge device consists of one or several capillaries (diameter: 0.01–1 mm, length/diameter from 10:1 to 1:1) through the dielectric that cover one or both electrodes (Figure 3.54). The capillaries operate as plasma sources and a plasma jet mode is observed. For operating voltages above some

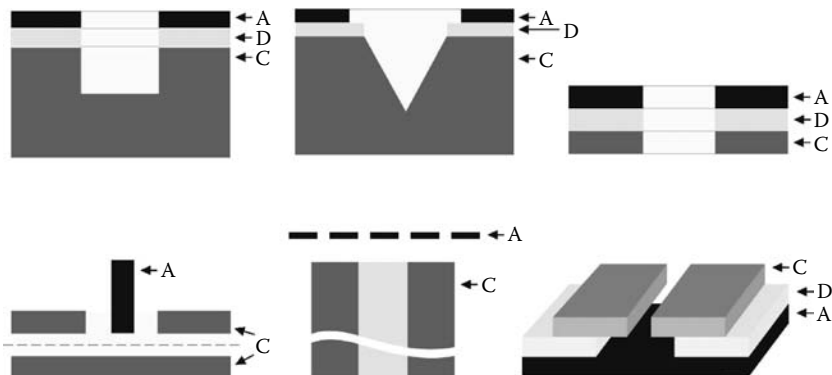


FIGURE 3.52 Microplasma geometries for single discharges or pixels in arrays. A, anode; C, cathode; D, dielectric. (From Becker, K. et al., *Plasma Phys. Contr. Fusion*, 47, B513, 2005.)

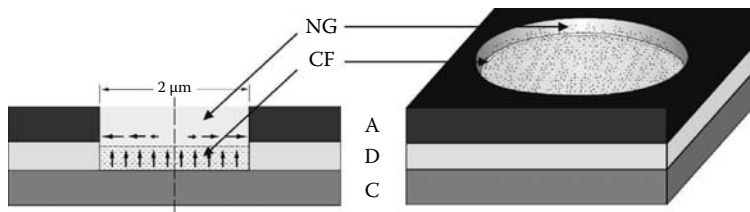


FIGURE 3.53 Cathode boundary layer discharge. A, anode; C, cathode; D, dielectric; CF, cathode fall; NG, negative glow. (From Becker, K. et al., *J. Phys. D: Appl. Phys.*, 39, R55, 2006.)

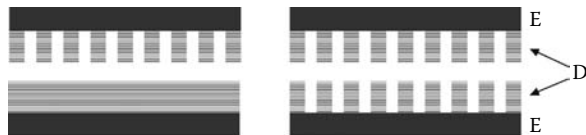


FIGURE 3.54 Scheme of a capillary plasma electrode discharge. E, electrode; D, dielectric. (From Becker, K. et al., *J. Phys. D: Appl. Phys.*, 39, R55, 2006.)

kHz the diffuse plasma changes into bright intense plasma formed by the overlapping plasma jets.

Arrays of microdischarges operating in nanostructured silicon or Al/Al₂O₃ multi-layer devices allow the generation of flat extended nonthermal atmospheric pressure plasmas with interesting short wave radiation originating from excimers. The nanosstructured silicon array consists of inverted square pyramid microcavities etched into p-Si. The emitting aperture is the pyramid base with $50 \times 50 \mu\text{m}^2$. A silicon nitride film covers the cavity surface, the Ni electrode is additionally isolated by a polyimide layer (Figure 3.55) [114]. The device operates by AC or bipolar DC voltage.

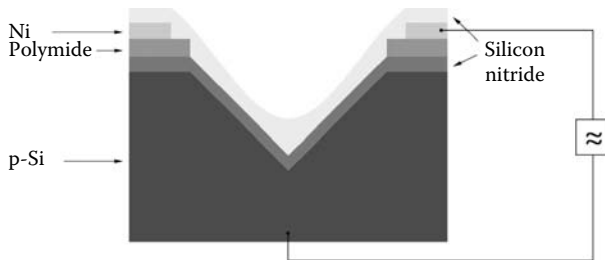


FIGURE 3.55 Scheme of an Si microplasma device with an inverted square pyramid microcavity. Ni and p-Si electrodes, silicon nitride and polyimide as dielectric. (From Becker, K. et al., *J. Phys. D: Appl. Phys.*, 39, R55, 2006.)

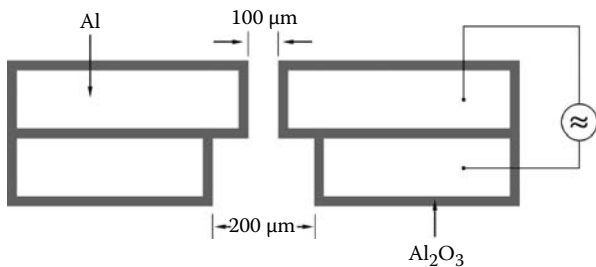


FIGURE 3.56 Diagram of an Al/Al₂O₃ microplasma device structure with two cylindrical cavities. (From Eden, J. et al., *Plasma Source Sci. Technol.*, 15, S67, 2006.)

One element of a Al/Al₂O₃ array consists of two conjoined cylindrical cavities in two Al foils (127 μm thick) with orifices of 100 and 200 μm , respectively. An Al₂O₃ layer on the surface of the foils (thickness 20–40 μm) and on the inner walls of the orifices (thickness 5–20 μm) assures the development of the plasma inside the cavity and protects against electrical breakdown elsewhere, see Figure 3.56. Such device operates at frequencies of some 10 kHz [112].

For low dimensions, high pressure, and high electron density the plasma will approach into a state of supercritical liquid and where quantum phenomena may become important [112,118].

3.8.12 COLD PLASMA JETS

A special type of microdischarges operating at atmospheric pressure is the cold plasma jet. In principle a plasma jet is built up of a combination of an electric field for plasma generation and a gas flow (see Figure 3.57). The jet device consists of cylindrical dielectric tubes and electrodes. At least one tube is the carrier of the gas flow of typically several liters per minute [125]. Atmospheric pressure nonthermal plasma jets are generated by nonthermal discharges like DBD, or RF discharges. Plasma jets can be classified according to the applied frequencies of the electric field for the discharge generation [120]. Pulsed DC-driven plasma jets, AC-driven jets operating with frequencies between 5 and 70 kHz and RF-driven jets using 13.56,

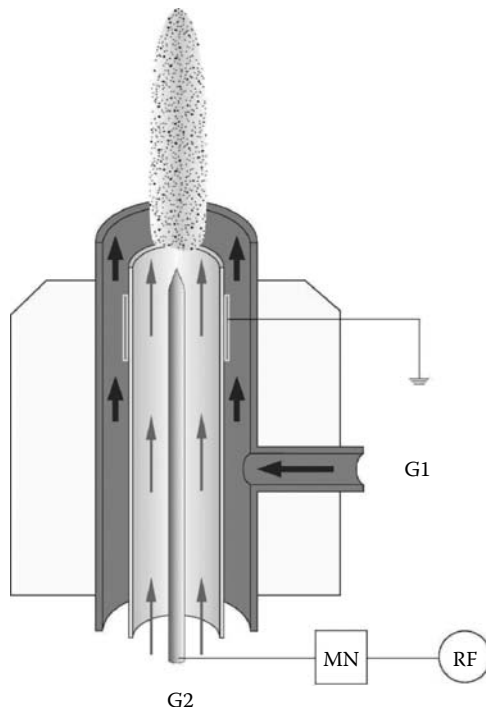


FIGURE 3.57 Scheme of a capillary jet with outer grounded ring electrode and inner powered rod electrode. G1 is the feed gas for plasma chemical reactions, admixed into the carrier gas (G2) outside the active plasma zone. (From Foest, R. et al., *Plasma Phys. Contr. Fusion.*, 47, B525, 2005.)

27.12, or 40.78 MHz as well as microwave powered jets were developed. DC and AC driven jets operate with voltages up to 10 kV. The glow to arc transition is inhibited by a pulsed operation regime, or resistive layers or dielectric barriers on or between the electrode surfaces. Configurations with outer electrodes, outer and central inner electrode, powered inner or outer electrode are developed. The discharge is generated on or near the open end of the device and is blown by gas stream into the surrounding environment with a length of some mm up to several cm. The generation of cold nonthermal plasmas can be supported by reduction of the input power and by increase of the heat losses [121]. Reduction of input power is possible by application of noble gases and small electrode gaps (some mm), small discharge currents, and reduction of duty cycle.

Plasma jets offer the advantage that the target of the plasma treatment is not positioned between the electrodes, the plasma is launched into the air and not limited by any boundaries. The diameter of the jet can be varied from some cm down to sub-mm. A local surface treatment of 3D structures as well as the arrangement of single plasma jets in an array for treatment of plane surfaces is possible [101,108]. The application of these exciting tools of plasma processing reaches from surface

TABLE 3.17
Microplasmas, Parameters, Applications

Microplasma	Plasma Parameter	Application
Hollow cathode glow discharge	$n_e: 5 \cdot 10^{16}$, $T_e: 1 \text{ eV}$ [124]	Excimer lamps, UV,VUV radiation [126]
DC-glow discharge	$n_e: 10^{13} - 10^{14} \text{ cm}^{-3}$, $T_e: 1.4 \text{ eV}$, $E_{\text{pos col}}: 1.4 \text{ kV/cm}$ [116]	Gas reforming, light sources, deposition, etching (Staack et al. [116])
Cathode boundary layer discharge	Pos. $U-I$ characteristic [127]	Excimer emission (Moseley and Schoenbach [127])
Capillary plasma electrode discharge	10 kHz, $n_e: 10^{10} - 10^{12} \text{ cm}^{-3}$ [128]	Flue gas cleaning, inactivation bacteria, (Becker et al. [129], Becker [114])
Al/Al ₂ O ₃ multilayer device nanostructured Si arrays	20 kHz, $10^4 10^6 \text{ W cm}^{-3}$, $n_e: 10^{13} - 10^{16} \text{ cm}^{-3}$ [112]	Medical applications (skin treatment), impurity detection (Eden et al. [112]), Photodetector [130]
Plasma jet	27.12 MHz, $n_e: 10^{12} - 10^{13} \text{ cm}^{-3}$,	Surface treatment, coating, medical applications (Foest [101])
Plasma needle	$n_{\text{radicals}}: 10^{13} \text{ cm}^{-3}$ [131]	Medical surface treatment (Stoffels et al. [132], Stoffels [133])

treatment for enhancing the surface energy, etching of various materials, thin film deposition, degradation of organic contaminants, inactivation of spores to killing of bacteria. Nonthermal plasma jets are sources of VUV radiation (e.g., Ar₂^{*} excimer continuum and atom lines of N, H, and O) [125] and radicals of organic compounds as precursors for thin film deposition [122]. The jet presented in Figure 3.57 is driven by 27.12 MHz as a RF capillary discharge between the outer grounded ring electrode and the central powered rod. The inert gas G2 flowing through the inner capillary is the carrier of the discharge, the feed gas (G1) for plasma chemical reactions, like silicon organic compounds vapor, flows through the outer capillary and is admixed to the plasma outside the active zone. An innovative version of an atmospheric pressure plasma jet is the Piezo-Plasma Pen working at a frequency of round about 119 kHz (eigenfrequency of the piezoceramics). A piezoelectric transformer generates high voltage starting with transversal oscillations of piezoceramic excited by 25 V RF voltage which is transformed into longitudinal oscillations which generate high voltage. This principle is proved for a hand-held unit with a power consumption of 6 W and a He gas-flow of 4 l/min [123].

Data and applications of selected microplasmas are presented in Table 3.17.

3.8.13 BEAM-GENERATED PLASMAS

Plasmas can be generated by the interaction of energetic beams of electrons. Plasmas of high ionization degrees are created in low-pressure environments [134]. The plasma generation by a magnetically confined electron beam in a low pressure (60 mTorr)

reactive gas atmosphere (Ar/SF_6) and its application to treatment of polymer surfaces is reported in [135,136].

3.8.14 PROPERTIES OF PLASMA SOURCES FOR PLASMA CHEMISTRY

The plasma sources have to satisfy different demands depending on the various applications. A plasma reactor for research and development purposes must have many ports for diagnostic tools as optical emission and absorption spectroscopy, mass spectrometry, Langmuir probes. Its potential of upscaling is important. Reactors in production lines must be matched to the selected production process. The following microscopic and macroscopic parameters and properties are important for technological applications (Figure 3.58), see also [137]. As already mentioned in the discussion of the various plasma sources the input parameters for plasma chemical processes are on one hand electrical as voltage and frequency, duty cycle, current and power for the plasma generation, external bias voltages of the substrate, magnetic field strength for plasma confinement, and/or ionization promotion. On the other hand nonelectrical parameter are important like gas pressure, gas flow, gas mixture, but also the temperature of the reactor walls, the electrodes and the substrate.

The magnetic field configuration can be achieved by various solenoids or by single and several permanent magnets. The application of solenoids is power consuming but allows an easy control and temporal variation of the magnetic field.

Plasma chemical reactors operate usually with a mixture of flowing inert carrier gas and the reactive component. The gas control system can be positioned in different places, upstream, into the plasma region (e.g., as a douche) or also downstream, in the remote afterglow plasma.

The dimensions of the reactor, the flow rate, and the pumping speed determine the residence time and the pressure regime: free fall (low-pressure ballistic movement without collisions) or diffusion determined (higher pressure) with laminar or turbulent flow. Most of the plasma chemical reactors operate as flow reactors.

The plasma chemical reactors for material treatment are constructed for batch or continuous operation. Examples for batch operation are the reactors of chip production in microelectronic industry for the wafer treatment in etch and deposition processes. Continuous operation is typical for the reactors for surface treatment of polymer foils to improve or enable the printability in dielectric barrier discharges or for thermal insulating coating of architectural glass by reactive sputtering in a DC magnetron discharge.

The reactor is determined by its shape and dimensions, if it is equipped with a single plasma source or an array, in a closed or open (e.g., in atmospheric pressure) configuration. The wall temperature is also important. Various electrodes are developed for special applications.

Concerning the substrate different types of reactors are possible. With fixed substrate position or moving substrate across the plasma zone (in continuous operation) or also rotating substrate for improving the homogeneity. Important is also the coupling of the substrate to the plasma [57]. A remote plasma source is a flowing afterglow with a low concentration of charge carriers, where surface processes are the result of long living radicals and energetic metastables. Plasma transport sources

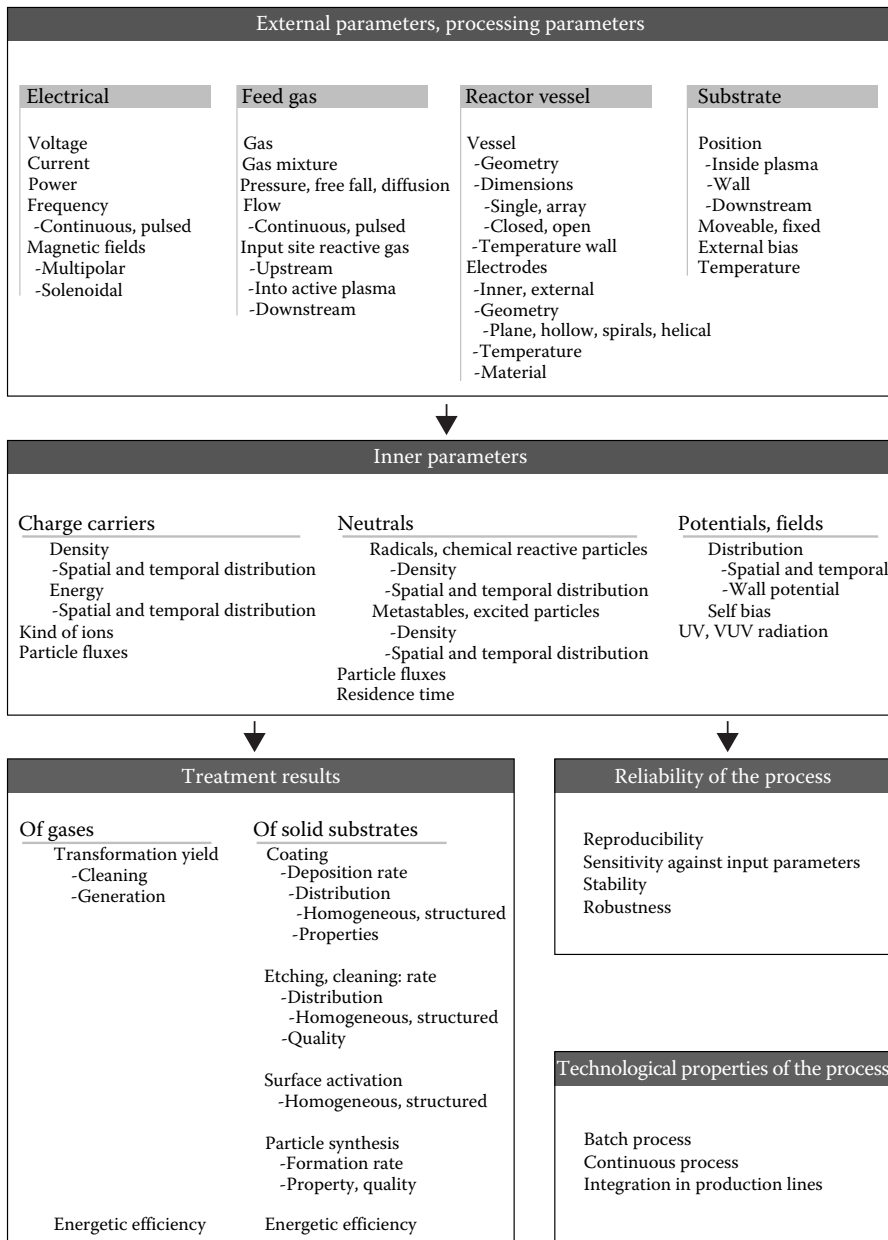


FIGURE 3.58 External and inner parameters of plasma chemical reactors, process results and properties.

are characterized by a separation of the active plasma zone and the work piece. High fluxes of charged particles combined with activated neutral particles interact with the substrate. The uniformity of the particle flux is less dependent on the power coupling.

Closed-coupled sources maximize the useful particle fluxes to the substrate. The homogeneity of the particle flux depends strongly on the position of the power coupling. The surface treatment of the substrate is also controlled by its temperature and bias voltage.

Fabrication processes include often some different production steps like surface cleaning, deposition of different materials with diverse feed gases, and also different plasma conditions. For this purpose the installation of clusters of different plasma reactors each with its specific task is used. The reactors are connected by a suitable transport system.

Plasma chemical reactors operating with various feed gases, especially for deposition processes, show not only deposition on the target surface, but also at the walls and on the installations inside the reactor vessel. These deposits are contaminants and the source of, e.g., gaseous decomposition products, adsorbed and later desorbed gases. Also the electrical conductivity can be changed. This will influence the plasma processes. Therefore, possibilities for surface cleaning and conditioning of the reactor are important for the reproducibility of the plasma chemical process.

The feed gas inlet system is an important part of the reactor. The source of the feed gas may be different in dependence of its properties. Permanent gases can be controlled by gas flow controllers, vapors of liquids demand a heating of the whole inlet installation to avoid condensation of the vapor along the feeding line. Thermal evaporators have been proved for the production of sufficient vapor flows.

The results of the plasma chemical treatment of gaseous or solid state materials can be evaluated on the one hand by the quality of the product, on the other hand for gaseous compounds by the rate of formation or transformation, for surface processes by the activation, etch and deposition rate. The energetic efficiency is an important parameter for gaseous processes.

Good reproducibility and low sensitivity against variations of the input parameters are essential for each commercial application of a plasma chemical process.

3.8.15 CONCLUSIONS

The presented plasma sources cover a broad field of parameters like gas pressure, charge carrier and radical density, electron and ion energy, ion energy at the substrate surface, and also density of UV radiation. Their scalability and timescales are different. The adjustment for the required plasma chemical application remains a challenge for scientific and engineering work. Furthermore, the history of the development of plasma sources shows the possibility of appearance of new source principles also in the future.

4 Nonthermal Plasma Chemical Reactors

CONTENTS

4.1	Principal Reactor Operation.....	137
4.2	Basic Reactor Models	139
4.2.1	Microphysical Kinetics	139
4.2.1.1	Plug Flow Model.....	140
4.2.1.2	Back Mixing Model	140
4.2.1.3	Closed Reactor.....	140
4.2.2	Example: Ozone Synthesis	141
4.3	Chemical Quasi-Equilibria	142
4.3.1	Introduction	142
4.3.2	Definition and Kinetic Background.....	143
4.3.3	Experimental Verification and Importance	147
4.4	Macroscopic Kinetics	151
4.5	Plasma Chemical Similarity.....	152
4.5.1	Introduction	152
4.5.2	Similarity Principles	153
4.5.3	Plasma Chemical Similarity: Positive Column of Glow Discharge	154
4.5.4	Application to the Flow Reactor	157
4.5.4.1	The Reactor Parameter R	158
4.5.5	Experimental Proof	159

4.1 PRINCIPAL REACTOR OPERATION

The principle of a nonthermal plasma chemical flow reactor is shown in Figure 4.1a. A mixture of reactants ($A_1 \dots A_k$) enters the so-called active zone (AZ) and is exposed to hot electrons (kinetic temperature $T_e = 1\text{--}10\text{ eV}$). The temperature T_g of the heavy particles remains small ($T_g \ll T_e$; nonthermal conditions). In the AZ the hot electrons start a chain of elementary reactions (ionization, dissociation, excitation, etc.) which result in highly reactive species (free atoms, radicals, ions, etc.). The consequence is the initiation of chemical reactions between heavy particles (radical reactions, ion–molecule reactions, ...). Moreover, heterogeneous reactions at metallic or semiconductor surfaces (electrodes, targets, ...) as well as the deposition of thin films (e.g., from organic reactants) occur.

After the AZ the chemically changed mixture enters the so-called passive zone (PZ). Because of the deionization and fast cooling of the electrons ($T_e \rightarrow T_g$) the PZ is characterized by a quite different chemical climate. Here recombinations, de-exitations, etc. prevail which create at the end a mixture of stable products

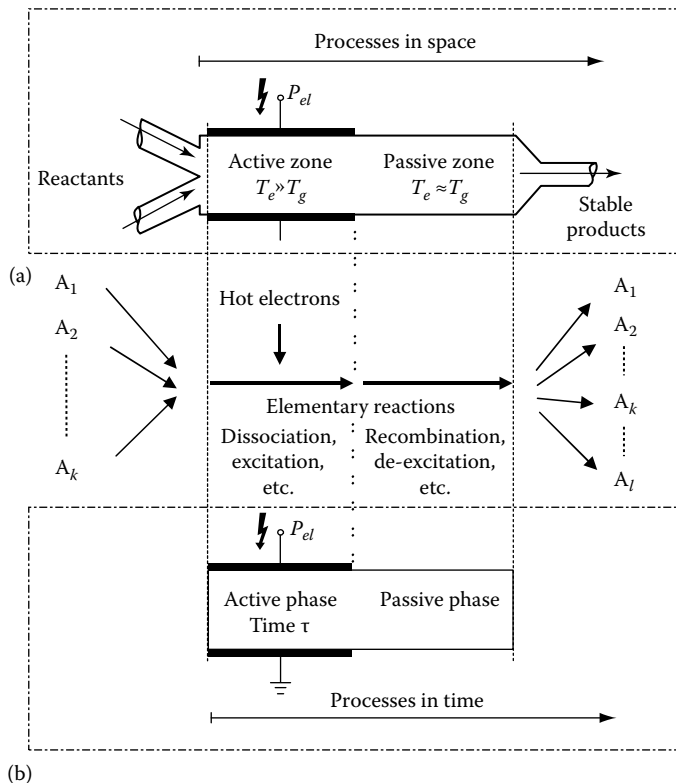


FIGURE 4.1 Scheme of a plasma chemical flow reactor (a) and of a closed reactor (b), respectively (with P_{el} electrical power input, T_e kinetic temperature of electrons, T_g gas temperature).

containing the input species ($A_1 \dots A_k$) but also new components ($A_{k+1} \dots A_l$). The double zone structure of every nonthermal plasma chemical flow reactor is well known. But very often the specific role of the PZ and its great importance for the final gas composition is underestimated.

There are conditions, namely in low-pressure plasmas, in which desired compounds originate nearly complete in the PZ. In this case a suitable control scheme for the manipulation of the PZ (e.g., by gas temperature control) considerably increases the efficiency of the whole reactor similar to the quench of an isothermal reactor. The quite different functions of the AZ and PZ especially in connection with so-called reversible chemical quasi-equilibrium states will be outlined in Section 4.3. The basis particle component of the AZ which guarantees the energy input in the reactant mixture is the hot electron gas. Hot electrons are produced by the different types of electrical discharges as glow discharges (DC, AC, RF, microwave) including hollow cathode discharges as well as barrier discharges, corona discharges, and plasma jets, see Section 3.8.

For reactor operation under no-flow conditions (closed reactor) the double structure is realized by two phases, an active phase (AP) of discharge operation followed by the passive phase (PP) (plasma off), characterized by the afterglow processes (compare Figure 4.1b). In practice the PP corresponds to the late afterglow of pulsed discharges.

4.2 BASIC REACTOR MODELS

4.2.1 MICROPHYSICAL KINETICS

For practical requirements the essential knowledge of the reactor operation reduces to the dependence of the output reactant composition in relation to the input parameters:

- Reactant composition at the reactor entrance
- Operating parameters of the reactor (geometry, pressure, flow rate, etc.)
- Operating parameters of the discharge (electrical characteristic, invested power, time regime, etc.)

Of course, the problem is very complex and due to interconnecting dependencies of the different quantities it should be solved as a whole. In a first approximation step the discharge operation is separated from that of the reactor. In this framework the discharge conditions (energy distribution function and concentration of the plasma electrons) are given and independent of the flow velocity, gas composition, etc. in the reactor.

At a fixed position in the reactor the temporal rate of one component A_i consists of a divergence term of the particle fluxes and a difference term of the gains (G_i) and losses (L_i) by particle collisions (particle balance equation):

$$\frac{\partial n_i}{\partial t} + \operatorname{div}(n_i \cdot \vec{w}_i) = G_i - L_i. \quad (4.1)$$

The mean molecular velocity \vec{w}_i is the sum of the mean particle velocity \vec{v} and the diffusion velocity \vec{V}_i . If thermo and pressure diffusion can be neglected ($p, T_g \approx \text{const}$) these velocities are given by

$$\vec{v} = \left(\frac{1}{n}\right) \sum n_i \cdot \vec{w}_i,$$

$$\vec{V}_i = - \left(\frac{D_i}{n_i}\right) \operatorname{grad} n_i,$$

with $n = \sum n_i$ and $n_i = [A_i]$. Here D_i is the diffusion coefficient and $[A_i]$ is the particle concentration (number density) of the component A_i .

In the most simple case the balance equation (4.1) is solved for a one-dimensional and stationary flow. Then two limiting cases are of great importance: the plug flow model (PFM) and the back mixing model (BMM).

4.2.1.1 Plug Flow Model

Here, the diffusion is neglected (diffusion coefficient $D_i \rightarrow 0$). The reactant mixture moves with the mean particle velocity $w_{iz} = v = v(z)$ along the axial reactor coordinate using the constraint condition $n = \text{const}$ and summing up all the particle sorts it follows

$$v \frac{dn_i}{dz} = S_i - \left(\frac{n_i}{n} \right) \sum S_j, \quad (4.2)$$

where

z is the axial reactor coordinate

$S_i = G_i - L_i$ the effective source term.

With the approximation of small chemical changes ($v \approx v_0 = \text{const}$, v_0 is the flow velocity without conversion) for a compound created in the reactor ($n_i \ll n$) solving of

$$v_0 \frac{dn_i}{dz} = S_i \quad (4.3)$$

results in $n_i = n_i(z)$. In the more general case ($v = v(z)$) the system of differential equations (4.2) must be solved together with the continuity equation of the mass flow

$$v \sum m_j n_j = v_0 \sum m_j n_{j0}$$

to get $n_i(z)$ and $v(z)$. Of course, (4.2) must be solved separately for both the reactor zones (AZ and PZ), fitting the solutions at the interface.

4.2.1.2 Back Mixing Model

Here, the diffusion prevails ($D_i \rightarrow \infty$) and provides a fast equalization of the particle concentrations along the z -axis. Within the reactor no variations $n_i = n_i(z)$ occur, but step profiles exist at the entrance $n_{i0} \rightarrow n_i$. In this case the particle balance equation is reduced to

$$v n_i - v_0 n_{i0} = l S_i, \quad (4.4)$$

where l is the length of the reactor zone under consideration.

The combined action of the AZ and PZ again is accounted for by fitting of the solutions for the AZ with $l = l_A$ and the PZ with $l = l_P \rightarrow \infty$.

In most cases the results of the PFM and BMM do not differ considerably for the exit concentration of the reactors (agreement within 10%–20%), but of course the handling of the BMM is much more convenient.

4.2.1.3 Closed Reactor

In the case of a closed reactor (system without flow) the term $\text{div}(n_i \vec{w}_i) = 0$ of (4.1) disappears. Consequently, the particle balance equation is simplified to

$$\frac{dn_i}{dt} = S_i - \left(\frac{n_i}{n} \right) \sum S_j \quad (4.5)$$

with $dn/dt = \sum S_j$.

4.2.2 EXAMPLE: OZONE SYNTHESIS

The approximation of the PFM will be illustrated for the basic mechanism of the ozone synthesis. The most significant processes of the O_3 production takes place via oxygen atoms. The microscopic reaction scheme is listed in Table 4.1.

The source terms S_i for the molar fractions $x_i = n_i/n$ of atomic and molecular oxygen and ozone (index 1, 2, and 3, respectively) then reads as follows:

$$\begin{aligned} S_1 &= 2k_1 n^2 x_e x_2 + k_3 n^2 x_e x_3 + k_6 n^2 x_2 x_3 - \gamma_2 n^3 x_1 x_2 - 2\gamma_4 n^3 x_1^2 - k_5 n^2 x_1 x_3 - \alpha n x_1 \\ S_2 &= k_3 n^2 x_e x_3 + \gamma_4 n^3 x_1^2 + 2k_5 n^2 x_1 x_3 + k_6 n^2 x_2 x_3 + \frac{\alpha n x_1}{2} - k_1 n^2 x_e x_2 - \gamma_2 n^3 x_1 x_2 \\ S_3 &= \gamma_2 n^3 x_1 x_2 - k_3 n^2 x_e x_3 - k_5 n^2 x_1 x_3 - k_6 n^2 x_e x_3 \\ \sum S_j &= k_1 n^2 x_e x_2 - \gamma_2 n^3 x_2 x_3 + k_3 n^2 x_e x_3 - \gamma_4 n^3 x_1^2 + k_6 n^2 x_2 x_3 - 0.5 \alpha n x_1. \end{aligned}$$

The solution of the following system of differential equations ($i = 1, 2, 3$)

$$\frac{dx_i}{d(z/l_A)} = \frac{\tau_0}{n} \frac{x_1 + 2x_2 + 3x_3}{x_{10} + 2x_{20} + 3x_{30}} \left(S_i - x_i \sum S_j \right)$$

with $\tau_0 = l_A/v_0$ results in $x_i = x_i(z/l_A)$, especially in the values $x_i(1)$ at the end of the AZ which must be continued in the PZ ($x_e = 0$) to get the final concentrations $x_i = x_i(\infty)$. Synthesis means $x_{10} = x_{30} = 0$; $x_{20} = 1$ and decomposition $x_{10} = x_{20} = 0$; $x_{30} = 1$. Because of the given low gas temperature ozone can be considered as a stable final product ($k_6 \approx 0$). Figure 4.2 shows the calculated concentration of O , O_2 , and O_3 as a function of the normalized reactor coordinate z/l_A of the reactor for fixed values of the ionization degree and the residence time τ_0 of the gas mixture in the AZ. Under the prevailing conditions in the back part of the AZ all particle concentrations transfer into constant values starting from the educt side of the gross reaction $3O_2 + e \rightleftharpoons 2O_3 + e$ as well as from the product side. After that the species

TABLE 4.1
Basic Mechanism of Ozone Synthesis

	Elementary Processes	Rate Constants
1	$O_2 + e \longrightarrow O + O + e$	$k_1(T_e)$
2	$O + O_2 + M \longrightarrow O_3 + M$	$\gamma_2 = 4.2 \times 10^{-35} \exp(1050/T_g)$
3	$O_3 + e \longrightarrow O_2 + O + e$	$k_3(T_e)$
4	$O + O + M \longrightarrow O_2 + M$	$\gamma_4 = 2.7 \times 10^{-32} T_g^{-0.41}$
5	$O_3 + O \longrightarrow 2O_2$	$k_5 = 2.0 \cdot 10^{-11} \exp(-2400/T_g)$
6	$O_3 + O_2 \longrightarrow 2O_2 + O$	$k_6 = 1.7 \cdot 10^{-9} \exp(-11300/T_g)$
7	$O + \text{wall} \longrightarrow 0.5O_2$	$\alpha = \varepsilon \bar{c}/2r$

The rate constants k_i and γ_i are given in $\text{cm}^3 \text{s}^{-1}$ and $\text{cm}^6 \text{s}^{-1}$, respectively, ε is the recombination probability, \bar{c} the thermal velocity, and r the radius of cylindrical reactor tube.

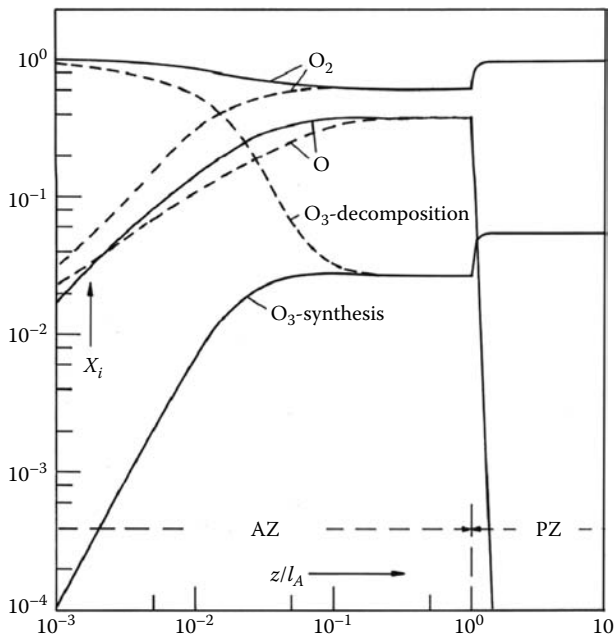


FIGURE 4.2 Development of the relative O -, O_2 -, and O_3 -concentration along the reactor coordinate of the AZ and PZ within the plug flow model. Conditions: $x_e = 10^{-6}$, $\tau_0 = 0.1$ s; $T_g = 300$ K, $n = [M] = 3 \cdot 10^{17}$ cm $^{-3}$, $\epsilon = 10^{-4}$, $r = 1$ cm, $3k_1 = k_3 = 9 \cdot 10^{-10}$ cm 3 s $^{-1}$.

relax along the PZ, whereas a considerable increase of ozone x_3 takes place. For high degrees of ionization x_e the differences in the O_3 amount at the exits of the AZ and PZ is enormous.

4.3 CHEMICAL QUASI-EQUILIBRIA

4.3.1 INTRODUCTION

Contrary to the thermal equilibrium, the term quasi-equilibrium describes physically and chemically well-defined states, related to special operation conditions of the reactors. To understand their character, it is indispensable to consider the double zone (or phase, respectively) structure of every plasma chemical reactor, as outlined in Section 4.1. In every case the statements of quasi-equilibrium states are related to the output of the PZ. Unstable products (e.g., free radicals) are not included! In practice this corresponds to flowing afterglows or the late afterglow of pulsed discharges. But they are formed in other types of closed reactors too. Such reactors are characterized by a small stationary AZ, separated in space and surrounded by an extended stationary afterglow PZ, as it is the case in many standard rf plasma sources.

Discussing the two limiting situations of low or high power input into the AZ $P \rightarrow 0$ and $P \rightarrow \infty$, which includes the limits $n_e \rightarrow 0$ and $n_e \rightarrow \infty$. The set of chemical rate equations results in two final compositions, which are qualified as [1,2]:

1. CEEC, Chemical equilibrium of electronic catalysis. The occurrence of a finite degree of conversion in a closed plasma chemical system at the limit of vanishing ionization is a very typical case, representing a kind of electronic catalysis: In principle already one hot electron (permanent regenerated) is able to convert a reactant mixture in this equilibrium state of altered composition.
2. CECD, Chemical equilibrium of complete decomposition. Large concentrations of hot electrons (high power input) result in the nearly complete decomposition of the reactants in the active zone (phase). The afterglow recombination processes yield a final composition of the reactant mixture according to the neutral gas reactions starting from the elementary constituents. Obviously this behavior must be a general characteristic equilibrium state of every nonisothermal plasma chemical reactor, too.

An important point regarding the experimental verification of the quasi-equilibrium states is the following one: Although these states are defined as limiting cases ($P \rightarrow 0$ or $P \rightarrow \infty$) in practice they can be observed already at moderate values of P .

4.3.2 DEFINITION AND KINETIC BACKGROUND

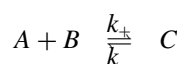
The reaction system is characterized by the type of reversible gross reaction:



(e symbolizes the hot electron) and some plasma parameters like the kinetic temperature of electrons T_e and gas temperature T_g . Under a plasma chemical quasi-equilibrium, we understand a stationary state of the composition of stable reaction products:

- Attainable from both sides of a reversible gross reaction (mentioned earlier)
- Independent of reactor parameters, as power input (degree of ionization), geometry, and type of the plasma zone as well as reactor dead zone
- Described by a modified mass action law whose constant differs from the usual one, but depends like the usual one on the gas temperature (the most important point). It is determined by a multitude of elementary processes of the reactor and is kinetic by nature.

In the case of the chemical equilibrium of thermal reactions (CETR) for the conversion



the mass action law reads

$$\frac{n_A n_B}{n_C} = \frac{k_-}{k_+} = K(T_g) \quad (4.7)$$

with n_i particle number density of component i .

Including electronic processes (4.6) we get for the closed system in the limit of vanishing electron concentration $n_e \rightarrow 0$ and $\tau \rightarrow \infty$ (τ duration time of active phase) [1–3]:

$$\text{CEEC} \quad \frac{n_A^0 n_B^0}{n_C^0} = \frac{k_-^0(n_e, T_e, T_g)}{k_+^0(n_e, T_e, T_g)} \xrightleftharpoons{T_e \geq T_{e,\min}} K^0(T_g). \quad (4.8)$$

The ratio of forward and backward rate coefficients depends, first of all, on the concentration n_e and temperature T_e of the electrons and on the gas temperature T_g . But in plasma chemistry very often conditions prevail where the electronic parameters can be canceled approximately. This is the case if the rate coefficients are proportional to n_e and nearly independent of T_e at values $T_e \geq T_{e,\min}$, that is $k_\pm^0(n_e, T_e, T_g) \approx n_e \cdot f(T_g, n)$. The minimum value $T_{e,\min} \approx 1 \text{ eV}$ will be surpassed in many plasma chemical systems [2,3].

The chemical equilibrium of complete decomposition ($n_e \rightarrow \infty$) is governed by afterglow processes mostly including neutral species. Then the gas temperature controls the conversion again

$$\text{CECD} \quad \frac{n_A^\infty n_B^\infty}{n_C^\infty} = K^\infty(T_g). \quad (4.9)$$

To demonstrate the different states of quasi-equilibria the basic mechanism of the ozone synthesis is used again



which was already discussed in the last section (see Table 4.1). The formation of a common quasi-equilibrium state for the synthesis and decomposition of ozone can be seen in Figure 4.2. It should be noted that this state is established already at relatively small ionization degree x_e for a moderate residence time τ_0 .

Figure 4.3 summarizes the calculated ozone concentration x_3 for the synthesis and decomposition in dependence on the ionization degree x_e at various residence times τ_0 at two reactor positions: the exit of the AZ ($z/l_A = 1$) and the exit of the PZ ($z/l_A \rightarrow \infty$). It is generally noticed that considerable differences of x_3 exist at these positions if x_e is larger or τ_0 is small. Furthermore, all curves of the PZ show a convergence to a nearly constant value $x_3 \approx 5 \text{ vol\%}$. The output concentrations of the reactor at $x_e \rightarrow \infty$ and $x_e \rightarrow 0$ at $\tau_0 \rightarrow \infty$ are almost equivalent and independent of the entrance composition (O_2 or O_3). The finite degree of conversion in a closed plasma chemical reactor ($\tau_0 \rightarrow \infty$ and $x_e \rightarrow 0$) represents the chemical quasi-equilibrium CEEC, defined above. The x_e -independent output for $x_e \rightarrow \infty$ denotes the CECD.

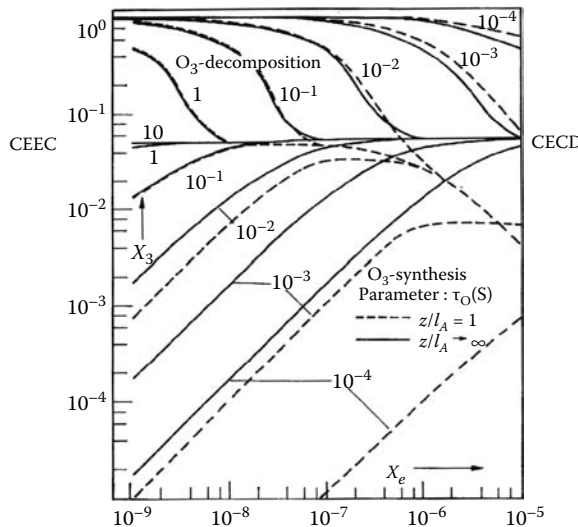


FIGURE 4.3 Relative concentration of ozone in dependence on the degree of ionization (broken curves: end of AZ; full curves: end of PZ). Rate constants and conditions as in Table 4.1 and in Figure 4.2.

For the basic ozone mechanism the case of CEEC can be derived analytically. It results in nonvanishing concentrations of ozone

$$\frac{n_{O_2}^0}{n_{O_3}^0} = \frac{k_5 + k_3 (n_e/n_O)^0}{\gamma_2 n} = K^0(T_g), \quad (4.10)$$

n is the total particle number density with the *finite* limiting value of the concentration ratio of electrons n_e and atomic oxygen n_O

$$\lim_{n_e \rightarrow 0} \left(\frac{n_e}{n_O} \right) = \left(\frac{n_e}{n_O} \right)^0 = \frac{1}{k_3} \frac{\alpha + \gamma_2 n n_{O_2}^0 + k_5 n_{O_3}^0}{2 n_{O_2}^0 k_1/k_3 + n_{O_3}^0}. \quad (4.11)$$

The existence of this finite ratio is essential for the finite conversion into O_3 in a closed reactor at $x_e \rightarrow 0$. For the CECD ($n_e \rightarrow \infty$) only a numerical solution is possible. The states of the CEEC and CECD are marked in Figure 4.3, too. At different gas temperatures the relevant concentrations of O_2 and O_3 are described by

$$\frac{n_{O_2}^\infty}{n_{O_3}^\infty} = K^\infty(T_g).$$

Figure 4.4 shows this dependence, too. Obviously an exponential dependence prevails (Arrhenius plot). Together with the CECD in Figure 4.4 the CEEC is also recognizable. For the used rate coefficients both quasi-equilibrium states coincide

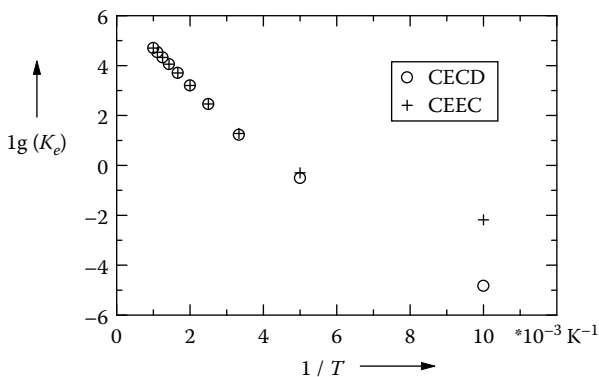


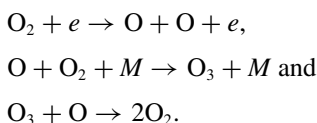
FIGURE 4.4 The constant $K_e(T_g)$ for the quasi-equilibrium states CEEC and CECD in the closed reactor. Rate constants as in Table 4.1 and in Figure 4.2.

$$K^\infty(T_g) = K^0(T_g) = K_e(T_g) \approx \frac{k_s}{\gamma_2 n}. \quad (4.12)$$

The conditions of the coincidence of the chemical compositions of the two quasi-equilibria is of considerable interest. Surprisingly, numerous experimental results confirm the suggestion that this is a more general case: Nonthermal plasma chemical conversion tends to reach CEEC = CECD.

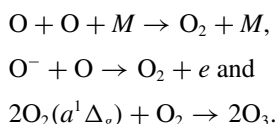
The kinetic background of the chemical quasi-equilibrium states has been extensively studied for different nonthermal plasma chemical systems, considering all relevant species and elementary reactions (see [2,4,5]). Generally, for CEEC = CECD the following conditions must be fulfilled:

- The gain and loss processes for stable final products are determined at vanishing power input ($P \rightarrow 0$) only by the collisions of neutral particles. The most important role of electron collisions is the generation of unstable intermediate particles (atoms, radicals, excited species) which influence the gain and loss of the final products, e.g.,



Disturbing process for the equalization: $O_3 + e \rightarrow O_2 + O + e$.

- Quadratic processes of unstable intermediate products are of minor importance, e.g.,



- For $P \rightarrow 0$ the important collisions of neutral particles govern the afterglow, which transfer the active plasma from complete decomposition to the final state of CECD. That means for both CEEC and CECD a very “similar chemical climate” exists. This includes: constant gas temperature and constant wall conditions (in the case of heterogeneous reactions).

4.3.3 EXPERIMENTAL VERIFICATION AND IMPORTANCE

In the following we present selected experimental results on the occurrence of chemical quasi-equilibria in nonthermal plasma reactors. The experiments were performed in a DC positive column, in an RF discharge, and a so-called spark discharge, respectively.

Figure 4.5 shows the ozone synthesis in the positive column of a DC O₂ glow discharge in a closed cylindrical glass tube at two different wall temperatures. The ozone concentration was detected using UV light absorption at 253.9 nm. In each case, the lower curves belong to the active phase AP (discharge operation). After discharge interruption (passive phase PP) the O₃ concentration reaches a value which is nearly independent of the ionization degree x_e , calculated from the current balance in the positive column. The development of a finite ozone concentration is clearly shown for $x_e \rightarrow 0$, denoting the CEEC. This value is independent of the special type of the discharge. Nearly the same value is reached using a weak spark discharge, produced by a Tesla transformer (here named Tesla spark discharge). The almost horizontal O₃ curves manifest the typical case of identical quasi-equilibria CEEC = CECD for the ozone synthesis as discussed in the last section. The strong dependencies of the level of the quasi-equilibria on the wall temperature correspond to the sensitive temperature dependence of the rate constants γ_2 and k_5 for the synthesis and decomposition of O₃ (compare Table 4.1).

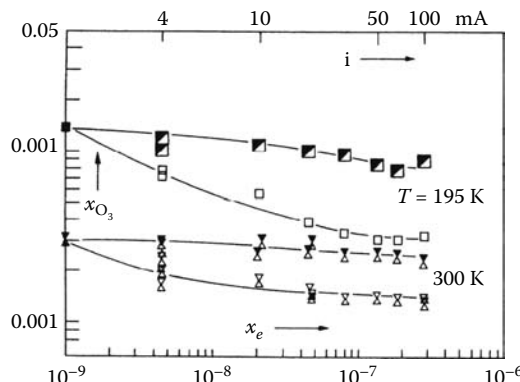


FIGURE 4.5 Relative ozone concentration x_{O_3} in dependence on the ionization degree in a closed reactor. Discharge: Positive column of a DC glow discharge. Tube: $L = 47$ cm, $r = 1$ cm, Al electrodes, input number density $n_0 = 5 \cdot 10^{17} \text{ cm}^{-3}$ pure O₂. Lower curves in each case: Active phase AP = discharge operation. Upper curves in each case: Passive phase PP after relaxation. Full symbols on left: Excitation for long time by a weak spark discharge.

Additionally, experimental results on the ozone production in a corresponding flow reactor (active zone AZ: DC positive column within a cylindrical glass tube, to see Figure 4.6 according the gross reaction $3\text{O}_2 + e \rightleftharpoons 2\text{O}_3 + e$ are shown in Figure 4.7 [5]. The ozone concentration in the PZ is nearly current-independent, of course depending on the gas pressure. For discharge currents above 20 mA the ozone concentration is decreasing. This is caused by the increasing gas temperature in the AZ, which—as in the closed reactor—affects sensitively the endothermic ozone production reactions. The current independent plateau of the relative ozone concentration

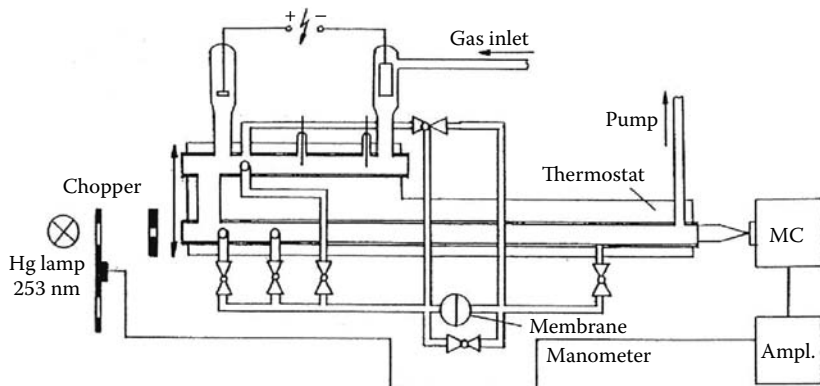


FIGURE 4.6 Experimental setup. The apparatus was fully placed in water (thermostat). MC: Monochromator, ampl.: LOOK IN amplifier.

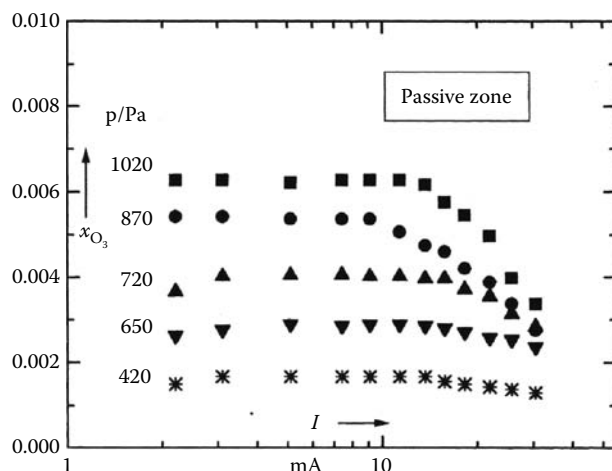


FIGURE 4.7 Dependence of the relative ozone concentration x_{O_3} on the discharge current I in the passive zone PZ of a flow reactor. AZ: Positive column of a dc glow discharge. Tube: $r = 1$ cm, Al electrodes, length of AZ = 20 cm. Conditions: $F = 79$ sccm. Parameter: Gas pressure.

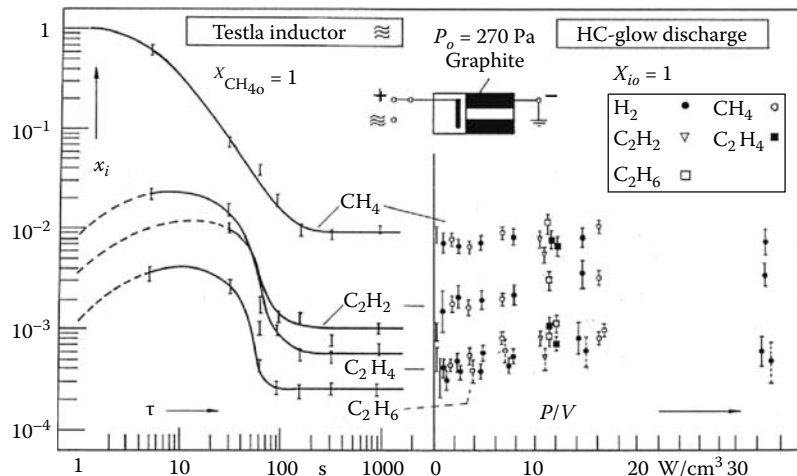


FIGURE 4.8 The formation of chemical quasi-equilibria in a closed reactor at different hydrocarbon and hydrogen input during the excitation by a Tesla spark discharge (left) and a hollow cathode glow discharge (graphite cathode, $D = 8 \text{ mm}$, $L = 30 \text{ mm}$). Input pressure in every case: $p = 400 \text{ Pa}$.

represents the case of identical chemical quasi-equilibria CEEC = CECD. The plateau represents a large variation of the ionization degree $x_e = n_e/n$ in the discharge of about two orders of magnitude.

The formation of identical chemical quasi-equilibria with CEEC = CECD also appears in the case of very complex plasma chemical processes. An example for this situation is the decomposition and formation of hydrocarbons in a hollow cathode glow discharge which operates in graphite cathodes. Etching processes, the formation of polymer layers, and complex homogeneous reactions take place. The product composition was detected by gas chromatography (see Section 6.6). Figure 4.8 (on the right-hand side) shows that an identical final gas composition is reached independent of the power density and the C/H ratio of the gas input. Obviously this complex process is controlled by the specific energy too. On the left-hand side of this figure the decomposition of CH_4 by the faint Tesla spark discharge (=low ionization degree) is shown. After short time the gas mixture reaches nearly the same stationary values as with the hollow cathode glow discharge. This fact demonstrates again that quasiequilibria are independent of the nonthermal plasma type.

As discussed earlier, the plateau of quasi-equilibria is independent of the reactor dead zone as well as of the plasma type. These results are illustrated for the CO_2 decomposition in a glass tube reactor under closed conditions according to the reversible gross reaction $2\text{CO}_2 + e \rightleftharpoons 2\text{CO} + \text{O}_2 + e$ [6]. The concentration of the reaction products was measured by the gaschromatographic technique. Figure 4.9 shows this conversion in an rf discharge at nearly constant power input. An extreme variation of the relative portion of the plasma zone does not influence the final composition of stable products. Different types of nonthermal plasmas create similar stationary compositions of stable reaction products at constant wall conditions (Figure 4.10).

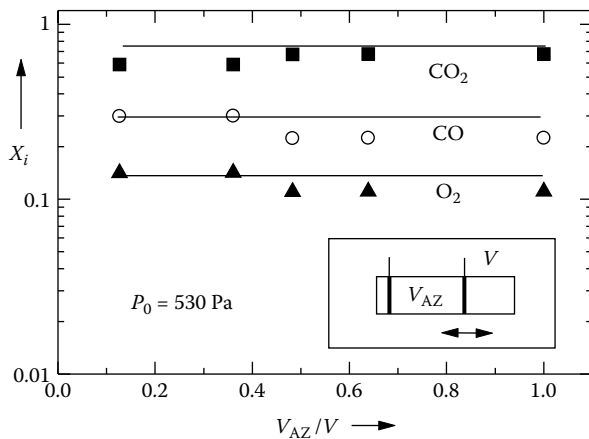


FIGURE 4.9 Stationary composition of the stable products of CO_2 decomposition in rf discharges depending on the volume of the reactor dead zone (glass tube reactor, $P = \text{const.}$, $f = 27.12 \text{ MHz}$).

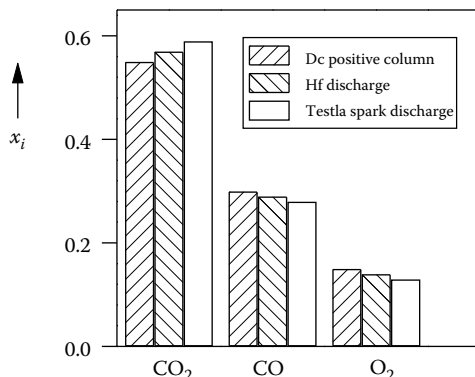


FIGURE 4.10 Stationary composition of stable reaction products for the CO_2 decomposition in different discharges types (glow discharge: $P = 10 \text{ W}$; rf discharge: $P = 10 \text{ W}$, $f = 27.12 \text{ MHz}$; Tesla spark discharge: $P < 0.1 \text{ W}$). Other conditions as in Figure 4.8.

In Figure 4.11 the change of the level of the CEEC in dependence on the input ratio of a CO/O_2 mixture AP (dc positive column, within cylindrical glass tube) is shown: The composition of the stable reaction products follows rather good the simple “electronically modified” mass action formula, given above, with $K^0 = 10^{16} \text{ cm}^{-3} = \text{const.}$ Surprisingly, the same value of K^0 describes also the pressure dependence of the CEEC [6].

The chemical quasi-equilibria are of practical significance and importance, based on the following facts:

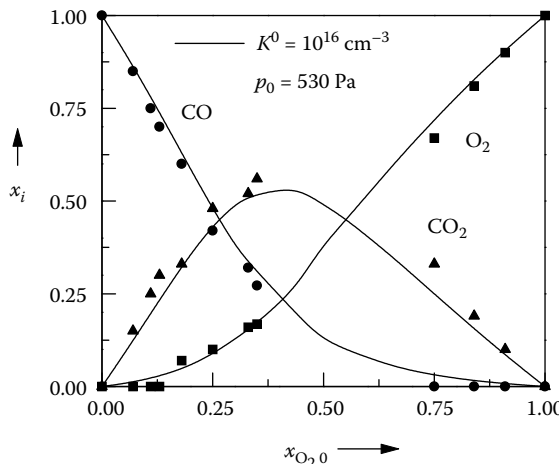


FIGURE 4.11 The chemical quasi-equilibrium CEEC in dependence on the input mixture O_2/CO (dc positive column, Al electrodes, $i = 30\text{ mA}$). Symbols: experiments, lines: Calculations with $K^0 = \text{const}$, according to (4.8).

- These states represent the basis for the so-called method of macroscopic kinetics (MAK). In the case $\text{CEEC} = \text{CECD}$ the specific energy $\tau_0 P/V_A$ is often the decisive quantity which in the kinetic curves $n_i = n_i(\tau_0 P/V_A)$ determines the mixture composition (compare Sections 4.4 and 4.5.4.1). With $\text{CEEC} \neq \text{CECD}$ the generalized MAK is relevant [3].
- Chemical quasi-equilibria are simple to verify. For instance, a few measurements with a closed reactive system allow the description of this as well as the corresponding flow reactor [3].
- The analysis of chemical quasi-equilibria allows the possibility of checking microscopic models. In this way an indirect determination of rate constants of unknown electronic collision processes was possible (see [4]).

4.4 MACROSCOPIC KINETICS

Generally, to solve (4.1), (4.2), and (4.4) the knowledge of the source terms S_i is necessary. The primary dependencies are

$$S_i = S_i \left(n_e, T_e \left(\frac{E}{n} \right), T_g, p, n_1, n_2, \dots \right).$$

In general the microphysical derivation of S_i is very difficult. Often many of the quantities influencing the source terms (energy distribution of electrons, various cross sections, rate constants, etc.) are not known, compare Section 9.1.

To bypass the enormous difficulties of complete microscopic kinetics in plasma chemistry a more coarse method was put to the test: macroscopic kinetics (MAK).

This method combines the chemical conversions in nonthermal plasma chemical reactors directly to important operation parameters (e.g., the power input, flow rate, ...) by means of macroscopic determined rate coefficients k_i in the competent reaction equations. By this, the method allows a very compact description of different plasma chemical reactors. For a long time the macroscopic kinetics was a pure phenomenological method, far away from first principles [7–9].

As a first step, the power input P of the reactor acts as the fundamental discharge parameter. Neglecting in a crude approximation the explicit influence of all other species n_1, n_2, \dots on the source term except that of the considered species n_i , one gets: $S_i = S_i(P, n_i)$ [9]. With the ad hoc ansatz

$$G_i = k_{Gi} \cdot P \quad \text{and} \quad L_i = k_{Li} n_i \cdot P$$

the integration of the PFM (4.3) results in the so-called kinetic curve

$$\frac{n_i(z)}{n_{i\infty}} = 1 - \exp\left(\frac{-k_{Li}zP}{v_0}\right) = 1 - \exp\left(\frac{-k_{Li}A \cdot z \cdot \tau_0 P}{V_A}\right), \quad (4.13)$$

where

$n_{i\infty} = k_{Gi}/k_{Li}$ is the “equilibrium concentration” at $P \rightarrow \infty$

A is cross section of the AZ.

The rate coefficients k_i must be determined experimentally as functions of the reactor operating conditions, for example, the gas pressure p . Kinetic curves have proved up to now their suitability for several chemical processes. But they are not a universal mean at all. Only in special cases the so-called specific energy $\tau_0 P/V_A$ (see (4.13)) is a true similarity parameter which determines n_i only in the shown combinations. Therefore, a more general base of MAK named generalized MAK has been developed and validated [1–3,6]. The starting point is a suitable schematic model of the non-thermal plasma chemical reactor. Within this concept the AZ and PZ of the reactor are represented as black boxes with input and output flows of only stable chemical components and with an effective source term for each of these species, representing a mean value. The reactor model adequate to this physical situation is the BMM, discussed previously. Further details can be found in Refs. [1–3]. In particular, it has been shown that chemical quasi-equilibrium states are especially important for this method. These states represent a characteristic phenomenon of the overall behavior of gas discharge reactors and reflects the basic role of gross reactions even for nonthermal plasma chemical conversions, see Section 4.3.

4.5 PLASMA CHEMICAL SIMILARITY

4.5.1 INTRODUCTION

The formulation and application of similarity principles starts with the foundation of modern physics. Today, many physical and process engineering disciplines make use of very efficient similarity methods and scaling laws. On the other hand plasma

chemistry seems to remain rather underdeveloped in this field. Until now, these principles were only considered in special cases. Some examples are mentioned:

- For high-power arc discharges (thermal plasmatrons and torches) detailed investigations on scaling and similarity were performed, but for the most part without satisfactory physical interpretation, see [10].
- Within a macroscopic description (compare Section 4.4) Warburg and his school [7], Becker [8] and Eremin [9] connected the efficiency of chemical reactions in gas discharges with important discharge parameters. Some of these pure empirical considerations include one fundamental point of view: the chemical changes of reactants during the flow through the discharge zone are determined by the power P deposited in the plasma volume V_A and multiplied by the residence time τ of the gas in the reaction zone. These discharge operation parameters are combined to the *specific energy* $\tau_0 P/V_A$ as the decisive quantity, and the mixture composition is then controlled by *kinetic curves* $n_i = n_i(\tau_0 P/V_A)$.
- In the field of glow discharge polymerization (film deposition) often the so-called Yasuda parameter Y is applied which combines the specific energy with the molecular weight of deposited monomers by $Y = W/(F \cdot M)$, where W is the invested electric energy [Ws], F the flow rate [sccm], and M the molecular weight [g/mol] [11,12].
- For various low-pressure nonthermal plasmas and ion beams, the etching rates have been summarized successfully using a similarity presentation [13].

On the other hand, the similarity principles of nonthermal plasmas, for example, of the low-pressure positive column, are mostly restricted to pure electronic similarity [14,15].

4.5.2 SIMILARITY PRINCIPLES

A very general starting point of the similarity analysis is the formulation and preparation of all the equations, relevant to the problem by transformation to dimensionless forms. The central equation for reactors in process engineering is the generalized equation of transport (heat, particles, momentum) given by the following generalized transport equation [16]

$$\frac{\partial \Gamma}{\partial t} + \operatorname{div}(\vec{w}\Gamma) - \operatorname{div}(\delta \operatorname{grad} \Gamma) + \epsilon f \Delta \Gamma - G = 0, \quad (4.14)$$

where

- Γ is the generalized transport quantity (mass, particle densities, energy, heat, etc.)
- $\operatorname{div}(\vec{w}\Gamma)$ the transport by convection and diffusion
- $\operatorname{div}(\delta \operatorname{grad} \Gamma)$ the transport by conduction (e.g., of heat)
- $\epsilon f \Delta \Gamma$ the transport by phase transitions (ϵ is the energy transfer coefficient and f the transfer area/volume)
- G the sources (e.g., effective source terms of particles)

By the systematic dimension analysis of (4.14) *ten dimensionless characteristic numbers* can be derived, beside the Reynolds number, Gay-Lussac number, Froude number, and Peclet number.

4.5.3 PLASMA CHEMICAL SIMILARITY: POSITIVE COLUMN OF GLOW DISCHARGE

The derivation of the relevant similarity parameters here will be demonstrated for the plasma chemistry in the *positive column of a glow discharge model reactor*. In this case the most important version of (4.14) is the particle balance equation of the different chemical species (4.1) written once again in modified manner [17]. For particles of kind i we have

$$\frac{\partial n_i}{\partial t} + \operatorname{div}(\vec{v} \cdot n_i) - \operatorname{div}(D_i \cdot \operatorname{grad}(n_i)) - S_i = 0.$$

The thermal energy balance of the neutral gas requires

$$\frac{\partial (\rho c_p T)}{\partial t} + \operatorname{div}(\vec{v} \rho c_p T) - \operatorname{div}(\lambda_w \cdot \operatorname{grad}(T)) - H = 0 \quad (4.15)$$

and the balance equations of particle numbers and energy of the electrons. The particle balance equation of electrons is given by

$$\frac{\partial n_e}{\partial t} + \operatorname{div}(n_e \vec{v}_e) - S_e = 0 \quad (4.16)$$

with $n_e \vec{v}_e = -\mu_e n_e \vec{E} - \operatorname{grad}(n_e D_e)$ and $\mu_e = \frac{e_0}{m_e} \tau_e$. The energy balance of electrons reads [18]

$$\frac{3}{2} \frac{\partial}{\partial t} (n_e U_e) + \frac{3}{2} \cdot \operatorname{div}(n_e U_e \vec{v}_e^*) + n_e \vec{v}_e \vec{E} + n_e H_e = 0, \quad (4.17)$$

where

$n_{i,e}$ is the particle number density of heavy particles i and electrons e , respectively

\vec{v} the gas flow velocity

\vec{v}_e the drift velocity of electrons (subscript “*” is the corresponding velocity for the flux of energy)

$D_{i,e}$ the diffusion coefficients of heavy particles and electrons, respectively

T the gas temperature

ρ the density

c_p the specific heat

λ_w the heat conductivity

U_e the mean energy of electrons

\vec{E} the electrical field strength

μ_e and τ_e are mobility and mean lifetime of electrons

effective source terms $S_{i,e}$ of heavy particles and electrons, H of heat production,

H_e of electron energy

From the detailed discussion of these equations (in a suitable dimensionless form) concerning the chemical point of view and *restricting on volume reactions* the following general principles of plasma chemical similarity for *homologous* points of two systems of the AZ result [17]

- Similar systems agree in the spatial and temporal distributions of all their components, expressed by identical values of

$$\frac{n_i \left(\frac{\vec{r}}{L_0}, \frac{t}{\tau_0} \right)}{n_0} \quad \text{with} \quad n_0 = \sum n_i \left(\frac{\vec{r}_0}{L_0}, \frac{t_0}{\tau_0} \right), \quad (4.18)$$

τ_0 is the residence time of gas mixture in the Active Zone, L_0 the characteristic length (e.g., of reactor); here subscript “0” are the reference parameters.

- The plasma chemical similarity is described by the correspondence in

$$\frac{n_i}{n_0}, \quad \frac{T}{T_0}, \quad \frac{n_e}{n_{e_0}}, \quad \frac{U_e}{U_{e_0}}, \quad i = 1, 2, \dots . \quad (4.19)$$

The conditions for this correspondence are the following one:

- From outside in chemical similar plasmas two reduced physical fields must be in correspondence

$$\frac{\vec{v} \left(\frac{\vec{r}}{L_0}, \frac{t}{\tau_0} \right)}{v_0}, \quad \frac{\vec{E} \left(\frac{t}{\tau_0} \right)}{E_0}. \quad (4.20)$$

Here, the geometrical similarity is manifested.

- The dimensionless similarity parameters of the problem are:

$$\frac{\tau_0 D_{i_0}}{L_0^2}, \quad \frac{\lambda_{W_0} T_0}{L_0 p_0 v_0} = P_e, \quad \frac{\lambda_{e_0} E_0}{U_{e_0}}, \quad \frac{\mu_{ion}}{\mu_{e_0}} \quad \text{and} \quad \frac{\lambda_{e_0}}{L_0}, \quad \frac{\tau_{e_0}}{\tau_0}, \quad (4.21)$$

P_e is the Peclet Number. Both later ones are a consequence of introducing kinetic reference parameters for the electron gas (subscript “0”).

- For plasma chemical similarity the correspondence of all the reduced source terms

$$\frac{\tau_0 S_i}{n_0}, \quad \frac{\tau_0 H}{p_0}, \quad \frac{\tau_{e_0} S_e}{n_{e_0}}, \quad \frac{\tau_{e_0} H_e}{U_{e_0}} \quad (4.22)$$

is required.

The widely general principle of plasma chemical similarity reflects the underlying electronical similarity of the plasma.

Starting from the Maxwell and Vlasov equations, it can be shown that in a collisionless plasma five independent similarity invariants exist [19]

$$C_1 = \frac{q_i E_i x_i}{m_i v_i^2}, \quad C_2 = \frac{q_i B_i x_i}{m_i c v_i}, \quad C_3 = \frac{m_i f_i v_i^5}{E_i^2}, \quad C_4 = \frac{m_i f_i v_i^5}{B_i^2}, \quad C_5 = \frac{x_i}{v_i t}. \quad (4.23)$$

The invariants C_1 and C_2 are criteria for similarity of particle trajectories in E- and B-fields. C_3 and C_4 are criteria for similarity of self-consistent fields produced by a plasma with distribution function f_i . C_5 is a criterion for similarity of nonstationary processes. Usually, in low-temperature plasmas, the self-consistent magnetic fields are small, therefore C_4 can be ignored. Extending this analysis to collisional plasmas, where the influence of collisions is important for the distribution function of the particles, the Boltzmann kinetic equation is invariant for binary collisions, if another invariant is introduced

$$C_6 = \Sigma_i f_i v_i^3 x_i, \quad (4.24)$$

where Σ_i is the total collisional cross section.

One should note that these similarity considerations include also binary collisions with neutrals and walls [20], but are violated as soon as non-binary processes like three-body recombination get important [21].

In our case (positive column of glow discharge) the so-called B-invariant similarity is relevant [14], which is based on fundamental invariant properties of the Boltzmann equation. Similar nonisothermal plasmas show identical energy distribution functions of electrons. In summary we are coming to the well-known similar conditions: Similarity exists for corresponding values of

$$\frac{E_0}{n_0}, \quad L_0 n_0, \quad \tau_0 n_0, \quad \frac{n_{e_0}}{n_0}, \quad T_0. \quad (4.25)$$

In transferring these principles to plasma chemical reactors some simplifications are necessary and possible. A far-reaching simplification is the restriction to stationarity and spatial homogeneity (e.g., by averaging over space and time). In this way from the energy balance of electrons (4.17) results a very practicable expression to estimate the ionization degree, which is fundamental for the reactor operation

$$\frac{n_e}{n} = \frac{2}{3} \frac{\tau_e n}{e_0 \delta U_e} \frac{P/V_A}{n^2}. \quad (4.26)$$

The mean energy loss of electrons per collision δ for elastic collisions is only $\delta_{el} = 2m_e/M \approx 10^{-4} \dots 10^{-5}$. Many energy losses from inelastic collisions δ_{inel} are one to two orders of magnitude larger than δ_{el} .

4.5.4 APPLICATION TO THE FLOW REACTOR

The subdivision of the reactor into two different zones and their joint action (compare Figure 4.1: AZ, plasma region and PZ, afterglow) is a prerequisite for applying the general principles of plasma chemical similarity to nonthermal flow reactors.

The most important question in reactor similarity is to define such conditions which result in the same spectrum of the reduced output values $x_i = n_i/n$ of the stable reaction products at corresponding input, inclusively identical chemical quasi-equilibria compositions.

The detailed distributions inside the combined reactor are of minor interest in this case. Then the difficulties mentioned can be overcome by restriction to the so-called back mixing model (see Section 4.2.1.2) of the reactor which assumes one-dimensional, steady-state flow (see Figure 4.12). With long enough PZ ($l_p \rightarrow \infty$) only chemical stable species leave the reactor. Within the scope of the one-dimensional back mixing model BMM (compare Section 4.2) the dimensionless balance equations of the stable products of kind i become

$$\begin{aligned} \frac{V_A}{v_0 \cdot A_0} \cdot \frac{\widehat{S}_i}{n} &= \frac{v \cdot A}{v_0 \cdot A_0} \cdot x_i - x_{i_0}, \\ \frac{v \cdot A}{v_0 \cdot A_0} &= \frac{\tau_0}{\tau} = \frac{\sum m_j \cdot x_{j_0}}{\sum m_j \cdot x_j}, \\ V_A \cdot \widehat{S}_i &= \iiint_{V_A} S_{i_A} dV + \lim_{l_p \rightarrow \infty} \iiint_{V_p} S_{i_p} dV \end{aligned} \quad (4.27)$$

with V_A , V_p the volume of the reactor zones, v_0 , v the flow velocities, A_0 , A the cross sections, x_{i_0} , x_i the relative concentrations ($x_i = n_i/n$ and $n = \sum n_j = \text{const.}$) and x_{i_0} the input values.

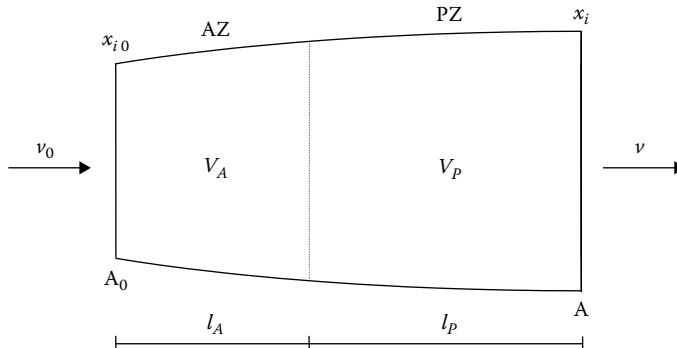


FIGURE 4.12 Schematic model for nonisothermal reactors under flow conditions.

The term \widehat{S}_i stands for an averaged effective and summed source rate (regarding particle gain and loss and the combination of AZ and PZ). The local rates S_{i_A} and S_{i_p} contain the well-known expressions for gain and loss by collisions, for example: $k_{ij}n_i n_j$.

Considering real plasma chemical conversions the microphysical analysis of \widehat{S}_i generally includes an overwhelming number of different species and reactions. For constant reactor cross section one gets from (4.27)

$$\frac{\tau_0 \cdot \widehat{S}_i}{n} = \frac{\sum m_j \cdot x_{j_0}}{\sum m_j \cdot x_j} \cdot x_{i_p} - x_{i_0},$$

$$\tau_0 = \tau_A = \frac{V_A}{v_0 \cdot A},$$

$$\tau_0 \cdot \widehat{S}_i = \tau_0 \cdot S_{i_A} + \lim_{l_p \rightarrow \infty} (\tau_p \cdot S_{i_p}).$$
(4.28)

According to (4.28) the condition for plasma chemical similarity can be formulated now:

Two reactors are plasma chemically similar (i.e., equal input values x_{i_0} result in equal output values of the passive zone x_{i_p}) if the reduced summed effective source terms $\tau_0 \widehat{S}_i / n$ are equal.

4.5.4.1 The Reactor Parameter R

Within the microscopic picture the detailed analysis of the different source terms is extremely expensive. The *analysis of various kinetic models* showed that the output values are given by five determining variables

$$T_g, \quad T_e, \quad n, \quad \tau_0, \quad \text{and} \quad x_e$$

which however appear in two combinations only (compare Section 4.2, basic ozone mechanism)

$$k_i(T_e) n \tau_0 x_e \quad \text{and} \quad k_j(T_g) n \tau_0.$$

With high precision the first one alone $n \tau_0 x_e = n_e \tau_0$ was sufficient for the representation of the output values. It is the direct consequence of the *combined action* of the AZ and PZ. For same temperatures T_g and T_e the combinations $n \tau_0 x_e$ and $n \tau_0$ are retained. Here, very surprisingly the first one alone $n \tau_0 x_e = n_e \tau_0$ was sufficient for the representation of the output values with high precision. General similarity rules for an AZ can be drastically changed by the tandem connection of a PZ. Here, the unique characteristic value for plasma chemical similarity is $\tau_0 n_e$ and $\tau_0 \cdot \widehat{S}_i / n = f(\tau_0 n_e)$. Because the electron concentration n_e is an inherent plasma parameter of the active zone and not given immediately, it would be very desirable to derive a connection to

the operating parameters of the reactor. This is possible via (4.26). Introducing the pressure $p = nkT$, one obtains

$$\tau_0 n_e = \varepsilon \frac{\tau_0 P}{p V_A} \quad \text{and} \quad \varepsilon = \frac{2}{3} \frac{\tau_e n}{\delta} \frac{kT}{e_0 U_e}. \quad (4.29)$$

Obviously, the main similarity quantity $\tau_0 n_e$ is determined by a new basic dimensionless reactor parameter R , which contains the former specific energy

$$R = \frac{\tau_0 P}{p V_A} = \frac{\tau_0 P}{(V_A n k T_g)} = \frac{W/N}{k T_g}, \quad (4.30)$$

where

W is the input of energy

N the number of particles

Regarding the physical meaning of this parameter, one sees:

R represents the energy invested per particle of the gas mixture during the flow through the active reactor zone in relation to the thermal energy $k T_g$.

The factor of proportionality ε in (4.29) is a true constant for constant gas and electron temperature. Of course, to guarantee corresponding values of T_g and U_e , extra conditions must be fulfilled, as already mentioned. But under some restrictions of the operation of nonisothermal plasma chemical reactor variations of T_g and U_e remain small and $\varepsilon \approx \text{const}$ is a tolerable approximation. The most important of these restrictions are sufficient high gas pressure and sufficient low Joule heating of the gas. The latter means nearly constant reduced field strength E/n and U_e (or T_e), respectively.

At small $R \rightarrow 0$ the reduced summed effective source terms are proportional to R , (i.e., $\tau_0 \hat{S}_i / n \sim R$), for created species with $\tau_0 n_e \sim R$. Large $R \rightarrow \infty$ results in $\tau_0 \hat{S}_i / n \rightarrow \text{const}$. and then the quasi-equilibrium states are reached and can be interpreted as the result of an electronically modified mass action law, which describes a complex chemical situation by a reversible gross reaction.

4.5.5 EXPERIMENTAL PROOF

To prove in a systematic manner the applicability of the dimensionless reactor parameter R , the separate variations of all the four quantities which are of influence should be analyzed with regard to changes of the output values $x_i = n_i / n$ at equal input. According to the analysis given, only such plasmas should be included, which show nearly equal gas and electron temperatures. The energy distribution function of electrons, neglecting Coulomb interaction, is mainly determined by the reduced electric field strength E/n . Therefore we have to look on such plasma conditions which do not differ too much in E/n .

As an example the similarity representation of measurements using geometrical similar positive columns as the active zone of a flow reactor is given [17]. Figure 4.13 shows the experimental arrangement.

The transition of E/n into a constant value at higher pressures is shown in Figure 4.14 for CO_2 discharges. It is a rather general experience that the value of E/n in electrical discharges controlled by bulk processes depends only weakly on current and pressure. In chemically active plasmas with many channels for generation and

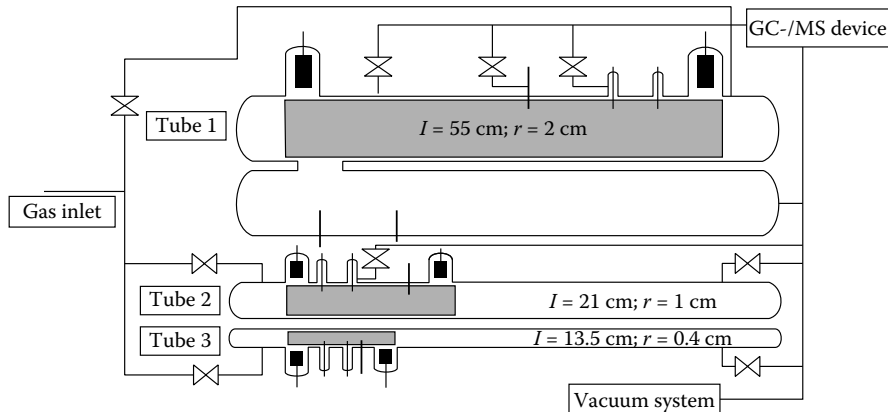


FIGURE 4.13 Schematic diagram of the positive column flow reactor with geometrical similar discharge tubes.

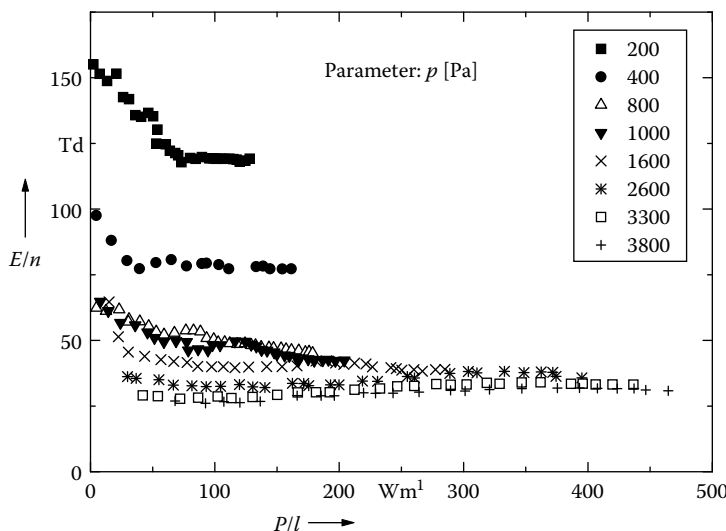


FIGURE 4.14 Reduced field strength E/n in the positive column of CO_2 discharges ($r = 0.4 \text{ cm}$).

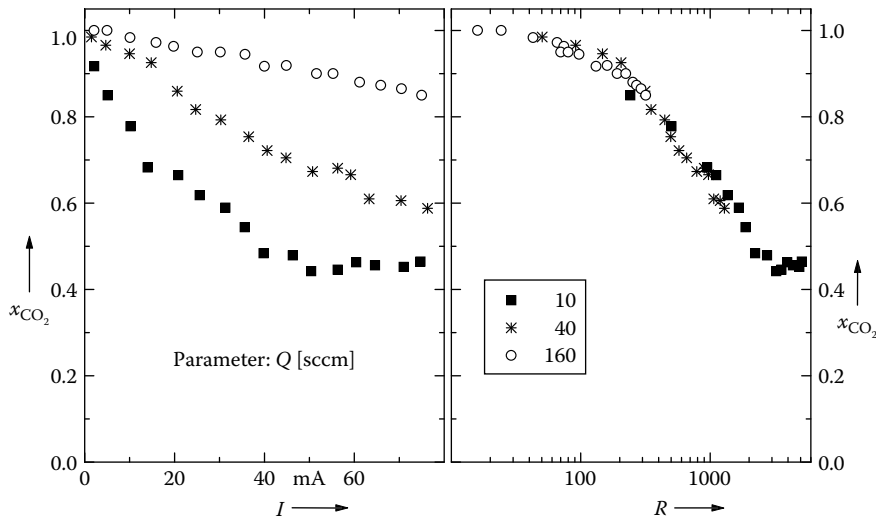


FIGURE 4.15 Dependence of the relative CO_2 concentration on the discharge current I and the reactor parameter R (tube 2 of Figure 4.13), $p = 1600 \text{ Pa}$.

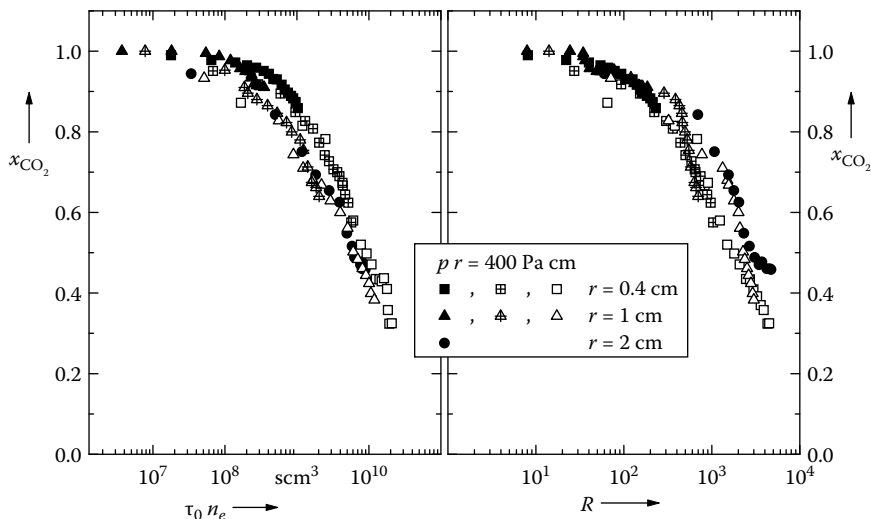


FIGURE 4.16 Dependence of the relative CO_2 concentration on $\tau_0 n_e$ and R at different values of τ_0 (tubes 1, 2, 3 of Figure 4.13).

loss of charge carriers the approximation $E/n \approx \text{const}$ should be useful in rather extended regions of the operation parameters.

The analysis of the chemical conversions was realized by gas chromatographic technique (detection of CO_2 , CO , and O_2). Figures 4.15 and 4.16 summarize some results for the decomposition of CO_2 . There is a clear compression of different

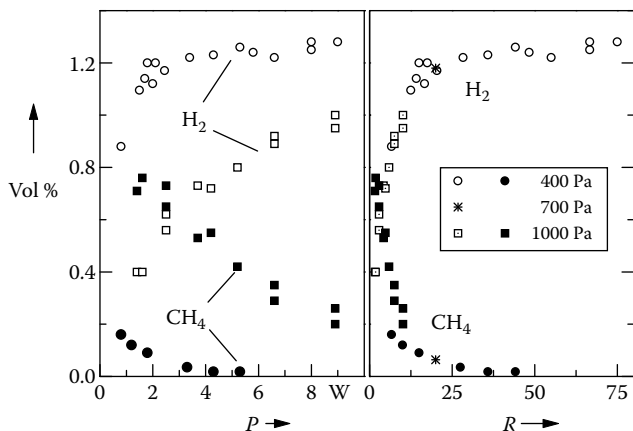


FIGURE 4.17 Measured concentrations of CH_4 and H_2 in dependence on the power input and on the reactor parameter R .

experimental data to one curve by using the similarity quantity $\tau_0 n_e$ or the reactor parameter R .

Experimental results on the chemical conversion of CH_4 in a microwave discharge ($f = 2\,330 - 2\,350$ MHz) in flowing Ar + 1% CH_4 mixtures, presented in Ref. [18], have been analyzed, too. The experiments were performed for different power, pressure and residence time. The volume of the active reactor zone remained constant ($V_A = 12 \text{ cm}^3$). Figure 4.17 shows the decomposition of CH_4 and the simultaneous generation of H_2 with increasing deposition of power as well as the obviously fusion of these different curves by introducing the reactor parameter R .

5 Elementary Processes on Surfaces in Plasma–Wall Interaction

CONTENTS

5.1	Adsorption and Desorption	164
5.2	Sticking Coefficients and Surface Loss Probabilities	165
5.3	Surface Coverage, Residence Time, and Adsorption Isotherms	167
5.4	Surface Diffusion	169
5.5	Energy Accommodation	169
5.6	Chemical Surface Reactions	170
5.7	Ion Bombardment in Plasma Processing	176
5.8	Particle Balance at Surfaces	178
5.9	Energy Balance at Surfaces	181

Plasma–surface interaction is one of the fastest growing branches in plasma physics and has got an important issue in the field of applied surface science. Its basic question includes the mastering of an old problem: the contact of different states of matter. The investigation and application of plasma–surface interaction plays an essential role in low-temperature plasma processing as etching, deposition, or modification of surfaces as well as in fusion research.

The characterization of plasmas in contact with solid surfaces is incomparably more complicated than that of unbounded plasmas. It requires the consideration of marked anisotropies and inhomogeneities, deviations from quasi-neutrality, exchange of energy and matter between plasma and solid, and may result in strongly non-linear equations containing many unknown quantities. The aim of understanding plasma–surface interaction is preferably an extensive description of the parameters that characterize the plasma and the solid surface (substrate) by taking into consideration particle and energy balances of the involved species. For example, the complex processes during etching or deposition of thin surface layers can be described via macroscopic rate equations depending on experimental conditions being realized in the plasma reactor. Typical experimental process parameters are gas mixture, gas flow, pressure, discharge power and frequency, reactor geometry, temperature, etc. On the other hand, the overall rates involve a variety of elementary processes, which have to be described by suitable models on a microphysical scale.

Elementary processes in plasmas—in particular during the interaction with surfaces—are rather complex. An experimental distinction of single phases of the

involved mechanisms is difficult. Depending on the impinging particle fluxes from the gas/plasma phase, on the energy distribution of the incoming species, and on the thermal conditions as well as on the electrical potentials in front of the substrate surface, different mechanisms are dominating. For example, in case of physical sputtering (PS) one has to investigate mainly interactions between directed, energetic ions and solids. Even in this case, an exact description is quite difficult, but it becomes nearly impossible for surface film reactions that proceed via intermediate molecular states. Examples for such processes are ion beam assisted etching (IBAE), plasma-enhanced chemical vapor deposition (PECVD), and plasma polymerization (PP). The mentioned intermediate states may include adsorption, surface diffusion, activation, chemical reaction, and desorption of different species.

5.1 ADSORPTION AND DESORPTION

Particles originating from the gas/plasma phase, which collide with a solid surface, can undergo several interactions [1]. They can be simply reflected from the surface or they can be adsorbed by forming a (weak) bond to the surface. After adsorption, the particles may diffuse along the surface or into the solid (bulk diffusion). Furthermore, they can react during their residence time at the surface with other adsorbed species or with surface atoms of the solid in order to form product molecules. Finally, depending on the binding energy of the particles, they may either desorb back into the gas phase or stick by forming a growing film.

A particle originating from the plasma may lose sufficient energy upon impact at the surface to be trapped in a binding potential in front of the surface: A new bond is formed. Two classes of bonds can be distinguished: physisorption and chemisorption.

In the case of physisorption, bonds are mediated by electrostatic forces as dipole–dipole interaction or dispersion forces, respectively. The released adsorption heat is in the order of $E_{ads} < 0.5 \text{ eV}$. Typical examples for physisorption are the adsorption of noble gases on metals at very low temperatures by van der Waals interaction (example Ar on Zr: $E_{ads} = 0.24 \text{ eV} \sim -25 \text{ kJ/mol}$) or the adsorption of nitrogen molecules on most surfaces. The induced dipole–dipole interaction may be calculated, for example, by the Lenard–Jones potential or by the image force for metallic (e.g., very conductive) substrates.

In the case of chemisorption, bindings are caused by valence forces of the exchanging electronic orbitals of adsorbed particles and substrate atoms. The adsorbed particles form a stronger chemical bond to the surface ($E_{ads} > 0.5 \text{ eV}$) as, for example, CO on metals (example CO on Pd: $E_{ads} = 1.43 \text{ eV}$ to -147 kJ/mol) or oxygen on most surfaces. The incoming molecules might break apart upon impact and the dissociation products are chemisorbed separately. This process of dissociative chemisorption occurs, for example, during passivation of metals or silicon by hydrogen molecules.

The potential curve for adsorption above a real substrate surface consists usually of a physisorbed precursor and a chemisorbed state. A qualitative potential diagram for the adsorption of a diatomic molecule A_2 is shown in Figure 5.1.

One can distinguish two potential curves above the surface for the molecule A_2 (a) and for the atom A (b), respectively. The difference in the potential energies for

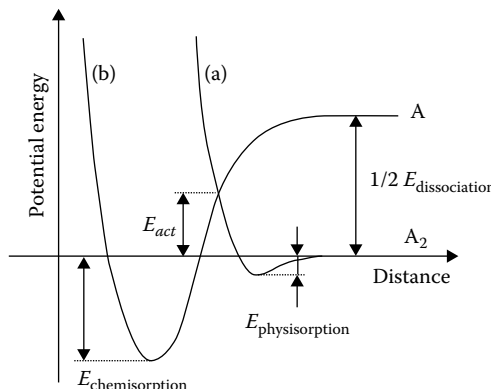


FIGURE 5.1 1D potential energy diagram showing a possible transition from molecular physisorption to dissociative chemisorption. Potential curves are presented for the molecule (a) and the atom (b).

A and A_2 at large distances from the surface corresponds to one half of the dissociation energy $E_{\text{dissociation}}$ of molecule A_2 . The adsorption of the molecule A_2 can be described as follows: A_2 approaches the surface at the vacuum level. Upon collision with the surface atom, it transfers kinetic energy to the solid and reduces thereby its potential energy becoming trapped into the physisorbed state with binding energy $E_{\text{physisorption}}$. If the crossover of the potential curve for A (b) with the potential curve for A_2 (a) is below the vacuum level, the molecule A_2 can directly dissociate and arrive into the chemisorbed state with binding energy $E_{\text{chemisorption}}$ as two atoms A. This mechanism is called dissociative chemisorption. If the crossover is above the vacuum level, as illustrated in Figure 5.1, the molecule A_2 can only chemisorb if it overcomes an activation barrier E_{act} . This may occur at higher substrate temperature via thermal activation or if the kinetic energy of the impinging molecule A_2 is sufficiently high.

Finally, the desorption of a particle from adsorption potential can be regarded as an excited or activated process again, which is described by an Arrhenius-like rate. In many cases, the thermal energy at room temperature is sufficient for the desorption of a physisorbed molecule back into the gas phase via thermal activation. As a consequence, the sticking coefficient for chemisorption of molecules at room temperature is often very small.

5.2 STICKING COEFFICIENTS AND SURFACE LOSS PROBABILITIES

Adsorption processes can be quantified using macroscopic parameters such as sticking coefficients and surface loss probabilities. The sticking coefficient γ describes the probability of an incoming particle to be trapped in a potential above the surface [2], for example, the rates of desorption and adsorption just differ by the sticking coefficient.

The sticking coefficient depends on various quantities of the gas/plasma–surface system, for example, the sticking probability decreases as the surface coverage

increases. However, the initial sticking coefficient also (e.g., at zero coverage) is affected by several surface properties:

1. With increasing depth of the potential well, the coefficient increases due to the trapping potential. For example, the initial sticking coefficient of N_2 on various faces of tungsten crystal differs remarkably from $\gamma = 0.1$ for (111) to $\gamma = 0.6$ for (100).
2. The coefficient decreases with increasing energy of incoming particles, since the kinetic energy has to be accommodated by the surface collision.
3. For large mass differences of the colliding partners (e.g., gas/plasma particles and substrate atoms), the sticking coefficients are small due to the low coupling of the incoming particle to the phonon spectrum of the solid.
4. It decreases with increasing substrate temperature due to the increasing velocity of the substrate atoms.

The surface loss probability β describes the loss of a particle upon impact, which includes sticking at the surface, but also surface reactions in which a reactive particle recombines at the surface to form a nonreactive volatile compound (example $\text{SiH}_3 + \text{H}_{\text{surface}} \longrightarrow \text{SiH}_4$). In many plasma experiments, as described in the following text, only the surface loss probability can be measured. The direct measurement of the sticking coefficient requires absolutely quantified sources of the species of interest, which is difficult to realize for the mixed conditions in plasmas. The distinction between the sticking coefficient and surface loss probabilities is often overlooked in the literature.

The rate of adsorption R_{ads} of a species A on a surface B is determined by the particle flux j_A , the sticking coefficient γ_A of A on B , and the state of the surface $f(\Theta)$:

$$R_{ads} = \frac{dn_{ads}}{dt} = \gamma_A j_A f(\Theta). \quad (5.1)$$

The sticking coefficient is dominated by the ability of the incoming species to transfer sufficient kinetic energy to the surface atoms to be trapped in the potential well. This transferred energy is then dissipated by the atom of the solid via phonon excitation. The energy being transferred from the impinging species to the surface atom can be roughly estimated on the basis of energy and momentum conservation in the binary collisions approximation. The maximum transferable energy T_{max} yields

$$T_{max} = E_0 \frac{4m_1 m_2}{(m_1 + m_2)^2}. \quad (5.2)$$

E_0 denotes the kinetic energy of the incoming species upon collision with the surface atom, m_1 the mass of the projectile, and m_2 the mass of the target atom. Equation 5.2 shows that for a light projectile impinging on a heavy target, the transferred energy is small. Thereby, the incoming species may be unable to lose sufficient kinetic energy to become chemisorbed, which leads to a small sticking coefficient. A typical

example is the low-sticking coefficient for the adsorption of atomic hydrogen on many materials. This is one reason for the long residence time of hydrogen in a plasma reactor volume.

The exact nature of a chemisorption process and the sticking coefficient depending on quantities such as impact angle and kinetic energy of the striking particle is usually identified by molecular dynamics.

5.3 SURFACE COVERAGE, RESIDENCE TIME, AND ADSORPTION ISOTHERMS

Any adsorption process depends on the actual state of the surface with respect to the identity of the topmost atom or the vibrational excitation of the solid. The surface structure can be characterized by the so-called degree of coverage, $\Theta = n_{ads}/n_0$, which represents the ratio of the surface density of adsorbed particles (n_{ads}) to the total density of available surface sites (n_0).

In general, the coverage is a function $f(\Theta)$ of surface morphology, vacant sites, etc. In the most simple case of physisorption, the function $f(\Theta)$ reflects the fraction of vacant sites, that is., $f(\Theta) = 1 - \Theta$.

Adsorption might also occur by a multistep process, where an incident species is first adsorbed in the physisorption well or, more general, into a weakly adsorbed state. In this surface state, it might be able diffuse along the surface and find an open bond (dangling bond) at the surface at which it chemisorbs. On the other hand, it can return into the gas phase via thermal desorption.

The residence time t in the weakly adsorbed state is described by the Frenkel equation [3]:

$$t = t_0 \exp\left(-\frac{E_{act}}{k_B T_S}\right). \quad (5.3)$$

Here, t_0 describes the smallest possible residence time in the weakly adsorbed state and corresponds to the inverse of the vibrational frequency of the surface bond, which is of the order of 10^{-12} – 10^{-13} s. E_{act} is the activation energy for thermal desorption, k_B is the Boltzmann constant, and T_S is the substrate temperature. The density of weakly adsorbed species n_{ads} can be expressed by rate equations, yielding

$$\frac{dn_{ads}}{dt} = j\sigma_{ads}n_0(1 - \Theta) - n_0\frac{\Theta}{t}. \quad (5.4)$$

The growth precursors with a flux j adsorb into the weakly adsorbed state at an empty site with a cross section σ_{ads} . The total number of surface sites is n_0 . The coverage in the weakly adsorbed state corresponds to $\Theta = n_{ads}/n_0$. The term $n_0\Theta/t_0$ defines the temperature-dependent desorption rate of weakly adsorbed species.

The adsorbed particles may leave the surface after a certain residence time τ_{des} , which is a statistical quantity. The activation energy of desorption E_{des} is delivered by the lattice in case of thermal desorption or by collisions with energetic particles as is the case in collisional desorption. In the steady state, there is a balance between

the elementary processes of adsorption (R_{ads}) and desorption (R_{des}). Solutions of the adsorption–desorption equilibrium result in adsorption isotherms that reflect the coverage–pressure dependence at a constant substrate temperature. In the most simple case, where every surface site is equivalent and only single monolayer adsorption occurs without any adsorbate–adsorbate interactions, one obtains, similar to (5.4), the following rate equation:

$$\frac{dn_{ads}}{dt} = R_{ads} + R_{des} = \gamma_A j_A (1 - \Theta) - \frac{n_{ads}}{t_{des}} = 0. \quad (5.5)$$

In this simple case, one gets the so-called Langmuir isotherm:

$$\Theta = \frac{n_{ads}}{n_0} = \left(1 + \frac{n_0}{\gamma_A j_A t_{des}} \right)^{-1}. \quad (5.6)$$

Since the balance depends essentially on the substrate temperature, Figure 5.2 shows corresponding Langmuir isobars $\Theta = \Theta(T_s)$ as functions of temperature for different process pressures and gases.

On the other hand, the adsorbed precursors can be transformed into the chemisorbed state with a time constant $t_{chemisorption}$. The growth rate therefore yields

$$\text{Growth rate} = \frac{n_0 \Theta}{t_{chemisorption}} \quad (5.7)$$

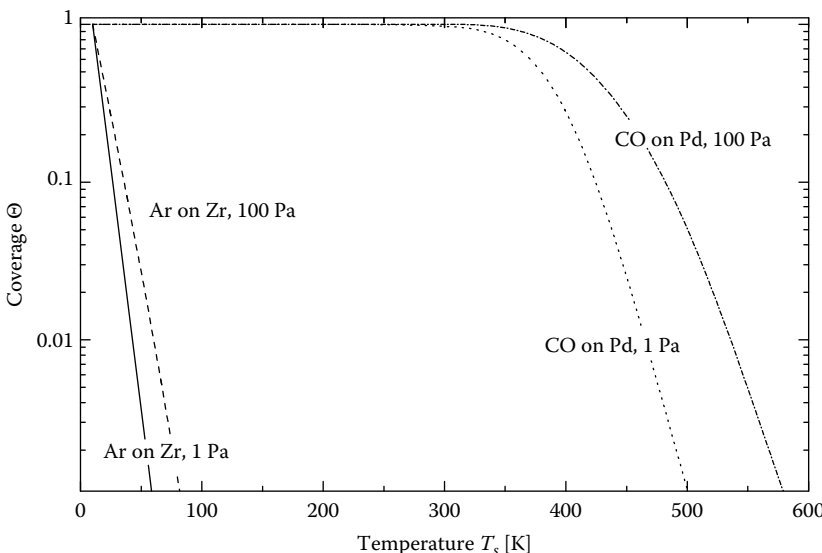


FIGURE 5.2 The initial coverage of Ar on Zr ($E_{des} = 0.24$ eV) and CO on Pd ($E_{des} = 1.43$ eV) in dependence on the surface temperature. The surface density is assumed to be $n_0 = 6 \times 10^{14} \text{ cm}^{-2}$. The initial sticking coefficient is assumed to be unity and the incoming particle flux j_A corresponds to the gas pressure (1 and 100 Pa, respectively).

and (5.4) modifies to

$$\frac{dn_{ads}}{dt} = j\sigma_{ads}n_0(1 - \Theta) - \frac{n_0\Theta}{t} - \frac{n_0\Theta}{t_{chemisorption}}. \quad (5.8)$$

This model yields a temperature-dependent chemisorption rate: If the substrate temperature increases, the rate of thermal desorption from the weakly adsorbed state increases (see (5.4) and (5.5)) leading to a decrease of Θ . Consequently, the growth rate decreases, because it is directly proportional to the coverage in the weakly adsorbed state. This is typical for epitaxial growth of crystalline silicon [4]. The growth precursors adsorb on terraces on the surface and diffuse to surface steps, where they are trapped, promoting film growth. At high surface temperatures, the thermal desorption becomes too fast compared with the time the precursors need to reach the chemisorption sites at the steps via surface diffusion. In consequence, the growth rate decreases with increasing substrate temperature. Additional surface reactions, like etching of the growing film as well as etching of the weakly adsorbed state, can be described as in (5.6).

5.4 SURFACE DIFFUSION

Impinging species, adsorbing into a weakly adsorbed state, may not be able to thermalize with the surface upon impact, but diffuse on the surface as *hot precursors* [5]. This has several consequences for the interpretation of the macroscopic growth rate. The surface diffusion in the *hot precursor* state can be incorporated into the chemisorption model. A typical example for adsorption via a *precursor state* is the adsorption of atomic hydrogen on hydrogen-terminated silicon surfaces [6–9].

The migration of atoms or molecules along the surface is one of the most important elementary steps of gas–surface interaction, reactive or nonreactive. The main reason for surface diffusion is the crystal structure and chemical composition of the substrate. Depending on the structure of the crystal face, diffusion coefficients may vary by orders of magnitude. Diffusion rates parallel to steps are greater than diffusion rates perpendicular to them. Both diffusion along the surface and diffusion into the near-surface layers of the solid are possible. In the latter case, one speaks of absorption or bulk diffusion.

5.5 ENERGY ACCOMMODATION

Plasma particles striking the solid surface exhibit a wide energy spectrum. In addition to low-energetic neutrals (atoms, molecules, radicals), there also exist particles with higher energy ($E \gg 1$ eV) that can be distributed on the different excitation modes.

If the energy of an incoming particle is too high for entering an adsorption process, or if the energy is too small for sputtering or implantation, respectively, or if it finds no suitable surface site, the particle will simply be reflected at the surface. Due to the energy transfer at such elastic scattering the substrate is heated until a thermal

equilibrium between gas phase (plasma) and solid surface is reached. A characteristic quantity for the energy exchange is the accommodation coefficient α :

$$\alpha = \frac{E_{in} - E_f}{E_{in} - E_S}, \quad (5.9)$$

where

E_{in} is the energy of the incident particle

E_f marks the energy of the scattered particle

$E_S = k_B T_S$ the thermal energy of the surface [1]

Scattering experiments of inert gases from a graphite surface have shown that especially for hot surfaces the energy transfer is incomplete.

For diatomic or polyatomic molecules, in addition to changes of kinetic energy (translation), the transfer involves de-excitation or excitation of vibrational and rotational modes during collision with the surface.

5.6 CHEMICAL SURFACE REACTIONS

Reactive species, impinging onto a surface, can react at the surface to form new species, which desorb. Two phenomenological types of reactions can be distinguished: the Eley–Rideal process and the Langmuir–Hinshelwood process [10,11].

In an *Eley–Rideal* reaction, incoming species A from the gas phase do not thermally equilibrate upon adsorption at the surface, but they react directly with a surface atom B to form a new product molecule AB , which desorbs. The occurrence of an Eley–Rideal mechanism can be identified by several criteria:

1. The reaction obeys first-order kinetics since it is directly proportional to the flux of incoming species A .
2. The impinging species are not in thermal equilibrium with the surface, which leads to hyperthermal kinetic energy of the desorbing products AB .
3. Eley–Rideal-type mechanisms have often a small cross section, since the incoming species have to directly break a chemical bond at the surface to form a volatile product on the time scale of a molecular vibration ($\sim 10^{-12}\text{--}10^{-13}$ s). In addition, this process can also be sterically hindered, resulting in a small cross section for this reaction.
4. The reaction rate changes when using isotopes of the reactants A or B .

The rate of an Eley–Rideal reaction with cross section σ_{reaction} for the interaction of impinging species A with flux j_A with adsorbed species B with a coverage Θ_B can be written as

$$\text{Reaction rate} \sim j_A \Theta_B n_0 \sigma_{\text{reaction}}. \quad (5.10)$$

An example for this type of reaction is the abstraction of hydrogen due to incoming atomic hydrogen from amorphous hydrogenated carbon film surfaces [12]. The cross section is 0.05 \AA^2 , which can be compared to the typical area of a surface site of $\sim 1 \text{ \AA}^2$,

yielding a reaction probability of 0.05 for H abstraction by atomic hydrogen from hydrocarbon film surfaces.

Since a reaction of Eley–Rideal type proceeds directly, the products are not in thermal equilibrium and, hence, the desorbed particles are hyperthermal. The cross sections of such reactions are rather small, because the interaction time of the direct reactions is quite small. The reaction rate scales proportionally with the coverage until a complete surface coverage is reached.

An incoming species *A* can also adsorb at the surface and thermalize prior to reacting with another adsorbed species *B* to form the molecule *AB*, which desorbs. This is called a *Langmuir–Hinshelwood-type* reaction. The occurrence of such a reaction is indicated by several criteria:

1. The reaction obeys second-order kinetics and is proportional to the coverage of species *A* and *B*.
2. The incoming species *A* thermalize at the surface, which leads to a kinetic energy of the desorbing molecules *AB* corresponding to the substrate temperature.
3. The cross section for this reaction is large, since both species *A* and *B* react in their adsorbed states, leading to a much longer interaction time compared to an Eley–Rideal-type reaction.
4. The reaction rate is insensitive on the used isotopes for reactants *A* and *B*, since the species react in thermal equilibrium with the surface and any initial momentum of reactant *A* is lost during its thermalization with the surface.

The rate of a Langmuir–Hinshelwood reaction with cross section σ_{reaction} of impinging species *A* leading to a coverage Θ_A with adsorbed species *B* with a coverage Θ_B at a surface with a total number of adsorption sites n_0 can be written as

$$\text{Reaction rate} \sim \Theta_A \Theta_B n_0^2 \sigma_{\text{reaction}}. \quad (5.11)$$

In summary, the reaction rate for the adsorption of growth precursors on surfaces can be estimated on the basis of the following:

1. Neutral, stable precursors have to overcome in many cases an activation barrier to transfer from the physisorbed into the chemisorbed state. Often, this activation barrier cannot be overcome by thermal activation at room temperature. However, since the potential well of the physisorbed state is shallow compared to the thermal energy at typical substrate temperatures (\sim room temperature), the adsorbed precursor desorbs thermally activated. As a result, stable neutral precursors are mainly reflected and their sticking coefficient is usually small.
2. Radicalic growth precursors have high potential energy at large distances above the surface, corresponding to the half of the dissociation energy, necessary for the formation of the radical. Upon approaching the surface, the radical converts its potential energy into kinetic energy, which has to be released via energy transfer to the atoms of the solid upon impact, in order

to become trapped in the chemisorbed state. This energy transfer depends on the masses of the solid target atoms and the impinging species: A heavy incoming particle can transfer more energy to a target atom compared to a light incoming particle. As a result, the sticking coefficient increases with the mass of the incoming radical.

3. The cross section for the direct reaction of an incoming radical with an adsorbed surface atom is usually small and depends on the type of isotope for the reactants. The cross section for the reaction of an incoming particle that adsorbs and thermalizes prior to reacting with another adsorbed particle is in general much larger. The energy distribution of the desorbing species is correlated to the kinetic energy of the incoming species plus the reaction enthalpy in the first case and correlated to the surface temperature in the latter.

These guidelines can only represent a *rule of thumb* for the estimation of sticking coefficients. In many systems not all of these criteria are fulfilled, since the probability for adsorption depends in detail on the multidimensional potential hypersurface above the surface as well as on the angle and energy distribution of the impinging species.

Sticking coefficients can be measured in a dosing experiment: A surface is exposed to a gas/plasma at a constant pressure, resulting in a constant surface collision rate. The dose is measured in Langmuir, which corresponds to the number of particles impinging onto a surface at a pressure of 10^{-6} mbar in 1 s. If the sticking coefficient would be unity, approximately one monolayer ($\sim 10^{15}$ surface atoms cm^{-2}) would be deposited at a dose of 1 Langmuir. After dosing of the surface, the resulting surface coverage of the adsorbate is measured via thermal desorption spectroscopy or other surface analysis techniques. From a modeling of the coverage in dependence on the dose, the sticking coefficient can be deduced.

The sticking coefficient can also be measured by modulated beam experiments. A particle beam source is used, striking a surface under ultrahigh vacuum conditions, and the reflected species are monitored via mass spectrometry. A modulation of the particle beam or the entrance of the mass spectrometer is necessary to separate the signals of the background gas from the signals of the directed beam component. In these experiments, the velocity distribution of the reflected particles can also be measured using time of flight methods. These types of measurements have been successfully used for the investigation of surface reactions of radicals like fluor on silicon surfaces [13]. For many growth processes, however, the dominant precursors are larger molecules, such as CH_x or SiH_x radicals for the growth of a-C:H or a-Si:H films. A particle beam source for these radicals is difficult to implement, and, therefore, only little experimental data exist on surface reactions of these growth precursors.

Since it is difficult to measure the sticking coefficients for typical growth precursors directly, the surface loss probabilities are often measured instead, using low-temperature plasmas as particle source [14–19]. The surface loss probability corresponds to the sticking coefficient plus the probability for an incoming species to react at the surface to form a volatile nonreactive product. This surface loss probability β has been investigated in methane and silane discharges, by the

measurement of the decay of CH_3 and SiH_3 , radicals respectively, in the plasma afterglow by ionization threshold mass spectrometry. In a pulsed plasma, the decay time of the density of reactive species after switching off the discharge depends on the efficiency of the chamber walls to act as a sink for these species:

1. If the surface loss probability is large, the species do not survive many wall collisions, leading to a decay time in the order of the travel time for the reactive species from the position of their formation in the plasma to the vessel walls.
2. If the surface loss probability is small, the species survive many wall collisions and the decay time is governed by the pumping speed of the plasma vessel.

A simple modeling of this decay yields $\beta = 10^{-3}$ for CH_3 and $\beta = 0.25$ for SiH_3 [20].

The surface loss probability can also be measured by depositing films inside a cavity, which is exposed to a discharge [14–19]. Growth precursors, emanating from the discharge, enter this cavity via a slit or a hole and build up a layer inside. From the analysis of the layer thickness profile, the surface loss probability can be determined. If the surface loss probability is high, films are only deposited in close proximity to the entrance of the cavity, since the species cannot survive many wall collisions. If the surface loss probability is small, the species will survive many wall collisions and the deposition profile inside the cavity becomes uniform. The variation of the film thickness inside the cavity can be modeled by Monte Carlo simulations, which follow the reflections of incoming growth precursors among the walls inside the cavity. Typical results for a cavity with a slit as entrance geometry are shown in Figure 5.3 for $\beta = 0.9$ and $\beta = 0.1$.

It can be seen that for high β (see Figure 5.3a), deposition is observed predominantly on the opposite side of the entrance slit, corresponding to the position of the first wall collision for incoming species. For small β (see Figure 5.3b), a uniform deposition is observed on all walls inside the cavity.

If the absolute flux of growth precursors to the surface is known, the sticking coefficient can be calculated from the absolute film thickness. Or, on the other hand, if the probability of forming a nonreactive volatile product is known, the sticking coefficient can directly be deduced from the surface loss probability.

As an example for the application of this technique, the deposition inside a cavity exposed to a hydrocarbon discharge is discussed in Refs. [14,15]. The comparison with the theoretical model yields for the deposition profile in a methane discharge $\beta = 0.65 \pm 0.15$ and in an acetylene discharge $\beta = 0.92 \pm 0.05$. In a methane discharge, the dominant contribution in the radical flux toward the surface consists of CH_3 radicals [21]. However, as mentioned earlier, the surface loss probability for CH_3 radicals is of the order of 10^{-3} . Thereby, the neutral growth precursor responsible for film formation inside the cavity in the methane discharge cannot be the CH_3 radical. In an acetylene discharge, the dominant radical should be the C_2H radical. Therefore, one assumes that the surface loss probability of $\beta = 0.92$ corresponds to the surface reaction of C_2H . In a methane discharge, however, larger hydrocarbon molecules

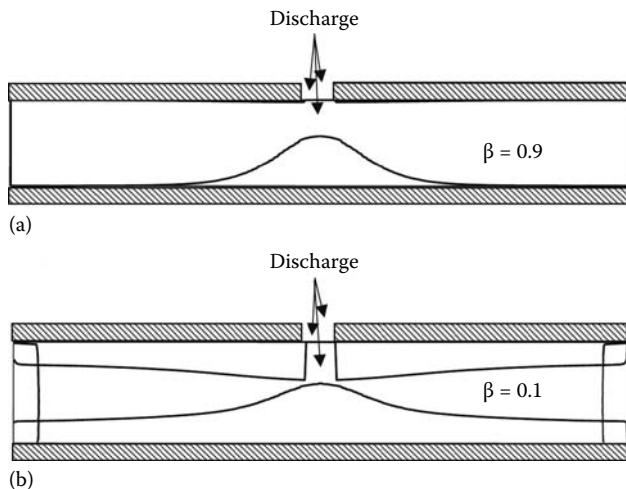


FIGURE 5.3 Modeling of film deposition inside a rectangular cavity with a surface reaction probability (a) $\beta = 0.9$ and (b) $\beta = 0.1$. Species from the discharge enter the cavity via a slit and result in deposition at different positions of the cavity.

are formed in the gas phase via molecule–molecule or ion–molecule reactions as identified by mass spectrometry [22]. These C_2H_x species in the methane discharge can efficiently contribute to growth, which is able to explain the high β value of 0.65 as measured in the experiment.

Example 5.1: Deposition of a-Si:H films

Amorphous hydrogenated silicon films (a-Si:H) are used in electronic applications for photovoltaics or flat panel displays [23,24]. These applications require a low defect density of the material. This is achieved by the incorporation of hydrogen in the growing film that saturates efficiently open bonds in the material. Any ion bombardment would deteriorate the film quality, since the displacement of silicon or hydrogen atoms in the growing film leads to open bonds, which act as recombination centers for electron transport in the final device. a-Si:H films are, therefore, usually deposited on the grounded electrode of a rf silane discharge, in order to limit the kinetic energy of the impinging ions to the plasma potential.

The dominant growth precursors in low-temperature plasmas from silane are SiH_3 radicals, if the depletion of the feed gas is in the range of 10% [25–27]. The formation of SiH_3 in the gas phase is well understood and follows at typical plasma pressures of several Pa the following reaction scheme:

1. The SiH_4 source gas is dissociated due to electron impact to form SiH_2 and two H atoms.
2. SiH_2 reacts with SiH_4 to form Si_2H_6 , which dissociates again to form SiH_3 .
3. Atomic hydrogen, created by the dissociation of SiH_4 , reacts also with SiH_4 to form SiH_3 and H_2 .

The surface loss probability of SiH_3 radicals on amorphous hydrogenated silicon films has been measured to $\beta = 0.25$ by several authors with various techniques [16–19]. This surface loss probability is also independent of substrate temperature T_s . However, the growth rate is temperature independent up to 350°C , corresponding to a sticking coefficient of $g = 0.1$ and increases by a factor of 2.5 above this temperature, corresponding to a sticking coefficient of $g = 0.25$ [17]. It is believed that the growth of a-Si:H films is due to the adsorption of SiH_3 radicals at dangling bonds on the surface. Below 350°C , the surface of the a-Si:H film is hydrogen-terminated and incoming atomic hydrogen or SiH_3 radicals abstract surface hydrogen to form H_2 or SiH_4 , respectively. The resulting dangling bonds act as chemisorption sites for incoming SiH_3 radicals [27–30]. Above a substrate temperature of $\sim 350^\circ\text{C}$, hydrogen desorbs from SiH surface groups, creating new open sites at the growing film surface, which act as additional adsorption sites for incoming SiH_3 radicals. As a consequence, the growth rate increases with increasing substrate temperature [17].

The amorphous hydrogenated silicon surface remains hydrogen oversaturated during growth at typical growth temperatures of 250°C , as known from infrared absorption measurements [30,31]. The defect density at this growing film surface is below 1% as measured by electron spin resonance measurements [32]. The experimental observation of a very low density of dangling bonds at the surface is in contradiction to the sticking coefficient of SiH_3 radicals of ~ 0.1 . The sticking coefficient of SiH_3 radicals of 0.1 would imply an average dangling bond density at the surface of the order of 10%, if incoming SiH_3 radicals directly chemisorb at an open bond upon impact. This problem was resolved by introducing a hot precursor state for SiH_3 prior to chemisorption at a dangling bond: SiH_3 adsorbs in a hot precursor state and diffuses on the surface to an open bond, where it chemisorbs. The fast surface diffusion of SiH_3 was also supported by molecular dynamic simulation, which indicated a migration length on the surface of $\sim 20 \text{ \AA}$ [33].

This description of a-Si:H film growth is based on the paradigm that SiH_3 is incorporated in the film only via chemisorption at dangling bond sites at the surface. The adsorption of SiH_3 on deuterated a-Si:D surfaces has been studied by von Keudell and Abelson [34] using *in situ* real-time infrared absorption spectroscopy. By following the isotope exchange, they observed that SiH_3 directly inserts into strained surface bonds at the growing film surface. The insertion reaction does not refute the *hot precursor* model. However, the experimental observation of a sticking coefficient of 0.1 for SiH_3 on the hydrogen saturated growing film surface can be due to the fact that the density of strained bonds at the surface is expected to be much higher compared to that of the dangling bonds (in the case of the silicon (100) surface, one Si–Si bond per Si atom in the first monolayer is strained). In that case, a reaction step based on the fast surface diffusion is no longer necessary, in order to explain the observed sticking coefficient of 0.1. The insertion model has been corroborated later by molecular dynamics modeling of SiH_3 chemisorption [35]. Recently, the dangling bond density at a growing a-Si:H film surface has been measured using cavity ring-down spectroscopy in reflection mode by Kessels [36].

They showed that the steady-state dangling bond density is by orders of magnitude too low to explain the observed absolute silicon growth rate. Based on these results, the conventional model for a-Si:H film growth based on SiH_3 chemisorption at dangling bond sites has to be revised. Amorphous hydrogenated silicon

growth occurs apparently via insertion of SiH₃ radicals into strained Si–Si surface bonds.

This example shows that although the macroscopic growth rate can easily be explained by the hot precursor model, the microscopic mechanisms can be different and require the knowledge of the detailed surface structure and morphology.

5.7 ION BOMBARDMENT IN PLASMA PROCESSING

The influence of ion bombardment on chemical reactions in a process plasma will be considered here. Ion bombardment during thin film growth from low-temperature plasmas plays a dominant role for many applications:

1. Physical sputtering by ion bombardment is used in deposition systems where sputtering of solid targets in an argon plasma is used to produce volatile growth precursors. These sputtered precursors can then produce thin films on a substrate that is placed in front of the sputter target. A typical example is the preparation of thin metallic films. In reactive magnetron sputtering (RMS), a reactive gas is added to the argon discharge. As an example, titanium-nitride films (TiN_x) are prepared from a titanium sputter target by adding N₂ to the argon discharge. For details see Refs. [37–39].
2. In most growth processes, sputtering of the growing film surface itself is not desired, since it reduces the effective growth rate or may deteriorate the quality of the material due to the formation of defects at the surface or in the bulk. For example, the production of device quality a-Si:H films requires the prevention of any bombardment with high energy particles, since the ion-induced defects act otherwise as recombination centers for the electron transport in the material. Consequently, the substrates for a-Si:H film growth are placed on the grounded electrode of an RF discharge reactor [23].
3. For the preparation of amorphous hydrogenated carbon films, however, ion bombardment is essential to produce dense films with superior material qualities. This is explained by the subplantation model [40,41]. Ions with kinetic energies above ~ 90 eV have a penetration range of a few angstrom, leading to their subplantation beneath the first few monolayers. Due to the incorporation of carbon atoms at interstitial network sites, compressive stress evolves that favors the formation of a dense sp³-hybridized network. By depositing films from monoenergetic carbon ions, amorphous sp³-coordinated carbon films can be prepared with a density and hardness close to that of a diamond.
4. Ion bombardment creates defects at the growing film surface due to sputtering or displacement of surface atoms. These open bonds can act as adsorption sites for incoming radicals. This leads to ion-radical synergism, since the effective sticking coefficient for radicals is enhanced by the ion bombardment. This ion radical for the adsorption of CH₃ radicals on amorphous hydrogenated carbon film surfaces has been proposed in a number of growth models for a-C:H film growth [42–44]. A nice confirmation of this

ion-radical synergism has been found by Shiratani et al. [20]. They measured the decay time of CH_3 radicals in the afterglow of a methane rf-discharge using ionization threshold mass spectrometry. It was observed that the decay of CH_3 radicals after switching off the methane discharge is characterized by two time constants corresponding to the two surface loss probabilities of 10^{-2} and 10^{-3} . This was explained by the fact that immediately after stopping the discharge, the ion bombardment disappears on the time scale of the confinement time for the ions in the discharge ($\sim\text{ms}$). The radicals, however, have a much longer confinement time, because they are not accelerated by electric fields. Immediately after the disappearance of the ions, only radicals are therefore present in the afterglow. The ion bombardment during plasma exposure creates dangling bonds at the surface. At these dangling bonds, the radicals present in the afterglow can adsorb more easily than at an undisturbed surface leading to an enhanced surface reaction probability of 10^{-2} . Since no ion bombardment is present in the afterglow, these chemisorptions sites are consumed by the adsorption of the radicals. After the complete saturation of all dangling bonds, a surface loss probability of 10^{-3} is measured, corresponding to the reactivity of CH_3 with a hydrogen saturated surface. A similar example for the occurrence of ion-neutral synergism exists for the etching of silicon in CF_4 discharges [13].

The influence of ion bombardment on thin film growth is summarized as follows:

1. An impinging ion leads to defects at the growing film surface due to displacement or sputtering of target atoms. This displacement depends on the energy transfer in a collision and, thereby, on the masses of projectile and target atom. A large displacement yield is obtained if the mass of the projectile matches the mass of the target atoms.
2. The threshold for physical sputtering depends on the surface-binding energy of the solid. A part of the momentum of the incoming ion has to be reversed by collisions to transfer kinetic energy to a surface atom directed away from the surface. This surface atom might then be able to overcome the surface-binding energy and be released from the solid.
3. With increasing kinetic energy of the projectile, impinging species penetrate deeper into the solid and the nuclear stopping becomes only dominant at the end of range. As a consequence, the maximum of the energy transfer and therefore the maximum amount of displacements occur further inside the solid.
4. The ion-induced formation of defects at the film surface can create adsorption sites for incoming radicals. This leads to ion-radical synergism during film growth.

These are only qualitative arguments and many of these effects can be quantified by computer codes like TRIM, SRIM, or TRYDIN [45]. However, for low ion energies or complex molecular ions, molecular dynamic simulation of ion–solid interactions

is the appropriate approach. Molecular dynamic calculations, however, are right now limited to small model systems and short time scales (\sim ps), which is much too short for typical time scales of thin film growth (\sim s to min).

Because of the high-level complexity of plasma–surface interaction, in technological applications approximative methods that permit to some extent generalizations have been favored. Simultaneously, the interest in the as much as possible exact handling of simplest models has considerably increased.

The sophistication of the phenomena at plasma–surface interaction is emphasized by the following items:

1. Combination of chemistry of neutral particles and charge carrier effects
2. Simultaneous appearance of erosion and deposition, sometimes even the formation of dust
3. Complexity of the plasma and surface structures

Originating from these points, a lot of problems arise in the optimization of plasma processes and they are often the reason for a discrepancy between empirical use in technological practice and exact physical description.

5.8 PARTICLE BALANCE AT SURFACES

An essential access to model the processes is the treatment of particle balances of the involved species on the basis of elementary mechanisms [46]. Since a variety of different particles are involved in the surface processes, one has, in principle, to establish a balance for each species. The several species originate on the one hand from the gas/plasma and on the other hand from interactions on the surface. The particle balances of the different particle sorts are linked to each other. However, such a balance equation system can only be solved for very simple and idealized systems. Alternatively, one has to simplify the system by restrictions.

In the following, a simple and idealized example will be discussed in more detail. The etching of a substrate B by means of surface film reaction (SFR) and chemical sputtering (CS) will be supposed. The processes are characterized by the cross section σ_{CS} and the reaction rate k_{SFR} . The gas/plasma should only contain the reactive etching component A that forms by reaction with B the product AB, as illustrated in Figure 5.4.

For those particles that originate from the bulk (B), the removal rate equals the etch rate R , and for those particles that arrive from the gas phase (A), the impinging rate must be equal to the removal or conversion rate, respectively:

$$\begin{aligned} \frac{dn_B}{dt} &= -k_{SFR}^B n_A n_B - \sigma_{CS}^B n_B j_A = R, \\ \frac{dn_{AB}}{dt} &= k_{SFR}^B n_A n_B + \sigma_{CS}^B n_B j_A - \frac{n_{AB}}{\tau_{des}^{AB}} = 0, \\ \frac{dn_A}{dt} &= \gamma_A j_A \Theta_B - n_A \tau_{des}^A - k_{SFR}^B n_A n_B = 0. \end{aligned} \quad (5.12)$$

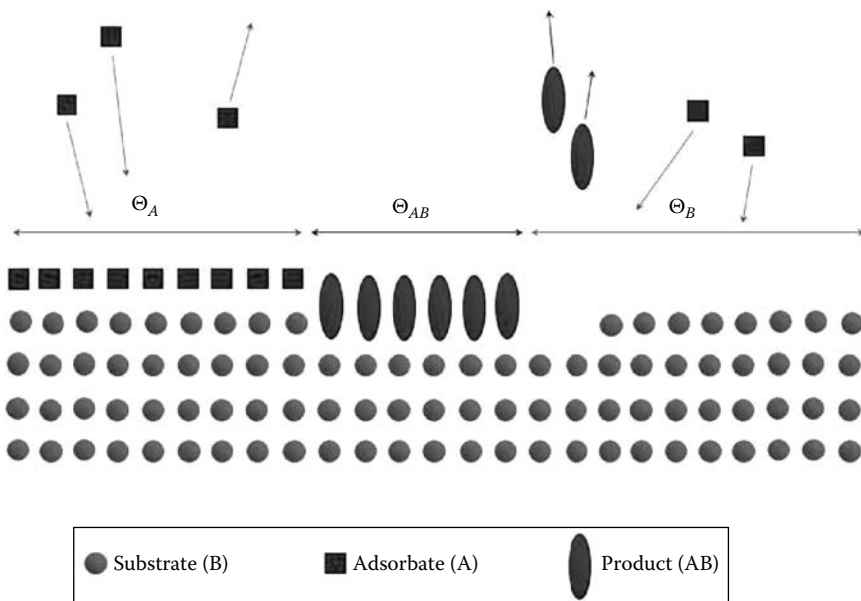


FIGURE 5.4 A supposed situation for modeling of reactive surface etching involving three components: adsorbed plasma species (A), solid surface atoms (B), and products (AB).

Under the assumption that at each B only either one A or one AB can be adsorbed, one obtains for the coverage

$$\Theta_A + \Theta_B + \Theta_{AB} = 1, \quad (5.13)$$

where $\Theta_A = n_A/n_0$, $\Theta_B = n_B/n_0$, and $\Theta_{AB} = n_{AB}/n_0$. Combining and solving (5.12) and (5.13), one obtains the normalized etch rate R/n_0 :

$$\frac{R}{n_0} = \left(\tau_{des}^{AB} + \frac{(\tau_{des}^A \gamma_A j_A)^{-1} + n_0 k_{SFR}^B (\gamma_A j_A)^{-1} + n_0^{-1}}{k_{SFR}^B + \sigma_{CS}^B \gamma_A^{-1} (\tau_{des}^A + n_0 k_{SFR}^B)^{-1}} \right)^{-1}. \quad (5.14)$$

This expression for such a simple example becomes much more difficult in real systems with more involved components and processes as considered here. Therefore, it is of importance to study some limiting cases of (5.14). For instance, at a very low adsorption of A (e.g., $\Theta_A \ll 1$), as is the case for high substrate temperatures where $\tau_{des}^A \approx 0$, or for low sticking coefficients $\gamma_A \approx 0$, the etch rate becomes

$$\frac{R}{n_0} = \left(\tau_{des}^{AB} + \frac{1}{j_A \sigma_{CS}^B} \right)^{-1}. \quad (5.15)$$

In this case, the etch rate R is mainly determined by the chemical sputtering of B and the desorption of the products. If the formed product molecule AB desorbs

immediately, the overall rate depends only on σ_{CS} . In contrast, in the case of a nearly complete coverage with A, that is, $\Theta_A \approx 1$, chemical sputtering can be neglected and the surface film reaction dominates:

$$\frac{R}{n_0} = \left(\tau_{des}^{AB} + \frac{n_0}{\gamma_A j_A} + \frac{1}{n_0 k_{SFR}^B} \right)^{-1}. \quad (5.16)$$

At very small flux densities of reactive particles j_A , the etching process is transport-limited, whereas at large $\gamma_A j_A$, the process is limited by the surface reactions.

In modeling the global etch mechanism, the basic processes mentioned earlier must be combined and have to be completed by volume processes in the plasma that supplies the various fluxes of particles to the substrate surface [47].

Example 5.2: Temperature dependence of chlorine plasma etching of GaAs

As already mentioned, a key question in modeling of the global surface modification processes is the description of relevant rates R in dependence on the process parameters. Among these parameters, the substrate temperature T_S is of special interest. A detailed investigation of the temperature dependence of the different rates $R(T_S)$ and surface properties can provide a lot of information on the kinetics and the interaction of the elementary processes of plasma–surface interaction because the different rate coefficients depend on T_S [46].

An interesting question in modeling of $R(T_S)$ is the interpretation of non-monotonous curves. In the case of plasma etching, there exist mainly three mechanisms for this behavior:

1. The etching or deposition process may proceed via different reaction channels that exhibit different temperature dependences (e.g., surface film reaction, chemical sputtering).
2. During the process, product molecules are formed that may react or desorb at different temperatures.
3. Different sensitivity of the elementary processes against temperature-dependent surface structures of the bulk material is required.

For example, the appearance of a maximum in the $R(T_S)$ dependence is quite general for etching via surface film reactions. At low temperatures, the concentration of reactants in the surface film is nearly saturated (full coverage). In this region, where $\Theta \approx 1$, the etch rate increases with increasing temperature according to the Arrhenius rate of a chemical reaction with constant reactants concentration. But at higher temperatures, normally the concentration of the surface film decreases due to faster desorption of adsorbed particles. Reaching a maximum, the decreasing supply of reactants results, finally, in a decreasing etch rate with further increasing temperature. The appearance of a minimum in the etch rate R can be modeled by the superposition of two or more processes of gasification, for example, of one mechanism with a maximum at low temperatures together with another mechanism that increases monotonically and dominates at higher temperatures. A possible combination of such mechanisms might be SFR and

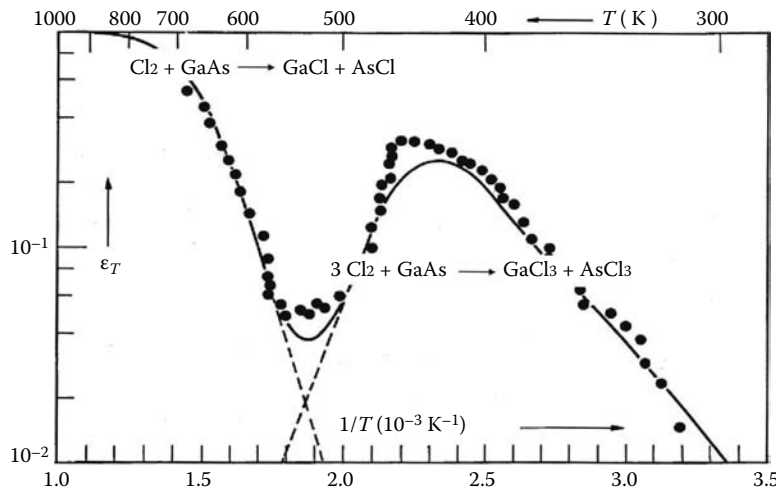


FIGURE 5.5 Total reaction probability of Cl_2 on GaAs in dependence on the substrate temperature.

CS. In the first reaction channel, etching occurs by conversion from a precursor weakly bound to the surface, and the latter etching occurs directly by the reactants arriving from the gas phase. A characteristic example for the combination of both reaction channels is the dry etching of silicon by fluorine-containing compounds.

A nonmonotonic $R(T_s)$ -curve due to the different desorption behavior of the formed products has been observed, for instance, during etching of GaAs by chlorine [48]. Starting at low temperature, the etch rate increases because of the large surface coverage of reactive species and increasing chemical reaction rates for the formation of GaCl_3 and AsCl_3 . At a higher temperature, the fast decreasing coverage of the origin species (Cl_2) and of the products (e.g., GaCl_3) vanishes and the formation of trichlorides stops. However, at these high temperatures desorption of the very fast formed layer of monochlorides (AsCl , GaCl) starts. The situation for the total reaction probability ϵ_T that is directly related to the etch rate $R(\epsilon_T) = (1/2)R/j_{\text{Cl}_2}$ is illustrated in Figure 5.5. The comparison of the measurements (points) with a simple model on the basic assumptions mentioned earlier yields typical quantities of the etch process like activation energies, residence times, etc.

One can conclude that the several elementary mechanisms of adsorption, diffusion, and desorption as well as the chemical reactions (CS, SFR) depend sensitively on the surface temperature T_s of the substrate, while the mechanisms of activation, physical sputtering, and implantation (at least in the relevant range) are almost independent of T_s .

5.9 ENERGY BALANCE AT SURFACES

For the energy balance during the plasma–surface interaction, one has to include the internal heat sources (energetic particle bombardment, radiation, surface reactions,

etc.) as well as the external sources (heating or cooling of the substrate) [49]. In the following, the energy balance in the plasma–surface interaction will be discussed.

When a solid comes into contact with plasma, energy transfer takes place. The substrate is heated and, after a certain time, it may reach a thermal equilibrium. This steady state is determined by a balance of energy gain Q_{in} from the plasma processes and energy losses Q_{out} due to conduction and radiation. The general power balance at the substrate is given by

$$Q_{in} = \dot{H}_S + Q_{out}, \quad (5.17)$$

where $\dot{H}_S = C_S dT_S/dt$ denotes the enthalpy of the substrate. It should be mentioned that the flux Q_{in} is the surface integral of the related energy flux density J_{in} over the substrate surface A_S :

$$Q_{in} = \int_{A_S} J_{in} dA. \quad (5.18)$$

In general, the total energy influx J_{in} is the sum of the fluxes due to the kinetic energy of electrons J_e and of ions J_i , the energy that is released when a positive ion recombines at the surface J_{rec} , the energy that is supplied when a gas phase species associate with another gas phase species at the surface J_{ass} , and the energy that is released if chemical reactions occur between gas phase species and the surface J_{chem} :

$$J_{in} = J_e + J_i + J_{rec} + J_{ass} + J_{chem}. \quad (5.19)$$

Contributions due to plasma radiation can mostly be neglected because the environment (gas, walls) is nearly at room temperature.

A certain part of energy is delivered by charge carriers to the substrate surface. In general, the mean kinetic ion energy is determined by the ion energy distribution function (IEDF). At elevated pressures, the energy distribution of the ions arriving at the substrate is affected by collisions in the sheath in front of the substrate. But at low pressures as is commonly the case, the maximum ion energy is determined mainly by the free fall energy $e_0 V_{bias}$, where V_{bias} is the potential drop across the sheath in front of the substrate that corresponds to the sum of the plasma potential V_{pl} and the substrate potential V_S :

$$V_{bias} = V_{pl} - V_S. \quad (5.20)$$

It should be emphasized that the simple expression of (5.20) for the mean kinetic energy of the ions striking the substrate is applicable in most cases of plasma processing. Only if the IEDF for the ions near the substrate is much more complex, the assumption of $e_0 V_{bias}$ for the kinetic energy is no longer justified.

In addition to the directed kinetic energy of the ions that originate from acceleration in the electrical field in front of the substrate, the ions also have thermal energy. However, this part can be neglected if the ions are nearly at room temperature. Hence, the contribution of the ions, which can be expressed as a product of the ion flux density j_i and their mean energy E_i , is

$$J_i = j_i E_i = j_i e_0 (V_{pl} - V_{fl}) = n_e v_{amb} e_0 (V_{pl} - V_{fl}) = 0.6 n_e \sqrt{\frac{k_B T_e}{m_i}} \cdot e_0 (V_{pl} - V_{fl}), \quad (5.21)$$

where the ambipolar diffusion $n_e v_{amb}$ has been approximated by the Bohm flux

$$j_i = 0.6 n_e \sqrt{\frac{k_B T_e}{m_i}}. \quad (5.22)$$

The substrate has been assumed to be at floating potential, that is, $V_s = V_{fl}$. Under low pressure conditions ($p < 10 \text{ Pa}$), the Bohm equation is applicable, because in the sheath almost no collisions occur. The Bohm equation yields the ion flux j_i by knowing the electron density n_e that equals the ion density n_i at the sheath edge.

In addition to kinetic energy, ions transfer a part of their potential energy when striking a surface. For metallic substrates, the neutralization of ions is caused by long-range interactions and may be accompanied by the emission of secondary electrons. The released recombination energy E_{rec} is given by

$$E_{rec} = E_{ion} - \Phi - \gamma_i \Phi \quad (5.23)$$

and the resulting contribution J_{rec} to the energy influx to the substrate due to the recombination is

$$J_{rec} = j_i E_{rec}, \quad (5.24)$$

where

E_{ion} is the ionization potential of the incident ion

Φ is the work function of the metal

γ_i is the yield of secondary electrons

Data for E_{ion} , Φ , and γ_i may be taken from the literature.

In general, the cooling effect due to sputtering of substrate material can be ignored because the energy $e_0 V_{bias}$ of the impinging ions is always smaller than 100 eV and the sputtering yield Y of most materials in this low-energy range is rather small ($Y = 0.1$) as well as the mean energy of the few sputtered particles ($\approx 5 \text{ eV}$). Therefore, the flux of sputtered surface atoms that may contribute to an energy loss of the substrate is negligible.

The electrons have to overcome the bias voltage V_{bias} in front of the substrate in order to reach the substrate surface and to transfer their energy. The kinetic energy of the plasma electrons arises from the integration over the electron energy distribution function (EEDF) from V_{bias} up to infinity, which yields in the case of a Maxwellian electron energy distribution the energetic influx J_e as

$$J_e = n_e \sqrt{\frac{k_B T_e}{2\pi m_e}} \cdot \exp \left\{ -\frac{e (V_{pl} - V_{fl})}{k_B T_e} \right\} 2k_B T_e. \quad (5.25)$$

An analysis of the charged plasma components by using the general equations (5.19) through (5.25) listed in the preceding text will in principle yield the part of surface heating caused by positive ions and electrons. Because several heat sources act together, for example, radiation, chemical reactions, neutrals, and charge carriers, it is possible to separate the contribution of the charge carriers by variation of the bias potential.

Example 5.3: Energy balance during thin film deposition

In a process plasma containing reactive species (e.g., N₂, O₂ and) in addition to energy transfer by charge carriers, the thermal balance of a substrate may also be influenced by atomic recombination (association) and exothermic reactions. Evidence for substrate heating by exothermic reactions on the processed surface has been reported, for example, with respect to plasma etching of silicon with fluorine-containing compounds [50] and during plasma cleaning of contaminated metal surfaces [51]. The percentage of the recombination energy that is used for surface heating varies with the chemical composition of the surface and of the plasma.

For a reactive oxygen plasma, the energy influx J_{ass} by atom recombination, that is, the formation of oxygen molecules, is described by

$$J_{ass} = j_O \Gamma_O E_{diss} = \Gamma_O \frac{1}{2} n_O \sqrt{\frac{8k_B T_g}{\pi m_O}} \cdot E_{diss}, \quad (5.26)$$

where

Γ_O is the association probability of O atoms on the substrate surface

T_g is the gas temperature (room temperature)

n_O is the density of O atoms

m_O is the mass of O atoms

E_{diss} is the dissociation energy of O₂ molecules

The contribution J_{chem} due to exothermic chemical reaction (i.e., surface oxidation) can be calculated by the product of the average energy E_{react} released per reaction with the flux density $j_{react} = j_O$ of the reactive oxygen radicals:

$$J_{chem} = j_{react} E_{react}. \quad (5.27)$$

The radical flux density j_O that has to be known in (5.26) and (5.27) is mainly determined by electron impact dissociation taking place in the negative glow of the discharge. If the growth rate of the oxide that is formed during the plasma process is known, one can easily estimate J_{chem} from the growth rate R_{dep} , the mass density ρ of the layer, and the average specific oxidation enthalpy h_{ox} :

$$J_{chem} = R_{dep} \rho h_{ox}. \quad (5.28)$$

Figure 5.6 shows an example for energy influxes Q_{in} measured for a weak radiofrequency (rf) plasma in argon and oxygen, respectively. The discharge power was kept constant at 15 W and the gas pressure at 1 Pa, while the substrate voltage

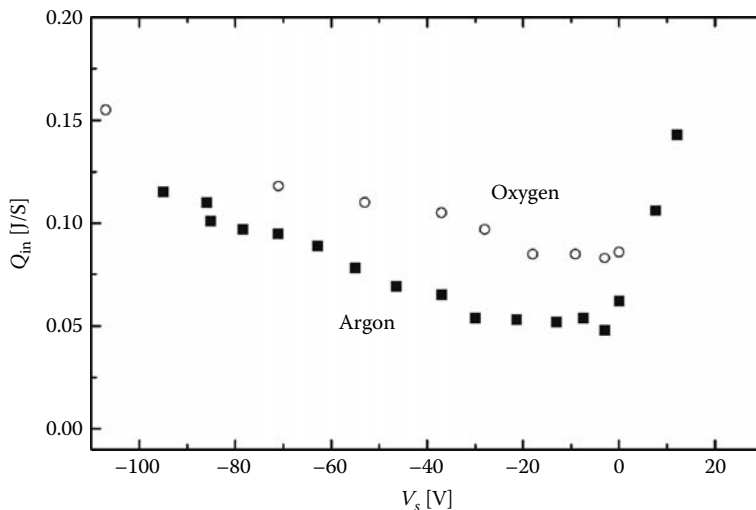


FIGURE 5.6 Measured integral energy influx from a weak rf plasma toward a copper substrate for argon and oxygen, as a function of the substrate voltage.

(V_s) was varied. A comparison of the measured total energy influx with different energetic contributions calculated on the basis of the equations mentioned earlier gives insight into the involved processes and dominant mechanisms that determine the thermal balance of a substrate during plasma treatment: For negative substrate voltages only the ions dominate, while the contributions of electrons and recombination become important for positive voltages. At floating potential, the energy influx from the plasma and, hence, the substrate heating shows a minimum. In principle, both gases (argon and oxygen) exhibit a similar qualitative behavior. However, the measured energy influx in the case of oxygen plasma is higher than that for an argon plasma. This observation is due to the processes of oxygen atom recombination (association) and surface oxidation that supply, in addition, chemical reaction heat.

The determination of the energy influx in practical applications of plasma discharge devices is important when it is necessary to know the surface temperature of an object immersed in the plasma. For example, in plasma processing it may be important to know the substrate temperature in order to avoid overheating of the substrate during processing.

Also the morphology and microstructure of the plasma-treated surfaces may be influenced by the thermal conditions at the substrate. It is well known that density and roughness of deposited films show a correlation with the substrate temperature and with the energy influx. This observation is illustrated in Figure 5.7, where thin aluminum films have been sputtered onto micro-sized silica powder particles. The layers deposited on the powder particles exhibit a rough, cauliflower-like structure, while films sputtered on the large substrates are comparatively smooth. An essential reason for the observed differences in surface roughness might be the different substrate temperatures that are reached during the sputter process. Although under comparable deposition conditions the energy flux toward a floating powder particle is the same as toward a flat substrate, the

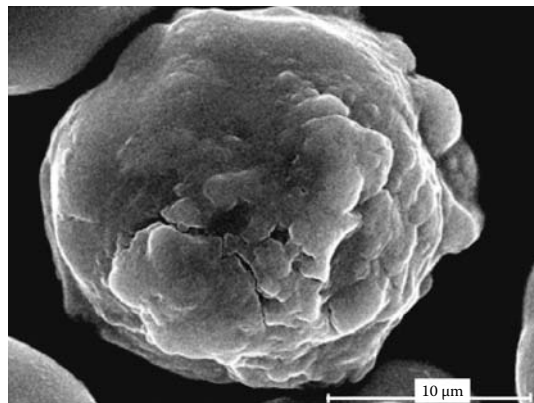


FIGURE 5.7 Scanning electron micrograph of Al-coated SiO_2 particles.

resulting equilibrium temperature may be quite different. Due to a much better heat conduction along the substrate holder, a Si wafer does not reach as high temperatures as microscopic powder particles that are mainly cooled by radiation. Hence, the rather high deposition temperature of the powder particles resulting from the thermal power during the sputter process causes an increased grain size and rough microstructure.

6 Plasma Diagnostics

CONTENTS

6.1	Probe Measurements	190
6.1.1	Overview	190
6.1.2	Elements of Probe Theory and Evaluation of the Probe Characteristic	191
6.1.3	Probe Measurements on More Complicate Conditions	193
6.1.3.1	Plasmas with Isotropic Non-Maxwellian EEDF	193
6.1.3.2	Plasmas with Anisotropic EEDF	194
6.1.3.3	Determination of the Second Derivative of the Probe Characteristic	194
6.1.3.4	Probe Measurements in rf-Discharges	194
6.1.3.5	Probe Measurements in Magnetron Discharges	195
6.1.3.6	Probe Measurements in Depositing Discharges	195
6.1.3.7	Probe Measurements in Discharges Containing Negative Ions	197
6.2	Microwave Interferometry	198
6.2.1	Introduction	198
6.2.2	Basic Principle	199
6.2.3	Experimental Arrangements	201
6.2.3.1	Mach-Zehnder Interferometer	201
6.2.3.2	Heterodyne Interferometer	201
6.2.4	Experimental Conditions	202
6.2.4.1	Probing Frequency and Frequency Stability	202
6.2.4.2	Path Length Variations	203
6.2.4.3	Steady State Operation	204
6.2.4.4	Components	204
6.2.5	Wave Transmission	205
6.2.6	Final Remarks	205
6.3	Emission and Absorption Spectroscopy	206
6.3.1	Introduction	206
6.3.2	Instrumental Techniques	206
6.3.3	Emission Spectroscopy	209
6.3.3.1	General Considerations	209
6.3.3.2	Concentration Measurements	211
6.3.3.3	Temperature Measurements	212
6.3.3.4	Degree of Dissociation of Hydrogen	216

6.3.4	Absorption Spectroscopy	216
6.3.4.1	General Considerations	216
6.3.4.2	Infrared Spectroscopy	219
6.3.5	Summary and Conclusion	225
6.4	Laser Induced Fluorescence Spectroscopy	226
6.4.1	Principles of Laser-Induced Fluorescence	227
6.4.2	Instrumentation and Experimental Techniques	229
6.4.3	Further Reading	230
6.5	Mass Spectrometry	230
6.5.1	Mass Spectrometer	230
6.5.1.1	Ion Source	232
6.5.1.2	Energy Analyzer	234
6.5.1.3	Mass Analyzer	234
6.5.1.4	Ion Detection	235
6.5.1.5	Coupling of the Mass Spectrometer with the Plasma Source	235
6.5.2	Ion Analysis	235
6.5.2.1	Sampling Orifice	236
6.5.2.2	Transfer Optics	237
6.5.2.3	Coupling	237
6.5.2.4	Gas Pressure	237
6.5.2.5	Calibration	238
6.5.2.6	Deduction of Data for Plasma Parameters	238
6.5.2.7	Determination of Ion Density	238
6.5.2.8	Examples for Mass Spectrometric Measurements in Chemically Active Plasmas	240
6.5.2.9	Conclusions	240
6.5.3	Neutral Plasma Components	241
6.5.3.1	Coupling	242
6.5.3.2	Electron Attachment Mass Spectrometry	242
6.5.3.3	Mass Spectrometric Investigation of Radicals	245
6.5.3.4	Threshold Ionization Mass Spectrometry	245
6.5.3.5	Ion Attachment Mass Spectrometry	247
6.5.3.6	Measuring Excess Energy	247
6.5.3.7	Measuring of Volatile Metal-Compounds	248
6.5.3.8	Conclusions	249
6.6	Gas Chromatography	249
6.6.1	Gas Chromatographic Separation of Stable Compounds	249
6.6.1.1	Principle	249
6.6.1.2	GC Equipment and Main Components	250
6.6.1.3	Basic Equation of Gas Chromatography	252
6.6.2	Examples	253

According to the broad spectrum of plasma components different tasks exist for the investigation of the plasma to understand the plasma processes and to control plasma chemical reactions characteristic for the various applications. Table 6.1 presents a summary of the plasma components, the experimental methods, and specific results.

In the following diagnostic methods are presented for the investigation of the electron component of the plasma, as probe measurements, and microwave interferometry. Next part deals with the methods for the study of the heavy particles in the gas phase: emission and absorption spectroscopy, also laser induced fluorescence spectroscopy. The final sections are devoted to mass spectrometry of ions and neutral particles including free radicals and gas chromatography of neutral components.

TABLE 6.1
Plasma Components and Diagnostic Methods

Plasma Components	Methods	Results	Section
<i>Electrons</i>			
Density	Probe MW-interferometry	$N_e(r, t)$ N_e	6.1 6.2
Energy	Probe	EEDF	6.1
<i>Ions</i>			
Composition	OES, OAS MS	Density, identification m/z	6.3 6.5
Flux	MS	j_v, N_v , surface	6.5.2
Energy	MS EA	Energy at surface	6.5.2
<i>Neutrals</i>			
Atoms	OES, MS ei	Identification, m/z	6.3, 6.5
<i>Molecules</i>			
Small molecules	OES, OAS MS ei	Identification, density m/z , density	6.3 6.5
Large molecules	OES, OAS MS ei, EAMS, CI, FI GC-Ms	Identification, density Spectrum, structure, m/z Identification, density	6.3 6.5 6.6
Radicals	OES, OAS FTIR, TDLAS, CRDS LIF, TALIF, DFWM MS ei, AMS, TIMS,	Identification, density Identification, density Identification, density Identification, density	6.3 6.3 6.4 6.5

N_e is the electron density, EEDF is the electron energy distribution function, m/z is the ion mass to charge ratio, MS is the mass spectrometry, OES is the optical emission spectroscopy, OAS is the optical absorption spectroscopy, j_v is the ion current density, N_v is the ion density, EA is the energy analysis, ei is the electron impact ionization, EAMS is the electron attachment mass spectrometry, CI is the chemical ionization, FI is the field ionization, GC-MS is the coupled gas chromatography-mass spectrometry, LIF is the laser-induced fluorescence, TALIF is the two-photon absorption laser-induced fluorescence, DFWM is the degenerated four wave mixing, FTIR is the Fourier transform infrared spectroscopy, TDLAS is the tunable diode laser absorption spectroscopy, CRDS is the cavity ring down spectroscopy. AMS is the appearance potential mass spectrometry, TIMS is the threshold ionization mass spectrometry, EAMS is the electron attachment mass spectrometry.

6.1 PROBE MEASUREMENTS

6.1.1 OVERVIEW

An electrical single or Langmuir probe is a small auxiliary electrode immersed into the plasma, the voltage current characteristic of which is measured with respect to a big reference electrode, the chamber wall, or one of the discharge electrodes. Positive or negative charge carriers (positive ions, electrons, negative ions) are attracted or repelled by the probe depending if the probe bias V is lower or higher than the potential V_s of the probe surrounding plasma. V_s is called space or plasma potential. The currents of the different charge carriers depend on the plasma parameters. Therefore the evaluation of the characteristic gives internal plasma parameters as floating and plasma potential, electron temperature, electron and ion density, mean electron energy and electron energy distribution function (EEDF) in spatial and temporal resolution. Monitoring of these parameters during a technological plasma process is of great importance to enhance reproducibility and process understanding, optimization, and control. Langmuir probes are well established in plasma diagnostics since tens of years [1]. There are some excellent reviews on probe diagnostics, such as [2–12].

Usually electric probes are of spherical, cylindrical, or plane geometry, see Figure 6.1. Because of the simple assembly cylindrical probes of few mm length are most commonly used. Usual probe materials are tungsten (high melting point) and platinum (high chemical resistivity). A possible probe circuit is shown in Figure 6.2. Here PMD is a probe measuring device performing the generation of the probe bias as a staircase voltage and the probe current measurement. A computer controls the measuring procedure, stores the measured current and voltage values, and processes the acquired data.

The use of Langmuir probes in chemically active plasmas is restricted because of etching of the probe material or deposition of the probe surface with insulating or metallic layers. The first problem especially occurs in fluorine-containing media and it may be solved using platinum as probe material; in chlorine containing plasmas tungsten may be used [13]. The second problem may be overcome or at least reduced

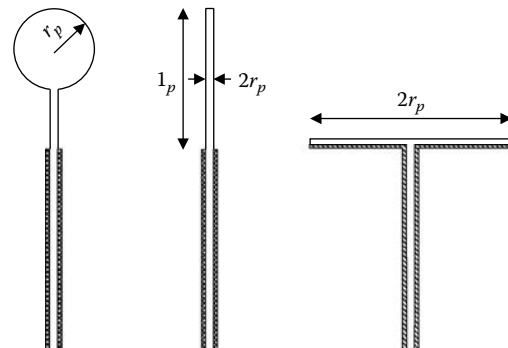


FIGURE 6.1 Probe shapes.

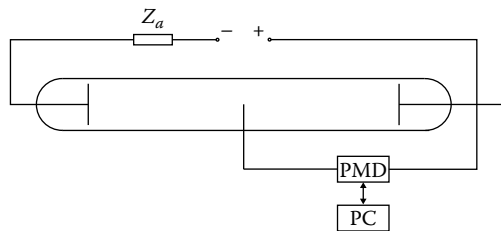


FIGURE 6.2 Probe circuit.

choosing an adequate measuring procedure and probe design (see Section 6.1.3.6). In the following a simple evaluation procedure for Langmuir probe characteristics is given, ignoring these and further problems. Afterward complications of the probe method are listed and measures are discussed to overcome them.

6.1.2 ELEMENTS OF PROBE THEORY AND EVALUATION OF THE PROBE CHARACTERISTIC

Many different working regimes of Langmuir probes depending on plasma parameters and gas pressure may be distinguished [5,6,10,11]. But this methodical aspect is of smaller importance for the evaluation of the probe characteristic, if only parameters of electrons and not of ions are determined and if the electrons do not suffer collisions with neutrals in the space charge region surrounding the probe (probe sheath). This is the case if the radius r_p of a cylindrical probe of 0.05 mm is chosen at pressures lower than 1 mbar. At higher pressures the probe radius should be not bigger than 0.05 mm/p[mbar]. This value can be given as a summary of the results presented in [14]. For probe measurements at higher pressures up to atmospheric pressure see [4,5,11,14–18], see also Section 6.1.3.6 (double probe). Furthermore the following conditions have to be fulfilled to ensure a relatively simple evaluation of the probe characteristic:

1. The influence of electric and magnetic fields occurring in the plasma on the movement of the charge carriers to the probe may be neglected.
2. The probe surface work function is constant along the whole probe surface and does not change during measurement.
3. There is only one kind of positive and negative charge carriers. No negative ions occur.
4. Fluctuations of plasma parameters do not occur.
5. An isotropic EEDF occurs in the plasma.

The probe characteristic is measured from voltages lower than floating potential V_f (i.e., the zero cross of the probe characteristic) up to voltages higher than plasma potential V_s . The characteristic shows an inflection point at V_s [19–21], see Figure 6.3. At probe voltages $V < V_s - 2(V_s - V_f)$ electrons are repelled by the probe. Only the attracted positive ions are able to reach the probe (ion saturation current $i_{+,sat}$). At voltages $V_s - 2(V_s - V_f) < V < V_s$ the total probe current comprises

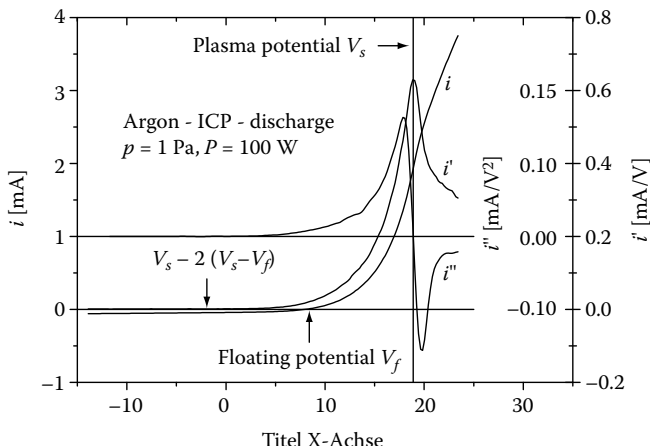


FIGURE 6.3 Example for a probe characteristic $i(V)$ and its first and second derivative.

of a current of attracted positive ions and also a current $i_{e,ret}$ of retarded electrons: $i = i_{e,ret} + i_{+,sat}$. At plasma potential no charge carriers are attracted or repelled by the probe. Here the random currents $i_{e0,+0} = (1/4)e_0 N_{e,+} \bar{v}_{e,+} S_p$ of electrons and ions flow to the probe (e_0 : elementary charge, n : density, \bar{v} : mean velocity, S_p : probe surface). Because of high ion mass and low ion temperature the relation $i_{e0} \gg i_{+0}$ holds and often i_{+0} is neglected (cold ion approximation [4,22,23]). At voltages higher than plasma potential only attracted electrons reach the probe (electron saturation current). Mostly the second derivative of a correctly measured probe characteristic has only two extreme values: a minimum and a maximum value near the plasma potential, see Figure 6.3. An additional maximum value at strongly negative probe bias may be caused by a group of fast isotropic electrons and an additional maximum near plasma potential can be caused by negative ions, but in most cases additional extreme values indicate problems with missing or incomplete rf-compensation or probe surface contamination (see below).

An isotropic electron velocity distribution function $F(v) = 4\pi v^2 f(v)$ occurs often in good approximation in most regions of a discharge. $F(v)$ is normalized to unity ($\int F(v) dv = 1$). An EEDF $F(U)$ with $eU = (m_e/2)v^2$ (m_e , v : mass and velocity of electrons) may be defined in this case as $F(U) = F(v)(dv/dU) = 4\pi v^2 f(v)(dv/dU)$. This definition ensures that also $F(U)$ is normalized to unity. The following expression for the electron retarding current $i_{e,ret}$ to any non-concave probe may be derived from a detailed consideration of the orbital motion of the electrons without having to assume the existence of a sheath region across which the probe to plasma potential is developed [4,24]

$$i_{e,ret}(V) = \frac{e_0^{3/2} N_e S_p}{2^{3/2} m_e^{1/2}} \int_{V_s-V}^{\infty} U^{1/2} F(U) \left(1 - \frac{V_s - V}{U}\right) dU, \quad V \leq V_s. \quad (6.1)$$

If a Maxwellian EEDF occurs, then it follows from (6.1)

$$i_{e,ret}(V) = i_{e0} \exp\left(\frac{V}{V_e}\right), \quad V \leq V_s \quad (6.2)$$

where

$$i_{e0} = S_p e_0 N_e \left(\frac{e_0 V_e}{2\pi m_e}\right)^{1/2} \quad (6.3)$$

is the thermal electron current, that is, the random electron current at a Maxwellian EEDF. V_e is the electron temperature in voltage units: $V_e = kT_e/e_0$ (k : Boltzmann constant, T_e : electron temperature).

In case of a Maxwellian EEDF the following evaluation of the probe characteristic has to be made:

1. Determination of the plasma potential from the inflection point, that is, from the maximum value of the first derivative or from the zero cross of the second derivative of the probe characteristic: $V_s = V(i'_{max}) = V(i'' = 0)$.
2. After extracting the electron retarding current from the total probe current $i_{e,ret}(V) = i(V) - i_{+,sat}(V)$ for $V < V_s$ [25,26] the electron temperature is obtained from the slope of the logarithmic electron retarding current $\ln(i_{e,ret}(V))$ for $V < V_s$, see Equation 6.2.
3. The electron density N_e is obtained from (6.3) with $i_{e0} = i(V)$. The positive ion density n_+ follows from the quasi neutrality of the plasma: $n_+ = N_e$.

6.1.3 PROBE MEASUREMENTS ON MORE COMPLICATED CONDITIONS

6.1.3.1 Plasmas with Isotropic Non-Maxwellian EEDF

A non-Maxwellian EEDF is indicated by the fact that the logarithmic electron retarding current is not a straight line. Then the EEDF is obtained by the twofold differentiation of (6.1) with respect to the probe potential V ($U = V_s - V$, $V \leq V_s$) [1,27], see also [4,24]

$$F(U) = \frac{2^{3/2} m_e^{1/2}}{e_0^{3/2} N_e S_p} U^{1/2} \frac{d^2 i_{e,ret}(V)}{dV^2}. \quad (6.4)$$

Using the normalization $\int F(U)dU = 1$ the electron density and the mean electron energy $\epsilon = e_0 \int UF(U) dU$ follow from (6.4) as

$$N_e = \frac{2^{3/2} m_e^{1/2}}{e_0^{3/2} S_p} \int_{-\infty}^{V_s} (V_s - V)^{1/2} i''_{e,ret}(V) dV, \quad (6.5)$$

$$\epsilon = e_0 \frac{\int_{-\infty}^{V_s} (V_s - V)^{3/2} i''_{e,ret}(V) dV}{\int_{-\infty}^{V_s} (V_s - V)^{1/2} i''_{e,ret}(V) dV}. \quad (6.6)$$

Because the relation $i''_{e,ret} \gg i''_{+,sat}$ is valid for low and medium values of $V - V_s$ often the measured total probe current is differentiated instead of the electron retarding current.

6.1.3.2 Plasmas with Anisotropic EEDF

In case of an anisotropic EEDF in an axisymmetric discharge a Legendre polynomial expansion of the EEDF has to be performed. The coefficients f_i of this expansion follow from the second derivatives of probe characteristics measured with a one-sided plane probe in different orientations [10,28–30]. Mean energy and density of electrons follow from f_0 and the drift velocity is derived from f_1 [11,31,32]. A generalized theory of electron retardation by Langmuir probes in anisotropic plasmas with no assumed symmetry is performed in [33] by expansion of the EEDF into a series of spherical harmonic functions.

6.1.3.3 Determination of the Second Derivative of the Probe Characteristic

The second derivative of the probe characteristic may be obtained by modulation of the probe current superposing an alternating voltage $v_{mod}(t)$ on the steady probe bias. The amplitude of one of the harmonics of the current is proportional to the derivative [4,10,18,34,35]. Presently often numerical techniques are used to differentiate the probe characteristic after measurement. One possibility is the non-recursive digital or FIR filtering of the characteristic recorded point by point at equidistant voltage values. Here each current value is replaced by a linear combination of itself and some neighboring current values [26], details in [36,37]. The distortion of the second derivative of the characteristic by the electrical or numerical differentiation is described by the convolution of the true derivative with an apparatus function [35–39]. Further differentiating techniques are listed in [11].

6.1.3.4 Probe Measurements in rf-Discharges

Technological plasmas often are generated by rf-discharges. Due to the varying plasma potential in these discharges an rf-current occurs in the probe circuit which is rectified at the nonlinear probe characteristic leading to distortions of the characteristic. The evaluation described here of such disturbed characteristics gives incorrect plasma parameters. Especially the electron temperature may be strongly overestimated. To avoid this problem the probe tip is forced to follow the varying plasma potential either by driving the probe with an rf-voltage (active rf-compensation) [40–43], or by increasing the impedance between probe and ground (introducing of blocking filters or self-resonant inductors connected in series to the probe tip) and decreasing the probe to plasma sheath impedance using an additional compensation electrode (passive rf-compensation) [44–47]. The blocking elements have to be placed to the probe tip as near as possible, but at least inside the metallic rf-reactor to avoid a big capacitively rf-current from probe tip connection to ground. Unfortunately often the rf-compensation is incomplete and a certain rf-perturbation remains. The evaluation of the characteristic has to be modified in this case [39,48,49]. Also rf-distortions of the probe characteristic are described by the convolution of the true characteristic with an apparatus function. Because this function is not a bell-shaped

but a U-shaped curve additional extreme values occur in the second derivative of the probe characteristic indicating bad rf-compensation [39,48].

6.1.3.5 Probe Measurements in Magnetron Discharges

Magnetron discharges are widely used in plasma-aided etching and deposition technologies. An overview about probe measurements in such discharges is given in [50]. The presence of a magnetic field generally reduces the current drawn from a plasma by a probe and causes an anisotropy of the EEDF. For a cylindrical probe the first effect is minimized if the probe axis is positioned perpendicular to the magnetic field lines and if the probe diameter is chosen as small as possible. The second effect appears if the ratio of magnetic field strength and pressure B/p is several of T/Pa [51]. In magnetron discharges this ratio is lower by about two orders of magnitude [50]. An anisotropy of the EEDF is not detectable there [52]. Based on measurements in a cylindrical magnetron discharge performed in argon at a pressure of 1.5 Pa in [50] was shown that in a weak magnetic field the error in the measured electron density obtained from the probe electron current at plasma potential according to Equation 6.3 caused by the magnetic field is not bigger than 20%.

6.1.3.6 Probe Measurements in Depositing Discharges

Surface contamination is generally a serious problem in probe diagnostics. Every new probe tip should be conditioned in the plasma bringing it to white heat ($T_p > 1500^\circ\text{C}$) by drawing a high electron saturation current [21]. In depositing plasmas probe contamination is the limiting factor of probe usefulness. Here a layer at the probe surface is formed which may disturb the probe characteristic. Generally, probe contaminations change the probe surface work function, causing a shift of the probe characteristic and/or a hysteresis [53,54]. Dielectric layers, such as polymer films or Al_2O_3 , additionally flatten the characteristic [54,55] causing an overestimation of electron temperature, whereas a conductive or semiconductive film, such as $\alpha\text{-Si:H}$ or SnO_2 , weakly disturbs the probe characteristic [54,56–58]. But also an influence of metallic layers was reported [59,60]. Probe contamination may lead to additional inflection points in the probe characteristic and thus to additional extreme values in its second derivative [55,61]. If insufficient rf-compensation as a reason may be excluded, such additional extreme values are a strong hint to probe contamination.

At first the following measures may be used to avoid probe contamination: Moving probe into plasma only during measurement, short plasma operating times, holding the probe at cleaning potential [62] or retracting the probe tip into its insulating capillary during nondata acquisition times [63]. Essential in the construction of cylindrical probes is the centering of the probe tip wire inside the insulating capillary [4,64].

6.1.3.6.1 Pre-Cleaning

The simplest possibility to carry out probe measurements in depositing plasmas is to clean the probe before each measurement by applying a voltage $V \ll V_s$ (ion bombardment) or/and $V > V_s$ (heating by a strong electron saturation current to red or white heat) and to perform the measurement in a time short compared with deposition time. Examples are given in [13] (plasma: N_2 , CCl_4 , CCl_4/N_2 ,

SF_6), [54] (precursor: aluminum isopropoxid, layer: Al_2O_5), [58] (precursor: tetramethyltin (TMT), layer: SnO_2 , [58] (plasma: $\text{Ar}/\text{C}_2\text{F}_3\text{Cl}$), [65] (plasma: CH_4/H_2 , layer: diamond-like). Additional argon plasma or oxygen plasma cleaning may be performed after each measurement [58,65]. In a silane plasma stable probe characteristics may be obtained if the probe ambient temperature is held at about 200°C [56,57].

6.1.3.6.2 Heated Probes

These probes have to be used, if the measuring time is bigger than the deposition time. In direct heated probes the tip consists of a heated wire which is in direct contact with the plasma. The wire temperature T_p during probe measurement has to be chosen below the limit of noticeable thermionic emission. If such a probe is used in an rf-discharge, both connections have to be rf-compensated [66]. Examples for the use of heated probes are given in [55] (plasma: $\text{Ar}/\text{benzene}$, $T_p = 850^\circ\text{C}$), [67] (plasma: $\text{Ar}/\text{benzene}$, $T_p = 1120^\circ\text{C}$), [68] (plasma: CF_4 , $T_p \approx 900^\circ\text{C}$), [69] (plasma: Ar/HMDSO , $T_p = 900^\circ\text{C}$), [70] (plasma: Ar/CF_4 , $T_p \approx 1500\text{ K}$). Sometimes a heatable probe is heated only during the non-data acquisition times [71] (plasma: acrylic acid, $T_p > 2000\text{ K}$). This eliminates the uncertainty of the probe bias due to the voltage drop along the probe wire during heating. Indirect heated probes may be used, if a lower probe temperature is sufficient [59,60] (plasma: potassium, $T_p \simeq 300/600^\circ\text{C}$).

Heated probes also may be used to determine the plasma potential directly, especially in depositing discharges. In this case the wire temperature has to be chosen to allow thermionic emission [8,72]. At probe voltages higher than plasma potential the emitted electrons are reflected back to the probe and the emissive probe characteristic is similar to that of the cold probe. At probe voltages lower than plasma potential the emitted electrons are rejected from the probe and appear as an effective ion current additionally to the current of plasma ions. This process depends directly on plasma potential rather than the electron kinetic energy. Thus it is not sensitive to plasma flow, non-isotropic plasma, and collisions of electrons with heavy neutral particles. The plasma potential may be determined from the branching point of the characteristic of the emissive and the cold probe and from the floating potential or the inflection point of the emitting probe. Unfortunately other plasma parameters than plasma potential are not detectable by means of emissive probes.

6.1.3.6.3 Floating Systems of More Than One Probe

Also a layer on the reference electrode can complicate the probe measurement. In this case double or triple probes may be used. The *double probe* method was developed originally for electrodeless discharges [73]. From the characteristic of a probe measured with respect to a second nearby, mostly identical, probe the electron temperature and the ion density may be derived [4,8,11,74–76].

Because the net current in the double probe circuit is zero, the maximum current is the ion saturation current. Thus only probe cleaning by ion bombardment is possible applying a high voltage between the two probes. Inserting a reference electrode allows probe cleaning by drawing an electron saturation current [75,76]. Furthermore both probe tips may be designed as heated probes. Often a symmetrical double probe

is considered to be less susceptible to rf-fluctuations, because it floats with the fluctuations [8] and therefore often no rf-compensation is used at double probe measurements in rf-plasmas [76]. Nevertheless sometimes an rf-compensation is employed [74,75]. The error in the electron temperature determination derived from a double probe characteristic measured in an atmospheric pressure discharge and using the evaluation valid for low pressure is less than 20 % [77].

A very short measurement of electron temperature and ion density is possible with a floating *triple probe* consisting of three identical probe tips [78,79] (plasma: Ar/hydrocarbons, layer: polymer, probe tips: wire loops heated directly prior measurement).

6.1.3.6.4 Other Probe Principles

With the *self-excited electron resonance spectroscopy* (SEERS) the volume averaged electron density and the electron to neutral collision rate in a cylindrical and strong asymmetrical rf-discharge at frequencies $f > 5$ MHz and pressures $p < 50$ Pa may be determined. The measured signal is a small part of the rf-discharge current detected with a sensor head mounted flat in the chamber wall made of the same material as the wall and therefore not disturb the technological process. Because an rf-current is measured there is no influence of polymer or other thin insulating layers on the measurement. The information about the plasma parameters is extracted from harmonics of the discharge current and a plasma physical model including the Maxwellian equations and the first three moments of the Boltzmann equation [80–82]. Some further probe principles applicable in chemically active plasmas are listed in [4,8,11].

6.1.3.7 Probe Measurements in Discharges Containing Negative Ions

Electronegative gases are used as isolators in high-voltage technology, for laser generation, and in most surface processing discharges. Negative ions in sometimes large concentrations n_- may occur in discharges containing NH₃, CH₄, SiH₄, O₂, H₂, halogens, or halocarbons [83]. Temperature and mass of positive and negative charge carriers become similar for $n_-/N_e \rightarrow \infty$ in electronegative plasmas. Thus also the absolute values of positive and negative saturation currents of a Langmuir probe characteristic become similar and floating and plasma potential coincide in this case [68,72]. At the other hand the result $n_+ > N_e$ where both n_+ and N_e are derived from the same characteristic do not always indicate the existence of negative ions because the positive ion density n_+ derived from the ion saturation current often is overestimated even in electropositive plasmas [11,14].

The relation $i_s \propto n_s(e_0|V - V_s|/2\pi m_s)^{1/2}$ for the current of particles of species s ($s = +, -, e$) is valid in thermal plasmas for a thin probe ($r_p/\lambda_D > 1$ with λ_D as the Debye length) at $e_0|V - V_s| \gg kT_e$ [72]. But it may be used also in nonthermal plasmas as a rough approximation [83,84]. Then the ratio $\alpha = n_-/N_e$ may be estimated in a quasi-neutral plasma ($n_+ = N_e + n_-$) as

$$\frac{n_-}{N_e} = \frac{(m_+/m_e)^{1/2} - (m_+/m_-)^{1/2}}{R - (m_+/m_-)^{1/2}} - 1, \quad (6.7)$$

where $R = (i_e + i_-)/i_+$ is the ratio of the negative $i_e + i_-$ to the positive i_+ particle current at the same absolute values of probe potential with respect to plasma

potential $V - V_s$. Remark: The term for α given in [83] is not correct. For a deeper analysis taking into account the change of the entrance velocity of the positive ions into the probe sheath at $V < V_s$ on replacing the electrons by negative ions look [72,85–87].

The evaluation described in Section 6.1.2, especially the determination of temperature and density of electrons according to (6.2) and (6.3), may be performed also at presence of negative ions if the thermal current i_{-0} of negative ions is much lower than the thermal electron current i_{e0} , that means at (V_- : temperature of negative ions in voltage units)

$$\frac{n_-}{N_e} \left(\frac{V_- m_e}{V_e m_-} \right)^{1/2} \ll 1. \quad (6.8)$$

The portions of negative ions and electrons may be separated sometimes in the second derivative of the probe characteristic and so temperature and density of negative ions may be determined directly [72,83,86,88]. But it has to made sure that no rf-distortion and probe contamination occur [61]. Assuming Maxwellian energy distribution functions for electrons and negative ions the ratio of the portions at $V = V_s$ is given by $i''_- / i''_e = i_{-0} / i_{e0} V_e^2 / V_-^2$ leading to

$$\frac{n_-}{N_e} = \left(\frac{i''_-}{i''_e} \right)_{V=V_s} \left(\frac{V_-}{V_e} \right)^{3/2} \left(\frac{m_-}{m_e} \right)^{1/2}. \quad (6.9)$$

The values of i''_- and i''_e at $V = V_s$ are obtained by extrapolation of the semi-logarithmic plots of the separated portions i''_- and i''_e to $V = V_s$.

An interesting method to get the negative ion density for $n_- < N_e$ was described in [89]. It is based on comparison of two probe characteristics, the first one taken in pure electropositive (Ar) plasma, the second one measured in electronegative (Ar/O₂) plasma. In [90] a more general approach of this method was given.

Langmuir probe independent methods to determine the negative ion density are mass spectrometry [83], photodetachment [83,84], and a method based on material etching by negative ions in reactive plasmas [91].

6.2 MICROWAVE INTERFEROMETRY

6.2.1 INTRODUCTION

Active probing with electromagnetic waves in the microwave range of frequencies allows for investigations with negligible perturbation, providing information about the plasma electron component. Wave plasma interaction can be manifold causing changes of amplitude, phase, or polarization state of the probing wave; the wave is being scattered and can completely be reflected. All interactions are being used for diagnostic purposes [92–96]. Interferometry, the oldest active microwave diagnostic, probes the dielectric properties of the plasma to determine the sightline integrated electron density [93,94]. The section describes in an elementary way the physics basis of the method and gives an overview of the interferometry techniques applied.

It should be mentioned that there are other microwave techniques successfully applied in chemically reactive plasmas like the microwave cavity resonator method not covered in this chapter [97]. The method makes use of the changes in resonance frequency and the resonator quality caused by the interaction of the microwave field with the plasma [98].

6.2.2 BASIC PRINCIPLE

Interferometry is based on comparing the phases of two waves of wave vector k and frequency ω , $E(z, t) = E_0 e^{i(kz - \omega t)}$, one traveling through the plasma the other one traveling along a reference path. Figure 6.4 gives the basic arrangement. The phase difference φ is determined by the optical path length difference ΔL_{opt} in units of wavelength λ , generally expressed by the line integrals of k along the reference and signal paths

$$\begin{aligned} \varphi = \varphi_{ref} - \varphi_{sig} &= 2\pi \frac{\delta L_{opt}}{\lambda} = \int_{L_{ref}} k_{ref} dz - \int_{L_{sig}} k_{sig} dz \\ &= \frac{\omega}{c} [L_{ref} - L_{sig}^{(out)}] - \int_{z_1}^{z_2} k_p(d) dz. \end{aligned} \quad (6.10)$$

In the last term free space propagation is considered outside the plasma along the reference L_{ref} , and the signal paths $L_{sig}^{(out)}$, $k_p(z)$ is the wave vector inside the plasma. For diagnostic applications the dispersion relation $k_p(\omega)$ for the plasma magnetized by a static field B can be derived with sufficient accuracy within the framework of the so-called magneto-ionic theory. Maxwell's equations are solved simultaneously with the equation of motion for the electrons under the following assumptions for the probing wave [99,100]

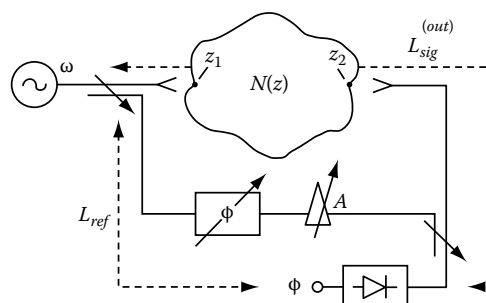


FIGURE 6.4 The Mach-Zehnder arrangement of an interferometer. A signal at frequency ω is split into two parts, one passing the plasma and the second serving as reference. They are combined at a diode acting as phase detector. The phase φ between the two signals is a measure of the line-integrated electron density through the plasma. (A: attenuator, Φ = phase shifter.)

- Electric field amplitude small that first-order perturbation theory can be applied.
- Angular frequency high that only electron, not ion acceleration needs to be considered.
- Phase velocity large compared to thermal plasma particle velocities.

With the refractive index $N_p = k_p c / \omega$, one finally gets the Appleton–Hartree equation $AN_p^4 - BN_p^2 + C = 0$, with $A, B, C = \text{constants}$, describing the plasma dispersion. The equation has two solutions for N_p^2 which describe the characteristic wave modes in a magnetized plasma. For wave propagation perpendicular to B , the characteristic modes are the linear polarized ordinary modes ($k_p \perp B, E \parallel B$), and extraordinary modes ($k_p \perp B, E \perp B$) and for propagation parallel B , the left- and right-hand circular polarized modes. Since the dispersion relations differ between these modes, the magnetized plasma is linear (Cotton–Mouton-effect) and circular (Faraday-effect) birefringent, a feature used in polarimetry techniques in particular in magnetic confinement fusion plasma diagnostics [96,101,102]. The ordinary-mode dispersion relation is identical to the dispersion relation of a nonmagnetized plasma $B = 0$. For convenience interferometry experimental arrangements use therefore ordinary mode-oriented sightlines. With ν the collision frequency and ω_{pe} the plasma frequency, the dispersion relation is

$$k_p^2 c^2 = \omega^2 - \frac{\omega_{pe}^2}{1 + (\nu/\omega)^2} + i \frac{\omega_{pe}^2 (\nu/\omega)}{1 + (\nu/\omega)^2} \quad (6.11)$$

with $\omega_{pe}^2 = N_e e^2 / (m_e \epsilon_0)$.

In case collisions can be neglected $\nu \ll \omega$, the imaginary part giving rise to wave attenuation disappears resulting in $k_p^2 c^2 = \omega^2 - \omega_{pe}^2$. The plasma dispersion under the simplifying assumptions given before is solely governed by the electron density through ω_{pe} . Propagation is possible for $\omega > \omega_{pe}$, for $\omega < \omega_{pe}$ the wave is exponentially damped. Considering explicitly the electron density dependency along z , the phase difference as defined in (6.10) then becomes

$$\begin{aligned} \varphi &= \frac{\omega}{c} \left[L_{\text{ref}} - L_{\text{sig}}^{(\text{out})} - \int_{z_1}^{z_2} \sqrt{1 - \left(\frac{\omega_{pe}(z)}{\omega} \right)^2} dz \right] \\ &\approx \frac{\omega}{c} \left[L_{\text{ref}} - (L_{\text{sig}}^{(\text{out})} + (z_2 - z_1)) + \frac{1}{2\omega^2} \int_{z_1}^{z_2} \omega_{pe}^2(z) dz \right]. \end{aligned} \quad (6.12)$$

In the second part of the equation the probing frequency has been chosen large compared to the plasma frequency. If the geometrical path length difference is made zero, φ becomes

$$\varphi = \frac{1}{2c\omega} \frac{e^2}{\epsilon_0 m_e} \int_{z_1}^{z_2} N_e(z) dz = \frac{1}{\omega} 5.303 \cdot 10^{-6} \int_{z_1}^{z_2} N_e(z) dz. \quad (6.13)$$

The integral on the right-hand side is the so-called line-integrated density or simply the line density, the quantity aimed at. If φ has been measured, the line density can readily be evaluated from (6.13). The approximation is usable for $\omega/\omega_{pe} \geq 2$.

To gain local information $N_e(r)$ a number of sightlines through the plasma and model assumptions on the density distribution are necessary. In case of circular density distribution Abel inversion on the basis of multi sightline measurements is possible [94,103].

6.2.3 EXPERIMENTAL ARRANGEMENTS

6.2.3.1 Mach–Zehnder Interferometer

The basic microwave interferometer in Mach–Zehnder arrangement is given in Figure 6.4. The signal generated by a microwave source with angular frequency ω is launched into the plasma with a horn antenna and collected with another one then guided to the phase meter. The reference path is generated by splitting and combining a part of the signal with the aid of directional couplers, guiding it along a path of equal length to the phase detector as well. Using in this basic arrangement a detector diode as the simplest phase meter, the combined microwave signal and reference amplitudes at the diode $V_D = A_S \cos(\omega t - \varphi) + A_R \cos \omega t$, are mixed by the quadratic term of the diodes $I - V$ characteristic $I_D = a_0 + a_1 V_D + a_2 V_D^2 + \dots$, to give a dc diode current component proportional to $A_S A_R \cos \varphi$ from which the phase can basically be determined [93,103,105]. Phase and amplitude adjustments for maximum phase sensitivity can be made in the reference path. The phase measurement is improved by introducing another diode detector with the reference signal shifted by 90° to generate a dc diode current proportional to $A_S A_R \sin \varphi$. From $\cos \varphi$ and $\sin \varphi$, the phase φ can uniquely be determined [106–109].

6.2.3.2 Heterodyne Interferometer

Direct phase measurement is possible by operating the probing and the reference path at slightly different frequencies after mixing the two as shown in Figure 6.5.

The signal $A_S \cos(\omega t - \varphi)$ carrying the phase information as introduced by the plasma is mixed with the reference signal $A_R \cos \omega_2 t$ in a microwave mixer M_S generating the intermediate frequency (IF) signal $A_{IF} \cos(\omega_{IF} t - \varphi)$ at frequency $\omega_{IF} = \omega_1 - \omega_2$ [105,110,111]. The mixing process is phase preserving. The phase shift φ introduced at the signal frequency ω_1 by the plasma transit is transferred to the intermediate frequency. Typically the IF frequency is chosen in the range of several tens of MHz that standard radio frequency techniques can be applied for accurate phase measurements (see below). The reference for the phase measurement is generated by directly mixing the signals of the two oscillators at ω_1 and ω_2 in reference mixer M_R . In the mm-wave range at probing frequencies of the order of 100 GHz, the two separate oscillators are typically locked to each other in a so-called phase locked loop (PLL) using a stable quartz oscillator at difference frequency ω_{IF} as the reference, to keep the difference frequency constant. The offset signal at ω_2 can also be derived from the probing oscillator signal at ω_1 introducing the frequency shift by applying single sideband modulation (SSBM) techniques [111], or by introducing it as a Doppler shift with the classical Veron-wheel [103,112,113].

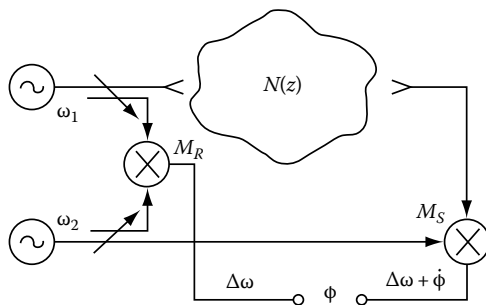


FIGURE 6.5 The heterodyne version of a Mach–Zehnder interferometer. The frequencies of plasma probing and reference beams differ by the intermediate frequency $\Delta\omega$. Mixing probing and reference signals in mixer M_R and after passing the plasma in M_S , signals at the difference frequency $\Delta\omega$ are generated where phase measurement can easily be conducted. Since the mixing process is phase preserving, the phase ϕ introduced by the plasma is present at $\Delta\omega$ too.

6.2.4 EXPERIMENTAL CONDITIONS

6.2.4.1 Probing Frequency and Frequency Stability

The choice of probing frequency is subject to various limitations. On one hand it must be high enough that the wave can propagate even at the highest densities expected $\omega > \omega_{pe}$. Density gradients eventually present perpendicular to the wave propagation direction give rise to refraction changing the beam path length and leading to misinterpretations of the measured phase shift. Refraction might also cause power losses at the receiving antenna. Increasing the probing frequency reduces both effects. In high-density plasmas therefore far infrared (FIR) and infrared laser (IR) are used [96]. On the other hand, according to (6.13), increasing the frequency reduces the phase sensitivity. In addition the sensitivity of the interferometer to fluctuations $\delta\omega$ of the probing frequency (jitter and drift) increases. Short-term frequency fluctuations much smaller than the probing frequency are considered $\delta\omega \ll \omega$ [114]. In case signal and reference paths are adjusted to equal length $\Delta L = 0$, the phase difference is solely determined by the plasma (6.13). The phase fluctuations are minimal $\delta\varphi = \varphi(\delta\omega/\omega)$. At finite ΔL , an additional contribution is present $\delta\varphi = (\Delta L/c)\delta\omega$, which can cause large errors since the phase contribution caused by the path length difference ΔL can be much larger than the optical path length change introduced by the plasma, $\Delta L > \int_{z_1}^{z_2} (\omega_{pe}^2/\omega^2) dz$. In case waveguides are used in signal and reference paths, the waveguide dispersion must be considered too, modifying the L -terms of (6.12) by a factor $\sqrt{1 - (\omega_c/\omega)^2}$, with the cutoff frequency of the waveguide.

Since improving the source frequency stability is the direct approach to reducing $\delta\varphi$, modern microwave interferometers operate with highly stable signal generators [115]. The stability is obtained by phase locking the microwave source to stable quartz oscillators, as shown in Figure 6.6. The measure results in a short term frequency stability of better 10^{-8} . This measure makes $\Delta L = 0$ path length adjustment [116] completely dispensable [117].

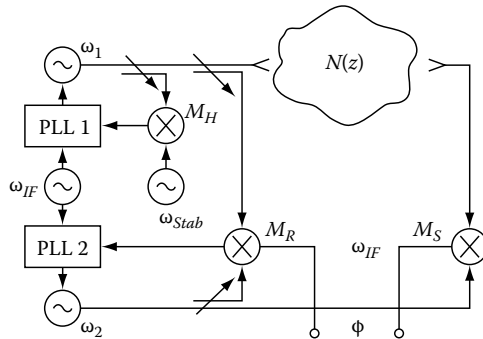


FIGURE 6.6 To obtain highest frequency stability in a heterodyne interferometer, both the difference frequency ω_{IF} of probing and reference signals and the probing frequency ω_1 are phase locked to highly stable quartz oscillators at frequencies ω_{IF} and ω_{stab} . The difference frequency generated in mixer M_R is compared in the PLL 2 circuit with a quartz oscillator at ω_{IF} resulting in a control signal which acts on the reference source at ω_2 in such a way that the difference frequency is phase locked to the ω_{IF} source. To keep the probing frequency ω_1 constant, the signal is mixed in M_H with a high harmonic (typically $n = 10$) of a stable source in the 10 GHz range. The difference frequency is phase locked with the aid of PLL 1 to the quartz oscillator as well, controlling source at ω_1 in such a way that $\omega_1 - n\omega_{stab} = \omega_{IF}$ is kept constant. (From Vowinkel, B., Private communication.)

6.2.4.2 Path Length Variations

In a similar way as frequency variations, path length variations δL cause phase fluctuations $\delta\varphi = (\omega/c)\delta L$, a contribution often difficult to quantify in the phase data interpretation. The mechanical movements and vibrations of beam guiding elements in particular those inside the plasma vessels are difficult to avoid. A way out is to probe the plasma with two separate waves of different frequency ω_1 and ω_2 , traveling along identical paths. In this *two-color interferometer* according to (6.13) each wave experiences a different phase shift $\varphi_{1,2}$, the common vibration error can be canceled. Let $\Phi_{1,2}$ be the two measured phases of the two separate interferometers $\Phi_{1,2} = \varphi_{1,2} + (\omega_{1,2}/c)\delta L$, the line density can be evaluated from

$$\int_{z_1}^{z_2} N_e(z) dz = \frac{1}{5.303 \cdot 10^{-6}} \frac{\omega_1 \omega_2^2 \Phi_1 - \omega_1^2 \omega_2 \Phi_2}{\omega_2^2 - \omega_1^2}. \quad (6.14)$$

The two sources at frequency ω_1 and ω_2 can be completely independent. The phases need to be measured separately with two phase meters. In the so-called *2ω- or dispersion interferometer* [118,119], the second signal is generated by frequency doubling from the first $\omega_2 = 2\omega_1$. The plasma is probed simultaneously at identical paths with signals at ω_1 and $2\omega_1$ giving rise to phase shifts $\varphi_1(\omega_1)$ and $\varphi_2(2\omega_1)$. After the plasma passage a second frequency doubler is used to generate the second harmonic of the probing signal at ω_1 , too. Both signals now have the same frequency

but different phases. They interfere at the power detector. The phase difference is given by

$$\Delta\varphi = 2\varphi_1(\omega_1) - \varphi_2(2\omega_1) = \int_{z_1}^{z_2} [2k_p(\omega) - k_p(2\omega)] dz. \quad (6.15)$$

It does not contain any path length and is insensitive to length variations. Phase fluctuations from length variations cancel at the detector and need not to be measured as necessary in the two-color interferometer. While mainly applied at high probing frequencies in the FIR and IR with laser interferometers [116], the basic two-color interferometer method is also applied at mm wavelengths [118].

6.2.4.3 Steady State Operation

Under long plasma pulse and steady state conditions high stability of the interferometer system is required. Phase changes are measured only during the plasma buildup and can reach many multiples of 2π . Interruption of the signal path destroys the information. Recovery is only possible at fixed probing frequency for plasma phase shift within $-2\pi \leq \varphi \leq 2\pi$. By varying the probing frequency, however, the line density can be determined in plasma columns existing prior to the interferometer operation.

Referring to (6.10), the frequency variation with rate $\partial\omega/\partial t$ introduces a phase variation or beat frequency, respectively, given by

$$\frac{\partial\varphi}{\partial t} = \frac{\partial\omega}{\partial t} \left[\Delta L \frac{\partial k}{\partial \omega} + \int_{z_1}^{z_2} \frac{\partial k_p}{\partial \omega} dz \right], \quad (6.16)$$

where ΔL is as before the net difference in waveguide length between the plasma and the reference paths. The frequency is swept at constant rate giving rise to a constant beat frequency. All information on plasma density is contained in the change of the beat frequency, compared to the vacuum case, from which the line density can be determined [121].

6.2.4.4 Components

To measure the phase shift φ of the probing wave the IF section of the interferometer contains a phase measuring device. At probing frequencies in the 100 GHz range of frequencies φ typically exceeds multiples of 2π which the phase meter must be able to handle. Electronic circuits exist separating the ranges $-2\pi \leq \varphi \leq 2\pi$ and counting multiples of 2π . It is especially important that during rapid changes the phase meter is able to follow to avoid so-called fringe losses, errors in counting multiples of 2π [122,123]. The temporal resolution τ of the interferometer is generally limited by the IF frequency $\tau > 2\pi/\omega_{IF}$. For a given rate of phase change $\Delta\varphi/\Delta t$ the IF bandwidth around ω_{IF} needs to have at least a bandwidth of [111]: $\Delta\omega_{IF} = \Delta\varphi/\Delta t$. As signal sources different types can be used

1. Sources including active semiconductor elements such as Gunn diodes or IMPATT (impact ionization avalanche transit time diode) elements.

- To increase frequency the output frequency of these devices might be doubled or tripled by driving further nonlinear solid-state elements.
2. Electron tube sources such as BWOs (backward wave oscillator), cyclotrons or klystrons.
 3. Electrically or optically pumped gas lasers.

Semiconductor and electron tube sources are tunable in a range of at least a few GHz. Therefore an offset of several GHz can readily be achieved making them especially suitable for heterodyne systems with PLL circuits for high-frequency stability [105,117].

6.2.5 WAVE TRANSMISSION

The probing wave must be guided from the source to the plasma and to the detector, antennas providing the interface between guided and free-space propagation at the plasma column. The antennas used in plasma diagnostics are typically aperture antennas whose size determines the beam pattern. They are designed to provide narrow beam width of about (10–20)°. The radiating structures are horns which are flared sections of a waveguide to meet the free space characteristic impedance. Lenses can be used to transform the divergent wave front of the horn into a plane wave or conversely focus a plane wave to approximately a point. Alternatively elliptical reflectors are used to reconcentrate power from one focal point of the ellipsoid where the feed horn is mounted to the other focal point. They are the standard focusing elements in quasi-optical systems (Gaussian optics) which can be used with advantage to form slim beams through the plasma [103,117,124,125]. The angular resolution or the spot size obtained are limited by the wave nature of the radiation. At millimeter wavelengths beam diameters are of the order of 1 cm.

In case distances are short between the source and the plasma, standard fundamental mode waveguides can be used. For larger distances oversized waveguides are used instead to avoid resistive losses which for mm waves are typically 5 dB per meter. Oversized waveguides have diameters at least 10 times the wavelength. Taper sections are needed to connect them reflection free to standard size waveguides.

6.2.6 FINAL REMARKS

The aim of this chapter on microwave interferometry was to make the reader familiar with one of the most important plasma diagnostic system to determine the line-integrated electron density. The basic physics behind was briefly reviewed and an overview was given of the various types of mm-wave interferometers in use. The experimental difficulties have been discussed and ways out have been shown. The main microwave components are reviewed very briefly. References are included where special designs are discussed in detail demonstrating the large variety of possibilities of experimental realization.

6.3 EMISSION AND ABSORPTION SPECTROSCOPY

6.3.1 INTRODUCTION

The investigation and understanding of plasma chemistry and physics requires detailed knowledge of plasma parameters, which can best be obtained by appropriate in-situ diagnostic techniques. The need for a better understanding of plasma physics and chemistry has stimulated the improvement of established diagnostic techniques and the introduction of new ones. Over the past decade, several new techniques have been successfully introduced, in particular for diagnostic studies of chemically reactive plasmas in which many short lived and stable species are produced. It has been possible to determine absolute concentrations of ground states using spectroscopy thereby providing a link with chemical modeling of the plasma. Another essential component needed to reach the objective of improved knowledge of molecular phenomena is to determine physical parameters of the plasma by an appropriate experimental methodology. In addition to an increasing extent the interaction of reactive species like atomic or molecular radicals with a surface is being studied.

Methods based on traditional spectroscopy have become amongst the most important in this field. The main goal of this chapter is to focus on the spectroscopic techniques for plasma diagnostics. The majority of molecular plasmas are characterized by high chemical reactivity due to the large concentrations of transient or stable chemically active species present. Noninvasive diagnostic methods have been developed for investigating this type of plasma, particularly optical emission spectroscopy (OES) and absorption spectroscopy (AS) with which this chapter is concerned. Methods based on OES and AS not only make use of resolved, discrete spectral lines (line positions and line profiles) but also of continuous spectral features. Since light emission is an inevitable consequence of the existence of a plasma it should be considered as a naturally (noninvasive) source of information for diagnostic purposes. When illuminated by low-intensity light the probing of plasmas by absorption spectroscopy can also be considered as noninvasive. Emission and absorption spectroscopy provide information about atom, molecule, including radical and ion densities in excited and ground states, as well as about gas, rotational, and vibrational temperatures. High temporal resolution can be achieved, while spatial resolution requires specific optical geometries and techniques, since OES and AS provide integrated emission or absorption intensities along the line of sight only.

6.3.2 INSTRUMENTAL TECHNIQUES

Electromagnetic radiation is emitted from low-temperature plasmas over a wide spectral frequency range extending from the vacuum ultraviolet (VUV) or even shorter wavelengths, through the ultraviolet and visible regions and out to the near, middle, and far-infrared. Modern OES spectrometers for detecting the radiation from molecular low-temperature gas discharges feature high spectral resolution (up to picometers), sensitivity near the single photon detection limit, and time resolution as short as nanoseconds. Surveys of the most important emission spectroscopy techniques and the principles of spectral photometry can be found in many different publications [126–131]. Signal recovery with CCD detectors has the advantage of

direct manipulation of digital data, simultaneous detection across a specific spectral window, high sensitivity and a dynamic range of the order of 10^5 . A wide variety of light sources, dispersive elements, detectors and data acquisition methods can be used for absorption spectroscopy [130]. The classic dispersion experiment for measuring the density of atomic or molecular states in a plasma by absorption spectroscopy uses a continuous light source in combination with a narrow bandwidth frequency filter, e.g., a spectrograph, with a detector suitable for the spectral range under investigation. The Fourier Transform Infrared (FTIR) technique uses a Michelson interferometer setup. The intensity depends on the (variable) optical path difference between the mirrors in the two arms of the interferometer. While one mirror is fixed the other is moved continuously between identical path length (maximum signal) and a shifted path length of $\lambda/2$ (zero signal). The inverse transform yields an absorption spectrum in the frequency domain. In contrast to dispersion techniques the FTIR spectrometer records the whole spectrum simultaneously (multiplex or Fellgett advantage). In principle the resolution of FTIR can be as high as 0.002 cm^{-1} , determined by the distance scanned by the moveable mirror, but at the expense of time resolution. Fractional absorptions as small as 10^{-4} can be measured.

The current development of tunable, narrow band light sources, such as tunable dye lasers, infrared diode lasers, or quantum cascade lasers, has led to their substitution as continuous light sources in AS experiments. These laser sources have the advantage of high spectral intensity, narrow bandwidth, and continuous tunability over the absorption line profile. Figure 6.7 shows an example of an experimental arrangement used to investigate the plasma chemistry and kinetics in a planar microwave

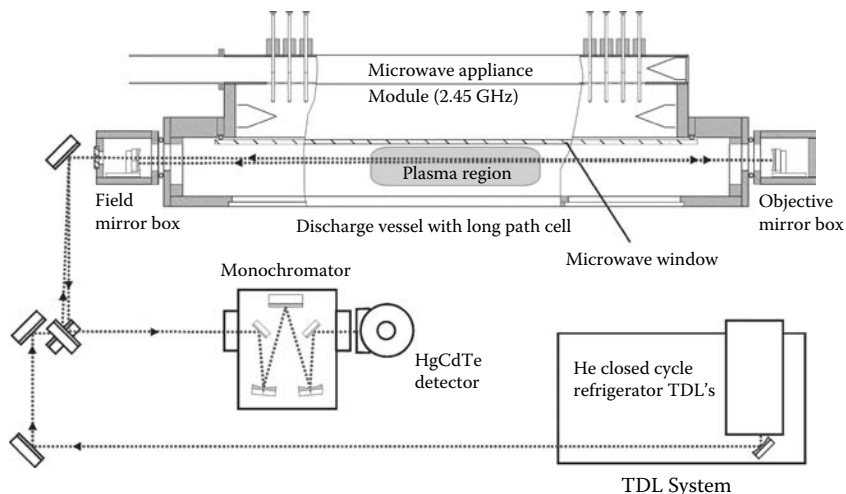


FIGURE 6.7 Experimental arrangement of a planar microwave plasma reactor (side view) with White cell multiple pass optical arrangements, and tunable diode laser (TDL) infrared source used for hydrocarbon (CH_4 , CH_3OH) plasma diagnostics. The path of the diode laser beam is indicated by dotted lines. (From Hempel, F. et al., *Plasma Source. Sci. Technol.*, 12, 598, 2003.)

reactor [132], in which a tunable diode laser (TDL) spectrometer [133] is combined with a White cell multiple pass optical arrangement to increase the absorption length and the sensitivity of the AS spectrometer [134,135]. The discharge configuration in planar microwave plasmas has the advantage of being well suited for end-on observations because considerable homogeneity can be achieved over relatively long plasma path lengths. The combination of the plasma source with the multiple pass optics of the White design provides the opportunity to use more than two passes through the chamber. The White geometry with two objective mirrors and one field mirror, allows different path lengths from 4 to 40 passes, (or more), through the plasma. The diode laser light beam enters and leaves the chamber through a KBr window and after passing through the plasma reactor is sent to a monochromator, which is necessary for mode selection and to block the broad band infrared emission from the discharge, before detection with a mercury cadmium telluride (HgCdTe) detector. Further improvements could be achieved by using long path cells with astigmatic optics instead of the White cell configuration.

Alternatively tunable infrared radiation can be generated using difference frequency mixing or optical parametric oscillators (OPO). Although in the past these systems had the disadvantage of rather low radiation power and were restricted to specific wavelength regions [136,137] new technical developments have led to solutions which provide up to a mW of single mode power and tunability of up to 100 cm^{-1} [138,139].

Cavity ring-down spectroscopy (CRDS) is another high-sensitivity laser absorption technique [140]. This method is based on the measurement of the intensity decay rate of a short laser pulse injected into an optical cavity formed by two very highly reflective mirrors which may also enclose the plasma. For each reflection of the laser pulse, a small fraction (depending on the reflectivity of the mirrors forming the cavity) leaks through one of the mirrors. Therefore, the light intensity detected outside the cavity decays incrementally with time to zero. Since the laser pulse is trapped in the cavity for many thousands of round trips, absorption path lengths in the kilometers range can be easily achieved, and absorptions as low as 10^{-9} can be measured with an acceptable signal-to-noise ratio [141,142]. In the visible spectral range CRD spectroscopy has been applied for density measurements of the SiH_2 radical and of nanometer-sized dust particles in silane plasmas [143] as well as for detecting N_2^+ ions in nitrogen discharges [144]. Near- and mid-infrared tunable diode lasers have been used as the light sources for CRD spectroscopy [145–148]. The recent development and commercial availability of quantum cascade lasers (QCL) offers an attractive new option for infrared absorption spectroscopy in the mid-infrared range (MIR). Recently, the potential application of pulsed and cw QCLs, as easily tunable MIR light sources, combined with cavity enhanced methods, like pulsed CRDS and cavity-enhanced absorption spectroscopy (CEAS), has been established [149].

As well as the implementation of innovative techniques like CRDS, the performance of the spectrometers used in plasma diagnostics have been greatly enhanced by improved technology. The introduction of CCD cameras, holographic gratings, tunable sources, and microprocessor instrument control and data collection are a few examples of the experimental innovations, which have become commercially available within the last decade.

Molecular plasmas are increasingly being used not only for basic research but also, due to their favorable properties, for materials processing technology. These fields of application have stimulated the development of infrared spectroscopic techniques for industrial applications. In order to exploit the capabilities of infrared TDLAS for effective and reliable online plasma diagnostics and process control in research and industry, compact and transportable tunable infrared multicomponent acquisition systems (IRMA, TOBI) have been developed [150,151]. These systems are mainly focused on

1. High speed detection of stable and transient molecular species in plasmas under non-stationary state excitation conditions
2. Sensitive (sub-ppb) trace gas detection with the aid of multi-pass absorption cells

The main disadvantage of TDLAS systems using lead salt diode lasers is the necessary cryogenic cooling of the lasers (and also of the detectors), since they operate at temperatures below 100 K. Systems based upon lead salt diode lasers are therefore typically large in size and require closed cycle refrigerators and/or cryogens like liquid nitrogen. Compared to lead salt lasers, QCLs allow the realization of very compact mid-infrared sources characterized by narrow line width combined with single-frequency operation and considerably higher power values, i.e., of tens of mW. The output power is sufficient to combine them with thermoelectrically cooled infrared detectors, which permits a decrease of the apparatus size and presents a new opportunity to design compact liquid nitrogen-free mid-IR spectroscopic systems. These positive features of quantum cascade laser absorption spectroscopy (QCLAS) can open up new fields of application in research and industry, including studies of gases in atmospheric, environmental, and plasma chemistry but also for in-situ control of industrial plasma processes.

Recently a compact quantum cascade laser measurement and control system (Q-MACS) has been developed for time-resolved plasma diagnostics, process control, and trace gas monitoring. The Q-MACS system contains a tunable quantum cascade laser which can be directed through a plasma or into a multipass cell for exhaust gas detection. Rapid scan software with real-time line shape fitting provides a time resolution of up to 100 ns for studying the kinetic processes of infrared active compounds in plasmas or gases. The Q-MACS-Basic system has been designed as a platform for various applications of QCLAS [135,152].

6.3.3 EMISSION SPECTROSCOPY

6.3.3.1 General Considerations

In low-temperature molecular plasmas a variety of processes, such as electron collisions, ion-molecule reactions, charge exchange and chemical reactions, lead to a large number of atoms, molecules, radicals, and ions in many different excited states. The generation of photons is mainly governed by the de-excitation of these species. Provided the influence of self-absorption inside the plasma is relatively small or negligible (referred to as optically thin plasma conditions) the emitted photons can be

detected outside the plasma. Even if self-absorption does occur, the spectral distribution of the emitted light still carries information on the plasma conditions. It contains information about the different kinds of plasma species, their number density and temperature, as well as about the strengths of internal or external electric fields.

The intensity of the spontaneous emission from molecules can be expressed as the number of photons emitted by a unit volume per second over all solid angles. The intensity of a spectral line from the $n', \nu', N' \rightarrow n'', \nu'', N''$ rovibronic (rotational vibrational electronic) transition may be written as

$$I_{n''\nu''N''}^{n'\nu'N'} = N_{n'\nu'N'} A_{n''\nu''N''}^{n'\nu'N'}, \quad (6.17)$$

where

- n are the quantum numbers describing an electronic state of the molecule
- ν and N are the corresponding vibrational and rotational quantum numbers, respectively

By convention the initial state is denoted by primes and the final state by double primes. $N_{n'\nu'N'}$ is the population density of the initial rovibronic level and A the corresponding transition probability for spontaneous emission.

A plasma diagnostic technique based on emission spectroscopy has the characteristics of an inverse problem. Usually, integral intensities of emission lines in the line of sight are measured within a solid angle with a certain spectral resolution. A local value of the intensity can be determined only if the plasma under investigation is homogeneous over the solid angle. Otherwise theoretical inversion methods have to be applied, such as Abel inversion in the case of cylindrical or spherical symmetry, or tomography. Measurements of spectrally, spatiotemporally, and phase-resolved emission of statistically generated discharges succeeded by the technique of cross correlation spectroscopy (CCS) [154]. The main advantage of this method is its high sensitivity (single photon counting) combined with a resolution in the sub-nanosecond and sub-millimeter range. On the basis of the measured spatiotemporally emission structure and a suitable modeling, conclusions are possible on the chemistry as well as on electrical fields and density of electron gas. Above all, the CCS was applied to study the microdischarges of dielectric barrier discharges in air at atmospheric pressure. This is illustrated in Section 8.1.1 on ozone generation. Other emission spectroscopic methods are successfully applied for determination of electron energy distribution function and electron density, also [155–157].

Gans et al. [156] determined the electron energy distribution function in a H₂ capacitively coupled 13.56 MHz discharge at 148 Pa time and space resolved (<5 ns, 0.5 mm) by using an analytical model of the excitation population dynamics and spectroscopic measurements of the excited state population of admixed rare gas atoms with known data for excitation and de-excitation processes, as excitation cross sections, cascading contributions from higher electronic states.

Measurements of Stark broadening of spectral lines can be used for determination of electron densities. This broadening is caused by a local perturbation of the electric field and therefore determined by the electron density N_e . The theory of Stark broadening is mostly developed for hydrogen atoms [158,159]. The half width $\Delta\lambda_s$

expressed in wavelength is equal to

$$\Delta\lambda_S = C^{-3/2} (N_e, T_e) N_e^{2/3}. \quad (6.18)$$

The broadening factor C shows only a weak dependence on electron density and temperature. The error for the determination of N_e is given to be 15%–20%. The application of atomic hydrogen lines is recommended for the measuring of electron density. The application of the Stark broadening requires the separation of other line broadening effects in the plasmas under study as instrumental broadening, Doppler broadening, and resonance broadening.

The measured, spatially localized line emission intensities allow the calculation of the population densities of the electronic or rovibronic levels of the species, provided transition probabilities are known and calibration of the spectrometer functions has been performed. The calculation of species densities in the *ground* state from measured line intensities is often also an inverse problem. It requires a theoretical model for the excitation and de-excitation processes, and knowledge of all necessary cross sections, transition probabilities and the electron energy distribution function (EEDF). These requirements are often nontrivial to achieve and in practice an easier approach is to use actinometry, described in the following section, in which the emission intensity is referenced to a known standard.

6.3.3.2 Concentration Measurements

6.3.3.2.1 Actinometry

Actinometry is an emission spectroscopy method, which offers the possibility of determining relative concentrations of ground state species from emission intensity measurements [160,161]. This technique requires the introduction of a selected gas as a minor impurity, an actinomer, into the feed gas stream. Typically a rare gas like argon is used. The actinomer indicates changes in the electron density or energy and is used for normalizing the emission intensity shown by the species of interest [162]. If actinometry is valid, then the emission intensity of the species of interest I_{spe} over the intensity of an emission line of the admixed actinomer I_{act} is proportional to the electronic ground state relative concentration n_{spe} , provided that the concentration n_{act} of the actinomer is known

$$n_{spe} = K n_{act} \frac{I_{spe}}{I_{act}}. \quad (6.19)$$

The factor K contains the spectral and geometrical factors of the detection system and the emission cross sections of the observed transitions. Clearly unless the factor K in (6.19) can be evaluated absolutely then the calculated n_{spe} values are only relative ones. The main conditions to be fulfilled to ensure valid actinometric measurements are

1. Excitation of emitting states of the species of interest and of the actinomer only by direct electron impact from their ground states
2. De-excitation by spontaneous emission
3. Similarity of the threshold $U_{thres\ act} = U_{thres\ targ}$ and shape of the electron-impact cross sections of both actinomer and target species

Recently a novel approach, two-gas actinometry (TGA) has been described [163]. A second actinomer gas was used to take into account dissociative excitation in processing plasmas. This method was employed to measure the degree of dissociation in an inductively coupled rf hydrogen plasma.

The applications of actinometry in plasma diagnostics are too numerous to mention here so only a few representative examples will be cited. Actinometry was developed to investigate the dissociation of CF_4 in many different types of discharge and to measure the dependence on discharge parameters, such as pressure and flow rate, of the density of atomic fluorine generated [164–168]. In several cases it has been combined with other diagnostic techniques like infrared absorption spectroscopy [169] or laser-induced fluorescence [170]. Within the last few decades actinometry has been developed from a steady state technique in CF_4 plasmas to a flexible dynamic method in a variety of different molecular systems and discharge types with the potential for spatial and time-resolved measurements. Like other diagnostic techniques actinometry is at its most powerful when it is combined with other plasma diagnostic techniques such as mass spectrometry, coherent anti Stokes Raman scattering (CARS), laser-induced fluorescence (LIF) or tunable diode laser absorption spectroscopy (TDLAS), and also with kinetic modeling.

6.3.3.2.2 Intensity Ratios of Resonance Multiplet Lines

Recently a new method to determine the concentration of B, Al, Si, Sc, Ti, V, Co, Ni, and Ga atoms in nonthermal plasmas using the intensity ratio of atomic lines has been proposed [171–173]. This method allows measuring the *absolute* particle densities of ground state atoms from *relative* intensities within resonance multiplets with the same upper level distorted by self-absorption. In the case of Boltzmann distribution over the sublevels of the ground state with the temperature T , the intensity ratio depends on the temperature T and the product NL , where N is the total population of the ground state and L the length of absorption, and is usually close to the atomic particle density. Hence, to determine the concentration N by using only one resonance doublet one has to know the temperature T . The common use of several doublets or a resonance multiplet allows not only the simultaneous and purely spectroscopic determination of the N and T values simultaneously, but also enables internal testing of the applicability of the method.

6.3.3.3 Temperature Measurements

Excited and ground state particles (atoms, ions, molecules, etc.) are characterized by their densities and velocity distribution functions, which may not be the same for different states and species in non-equilibrium plasmas. Distribution functions may also be introduced for describing populations of various excited states. The conventional concept of temperature is only valid if a Maxwell–Boltzmann situation applies (local thermodynamic equilibrium). This is often not the case for low-pressure plasma and so the idea of temperature may not be meaningful or the values should be considered as effective quantities only—characteristic of the average energy. In the literature (especially in application oriented work) one finds reference to many different effective temperatures, namely: *Gas* (also called *translational* or *kinetic*), *rotational*, *vibrational*, and even the *excitation* temperature of certain groups of

excited atomic levels. Hence in non-equilibrium plasmas the concept of temperature may have a certain physical meaning, but often it is rather artificial.

6.3.3.3.1 Translational Temperature

The gas (kinetic) temperature T is a very important plasma parameter, since the rate coefficients of chemical reactions usually show an exponential increase with T . On the other hand, even in a monoatomic gas the plasma density distribution cannot be calculated without knowledge of the temperature distribution. Determination of the gas temperature or attempts to do that by emission and absorption spectroscopy are rather common in plasma diagnostics [174–196]. A measurement of the Doppler broadening of spectral lines is a well known and widely used method of temperature determination in gas discharge plasmas [128,129]. For a single spectral line the full width half maximum (FWHM) of the Doppler profile is

$$\Delta\lambda_d = \sqrt{\frac{8kT \ln 2}{mc^2}} \lambda_m, \quad (6.20)$$

where

$\Delta\lambda_d$ [nm] is the FWHM of the Gaussian line profile

T [K] is the neutral gas temperature

m [kg] is the particle mass

λ_m [nm] is the wavelength at line center

One can see that for plasma diagnostics it is better to use lines with longer wavelengths emitted by lighter species. It should be noted that implementation of the method is not that simple in practice. The main problems are

1. The determination of the instrumental function of the spectrometer
2. Taking into account the multiplet and fine structure of lines
3. Extraction of the Doppler broadening contribution from the measured line profile (so-called deconvolution)

Moreover, in non-equilibrium molecular plasmas the velocity spectra of excited and ground state species can be different. Nevertheless, the determination of translational temperatures from Doppler broadening of atomic and molecular hydrogen lines is often used in non-equilibrium plasmas [176,180,182,186,189,191]. In the case of H_{alpha} and D_{alpha} spectral lines, which are of special importance, it is necessary to take into account their fine structure [194].

6.3.3.3.2 Rotational Temperature

When the populations of rotational levels in excited vibronic states n', v' are close to a Boltzmann distribution, the rotational temperature $T_{rot}(n', v')$ for this state is given by

$$N_{n'v'N'} = c_{n'v'} g_{a,s} (2N' + 1) \exp \left(-\frac{hcE_{n'v'N'}}{kT_{rot}(n', v')} \right), \quad (6.21)$$

where

$c_{n'v'}$ is a normalizing constant

$g_{a,s}$ is the nuclear spin degeneracy of the $n'v'N'$ level ($g_{a,s} = 1$ for heteronuclear diatomics)

$E_{n'v'N'}$ is the term value [cm^{-1}]

h, c, k are universal constants

The rotational temperatures have definite physical meaning if the time of rotational relaxation in a certain vibronic state is much smaller than the mean lifetime of the rotational levels. In this case the rotational distribution of the populations is close to a Boltzmann distribution, with the temperature $T_{rot}(n', v')$ equal to the translational temperature T of the colliding particles (assuming they have a Maxwell velocity distribution).

Non-equilibrium population distributions over rotational levels of excited electronic states of molecules have often been observed in gaseous discharge plasmas and in flames [177,179,191,192,197]. Their characteristic feature is a large excess of population in higher rotational levels. Such a non-Boltzmann behavior of the populations should be taken into account in the determination of gas temperature from the low energy part of the distributions (a detailed analysis of various mechanisms responsible for the effect can be found elsewhere [187,189]).

In low-pressure plasmas the radiative lifetimes of rotational levels in excited vibronic states are often much smaller than those of the rotational relaxation in the specified excited vibronic states. If this is the case the rotational population distributions [187–190] as well as the corresponding rotational temperatures [177,182] in the ground and excited vibronic states can be related in the framework of specific kinetic models. The simplest is the so-called corona-like model which is based on the assumption of dominant, direct, electron impact excitation and spontaneous decay of rovibronic levels [182,187–190]. In this case the measurement of an intensity distribution of the rotational structure of emission bands may be used for the determination of the ground state rotational temperature, which is often close to the gas temperature [177,178,188,189,192,194,197–199].

In the case of unresolved or partly resolved rotational structure the band shape has to be calculated theoretically and compared with experimental values to derive information about temperature. Many papers describe how nitrogen band emission spectra can be used to determine temperature in low-pressure discharges [179]. Also at higher pressures such as in barrier discharges, rotational temperatures have been derived from N_2 band shapes [186]. Stalder and Sharpless [184] compared experimental and calculated spectral emission of C_2 Swan band transitions to estimate the temperature in H_2 – CH_4 plasmas used for thin diamond film deposition.

The possibility of determining the gas temperature from the measured rotational intensity distributions is directly connected with the applicability of specific theoretical models to the plasma under study. The rates of the required elementary processes are, as a rule, not known. Therefore, it is not possible even to estimate the applicability *a priori*. So in each particular case it is necessary to accompany the intensity measurements with supplementary methods of temperature determination (Doppler broadening, CARS, thermoprobe, etc). The other possibility (especially suitable for

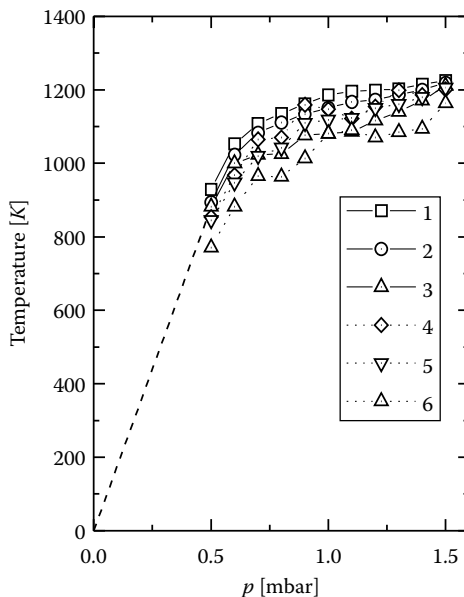


FIGURE 6.8 Translational and rotational temperatures in a planar microwave discharge ($64\% \text{H}_2 + 16\% \text{D}_2 + 20\% \text{Ar}$, $P = 1.5 \text{kW}$) and their dependence on pressure, 1, 2, and 3: translational temperatures derived from Doppler broadening of D_α , H_α , and H_2 spectral lines respectively; 4, 5, and 6: rotational temperatures of the $\text{X}^1\Sigma_g^+$, $v = 0$ state of H_2 obtained from the $Q(0-0)$, $Q(1-1)$, and $Q(2-2)$ branches of the Fulcher- α bands. (From Röpcke, J. et al., *J. Phys. IV*, 8, 207, 1998, *Third International Workshop on Microwave Discharges-Fundamentals and Applications*, April 20–25, 1997, Fontevraud Abbey, France.)

applications in plasma technology) is the application of internal checks within the method—to use simultaneously the emission of several different bands and band systems [177,188], different isotopomers (like H_2 , HD , and D_2 [192]), or different molecules [175,191] to determine T , which has obviously a specific value for every condition.

As an example Figure 6.8 shows the results obtained in a planar microwave discharge [175]. Agreement was found to be within 10%–15% between the rotational temperature, derived from the (0–0), (1–1), (2–2) Fulcher- α bands, and the translational temperatures of hydrogen and deuterium atoms and hydrogen molecules.

6.3.3.3 Vibrational Temperature

Population density distributions over vibrational levels have a non-Boltzmann character in gas discharge plasmas [200]. Nevertheless, the vibrational temperature T_{vib} is widely used for very rough estimates of these distributions. Since the original measurement of the emission band intensities has been proposed for determining T_{vib} in N_2 discharges by OES [201], the method has often been used in low-pressure plasma diagnostics. In particular, it looks promising for the in-situ control of temperature during plasma processing. The method has been generalized by taking into account the resolved rotational structure of H_2 bands [196], which is important for

light molecules. Subsequently the method of determining T_{vib} from the relative intensities of Q-branch lines in the Fulcher- α bands was revised and simplified due to the changes of the $d^3\Pi_u \rightarrow a^3\Sigma_g^+$ transition probabilities and cross sections of the $d^3\Pi_u \leftarrow X^1\Sigma_g^+$ electron impact excitation [202]. Also the emission of the H₂ radiative dissociation continuum ($a^3\Sigma_g^+ \rightarrow b^3\Sigma_u^+$) has been employed as a source of information for the spectroscopic diagnostics of non-equilibrium plasmas [202,203]. This new method has been used in studies of capillary arc [202] and pulsed microwave discharges [199]. In both cases a remarkable difference between T_{vib} and T was observed. This observation is in accordance with previous CARS measurements in other discharges [200,204]. In pure H₂ plasmas the values of T_{vib} obtained by two independent OES methods are in rather good agreement for $T_{vib} = 3\,000 - 5\,000$ K [202].

6.3.3.4 Degree of Dissociation of Hydrogen

Dissociation processes in low-temperature hydrogen-containing plasmas can be investigated by several different approaches, namely, actinometry (see Section 6.3.3.2.1), absolute atomic line intensities [201,205,206], relative atomic and molecular line intensities [207,208], laser induced fluorescence [209], or vacuum ultraviolet absorption methods [210]. When using atomic emission the electron impact dissociative excitation process should be taken into account in molecular plasmas which have a low degree of dissociation [206]. Since this work, various methods based on relative intensity measurements have been assessed and compared [208]. It was shown that the fine structure makes an important contribution in the balance equations for the calculation of emission rate coefficients of the direct and dissociative excitation of H _{α} and H _{β} lines [210].

A new spectroscopic method considers the non-resolved fine structure of Balmer lines in the kinetics of excitation and deactivation of hydrogen atoms in non-equilibrium plasmas [212–215].

Based on measurements of the relative line intensities of atomic and molecular hydrogen and the gas temperature and using a simple excitation-deactivation model the density of molecular hydrogen was studied in microwave discharges in H₂-Ar-B₂H₆ gas mixtures ($f = 2.45$ GHz, $P = 1.2 - 3.5$ kW, $p = 1 - 8$ mbar). The experimental arrangement of the planar microwave plasma reactor and the optical system is shown in Figure 6.9. Details of the reactor and the arrangement for emission spectroscopy can be found elsewhere [171,216]. The experimental values of $[H]/[H_2]$ obtained for two different distances from the microwave window are shown in Figure 6.10. From Figure 6.10 one may see that the density ratio increases noticeably with MW power at a distance of 2 cm from the optical axis from the MW window, while for the greater distance of 4 cm the variation of the density ratio does not exceed the experimental error.

6.3.4 ABSORPTION SPECTROSCOPY

6.3.4.1 General Considerations

The methods of absorption spectroscopy are of great importance in plasma diagnostics because they provide a means of determining the population densities of species

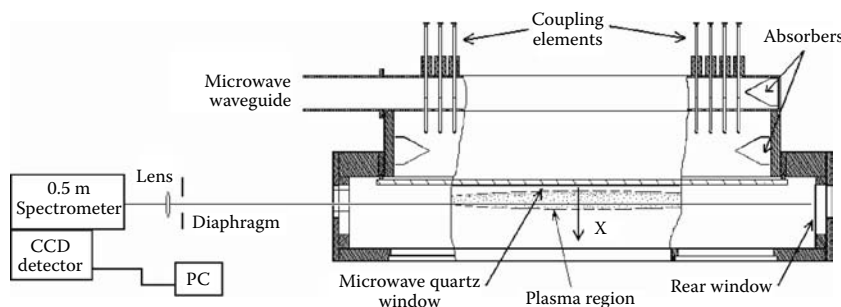


FIGURE 6.9 Microwave discharge plasma reactor with the optical emission spectroscopy arrangement for recording spectra. (From Lavrov, B.P. et al., *Plasma Source. Sci. Technol.*, 12, 576, 2003.)

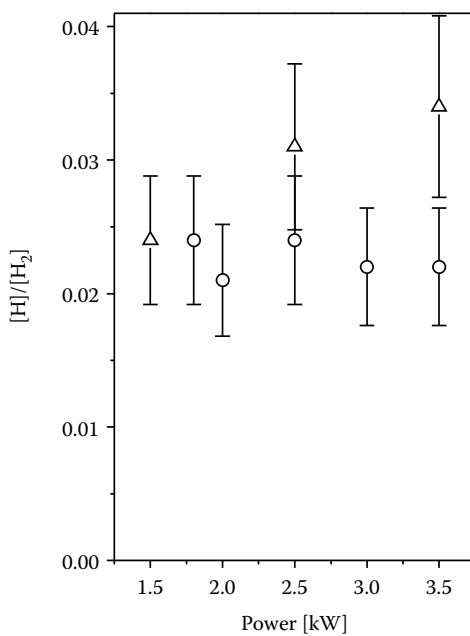


FIGURE 6.10 The concentration ratio of atomic and molecular hydrogen as a function of the axis of observation below the microwave window: \circ for 4 cm and Δ for 2 cm distance. (From Pipa, A.V., On determination of the degree of dissociation of hydrogen in non-equilibrium plasma by means of emission spectroscopy, PhD thesis, University of Greifswald, Greifswald, Germany, 2004.)

in both ground and excited states. The spectral line positions provide species identification while line profiles are often connected with the gas temperature and relative intensities provide information about population densities. An important advantage of AS over OES methods is that only relative intensities need to be measured to determine absolute concentrations, avoiding the problems of complete instrument

calibration inherent in the OES methods. Absorption spectroscopy has been applied across the spectrum from the VUV to the far-infrared (FIR).

Two principle cases need to be distinguished:

1. The measurement of the absorption of light emitted by the plasma itself (*self absorption or reabsorption*)
2. Absorption of an external light source

In the case of self-absorption measurements the light from the plasma is measured with and without a retroreflector or compared with the direct light emitted from an identical plasma. This ensures identical line profiles for the emitted and the absorbed light. This method is particularly important for checking the optical thickness of the plasma. Further discussions about self-absorption can be found in [127,128]. The probing light intensity of an external light source in case 2 has to be low to avoid saturation effects of the excited states of the species under investigation.

In the case where an external light source has much higher intensity than that of the plasma itself, the absorption of radiation can be described by the Beer–Lambert law which is

$$I_v(l) = I_v(0) \exp(-\kappa(v)l), \quad (6.22)$$

$$\kappa_i(v) = n_i \sigma_i(v), \quad (6.23)$$

where

$I_v(0)$ and $I_v(l)$ are the fluxes of the radiation entering and leaving the plasma

l is the length of the absorbing (homogeneous) plasma column

$\kappa(v)$ is the absorption coefficient

n_i is the concentration under study

σ_i the absorption cross section

Figure 6.11 illustrates this situation [135].

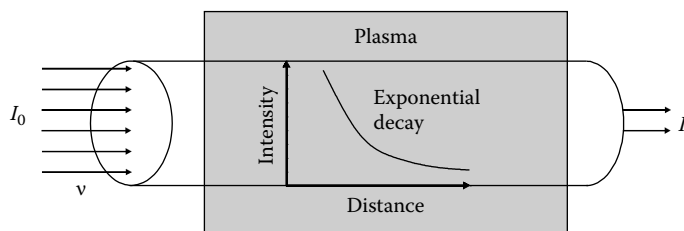


FIGURE 6.11 Absorption of external radiation in a plasma according to the Beer–Lambert Law.

6.3.4.2 Infrared Spectroscopy

6.3.4.2.1 Studies of Plasma Chemistry in Microwave Plasmas Containing Hydrocarbons

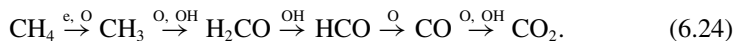
Low-temperature plasmas, in particular microwave and radio frequency (RF) plasmas, have high potential for applications in plasma technology. In molecular low-temperature plasmas, the species and surface conversion is frequently governed by high degrees of dissociation of the precursor molecules and high amounts of chemically active transient and stable molecules present. For further insight into plasma chemistry and kinetics a challenging subject is to study the mainly electron-induced plasma reactions leading to entire series of different chemical secondary reactions involving the whole group of substances making up the source gas molecules. Hydrocarbon precursors are of special importance, since they are used in a variety of plasma-enhanced chemical vapour deposition (PECVD) processes to deposit thin hydrocarbon films. In all cases, the monitoring of transient or stable plasma reaction products, in particular the measurement of their ground state concentrations, is the key to improved understanding of fundamental phenomena in molecular non-equilibrium plasmas which can in turn be applied to many other aspects of plasma processing.

In recent years several types of microwave discharge containing hydrocarbons as precursor gases have been at the center of interest. The most recent applications of TDLAS for plasma diagnostic purposes include studies in which many different species have been monitored under identical plasma conditions [134,217]. This experimental data has frequently been used to model plasma chemical phenomena.

In an Ar/CH₄/N₂/O₂ plasma apart from the precursor molecule, the most abundant species in a methane-containing plasma were determined to be H₂O and CO, see Figure 6.12. When comparing the amount of CH₄ added to the discharge and the measured CO concentration values it turns out that methane is mainly converted into CO and only to a lesser extent into HCN and CO₂. However, the CO₂ selectivity, i.e., [CO₂]/([CO] + [CO₂]), increases with higher amounts of oxygen in the discharge.

In order to elucidate the underlying reactions participating in Ar/CH₄/N₂/O₂ plasmas one of the well-known intermediate molecules for the conversion of CH₄, namely, formaldehyde (H₂CO) and the concentration of OH were measured. For higher oxygen flows less H₂CO was found in the discharge whereas the concentration of the OH radical was found to increase.

The behavior of the carbon-containing molecules mentioned previously can be understood qualitatively in terms of a model which was developed for a H₂/CH₄/O₂ plasma [133,218]. Although the base gas was changed (Ar instead of H₂) the major reactions for the conversion of CH₄, as shown in (6.24), should still be valid since mainly O or OH are involved. The prediction of the model calculation for the OH concentration is 5 · 10¹¹ cm⁻³ which agrees well with the values obtained in the experimental study.



After the dissociation of CH₄ into CH₃ the main conversion path terminates at H₂CO at low oxygen flows. With a higher oxygen content more radicals (O, OH) are available

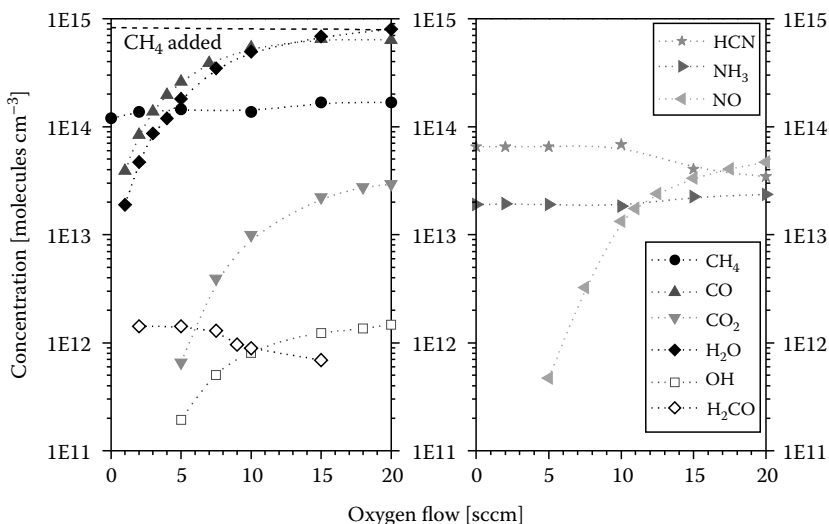


FIGURE 6.12 Most abundant molecular species and their concentrations in an Ar/CH₄/N₂/O₂ plasma (420 sccm Ar, 10 sccm CH₄, 10 sccm N₂, 0–20 sccm O₂; 1.5 mbar). (From Welzel, S. et al., *J. Phys. Conf. Ser.*, 86, 012012, 2007.)

which first leads to a conversion into CO and finally into CO₂. Formaldehyde, as the intermediate molecule is further converted leading to the observed maximum in [H₂CO] at lower oxygen flows. The more CO₂ is produced with higher oxygen flows—as the final product of the CH₄ conversion path—the more the CO₂ selectivity increases, i.e., the relative concentration of CO₂ over CO increases. However, all the measurements were performed in a discharge regime which is still oxygen poor [133]. As a result CO remains the most abundant molecule due to an incomplete conversion of CH₄ to CO [219].

The production of NO in combination with several other molecules in a planar microwave plasma created from a mixture of Ar, CH₄, N₂, and O₂ has been studied by Zijlmans et al. [220]. The molecules were detected by means of in-situ TDLAS and by absolute mass spectrometry (MS). The time resolution of the TDLAS measurements was in the range of 0.1–1 s. Three groups of molecules can be distinguished in terms of their molecular abundances: CO is the main component, together with H₂O, N₂, and H₂. The molecules CH₄ and O₂ are significantly depleted, but still present in finite amounts. The third group is formed by several other species like NH₃, NO, and HCN. The combination of both TDLAS and MS allowed a clear distinction to be made between the etching and deposition modes of the microwave reactor [220].

6.3.4.2.2 On NO_x Production and Volatile Organic Compound Removal

Recent concerns about air quality have led to increasing research in the field of pollution abatement from gas exhausts. Apart from conventional techniques, such as catalysis, scrubbers, and active carbon, the use of electric discharges is a promising technique for toxic gas removal, especially when these gases are present in low

concentrations [221–226], see also Section 8.1.2. There is of course a wealth of literature dealing with the NO_x and VOC problem and so only three examples dealing with new aspects are presented here.

One of the key issues when studying plasma processing for gas treatment is to make sure that no undesirable by-product results from the process. Among them, NO_x are readily produced in air plasmas. The production of undesirable NO and NO_2 and the removal of acetylene, an example of a Volatile Organic Compound (VOC), has been studied in a pulsed low-pressure dc discharge in air. The influence of changing pulse duration, of the pulse repetition rate and of a photocatalyst is reported.

Both NO and NO_2 could be measured ex situ simultaneously using TDLAS spectroscopy downstream of the plasma region. In contrast to what was expected, the use of short pulses did not lead to an effective curtailment of the NO_x production. It was found that the NO_x formation depended only on the average power injected into the plasma independent of the pulse duration and repetition rate. In order to explain this feature a simplified analytical calculation has been developed which considers about 30 kinetic reactions involved in NO_x formation. The calculations lead to a fair agreement with the experimental results [227].

The disadvantage of downstream experiments, being separated from the plasma region and being naturally limited in time resolution, has also been overcome in DC discharges. TDLAS has been applied in situ in a pulsed low-pressure DC discharge of dry air. Under these experimental conditions a time resolution of about 1 ms could be achieved, which was an important step for analyzing plasma chemical phenomena in single discharge pulses. It was found that the NO concentration is approximately proportional to the product of the pulse current and the pulse duration. The role of vibrationally excited nitrogen molecules in NO formation was discussed. Numerical computation of a simplified kinetic model for NO formation, taking into account the $\text{N}_2(\text{A})$ excited metastable state, showed good agreement, see Figure 6.13 [228].

A higher time resolution, up to nanoseconds, using pulsed QCL, has opened up a new approach for studying kinetic phenomena in molecular plasmas in real time and in situ. The scan through an infrared spectrum is commonly achieved by two different methods. In the inter pulse mode a bias DC ramp is applied to a series of short laser pulses of a few tens of nanoseconds [229,230]. Another option is the intra pulse mode, i.e., scanning in single, longer pulses and acquiring an entire spectrum [231]. Since this scan is performed in tens up to a few hundred nanoseconds a time resolution below 100 ns is feasible for quantitative in-situ measurements of molecular concentrations in plasmas. This fits very well for making measurements of rapidly changing chemical processes. The time decay of NO in single discharge pulses has been studied based on this new approach for fast in-situ plasma diagnostics Figure 6.14. At the center of interest was the kinetics of the destruction of NO in a pulsed DC discharge. It transpires that the QCLAS measurements, accompanied by simplified model calculations, serve as a powerful noninvasive temperature probe with a remarkable time resolution up to the sub-microsecond timescale giving insight into the gas heating dynamics [232].

Lastly, the effect of combining plasmas and photocatalysts for VOC removal was investigated in a pulsed low-pressure DC discharge. The photocatalyst was TiO_2 while the VOC was acetylene (1000 ppm) diluted in dry air. The temporal evolution of

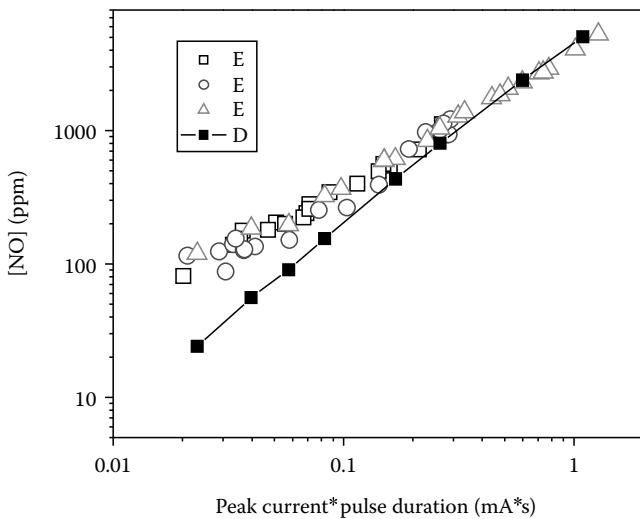


FIGURE 6.13 Influence of the product (peak current times pulse duration) on NO formation: squares 80 mA, 1 ms; circles 40 mA, 2 ms; triangles 40 mA, 4 ms; stars 80 mA, 2 ms. The solid line is the result of numerical computation. (From Gatilova, L.V. et al., *Plasma Sources Sci. Technol.*, 16, S107, 2007.)

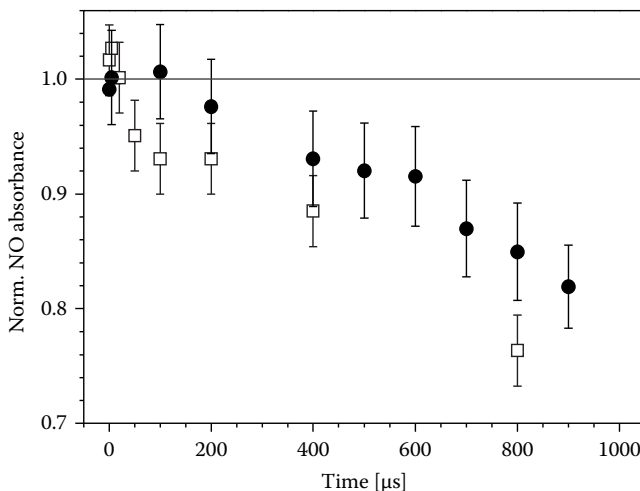


FIGURE 6.14 Decay of the NO absorbance in a pulsed DC discharge containing 0.91% NO in an Ar-N₂ mixture for static (full) and flowing (open) gas conditions. (From Welzel, S. et al., *Plasma Sources Sci. Technol.*, 16, 822, 2007.)

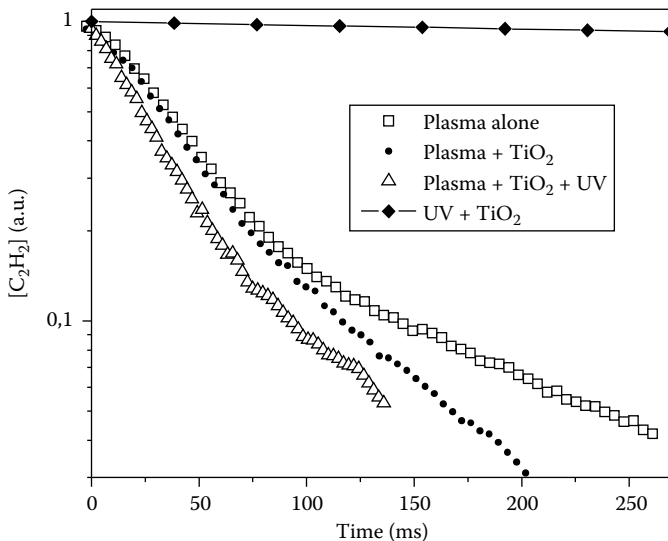


FIGURE 6.15 Time evolution of C_2H_2 concentration during a 1 000 ms plasma pulse; open squares plasma only; solid circle plasma + TiO_2 ; open triangles plasma + TiO_2 + UV; solid diamonds UV + TiO_2 ; total pressure 210 Pa, discharge current 3 mA. (From Rousseau, A. et al., *Appl. Phys. Lett.*, 87, 221501, 2005.)

the C_2H_2 concentration was measured by TDLAS during the plasma pulse of 1s. The combination of the nonthermal plasma with photocatalysis leads to a strong increase (a factor 25) of the photocatalytic activity. Under the experimental conditions used, UV generated by the plasma is not sufficient to ensure such a synergistic effect. The main results of this study was, that UV irradiation promotes adsorption of oxidative neutral radicals produced by the plasma as well as adsorption of C_2H_2 ; this leads to higher oxidative species concentration on the TiO_2 surface, which enhances the photocatalytic activity, see Figure 6.15 [233].

6.3.4.2.3 In-Situ Monitoring of Silicon Plasma Etching

During the last 40 years plasma etching has become a fundamental feature for processing integrated circuits. The optimization of the plasma chemistry of the etching processes includes the identification of the mechanisms responsible for plasma-induced surface reactions combined with the achievement of uniformity in the distribution of molecules and radicals for homogeneous wafer treatment.

In etch plasmas used for semiconductor processing, concentrations of the precursor gas NF_3 and of the etch product SiF_4 were measured online and in-situ using an experimental arrangement, designated the Q-MACS Etch System, which is based on QCLAS. In addition, the etch rates of SiO_2 layers and of the silicon wafer were monitored, including plasma etching endpoint detection. For this purpose the Q-MACS

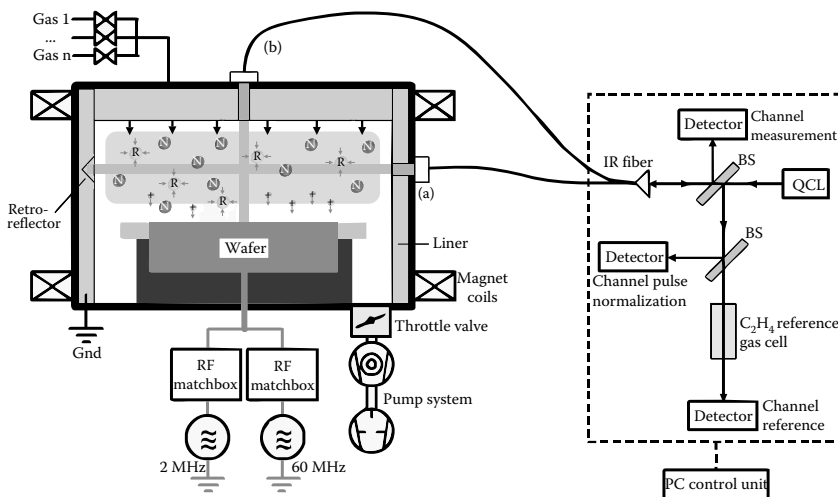


FIGURE 6.16 Experimental arrangement of the MERIE plasma etching reactor and the three channels Q-MACS Etch system: (a) side access and (b) top access monitoring. (From Stancu, G.D. et al., *Chem. Vap. Deposition*, 13, 351, 2007.)

Etch System functioned in an interferometric mode. The experiments were performed in an industrial dual frequency capacitively coupled magnetically enhanced reactive ion etcher (MERIE), which is a plasma reactor developed for dynamic random access memory (DRAM) technologies Figure 6.16.

The quantum cascade laser system Q-MACS Etch consists of a pulsed infrared QCL source with the laser wavelength tunable in the range $1\,027\text{--}1\,032\,\text{cm}^{-1}$, optical components, detectors, and data acquisition cards controlled by a PC. From Figure 6.16 it can be seen that the IR beam is split into three channels using two IR transparent ZnSe beam splitters (BS). The main part of the beam is coupled into an IR fiber using an off-axis parabolic (OAP) mirror, and then collimated into the plasma reactor using either lenses or OAPs. The second channel, operating as a pulse normalization channel, is used to reduce the fluctuation intensities of the QCL from pulse to pulse. In the third channel a reference spectrum of C_2H_4 is measured through a reference gas cell in order to calibrate the spectral region and to correct drifts of the laser frequency due to temperature instability of the laser chip.

Industrial requirements, such as

1. No open optical path
2. The availability of just one optical access port

makes coupling the infrared beam into the reactor a challenging task. The solution presented here is based on the use of (a) mid-infrared fibers and (b) internal reflections in the reactor chamber.

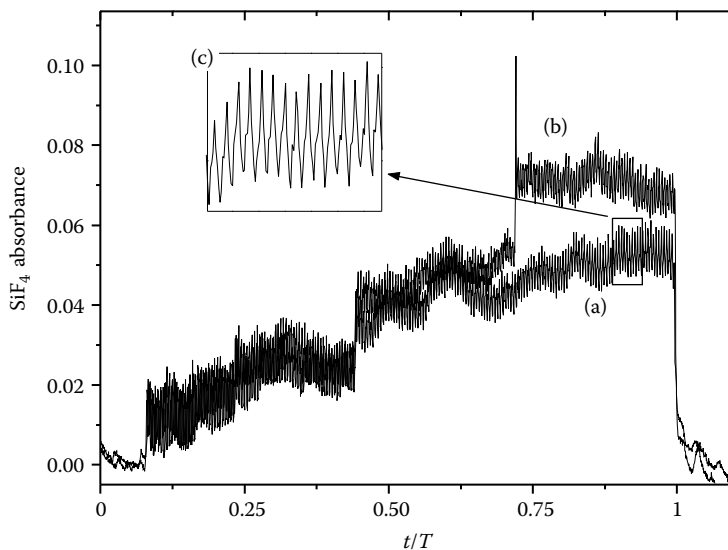


FIGURE 6.17 Silicone etching by NF_3 plasma. SiF_4 absorbance monitoring using QCLAS for: (a) a complete plasma etching process, (b) complete plasma etching process with injection of 2% SiF_4 , (c) SiF_4 concentration variation due to changes of the magnetic field. The experiments were performed using a process wafer. (From Stancu, G.D. et al., *Chem. Vap. Deposition*, 13, 351, 2007.)

In Figure 6.17 an example of on-line in-situ monitoring of the SiF_4 absorbance during a deep trench etch processes is shown. Figure 6.17c shows the enlarged temporal behavior of the measured concentration. Changes of the concentration due to plasma density over the wafer are clearly visible and further prove the sensitivity and time resolution of the method. Focused on sensitive and fast concentration measurements of key molecular components, while ensuring compactness, robustness, and long-term stability, this new class of process control equipment has the potential to become implemented into other fields of plasma technology [234].

6.3.5 SUMMARY AND CONCLUSION

During the past few years a variety of phenomena in molecular non-equilibrium plasmas in which many short-lived and stable species are produced have been successfully studied based on methods of emission and absorption spectroscopy, with which the present contribution is concerned. It has been possible to determine absolute concentrations of ground states using spectroscopy thereby providing a link with chemical modeling of the plasma, the ultimate objective being a better understanding of the chemical and reaction kinetic processes occurring in the plasma. The other essential component needed to reach this objective is to determine physical parameters of the plasma, for example, temperatures, degrees of dissociation, and dynamics of reaction kinetic processes; the present chapter discusses methods for

achieving this. The need for a better scientific understanding of plasma physics and chemistry has stimulated the application of TDLAS, which has proven to be one of the most versatile techniques for studying molecular plasmas. Based on the recent development of quantum cascade lasers the further application of this method of high-resolution mid-infrared spectroscopy to industrial applications has become a reality.

6.4 LASER INDUCED FLUORESCENCE SPECTROSCOPY

Atoms and ions both in their ground states and excited levels play a key role in reactive plasmas. The spatial and temporal density distributions of these particles are central parameters to understand the complicated chemical kinetics of heavy particles. In order to reveal details for modeling, state-selective densities for the reactive species are required for the refinement and validation of physical models. Laser-induced fluorescence measurements address this issue experimentally.

Laser-induced fluorescence (LIF) is a diagnostic technique for measuring properties of excitable atomic species (atoms, molecules, ions) [235]. Usually, tunable laser light is employed to excite atoms or ions. The subsequent re-emission, the fluorescence, is then detected, mainly to infer densities and temperatures of the emitting particles. Different from laser absorption techniques (see Section 6.3), laser-induced fluorescence gives spatially resolved information on the excited state. However, LIF results are relative measurements, i.e., a calibration is required for a quantitative interpretation of experimental results. The spatial resolution is given both by the exciting laser beam and the observation arrangement. An attractive option of LIF is its potential to provide two-dimensional measurements by observing a laser sheet with appropriate camera systems. High time resolution may be attained by short-pulse excitation with pulsed lasers.

LIF is a long established technique in laser spectroscopy; for a review see [236]. Compared to sophisticated techniques like coherent anti-Stokes Raman scattering (CARS), the experimental effort is less complicated. LIF is applied in many engineering and natural science contexts; an example is the investigation of combustion systems [237].

Since LIF is a state-selective measurement, the laser light is to be tuned to an atomic transition. If small-band, tunable laser light sources are employed, any particle property reflected in absorption line shape can be inferred. Hence, in addition to the density, also the temperature of excitable atoms or ions can be determined [238]. More specifically, tuning techniques allow one to access all parameters determining the absorption line shape, i.e., drift velocities, collisional de-excitation rates by collisional quenching, and even details of ionic distribution functions [239]. And scanning the laser over split levels gives access to electromagnetic fields. for example, the combination with absorption to Stark-states may be employed to derive small electric field strengths as occurring in low temperature plasmas [240].

The remainder of this section introduces basic physics background for LIF measurements. A brief overview on tools is part of a practically oriented section. A selection of applications relevant to plasma chemistry will finish the section.

6.4.1 PRINCIPLES OF LASER-INDUCED FLUORESCENCE

The basic physics of LIF can be revealed in figures of radiative excitation and subsequent spontaneous emission. Figure 6.18 shows a schematic Grotian diagram with some selected transitions. The typical three-level excitation scheme is shown with bold symbols and lines indicating transitions (atomic levels are indicated by $| \cdot \rangle$)

$$\begin{array}{c} |0\rangle \quad \xrightarrow{\text{Laser excitation}} \quad |*\rangle \quad \xrightarrow{\text{fluorescence}} \quad |e\rangle \\ \hline \end{array}$$

Usually, a well-populated state is excited ($|0\rangle \rightarrow |*\rangle$ in Figure 6.18) by laser irradiation. In plasma chemistry, ground state atoms, e.g., N or O, are to be explored. Here, short wavelengths are required for excitation and two-photon excitation schemes (two-photon absorption LIF - TALIF; double arrow upwards in Figure 6.18) are used [241]. It is convenient if the excited state decays to a different state, say $|e\rangle$. Then, the observation wavelength of fluorescence (bold double lined arrow in Figure 6.18) is easily separable from the excitation wavelength. Nonetheless, two-level LIF are applied as well ($|e\rangle \equiv |0\rangle$). Techniques with further excitation can be used to detect, the opto-galvanic effect which is a sensitive measurement of changes in the discharge current due to photo-ionization [242]. Electric fields can be measured by scanning the wavelength of a second laser to depopulate $|*\rangle$ to Stark-split levels $|*\rangle \rightarrow |s_j\rangle$. Since lifetimes of levels with high principal quantum numbers—for which the Stark effect is largest—is high, the effect of depopulation is observed through fluorescence $|*\rangle \rightarrow |e\rangle$ in an accessible spectral range [240].

For a quantitative analysis of LIF, population models of the involved atomic states are required. A rigorous treatment of LIF is achieved by solving the density matrix

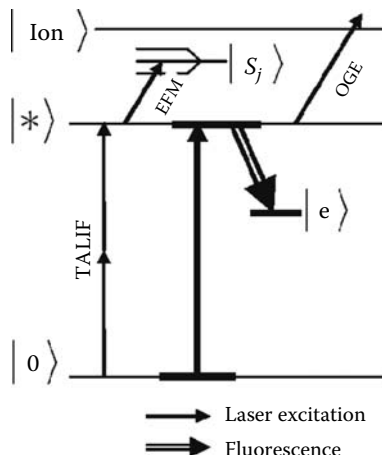


FIGURE 6.18 Simplified term diagram depicting some relevant excitation schemes for laser induced fluorescence. $| \cdot \rangle$ designates atomic levels. TALIF shows two-photon absorption excitation. OGE indicates photo-ionization (opto-galvanic effect). EFM shows transitions which may be involved in electric field measurements.

master-equation [243]. This treatment is required if coherence effects need to be considered. However, in many applications a population density model is sufficient, i.e., a set of rate equations. A simplified version of which reads for the laser-excited state $|*\rangle$

$$\frac{dn_{|*}\rangle}{dt} = \underbrace{\left(n_{|0\rangle} - \frac{g_{|0\rangle}}{g_{|*}\rangle} n_{|*}\rangle \right) B_{0*} \times I_v}_{\text{Laser excitation}} - \underbrace{\left(\sum_k A_{*k} + \frac{1}{\tau_q} + \dots \right) n_{|*}\rangle}_{\text{Depopulation}}. \quad (6.25)$$

Here, A and B designate the Einstein coefficients for spontaneous emission and absorption. Usually, quenching processes summarized by the rate $1/\tau$ may lead to additional depopulations of the excited state. Solving the full set of rate equations for relevant population densities n_i is straightforward but may become complicated by details of the spatial and temporal dependencies of the laser power spectral density [235]. Dependent on the specific atomic system and the particle density, amplified spontaneous emission due to population inversion at higher densities and photoionization are further processes to be included in a full description of LIF [236].

While quantitative results are due to a solution of the full set of rate equations, the dependency of (6.25) on the power spectral density I_v of the laser leads to saturation effects in typical fluorescence schemes: In increasing I_v , induced radiative processes (absorption and induced emission) govern. Then, the density population cannot exceed a relative equilibration given by the ratio of statistical weights of the levels involved

$$\lim_{I_v \rightarrow \infty} \frac{n_{|*}\rangle}{n_{|0\rangle}} = \frac{g_{|*}\rangle}{g_{|0\rangle}}. \quad (6.26)$$

Moreover, the fluorescence intensity increases linearly with I_v at low laser intensities. In case of TALIF the fluorescence increases quadratically (I_v^2), since two photons are involved. (6.25) has to be modified accordingly. In case of saturation, the spatial variation of I_v enters since the low laser power spectral density in the spatial wings leads to unsaturated scattering volume. Differences in absorption line broadening mechanisms may lead to spectrally dependent saturation, the so-called hole-burning [235]. This saturation effects should be considered when outlining an experimental setup (e.g., avoidance of (partial) saturation/user power monitoring, etc.).

Specific features of excitation schemes are due to optical selection rules. Since laser light is polarized, details of the atomic physics of the excitation scheme with respect to polarization should be accounted for. For example, if a weak magnetic field gives the quantization axis, Δm selection rules (where m is a angular momentum projection quantum number) according to the longitudinal and perpendicular Zeeman effect, respectively, should be accounted for. In extreme cases, the selective population of degenerate levels may even affect the fluorescence emission characteristics. For two-photon excitation, angular momentum conservation may lead to different excitation branches than for single photon excitation.

6.4.2 INSTRUMENTATION AND EXPERIMENTAL TECHNIQUES

LIF is a highly feasible experimental technique. It gives space and time-resolved results. Figure 6.19 shows schematically an experimental setup: A laser beam is led into a plasma to excite specific atomic species (atoms in different levels, molecules, ions, etc.). The fluorescence is observed by means of an observation optics guiding the scattered light into a spectral filter which is employed to suppress unwanted plasma emission. In case of two-level LIF, special care has to be taken to suppress laser stray light. A photodetector is then used to measure the fluorescence power spectral density. The spatial resolution is given by the fluorescence volume along the laser-beam cut-out from the observation cone.

The specifics of experimental layouts are determined by the measurement requirements. Aspects which enter the choice of the laser are the required excitation wavelength, spectral width, and stability of the laser light. The stability is affected by a proper outline of the laser resonator. Stable mode operation with simultaneous tunability is particularly an issue for pulsed laser systems. To give a typical number, the Doppler width of an absorption profile of a neon transition at room temperature is about $\Delta\nu_{|0\rangle} \approx$ few GHz. Modern laser systems easily provide much smaller bandwidths $\Delta\nu_{|0\rangle} <$ few 10 to 100 MHz thus allowing scanning the absorption line. If one might wish to provide a broadband excitation to excite all particles rather in a statistical ensemble, a caveat should be noticed that broad-band excitation is mostly multimode operation which may require complicated corrections [244]. In addition to the actual laser system, a well-defined power attenuation allows one to examine saturation effects. In practice, turnable polarizers may be used. In addition, a variation of the polarization of the incident laser beam gives experimentally access to details in the excitation. Laser-beam diagnostics, moreover, allow one to examine potential details of spatial variations of saturation. A monitoring of the laser power or pulse energy should be part of the setup.

Tunable laser sources are provided by solid state active media or dye lasers. Frequently, the tunable laser itself is excited by a second laser. To conclude it is to be mentioned that laser development is a fast evolving field, still. Therefore,

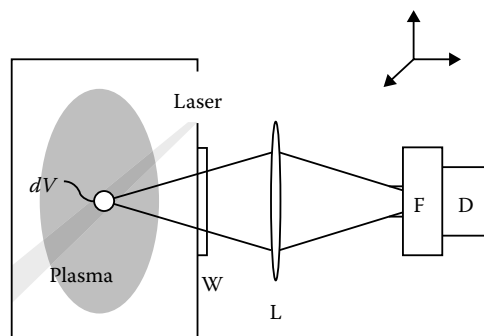


FIGURE 6.19 Schematic experimental setup for laser-induced fluorescence. (dV : fluorescence volume, W: vessel window, L: observation optics, F: spectral filter, D: detector.)

long-standing recommendation for the choice of specific laser systems can barely be given but the reader is referred to respective commercial sections of general physics journals.

The outline of the observation optics is a typical issue in optical engineering. In LIF, spectral transmission characteristics should be considered also in conjunction with supplementary measurements like calibrations. Generally, a spectral filter such as an interference filter can be employed to suppress plasma radiation and the intense background of laser stray light. The choice of the detector is determined by the required temporal resolution and spectral response. Photomultiplier tubes, avalanche diodes, or even intensified charge coupled devices (ICCD) are used to detect the fluorescence light with different response times and spatial resolution up to 2D imaging.

Absolute measurements of fluorescence signal require calibration measurements [245]. For this purpose, well-defined scattering processes such as Rayleigh scattering, or titration techniques are employed. A different option is the combination detection of LIF along the plasma with absorption measurements or even the consideration of radiation transport [246]. The calibration procedure gives the sensitivity of the detection (measure, e.g., in photons per mV). Calibration measurements should also be used to determine the measurement uncertainties; a particular caveat has to be raised since many quantities may cancel in a formal treatment of calibration, but the errors do not.

6.4.3 FURTHER READING

The overview given in the previous sections gives a survey of potentials and limits of LIF as a diagnostic technique. For further background in general laser spectroscopy, the monograph [235] is an outstanding entry. Specific to plasma chemistry, a compilation by Amorim et al. [236] serves as an excellent overview. Table 6.2 reviews and partly updates this compilation. This table may serve as a more specific entry to the field to those readers who consider an application of laser-induced fluorescence.

6.5 MASS SPECTROMETRY

Gas discharge physics is connected with mass spectrometry since the beginning of this measuring technique. Thomson [277] constructed the first apparatus, the parabola spectrograph, with a dc discharge as ion source. The position of the parabola on the detector plate is related to the ion mass (m/z , ion mass m , charge z), its length depends on the ion energy distribution. For the first time, isotopes of a nonradioactive element ^{20}Ne and ^{22}Ne were detected in the canal rays by the two parabolas. The parabola spectrograph with its possibility of ion identification by the mass/charge relation and of the ion energy distribution can be denoted as the first plasma monitor.

6.5.1 MASS SPECTROMETER

A complete mass spectrometer consists of the gas inlet, an ion source, the mass analyzer and ion detector. For more details, see textbooks on mass spectrometry like [278–280]. Commercial plasma monitors, constructed also for ion and for neutral gas

TABLE 6.2**Examples of Atomic Species (Atoms, Ions, Molecules) Relevant to Plasma Chemistry Detected by LIF**

Species	Plasma	Laser λ_{0*} (nm)	Fluorescence λ_{*e} (nm)	Reference
Al	RF	394	396	[247]
As	RF	193	245	[248]
Cu	RF	325	325, 510	[249]
Fe	Magnetron	302	382	[250]
Ge	RF	265	275	[251]
Mo	RF	313	317	[247]
Si	RF	251	253	[252]
Zn	RF	214	214	[249]
BCl	RF	272	272	[253]
CCL	RF	278	278	[254]
CF	Pulsed	193	194	[255]
CF ₂	Pulsed	248, 266	257, 271	[255]
Cl ₂ ⁺	RF	386	396	[256]
CH	ECR	387	390	[257]
CH	ECR	413	430	[257]
CH	Microwaves	314	314	[258]
N ₂ ⁺	dc	391	428	[259]
NH	dc	336	336	[260]
OH	Post-discharge	281, 284	312	[261]
SiCl	Post-discharge	275, 295	280	[262]
SiH	RF	413	413	[263]
SiH ₂	Post-discharge	580	618	[264]
SiN	dc	396	414	[265]
SiO		221	248	[266]
C		280*	910	[267]
Cl		210*	904	[268]
Cl		233*	725, 775	[269]
F		170*	776	[270]
H		205*	656	[271]
N		211*	869	[272]
N		207*	752	[273]
N		207*	742-747	[238]
O		226*	845	[272]
S		288*	VUV	[274]
I		305*	VUV	[275]
Xe		250*	828	[276]

* Indicates two-photon absorption LIF schemes. RF, radio-frequency source; ECR, electron cyclotron resonance heated source; dc, dc discharge.

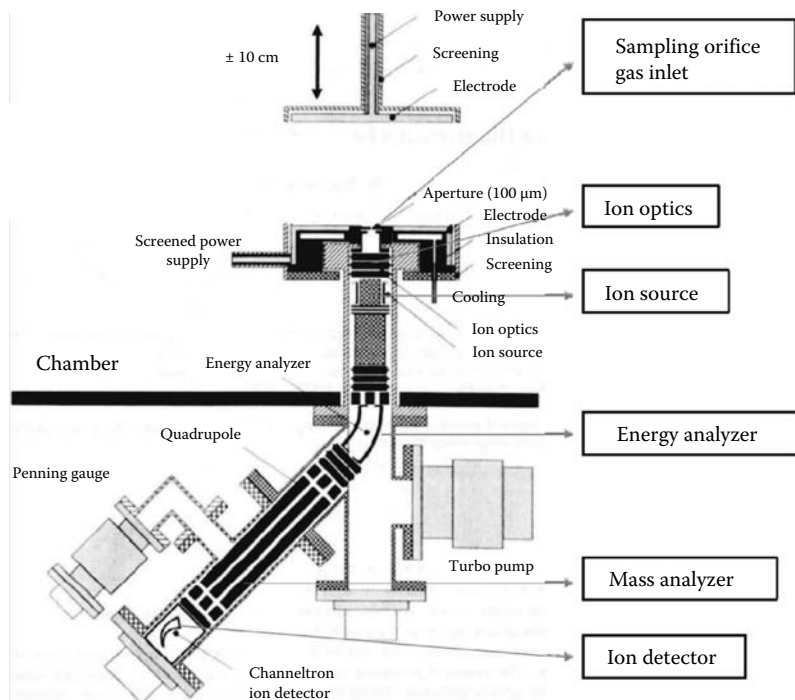
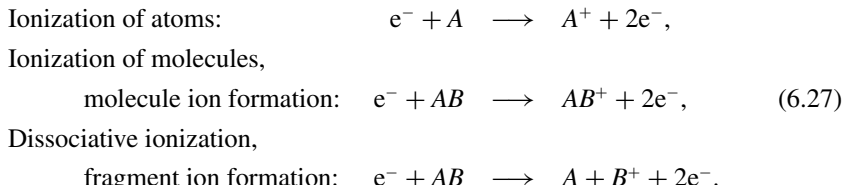


FIGURE 6.20 Mass spectrometer with the main elements of the plasma monitor of Hiden Analytical Company. (From Zeuner, M. et al., *J. Appl. Phys.*, 79, 9379, 1996.)

analysis of plasmas, are equipped with an ion energy analyzer between ion source and mass analyzer (see Figure 6.20): This position offers the possibility to control the energy distribution of the ions produced in the ion source.

6.5.1.1 Ion Source

The mass spectrometric investigation of heavy particles is possible for charged particles only, therefore neutral atoms and molecules must be ionized in an ion source. Electron impact ionization is a common method for positive or negative ion formation. The following ionization processes are important



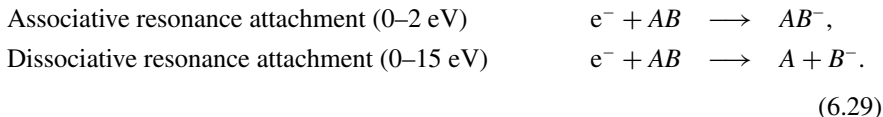
Higher energetic electrons can generate multiple charged ions as A^{++} or AB^{++} . The ion current i_v^+ produced in the ion source by an electron current i_e^- depends on the

gas density n_n , the partial ionization cross section σ_ν and the length l of ionization region

$$i_\nu^+ = i_e^- n_n \sigma_\nu l. \quad (6.28)$$

The ionization cross section for positive ion formation starts at the ionization energy for most molecules between 5 and 15 eV and has a broad maximum around ~ 70 eV. The appearance energies for the fragment ions can be essentially higher.

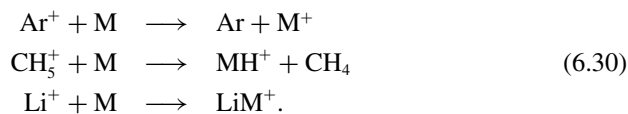
The formation of negative ions by attachment processes requires low energetic electrons, see [281]



In the electron impact ion source a heated filament (tungsten, thoriated tungsten, rhenium) emits the electrons which are usually accelerated by a static electric field to energies in the range between 5 and 100 eV for generation of positive ions; for negative ion formation lower electron energies are necessary. The electron beam crosses the chamber with the gas probe. Additional electrodes extract the ions out of the ionization chamber and form the ion beam. Ion sources for positive ion formation in commercial mass spectrometers mostly use electron energies of 70 eV. The electron impact ion source usually operates with a gas pressure of 10^{-3} Pa to ensure a maximum of a single-electron collision with a heavy particle. If the electron impact ionization generates the molecular ion it is possible to determine the molecular mass. The dissociative ionization generates a characteristic spectrum of fragment ions.

This pattern allows conclusions on the molecular structure. The investigation of a mixture of different gases may be complicated by the various fragment ions originating from the different gases. The fragmentation can be reduced by application of low energetic electrons (~ 20 eV) and of molecules with sufficient probability for negative ion formation by associative resonance attachment, see Section 6.5.3.2.

The fragmentation of the parent molecule is avoided by chemical ionization [282]. This ionization is induced by charge transfer reactions or ion molecule reactions between the gas under study and a reactant gas which is ionized by electron impact or ion attachment



Chemical ionization requires a pressure of 30–100 Pa and analyte admixtures of $10\text{--}10^4$ ppm in order to achieve sufficient numbers of reactions and to enable the transfer of excess energy from the generated ions to the gas.

Field ionization as a mild ionization process shows low fragmentation also [283], see [284,285].

6.5.1.2 Energy Analyzer

The measurement of the energy of the plasma ions is possible by a retarding field analyzer. Here, the energy distribution is obtained by the first derivative of the I-U characteristic assuming an ion movement parallel to the retarding electrical field. Ion optical elements are more convenient which directly provide the energy distribution and diverts the ions in an off-axis direction. Commercial instruments use electrostatic sector fields, often 45° , and cylindrical mirror analyzers. The electrical field acts perpendicular to the flight direction of the ions Figure 6.21. The energy range reaches up to 1000 eV for positive and negative ions, a scan energy at 0.05 eV increments and a resolution power of 0.25 eV FWHM is indicated.

6.5.1.3 Mass Analyzer

Static analyzers separate the ions according to their m/z by a static magnetic sector field and for improvement of the resolution power $m/\Delta m$ by an additionally static electric field (double focussing instruments). The resolution power can be very high ($>10^5$). In this case, a determination of the elemental formula of the ion is possible using the exact masses of the single elements. The transmission is independent of the ion mass. But these instruments are large due to the necessary long ion path, which also requires a very good vacuum, heavy and expensive.

Dynamic instruments [286] separate the ions by time-varying electromagnetic fields, e.g., Fourier transform ion cyclotron resonance mass spectrometers, omegatrons, time-of-flight and quadrupole instruments.

Quadrupole mass spectrometers are widely used instruments for low-resolution applications and most important in plasma diagnostics [287]. The ions fly through an electrical quadrupole field generated by four parallel conducting hyperbolic, in practice mostly cylindrical rods Figure 6.22. The ions oscillate transversal in direction to the rods. Depending on the potentials only one kind of ions defined by m/z has a stable path, the others are deflected to the rods. The resolution power $m/\Delta m$ increases

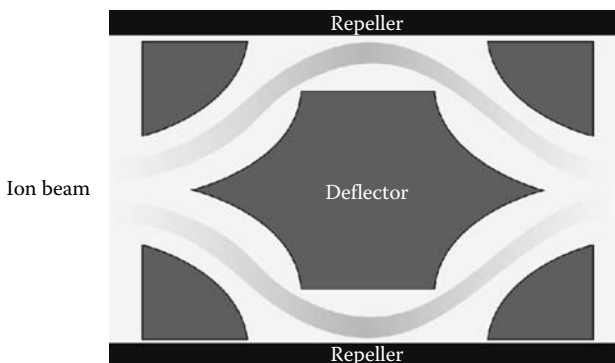


FIGURE 6.21 Scheme of a cylindrical mirror analyzer. (From Zeuner, M., Corpuscular diagnostics of plasma polymerization processes, in H. Biedermann, ed., *Plasma Polymer Films*, pp. 85–142, Imperial College Press, London, U.K., 2004.)

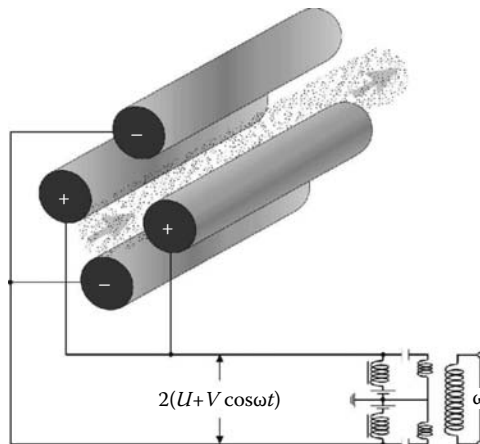


FIGURE 6.22 Scheme of a quadrupole mass analyzer.

linearly with the mass number. The peak width is constant over the whole mass range and slightly smaller than one mass unit.

The resolution power and transmission can be varied by adjusting the electrical parameters of the quadrupole field. These instruments are light and short (~ 30 cm). A base pressure of 10^{-3} – 10^{-4} Pa is sufficient. Commercial spectrometers are available with a mass range of 1–100, 1–300 up to 1–2 500 amu. The use of quadrupole mass spectrometers is widespread (therefore these instruments are relatively cheap) as gas analyzers in vacuum technique, for chemical analysis combined with gas chromatography (GC-MS), and last not least in plasma diagnostics in fundamental research and process control.

6.5.1.4 Ion Detection

The ion detection is usually performed by ion multipliers or channeltrons using counting technique with a dynamic range of seven decades. Faraday collectors are optionally applied. The reliable counting technique ensures high sensitivity independent of mass and chemical nature of the ion [278] as well as a high time resolution. Time-resolved measurements are reported with gate times of $30\ \mu\text{s}$ [288,289] down to $4\ \mu\text{s}$ [290].

6.5.1.5 Coupling of the Mass Spectrometer with the Plasma Source

The problems of coupling of the mass spectrometer with the plasma source are different for ion and neutral particle diagnostics and will be discussed in relation to these tasks.

6.5.2 ION ANALYSIS

The investigation of ion composition of plasmas is a topic of plasma diagnostics, but it is also correlated with the plasma as a chemical analytic tool [291]. Here, the plasma mass spectrometry is discussed as a method of plasma diagnostic. The study

of the plasma ions has two different aspects, one is strongly coupled with the plasma chemistry. The ions are a product of reactive processes as well as a reactant in plasma chemical reactions in the volume and also essential in surface reactions on substrates, electrodes, and walls. The task is the identification of the nature of these ions, that is, their chemical composition and charge. The other aspect is more related to the diagnostic of selected plasma properties. For this purpose, it is necessary to measure the kinetic energy of these heavy particles.

The ion analysis of a plasma concerning the nature and the energy of these heavy, charged particles as well the flux density on the substrate, electrode, or wall surface by mass spectrometric methods is a noninvasive diagnostics. Only a small orifice is necessary for the transfer of the ions from plasma into the mass spectrometer. Reviews of this diagnostic method were given in the past by [292–299].

6.5.2.1 Sampling Orifice

The orifice is an essential part of the ion diagnostics of plasmas. The diameter of the orifice should be smaller than the thickness of the space charge sheath in front of the surface. So the disturbance of the plasma will be small. The diameter should be large in relation to its length. Wall recombination of ions is minimized in this region and the acceptance angle will be not limited by the geometry of the orifice. For low-pressure plasma conditions often an orifice diameter of 100 μm is smaller than the sheath thickness. In a collision-free sheath the sampled ions originate from the plasma bulk.

The flight of the ions to the surface under study is not only perpendicular. The ion current in a Cl_2 discharge shows an angular distribution of $\sim 6^\circ$ which varies with ion energy [300]. In a CF_4 rf plasma the angular distribution of CF_2^+ and CF^+ ions was measured to 5° for high energies and near 15° in the low energy range [301]. For measurements especially of the ion energy distribution the acceptance angle of the orifice and the ion optical system is essential, as discussed in [302–304], see also Figure 6.23.

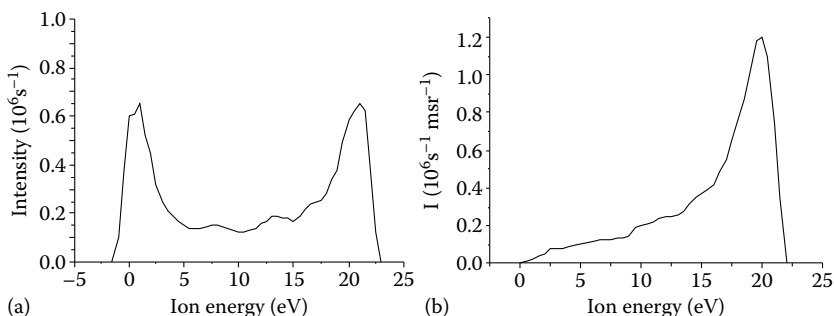


FIGURE 6.23 Energy distribution of Ar^+ ions measured at the grounded electrode of an RF discharge in Ar. (b) Shows the IED of (a) after division by the corresponding solid angle of acceptance. (From Hamers, E. et al., *Int. J. Mass Spectrom.*, 173, 91, 1998.)

6.5.2.2 Transfer Optics

The transfer from the orifice to the energy analyzer is performed by an ion optical system of electrostatic lenses. Its construction can be supported by an appropriate software, for example, SIMION (Ion and Electron Optics Simulator).

6.5.2.3 Coupling

The connection of the plasma with the mass spectrometer requires the coupling of two electrical devices with minimal disturbances of both systems.

Current plasma chemical devices are mostly metallic and the mass spectrometer is flanged at the grounded wall [288,305,306], the grounded electrode [307,308] (see Figure 6.20), or the grounded as well as the powered electrode of an rf discharge [309]. For measurements at the powered electrode of an rf discharge a biasing of the mass spectrometer at the dc bias potential of the electrode is possible [310].

The investigation of the ions in the positive column of a dc discharge in a dielectric glass tube requires a reference potential for the acceleration of the ions. The floating potential of a wall probe near the sampling orifice has proven itself suitable for this purpose [311,312].

6.5.2.4 Gas Pressure

The gas pressure in the mass spectrometer should be lower than 10^{-3} Pa to avoid collisions and reactions between the ions and gas molecules. Therefore differential pumping and an orifice as small as possible are necessary. The gas density decay $n_g(x)$ behind the orifice (radius R) is given by [295,299,313]

$$n_g(x) = \frac{n_0}{2} \left(1 - \frac{x}{\sqrt{R^2 + x^2}} \right) + n_a \quad (6.31)$$

with x the distance from the orifice, n_0 the gas density in the plasma vessel, mean free path λ , n_a the gas density (residual gas pressure) in the analyzer, mean free path λ_a .

The relative number of ions n^+/n_0^+ flying without collision from the orifice to the collector in the distance x can be estimated as

$$\frac{n^+}{n_0^+} = \exp \left(-\frac{x}{\lambda} \left(\frac{1}{2} + \frac{\lambda}{\lambda_a} \right) + \frac{1}{2} \sqrt{\frac{R^2}{\lambda^2} + \frac{x^2}{\lambda^2}} - \frac{R}{\lambda} \right). \quad (6.32)$$

Ion neutral collisions may disturb the flight path by scattering and can change the species of the ions by ion-molecule reactions.

A detailed review of fundamental aspects of ion extraction in the inductively coupled plasma mass spectrometry (ICP-MS) at atmospheric pressure especially for analytic purposes is given by [314], but these treatments are useful also for plasma diagnostics. Here, the discharge contacts the sample with a 1 mm orifice and a supersonic jet streams to the skimmer. The ion optics and the mass spectrometer are situated behind the skimmer. The region between sampler and skimmer is evacuated to ~ 100 Pa by a mechanical vacuum pump, the region behind the skimmer with the analyzing system is evacuated by high vacuum pump to $\lesssim 10^{-2}$ Pa. A critical

discussion of the origin and possible disturbance (e.g., by ion molecule reactions) of the identified ion population is necessary.

6.5.2.5 Calibration

The calibration of the energy scale of the energy analyzer is possible by means of a thermal Na⁺ ion source with heated sodium silicate (Na₂O · n SiO₂). The calibration of the spectral sensitivity of the mass analyzer can be done with a mass spectrum of a substance with an ample number of fragment ions measured by a magnetic mass spectrometer with negligible mass discrimination or by comparison with electron impact ionization cross sections for the formation of fragment ions with marginal kinetic excess energy [315]. Faraday cup measurements can be used for the calibration of the sensitivity of the ion multiplier. The identification of ions and ion reactions in a more complicated spectrum can be facilitated by observation of the natural isotope distribution and/or application of an isotopic labeling technique [316].

6.5.2.6 Deduction of Data for Plasma Parameters

6.5.2.6.1 Ion Energy

The ion energy distribution is determined by the flight of the ions through the potential drop in the sheath and the physical processes therein as interaction with the rf-sheath potential, charge transfer reactions, and ion molecule reactions.

The shape of the ion energy distribution gives information of the site of ion formation. The maximum energy (~ 40 eV) of the SF_x⁺ ions measured at the grounded electrode indicates their origin in the plasma bulk (Figure 6.24) [307]. The high energy peak (~ 650 eV) of the negative ions (Cl⁻ and F⁻) at the grounded electrode of a capacitively coupled RF discharge indicates that these ions are generated at the surface of the powered electrode (Figure 6.25) [308]. The high energy of these ions is sufficient to surmount the retarding sheath potential. For ion flight times in the sheath comparable to the rf oscillation period the ion energy distribution (IED) is modulated (Figure 6.24). The energy dispersion ΔE of the plasma peak is given by [317]

$$\Delta E = \frac{8 e U_{rf}}{3 \omega d} \sqrt{\frac{2 e U_{dc}}{m_i}} \quad (6.33)$$

with U_{rf} the rf sheath potential, ω circular frequency of rf voltage, d sheath thickness, m_i ion mass, and e elementary charge. The mean energy of the plasma peak corresponds to the dc sheath potential U_{dc} .

A calculation of the sheath thickness is possible [310].

6.5.2.7 Determination of Ion Density

For diffusion dominated plasmas the current density j_v^+ depends on the ion density n_v^+ as $j_v^+ = b^+ E n_v^+$. The relative ion densities in the plasma volume are given by [318]

$$\frac{n_v^+}{n_\mu^+} = \frac{b_\mu j_\mu^+}{b_v^+ j_v^+} \quad (6.34)$$

with E the electrical field and b^+ the ion mobility.

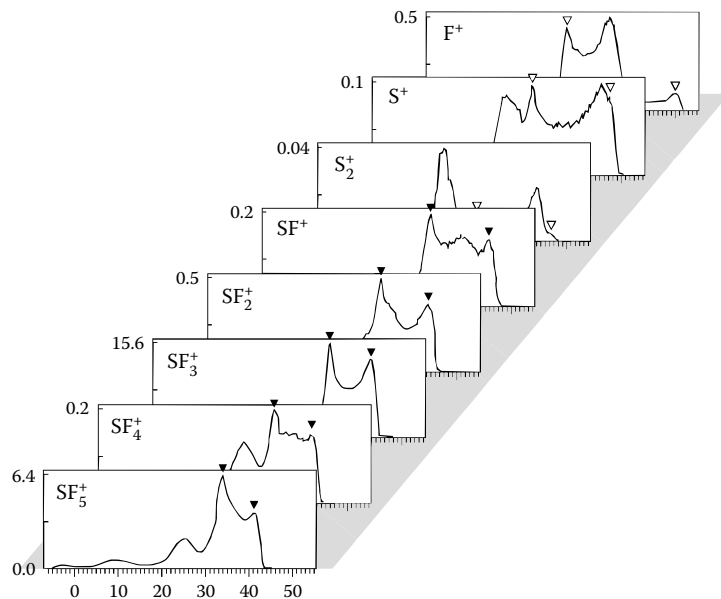


FIGURE 6.24 IED of positive ion of an rf discharge in SF₆ measured at the grounded electrode. The triangles indicate the width of the plasma peak. (From Foest, R. et al., *Phys. Rev. E*, 54, 1876, 1996.)

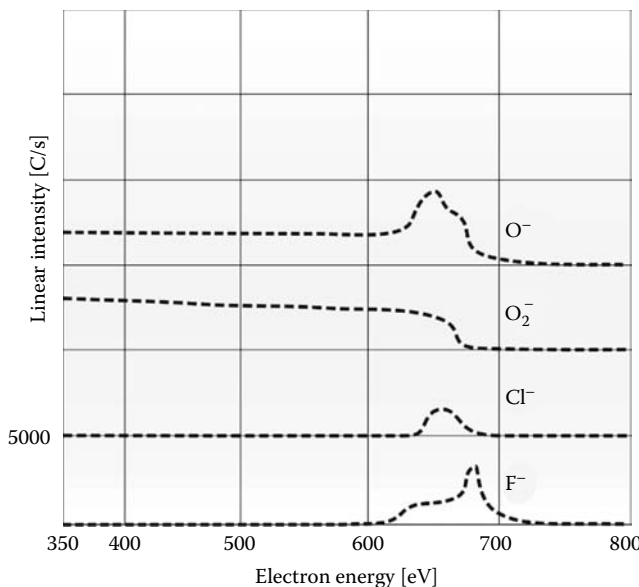


FIGURE 6.25 Energy distribution of negative ions measured at the grounded electrode of a capacitively coupled rf discharge in O₂. V_{rf} 1600 V, V_{dc} (bias) at the powered electrode up to 650 V. (From Zeuner, M. et al., *J. Appl. Phys.*, 79, 9379, 1996.)

The ion density near the sampling orifice in the electrode is determined by integration of the measured ion flux energy distribution $d\Gamma_i/d\varepsilon_i$ over ε_i divided by the ion velocity [319]

$$n_i = \int \frac{d\Gamma_i}{d\varepsilon_i} \sqrt{\frac{m_i}{2\varepsilon_i}} d\varepsilon_i. \quad (6.35)$$

6.5.2.8 Examples for Mass Spectrometric Measurements in Chemically Active Plasmas

The mass spectrum of the plasma ions shows the diversity of the ion species. One example is given by the investigation of the ion population of an inductive coupled rf discharge (27 MHz, 1.2 kW) in an Ar/H₂/CH₄ mixture (250/25/0.5 sccm, 4 mbar total pressure) for diamond deposition, see Figure 6.26 [320]. This result demonstrates the reactivity in this plasma by formation of higher hydrocarbon ions with only a small admixture of methane.

The plurality of ion formation processes shows the investigation of SiH₄ plasmas of an expanding thermal cascade arc with a broad spectrum of positive (Figure 6.27) [321] and of an RF discharge with impressive population of negative ions (Figure 6.28) [322].

6.5.2.9 Conclusions

The plasma ion mass spectrometry is an effective method for the diagnostics of various reactive plasma components as positive and negative ions. The mass spectrum is characterized by a relative simplicity in comparison with the optical spectrum. Additionally, the plasma monitoring gives information on the ion energy. These data are valuable for the understanding of plasma and discharge physics as well as of various plasma chemical volume reactions and surface processes such as cleaning,

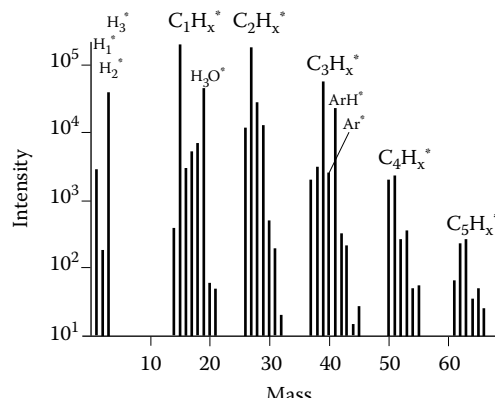


FIGURE 6.26 Positive ion mass spectrum of inductive coupled rf discharge in Ar/H₂/CH₄ mixture (500:100:1). (From Awakowicz, P. et al., *Diam. Relat. Mater.*, 6, 1816, 1997.)

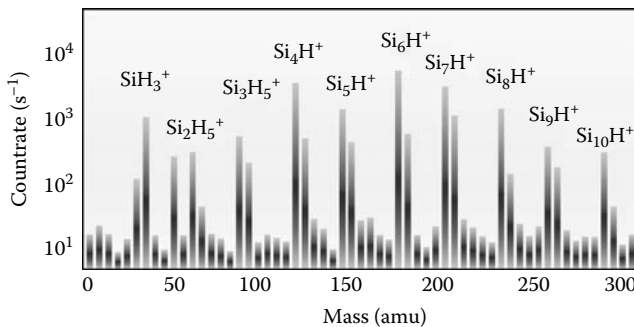


FIGURE 6.27 Mass spectra of positive ions of an expanding cascade arc plasma. (From Kessels, W.M.M. et al., *Appl. Phys. Lett.*, 72, 2397, 1998.)

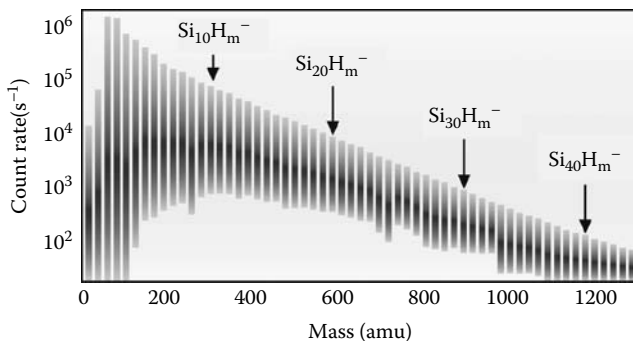


FIGURE 6.28 Negative ions in an RF discharge in SiH₄. (From Hollenstein, C. et al., *J. Vac. Sci. Technol. A*, 14, 535, 1996.)

etching, and thin film deposition. Mass spectrometry is an effective tool for process control in industrial plasma chemical applications.

6.5.3 NEUTRAL PLASMA COMPONENTS

The mass spectrometric analysis of neutral components in plasmas is applied to stable atoms and molecules but also to free radicals. The investigation of stable neutral nonreactive components is extensively discussed in textbooks of mass spectrometry, [279,323].

The mass spectrometric analysis of neutral particles requires their ionization in an ion source. Each compound is characterized by its molecular ion with the mass number m/z (not visible for all compounds) and the fragment ions with different mass numbers and intensities. These mass spectra are compiled for many substances, see [324]. The definite identification of the neutral component may be supported by consideration of the mass spectrum determined by the isotopic components with their various abundances. The quantitative analysis of more complicated mixtures with the interference of the various cracking pattern demands the decomposition of

the mass spectra to find the concentrations of the different components quantitatively. Unknown mixtures of gases like plasmas are treated successfully by Bayesian analysis [325,326].

The quantity of the neutral components can be deduced from the ion intensity taking into account the ionization cross section and the relative sensitivity of the mass analyzer or by calibration of the mass spectrometer with the corresponding gases.

6.5.3.1 Coupling

For processing pressures lower than 10^{-3} Pa the mass spectrometer can be inserted directly into the reaction chamber. For higher pressures the spectrometer is situated in a differentially pumped housing which is separated from the reaction chamber by a small orifice. The application of a leak valve or a tube with low conductance is possible. The application of a short orifice improves the detection of reactive species because of the low probability of wall collisions and therefore low loss rate. The diameter of the sampling orifice should be smaller than the mean free path of the gaseous molecules to minimize the disturbance of the plasma and to ensure a molecular flow. The composition of the gas in the ion source is determined by the properties of the pumping system for each component. Modifications of the gas flow composition can be avoided by a molecular flow through the orifice as well as in the high vacuum pumping system. The molecular flow through the orifice is limited to pressures up to 10^3 Pa due to minimum orifice diameters of $10\text{ }\mu\text{m}$.

The investigation of atmospheric pressure plasmas requires an essential reduction of the pressure between the sampling orifice and the mass spectrometer. For qualitative measurements of stable components the coupling is possible by a long capillary tube [327].

The application of a molecular beam system with a sampling orifice in the line-of-sight with the ionizer allows a quantitative determination of the plasma components including nonstable species such as radicals [328], see also [329,330]. The beam forming system comprises three differentially pumped stages and for modulated beam techniques a chopper. The application of a rotating skimmer within the first pumping stage allows an effective separation of the vacuum system from plasma system operating at higher pressure is what considerably improves the beam to background ratio [331].

The identification of the heavy neutral plasma components can be improved using ionization techniques with low decomposition (low energy of ionizing electrons, EAMS, chemical ionization, field ionization MS). A method for the mass spectrometric identification of single components in a gas mixture originating from a plasma chemical reactor with troublesome overlapping of decomposition pattern is proposed by [332]. The cryotrapping assisted mass spectrometry operates with a fast cooling in a cold trap and slow warming of the target gas mixture with different evaporation and therefore separation of single components.

6.5.3.2 Electron Attachment Mass Spectrometry

The electron attachment mass spectrometry (EAMS) investigates negative ions which are generated by attachment of low energetic electrons ($<10\text{ eV}$) by neutral species

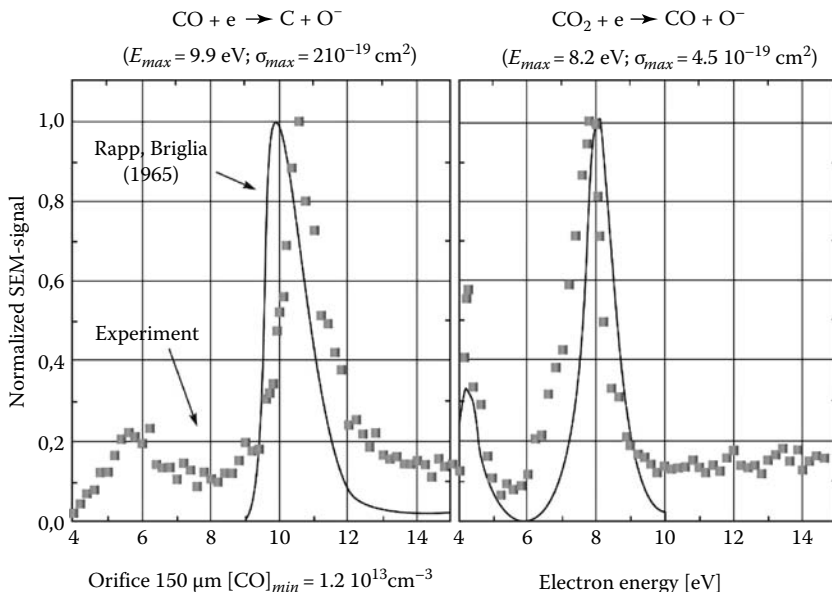
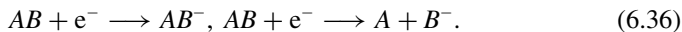


FIGURE 6.29 O^- -peaks generated by dissociative attachment of electrons by CO and CO_2 together with the reaction cross sections. (From Rapp, D. and Briglia, D.D., *J. Chem. Phys.*, 43, 1480, 1965.)

in the electron impact ion source. The dominant ion formation processes are



In polyatomic molecules the excess energy can be redistributed by internal degrees of freedom, and the parent ion is stabilized and can be detected [333]. Smaller molecules decay by dissociation into stable fragments. The dissociative electron attachment includes an intermediate metastable state and shows as a resonance process a peaked shape of the cross section. This results in a characteristic peak of the fragment ion in dependence on the electron energy. In Figure 6.29 the O^- -peaks generated by dissociative attachment of CO and CO_2 are presented together with the concerning reaction cross sections of Rapp and Briglia [334]. Because of the low electron energy the fragmentation is much lower than in conventional mass spectrometry ion sources with electron energies around 70 eV.

Radicals and large molecules such as polymers have a large electron attachment cross section. Also, vibrationally excited molecules can be distinguished due to their large cross sections; for example, for H_2 the dissociative attachment cross section for an internal energy of 3 eV is 10^5 times higher than for the ground state molecule [335]. Data of electron attachment of plasma processing gases (mainly F and Cl containing gases) are compiled in [336], see also [337] for energies < 0.5 eV.

Practical application of the EAMS is used for the investigation of larger neutral molecules by direct measurement of the concerning negative ions and for investigation of smaller neutral species which are identified by measurement of the dissociative products, as F^- , in dependence on the electron energy. Each compound is characterized due to the resonance process by a narrow peak shaped according to their attachment cross sections for the specific electron energy.

The experimental equipment for the EAMS consists usually of a quadrupole mass spectrometer with electron impact ion source, energy analyzer, quadrupole mass filter, and ion detector, evacuated by a turbo molecular pump. The device is separated from the plasma reactor by an orifice with a diameter of 100–200 μm , which is situated in the reactor wall. The neutral species flow out of the plasma vessel through the orifice into the ion source with the ionizing electrons. These electrons are generated by a hot filament and accelerated by a potential between the filament and a grid surrounding the attachment region in the source. The electron energy can be scanned from 0.5 to 10 eV with an energy resolution of 0.1 eV. A calibration of the energy scale is possible by using the dissociative attachment of O_2 with the resonance peak at 6.7 eV for O^- -generation [281].

The EAMS is applied preferentially for the investigation of fluorocarbon gases used for plasma processing in semiconductor industry [333,338–341]. In a 13.56 MHz capacitively coupled CF_4 discharge (15 mTorr, 2.5 sccm, ≤ 30 W) C_2F_6 and C_3F_8 could be identified; C_2F_6 and C_4F_8 plasmas were also investigated and series of anions C_nF_{2n-k} were found, which may originate from C_nF_{2n-k+1} [333]. A C_5F_8 plasma is investigated by [340]. Figure 6.30 presents the F^- -signal which shows several resonance peaks.

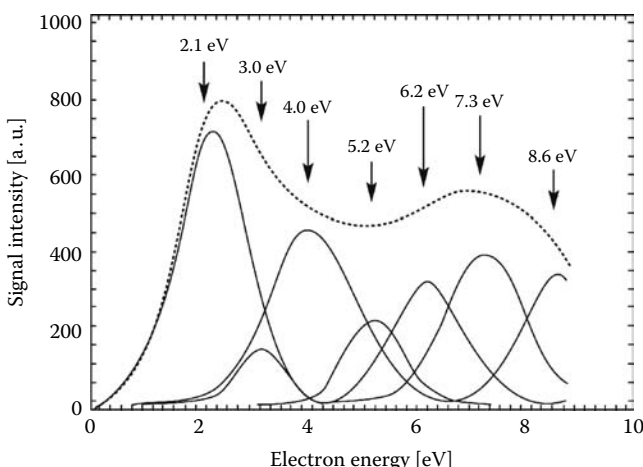


FIGURE 6.30 F^- -signal of neutral gas from a C_5F_8 plasma in dependence on the electron energy. The peaks at 2.1, 6.2, and 8.6 eV can be attributed to C_5F_8 , the 7.3, 4.0, and 3.0 eV peaks to CF_4 , C_2F_6 , and C_3F_8 . (From Imai, S. and Tachibana, K., *Jpn. J. Appl. Phys.*, 38, L888, 1999.)

6.5.3.3 Mass Spectrometric Investigation of Radicals

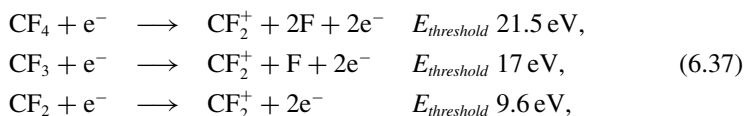
As already mentioned earlier, many mass spectrometric methods are suited more or less for the investigation of radicals in reactive plasmas. In the following, methods are discussed which are specially developed for radical investigations. A comprehensive review of mass spectrometry of free radicals also in plasmas is given by [342]. The study of the reactive radicals by mass spectrometry requires the consideration of their high reactivity in the sampling process. Disturbances by losses in surface reactions can be largely avoided for low pressures by application of short ideal sampling orifices and for higher pressures by use of modulated beam techniques.

6.5.3.4 Threshold Ionization Mass Spectrometry

The mass spectrometric investigation of the radicals requires the electron impact ionization of the neutral plasma components as a mixture of feed gas molecules, product molecules, as well as radicals. For example, in a CH₄ plasma CH₃ radicals are created. In the mass spectrum there is an overlap of the CH₃⁺ ions originating from the CH₃ radical and CH₃⁺ ions as fragment ions of CH₄. These ions can be distinguished by their appearance energy. The appearance energy of CH₃⁺ from CH₃ radical, that means its ionization energy, is 9.8 eV, the appearance energy of CH₃⁺ from CH₄ is 14.3 eV. In this way an energy scan of the ionizing electrons enables the identification of the radical. The determination of the radical density requires the knowledge of the sensitivity of the apparatus and the partial electron impact ionization cross sections for the formation of the relevant ion from the radical under study [343]. For the radical measurements, losses of these reactive particles on the path between plasma and ion source by wall recombination must be avoided, but generation of additional radicals at the hot filament surface should be prevented.

Mass spectrometric investigations of radicals were reported of SiH₄-discharges [343], of Ar-H₂-N₂-SiH₄ plasmas [344], and of an expanding Ar/C₂H₂ plasma [330].

Plasmas in fluorocarbon feed gases are important for plasma processing as thin film deposition and plasma etching. Essential reactants are various radicals, as CF, CF₂, and CF₃. Electron impact induced CF₂⁺ ion formation processes in CF₄ are [336]



see also Table 6.3.

Investigation of a capacitively coupled RF discharge in CF₄ 20 Pa, 13.56 MHz by threshold mass spectrometry allows the identification CF_x radicals. The differential pumped quadrupole mass spectrometer is coupled to the grounded plane electrode by an orifice (2r 100 μm), Figure 6.31.

The energy of the ionizing electrons can be scanned in the low energy range between 0.5 and 35 eV. A scan of the CF₂⁺ ions for electron energies of 5 eV up to 35 eV in pure CF₄ gas and for various plasma operating times (10, 30, 60, and 70 min) are shown in Figure 6.32. The onset thresholds for new CF₂⁺ generation processes

TABLE 6.3

Parent Neutral Radicals and Molecules and Their Parent or Fragment Ions with the Respective Ionization/Appearance Energies/eV

Ions	Parent Neutral					
	CF	CF ₂	CF ₃	CF ₄	C ₂ F ₆	C ₃ F ₈
CF ⁺	11	14.1	20.7	29.1	18	21
CF ₂ ⁺		9.6	17	21.5	17.5	26.6
CF ₃ ⁺			9.6	15.9	15.4	15.2

Source: Christophorou, L.G. and Olthoff, J.K., *Fundamentals Electron Interactions with Plasma Processing Gases*, Kluwer Academic/Plenum Publishers, New York, 2004.

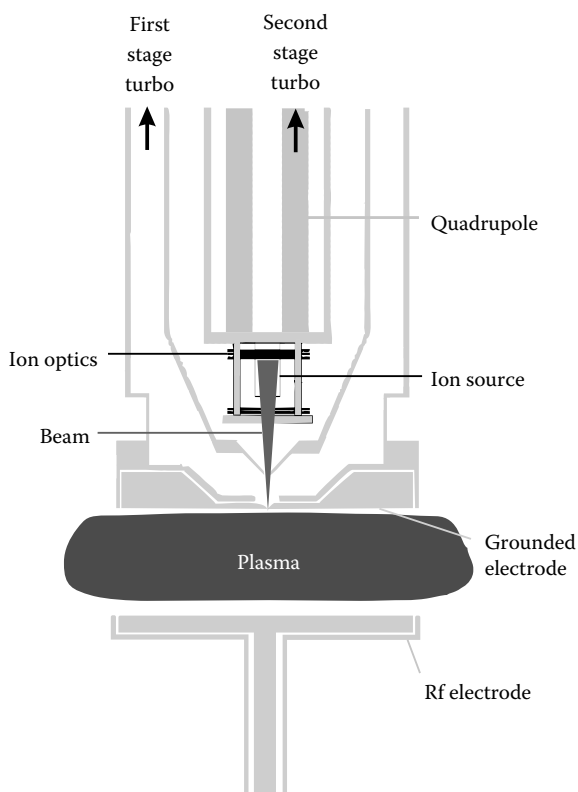


FIGURE 6.31 Capacitively coupled rf discharge with differential pumped quadrupole mass spectrometer separated from the plasma by an orifice ($2r = 100 \mu\text{m}$) in the grounded plane electrode. Apparatus for TIMS of CF_x radicals.

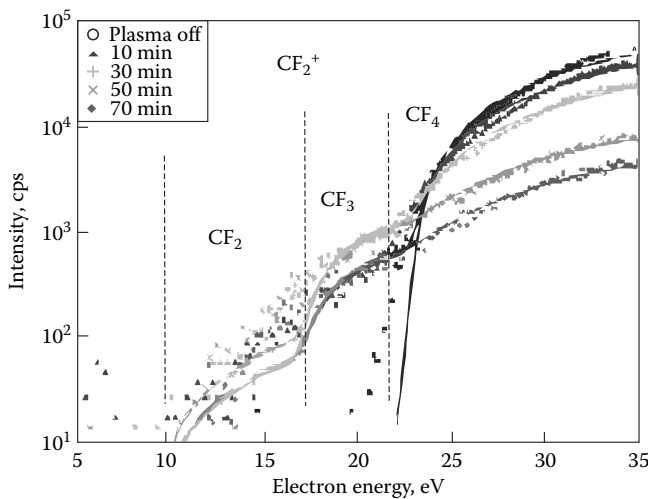


FIGURE 6.32 Scan of CF_2^+ ions for electron energies 5–35 eV in CF_4 (plasma off) and various plasma operating times. Capacitively coupled rf (13.56 MHz) discharge in CF_4 (20 Pa). CF_x indicates the parent radical/molecule of the CF_2^+ ion.

are clearly visible. In the interval between 10 and 17 eV the parent molecule is the radical CF_2 , in the range 17–21.5 eV the observed CF_2^+ is a fragment ion of CF_3 and for electron energies higher 21.5 eV a fragment ion of CF_4 .

In this way the evidence for the existence of CF_2 and CF_3 radicals is demonstrated. The decrease of CF_4 with increasing discharge time by thin film deposition is visible. A quantitative evaluation of the radical concentration requires the knowledge of the concerning reaction cross sections; data are compiled by [336].

6.5.3.5 Ion Attachment Mass Spectrometry

The chemical ionization of radicals by the attachment reaction between Li^+ ions and radicals is applied by Fujii [345], see also [346]. In the ion source Li^+ ions are produced by heating of a glass bead with lithium oxide in an aluminosilicate matrix. The ion source operates in the 10 Pa region, the ions are analyzed in a quadrupole mass spectrometer. In a CH_4 microwave discharge radicals like $\text{C}_n\text{H}_{2n-1}$ ($n = 2 - 11$) and $\text{C}_n\text{H}_{2n+1}$ ($n = 2 - 11$) could be measured.

6.5.3.6 Measuring Excess Energy

The application of an energy analyzer between the ion source and the mass analyzer offers the possibility to identify parent molecule ions and fragment ions. If the electron impact ionization occurs via a higher excited state the kinetic excess energy is distributed according to the conversion of momentum between the fragments like $m_1/m_2 = E_2/E_1$.

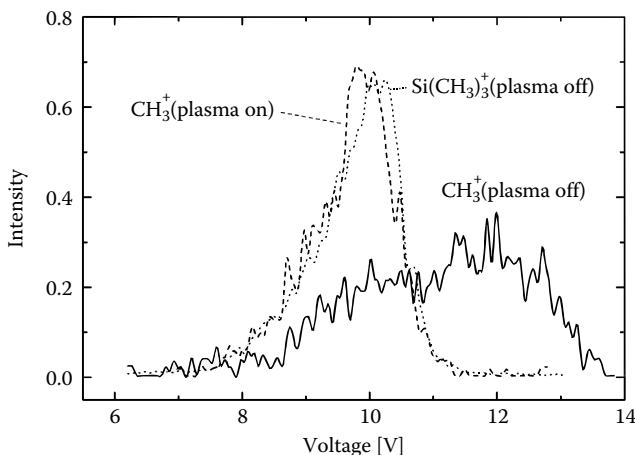
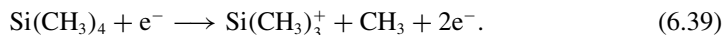


FIGURE 6.33 Energy distribution of CH_3^+ ions generated in the ion source coupled with a planar reactor filled with a $\text{Si}(\text{CH}_3)_4/\text{Ar}$ mixture. The energy of 10 eV accords to the potential of the ion source in relation to energy analyzer. The CH_3^+ ion (plasma off) originates from the $\text{Si}(\text{CH}_3)_4$, the CH_3^+ ion (plasma on) originates from CH_3 radical or small molecules as CH_4 . (From Foest, R., Massenspektrometrische Untersuchungen der Ionen und Neutralteilchen von RF-Entladung mit silizium-organischen Zumischungen, PhD thesis, Ernst Moritz Arndt University, Greifswald, Germany, 1998.)

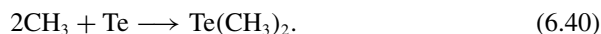
One example may be the electron impact ionization of $\text{Si}(\text{CH}_3)_4$, see also Figure 6.33



The broad energy distribution of the CH_3^+ ions identify this ion as a light fragment ion in contrast to the small energy distribution of $\text{Si}(\text{CH}_3)_3^+$ as a heavy fragment. Under plasma conditions CH_3^+ ions show a small energy distribution, indicating this ion as a parent ion of the CH_3 radical or the heavy fragment ion of CH_4 [347,348].

6.5.3.7 Measuring of Volatile Metal-Compounds

Methods for mass spectrometric identification of radicals use the chemical reactivity of radicals with a Tellurium surface



This compound can be identified by mass spectrometry. This technique has proven its suitability for the investigation of CH_3 , CF_3 , CF_2H , C_2F_5 , and F radicals in the presence of parent hydrofluorcarbons at five orders of magnitude higher pressures [349].

6.5.3.8 Conclusions

Mass spectrometry is an effective tool also for the investigation of neutral particles in plasmas. According to the small orifice coupling plasma and mass spectrometer, the disturbance of the plasma is very small. New methods for particle sampling from the plasma as modulated beam techniques improve the sensitivity also for radical detection in higher pressure plasmas. The conventionally applied electron impact ionization allows often an identification of the parent molecule, the fragmentation generates an specific fingerprint and is connected with the structure of the parent molecule. Ionization techniques with low fragmentation, as electron attachment mass spectrometry (EAMS) and field ionization mass spectrometry and ion attachment mass spectrometry are developed. Such methods and the threshold ionization mass spectrometry are also successfully applied for the investigation of free radicals. The plasma mass spectrometry is a powerful tool for plasma research and process control.

6.6 GAS CHROMATOGRAPHY

The gas chromatography (GC) allows the sensitive detection of the composition of stable reaction products at the outlet of plasma chemical reactors. Therefore, the GC is an important completion to the standard techniques, as emission spectroscopy, mass spectrometry and probe diagnostics, which characterize the plasma parameters themselves. Traditionally, the GC was mainly applied in the chemical analysis and process controlling [350,351]. The product analysis by GC in the plasma chemistry was realized in selected cases only, see [153,352–355]. This situation changed with the development of powerful separation columns, sensitive micro detectors and easy sample handling. Nowadays the GC finds many applications in the field of plasma chemistry, too [356–359].

The main *potential and advantages* of the GC can be summarized as follows:

- Separation of complex permanent gas mixtures as well as evaporable substances (e.g., liquids).
- Qualitative and quantitative analysis of complex mixtures. Identification of compounds by the combination with mass spectrometry (MS).
- High detection sensitivity depending on the used detector (mass flow: down to 10^{-14} g/s, concentration: ppb range).
- Fast sample analysis and easy automation (sample extraction and analysis). The so-called express GC realize the analysis on second level (see [357]).

6.6.1 GAS CHROMATOGRAPHIC SEPARATION OF STABLE COMPOUNDS

6.6.1.1 Principle

The principle of the component separation in a substance mixture (named sample) is caused by their distribution between two non-mixable phases: a stationary phase (solid and/or liquid, filled in the so-called separation column) and the mobile phase (carrier gas, flowing through the column, and containing the gaseous sample mixture). The distribution between the stationary and mobile phase results from

kinetic effects (absorption–desorption equilibrium) or the development of phase equilibria (solution–evaporation).

In most cases of gas chromatographic analysis a defined sample volume of the plasma chemical reactor is injected at the input of the separation column by valves in the near atmospheric pressure flowing carrier gas (mobile phase). Because of their different kinetic properties, the single components of the injected sample need a different time for traveling through the separation column (retention time). At the column outlet the separated single gas components are detected. This technique is named elution chromatography.

6.6.1.2 GC Equipment and Main Components

In Figure 6.34 a typical PC controlled setup is shown. The gaseous sample is extracted by a needle valve from the reactor into the sample inlet device. This module can be pumped separately. The sample volume (1) (typical volume: about 1 mL) is injected via a *two position valve* (2) into the mobile phase (carrier gas). In this way the sample is transferred to the inlet of the separation column(s) which are located in the thermostat (3) of the GC. In the shown setup two different columns (4, 5) can be operated, depending on the composition of the gas mixture. The columns GS-Q and PLOT 5A cover a wide field of separation problems.* The single components are detected by a mass spectrometer system (MS). The connection of the GC column with the quadrupole mass spectrometer is realized via an interface. The details are sketched in Figure 6.35a. In the MS the components are ionized by typically 70 eV electrons.

The chromatogram peak results from the total ion current (sum of all mass peaks) of the fragments of one component, collected by the detector (here a channeltron).

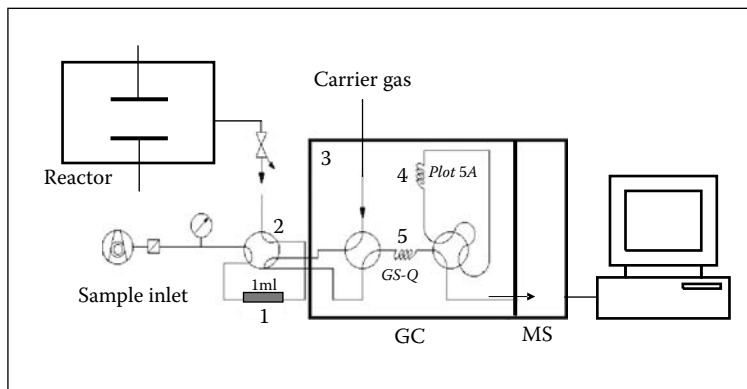


FIGURE 6.34 Scheme of gas chromatograph-mass spectrometer combination (GC-MS), 1: sample volume, 2: two position loading valve, 3: thermostat, 4, 5: separation columns, GS-Q: fused silica capillary column, PLOT 5A: molsieve column.

* The GS-Q is a fused silica capillary column (length about 25 m, inner diameter of 0.3 mm). The PLOT 5A is a molsieve column.

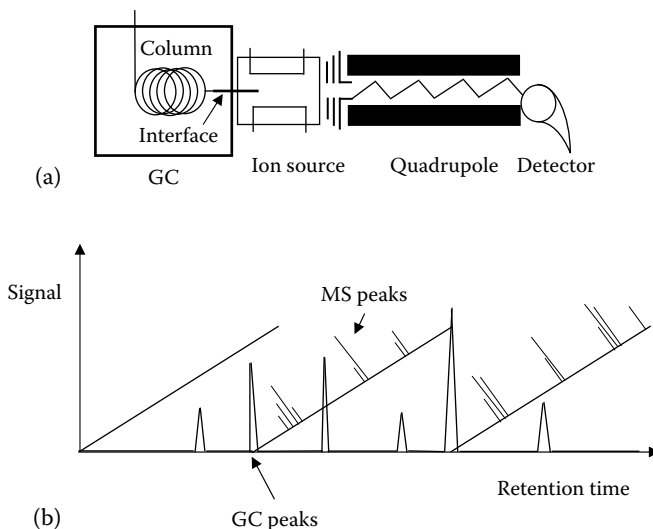


FIGURE 6.35 Scheme of a gas chromatograph coupled to a mass spectrometer (a) and sketch of a gas chromatogram (chromatogram peaks, mass peaks) (b).

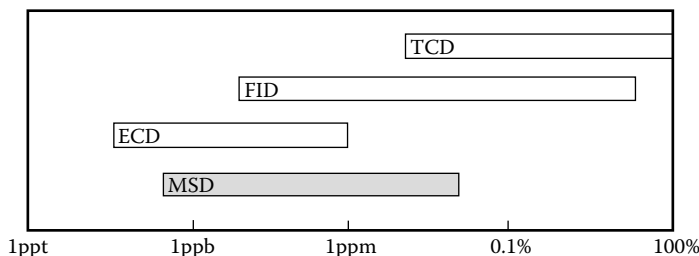


FIGURE 6.36 Important detectors, their sensitivities, typical carrier gases, and detectable gases.

TCD: thermal conductivity detector (universal), carrier gases: He, H₂, Ar, N₂, . . . ; FID: flame ionization detector (hydrocarbons), carrier gases: He, Ar, N₂, . . . ; ECD: electron capture detector (electronegative gases), carrier gas: N₂; MSD: mass spectrometer detector (universal, traces), carrier gases: He,

The mass spectra of the single components are an important tool for the identification of unknown substances, too. In Figure 6.35b a schematic *gas chromatogram* is shown. It consists of six components (chromatogram peaks) which appear after different retention times at the column outlet. The concentration of the single components is proportional to the chromatogram peak area. In this way, after the calibration with defined gas mixtures, a *quantitative analysis* of the sample composition is possible.

An overview on different detector types, their sensitivity, carrier gases and fields of application is given in Figure 6.36.

6.6.1.3 Basic Equation of Gas Chromatography

The basic equation of gas chromatography is discussed for the case of separation columns with a liquid stationary phase.* The separation process is controlled by the distribution coefficient K_i of the component i . If the distribution coefficients K_i are different for the components, the gas mixture (traveling through the column with the mobile phase) will be separated into their single compounds (substances). K_i is defined as

$$K_i = \frac{X_i}{Y_i} \quad \text{with} \quad X_i + Y_i = 1, \quad (6.41)$$

where

X_i is the relative amount of substance i in the stationary phase

Y_i is the relative amount of substance i in the mobile phase

Here equal volumina of the stationary and mobile phase are assumed.

Under the assumptions of the so-called linear (ideal) chromatography:

- Immediate adjustment of the phase equilibrium between solution/evaporation
- No axial diffusion
- Constant flow velocity u of mobile phase along the column (= flow velocity of the carrier gas)
- K_i is no function of the particle concentration n_i of component i , i.e., $K_i \neq K_i(n_i)$,

the basic equation of chromatography can be written as[†]

$$w_i = u * Y_i = \frac{u}{(1 + K_i)}, \quad (6.42)$$

where w_i is the traveling velocity of component i through the column.

The retention time t_{ri} of component i follows from

$$t_{ri} = \frac{L}{w_i} = \left(\frac{L}{u} \right) * (1 + K_i) = t_m + t'_i, \quad (6.43)$$

where

L is the length of separation column

t_m is the pure traveling time of the mobile phase (carrier gas) through column

t'_i is the relative retention time.

Therefore, a successful separation process of complex mixtures requires different K_i values of the single components i .

* The discussion for a solid stationary phase is quite analogous.

[†] This equation can be easily explained, because the value of Y_i is identical with the temporal fraction in which *all* the molecules of component i are in the mobile phase. In this time the molecules are traveling with the velocity u of the mobile phase.

6.6.2 EXAMPLES

Beside others, the GC-MS setup has been applied to the chemical analysis of reaction products formed in the dielectric barrier discharge operating at atmospheric pressure [356] (see Section 3.8). Mixtures of CH₄ and CO₂ were converted partially into a large number of substances. In Figure 6.37 the separation efficiency of the GC is illustrated. The gas chromatogram shows the separated complex calibration mixture, necessary for the quantitative determination of the expected reaction products. In Figure 6.38

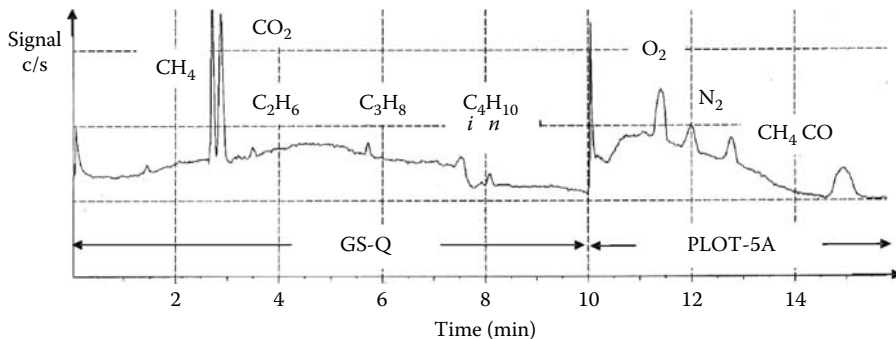


FIGURE 6.37 Analysis of a complex calibration mixture by the combined action of the GS-Q and PLOT 5A column with the SHIMADZU GC-MS QP 5000 (comp. Figure 6.34); sample mixture ($p = 1$ mbar, $V = 1$ mL) of CO₂, O₂, N₂, CH₄, CO (each 5 vol.%) and C₂H₆, C₃H₈, *i*-C₄H₁₀, *n*-C₄H₁₀ (each 100 ppm).

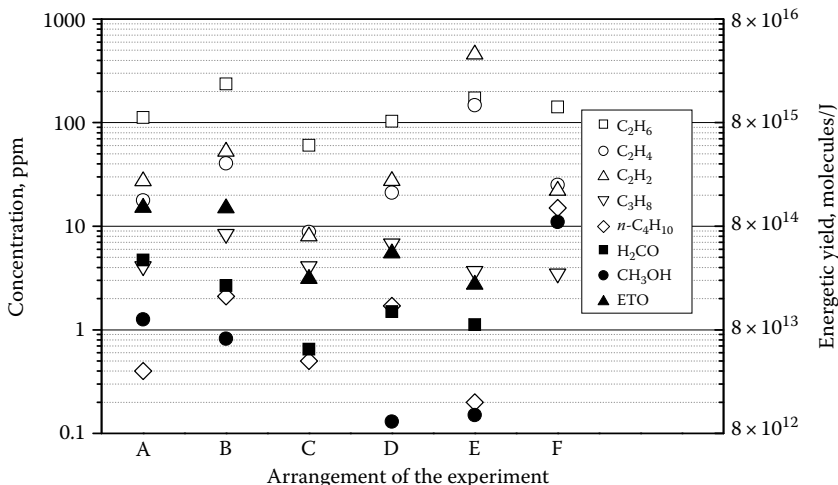


FIGURE 6.38 Comparison of the chemical efficiencies of the dielectric barrier discharge in mixtures of CH₄ with CO₂ for different experimental conditions A–E for different operation conditions of the discharge. (From Kozlov, K.V. et al., *Plasma Polym.*, 5(3–4), 129, 2000.) ETO: ethylene oxide.

selected results of these investigations are summarized. By the GC-MS it was possible to detect many compounds in a large concentration range over several orders of magnitude. Finally, the experimental results allowed a better understanding of the reaction mechanisms under the conditions studied.

Further examples of GC diagnostics are shown in Figures 4.8 and 4.9. By the GC, operating with a molsieve column and flame ionization detector FID (comp. Figure 6.36), the formation of hydrocarbons in a graphite hollow cathode glow discharge was analyzed (Figure 4.8). In this way the formation of chemical quasi-equilibria in low-pressure discharges was studied. The decomposition of CO₂ in RF discharges was investigated by a GC equipped with a thermal conductivity detector TCD (Figure 4.9). After the necessary compression of the low pressure sample to atmospheric pressure, the quantitative detection of CO₂, CO, and O₂ was realized.

More examples can be found in the given references.

7 Surface and Thin Film Analysis

CONTENTS

7.1	Fourier Transform Infrared Spectroscopy	258
7.1.1	Basics of Absorption Spectroscopy in the Mid-Infrared Spectral Range	258
7.1.2	Principle of Fourier Transform Infrared Spectroscopy	261
7.1.3	IR Spectroscopic Techniques for Analysis of Interfaces and Thin Films	263
7.1.3.1	Infrared Reflection-Absorption Spectroscopy	264
7.1.3.2	Evanescence Wave Spectroscopy	265
7.1.3.3	Internal Reflection Element Using Mid-Infrared Transmitting Fiber	267
7.2	X-Ray Photoelectron Spectroscopy (XPS)	271
7.2.1	Experimental Setup	271
7.2.2	Analysis of XPS Spectra	273
7.2.3	Actual Trends in X-Ray Photoelectron Spectrometry Development	274
7.3	Analysis with Ion Beams by Energy Loss Spectroscopy	276
7.3.1	Rutherford Backscattering Spectrometry	276
7.3.2	Elastic Recoil Detection Analysis	277
7.4	Matrix-Assisted Laser Desorption/Ionization, Secondary Ion Mass Spectrometry	278
7.5	X-Ray Diffraction and Reflection	280
7.5.1	Grazing Incidence X-Ray Diffractometry	280
7.5.2	X-Ray Reflectometry	282
7.6	Radical Investigation by Electron Spin Resonance	282

An important application of plasma chemistry is the reactive treatment of surfaces and the deposition of thin films. The analysis of these surfaces and films is essential for understanding of the mechanisms of the treatment and deposition processes which facilitate developments and optimization activities, too. The diagnostics include conventional chemical, like elementary analysis, and physical methods, like microscopy, or methods which are specially developed for this purpose. An overview on thin film and surface properties and corresponding diagnostic methods are presented in Table 7.1.

TABLE 7.1**Surface and Thin Film Properties and Methods of Analysis**

Thin Film/Surface Properties	Thin Film/Surface Analysis
Thickness	XRF ^a , SEM ^b , XR ^c , ellipsometry
Density	XR ^c , ellipsometry
Grain size	XRD ^d , TEM ^e , SEM ^b , AFM ^f
Surface topography	SEM ^b , TEM ^e , AFM ^f
Hardness	Brinell-, Vickers-, Rockwell-Hardness
Stress, strain	XRD ^d , substrate curvature
Wettability	Contact angle methods
Optical properties	Refractometry, ellipsometry
Refraction index, reflectivity, absorbance	Four point method
Resistivity	AAS ^g , AES ^h , ICP-MS ⁱ , XPS ^j , EDX ^k , SIMS ^l ,
Chemical composition	XRD ^d , RBS ^m , ERDA ⁿ , ESR ^o , GDMS ^p
Constitution/structure	XPS ^j , FTIR ^q , Raman spectroscopy, NMR ^r , SIMS ^l , XRD ^d , LEED ^s
Phase composition	XRD ^d , TEM ^e

^a XRF: x-ray fluorescence analysis
^b SEM: scanning electron microscopy
^c XR: x-ray reflectometry
^d XRD: x-ray diffractometry
^e TEM: transmission electron microscopy
^f AFM: atomic force microscopy
^g AAS: atom absorption spectroscopy
^h AES: Auger electron spectroscopy
ⁱ ICP-MS: inductive coupled plasma mass spectrometry
^j XPS: -ray photoelectron spectroscopy
^k EDX: energy dispersive x-ray spectroscopy
^l SIMS: secondary ion mass spectrometry
^m RBS: Rutherford back scattering
ⁿ ERDA: elastic recoil detection analysis
^o ESR: electron spin resonance
^p GDMS: glow discharge mass spectroscopy
^q FTIR: Fourier transform infrared spectroscopy
^r NMR: nuclear magnetic resonance
^s LEED: low energy electron diffraction

This chapter deals with physical methods such as XPS, XRD, RBS, ERDA, FTIR, MALDI-ToF, SIMS, and ESR. Here the principles of the methods will be explained and illustrated by examples of plasma chemistry.

Typical chemical methods and other physical methods like ELMI, AFM, as well as electrical methods are dealt in related textbooks

The diagnostics of solids by probing with beams can be classified as in Table 7.2.

TABLE 7.2
Excitation and Emission Processes for Surface and Thin Film Analysis

Excitation by			
Emission of	Photons	Electrons	Ions
Photons	Diffraction, Reflection (XRD ^a , GIXD ^b , XR ^c) X-ray spectroscopy (XRF ^f)	X-ray spectroscopy (EDX ^d) Electron-induced photons (GDOS ^e)	Ion-induced photons (GDOS ^e)
Electrons	Ellipsometry Infrared spectroscopy (FTIR ^g , IRRAS ^h , ATR ⁱ) Electron spin resonance (ESR ^j)	Scanning electron microscopy (SEM ^m) Diffraction (LEED ⁿ , RHEED ^o) Electron energy loss spectroscopy (EELS ^p) Auger electron spectroscopy (AES ^q)	Ion-induced secondary electrons
Ions	Photo desorption of ions, Mass spectrometry (MALDI-ToF MS ^r)	Mass-spectrometry (EI-MS ^s) Electron-induced desorption (EID ^v)	Secondary ion mass spectrometry (SIMS ^t , ToF-SIMS ^u) Back scattering of ions (RBS ^w , ERDA ^x , ISSY ^y , GDMS ^z)

^a XRD: x-ray diffractometry^b GIXD: grazing incidence x-ray diffractometry^c XR: x-ray reflectometry^d EDX: energy dispersive x-ray spectroscopy^e GDOS: glow discharge induced optical spectroscopy^f XRF: x-ray fluorescence analysis^g FTIR: Fourier transform infrared spectroscopy^h IRRAS: infrared reflection absorption spectroscopyⁱ ATR: attenuated total reflection^j ESR: electron spin resonance^k XPS: x-ray photoelectron spectroscopy^l UPS: ultra violet photoelectron spectroscopy^m SEM: scanning electron microscopyⁿ LEED: low energy electron diffraction^o RHEED: reflection high energy electron diffraction^p EELS: electron energy loss spectroscopy^q AES: Auger electron spectroscopy^r MALDI-ToF MS: matrix-assisted laser desorption / ionization time of flight mass spectrometry^s EI-MS: electron impact ionization mass spectrometry^t SIMS: secondary ion mass spectrometry^u ToF-SIMS: time of flight secondary ion mass spectrometry^v EID: electron induced desorption^w RBS: Rutherford back scattering^x ERDA: elastic recoil detection analysis^y ISS: low energy ion scattering spectroscopy^z GDMS: glow discharge mass spectrometry

7.1 FOURIER TRANSFORM INFRARED SPECTROSCOPY

7.1.1 BASICS OF ABSORPTION SPECTROSCOPY IN THE MID-INFRARED SPECTRAL RANGE

Infrared (IR) absorption spectroscopy is applied for the analysis of the chemical composition and molecular structure of gases, liquids, thin solid films, and interfaces. The interaction of electromagnetic radiation in the infrared spectral region with matter can result in excitation of the molecule to higher vibrational states, for example, the fundamental vibrational bands in the mid-infrared at wavelengths between 2 and 20 μm or corresponding wave numbers $\bar{\nu} = 1/\lambda$ from 5000 to 500 cm^{-1} . The absorption of power from waves occurs by changing the electric dipole moment during the oscillation only. That means that the vibrational mode is IR-active. The theory of molecular transitions in the IR spectral range, including their quantum mechanical selection rules, has been presented by many authors in detail [1–4]. Complex molecules show a lot of vibrational modes which are mostly IR-active. The frequency of the observed bond length (stretching) and bond angle (deformation) vibrations is mainly determined by the atomic masses in the molecule, their bond strengths, and molecular geometry. Furthermore, the molecular surroundings and interaction of the absorbing molecular groups in gas phase, liquid or solid state have influence on the frequency. One advantage in the interpretation of the measured IR spectrum is that strong vibration modes in complex molecules are limited to a small number of atoms. The corresponding characteristic frequencies are approximately independent from the molecular structure and can be used for the analysis of characteristic groups. Each material is characterized by a *fingerprint* in the spectral region between 1500 and 900 cm^{-1} for identification. Here, the vibrations of single bonds are localized. Other interesting spectral ranges provide information about double bonds (1800–1500 cm^{-1} , e.g., C=O, C=N, C=C), triple bonds (2300–2100 cm^{-1} , e.g. C≡N, C≡C), and vibrations of heterogeneous X–H chemical bonds, e.g., C–H (3200–2800 cm^{-1}), N–H and O–H (4000–3000 cm^{-1}). Furthermore, the interaction of absorbing X–H species and formation of hydrogen bridge bonds may result in strong broadening of the absorption bands.

Table 7.3 gives an overview about selected molecular groups and their characteristic group frequency and wave number, respectively. Figure 7.1 shows exemplarily the different normal modes of the CH₂ molecular group which is present in many organic compounds.

The classical absorption spectroscopy is based on the measurement of the transmittance $T = I/I_0$, where I_0 is the initial intensity impinging on a sample and I is the reduced intensity after transmission of an absorbing sample of the thickness d , see Figure 7.2.

The absorption of the infrared radiation at any wave number by a homogeneous medium is defined quantitatively by the Beer–Lambert–Bouguer law

$$A(\bar{\nu}) = -\log_{10}\left(\frac{I}{I_0}\right) = \alpha(\bar{\nu}) \cdot d = \varepsilon(\bar{\nu}) \cdot c \cdot d. \quad (7.1)$$

TABLE 7.3**Selected Wave Number Range of Characteristic Molecular Groups**

Vibration	Functional Group	Wave Number [cm ⁻¹]	Intensity	Comments
C–C def.	–(CH ₂) _n –	725–720	w-m, rocking	n > 3, skeletal
C–F def.	–C–F	830–520	s	General range
Si–C str.	–OSiCH ₃	850–840	s	Siloxanes
C–H def.	–C=CH ₂	895–885	s	CH ₂ out of plane
O–H def.	Carboxylic acid	955–915	s, out of plane	
Si–H def.	Si–H	985–800	m-s	General range
C–O stret.	–CH ₂ –OH	1085–1030	s	Sat. prim. alcohols
C–N stret.	–CH ₂ –NH ₂	1090–1065	m	Prim. aliph. amines
C–F stret.	–C–F	1100–1000	vs	Aliph. fluorinated
–(SiO) _n –	–(SiO) _n –	1100–1000	s	Siloxanes
C–O–C		1150–1060		Sat. aliph. ethers
C–N stret.	–CH ₂ –NH–CH ₂ –	1190–1170	m	Sec. aliph. amines
C–F stret.	–CF ₃	1350–1120	vs	
C–F stret.	–CF ₂	1350–1120	s	
O–H def.	–OH	1350–1260	s, in plane	Prim./sec. alcohols
C–H def.	–CH ₃ –	1390–1370	m-s, symm.	Alkane
C–F stret.	–CF	1400–1000	s	General range
C=C	–C=C–	1465–1430	vs	Aromatic
C–H def.	–CH ₃ –	1465–1440	m, asymm.	Alkane
C–H def.	–CH ₂ –	1480–1440	m, scissoring	Alkane
C=C	–C=C–	1525–1470	vs	Aromatic
C=C	–C=C–	1590–1575	vs	Aromatic
C=C	–C=C–	1625–1590	vs	Aromatic
C=C stret.	–CH=CH ₂	1645–1640	w-m	Alkene
N–H def.	–NH ₂	1650–1580	m-s	
C=N stret.	–C=N–	1690–1640	w	
C=O stret.		1850–1550		
C≡C stret.	–C≡CH	2140–2100	w-m	Monosubst.
Si–H stret.	–Si–H	2250–2100		General range
C≡N stret.		2260–2200	m	
C–H stret.	–CH ₂ –	2870–2840	m, symm.	Alkane
C–H stret.	–CH ₃ –	2870–2840	m, symm.	Alkane
C–H stret.	–CH ₂ –	2940–2915	m-s, asymm.	Alkane
C–H stret.	–CH ₃ –	2975–2950	m-s, asymm.	Alkane
C–H stret.	–CH=CH ₂	3030–2995	m	CH str. of CH
C–H stret.	=C–H	3080–3010	m	Aromatic
C–H stret.	–CH=CH ₂	3095–3075	m	CH str. of CH ₂
N–H stret.	–NH ₂	3450–3250	w-m	Prim. amines
O–H stret.	–OH	3550–3230	m-s	Hydr. bonded

Source: Socrates, G., *Infrared Characteristic Group Frequencies—Tables and Charts*, Johh, Wiley & Sons, Inc., New York, 1994.

vs, very strong; s, strong; m, middle; w, weak; stret, stretching; def, deformation.

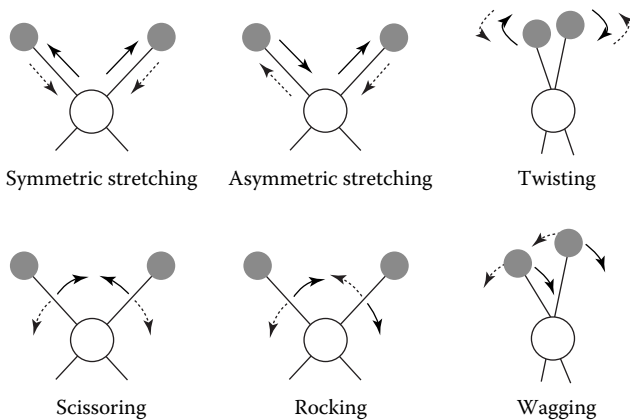


FIGURE 7.1 Normal modes of stretching and deformation vibrations in the CH_2 molecular group.

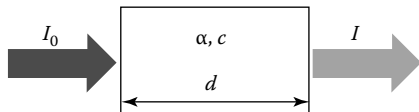


FIGURE 7.2 Principle of transmission spectroscopy.

The absorbance $A(\bar{\nu})$ in relation (7.1) is usually defined as the negative decadic logarithm of the transmittance $T = I/I_0$.

Here $\alpha(\bar{\nu})$ is the decadic absorption coefficient at wave number $\bar{\nu}$, $\varepsilon(\bar{\nu})$ the molar absorptivity in m^2/mol , c the concentration of absorbing species in mol/m^3 , and d the path length in the sample. Alternatively, the negative natural logarithm is applied in relation (7.2) with the corresponding absorption coefficient $\alpha'(\bar{\nu})$, the absorption cross section $\sigma(\bar{\nu})$ of a single particle, and the number density of the absorbing particles n .

$$A'(\bar{\nu}) = -\ln \left(\frac{I}{I_0} \right) = \alpha'(\bar{\nu}) \cdot d = \sigma(\bar{\nu}) \cdot n \cdot d. \quad (7.2)$$

The absorption coefficient $\alpha(\bar{\nu})$ is connected with $\alpha'(\bar{\nu})$ and the imaginary part k of the complex refractive index $\tilde{n} = n + ik$ at the wavelength λ , respectively, at the wave number $\bar{\nu}$, according to

$$\alpha \cdot \ln 10 = \alpha' = \frac{4\pi \cdot k}{\lambda} = 4\pi \cdot \bar{\nu} \cdot k. \quad (7.3)$$

Thus, it is possible to calculate the concentration of the absorbing species if the absorption coefficient is known. The Beer–Lambert–Bouguer law for quantitative analysis is only exact if no interaction occurs between the absorbing species. In the frame of its validity, the concentration can be calculated using the maximum

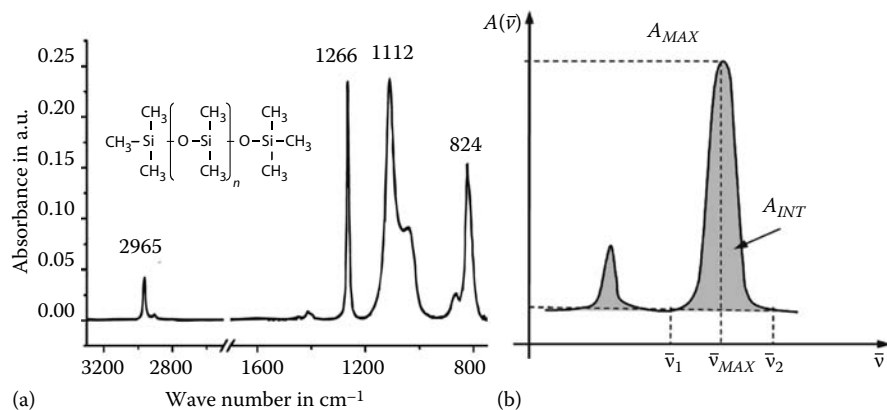


FIGURE 7.3 IR absorption spectrum (a) of a 85 nm thin film from polydimethylsiloxane (SILFAR® 1000) with characteristic absorptions at 2965 cm⁻¹ (asymmetric stretching of C–H in CH₃-group), 1 266 cm⁻¹ (symmetric deformation of Si–CH₃), 1 112 cm⁻¹ (asymmetric stretching of Si–O–Si backbone), and 824 cm⁻¹ (symmetric rocking of Si–(CH₃)₂). (b) The principle of the integral absorbance for determining the concentration of absorbing species is shown.

absorbance $A_{MAX}(\bar{\nu}_{MAX})$ of the absorption line; however the instrumental parameters have strong influence on this maximum absorbance. Therefore, the calculation of the integral absorbance A_{INT} over the absorption line (7.4) is more favorable. The area below the absorption line is proportional to the concentration of absorbing species. Figure 7.3 shows as an example the absorption spectrum of a polydimethylsiloxane (PDMS) thin film with characteristic absorption bands (taken by FT-IRRAS, Figure 7.3a), and the definition of the integral absorbance (Figure 7.3b)

$$A_{INT} = \int_{\bar{\nu}_1}^{\bar{\nu}_2} A(\bar{\nu}) \cdot d\bar{\nu}. \quad (7.4)$$

7.1.2 PRINCIPLE OF FOURIER TRANSFORM INFRARED SPECTROSCOPY

In comparison with conventional broadband IR spectroscopy using dispersive optical elements for the wave number tuning, the FTIR technique [6] allows one to measure simultaneously all wave numbers in the chosen spectral range by means of the interferometer. The principal scheme of FTIR spectrometer with a Michelson interferometer is shown in Figure 7.4.

The interferometer consists of two mutually perpendicular plane mirrors. One of them (M_1) is fixed and the other (M_2) can move along the axis which is perpendicular to its plane. The infrared radiation emitted by a broadband IR source is divided by the beam splitter (BS) where the infrared beam is partially reflected to the mirror M_1 and partially transmitted to the mirror M_2 . After both space-coherent beams return to the beam splitter, they interfere and are again partially reflected and transmitted. The path difference of the two interfering beams is equal to $2 \cdot \delta$, where δ is the M_2 mirror

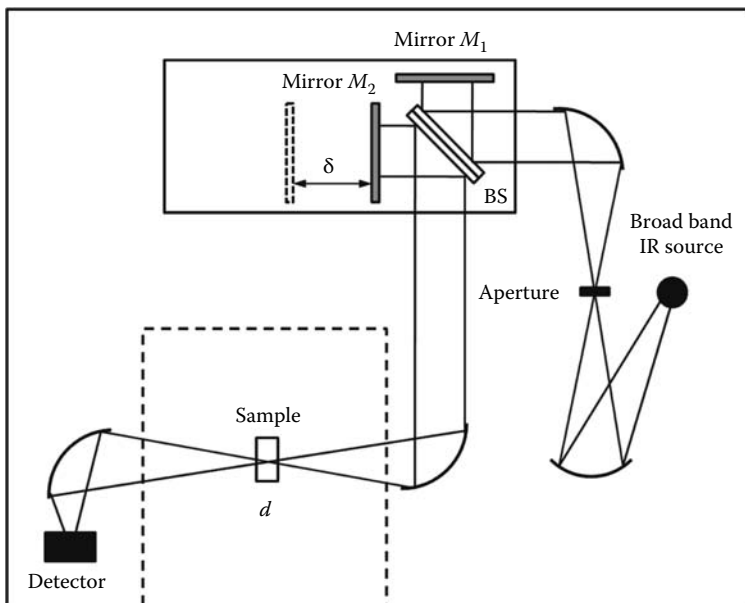


FIGURE 7.4 Principle of the FTIR spectrometer with Michelson interferometer, BS: Beam splitter, δ : Mirror displacement, d : Sample thickness (absorption path length).

displacement. The output intensity I_0 transmits the sample section and is focused on a detector. The detector measures the intensity I of the infrared radiation as a function of the mirror displacement δ - the interferogram $I(\delta)$. For the broadband IR source the measured interferogram is the result of the overlay of interferograms corresponding to each wave number. In such case the main relation in the FTIR spectroscopy is represented by the integral for the amplitude spectrum $B(\bar{\nu})$ of the investigated IR radiation including all instrumental effects

$$B(\bar{\nu}) = \int_{-\infty}^{+\infty} I(\delta) \cdot A(\delta) \cdot \exp(i \cdot 2\pi \cdot \bar{\nu} \cdot \delta) \cdot d\delta. \quad (7.5)$$

The IR amplitude spectrum $B(\bar{\nu})$ is calculated from the interferogram $I(\delta)$ by computing the integral (7.5). For monochromatic radiation the value $B(\bar{\nu})$ provides the intensity of the source at a wave number $\bar{\nu}$ as modified by the instrumental characteristics. This procedure is implemented using a fast Fourier Transform in the standard data processing software of FTIR spectrometers. In the case $A(\delta) = 1$, the amplitude spectrum $B(\bar{\nu})$ corresponds to the Fourier transformed function $I(\delta)$. Because of the limited displacement δ_{max} of the moving mirror, the apodisation function $A(\delta)$ is introduced. In the case $|\delta| > \delta_{max} = \Delta$ the apodisation function has a value $A = 0$, whereas $A = 1$ is valid for $\delta \sim 0$. By use of the boxcar function $A(\delta) = 1$ for $-\Delta \leq \delta \leq +\Delta$, and $A(\delta) = 0$ elsewhere, the spectrum is convoluted with the Fourier transformed symmetric boxcar function (7.6).

$$F[A(\bar{v})] = 2 \cdot \Delta \cdot \text{sinc}(2\pi\bar{v}\Delta) = \frac{2 \cdot \Delta \cdot \sin(2\pi\bar{v}\Delta)}{2\pi\bar{v}\Delta}. \quad (7.6)$$

The convolution with the *sinc* function results in strong side lobes in the interferogram. Suppression of the magnitude of these side lobes can be realized by usage of other apodisation functions. Different forms of apodisation functions have been studied, for example the apodisation functions Norton–Beer [7,8] and Happ–Genzel [5]. Norton and Beer showed that there is a distinct empirical boundary relation between the full width at half-height (FWHH) and the side lobe amplitude [7,8]. The narrower the FWHH, the greater is the side lobe amplitude. The use of the specific apodisation function depends on the experiment being performed. A function like the Norton–Beer weak function should be applied, if either high resolution or accuracy for quantitative analysis is required. Stronger apodisation functions can be applied for spectra containing both weak and intense bands, especially when their width is comparable with the instrumental resolution. Taking into consideration the maximum displacement Δ of the interferometer mirror and boxcar apodisation the received spectral resolution is given by $\Delta\bar{v} = \Delta^{-1}$. Additionally, the beam collimation in the interferometer has influence on the resolution.

The Fourier transform of the interferogram represents the single channel spectrum which contains instrumental effects, for example, the source and detector characteristics as well as the transmission properties of all the optical elements in the spectrometer. Therefore, in the IR spectroscopy two single channel spectra are taken to measure $I_0(\delta)$ without and $I(\delta)$ with the absorbing sample of thickness d , respectively. The corresponding negative decadic logarithm of the amplitude spectra $\log(I/I_0)$ in absorbance units versus \bar{v} in reciprocal cm provides the usual representation of the IR absorption spectrum.

The advantages of the FTIR spectroscopy [6,9] are

1. Reduced measuring time due to the fast mirror movement and detection of the complete spectrum
2. Increased accuracy due to laser-assisted determination of the mirror position (Connes advantage)
3. Increased transmission of radiation due to the usage of circular apertures instead slits or grids in dispersive spectrometers (Jacquinot advantage)
4. Increased intensity at the detector due to the broadband intensity in comparison with low intensity at selected wave number in dispersive spectrometer (Fellgett advantage)

7.1.3 IR SPECTROSCOPIC TECHNIQUES FOR ANALYSIS OF INTERFACES AND THIN FILMS

By use of the conventional transmission arrangement, that is, the measurement of the transmitted IR radiation in a single path through an absorbing sample of thickness d , according to Figures 7.2 and 7.4, the IR analysis provides information about the chemical composition and molecular structure, and the absolute concentration

of absorbing species. In contrast to methods in surface analysis, for example, x-ray photo electron spectroscopy, the standard IR spectroscopy is not surface sensitive. Nevertheless, the specific IR spectroscopic techniques based on specular and internal reflection are widely applied for the analysis of interfaces and thin films. The transmission and reflection of infrared radiation can be described in both rigorous by means of the Maxwell equations and non-rigorous by use of the classical equations of Fresnel and Snell's law.

The following methods are of special interest in thin film and interface analysis:

- Infrared Reflection-Absorption Spectroscopy (IRRAS)
- Evanescent Wave Spectroscopy (EWS)

7.1.3.1 Infrared Reflection-Absorption Spectroscopy

The infrared reflection-absorption spectroscopy (IRRAS) [10–12] involves a double pass through a thin film on a highly reflective (metallic) surface. The analytical description of reflection-absorption spectroscopy considers the propagation of the electric wave field in a three-phase, optically isotropic medium. Reflection occurs at the planar, parallel optical boundaries between media. The typical system consists of the ambient (air/vacuum), a thin film of interest and an optically thick metallic film as substrate. The formation of a standing wave due to interference of incoming and reflected wave at the metallic substrate is characterized by disappearing electric field strength near the metallic surface. By use of the IR reflection technique the analysis of a thin film ($d \ll \lambda$) provides usually a weak absorption compared with the standard transmission arrangement using self-supporting thin film. This effect can be reduced by the careful selection of material and geometry [7,8]. The degree of reflected or transmitted IR radiation at an interface depends on the polarization state and angle of incidence of the incoming radiation as well as the optical constants of the two adjacent media. Whereas no interaction of the radiation at perpendicular polarization with the thin film for all angles of incidence occurs, the parallel polarized radiation and grazing incidence results in sufficient electric field strength and absorption, see Figure 7.5. For highly reflecting metallic surface and angles of incidence lower than 80° , the change in reflectivity can be expressed by (7.7), [10,13]

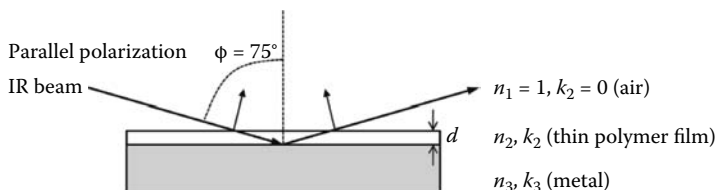


FIGURE 7.5 Principle of IR reflection absorption spectroscopy (IRRAS) of thin film with thickness d at parallel polarization and grazing incidence.

$$\Delta R = \frac{R_0 - R}{R_0} = \frac{4 \cdot \sin^2 \varphi}{n_2^3 \cdot \cos \varphi} \cdot \frac{4\pi \cdot k_2}{\lambda} \cdot d = \frac{4 \cdot \sin^2 \varphi}{n_2^3 \cdot \cos \varphi} \alpha' \cdot d. \quad (7.7)$$

R_0 and R are the reflectivity without and with an absorbing thin film, respectively, and k_2 is the imaginary part of the complex refractive index of the thin film.

Further, in the case of a weakly absorbing thin film ($\alpha' \cdot d \ll 1$), it follows from the Beer–Lambert law the approximation $\Delta I = (I_0 - I)/I_0 \sim \alpha' \cdot d$ and the ratio of absorption of a thin film comparing IRRAS and transmission experiment is expressed by

$$\frac{\Delta R}{\Delta I} = \frac{4 \cdot \sin^2 \varphi}{n_2^3 \cdot \cos \varphi}. \quad (7.8)$$

For example, using the arrangement with a thin polymer film ($n_2 = 1.5$) of thickness d , ambient vacuum ($n_1 = 1$), and an angle of incidence $\varphi = 75^\circ$ the sensitivity in the IRRAS experiment is increased by the factor of about four compared with the transmission experiment. By use of proper experimental condition the received IRRAS spectrum corresponds practically to the transmission spectrum [14]. The advantage of this technique is that thin films can be prepared on the metallic substrate by plasma deposition processes or spin/dip coating procedure in order to study the interaction of the nonthermal plasma with polymer surfaces and thin organic films *in situ*. For example, it has been investigated the plasma modification of polymer surfaces [15], as well as the plasma solidification of liquid polydimethylsiloxane films [16].

7.1.3.2 Evanescent Wave Spectroscopy

The evanescent wave spectroscopy (EWS) in the IR spectral range is well known as the *attenuated total reflection (ATR) spectroscopy* [17].

When radiation passes into a medium 1 with higher refractive index n_1 than the surrounding medium 2 with n_2 , the radiation will be trapped inside if the angle of incidence φ at the reflecting surface in the medium 1 exceeds the critical angle $\varphi_c = \sin^{-1}(n_2/n_1)$. A standing wave is established in front of the reflecting interface. The radiation is totally reflected at proper conditions and propagates through the medium 1. In the medium 2 with lower refractive index an evanescent wave is observed for the electric field strength $E(z)$ (7.9) with characteristic penetration depth d_p (7.10), see Figure 7.6.

$$E(z) = E_0 \cdot \exp\left(-\frac{z}{d_p}\right), \quad (7.9)$$

$$d_p = \frac{\lambda}{2\pi \cdot n_1 \cdot \sqrt{\sin^2 \varphi - (n_2/n_1)^2}} \quad (7.10)$$

with λ the vacuum wavelength.

Without absorption in medium 2 the Pointing vector in z -direction disappears averaged over the time. In the interesting case of an absorbing medium 2, the reflected intensity is reduced. ATR spectroscopy is used for chemical analysis of the interface of bulk material (semi-infinite sample $d \gg d_p$), or for thin films

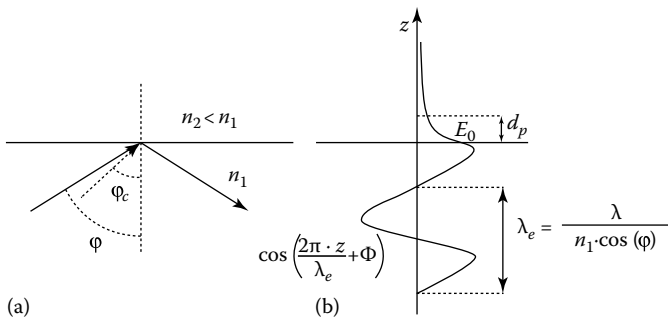


FIGURE 7.6 Principle of evanescent wave spectroscopy. Total reflection in the case $\varphi > \varphi_c$, ray path (a) and formation of standing wave in medium 1 and penetration of the electric field $E(z)$ in semi-infinite medium 2 described as evanescent wave (b).

($d \ll d_p$) as the medium 2. The efficiency of the ATR analysis is characterized by the effective thickness d_e of the sample, which defines a sample thickness of the investigated material having the same absorption as in the transmission experiment.

In case of a bulk material the sampling depth is defined by the full absorption of the evanescent wave and results in the value of about $3d_p$ [9]. Generally, the ATR spectrum is determined by the coupling of the evanescent wave to the absorbing medium. This coupling is influenced by the electric field strength, depth of penetration, sampling area, and index matching [6].

In the interesting case of thin film analysis the effective thickness is independent on d_p and the wavelength, but the effective thickness depends on the polarization state of the IR radiation ($d_{e\perp}$, d_{ell}) according to (7.11) with the refractive index n_2 for the thin film and non-absorbing ambient medium n_3

$$d_{e\perp} = \frac{4 \cdot n_2/n_1 \cdot d \cdot \cos \varphi}{1 - (n_3/n_1)^2},$$

$$d_{ell} = \frac{4 \cdot n_2/n_1 \cdot d \cdot \cos \varphi}{1 - (n_3/n_1)^2} \cdot \frac{[1 + (n_3/n_2)^4] \cdot \sin^2 \varphi - (n_3/n_1)^2}{[1 + (n_3/n_1)^2] \cdot \sin^2 \varphi - (n_3/n_1)^2}. \quad (7.11)$$

However, strong influence of the polarization state on the effective thickness is only observed near the critical angle φ_c . In the case of a thin film, the critical angle is determined by the refractive index of the ambient medium and not by the thin film!

High-sensitive ATR spectroscopy can be performed due to multiple total reflections at the sample surface using an internal reflection element (IRE) in contact with the thin film of interest. The IRE may be realized by a parallelepiped, see Figure 7.7.

For example, the arrangement consists of chalcogenide glass (IRG 100: Ge-Sb-Se, $n_1 = 2.6$) for the IRE, the thin polymer film ($n_2 = 1.5$) of the thickness d , the ambient medium vacuum or air ($n_3 = 1$), and the angle of incidence $\varphi = 45^\circ$. This provides a

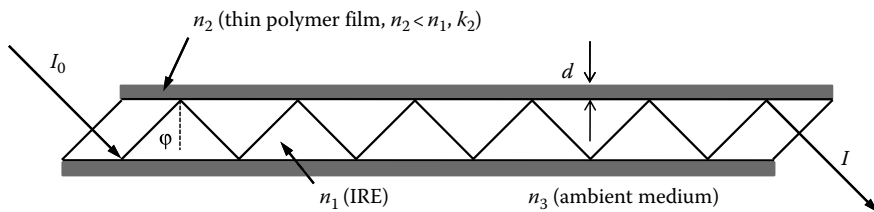


FIGURE 7.7 Principle of attenuated total reflection (ATR) spectroscopy using parallelepiped as internal reflection element (IRE) with deposited thin polymer film of thickness d on both surfaces of the IRE.

ratio between effective and geometric thin film thickness of $d_e/d \sim 2$, corresponding to (7.11). Taking into account 12 total reflections in the sample region according to Figure 7.7, the sensitivity of the ATR spectroscopy is about 24 times higher compared with the standard transmission spectroscopy. By use of a parallelepiped as IRE, the ATR technique was successfully applied for in situ diagnostics of polymer surface modification in nonthermal reactive plasmas [15].

7.1.3.3 Internal Reflection Element Using Mid-Infrared Transmitting Fiber

Sensitive evanescent wave spectroscopy can be achieved due to high number of internal reflections by use of optical step-index fiber for the internal reflection element (IRE). Fibers transmitting infrared radiation can be divided into three large groups: glass fibers, crystal fibers and hollow waveguides [18,19]. Progress was mainly achieved in the development of infrared fibers in connection with remote sensor applications and power delivery applications [20,21]. IR transmitting fibers for the interesting mid-infrared (MIR) spectral region consist of chalcogenide glass, halide, and hollow fibers [18,19]. The application of MIR fibers as sensors for studying plasma-assisted thin film deposition/etching or plasma surface modification in non-thermal reactive plasmas needs sufficient stability of the fiber material in the plasma environment (ion bombardment, UV radiation, temperature). Therefore, the step-index chalcogenide glass (As-Se-Te) fiber with diameter 750 or 250 μm was used for internal reflection element (IRE) [22]. The core refractive index is $n_{\text{core}} = 2.82$ at a wavelength $\lambda = 4 \mu\text{m}$. This fiber material is stable under nonthermal plasma conditions (glass transition temperature about 136°C) and has relatively low optical losses, about 1 dB/m from 2 to 10 μm , in comparison with crystalline fibers. In the considered case of MIR radiation with wavelength in the range of between 3 and 16 μm and a fiber radius R in the order of few hundred microns, the propagation of the IR radiation in the fiber can be described in the limit of geometric optics. For the description of ray propagation in optical fibers it is convenient to use the axial angle δ , which is the angle between the ray path and the tangent plane of the fiber core surface. The rays enter and propagate in the fiber core with constant refractive index n_{core} within a limited solid angle of incidence defined by φ_0 , according to (7.12) and Figure 7.8

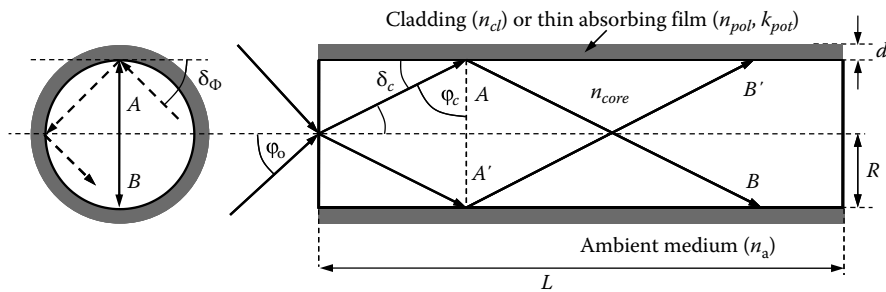


FIGURE 7.8 Schematic of the ray propagation in the step-index fiber as internal reflection element with meridional ray ($\delta_\phi = \pi/2$) crossing the fiber axis between reflection points A and B, and the skew ray for $\delta_\phi < \pi/2$ (dashed line).

$$n_0 \cdot \sin \varphi_0 = n_{core} \cdot \sin \delta_c = n_{core} \cdot \cos \varphi_c = (n_{core}^2 - n_{cl}^2)^{1/2} \approx n_{core} (2\Delta)^{1/2}, \quad (7.12)$$

where

n_0 and $n_{cl} < n_{core}$ are the refractive index of the ambient medium (e.g., air $n_0 = 1$) and fiber cladding

δ_c is the critical angle for total reflection ($\sin \varphi_c = \cos \delta_c = n_{cl}/n_{core}$)

The quantity $n_{core} (2\Delta)^{1/2} = n_{core} [2 \cdot (n_{core} - n_{cl}) / n_{core}]^{1/2}$ in (7.12) is the numerical aperture of the fiber. The radiation can propagate for angles $\delta < \delta_c$ by meridional rays containing the core axis or by skew rays (helical-like path for $\delta_\phi < \pi/2$). The skew rays are not confined in a single plane, see Figure 7.8 left. However, in the case of a phase shift after reflection between perpendicular and parallel polarized light to the plane of incidence the propagation of a limited number of modes remains. This number of modes in the step-index fiber is the fiber parameter V according to [23,24],

$$V = \frac{2\pi R}{\lambda} \cdot (n_{core}^2 - n_{cl}^2)^{1/2} \approx \frac{2\pi R}{\lambda} \cdot n_{core} \cdot (2\Delta)^{1/2} \quad (7.13)$$

with λ the vacuum wave length.

For application of the geometric optics the fiber parameter should be $V \gg 1$. Considering multimode chalcogenide glass fibers with core diameter larger than $250 \mu\text{m}$ the fiber parameter is greater than 250. Both criteria, ($V \gg 1$, $R \gg \lambda$) are satisfied and, consequently, the ray analysis can be used.

In the case of an absorbing medium instead of the cladding, for example, a thin polymer film with refractive index n_{pol} and absorption k_{pol} , the propagating rays in the fiber lose some of their intensity due to attenuated total reflections. The number of total reflections per length unit from the ray path through the fiber IRE can be calculated by the relation

$$\frac{N_{IRE}}{L_{IRE}} = \frac{\tan \delta}{2 \cdot R \cdot \sin \delta_\phi}. \quad (7.14)$$

For example, by use of chalcogenide glass fiber (diameter $250 \mu\text{m}$, $n_{core} = 2.82$, $n_{pol} = 1.5$), the reflections per length unit for an assumed angle of incidence

$\delta = 45^\circ < \delta_c$ amounts to about 200 total reflections per 50 mm fiber length for meridional rays.

For a given pair of the angles (δ, δ_ϕ) the attenuation coefficient per length unit (γ_F) of the fiber IRE in contact with the absorbing thin film is defined as

$$\frac{I(\delta, \delta_\phi, z)}{I_0} = \exp(-\gamma_F \cdot l). \quad (7.15)$$

The attenuation coefficient γ_F of a ray can be found by summation of the intensity loss at the reflection points per length unit l of the fiber. According to Snider and Love [23] the attenuation coefficient γ_F of a ray is related to the absorption coefficient α'_{pol} of the absorbing polymer material

$$\gamma_F = \frac{\alpha'_{pol}}{V} \cdot \left(\frac{\delta}{\delta_c} \right)^2 \cdot \left[1 - \left(\frac{\delta}{\delta_c} \right)^2 \cdot \sin^2 \delta_\phi \right]^{-1/2} \quad (7.16)$$

with $0 \leq \delta < \delta_c$ and $\alpha'_{pol} = 4\pi \cdot k_{pol}/\lambda$. The attenuation has a maximum when the ray is meridional, that is, $\delta_\phi = \pi/2$, and decreases with increasing skewness. Usually, the attenuation coefficient will be dominated by the meridional rays, which means $\delta_\phi \sim \pi/2$ [23].

Taking into account meridional rays only, the intensity loss is given by the integral (7.17) over the angular distribution $g(\delta)$ from $\delta = 0$ to the maximum angle δ_{MAX} .

$$\frac{I(l)}{I_0} = \frac{\int_0^{\delta_{MAX}} g(\delta) \cdot \exp[-\gamma_F(\delta) \cdot l] \cdot d\delta}{\int_0^{\delta_{MAX}} g(\delta) \cdot d\delta} = \exp(-\Gamma_F \cdot l). \quad (7.17)$$

Further, with the assumption of weak absorption ($\gamma_F \cdot l \ll 1$) the integral can be solved analytically, and in the case that the maximum angle δ_{MAX} is far from the critical angle δ_c the ratio between the effective evanescent wave absorption coefficient Γ_F and the absorption coefficient α'_{pol} of a polymer sample is given by [25]

$$\frac{\Gamma_F}{\alpha'_{pol}} = \frac{2}{3 \cdot V} \cdot \left(\frac{\delta_{MAX}}{\delta_c} \right)^2 = \frac{2}{3 \cdot V} \cdot \left(\frac{n_{core}}{n_{pol}} \cdot (2\Delta)^{1/2} \right)^2. \quad (7.18)$$

The approximation used here for evanescent wave spectroscopy is valid in the limit $\Gamma_F \cdot l \leq 0.2$ and $\delta_{MAX}/\delta_c \leq 0.3$ and shows a linear relation between Γ_F and α'_{pol} .

The optical signal transmitted along the fiber is distorted because of dispersion effects. It is convenient to distinguish the intermodal and intramodal dispersion. The first kind of dispersion is present whenever more than one mode exists in the fiber. The modes with higher δ angles propagate more slowly along the fiber than those with lower angles. The energy pulse of the initial signal is broadened. The intramodal dispersion occurs because of the Fourier transformation of the single mode which

consists of a distribution of propagating waves with $\lambda \pm \Delta\lambda$. Every spectral component undergoes the appropriate time delay. Intramodal dispersion contains generally two independent contributions from the core material ($d\eta/d\lambda$) and from the mode guiding ($d\delta/d\lambda$). The former is referred to as material dispersion and the latter as waveguide dispersion.

The total transmission loss of optical fibers is expressed by the sum of losses due to scattering and absorption. Both processes are present even in highly pure and structurally perfect materials (intrinsic losses). The frequency range of maximum intrinsic transparency in glasses and crystals is known as the optical window, limited by the multiphonon edge (far IR) and by the Urbach tail at the short wave length side (absorptions from electronic band gap excitations). The other source of the intensity attenuation at short wavelength is scattering (mainly Rayleigh scattering). Besides such loss mechanisms, there are also macroscopic losses due to bending of the fibers, imperfection of the core cross-section, etc.

For example, a single channel IR transmission spectrum of about 1 m long step-index chalcogenide glass fiber is shown in Figure 7.9. The used core-only fiber is covered with a protecting polyamide layer. The transmission spectrum of the chalcogenide glass fiber is determined by both, the absorption bands from the polyamide including H_2O and CO_2 impurities and the structural imperfections and impurities (Se–H) of the fiber material.

The fiber losses as well as the dispersion do not influence crucially the application of the optical fibers as IRE in the evanescent wave spectroscopy. Any absorption spectrum of a thin film deposited on the fiber core is taken with regard to the background

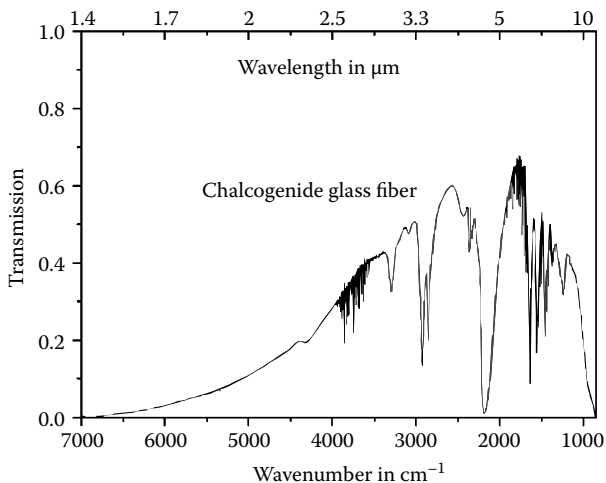


FIGURE 7.9 Single channel transmission spectrum of step-index chalcogenide glass fiber (core diameter 750 μm) with protecting polyamide taken by the FTIR spectrometer Bruker Vector 22 and MCT detector. Characteristic absorption bands from polyamide, as well as H_2O , CO_2 , and Se–H ($2200\text{--}2800\text{ cm}^{-1}$) can be seen. (From Li, K., Investigation of plasma polymerization in RF discharge by novel fibre based FTIR diagnostic tool, PhD thesis, University of Greifswald, Greifswald, Germany, 2002.)

spectrum. The fiber IRE for in situ studies of organic thin film deposition/etching in reactive nonthermal plasmas was realized by guiding the fiber through the plasma reactor and removing the polyamide protection layer from a part of the fiber in the plasma zone [22,26].

7.2 X-RAY PHOTOELECTRON SPECTROSCOPY (XPS)

7.2.1 EXPERIMENTAL SETUP

XPS is the most widely used surface analysis technique for plasma-modified surfaces and plasma-enhanced deposited thin films. Especially, biomaterial surface modification pushed the advancement of devices and techniques [27,28]. The XPS, also known as ESCA (electron spectroscopy for chemical analysis) determines surface elemental compositions, its molecular state, unpaired electrons, organic groups, surface heterogeneity, lateral surface variation, and allows the identification of specific valence bands [29].

Performing an XPS measurement, a sample is irradiated with soft x-rays. In most cases, Mg K α (1253.6 eV) or Al K α (1486.6 eV) x-rays are used (see Figure 7.10 with a schematic view of an XPS device and photoelectric process for 1s electron emission). The x-ray photons interact with the atoms in the surface region causing core electrons to be emitted by the photoelectric effect. The energy and the amount of the emitted electrons are analyzed. The measured kinetic energy of the electrons is given by

$$E_k = h\nu - E_b - \phi, \quad (7.19)$$

where

$h\nu$ is the energy of the photons

E_b is the binding energy of the atomic orbital the electron originates from

ϕ is the spectrometer work function

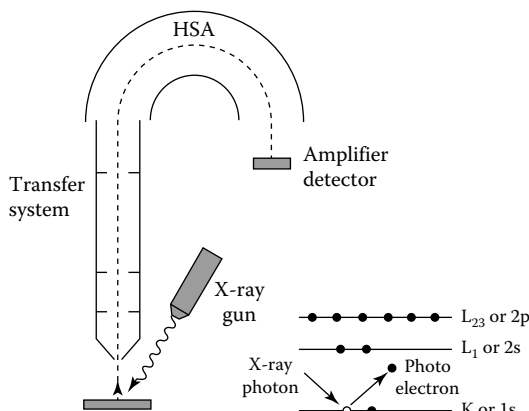


FIGURE 7.10 Schematic view of an XPS device and photoelectric process for 1s electron emission. HSA, hemispherical energy analyzer.

The main parts of an XPS device are: x-ray source, electron optic, energy analyzer and detector. In modern spectrometers, the x-rays are energy filtered or monochromatized using a quartz crystal to get x-rays with small energy width. The monochromatic x-rays enable a higher energy resolution and prevent additional peaks (satellites). A hemispherical analyser (HSA) is applied to measure the energy of the electrons emitted. Small pass energies of the HSA reduce the signal peak width.

Each element has a unique set of electrons in orbitals with well-defined binding energies. The kinetic energy of an emitted electron is characteristic for its source orbital and hence for each element.

The number of electrons measured for a given transition is proportional to the number of atoms at the surface. For that reason, XPS can be used to identify and determine the concentration of the elements in the surface excluding hydrogen and helium. The number of electrons counted in dependence of binding energy yields an XPS spectrum, see Figure 7.11.

Quantitative data can be obtained from the peak areas divided by the atomic sensitivity factors (ASF) which depend on the XPS instrument. Concentrations down to 0.1 at% can be detected. Variations in the elemental binding energies arise from differences in the chemical neighborhood and binding state. These chemical shifts can be used to identify the chemical state of the materials being analyzed.

In the case of conducting samples, the detected electron energies can be referenced to the Fermi energy of the spectrometer. An absolute energy scale can be established. Energy calibration is significant for nonconducting samples. Electrons leaving the sample surface cause a potential difference between the sample and the

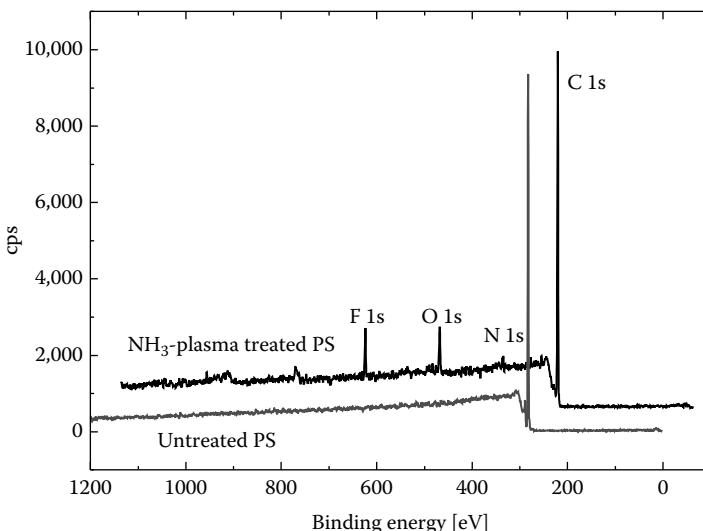


FIGURE 7.11 Wide scan—comparison between untreated polystyrene (PS) and NH₃-plasma-treated PS after chemical derivatization of amino groups by trifluoromethylbenzaldehyde introducing a F 1s peak.

spectrometer. The consequence can be peaks shifted in energy which will complicate their identification. A hot filament electron source is usually applied to compensate the charge of electrons leaving the surface. Nevertheless, the measured spectrum should be calibrated to at least two peaks with well-known positions.

While the path length of the x-ray photons inside the target is several micrometers, that of the electrons is some nanometers, only. Thus, XPS is restricted to a surface depth of maximal 10 nm in polymers. Electrons leaving the surface without energy loss produce the peaks in the spectra. The background is formed by the electrons that undergo inelastic loss processes before emerging, see Figure 7.11 [29–32].

7.2.2 ANALYSIS OF XPS SPECTRA

The analysis of an XPS measurement starts with the identification of the peaks in the spectrum. The first step is to define an approximation to the background signal. The background results from electrons which are scattered in the surface material. There are several background algorithms known for XPS spectra, which are more or less useful approximations, Linear, Shirley, or universal cross-section Tougaard backgrounds are used in most cases. Linear backgrounds provide good results for polymers [29]. Energy loss processes occur above an energy threshold and the linear approximation fits well. On the other hand, spectra of metals exhibit sharply rising backgrounds under the peaks. In these cases, an approximation due to Shirley is used quite often. Tougaard announced three-parameter universal cross sections for materials with sharp rising backgrounds such as metallic aluminum where the approximation according to Shirley failed, too [33].

Not all peaks in XPS data are due to the ejection of electrons by a direct interaction with the incident photons. The most important additional peaks are Auger peaks, satellites, and plasmons. An Auger process includes the decay of a more energetic electron to fill the vacant hole created by the x-ray photon, combined with the emission of an electron with an energy characteristic of the difference between the states involved in the process. Satellite peaks can be generated by nonmonochromatic x-ray sources. These peaks are shifted to higher kinetic energies. Energy shift and proportion to the main peaks in the x-ray spectrum are characteristic for the anode material and well known. Another source of peaks in the background signal is due to resonant scattering of photoelectrons with other electrons in the surface region. In the case of insulating samples, there is a fairly sharp peak at 20–25 eV higher binding energy than the main peak. This effect is much stronger in metals. Energy loss lines due to interaction with conductive electrons are obtained in well-defined distances to the main peak and are characteristic for each metal. The energy difference between the main peak and the loss peak is called plasmon energy.

Some photoelectric processes lead to ions in excited states. In this case, the kinetic energy of the photoelectrons is reduced resulting in a peak with a few eV higher binding energy. For carbon in aromatic compounds, the typical shake-up process involves the $\pi \rightarrow \pi^*$ transition.

Additionally, valence lines and bands are present in the spectrum region between the Fermi level and 10–20 eV. Molecular orbitals and solid state energy bands are

responsible for these lines. The valence band region is more sensitive to the molecular structure than core lines. So, several hydrocarbons like polyethylene and polypropylene have got the same C 1s spectrum but are clearly distinguished by their valence band spectra. Unfortunately, the intensity is up to two magnitudes lower in the valence band region [29].

The atomic concentration of the elements is calculated from peak area and ASF, if the background is established and the elements are identified. ASF tables are only accurate for homogenous materials. Unfortunately, most samples vary in composition with depth. Therefore, differences occur in one element in one sample between transitions at low binding energy (high kinetic energy) and high binding energy (lower kinetic energy).

A more detailed analysis of peak shape is often applied to quantify different binding states of one element. For this purpose, measured peaks are approximated by synthetic curves. Peak fitting is a complex process. A fitting procedure without constraints very often yields incorrect results. The most popular lineshapes for routine analysis of XPS spectra are based on Gaussian and Lorentzian functions [34]. Figure 7.12 shows an example for the analysis of an NH₃ plasma-treated polystyrene (PS) sample.

7.2.3 ACTUAL TRENDS IN X-RAY PHOTOELECTRON SPECTROMETRY DEVELOPMENT

To meet the demands of advanced plasma chemical modification processes, some new technical features and process developments will be described briefly.

The measurement of energetically highly resolved XPS spectra is necessary to distinguish different functional groups by curve-fitting methods. A reduced peak FWHM (for instance, below 1 eV for C 1s spectra) enables the parallel quantification of different functional groups, see Figure 7.12) [37,38]. But primary, secondary, and tertiary amines or alcohols and ethers can not be distinguished by curve fitting, because the chemical shifts are too small. Thus chemical derivatization [39–41] is of special importance to quantify, for instance, the density of amino groups after plasma treatment [41], compare Figure 7.12a and b.

There are several methods to obtain information on the depth of an element in the sample. A first simple check concerning the homogeneity of the sample can be done by comparing the results of two peaks of one element with different kinetic or binding energies. Real depth profiling can be accomplished using controlled erosion of the surface by sputtering. Furthermore the background can be analyzed to get information on the depth of elements [42]. A very good approach to improved depths information is to change the angle θ between the surface normal and the angle of entrance to the analyzer. At 90° electrons escaping the sample surface have got a maximum information depth. In the case of angle-resolved XPS (ARXPS) the analysis depth d is reduced to $d \cdot \cos \theta$. Some XPS instruments use detectors that collect spectroscopic and angular information simultaneously [43].

XPS usually analyzes macroscopic areas of some mm², because x-ray sources are showers. Lateral resolution can be increased by focussing the x-ray source to about 7 μm [45]. The local resolution can be improved in the sub-μm range by

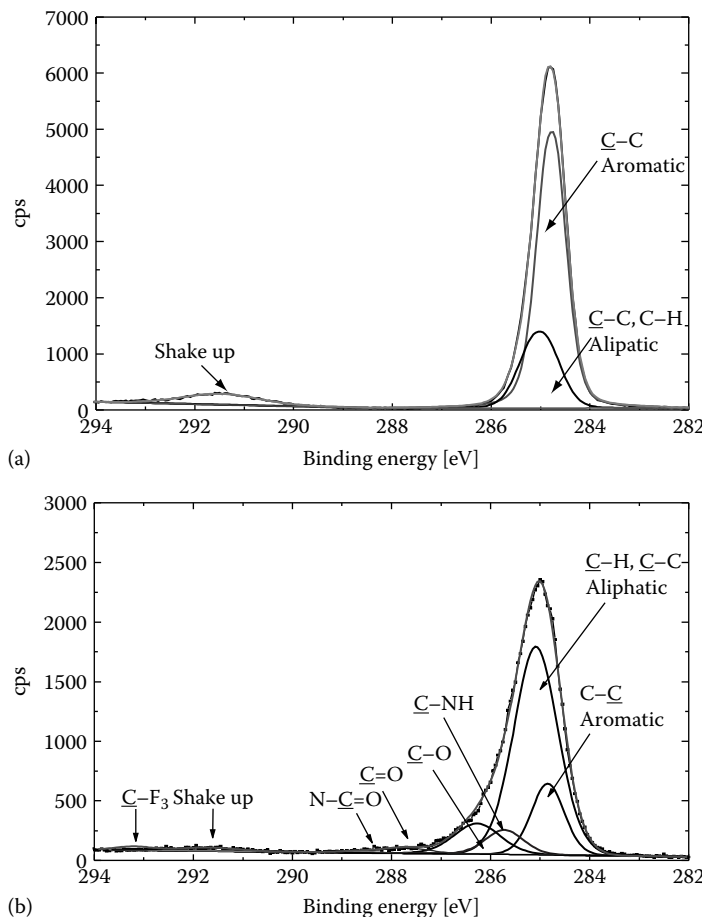


FIGURE 7.12 C 1s peak fitting of (a) PS and (b) NH₃ microwave plasma-treated PS. Position and content of the shake-up, aromatic, and aliphatic peaks of the PS sample agree very well with known values from the literature. (From Beamson, G. and Briggs, D., *High Resolution XPS of Organic Polymers*, John Wiley & Sons, Chichester, U.K., 1992.) On the plasma-treated PS, typical N containing functional groups were detected like amines (C-NH) and amides (N-C=O) in contrast to the much narrower peak of the untreated material. The CF₃-peak was generated by the derivatization of the sample. However, oxygen functional groups were created upon contact with air. (From Steffen, H. et al., *Plasma Process. Polym.*, 4(SI), S392, 2007.)

combining XPS with PEEM (photo emission electron microscopy). Photoelectrons may be collected from the surface in two dimensions to generate elemental or chemical state images of the surface. With the help of a synchrotron radiation source, a lateral resolution of less than 200 nm was detected this way [46].

A particular interesting development is imaging XPS. The local resolution is about 3 μm with conventional x-ray sources [47]. Such images (see Figure 7.13) could be obtained from plasma chemical micropatterned polystyrene surfaces [44].

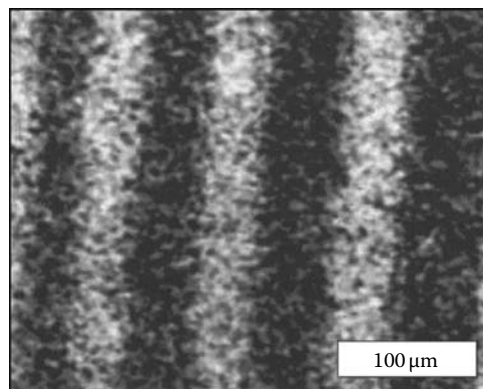


FIGURE 7.13 XPS O 1s image of a lateral chemical micropattern created by a multistep microwave plasma process. (From Schröder, K. et al., *Surf. Interface Anal.*, 36, 702, 2004.)

7.3 ANALYSIS WITH ION BEAMS BY ENERGY LOSS SPECTROSCOPY

In this section the surface analysis due to interaction of ion beams with material surfaces will be presented.

7.3.1 RUTHERFORD BACKSCATTERING SPECTROMETRY

For the RBS method [48] a sample is irradiated with light energetic ions, in most cases hydrogen, helium, or neon of a few MeV are used. At a backward angle close to 180° relative to the beam direction the number and the energy of projectile ions backscattered from the target are measured (Figure 7.14a).

Since these values are dependent on the mass respectively on the nuclear charge of the scattering atoms and because the projectiles sustain an energy loss in the

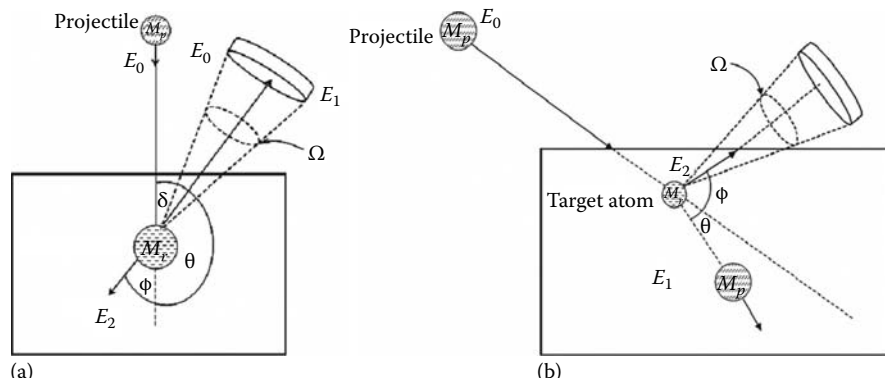


FIGURE 7.14 Measuring principle for RBS (a) and ERDA (b).

material it is possible to determine the elemental composition as a function of depth. The energy of the scattered projectile is

$$E_1 = E_0 \left[\frac{(M_T^2 - M_P^2 \sin^2 \theta)^{1/2} + M_P \cos \theta}{M_P + M_T} \right]^2, \quad (7.20)$$

where

M_P is the mass of the projectile with initial energy E_0

M_T is the mass of the target nucleus

θ describes the scattered angle of the scattered particle with the mass M_P relative to the incident trajectory

While this equation correctly determines the backscattered energies relative to measurement angle, it does not describe the angular distribution of the backscattering probability. For the backscattering probability the differential cross-section of the backscattering will be needed [48]

$$\frac{d\sigma(\theta)}{d\Omega} = \left(\frac{Z_T Z_P e^2}{16\pi \epsilon_0 E} \right)^2 \cdot \frac{1}{\sin^4 \theta/2} \frac{\left(\left(1 - ((M_P/M_T) \sin^2 \theta)^2 \right)^{1/2} + \cos \theta \right)^2}{\left(1 - ((M_P/M_T) \sin^2 \theta)^2 \right)^{1/2}}, \quad (7.21)$$

where Z_P and Z_T are the atomic numbers of the incident and the target nuclei. Layer thickness and concentration profile can be determined from the energy difference $E_1 - E_0$, see (7.20), of the backscattered projectile. The number of the detected backscattered projectile ions gives information about the concentration of the target element. From the differential Rutherford cross section (7.21) the atomic number Z_T of the target atom can be calculated. RBS is a standard free and absolute method. It is more sensitive for heavier components of a the sample.

7.3.2 ELASTIC RECOIL DETECTION ANALYSIS

The sample which should be analyzed is irradiated with high energetic heavy ions under grazing incidence conditions (see [49,50]). Light elements (e.g., H, D) from the sample are scattered in forward directions. The energy as well as the number of outscattered atoms (recoils) of the sample components are measured at a fixed angle relative to the beam direction, see Figure 7.14b. The mass identification can be done by ToF (time of flight) methods ($E = M/2 \cdot v^2$). The element concentration can be estimated from the number of the forward scattered atoms. Layer thickness and concentration profile will be determined from the energy difference $E_2 - E_0$ of the forward scattered sample atoms

$$E_2 = E_0 \frac{4M_P M_T \cos^2 \phi}{(M_P + M_T)^2}. \quad (7.22)$$

Using (7.23) the differential Rutherford cross section for the forward scattered sample atoms with the atomic number Z_T can be calculated

$$\frac{d\sigma_T(\phi)}{d\Omega} = \left(\frac{Z_p Z_T e^2}{2E_0} \right)^2 \left(\frac{M_p + M_T}{M_T} \right)^2 \cdot \frac{1}{\cos^3 \phi}. \quad (7.23)$$

ERDA is a technique for quantitative analysis in particular of light elements in solids. Information about hydrogen analysis with ERDA can be found in a review from Lanford [51]. The ERDA method provides absolute concentration values and is not affected by matrix effects. Furthermore, ERDA is noninvasive, that is, the sample is not damaged on a macroscopic scale.

7.4 MATRIX-ASSISTED LASER DESORPTION/IONIZATION, SECONDARY ION MASS SPECTROMETRY

The matrix-assisted laser desorption/ionization time of flight mass spectrometry (MALDI-ToF MS) is a technique successfully applied for polymer analysis [53–55] and is therefore an interesting tool for the investigation of plasma polymers [56] and plasma-induced processes on polymer surfaces [57,58] (see Figure 7.15). This method includes a soft ionization technique for the investigation of large organic molecules compared with conventional electron impact fragmentation and ionization of polymer molecules. The analyte is mixed (1:10⁵) and co-crystallized with matrix molecules (e.g., 2,5-dihydroxy benzoic acid, 3,5-dimethoxy-4-hydroxycinnamic acid, 2-(4-hydroxyphenylazo) benzoic acid). The matrix encloses completely the single analyte molecules. The sample is prepared usually on a metal plate. Matrix molecules are

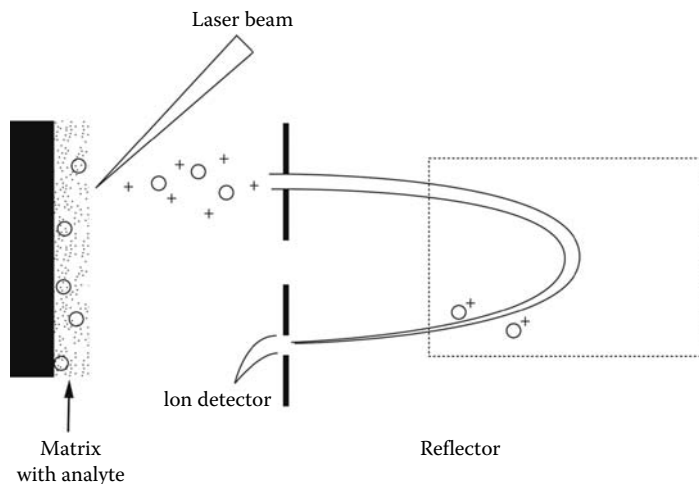


FIGURE 7.15 Scheme of MALDI-ToF, matrix with analyte, ToF mass spectrometer with reflector and ion detector.

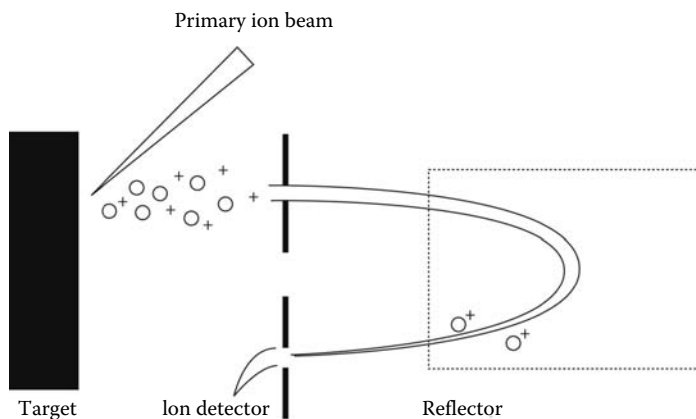


FIGURE 7.16 Scheme of ToF-SIMS apparatus.

distinguished by a high evaporation enthalpy and a strong absorption for the laser radiation, for example, for 337 nm of a nitrogen laser. Irradiation with the intensive short (some ns) laser pulse leads to desorption of the matrix with the analyte and is combined with the ionization of desorbed material. These ions are analyzed in the ToF-MS. The mass spectrum of the analyte is obtained after subtraction of the pure matrix spectrum. In particular, MALDI allows the investigation of molecules with mass larger than 10^5 u.

Secondary ion mass spectrometry (SIMS) is a method for analyzing the composition of solid surfaces and thin films by mass spectrometric investigation of the secondary ions (positive and negative) emitted from the target after irradiation with a focused energetic ion beam [59,60] (see Figure 7.16). The chemical element or molecular composition of the surface can be determined. The ion beam operates typically in the keV energy range and is focused to less than 1 μm diameter at the target surface. Various ions such as He^+ , Ne^+ , Ar^+ , Xe^+ , O^- , and O_2^+ , as well SF_5^+ are used. Cs^+ and Ga^+ ions enhance the emission of negative ions. Cluster ions like C_{60}^+ increase the yield of emitted fragments with higher molecular weight. The time of flight mass spectrometers are very suitable for SIMS because of their high mass range and resolution, high transmission and parallel mass detection. SIMS represents a very sensitive method with a detection limit of 10^{12} – 10^{16} atoms per cm^3 . Static SIMS operates in a slow sputtering mode with an ion dose lower than 10^{13} ions/ cm^2 and is used for study of the top two to three monolayers (nearly 10–20 Å). Dynamic SIMS with continuous sputtering allows the investigation of depth profiles of materials. The charging of insulating samples by emission of secondary electrons and the bombardment of the primary positive ions is avoided by pulses of low-energy electrons between the pulses of primary ions.

The influence of substrate temperature during plasma deposition, the polymer damage by plasma treatment, or the functionalization of polymers in plasmas were studied by ToF-SIMS investigations, see [61]. The results are interpreted by comparing the characteristic peak intensities of the relevant secondary ions.

The derivation of reliable quantitative conclusions from the complicated ToF-SIMS spectra requires the application of statistical methods as multivariate analytical techniques [61,62]. Static ToF-SIMS and XPS are used for the study of plasma polymers deposited on a silicon wafer in an inductive coupled 13.56 MHz discharge in a 2.67 Pa allylamine ($\text{CH}_2=\text{CH}-\text{CH}_2-\text{NH}_2$) atmosphere. The application of the multivariate analysis of the ToF-SIMS spectra shows a decreasing primary amines concentration and increasing cross-linking in the plasma polymer with rising plasma power [63].

The plasma-enhanced chemical vapor deposition of silicon nitride-like and silicon oxynitride-like films in Argon containing bis(dimethylamino)dimethylsilane (BDMADMS 1sccm, Ar 21 sccm) has been studied by ToF-SIMS together with infrared and XPS analysis [64]. A transition from an organic material into an inorganic silicon nitride-like coating is observed by increasing input power (100–700 W) in a 13.56 MHz inductively coupled rf discharge. With increasing O_2 (0–4 sccm) concentration at high input power a transition was observed from inorganic silicon nitride-like via oxynitride-like to oxide-like deposition.

The efficiency of static ToF-SIMS was demonstrated for the deposition of thin CF_x films using a pulsed Ga^+ ion source and applying multivariate analysis [65]. Here, silicon and polyethyleneterephthalate (PET) substrates are coated in a pulsed dc Ar/ CHF_3 discharge ($t_{on} = 1$ ms, $t_{off} = 9$ ms, peak power 8 W, total pressure 0.8 mbar). Differences in the film growth and CF_x cross-linking are detected in dependence on the substrate nature.

7.5 X-RAY DIFFRACTION AND REFLECTION

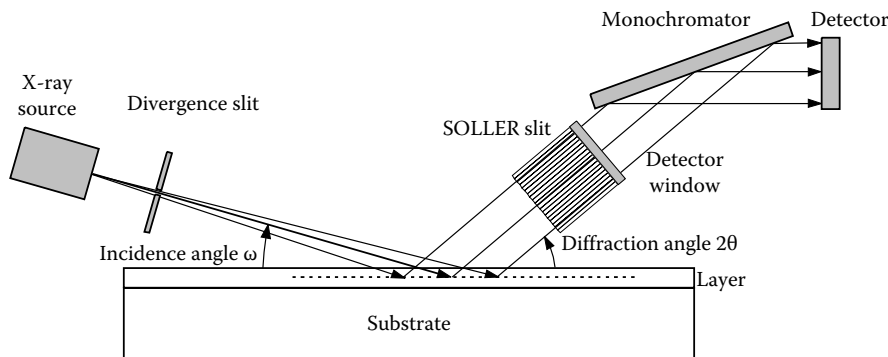
To understand the plasma wall interaction in detail a close look at the deposition/reaction region is necessary, this is usually the substrate area. Particular interest is on the nondestructive analysis of film properties in the nanometer range. In this chapter the basics of x-ray techniques grazing incidence x-ray diffractometry, GIXD, and x-ray reflectometry, XR, will be presented. Advantages and disadvantages of these methods will be discussed in comparison with other thin film analyses methods.

7.5.1 GRAZING INCIDENCE X-RAY DIFFRACTOMETRY

The observation of x-ray diffraction from very thin films (analyzed film properties see Table 7.4) is often hampered by weak diffraction intensities due to the smallness of the diffraction volumes. Thin polycrystalline films can be studied with advantage in the highly asymmetric Bragg case [66]. In this technique the diffraction volume can be increased by decreasing the angle of incidence. The optical path in GIXD is depicted in Figure 7.17. The reflection positions are equal as in normal Bragg–Brentano geometry for the polycrystalline film, but in the GIXD technique the substrate reflections are suppressed and the film intensities strongly increase. In the analysis of surface layers, the information depth of x-rays is an important parameter, in particular, if gradients of structure parameters are observed [67]. The film information depth strongly depends

TABLE 7.4**X-Ray Techniques and Alternative Methods of Thin Film Analysis**

Film Property	X-Ray Method	Alternatives
Phase composition	GIXD: Bragg angle, intensity	TEM
Chemical composition (concentration depth profile)	GIXD: Bragg angle	EDX, XPS, RBS, ERDA
Macrostress	GIXD: Bragg angle	Substrate curvature, laser optics
Grain size	GIXD: line profile, line width	TEM, SEM
Microstrain	GIXD: line profile	
Preferred orientation	GIXD: intensity, polfigure	
Crystal structure	GIXD: Rietveld analysis, structure refinement	
Thickness	GIXD: intensity, XR: Kiessig fringes	Interferometry, piezoelectric crystal, ellipsometry, TEM ellipsometry
Density	XR: critical angle of total reflection	
Surface roughness, interface roughness	XR: amplitude of Kiessig fringes	SEM, ellipsometry, AFM
Diffusion behavior	In situ GIXD, thermal and time resolved: intensity	SIMS, AES, combined with sputtering
Crystallization rate, melting point	In situ GIXD, thermal and time resolved: intensity	

**FIGURE 7.17** Schematic diagram of grazing incidence x-ray diffractometry, 2θ Bragg angle, ω angle of incidence (asymmetric Bragg case).

on the thickness d , the mean absorption coefficients of the film, and the incidence angle ω of the x-ray beam. By variation of incidence angle ω the gradients of structure parameters can be measured. A further advantage of GIXD compared to the Bragg–Brentano geometry is that the information depth is independent of the Bragg angle 2θ if the incidence angle ω is small.

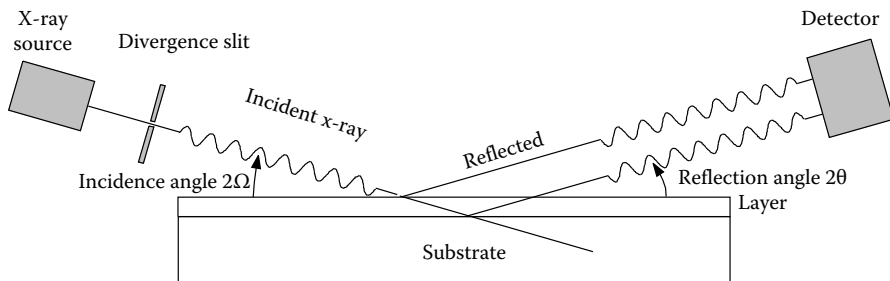


FIGURE 7.18 Schematic diagram of x-ray reflectometry.

7.5.2 X-RAY REFLECTOMETRY

The measurement of x-ray reflectivity around the critical angle for total reflection allows the accurate determination of film thickness, mass density, as well as surface and interface roughness irrespective of the crystalline structure. X-ray reflectometry is equally well applicable to crystalline, polycrystalline, and amorphous materials; it only requires a sufficiently flat sample. The basic principle is shown in Figure 7.18. It corresponds to the symmetrical Bragg-geometry. In the case of thin films on a substrate constructive interference occurs between the beam reflected at the surface and the beams reflected at the interfaces. Constructive interference results in intensity maxima called *Kiessig fringes*, whose angular spacing is characteristic for the thickness of the layers. The reflected intensity can be calculated by a recursive formula taking the Fresnel coefficients for all corresponding interfaces into account. Using Debye–Waller factor modified Fresnel coefficients to account the roughness in x-ray reflectometry, the reflectivity of a layer can be calculated [68]. On the basis of such an algorithm (Parrat recursive formula) the modeling of reflectometry measurements yields thickness, surface and substrate roughness, and mass density.

A detailed description of x-ray methods for thin film analysis was recently presented by Wulff and Steffen [69]. Grazing incidence x-ray diffractometry (GIXD) and x-ray reflectometry (XR) have been established as well-suiting tools for investigations of chemical, physical, and crystallographic properties of thin films. They are nondestructive techniques; therefore a sample can be reused and can be measured with other techniques. A usable combination of GIXD and XR requires crystalline films whose thickness does not exceed the upper physical absorption limit for the reflectometry measurements.

Table 7.4 gives an overview of the possibilities of x-ray methods and alternative techniques for thin film analysis.

7.6 RADICAL INVESTIGATION BY ELECTRON SPIN RESONANCE

Radicals are atoms or molecules with one unpaired electron at least, and show high chemical reactivity, for example, O^\bullet , NO^\bullet . Plasma-treated material surfaces or

deposited thin films in plasma processing are often characterized by macroradicals at the surface or in thin films [70].

An unpaired electron is connected with a magnetic spin moment. This magnetic moment generates energy splitting into two energy levels in an external magnetic field. Transition between these two levels can be induced by external electromagnetic radiation of suitable frequency. At an external magnetic field H_0 the frequency ν for which the external radiation is in resonance with the paramagnetic substance is given by

$$\nu = \frac{1}{h} (g\mu_0 H_0), \quad (7.24)$$

where

h the Planck constant

g the Landé factor

μ_0 the Bohr magneton

The ESR spectroscopy measures the absorption of electromagnetic wave energy at the resonance using a monochromatic radiation (e.g., microwaves) and a scan of the external magnetic field. The position (g -value) and shape of the absorption spectrum are determined by the nature of the radical, whereas the line intensity depends on the radical concentration.

The impact of radicals in a thin film is different; they can generate dielectric losses and according to their reactivity with water or oxygen they cause aging effects. In particular, radicals near the surface influence the chemical interaction with surrounding media [71].

ESR studies on radical generation and recombination in thin plasma polymers deposited in a c-C₄F₈ rf discharge show radical densities of $\approx 10^{20}$ cm⁻³. Storage on air reduces the radical number with a half time of 24 h [71].

The formation of radicals on conventional synthetic polymers is studied by [72–74]. Powdered TEFLON treated by Ar and oxygen plasmas is studied by ESR technique. Midchain ($-\text{CF}_2-\text{CF}-\text{CF}_2-$), endchain ($-\text{CF}_2-\text{CF}_2-$) radicals and peroxy radicals in O₂ plasma were identified. Peroxy radical formation was also observed on plasma-treated polyethylene surfaces after exposure to air.

The treatment of natural fibers like wool in a gas flow of a gliding arc discharge plasma at atmospheric pressure leads to the formation of radicals on the wool fiber surface as shown by ESR techniques [75].

Studies of radicals on surfaces are possible also by chemical methods, for example, by application of the stable radical DPPH (2,2-Diphenyl-1-pikrylhydrazyl). Furthermore, the reaction of nitric oxide or iodine in combination with XPS measurements can also be applied for radical detection [76].

8 Selected Applications

CONTENTS

8.1	Volume Plasma Chemistry	286
8.1.1	Ozone Synthesis in Barrier Discharges: Basic Mechanism and Discharge Operation Models	286
8.1.1.1	Chemistry of Ozone Formation in Gas Discharges	288
8.1.1.2	Brief Review of the MD Models	290
8.1.1.3	Spatiotemporally Resolved Plasma Diagnostics of the Microdischarges in Air and N ₂ /O ₂ Mixtures	293
8.1.1.4	Concluding Remarks	295
8.1.2	Plasma Treatment of Flue and Exhaust Gases	296
8.1.2.1	Overview of Methods for Pollution Control	296
8.1.2.2	Selected Plasma Treatment Applications	299
8.1.2.3	Concluding Remarks	305
8.1.3	Plasma Chemistry of Excimer Light Sources	306
8.1.3.1	Main Processes of Excimer Formation in Rare Gases	307
8.1.3.2	Main Processes of Excimer Formation in Rare Gas Halide Mixtures	309
8.2	Plasma Surface Chemistry	312
8.2.1	Plasma Etching	313
8.2.1.1	Plasma Etching, Micro- and Nanostructures	313
8.2.1.2	Basic Mechanisms of Plasma Etching	315
8.2.1.3	Etch Chemistry	318
8.2.1.4	Reactors for Plasma Etching	320
8.2.1.5	Trench Etching	322
8.2.1.6	Conclusions	323
8.2.2	Biological Decontamination up to the Level of Sterilization	323
8.2.2.1	Plasmas as New Prospects for Hygiene and Life Science	323
8.2.2.2	Some Basics of Biological Decontamination and Sterilization	324
8.2.2.3	Microbicidal Effects of Plasmas	326
8.2.2.4	Examples of Plasma Processes for Sterilization	331
8.2.2.5	Outlook	332
8.2.3	Surface Modification	332
8.2.3.1	Polymers	334
8.2.3.2	Metals	340
8.2.3.3	Textiles	343

8.2.3.4	Biomedical Applications of Plasmachemical Surface Functionalization	348
8.2.3.5	Plasma Medicine	357
8.2.4	Plasma-Enhanced Chemical Vapor Deposition.....	362
8.2.4.1	Organic Thin Films/Plasma Polymerization	363
8.2.4.2	Inorganic Thin Films	382
8.3	Pulsed Electrical Discharges in Liquids	392
8.3.1	Background	392
8.3.2	Experimental Systems	393
8.3.3	Selected Experimental Results	395
8.3.4	Summary	397
8.4	Nano- and Microparticles	398
8.4.1	Particle Synthesis in Plasma.....	399
8.4.2	Formation and Deposition of Nano-Sized Clusters in Plasma	402
8.4.3	Modification of Particles in Plasma	405

In the first part of this chapter, examples of applications of volume plasma chemistry with gaseous reaction products are presented. The reactions take place in the volume, as pure gas phase reactions, or in heterogeneous processes with participation of the surface of substrates, electrodes, or walls, sometimes assisted by catalytic effects. The second part concerns applications of surface chemistry. Here, the plasma chemical reactions result in changes of surface properties. The reactions may involve volume processes but the essential reactions take place at the surface.

8.1 VOLUME PLASMA CHEMISTRY

The unique volume plasma chemical process that produces a larger quantity of products and as achieved industrial maturity is the ozone synthesis. Other processes such as methane reformation with the goal of generation of higher hydrocarbons or the production of synthesis gas are until now a topic of research. More successful is the application of plasmas for the fragmentation of greenhouse gases, pollution control, odors, flue gases, diesel exhausts, and volatile organic compounds (VOCs). The concentration of the material of interest is small, typically <1000 ppm [1]. The formation of excimers as a source of UV radiation is the result of plasma chemical volume processes. Applications of volume plasma chemistry are summarized in Table 8.1.

8.1.1 OZONE SYNTHESIS IN BARRIER DISCHARGES: BASIC MECHANISM AND DISCHARGE OPERATION MODELS

The ozone generation belongs to the most important applications of nonthermal plasma volume chemistry. There is no alternative effective way for its thermochemical production.

The first ozone generator was developed by Werner von Siemens in 1857 [3]. The application of ozone is based on its high oxidation potential. Historically, it is linked to the purification of drinking water. The first installations were realized already at the beginning of the twentieth century in Nice, Paris, and St. Petersburg. Nowadays,

TABLE 8.1
Applications of Volume Plasma Chemistry

Plasma Volume Chemistry		Section
Synthesis	Ozone Higher hydrocarbons from methane	8.1.1
Fragmentation	Methane into synthesis gas Greenhouse gases	
	Pollution control [2]	
Cleanup of gases	Odors Flue gases Diesel exhaust (NO/NO _x) VOCs	8.1.2
Excimer generation	Light sources	8.1.3

the applications of ozone include, for example, water purification, cleaning, and sterilization processes in the pharmaceutical industry and medicine, and cover the wide field of environmental protection.

Large ozone installations have a power consumption until megawatts. They consist of many parallel operating single cylindrical discharge tubes with a still quite similar geometry as the historical installation of Werner von Siemens.

It should be recognized that even nowadays, after more than a hundred years of the research of ozone generation process in the barrier discharge (BD, sometimes also referred to as dielectric-barrier discharge (DBD) or silent discharge), despite a great number of scientific publications put forth mostly in the last few decades, our knowledge of the subject appears to be insufficient to provide an adequate quantitative theoretical description for the system under consideration [4–6]. This means that, for example, to solve a problem of optimization of the operating conditions of an ozonizer, or to develop a new, more efficient type of ozone generator, we are not able to use a computer simulation technique instead of the hard way of empirical search. The reason for such a state of affairs seems to be not a technical one (e.g., a necessity to use three-dimensional computer models instead of two-dimensional ones, or an inevitable need to include several hundreds of elementary reactions into the kinetic scheme). Actually, the reason is our poor understanding of the physics of electrical breakdown as the initial and determining stage of the consequent plasma-chemical processes.

A BD in oxygen, air, or mixtures O₂/N₂ consists of a number of microdischarges (MDs, sometimes also referred to as partial discharges [7] or discharge filaments [4]) of nanosecond duration, randomly but uniformly distributed over the dielectric surface. Under the typical conditions of the BD operation (discharge gap width of 1–2 mm, dielectric: glass of 1–2 mm thickness, and dielectric constant $\epsilon = 5–7$, gas pressure: 1–3 bar), these MDs can be treated as tiny plasma-chemical reactors that act independent from each other [4,5,8]. That is why the study of the dynamics of a single MD is one of the most important research topics in the field of BD physics

and chemistry. It is hard to carry out any experiment with a single MD, since high temporal resolution (in a sub-nanosecond range) and spatial resolution (down to 10^{-1} – 10^{-2} mm) is required. Moreover, in the case of a commonly used parallel-plane electrode arrangement, it is usually impossible to predict the location of an MD emergence. Thus, it is no wonder that a great deal of effort has been devoted to computer simulation of MD development [9–15].

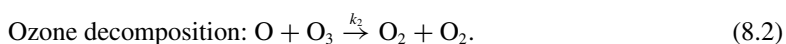
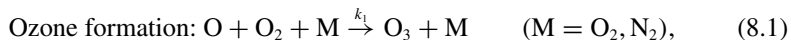
As regards experimental findings, the following important milestones should be mentioned:

- 1972—Identification of separate MDs [7]
- 1980—Streak-photography of single MD [17,18]
- 1983—Accurate measurement of MD current pulses [19]
- 1995—Determination of the spectrally resolved spatiotemporal distributions of MD luminosity by means of cross-correlation spectroscopy (CCS) [20,21]

It should be mentioned that the authors [20] also used their experimental data for a qualitative characterization of the spatiotemporal structure of electric field within an MD channel. A remarkable progress in experimental investigation of MD evolution was achieved during the last few years [21–23]. The authors [22] reported their results of an accomplished procedure of a BD plasma diagnostics by means of the spatially resolved CCS, including the quantitative estimation of the electric field, relative electron density, and ozone yield within an MD channel. These measurements and calculations were performed for a BD with the symmetrical electrode arrangement, discharge gap width of 1.2 mm, in air at atmospheric pressure, that is, under typical conditions of ozone generation technologies. Experimental data [20–23] and their sophisticated kinetic analysis provide, essentially, a deeper understanding of the MD mechanism as well as a detailed quantitative description of the chemical activity of plasma within the MD channel.

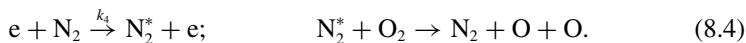
8.1.1.1 Chemistry of Ozone Formation in Gas Discharges

In order to understand in what way the physics of electrical breakdown determines the chemical activity of a BD plasma, it seems reasonable to begin with the analysis of the chemical mechanism of the formation of ozone, usually the dominant product of plasma synthesis. This mechanism was established relatively long ago, and at present the kinetic schemes for ozone generation in oxygen and air may be regarded as sufficiently reliable ones [4,5]. Generally, under the typical conditions for an ozonizer, there are only two dominant reaction channels as follows:



Therefore, atomic oxygen can be regarded as a sole precursor of ozone, and the conversion degree for the gross reaction $\text{O} + \text{O}_2 \rightarrow \text{O}_3$ is determined by the ratio of the rate constants k_1/k_2 as well as by the background (initial) concentration of O_3 .

Due to comparatively strong temperature dependence of the rate constant $k_2(T)$, this conversion degree may be considerably decreased by a local temporary gas heating within the MD channel (i.e., it depends upon the power density profile). Obviously, a spatial distribution of the power density is determined by the spatiotemporal structure of an MD and, consequently, by its mechanism. This can be the first possible way to affect chemical yield of ozone by means of influencing the characteristics of electrical breakdown in an ozonizer. The second way is related to the reactions leading to the formation of atomic oxygen:



Here the asterisk denotes the triplet excited states of molecular nitrogen (A, B, and C, [5,13,22]). Within the frame of the concept of local equilibrium (i.e., an equilibrium between electric field and electron energy distribution function), for a given composition of a mixture ($N_2 + O_2$), the rate constants k_3 and k_4 may be treated as the sole functions of the reduced field strength E/N . It should be noted that in air, the channel (8.4) seems to provide up to 50%–70% of the total yield of atomic oxygen, the second elementary reaction shown in this scheme being a dominant process among the different pathways of N_2^* relaxation [9,14,22].

In accordance with the simplified scheme (see (8.3) and (8.4)), the maximal possible energetic yield of atomic oxygen can be calculated as a ratio of O-atoms production rate to electric power released by drifting electrons, as follows:

$$Y_{O,max} \left(\frac{E}{N} \right) = \frac{k_3(E/N)[O_2] + k_4(E/N)[N_2]}{e E w_e(E/N)}, \quad (8.5)$$

where

e is the elementary charge

$w_e(E/N)$ is the drift velocity of electrons

Square parentheses are used to denote the concentrations of the corresponding species. Actually, Equation 8.5 takes into account the branching of electron energy losses. The explicit dependence of $Y_{O,max}$ upon the parameter E/N reveals the dependence of the energetic yield of ozone upon the spatiotemporal structure of a single MD, the latter being defined as the spatiotemporal distributions of electric field $E(r, t)$ and electron density $n_e(r, t)$. In order to complete the consideration of energy losses within the channel of a separate MD in an ozonizer, the ion drift should be taken into account as well. Obviously, the value of ion losses also depends on the mechanism of electrical breakdown, and it has to be included into the general formula for energetic yield of ozone

$$Y_{ozone} \left(\frac{E}{N} \right) = \frac{C \{ Y_{O,max}(r, t) P_e(r, t) \}}{\{ P_e(r, t) + P_i(r, t) \}}, \quad (8.6)$$

where C is the conversion degree for the gross reaction $O + O_2 \rightarrow O_3$ ($0 < C < 1$); the local power densities for electrons and ions are defined as $P_e(r, t) = en_e(r, t)$

$E(r, t) w_e(r, t)$ and $P_i(r, t) = e n_i(r, t) E(r, t) w_i(r, t)$, respectively; the parentheses {} denote integration over the entire MD volume and over the time of its existence (to be more precise, from the moment of an appearance of the first electrons until the vanishing point for positive and negative ions within the MD volume).

8.1.1.2 Brief Review of the MD Models

Generally, a complete model of the MD in an ozonizer includes the descriptions for electrical breakdown (time scale: 10^{-8} – 10^{-7} s), chemical kinetics (10^{-6} – 10^{-4} s), and the consequent diffusion and heat transfer occurring in millisecond scale [4,5]. In the following, the attention is focused only on the first phase of the MD development, and the term *model* is related to the process of electrical breakdown of the discharge gap of an ozonizer. All the proposed physical models of MD mechanism appeared either as a result of interpreting experimental observations and measurements or by means of the powerful technique of computer simulation. It should be noted, however, that in the latter case a model is implicitly defined by a choice of initial and boundary conditions for the coupled Poisson and continuity equations (i.e., in fact, before the simulation procedure itself).

8.1.1.2.1 Model of Avalanche-to-Streamer Transition

The first attempt to provide a full theoretical description for a single MD in an ozonizer by means of two-dimensional numerical modeling was made by the authors [10]. It is interesting to mention that at the time when this modeling was being carried out, there were no reliable experimental results concerning microscopic structure of the MD. So it was some kind of an ab initio computation, and only a few years later it has become clear that its results essentially disagree with experimental data. Initial and boundary conditions used in the model under consideration (initial electric field somewhat higher than the corresponding Paschen value; initial avalanche starts from about 10^6 electrons located near the cathode) account for the mechanism of *avalanche-to-streamer transition*, see Figure 8.1. The authors [11] later assumed this mechanism to control the efficiency of the ozonizer with a 5 mm discharge gap in order to interpret experimentally obtained dependence of the ozone yield on the working

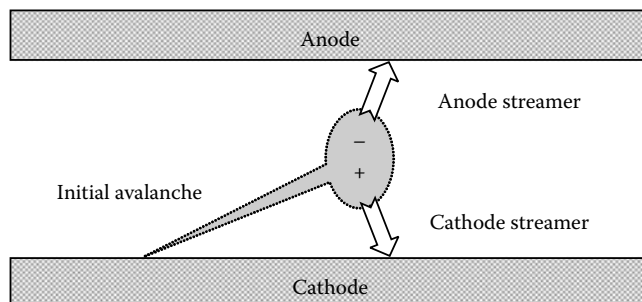


FIGURE 8.1 Schematic illustration for the breakdown mechanism within the frame of the model of *avalanche-to-streamer transition*. Time axis is directed from the left to the right, and for the discharge gap width of about 1 mm, it has a scale range of a few nanoseconds.

pressure of oxygen. The origin of this model belongs to the field of the physics of electrical breakdown in the long gaps (characteristic size in the 10^1 – 10^2 cm range). Under such conditions, any starting from the cathode avalanche may be expected to reach a critical number of electrons in it necessary to cause a transition to the streamer. For the ozonizers (gap width of a few millimeters), this mechanism has never been observed experimentally and it seems to be hardly possible, excepting probably only the case of the devices with pulse feeding voltage (rise time of about 1 kV/ns [18]).

8.1.1.2.2 Model with a Pulsed Electric Field

This model may be considered as a semiempirical one based on the results of the first measurements of the microdischarge current pulse [19]. In order to simulate the experimentally observed current pulse within the frame of a simplified zero-dimensional (homogeneous) kinetics, the authors [11,19] used a corresponding pulse variation of the reduced field (Figure 8.2). Despite complying with the current measurements and using an extremely detailed kinetic scheme, the model failed to provide a reasonable estimate for the ozone yield [5].

8.1.1.2.3 Accumulation of Positive Space Charge Followed by the Cathode-Directed Streamer

This model has been widely used in a number of computer simulations for MD development since 1986 [12]. The first experimental evidence for the existence of a cathode-directed streamer in a BD was obtained by means of the technique of

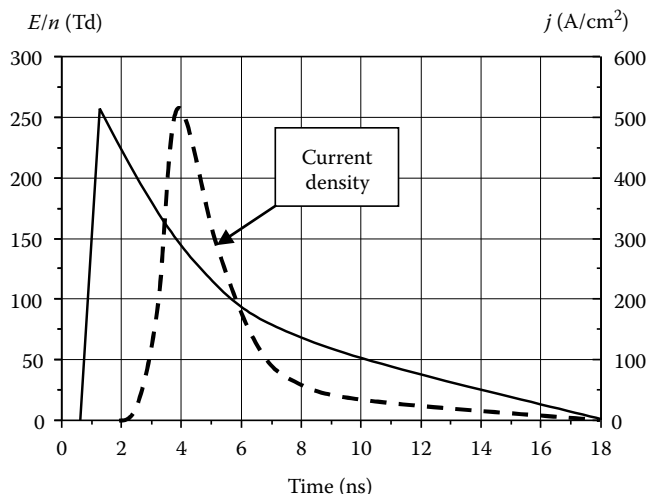


FIGURE 8.2 Schematic illustration for the model of the *pulsed electric field* used in the computer simulation of the MD in oxygen. Assumed variation of the reduced field (solid line), and calculated current density (dashed line, right y-axis), is fitted to comply with the results of experimental measurements of the MD current.

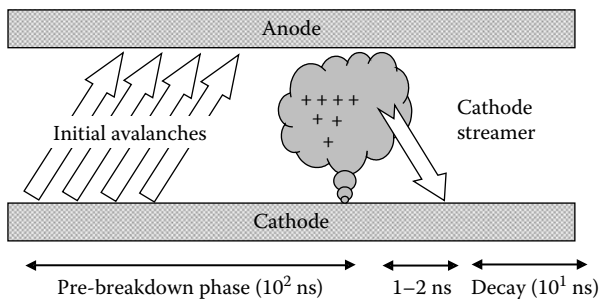


FIGURE 8.3 Schematic illustration of the breakdown mechanism for the model of *cathode-directed streamer, caused by a positive space discharge*. Time axis is directed from the left to the right. *Initial avalanches* denote here a continuous process, including the electron drift, ionization, and the secondary emission from the cathode.

streak-photography. To interpret their results, the authors [17,18] formulated the basic ideas of the breakdown mechanism, schematically presented in Figure 8.3.

All the later investigations of the model under consideration have been carried out by means of computer modeling. The authors [12] demonstrated that if the development of the breakdown begins with a single electron emitted from the cathode, then for a sinusoidal feeding voltage, the development of the MD proceeds according to the model presented in Figure 8.3, but for the impulse voltage, the mechanism of the *avalanche-to-streamer transition* can be realized. Such a transformation of the MD mechanism caused by an increase of the voltage pulse steepness has been found to result in considerable growth of the energetic yield of ozone due to the decrease of ion losses. However, the latter conclusion disagrees with the modeling results [9,13–15], according to which the fraction of ion losses appears to be very low even in the case of a sinusoidal feeding voltage. According to the described model, the development of the cathode-directed streamer is caused by the distortion of electric field due to a positive space charge within the MD channel (Figure 8.3). Accumulation of this charge occurs during the prebreakdown phase of MD development, which can take up to 10^{-7} s [12,14]. The final phase of decay is characterized by the deposition of the charge carriers (electrons and ions) onto a dielectric surface, resulting in a monotonous decrease of electric field.

8.1.1.2.4 Accumulation of Negative Space Charge Followed by the Cathode-Directed Streamer

This model appeared as a result of the attempts to give a reasonable interpretation to certain experimental findings of the authors [20,21], in particular to the existence of a weak but profound prebreakdown anode glow of microsecond duration. Some ideas of the MD mechanism including an accumulation of the negative space charge during the prebreakdown phase have been stated in [20], and a more detailed description of the corresponding physical model (Figure 8.4) is presented in [22]. However, this model has not been used in computer simulations as yet.

Contrary to the MD mechanisms described earlier, the scheme in Figure 8.4 takes into account surface charge left on the dielectric electrodes after a previous

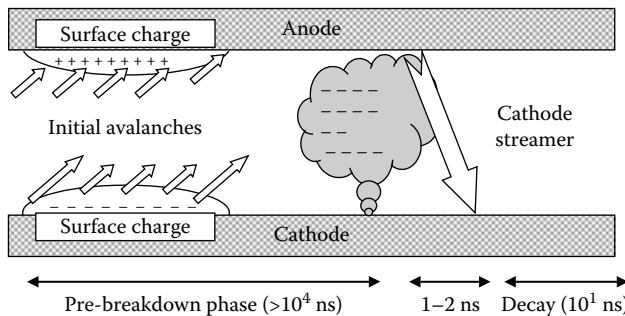


FIGURE 8.4 A scheme for the microdischarge mechanism, based on the assumption of a pre-breakdown accumulation of the negative space charge within the MD channel. Initial avalanches are caused by a local field enhancement due to the surface charges on the dielectric electrodes. It is also assumed to be a continuous process including electron drift, ionization, attachment and secondary emission from the cathode (see text for details).

MD. Initial electric field is therefore assumed to be nonhomogeneous, the mean value of the field strength being considerably lower than that corresponding to the Paschen law (probably proportional to the ratio of the burning and ignition voltages of the BD). Under such conditions, ionization may be expected to occur mostly near the charged dielectric surface, and attachment at the center of a gap [6]. An appearance of the negative space charge causes rearrangement of initial electric field, the maximum of the field strength being located exactly on the anode surface. The duration of this *prebreakdown* phase of the MD development is at least a few μs . Cathode-directed streamer starts from the anode surface and propagates through the medium enriched with negative ions, and its velocity depends on electronegativity of the feeding gas.

8.1.1.3 Spatiotemporally Resolved Plasma Diagnostics of the Microdischarges in Air and N₂/O₂ Mixtures

As already mentioned, an essential progress in experimental investigation of the MD in an ozonizer in air at atmospheric pressure has been achieved recently by means of the spatially resolved CCS technique [20–23]. Quantitative estimates for electric field strength $E(x, t)$ and for relative electron density $n_e(x, t)/n_e^{\max}$ were derived from the experimentally determined spatiotemporal distributions of the luminosity for the spectral bands of the 0–0 transitions of the second positive system of N₂ ($\lambda = 337.1 \text{ nm}$) and the first negative system of N₂⁺ ($\lambda = 391.5 \text{ nm}$). Some of these results are presented in Figure 8.5. A cathode-directed wave of electric field is clearly seen in this figure. High electric field strength is observed mostly near the cathode, and a high electron density, on the contrary, near the anode.

The streamer starts directly from the surface of the anode and crosses the gap with an increasing velocity that reaches 10⁶ m/s. Electric field strength of the streamer grows respectively from 120 Td at the anode to 240 Td at the cathode. The authors [20,21,23] confirmed also that there are three distinct phases of the MD development. The pre-breakdown phase lasts for a period of more than 0.5 μs . It is characterized by a continuous glow on the glass surfaces of both electrodes. During the last 100 ns

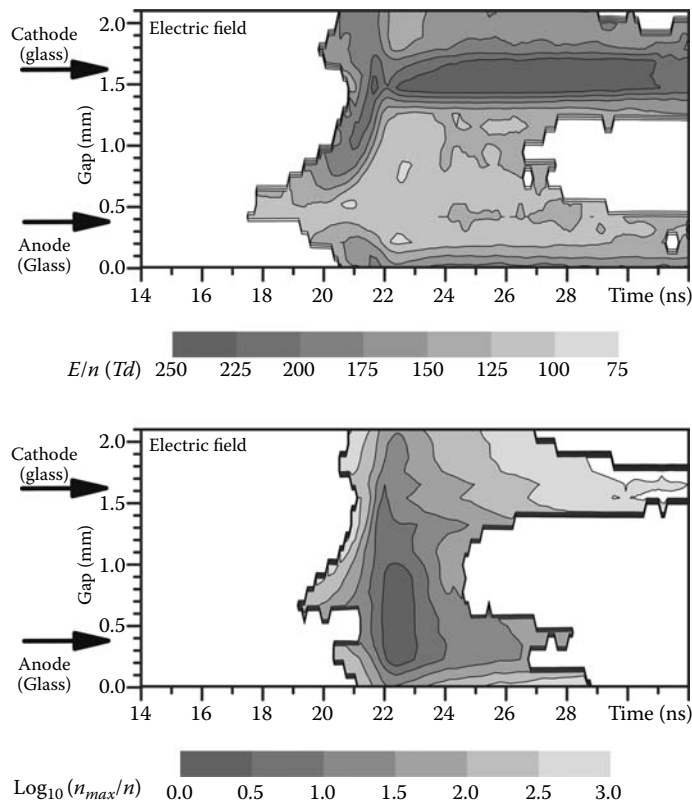


FIGURE 8.5 Results of [21]: Calculated distributions of electric field and density. Positions of the electrode tips (semispherical glass electrodes of the radius of curvature 7.5 mm were used, see [21] for more details) are pointed at the left by the arrows. (From Kozlov, K.V., Dobryakov, V.V., Monyakin, A.P., Samoilovich, V.G., Shepeliuk, O.S., Wagner, H.-E., Brandenburg, R., and Michel, P., Cross-correlation spectroscopy in investigations of filamentary gas discharges at atmospheric pressure, in Ochkina, V.N., ed., *Selected Research Papers on Spectroscopy of Nonequilibrium Plasma at Elevated Pressures*, Vol. 4460, pp. 165–176, Society of photo-optical Instrumentation Engineers, Bellingham, WA, 2002.)

of the pre-breakdown phase, the maximal light intensity is observed on the anode. The third phase of the MD is a phase of decay of the light and current pulses.

The authors [21] used their experimental data and the results of their processing to test the validity of the considered physical models of electrical breakdown in a BD, in particular the model of accumulation of positive space charge followed by the cathode-directed streamer (CDS), and the model of accumulation of negative space charge (NSC). They came to the conclusion that their results provide an unambiguous experimental evidence in favor of the model NSC. Taking into account the initial conditions assumed for the model CDS, we may expect this model to describe some special cases of a BD operation. For example, it can account for the first electrical

breakdown event in an ozonizer (i.e., at the moment when an ozonizer is just switched on), since only at this moment there are no surface charges on the dielectrics. Also, in some laboratory experiments, the BD was operated in a special single-pulse mode when the periodical slow voltage pulses were applied to the discharge cell. In order to get rid of a surface charge, a rest time interval of about 30 min between the successive single pulses was provided [18]. Obviously, for an ordinary (continuous) operation mode of a BD, the model NSC should be used. Therefore, it is very important to distinguish between two different modes of a BD operation: single pulse and continuous. To provide a correct theoretical description of the MDs for an ordinary continuous mode, a model should be used, which takes into account the existence of initially nonuniformly charged dielectric surfaces.

In order to propose a qualitative description of the influence of the MD spatiotemporal structure on the kinetics of ozone synthesis, the authors [22] used the following semiempirical method. From the arrays of electric field strength $E(x, t)$ and relative electron density $n_e(x, t)/n_e^{max}$, the spatially resolved kinetics of the formation of atomic oxygen and triplet nitrogen N_2^* by the reactions (3,4) in a nanosecond time scale were calculated. The rate constants $k_3(E/n)$ and $k_4(E/n)$ were taken from [14]. Since the relative values of electron density were used, the results of these kinetic calculations also contain an unknown constant. However, this constant does not depend on the space-time coordinates. Therefore, thus calculated spatiotemporal distributions of the relative concentrations of considered species may be expected to represent the real kinetics within the MD channel. The latter results lead to the following important conclusions concerning chemical activity of plasma within the MD channel.

There are two distinct regions with essentially different plasma properties of plasma within the MD channel. Electric field near the cathode is higher than near the anode; electron density, on the contrary, is considerably lower. Furthermore, different physical properties of these regions result in a noticeable difference in chemical kinetics. For example, as it was demonstrated in [22], the properties of the plasma in the region near the anode favor dissociation of molecular oxygen by direct electron impact. In the case of the excitation of triplet nitrogen states, the contributions of both regions to this process appear to be comparable.

8.1.1.4 Concluding Remarks

Various physical models (that were explicitly or implicitly used in a number of computer simulations of coming into being, development, and decay of a separate MD) are distinguished, actually, by the choice of initial and boundary conditions for the coupled Poisson and continuity equations. Assuming essentially different mechanisms of electrical breakdown, they determine different contributions of the terms in (8.6), corresponding to the conversion degree for ozone formation, fraction of electron losses, and maximal yield of atomic oxygen, respectively. All these models fail to provide a reasonable interpretation for the detailed spatiotemporal structure of a real MD in air [6]. Use of the briefly described improved physical model of the MD development under the conditions of initially charged dielectric surface [16] in a computer simulation may be expected to avoid discrepancies between theoretical

results and experimental data. It should be noted, however, that this model needs a detailed information concerning the distribution of a surface charge over the dielectric electrode, as well as the values of the secondary emission coefficient (for electrons and ions) for a charged dielectric surface, which have never been measured.

There are also two essential gaps in the understanding of the MD behavior near the cathode surface that should be filled, in order to develop an adequate numerical model for it. In the case of a dielectric cathode, there is a need to simulate a three-dimensional surface discharge (Lichtenberg figures) which has been proved to occur simultaneously with a volume breakdown within the MD channel. In the case of a metallic cathode, there is an evolution of the cathode sheath. Formation of the normal cathode sheath under atmospheric pressure with the reduced field strength of some thousand Td [15] seems hardly possible, and the mechanisms leading to a complete or partial destruction of this sheath are not quite clear.

8.1.2 PLASMA TREATMENT OF FLUE AND EXHAUST GASES

Today the world is faced with a number of environmental problems like acid rain, global warming, or ozone accumulation in the lower atmosphere. Common pollutants emerge from the burning of fossil fuels and coal in power plants, chemical production plants, diesel engines, and motor vehicles. Besides gaseous components like VOCs harmful ultrafine particles, or aerosols, there are also substances with unpleasant odors. Nonthermal plasma (NTP) techniques offer an innovative approach to solve some of these environmental problems.

A strong electric field causes ionization of an airstream and, besides the formation of charge carriers (electrons, ions), also causes a lot of radicals. These highly reactive species can lead to partial or total oxidation of air pollutants. Since the typical concentration range of the pollutants is mostly in the order of several hundred parts per million (ppm), direct interactions between the electrons and pollutants are usually negligible.

8.1.2.1 Overview of Methods for Pollution Control

Fields of NTP applications range from air-pollution control systems for electrostatic precipitation to sterilization [24–26]. Table 8.2 shows an overview of different plasma methods for pollution control and diverse examples. One of the most important applications of NTP is the corona discharge. This type of discharge is preferably applied in electrostatic precipitators for aerosol removal. It was demonstrated originally by Cottrell in a large-scale application for the collection of sulfuric acid mist [45]. Meanwhile large-scale facilities of pulsed corona processing for industrial incinerators or collecting fly ash from a pulverized coal-fired power plant are state of the art. Figure 8.6 shows typical electrostatic precipitator configurations. The discharge electrodes contain parts with small radius of curvature or sharp edges, which cause locally high electric fields to enable corona discharge. Typical electrode plate distances are 0.2–0.4 m; the applied voltage can reach 50–110 kV. The corona discharge can be characterized by a weak glow in the high field region of the discharge electrode. Depending on the discharge conditions, the breakdown is accompanied by streamer

TABLE 8.2
Overview of Different Plasma Methods for Pollution Control

Nonthermal Plasmas	Examples
Corona discharge	Electrostatic precipitators (review) [27], applications in cement industry [28], pulsed streamer corona for gas cleaning [29,30], DC corona streamers induced by UV irradiation for NO_x or SO_x removal and VOCs decomposition [31], scale-up for a coal-fired power plant [32], plasma-based total treatment of waste and low-grade fuels [33], kinetic analysis of NTPs used for pollution control [34]
DBD	NO_x and SO_2 , removal, VOCs decomposition (reviews) [24,34,35]
High-frequency discharge	Oxidation of carbon and methane using a high-frequency pulsed plasma [36]
Glow discharge	DC glow discharge in atmospheric pressure air as a means of pollution control [37,38]
Microwave	Control of NO_x and ammonia emissions [39]
Microhollow cathode	Applications for plasma chemical synthesis and pollution control become feasible [40]
<i>Indirect plasma methods</i>	
UV	Pollution and odor control [41]
Ozone	Ozone injection for NO control [42], removal of sulfur dioxide and nitrogen oxides [43], effect of ozone injection on the catalytic reduction of nitrogen oxides [44]

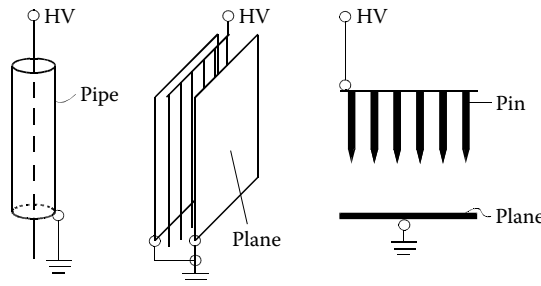


FIGURE 8.6 Corona discharges.

propagation toward the other electrode. In the high field region the electrons, positive and negative ions are generated.

Other advantageous types of discharge reactors for environmental applications are DBD implementations. A DBD is characterized by two electrodes with at least one insulating layer as a dielectric barrier in between (see Figure 8.7) The dielectric barrier inhibits the flow of the direct current.

The DBD stands out due to the fact that it can be operated in a wide range of pressure (mbar up to atmospheric pressure); the electrode distance reaches from the tenth of a millimeter up to a couple of millimeters. Generally, the DBD can be operated with sine wave or square wave alternating voltages in the frequency range

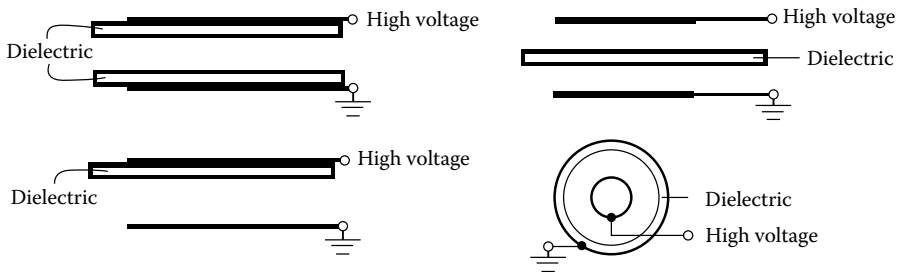


FIGURE 8.7 DBD configuration.

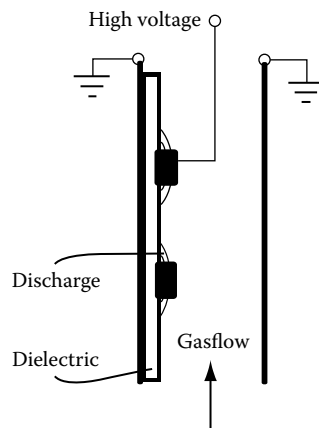


FIGURE 8.8 SD-DBD configuration.

of some Hz up to some 100 kHz. Due to the extent of the possibilities for different configurations and discharge parameters, the properties of the discharge show rather complicated connections. The discharge is characterized by a strongly increasing electric field toward the cathode and a high electric field around the cathode due to field distributions by space charges [46].

Meanwhile a lot of different special reactor configurations were developed and tested on the basis of DBD for plasma production. Figure 8.8 depicts a so-called surface discharge (SD)-DBD. In this case, one electrode is positioned on top of a dielectric while the second one is on its reverse side. In another arrangement, the second electrode is part of a coplanar electrode system where both electrodes are on the same side (at least one electrode is covered by a dielectric) [47,48].

In addition to these configurations, another established reactor type is the dielectric pellet packed-bed reactor shown in Figure 8.9. It uses dielectric pellets that are held between a dielectric and two metal electrodes to which high-voltage AC is usually applied. Special ferroelectric pellet packed-bed reactors were developed as a type of electrostatic precipitator and were found to be effective not only in collecting particles but also for VOC decomposition and odor removal. The most commonly used ferroelectric material is barium titanate. When the ferroelectric materials are exposed

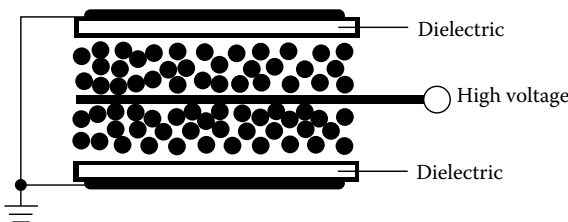


FIGURE 8.9 Packed-bed reactor.

to an external electric field, the pellets are polarized and a high field is created at each contact point of the pellets. This ends up in microdischarges at each pellet and in the surroundings. Packed-bed reactors can easily be modified to incorporate a catalyst.

8.1.2.2 Selected Plasma Treatment Applications

8.1.2.2.1 Soot and VOC Decomposition

There are various technical processes that generate waste streams containing toxic gases and aerosols mixed with air. Mainly submicron soot particles pose short- and long-term health risks. The reasons for this are the particle-bound polycyclic aromatic hydrocarbons (PAHs). The main sources of submicron particles are the different combustion processes. The potential to use DBDs for the decomposition of pollutants or toxic molecules was demonstrated in various contexts [24].

In many treatment applications of common DBD configurations, the flow rate, frequency, and power consumption are fixed parameters. The geometrical properties of the reactor (especially length and cross section) influence the results of the plasma treatment to a large extent. The residence time is determined by the geometry of the reactors, which should be optimized for a successful treatment. In the case of soot-containing flue gas, especially, a high residence time of particulates should be promoted.

The preferred system for the treatment of soot combines both plasma and filter techniques. In this case, a special DBD configuration consists of two electrodes: one of these is porous and gas-permeable: The porous electrode is made of high-performance electrically conductive SiC-ceramics or sintered metal filter. Figure 8.10 shows a scheme of the reactor configuration (one unit). The reactor consists partly of a wall flow filter with the channels at one end open and the outlet end plugged (in the shape of a honeycomb). The dielectric barrier electrode is mounted in the axis of the channels.

In this way, a plasma-processing station is formed by the two electrodes. In order to decompose the toxic and soot-containing harmful substances, the flue gas is first introduced into the processing station, in which it is subject to plasma processing, and from which flue gas is let out through the porous electrode, which is gas-permeable but filters and holds back the soot particles. Figure 8.11 shows a photograph of such a scaled up reactor with 108 inlet channels (active length of each channel: 28.5 cm, width of the honeycomb channels: 5.6 cm).

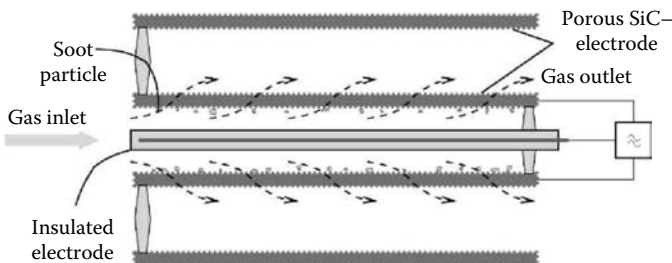


FIGURE 8.10 Scheme of the reactor configuration.

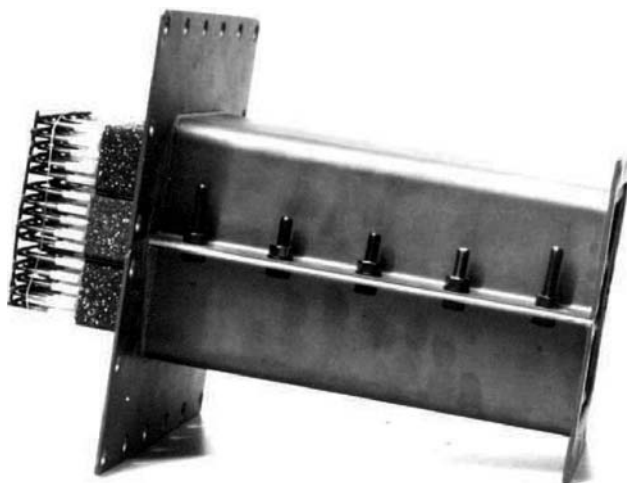


FIGURE 8.11 Photograph of a scaled up reactor with 108 inlet channels.

The degree of soot reduction depends mainly on the pore size of the ceramics. Normally the back pressure rises without any cleaning or regeneration due to the collection of particles. During plasma treatment, the back pressure remains almost constant. In this way, a continuous regeneration of the reactor can be achieved. The reaction products are CO and CO₂.

The soot decomposition is achieved in a cold oxidation process during all engine operation conditions, and no filter regeneration by promoting the combustion of the collected particulate matter is necessary. Depending on the load of soot, the process of treatment can be controlled by the pulse break ratio of the sustaining voltage. Hence, the dissipated power in the discharge can be optimized in a simple way.

The example in Figure 8.12 shows the regeneration of a soot-loaded reactor in air. The process is completed after a short time, and the pressure at the inlet remains almost constant after 30 min.

In order to analyze the results, a simple DBD-configuration was used while a porous electrode served as a filter element and soot carrier [49,50]. The diagnostic was done by an FTIR spectrometer. Gas pipes and the DBD chamber were heated and the temperature controlled. Reaction rates were determined from the time behavior

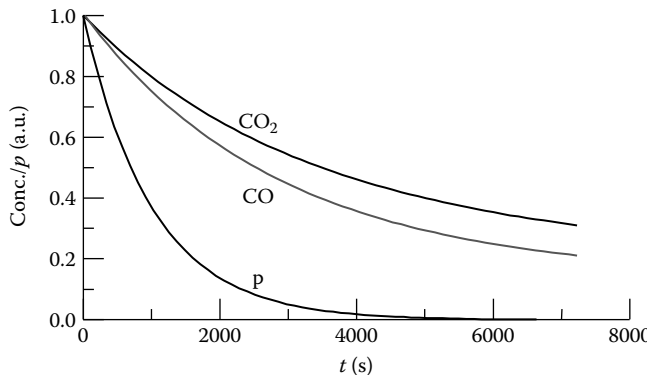


FIGURE 8.12 Time behavior of the reaction products and back pressure p .

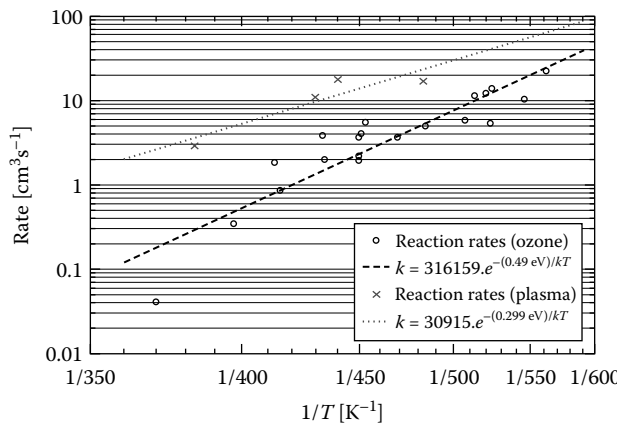


FIGURE 8.13 Plot of the estimated reaction rates versus $1/T$. The circles mark the measurements with ozone externally generated, while the crosses refer to the decomposition inside a discharge.

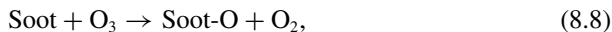
of the reaction products. Commercial ozone generator, which represents an ordinary DBD configuration, served as ozonizer. In the first step, soot was treated with a pure oxygen/ozone mixture without plasma interaction. Several measurements at different temperatures of up to 620 K were performed. Figure 8.13 (circle-points) shows the estimated reaction rates as an Arrhenius plot. The activation energy was estimated to be $E_{O_2} = 0.46$ eV.

In the next step, soot was decomposed inside a DBD configuration. Again the carrier gas was oxygen. In addition to the previous measurements, reactions with free radicals or excited atoms/ions were now possible [51,52]. Furthermore, a heating of a substratum by a plasma was reported [53] and should be taken into account. The reaction rates at different temperatures in the range of 370–520 K were estimated (Figure 8.13, “cross”-points) [54]. The rates are significantly larger and the activation

energies lower, respectively. In terms of temperature dependence, the results are similar to those for pure ozone treatment but parallel shifted to higher reaction rates. The activation energy was estimated to be $E_{DBD} = 0.30\text{ eV}$.

Furthermore, the soot was analyzed using XPS. The decomposition temperature was chosen as 433 K. As expected, both an increase of the oxygen bound into the soot surface and a decrease of the carbon fraction was found [55].

The results suggest that the decomposition process in oxygen is a three-stage process:



Soot* means partly decomposed soot; HC denotes hydrocarbons.

In addition to the reaction of soot with ozone, reactions with nitrogen oxides are known [56–58]. The electric parameters of the DBD were chosen in such a way that the discharge served as a source of NO_x . The results have shown that the decomposition of the soot–oxygen complex (soot-O) (which corresponds to the decomposition of soot) is very slow at this low temperature without ozone. It suggests further that, at least at this temperature range, the reaction with ozone is the most important process in the decomposition of the soot–oxygen complex.

In addition, the possibility of VOC decomposition was tested with the reactor configuration described earlier. Using GC-MS tests, the polycyclic aromatic hydrocarbons PAH-16, coronene, and other compounds were examined, which are particularly dangerous since they enhance the mutation of cells and may be carcinogenic. The PAH were significantly reduced by the reactor, from $21.38\text{ }\mu\text{g/m}^3$ down to $<0.3\text{ }\mu\text{g/m}^3$ [50]. Hence, it is assumed that the PAH adsorbed at the soot can be removed and also decomposed.

8.1.2.2.2 NO_x Removal

During the past several years, the control of NO_x emissions has become an issue of growing interest because nitric oxide (NO) is harmful to human health and causes damage to vegetations. In addition, NO_x emissions are a leading contributor to acid rain. The scientific literature offers a wide spectrum of publications concerning the decomposition of NO in DBDs. Yet Berthelot [59] observed the conversion of nitric oxide into N_2 , O_2 , and N_2O as well as the creation of higher nitric oxides plus oxygen, which interact with the NO. A complete decomposition of NO as shown in [60] results from the following reaction:



It is mainly the existence of N-radicals that enhances such reactions. Reactive oxygen is one of the by-products, while the concentration of oxygen generally does not rise significantly during the experiments. Nevertheless, manifold possible reactions have to be considered: Atomic oxygen may decompose NO during an oxidation and create N_2O and NO_2 . HNO_2 as well as HNO_3 is produced from higher nitric oxides.

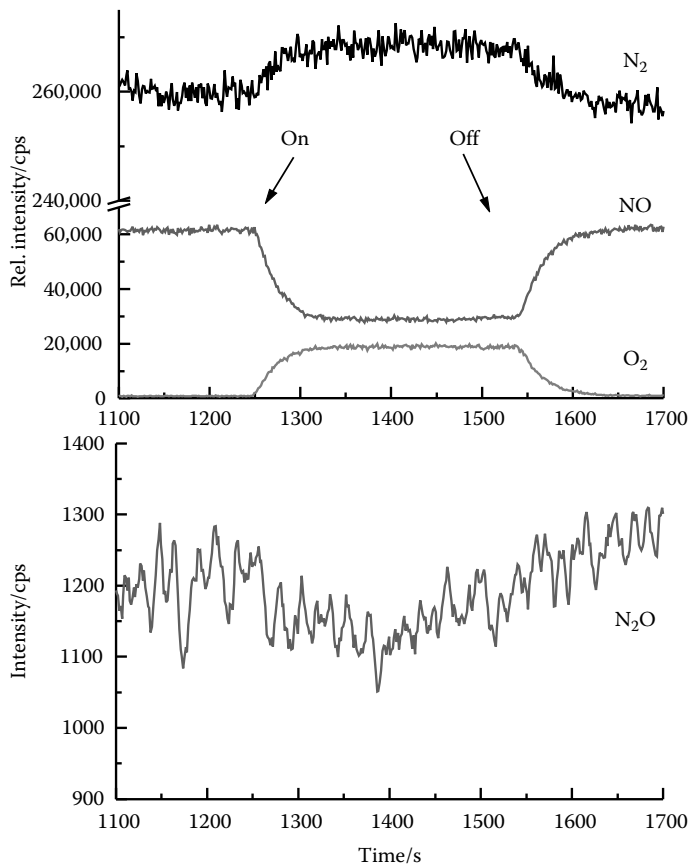


FIGURE 8.14 Reductive decomposition of NO.

Figure 8.14 shows an example of the reductive decomposition of NO in a DBD, which was recorded with a plasma monitor system.

The more stable molecular oxygen will be created according to



In experiments with mixtures of $\text{N}_2/\text{NO}/\text{O}_2/\text{H}_2\text{O}$, one can observe a decrease of the NO decomposition in the discharge. Even for optimal discharge parameters, NO_x can only be reduced to just below 50%. The activation and dissociation energies of O_2 and H_2O , remain below those of N_2 . Excited N_2 -molecules transfer their energy onto H_2O and O_2 to the disadvantage of an optimal NO_x processing.

The detected amounts of the concentration of NO_2 and N_2O correspond to those in the measurements without additional water. From the higher remaining concentration of NO_x , one can therefore conclude that a higher concentration of nitric oxides or

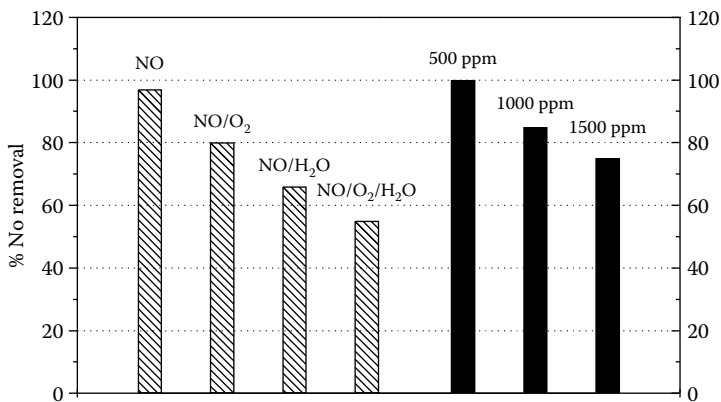


FIGURE 8.15 NO decomposition for different gas compositions N₂ carrier gas with 750 ppm NO 3% O₂ or 3% H₂O or 3% O₂/3% H₂O (shaded columns) and N₂ carrier gas with different (500, 1000, and 1500 ppm) NO concentrations (black columns).

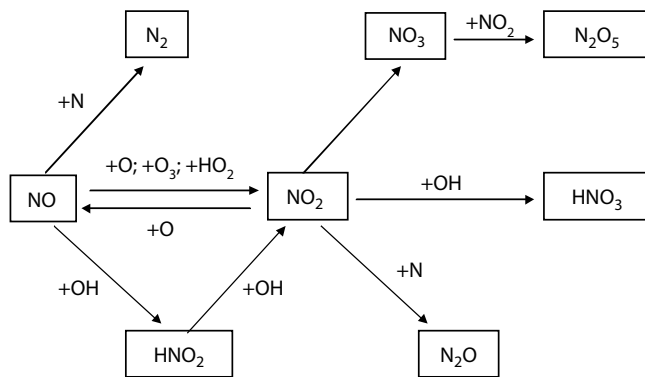


FIGURE 8.16 Scheme of the NO_x chemistry.

nitric acid are additional products. Hence, the NO decomposition is predominantly oxidative.

Figure 8.15 shows as an overview of the dependence of the NO decomposition for different gas compositions and concentrations. A scheme of corresponding reaction pathways is given in Figure 8.16 in the case of oxidative decomposition of NO.

Real diesel exhaust gases exhibit nearly identical behavior as reported earlier. In these gas systems, NO is only oxidized to NO₂ via direct or indirect reactions. Gases such as ammonia, HC, N₂H₄, and catalytic materials are used for NO₂ remediation [26,41]. Many investigations have shown that the conversion of NO to NO₂ is an important intermediate step in the de-NO_x process.

8.1.2.2.3 Odor Control

In further experiments, we set up different plasma reactor arrangements. Different SD-DBD configurations with structured electrodes were developed and tested for

odor control [61,62]. In addition to a stacked SD-DBD system, an SD-DBD with structured electrodes mounted in the center of a pipe was used. In this system, the pipe served as a casing and a flow path. The gas back pressure of this system is very low. In the experiments conducted, the active areas of structured electrodes had an extent up to 600 cm^2 .

In a typical operation mode, one of the electrodes formed the high-voltage electrode and the second one was grounded. The plasma was produced in a small part of the reactor, and the waste gas is mostly not in contact with the plasma part. Therefore, this mode is predominantly applied for reactions by long living species like ozone. In another control mode, the SD-DBD was sustained by sine wave pulse voltages. The polarity was chosen as necessary. The grounded casing was situated in front of the plasma electrodes. Positive or negative ions were extracted from the discharge side by a potential difference. These ions penetrated the waste gas, making it a promising treatment method.

The reactors and methods described earlier were used in different ways. In the first method, the reduction of odors resulting from the production of French fries was tested. The waste air cleaning system has different components and openings for gas samples on different spots. At first, the waste air from a deep-fryer reaches a high-efficiency particulate air filter made of foam material. This material works as a sorption agent, and a prefiltration of water and oil aerosols is carried out there. Due to this fact, systems like the plasma reactor or an activated carbon filter are largely spared. The process diagnostics were done using UV-absorption spectroscopy (ozone concentration), thermal desorption GC/MS (odor substances), FTIR (reaction products), and olfactometry (odor). For smell analysis, we took gas samples of approximately 81 from the process gas during the preparation of French fries in different places within a period of 2 min. For the determination of the basic level of smells, further samples of the untreated and unloaded air were taken from the surroundings.

For additional investigations, we introduced further plasma reactor configurations than those described.

Figure 8.17 shows a comparison of the common SD-DBD configuration and the pulsed SD-DBD with the odor strength of the raw gas. In the mode of sine wave pulse voltages, there is near total odor reduction. Due to the grounded casing in front of the plasma electrodes, positive or negative ions are extracted from the discharge side. Thanks to this potential difference, the ions penetrate the waste gas. We assume that the penetration of the waste air enables efficient decomposition of VOCs through additional ion–molecule reactions. The experiments showed a correlation of odor strength with odorous compounds such as VOCs. The VOCs were identified mainly as aldehydes.

8.1.2.3 Concluding Remarks

Nonthermal plasma techniques offer an innovative approach for air pollution control. There are various devices for nonequilibrium discharges and methods for pollution control. Different reactor configurations were developed and tested for some arrangements. The most important applications of nonthermal plasmas use corona discharge

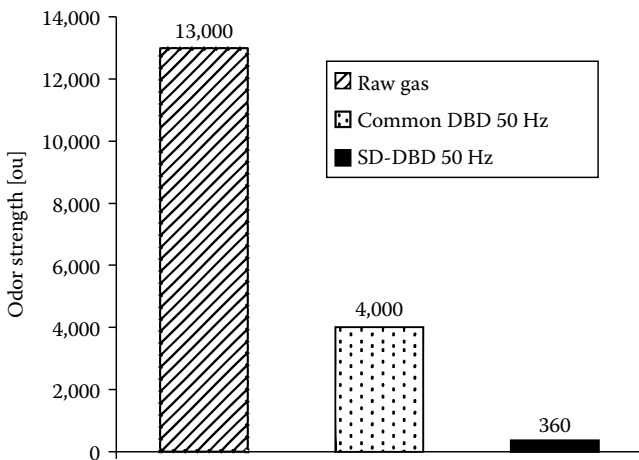


FIGURE 8.17 Odor strength after different treatment procedures.

and DBDs. Advantageous and successful implementations of nonthermal plasmas are oxidative decomposition of aromatic hydrocarbons, destruction of hazardous waste, electrostatic precipitator applications, plasma-chemical synthesis (ozone), removal of sulfur dioxide and nitrogen oxides, decomposition of soot, reduction of odors, and antimicrobial treatment of air. In the case of configurations in interiors such as recirculating air operation, one has to consider the possible emergence of by-products.

8.1.3 PLASMA CHEMISTRY OF EXCIMER LIGHT SOURCES

Plasma-chemical processes also have great importance for the generation of radiation like ultraviolet (UV) and vacuum ultraviolet (VUV) radiation, resulting from decaying excimer complexes. Excimers (*excited dimers, trimers*) are weakly bound excited states of molecules that do not possess a stable molecular ground state under normal conditions [63]. Their spontaneous emission lifetime is of the order of nanoseconds, and during the dissociation of the excited molecule by passing the excited molecular state into the ground state the binding energy is emitted in the form of continuum radiation. Depending on the desired wavelength range, different gas systems are used. In particular, rare gas (He_2^* , Ne_2^* , Ar_2^* , Kr_2^* , Xe_2^*) and halogen (F_2^* , Cl_2^* , Br_2^* , I_2^*) excimers as well as rare gas halide exciplexes* (ArF^* , KrF^* , XeCl^* , XeF^* , and so on) are of special interest for diverse applications. The corresponding maxima of the emission wavelengths are given in Table 8.3.

As sources of intense coherent UV and VUV radiation, excimer lasers have been used in photophysical and photochemical research, in micromachining of materials, as well as in medical fields like ophthalmology and psoriasis therapy [63,64]. The stimulated (laser) excimer emission is usually generated in pulsed high-pressure glow discharges. Because the emission of excimers results from a transition between a weakly bound upper state and a repulsive ground state, self-absorption or radiation

* Excited dimers/trimers of atoms of different elements that are commonly referred to as excimers.

TABLE 8.3

Matrix of Rare Gas (Rg_2^*), Halogen (X_2^*), and Rare Gas Halide (RgX^*) Excimers and Their Emission Maxima

Rare Gas (Rg)	He	Ne	Ar	Kr	Xe
Halogen (X_2)					
	74 nm	83 nm	126 nm	146 nm	172 nm
F	157 nm	108 nm	193 nm	248 nm	354 nm
Cl	259 nm		175 nm	222 nm	308 nm
Br	289 nm		165 nm	207 nm	282 nm
I	342 nm			190 nm	253 nm

trapping do not take place and excimers have also become attractive as incoherent light sources [60,65,66]. Modern excimer lamps are based on the efficient fluorescence of UV and VUV radiation of excimers, which is converted into visible light by means of appropriate phosphors. DBDs, capacitive discharges, and microwave excitation have been used to drive excimer lamps. Industrial applications of excimer lamps are cleaning of substrates, water and air purification, UV curing and modification of polymer surfaces, low-temperature oxidation of semiconductors, and UV-induced deposition of different materials [67,68]. In addition, flat-panel plasma TV sets are a modern excimer application. A plasma display panel (PDP) is essentially a matrix array of very small discharge cells, where the plasma in each cell is generated by DBD [69].

In the following, the main plasma-chemical processes required to form excimers in rare gases and rare gas halide mixtures are discussed.

8.1.3.1 Main Processes of Excimer Formation in Rare Gases

The efficient excimer formation requires electrons (e^-) with an energy of at least 10 to 25 eV. These electrons are able to generate excited atoms (Rg^*) or ions (Rg^+) of the rare gas in direct collisions of electrons with rare gas atoms (Rg) in their ground state according to



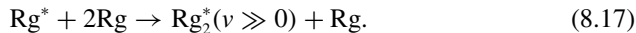
In excimer light sources, the generation of rare gas ions is usually dominated by stepwise excitation of excited rare gas atoms (Rg^*) to the higher excited atoms (Rg^{**}) via



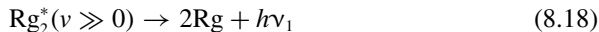
followed by the stepwise ionization mainly according to



Depending on the pressure, excited rare gas molecules in vibrationally excited states are produced in three-body collision processes of the lowest excited rare gas atoms with two rare gas atoms in their ground state via the reaction



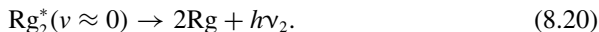
In a next step, the highly vibrationally excited molecules either decay radiatively toward the unstable ground state connected with the dissociation into two rare gas atoms according to



or undergo vibrational relaxation

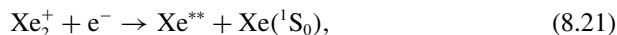


with subsequent radiative dissociation of the relaxed lowest vibrational state into two rare gas atoms



These radiative transitions are attributed to bound-free transitions, and they result in the first (8.18) and second (8.20) continuum. Depending on the pressure, the radiation process (8.18) competes with the vibrational relaxation process (8.19). In addition, the radiation process (8.20) is in competition with the quenching of $\text{Rg}_2^*(v \approx 0)$ by rare gas atoms and by itself, which leads to a decrease of the efficiency of the emission at high pressures.

As an example, the pumping mechanism involved in the formation of xenon excimers in DBDs is illustrated in Figure 8.18. The reaction scheme includes electrons, ground state xenon ($\text{Xe}({}^1\text{S}_0)$) atoms, the excited atomic ($\text{Xe}({}^3\text{P}_2)$, $\text{Xe}({}^3\text{P}_1)$, Xe^* , Xe^{**}) and molecular ($\text{Xe}_2^*(1_u, 0_u^-; v \approx 0)$, $\text{Xe}_2^*(0_u^+; v \approx 0)$, $\text{Xe}_2^*(1_u, 0_u^-; v \gg 0)$, $\text{Xe}_2^*(0_u^+; v \gg 0)$) states, and the atomic (Xe^+) and molecular (Xe_2^+) ions, where Xe^* and Xe^{**} represent the lumped 6s' and 6p levels, respectively. Electrons generated in the microdischarge excite and ionize the xenon atoms according to the reactions given by (8.13) through (8.16). The main electron loss in the discharge results from the electron-ion recombination



where the molecular ions are the predominant positive charge carrier. They are rapidly produced via the three-body reaction



The xenon excimer radiation results from the reaction processes given by (8.17) through (8.20), where Rg^* denotes $\text{Xe}({}^3\text{P}_2)$ and $\text{Xe}({}^3\text{P}_1)$, respectively. At pressures

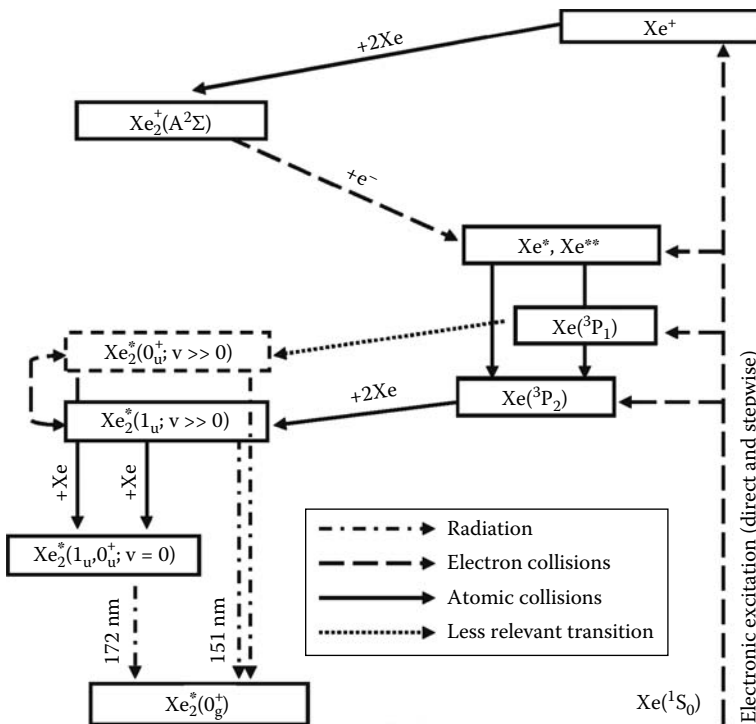
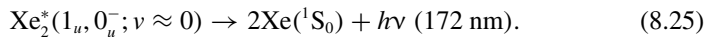
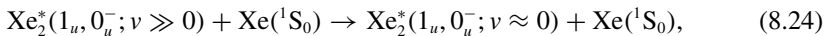
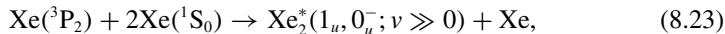


FIGURE 8.18 Scheme of kinetic pathways for the formation of Xe_2^* excimer radiation in a DBD. (From Adler, F. and Müller, S., *J. Phys. D: Appl. Phys.*, 33, 1705, 2000.)

above 10 Torr, the first continuum of the xenon excimer appears peaking at a wavelength of about 151 nm [70]. It can be observed in DBDs in the medium pressure range below 250 Torr only [71]. At pressures above 100 Torr, i.e., in the DBD considered, the second continuum radiation of the xenon excimer is predominant with an emission maximum at 172 nm. The main reaction pathway to produce the excimer radiation reads



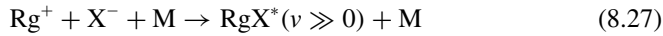
8.1.3.2 Main Processes of Excimer Formation in Rare Gas Halide Mixtures

Rare gas halide excimer transitions are widely used in commercial lasers [63] and in excimer lamps [67]. Typical rare gas halide lasers consist of a light buffer gas, a heavy rare gas (Rg), and a halogen (X). A large number of atomic, molecular, and ionic species are generally involved in the formation of rare gas halide excimer. The energetic electrons generated in the pulsed high-pressure glow discharge (or in the microdischarge of the DBD) excite and ionize the heavy rare gas according to

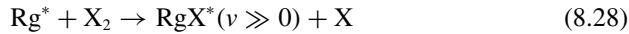
the reactions given by (8.13) through (8.16). In addition, electrons of low energy collide with the halogen molecule and form negative halide ions via the dissociative attachment reaction



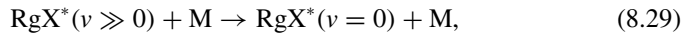
The main pathway to form the RgX^* exciplex is the three-body recombination



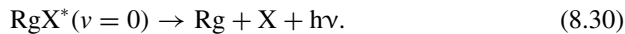
of positive rare gas ions with negative halide ions. Here, the third partner M, e.g., from the buffer gas, absorbs the remaining energy and a part of the momentum in this collision process. Furthermore, the harpooning channel via the two-body reaction



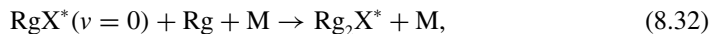
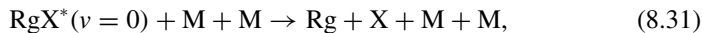
of an excited rare gas atom with the halogen molecule plays an important role in the formation of exciplexes. Similar to the rare gas excimers, the exciplex molecules are formed in a high vibrational level. The transition to the lowest vibrational level occurs by the vibrational relaxation reaction



where M is the buffer gas (or the heavy rare gas). Thus, the density of M has to be chosen in such a way that the time of vibrational relaxation is small compared to the lifetime of spontaneous emission of the upper laser level $\text{RgX}^*(v = 0)$. The unstable molecule $\text{RgX}^*(v = 0)$ disintegrates within a few nanoseconds by photon emission into a rare gas and a halide atom according to



The efficient generation of rare gas halide exciplexes requires large neutral and electron densities. However, the radiative process (8.30) is in competition with several quenching processes so that too large species densities result in a too fast destruction of the rare gas halide exciplexes particularly by three-body reactions



where triatomic species (Rg_2X^*) can be formed.

As an example, Figure 8.19 shows the main plasma-chemical reactions involved in the formation of XeCl^* in discharge-pumped laser systems. The discharge mixture consists of neon as buffer gas, xenon as heavy rare gas, and hydrogen chloride as halogen donor with the initial composition of 1000/8/0.8 of the Ne/Xe/HCl mixture at a pressure of 3 bar [72]. The reaction scheme includes the heavy particles Ne , Ne^* , Ne^{**} , Ne^+ , Xe , Xe^* , Xe^{**} , Xe^+ , Xe_2^* , Xe_2^+ , NeXe^+ , HCl ($v = 0, 1, 2, 3$), H , Cl , Cl^- ,

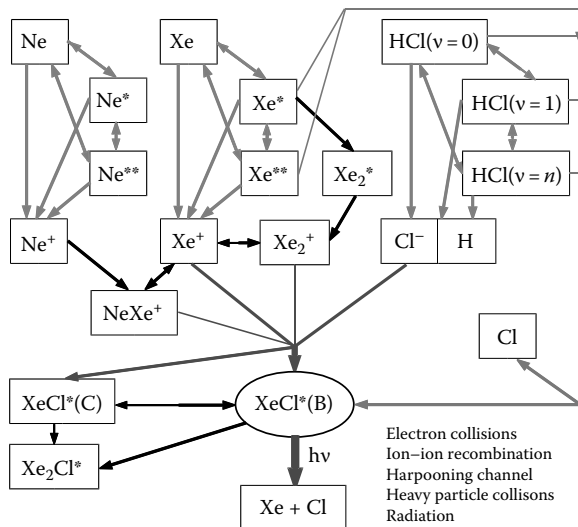


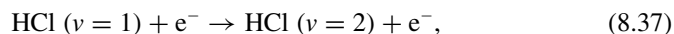
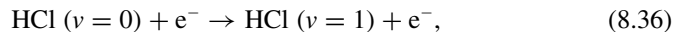
FIGURE 8.19 Reaction kinetics in XeCl^* laser discharges.

$\text{XeCl}^*(\text{B})$, $\text{XeCl}^*(\text{C})$, and Xe_2Cl^* , electrons, and laser photons. Here, the excited $1s_{5.2}$ and $2s_{10..1}$ atomic states of neon and xenon are grouped into the excited levels Ne^* , Xe^* and Ne^{**} , Xe^{**} , respectively.

Collisions of electrons with the atoms of xenon and neon lead to their excitation and ionization according to the reactions (8.13) through (8.16). Because of the lower excitation and ionization energy of Xe, the multistage process

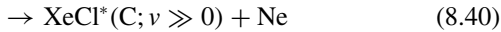
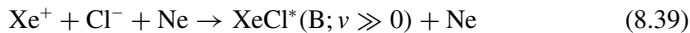


is predominant for the generation of positive ions and electrons after the ignition of the discharge. For the halogens F_2^* , Cl_2^* , Br_2^* , and I_2^* in their ground state, the process (8.26) leads to the formation of negative ions already when the energy of the attaching electron is zero. In contrast to these halogens, the energy threshold for electron impact vibrational excitation of hydrogen chloride in its vibrational ground state is lower than that for dissociative attachment of electrons. Thus, the formation of negative ions occurs by collisions of electrons of low energy with vibrationally excited states $\text{HCl}(v > 0)$, which have a lower threshold for dissociative electron attachment than $\text{HCl}(v = 0)$. The corresponding multistage process reads



It finally leads to the production of the required negative chlorine ion and hydrogen.

The ion–ion recombination reaction induced by Ne



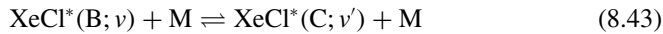
results in the formation of the vibrationally excited B and C states of the XeCl molecule, where $\text{XeCl}^*(\text{B}; v \gg 0)$ is predominantly produced. The collision reaction between Xe^* and HCl ($v = 0$) is thermoneutral, i.e., its branching ratio is almost zero with respect to the formation of XeCl^* . Thus, the upper laser level is mainly formed via reaction (8.39), while the harpooning reaction



plays a minor role only. The vibrational relaxation



results mostly from collisions with the buffer gas neon and the unstable $\text{XeCl}^*(\text{B}; v = 0)$ molecule decomposes within 11 ns by emission of photons with a maximum intensity at the wavelength 308 nm [73]. All vibrational levels $\text{XeCl}^*(\text{B}; v)$ and $\text{XeCl}^*(\text{C}; v)$ are not only subject to vibrational relaxation but also to exchange reactions



by collisions with $\text{M} = \text{Ne}$, Xe , HCl , Cl , e^- as well as quenching in two-body reactions



and three-body collision processes



leading to the generation of Xe_2Cl^* . Further details of the vibrational and quenching kinetics of XeCl are given in [74].

8.2 PLASMA SURFACE CHEMISTRY

Low-temperature, nonthermal plasmas are effective tools for surface treatment of materials in a broad field of applications. The use of plasmas offers the possibilities of selective control of various parameters and as dry processes with low material and energy insert they are environmentally friendly. Plasma surface chemistry

is distinguished from physical processes by chemical reactions that change the chemical state of the surface. Pure physical processes such as sputtering or ion implantation are beyond the scope of this chapter. A systematic compilation of the treated plasma surface chemical processes is given in Table 8.4 together with material transfer from or on the target surface as well as some applications of the selected processes. Deposition and etching transfer weighable materials. In activation processes, the material transport is negligible; sometimes only the chemistry is changed. The coating and deposition processes that are discussed here are known as plasma-assisted chemical vapor deposition (PACVD). The chapter is organized as follows. The first part deals with plasma etching, especially for the formation of micro- and nanostructures in the microelectronic industry. Biological decontamination and sterilization are covered in the next part. Surface modifications of polymers, textiles, and biomedical applications and plasma medicine are treated in further sections. The following treats various fields of plasma enhanced chemical vapor deposition (PECVD) of organic thin films, including diamond, a-C:H films, plasma polymers, and inorganic films. Electrical discharges in liquids and nano- and microparticles are further topics.

8.2.1 PLASMA ETCHING

8.2.1.1 Plasma Etching, Micro- and Nanostructures

A standard technique for the removal of material from a surface is etching Figure 8.20. Wet etching is a long-established technique that uses aggressive chemical liquids such as acids, bases, or other chemical compounds also in mixtures according to the chemical properties of the treated substance. Wet etching is very species selective but isotropic.

Plasma etching is a key process step, e.g., in microelectronic production, in the nanoelectronic industry, and for micromachining of materials [75,76]. It is a dry etching procedure that is characterized by the application of plasmas for the activation of primary nonreactive gases by dissociation or ionization. The plasma generates energetic ions reacting with surfaces by physical and/or chemical processes. Using the electric field near the surfaces, ion-induced anisotropic etching gets possible. The dry etching process is species selective by the generation of volatile products in reactions of activated species with the substrate.

8.2.1.1.1 Application of Plasma Etching in Micro- and Nanoelectronics

The demands on etching technology are growing rapidly according to the increasing number of transistors on a processor chip. Moore's law is based on the observation of a doubling of the transistors per chip every 2 years. This is necessarily coupled with a decrease of the structure width, typically the width of the current lines or of a dielectric region [77]. In the 1970s, the structure width was about 10 µm and $2 \cdot 10^3$ transistors were integrated on a chip. Nowadays, using extreme ultraviolet lithography, structure widths of 35 nm and $2 \cdot 10^9$ transistors per chip can be achieved (Intel) Figure 8.21. This development is connected with an increase of, e.g., the maximal memory capacity and the upper limit frequency, but also with a drastic miniaturization.

TABLE 8.4 Applications of Plasma Surface Chemistry
Plasma Surface Chemistry

Target	Process	Material	Mass Transfer	Applications (Examples)	Sections
Solids	Etching		$\Delta m/m < 0$	Microelectronics structuring, micromachining	8.2.1
	Cleaning		$\Delta m/m \sim 0$	Industrial production	8.2.3.2
	Decontamination		$\Delta m/m \sim 0$	Sterilization	8.2.2
	Surface activation, functionalization deposition		$\Delta m/m \sim 0$	Wettability, printability, adhesion, settlement probability of cells	8.2.3
		Organic films: Carbon depositions Diamond, DLC (a-C:H)	$\Delta m/m > 0$	Hardness, wear resistance, frictional properties, scratch resistance, corrosion protection, medical biocompatible coating, optical coating electronics, nanotechnology	8.2.4.1
		Nanotubes, graphene		Corrosion protection, insulator in thin film capacitors, microelectronics mask material, scratch-resistant coatings, antisoilng and antibonding coating, optical coating	
		Plasma polymers: Hydrocarbons Fluorocarbons Siliconorganics		Sensors, antibacterial coating	
		Composite films Inorganic films: TiN, a-Si:H, TCO Metal oxides	$\Delta m/m > 0$	Hardness, wear resistance, photovoltaic, decorative coatings High k dielectrics, nanoelectronics	8.2.4.2
Liquids	PEALD				8.3

TCO: transparent conducting oxides; PEALD: plasma-enhanced atomic layer deposition; DLC: diamond-like carbon.

Etching		
Wet etching		Selective, isotropic
Dry etching		
	Gas etching	Selective, isotropic
	Beam etching	
	Ion milling	Nonselective, anisotropic
	Reactive ion beam etching	Selective, anisotropic
	Chemically assisted ion beam etching	Selective, anisotropic
	Plasma etching	
	Reactive neutral gas etching	Selective, isotropic
	Sputter etching	Nonselective, anisotropic
	Reactive ion etching	Selective, anisotropic
	Ion-enhanced energy-driven etching	Selective, anisotropic
	Ion-enhanced inhibitor-controlled etching	Selective, anisotropic

FIGURE 8.20 Classification of etching types. (From Deutsch, H. et al., *Contrib. Plasma Phys.*, 29, 263, 1989.)

This leads to a rapid increase of applications, e.g., in science, medicine, and telecommunication. Perspectives in nanoscale etching are discussed in [79].

The diameters of the Si-wafers for the fabrication of integrated circuits were 25 mm in the middle of the 1960s. Nowadays, diameters of 150–300 mm are used, and diameters of 450 mm are predicted for 2012.

8.2.1.2 Basic Mechanisms of Plasma Etching

Plasma-assisted dry etching is characterized by four basic mechanisms [89].

1. Physical sputtering: Ion beam sputtering is a purely physical process. An ion with a kinetic energy above the threshold energy (~ 20 eV) collides with a target atom, and the momentum transfer results in the ejection of atoms from the surface. Sputtering is possible for all materials of interest, but has a low selectivity, a low etch rate, and, due to the high ion energies used, a high damage rate of the target material. Redeposition of sputtered material is possible. Using directed ion bombardment of the surface in an electric field, the etch process gets anisotropic.

Ion milling techniques also use physical sputtering. Usually, inert gas ions as Ar^+ with energies of 500–800 eV bombard the surface at perpendicular

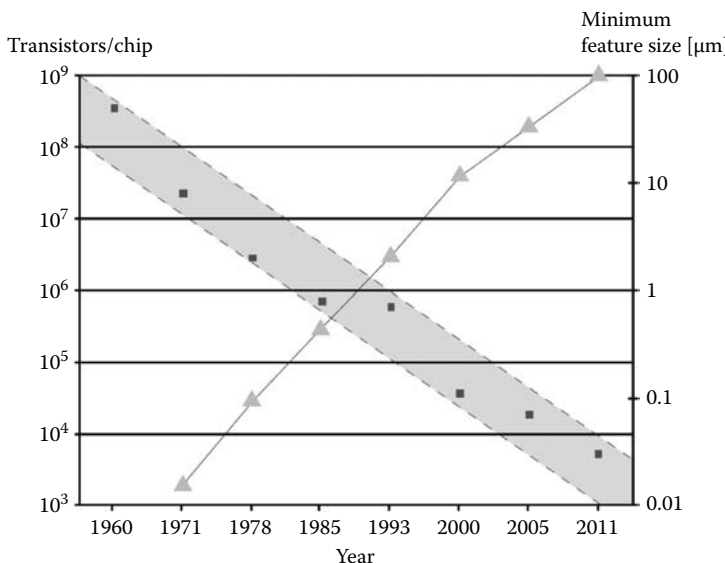


FIGURE 8.21 Minimum feature size/structure width (■), and number of the transistors per chip (▲) in dependence on time. Moore's law. (From Fahrner, W., *Nanotechnologie und Nanoprozesse*, Springer, Berlin, Germany, 2003.)

incidence. Redeposition of sputtered material is avoided operating at low pressures (<0.01 Pa).

2. Chemical etching: Neutral radicals generated inside the plasma can react with substrate materials. The volatile reaction products leave the surface. A product is called volatile if the vapor pressure is larger than 10^{-2} Pa at operating temperature [80]. The formation of volatile reaction products depends on the chemical properties of the radical and the substrate. Therefore, this process is very species selective but isotropic due to the isotropy of the inflow of the radicals from the plasma Figure 8.22a [76].

Pure chemical etching is used, e.g., for plasma stripping or plasma ashing in barrel reactors to remove residues of photoresist from wafers in 13.56 MHz discharges in O₂ or O₂/N₂ [81]. The plasma does not contact the wafers and generates O radicals, which oxidize the organic photoresist to CO, CO₂, and H₂O. Also, radicals in downstream microwave plasmas are used for pure chemical etching [82].

3. Physical-chemical etching: The reactivity of the surface can be enhanced utilizing the kinetic and potential energy of impinging ions. Heating and breaking of bonds on the surface facilitates the formation of volatile compounds by reactions with neutral radicals. Ion collisions on the thin polymer surface enhance the diffusion of radicals, provide the desorption energy for the etch products, and enhance their diffusion through the polymer film into the gas phase [83,84]. Also, the activation of adsorbed working gas molecules is possible. This process is selective, determined by the chemistry

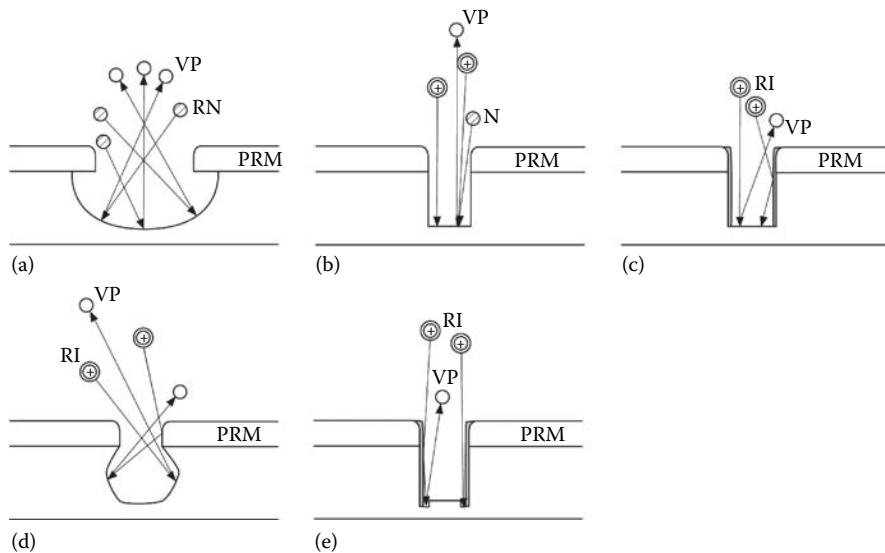


FIGURE 8.22 Various etching processes: (a) chemical etching, isotropic etching with under etching; (b) ion-induced etching; (c) reactive ion etching, with sidewall protection by inhibitor film; (d) bowing by transversely impinging reactive ions; and (e) trenching by ions reflecting from inhibitor films at sidewalls (PRM: photoresistant mask, VP: volatile reaction products, RN: neural radicals, N: neutral gas molecules, RI: reactive ions).

of radicals and substrate, and anisotropic, determined by the direction of the impinging ions Figure 8.22b [76].

For etch processes operating at direct contact between substrate and plasma, the reactions are a mixture of physical and chemical reactions. Ions are accelerated to the substrate due to its self-bias or bias potential. This directed flux of energetic ions leads to an anisotropic etching by an ion-enhanced, energy-driven mechanism. Disturbances of the direction of the ion beam from the plasma lead to a bowing of the etch profile Figure 8.22d [76]. Such perturbations of an ideal beam are broadened angular distribution of the ions leaving the plasma or can be caused by collisions of ions with neutral gas molecules in the sheath.

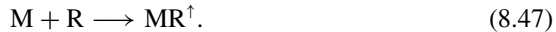
4. Ion-enhanced inhibitor: Plasmas containing, e.g., hydrocarbons tend to form plasma polymers on surrounding surfaces. Also, during the plasma etch procedure, the formation of plasma polymers is observed. The deposition of such inhibitor films at vertical side walls prevents the action of the etching radicals, but on the other hand the energetic ions avoid the deposition of inhibitor film on horizontal surfaces. In this way, the sidewall passivation enhances the anisotropy Figure 8.22c [76]. The reflection of ions from the dielectric inhibitor films at the sidewalls can cause trenches Figure 8.22e [76]. The formation of polymeric films in active etching plasma can be enabled by the chemistry of the etching gas, suitable gas admixtures, or by etch products, e.g., of the photoresist.

8.2.1.3 Etch Chemistry

The basic equations for plasma etching are

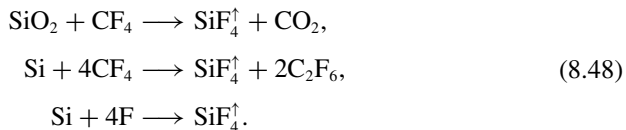


Etch gas RB is activated in the plasma, e.g., by electron collision



The radical R reacts with the substrate material M. The volatile etch product MR^\uparrow is formed. Desorption of etch product can be enhanced by ion collisions.

The etch process of Si and SiO_2 can be written by the gross reactions



Here, the source of F can be, e.g., SF_6 .

The etch product desorption is enhanced by ion bombardment of the surface.

The application of other fluorocarbons such as C_2F_4 , C_4F_{10} , and C_2F_6 leads to the deposition of plasma polymers for small F/C ratios, low bias to the treated surface, and admixture of H_2 . Etching is enhanced for high F/C ratios, increasing bias of the treated surface, and admixture of O_2 [85].

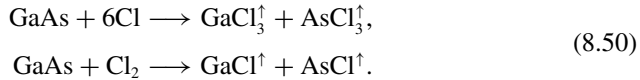
Aluminum etching is determined by the formation of Al_2Cl_6 and AlCl_3 . Cl_2 etches Al without activation. Anisotropic etching is possible in an ion-enhanced process with inhibitor chemistry using admixtures such as CCl_4 , CHCl_3 , and SiCl_4 to the Cl_2 feedstock [98].

The etching of GaAs in a CH_4/H_2 plasma can be summarized as



(see [86]).

Overall etch reactions of GaAs in a Cl_2 plasma are



Complex etch processes with different reaction rates, temperature dependences and different residence times of reaction products lead to temperature dependencies of the etching rate [78]. A discussion of the rate basing on a detailed particle balance on surfaces is given in Chapter 5.

The observed etching rates vary considerably for different systems. Si etching in SF_6 plasmas achieve rates of some $\mu\text{m}/\text{min}$ [87], GaAs in Cl_2 -based plasmas 300 nm/min, InP in CH_4/H_2 -based plasmas 30 nm/min [88].

The etching rate depends not only on various process parameters, but also on the loading of the materials in the reactor. The consumption of reactive radicals increases with increasing loading and therefore the radical concentration and etching rate decreases.

Important characteristic data for dry etching technology are [88]

- Etching rate
- Selectivity (etching rates for different materials)
- Directionality (isotropic or anisotropic)
- Sidewall angle
- Etched surface quality
- Material damage
- Uniformity
- Reproducibility

Besides these important parameters, the reactive gas phase must be free of dust particles to avoid disturbances of the microstructures by deposited dust particles (see also Section 8.4). In Table 8.5, etching gases are summarized for various materials.

TABLE 8.5
Etching Gases for Various Materials

Silicon	CF ₄ /O ₂ , CF ₂ Cl ₂ , CF ₃ Cl, SF ₆ /O ₂ /Cl ₂ , Cl ₂ /H ₂ /C ₂ F ₂ /CCl ₄ , C ₂ ClF ₅ /O ₂ , SiF ₄ /O ₂ , NF ₃ , CCl ₄ , C ₂ ClF ₅ /SF ₆ , C ₂ F ₆ /CF ₃ Cl, Br ₂ , CF ₃ Cl/Br ₂ , HBr
SiO ₂	CF ₄ /H ₂ , C ₂ F ₆ , C ₃ F ₈ , C ₄ F ₈ , C ₄ F ₆ , CHF ₃
Si ₃ N ₄	CF ₄ /O ₂ /H ₂ , C ₂ F ₆ , C ₃ F ₈ , CHF ₃ , NF ₃ , CHF ₃ /O ₂ , CH ₃ F, SF ₆
Organics, polymers	O ₂ , CF ₄ /O ₂ , SF ₆ /O ₂
Silicides	CF ₄ /O ₂ , NF ₃ , SF ₆ /Cl ₂ , CF ₄ /Cl ₂
Al	BCl ₃ , BCl ₃ /Cl ₂ , CCl ₄ /Cl ₂ /BCl ₃ , SiCl ₄ /Cl ₂
Cr	Cl ₂ , CCl ₄ /Cl ₂
Cu	Cl ₂ /Ar
Mo, Nb, Ta, Ti, W	CF ₄ /O ₂ , SF ₆ /O ₂ , NF ₃ /H ₂
Au	C ₂ Cl ₂ F ₄ , Cl ₂ , CClF ₃
GaAs	BCl ₃ /Ar, Cl ₂ /O ₂ /H ₂ , CCl ₂ F ₂ /O ₂ /Ar/He, CCl ₄ , PCl ₃ , HCl, Br ₂ , COCl ₂ , SiCl ₄
InP	CH ₄ /H ₂ , C ₂ H ₆ /H ₂ , Cl ₂ /Ar, Cl ₂ /O ₂ , HBr, CF ₃ Br, Br ₂ , HI, CH ₃ I, I ₂
NiFeCo	Ar/Cl ₂ , N ₂ /Cl ₂ , H ₂ /Cl ₂

Sources: Shul, R.J. and Fleming, J.G., Bulk si micromachining for integrated microsystems and MEMS processing, In Shul, R.J. and Pearton, S.J., eds., *Handbook of Advanced Plasma Processing Techniques*, Springer, Berlin, Germany, pp. 419–458, 2000; Grill, A., *Cold Plasma in Materials Fabrication from Fundamentals to Applications*, IEEE, New York, 1994; Boeing, H.V., *Fundamentals of Plasma Chemistry and Technology*, Technomic, Lancaster, PA, 1988; Richter, H.H. et al., Plasma etching in microelectronics, in *Low Temperature Plasmas: Fundamentals, Technologies and Techniques*, in Hippler R. et al., eds, pp. 655–674, Wiley-VCH, Weinheim, Germany, 2008.

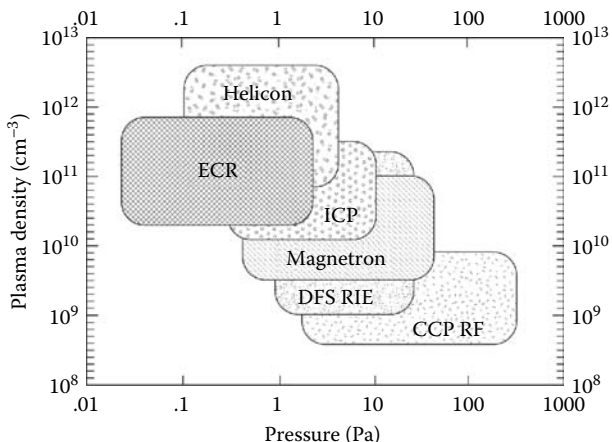


FIGURE 8.23 Plasma etch reactors for manufacturing of large-scale integrated electronic devices with operating pressure and plasma density. (From Abe, H. et al., *Jpn. J. Appl. Phys.*, 47, 1435, 2008.)

8.2.1.4 Reactors for Plasma Etching

The principal features of reactors for etching were already discussed in the chapter on plasma sources. Figure 8.23 shows the plasma reactors used for manufacturing of large-scale integrated electronic devices that depend on operating pressure and plasma density. Low pressure reduces the neutral radical density and therefore the isotropic etching by these particles. Also, the thickness of the sidewall-protecting films will be reduced. The general trend for the operation of plasma reactors for LSI manufacturing is directed to low pressure and high plasma density [81]. Low-density reactors are the capacitively coupled parallel plate RIE (reactive ion etching) rf reactors (CCP RF). Higher densities are achieved in the dual frequency superimposed capacitively coupled RIE reactors (DFS RIE). Lower pressures and higher plasma densities are typical for magnetic field enhanced RIE reactors (MERIE; magnetron-, helicon-, ECR-reactors). Higher plasma densities (ICP) can also be obtained by inductively coupled plasma reactors.

Characterization and control of the etch process requires the measurement of three categories of parameters [92]:

1. Machine parameters, such as power, pressure, partial pressures, and flow rate
2. Plasma parameters, such as potentials, densities of charge carriers, and neutral radicals
3. Process parameters, such as etching rate, anisotropy, selectivity, uniformity, and endpoint monitoring

The various methods of plasma diagnostics, like probes, optical emission and absorption spectroscopy, laser methods, and ion mass and energy analyzers are

discussed in Chapter 6. Plasma diagnostics is in particular informative near the wafer surface.

For high density, low pressure etching in different plasma sources it could be shown that the etch rate (e.g., of SiO_2 in a CF_4 plasma) depends only on the plasma parameters in front of the wafer [93]. The etch process occurs by ions and neutrals, e.g., F atoms. Also, the deposition of polymers (by CF_2) has to be taken into account. The etch rate R using the experimental values of ion current density J_i and its energy E_i as well as the neutral fluxes of the etching J_e and depositing J_d species (which are proportional to the particle densities) are given by

$$R = \frac{K_{es} J_i E_i [1 - C_{sp} (J_d/J_e)^2]}{1 + A_s (J_i E_i / J_e)}, \quad (8.51)$$

K_{es} , C_{sp} , and A_s being constants. The etch rates of SiO_2 in CF_4 plasmas determined in different tools (electron cyclotron reactor [ECR], helicon reactor [HRF], magnetically confined inductively coupled plasma [MCICP], and RIE) are presented in Figure 8.24 according to Equation 8.51 using experimental values of the plasma parameters. Equation 8.51 fits the data of the different tools very well [93].

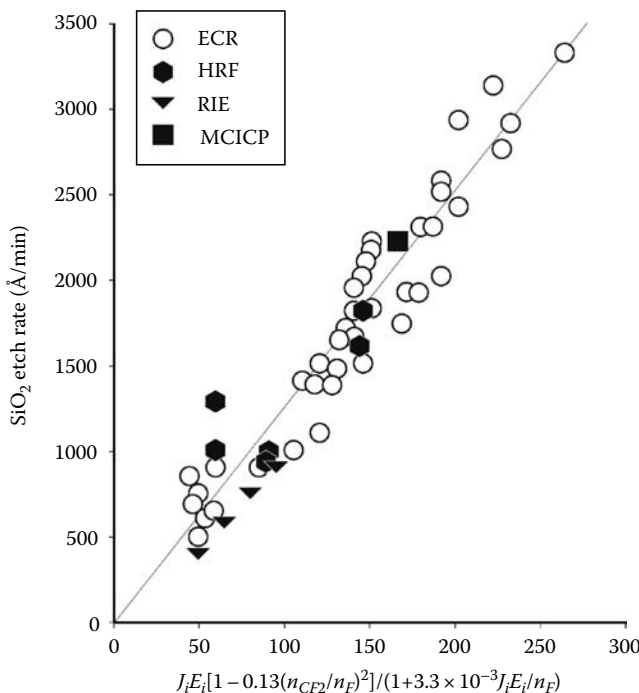


FIGURE 8.24 Etching rates of SiO_2 in CF_4 plasmas in ECR, RIE, MCICP, and HRF reactors, experimental and calculated data (8.51). (From Hershkowitz, N. et al., *Phys. Plasmas*, 3(5), 2197, 1996.)

8.2.1.5 Trench Etching

An important task for plasma etching is the formation of small, deep trenches with aspect ratios (deep/width) beyond 10:1 in micromechanics as well as in microelectronics [94,95]. Here, one reliable technique for this application will be presented in more detail. Such features can be produced by deep reactive ion etching (DRIE) with a directed ion beam. Ion inhibitor techniques using the sidewall protection are very well suited for directional etching. SF₆/C₄F₈ generates plasma polymers. According to the temperature dependence of the film formation, cooling systems with He or liquid nitrogen for the generation of constant wafer temperatures are applied. Modern etch reactors are equipped with an inductive coupled plasma source to generate a high-density plasma with high concentrations of ions and radicals and additionally with a capacitive coupled plasma source for generation of fluxes of directed ions to the wafer surface by the bias.

The following methods are used for the formation of passivating layers:

1. Plasmas with gases for the formation of nonvolatile siliconoxy halogens
2. Freezing the volatile etch products at the feature wall by wafer cooling
3. Plasmas with gases that form plasma polymers
4. Removal and redeposition of mask material

The feeding of the inhibitor forming gases into the plasma can be done

1. Directly to etch gas
2. Sequentially (time-multiplexed) from the etch gas (pulsed-mode DRIE)

An example of a pulsed-mode DRIE procedure is the advanced silicon etch (ASE®) process [95]. It works in a reactor with inductive coupled plasma (13.56 MHz) and a wafer chuck independently biased by a low power 13.56 MHz generator. This allows an independent bias control of the wafer. The working gases are C₄F₈ and SF₆.

The etch procedure includes the *repetition* of three steps:

1. All surfaces are passivated by thin fluorocarbon plasma polymer film using the C₄F₈ based plasma.
2. With an SF₆-based plasma and DC bias of the wafer, energetic ions bombard the surface and remove the polymer film mainly parallel to the wafer surface. The base of the trench is cleaned. The sidewalls are protected by the polymer layer.
3. The pure silicon surfaces are etched isotropically by the neutral fluorine radicals generated in dense inductive coupled plasma. The sidewalls are protected by the polymer films.

The chemistry of the Si etching in an SF₆ plasma [96] starts with the electron impact induced dissociation of SF₆:



The F radicals react with the Si and generate SiF, then stepwise SiF₂, SiF₃, and finally the volatile SiF₄. Loss processes for F atoms are recombination reactions such as



The admixture of O₂ avoids the deposition of sulfur by generation of SO₂.

8.2.1.6 Conclusions

Plasma etching is an advanced method for material processing not only in microelectronics but also in micromachining. Until now, the requirements for miniaturization have been fulfilled down to structure widths of about 50 nm. Future tasks will be the etching of new metals and complex oxides. Further developments of polymer electronics may be connected with the introduction of microstructuring of polymers by plasma etching. Improvements of the established procedures should reduce the consumption of etching gases with their high global warming potential.

8.2.2 BIOLOGICAL DECONTAMINATION UP TO THE LEVEL OF STERILIZATION

8.2.2.1 Plasmas as New Prospects for Hygiene and Life Science

In nonthermal plasmas, the neutral background gas enthalpy is usually not significantly increased. This enables the treatment of heat-sensitive materials and biological tissues. In many studies, the inactivation or removal of biological contaminants such as pathogens has been demonstrated and opens up new fields of applications. For sensitive goods, e.g., medical instruments and implants that cannot be treated by classical thermal or chemical methods,* nonthermal plasmas introduce an alternative for sterilization. Plasma-based sterilization and disinfection technologies for packaging will lead to safer products with longer shelf life in food and pharmaceutic industry. Electrical discharge–driven ozone generators are used for water treatment for about 100 years; new activities consider the generation of plasmas inside liquids as well. The use of plasmas for the decontamination of exhaust gases and room ventilation air (e.g., in hospitals, laboratories, and cabines) has been demonstrated and is on the way to commercialization. The therapeutic application of plasmas in medicine for electrosurgery (e.g., coagulation for wound sealing and nonspecific removal or cutting of tissue) is already known, and the new arising interdisciplinary area of plasma medicine addresses the disinfection of chronic wounds, the generation of sublethal effects (e.g., affection of metabolic cell functions) for healing stimulation, and the removal of tissue without unwanted inflammatory reactions [98,99].

The American inventor Smith granted a patent on a process for destroying insect life and microorganism based on spark and corona discharges [100] already in 1920. The first report on plasma as a sterilizing agent was by Menashi in 1968 [101]. By means of pulsed RF-driven corona-type discharges in argon at atmospheric pressure, the inner surface of vials in times of less than 1 s was sterilized. The biocidal effect

* Classical sterilization processes uses wet (autoclaves) or dry heat. The most widely used sterilants in chemical processes for heat-sensitive products are ethylene oxide, hydrogen peroxide, and glutaraldehyde.

was thought to be due to microincineration, i.e., intense heating of the contaminants in a time too short to appreciably heat the glass container [102]. In the following years, many investigations using plasmas at low, medium, and atmospheric pressure* in different configurations and gases, including gas mixtures commonly used for etching, were carried out. In the 1980s, *plasma-assisted* gas sterilization systems working at medium pressure were developed and commercialized. In these process, gases with biocidal properties of their own are used, while *plasma-based* decontamination and sterilization refer to plasma-activated processes in otherwise nonbiocidal gases. Since the 1990s, an increasing number of studies on atmospheric pressure discharges (e.g., barrier discharges, plasma jets) for biological decontamination have been registered. For further details on low- and medium-pressure plasma sterilization, the reader is referred to the review articles of Moisan et al. and Lerouge et al. [102–104]. Comprehensive reviews on the activities at atmospheric pressure, including descriptions of the plasma sources, can be found in the articles of Boudam et al. [105], Ehlbeck et al. [106], and Laroussi ([107], chapters 9.9 in [26] and 32 in [108]).

This chapter will focus on the elementary processes of antimicrobial treatment by means of nonthermal plasmas. First, some definitions and basics will be introduced (Section 8.2.1.2.2). The elementary processes will be summarized and discussed in Section 8.2.1.2.3. Finally, some selected examples on plasma-based and plasma-assisted processes for antimicrobial surface treatment will be given (Section 8.2.1.2.4). Tissue processing as well as water and gas decontamination are outside the scope of this chapter. To inform about therapeutic applications, the reviews of Stoffels (chapters 9.10 in [26] and 33 in [108]), Fridman et al. [98] and Kong [99] are recommended, see also Section 8.2.2.4. For gas decontamination see, e.g., [109–111] and section 8.2.3.1.6.

8.2.2.2 Some Basics of Biological Decontamination and Sterilization

8.2.2.2.1 Classification and Terms

Biological decontamination means the inactivation or removal of biological material, including microorganisms, pyrogens, fungi, viruses, and even prions. One aspect is the antimicrobial treatment, defined as *the inactivation of microorganisms with the purpose to reduce infections*. Thus, antimicrobial treatment is a collective term for *disinfection, sterilization, and aseptic* as well as *antiseptic*, which all have different definitions. Disinfection means *to put dead or living material in a situation where it is not longer able to contaminate*. The practical advice of the national authorities for conforming disinfection is a measurable reduction of pathogenic microorganisms by at least a factor of 10^5 . Sterilization is strictly defined as *the complete absence of viable microorganisms*. Since this cannot be proven experimentally, a sterility assurance level (SAL) of 10^{-6} has been defined for practical purposes, i.e., an assurance of less than one chance in one million that viable microorganisms are present in products after sterilization is required [112]. However, since the maximum detection limit of microbiological tests is practically at 10^{-2} microorganisms per object, a measurable reduction of 10^6 steps is instructed (with doubling of intensity to fulfill

* Pressure ranges: low pressure: 0.1 … 100 Pa; medium pressure: 100 Pa … 3.000 Pa; atmospheric pressure: 101 325 Pa = 1013.25 mbar.

overkill conditions). The terms aseptic and antiseptic refer to avoiding or inactivating pathogens to prevent infections. While antiseptic is correlated to living matter, aseptic is correlated to surfaces and products.

8.2.2.2.2 Materials and Methods

Antimicrobial effectivity is usually investigated by the comparison of the number of viable microorganisms (MO) on treated and untreated test samples with a given initial number. MO for such test are often vegetative bacteria (most common is *Escherichia coli*) or endospores of bacteria (e.g., spores of *Bacillus atrophaeus*, formerly named *Bacillus subtilis*). Endospores are a dormant form of the bacterium with a high resistance to hostile physical and chemical conditions and thus considered as good indicators. Test objects are usually sterile strips, plates, or dishes made of plastic, glass, or paper. MO containing solution (usually saline) can be dropped (*spot contamination*) or sprayed (*spray contamination*) on the test objects and must be dried under aseptic conditions. The average density of initial load derived from the literature varies between 10^6 and 10^4 MO/cm².

By default, the recovery of surviving MO on test objects is performed by the plate count method, also referred to as the *direct cell counting method*. Therefore, test objects are washed with buffered saline and an aliquot is serially diluted. The diluted solution is spread onto plates with a culture medium (agar). After incubation for several hours to days, surviving MO will form discernible colonies on the plates. The number of colonies per plate is counted, and by taking into account the dilution factor the MO concentration is derived as the number of colony-forming units per milliliter or object N [CFU/object]. This method is applied if viable MO are present on all test objects. The detection limit of the direct cell-counting method depends on the volume of the washing solution and the aliquot (practically at $10^1 \dots 10^2$ MO/object). To recover surviving spores when less than a few hundred are expected, the washing solution may be filtered through a membrane, which is directly laid onto the culture medium and incubated. The detection limit of *membrane filtration* is 1 MO/object. If test objects with and without viable MO occur simultaneously, the *fraction negative method* should be used, i.e., treated test objects are incubated completely in nutrient solution (broth) whose turbidity visually gives the evidence for microbial growth. Based on a Poisson distribution, the mean number of survivors per test object m is calculated from the number of test objects without viable MO n_0 related to the total number of identically treated test objects n, namely, $m = -\ln(n_0/n)$. The detection limit of this method depends on n_0 and is practically at $10^{-1} \dots 10^{-2}$ MO/object [113].

8.2.2.2.3 Inactivation Curves and D-Values

The physical and chemical processes during plasma treatment of MO can be analyzed by means of inactivation curves (IC), also referred to as survival curves. In IC, the decimal logarithm of the number of CFU per object or unit volume as a function of corresponding intensity—usually the treatment time—is plotted. When no survivors are found, the value may be determined by the inverse of the number of treated objects n, with attention to the detection limit of the corresponding method (see previous section). Ideally, the microbicidal effect is continuous and the number of survivors will follow an exponential decay, i.e., a line in the IC. The relationship

between the concentration of survivors N and intensity I is given by Equation 8.54

$$\lg \left[\frac{N(I)}{N_0} \right] = -kI, \quad (8.54)$$

where

N_0 is the initial concentration of MO

k is the inactivation rate constant

Based on this consideration other quantities can be defined (see Table 8.6). Commonly used is the D -value (decimal value or decimal time) as the treatment time required to reduce 90% of an initial contamination, i.e., the reciprocal slope of a linear IC.

8.2.2.3 Microbicidal Effects of Plasmas

8.2.2.3.1 Biocidal Agents Produced in Plasmas

Table 8.7 summarizes the possible microbicidal components of plasmas and its corresponding biocidal or sporocidal effects.

Ultraviolet (UV) radiation ($\lambda = 200\text{--}300\text{ nm}$) with doses of several mW s cm^{-2} is known for its lethal effects on MO. Thus various UV lamps have been developed

TABLE 8.6
**Quantities Used for the Conformation
of Antimicrobial Treatment**

Quantity	Symbol	Definition
D -value	D	$D = t/\lg[N_0/N(t)]$
Reduction factor	R	$R = \lg[N_0] - \lg[N(t)]$
Survival probability	S	$\lg S = \lg[N(t)/N_0]$

TABLE 8.7
Microbicidal Components of Plasmas

Component	Effect on Microorganisms
(V)UV radiation	Inactivation of DNA and RNA Wall/membrane/coat erosion
Radicals and low molecular products	Erosion of wall/membrane/coat Interference with metabolic pathways Oxidation of proteins, DNA, RNA, enzymes, etc. Natural signal stimulation (e.g., NO)
Charged particles (ions)	Etching/perforation of wall/coat Irreversible electroporation (lysis) Catalysis of peroxidation processes
Pulsed electric fields	Irreversible electroporation (lysis)
Heat	Denaturation of enzymes (moist heat) Oxidation (dry heat)

for sterilization and disinfection. The main effect of UV photons on MO is the dimerization of thymine bases in DNA and RNA strands, which inhibits proper cell replication. Furthermore, UV radiation can break the chemical bonds of MO material, inducing or advancing the erosion of outer structures (e.g., photo-induced etching). Effects of vacuum ultraviolet (VUV) radiation ($\lambda \sim <200\text{ nm}$) has been discussed previously (e.g., [114,115]).

Numerous radicals and low-molecular species can be produced in nonthermal plasmas. Especially in air plasmas reactive oxygen- and nitrogen-based species (ROS and RNS) are formed, e.g., O, O_2^* , O_3 , NO, NO_2 , and superoxide anions O_2^- . In presence of a certain level of humidity hydroxyl radicals, OH will be produced. ROS are naturally produced in many biological systems too, along with superoxides, hydrogen peroxide, etc. They have strong oxidative effects and are capable of damaging many organic molecules including nucleic acids, lipids, and amino acids. OH radicals attack unsaturated fatty acids, leading to the adverse effect on the barrier functions of cell membranes. OH radicals can further form hydrogen peroxide (H_2O_2), a well-known sterilizing agent. Atomic oxygen or oxygen metastables destroy proteins or can lead to an erosion of the outer structures by reactive etching. Ozone O_3 is a powerful oxidizing agent, which reacts directly with organic double bonds and gives rise to additional ROS. Besides damage to outer structures, biochemical reactions induced by ROS can interfere with metabolic pathways of MO and cause oxidative stress and cell death via apoptotic signaling.* O_3 can irritate the cell respiration, nitric oxide (NO) can trigger several metabolic pathways causing inactivation of MO [107]. Since ROS can penetrate through the pores of foils, items in sterile packaging may be sterilized [102,116]. Peroxidation processes both inside and outside biological organisms can be catalyzed by positive and negative ions [117].

The role of ions is discussed controversially. On one side, it is believed that electrical charges can accumulate on the outer surface of the cell membrane. The induced electrostatic force can overcome the tensile strength of the membrane, causing the rupture of the cell. The smaller the radius of the MO, the stronger the electrostatic force [107]. Thus, the scenario is more probable to occur for bacteria with irregular surfaces, like gram-negative bacteria.[†] There exist a number of contributions containing SEM pictures of treated cell with morphological damages (e.g., [107,118] and references therein). In contrast, the authors of [117] claim that effects of charged species are chemical and not related to physical phenomena.

Ion-catalyzed peroxidation processes mostly occur on the cell membrane. This is effected by the environment of the cell, i.e., it depends not only on the amount of water in the surrounding gas but also on the humidity and composition of the medium surrounding the MO.

Functions and membrane transport processes in cells can be controlled by external pulses of electric fields. An overview on the emerging field of *bioelectrics* is given in [119]. Reversible electroporation by local electric fields produced in plasmas may

* Apoptotic signaling is responsible for apoptosis, the so-called programmed cell death. It has to be distinguished from necrosis, which is a traumatic event that results from acute cellular injury.

[†] Gram staining is an empirical method of differentiating bacterial species based on the chemical and physical properties of their cell walls. One decides between gram-positive and gram-negative bacteria.

enhance the infiltration of bioactive plasma compounds (e.g., short-lived ROS) into cells. Higher electric fields cause irreversible membrane damage, and thus lysis of cells and nanosecond pulses with high amplitudes have the potential to affect transport processes across subcellular membranes or cause apoptosis. However, electric fields as well as heat are not considered to play a dominant role in the inactivation by means of nonthermal plasmas.

The mechanisms of plasma interaction with MO are rather complex and can be very specific. They are not only determined by the type of MO but also by its environment and condition.

8.2.2.3.2 Processes of Decontamination

Quite different inactivation kinetics were observed by means of plasmas. Beside IC with a single line (continuous effect, exponential decay of CFU), curves with two or more consecutive lines, each with different D_i (number of phase $i = 1, 2, 3$) have been observed. The multitude of different IC disclose the high complexity of physical and biochemical processes by means of plasmas. Often the effect of the plasma is not continuous, i.e., several processes are involved, and indeed synergistic effects are possible. The kinetics of inactivation depends on the type of MO, the type of substrate, as well as the specific plasma parameters and conditions (gas or gas mixture, plasma generation method, direct or remote exposure of samples*). In Figure 8.25, IC with two inactivation phases (with $D_1 < D_2$) are shown (see figure caption for experimental details).

In medium- and low-pressure plasmas, the UV photons are considered to play a dominant role [102,114]. In the examples shown in Figure 8.25, the first phase with the smaller D -value is due to the inactivation of genetic material of isolated MO (endospores) or of the first layers of stacked spores by UV irradiation. The D_1 -value in Figure 8.25 decreases with the nitrogen content due to the optimization of UV emission that is caused by the molecular band of NO in these plasmas. This phase stops after a certain treatment time because of the limited penetration depth of UV photons into stacked spores or spores covered with various debris. The following, slower phase is attributed to erosion processes of the covering material. Photon-induced intrinsic desorption by UV leads to the formation of volatile by-products (e.g., CO, CH_x) from the MO material. Furthermore, reactive species from the plasma (O , OH , O_2^*) are adsorbed on the MO and subsequently undergo chemical reactions forming VOCs and CO_2 and H_2O (spontaneous etching). Recent experiments where spores of *Bacillus atrophaeus* were exposed to beams of hydrogen atoms and Ar^+ ions have shown that chemical sputtering due to the simultaneous impact of H atoms and argon ions at around 100 eV causes a very effective etching and perforation of spore coats [120]. The etching process can be enhanced by UV photons (UV-induced etching), and the erosion rate increases with substrate temperature. It has also been described in the literature that UV inactivation can come into action again when the remaining living MO have been sufficiently uncovered from debris. In [121] spot (about $1.4 \cdot 10^7 \text{ MO/cm}^2$) and spray contaminated ($6.4 \cdot 10^4 \text{ MO/cm}^2$) samples were treated with identical plasmas (low-pressure microwave-sustained planartron discharge).

* Remote exposure (or afterglow): The sample is placed at some distance from the plasma and thus charged and short-lived species are not in contact with it.

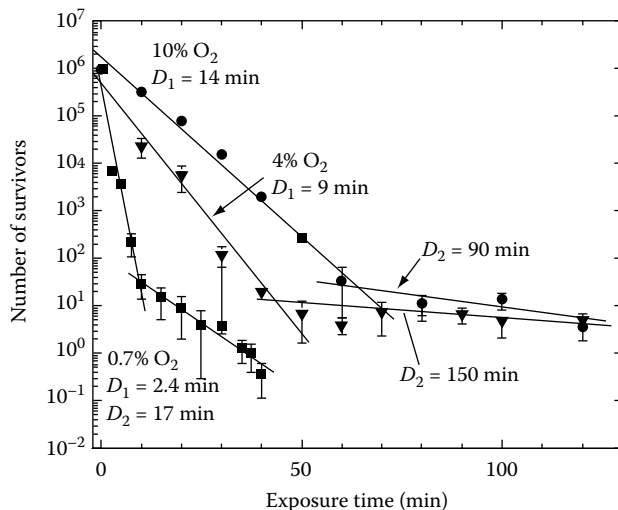


FIGURE 8.25 IC of *Bacillus atrophaeus* spores observed in the flowing afterglow of a microwave sustained discharge (pressure 667 Pa, power 100 W, frequency 2.45 GHz, volume of afterglow-chamber 20 l) in N₂/O₂ gas mixtures. Data points: mean of CFU/object; error bars: rms deviation; solid lines: least square fits. (From Boudam, M.K., Moisan, M., Saoudi, B., Popovici, C., Gherardi, N., and Massines, F., Bacterial spore inactivation by atmospheric-pressure plasmas in the presence or absence of UV photons as obtained with the same gas mixture, *J. Phys. D Appl. Phys.*, 39(16), 3494–3507, 2006. With kind permission from the Institute of Physics.)

As a result, a 20 times higher power density necessary for equivalent inactivation of spot-contaminated samples was investigated. Similar effects of the initial microbial load were studied by means of plasmas at atmospheric pressure (e.g., [122]).

In atmospheric pressure discharges, under specific operation conditions, the UV photons can be the dominant biocidal agents as well [105]. However, in most of the plasmas driven at atmospheric pressure, no sufficient dose of UV emission is produced (in most atmospheric air plasmas, there is almost no radiation below 300 nm, see, e.g., [123]). In Figure 8.26, antimicrobial treatment of spot-contaminated polyethylene strips (about 3 10⁶ MO/cm²) by means of plasma jets* in argon at atmospheric pressure are given.

In previous studies, the generation of UV and VUV radiation as well as ROS has been investigated by means of optical spectroscopy in similar arrangements [125]. ROS (O, O₃, NO, OH) are formed by excitation of air compounds, mixed into the expanding argon gas from the surrounding air. UV radiation above a wavelength

* The plasma jet configuration used in the experiment consists of a nozzle made of ceramics (inner diameter of outlet about 7 mm) and a concentric needle electrode. The argon gas flows through the nozzle (gas flow of 20 slm) and the RF voltage (power: 20 W) is coupled to the center electrode via a matching network. The grounded electrode is a ring placed at the nozzle outlet. The plasma is generated in the nozzle starting from the point of the needle electrode and expands into the surrounding air outside the nozzle. Depending on the gas flow rate and the applied power, the plasma jet has a length of up to 10 mm measured from the nozzle outlet and a diameter of about 8 mm.

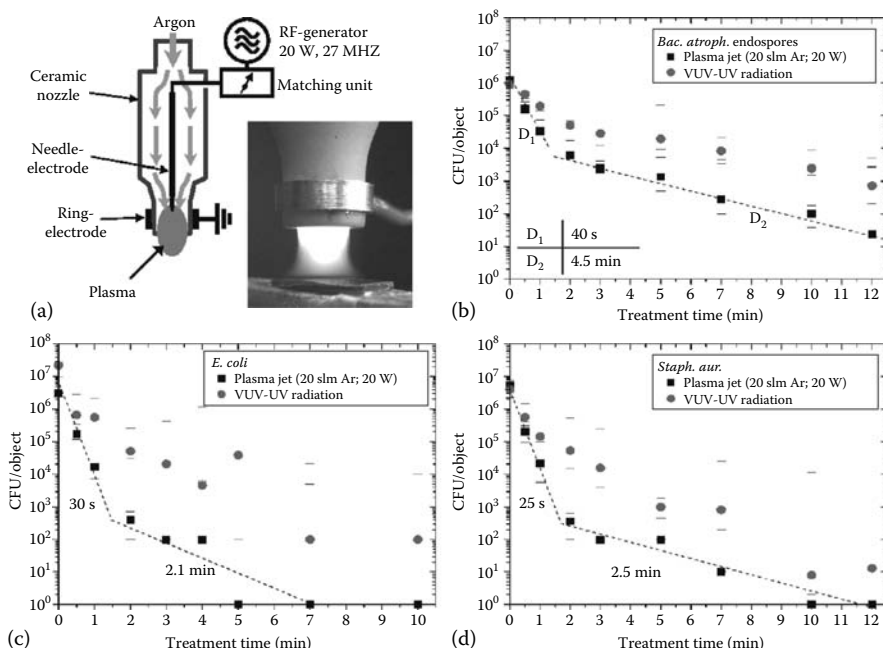


FIGURE 8.26 (a) Decontamination of spot-contaminated test-strips by means of RF-driven plasma jets in argon at atmospheric pressure on (b) *Bacillus atrophaeus* spores, (c) *E. coli*, and (d) *Staphylococcus aureus* bacteria. Data points: median of CFU/object; Error bars: spread between minimum and maximum; detection limit 1 MO/object (membrane filtration). Comparison between direct exposure and treatment with the sample beneath a VUV/UV transparent filter. The dashed lines are only a guide for the eye.

of 220 nm is due to molecular bands of NO, while Argon excimers (Ar_2^*) produce VUV radiation at about 120 nm. The radiation reach the sample due to the high argon gas flow. To evaluate its effect, the inoculated samples were additionally treated with a UV and VUV transparent MgF_2 -plate positioned between the plasma and the sample. For gram-negative (*E. coli*) as well as gram-positive vegetative bacteria (*Staphylococcus aureus*) and endospores (*B. atrophaeus*), a time-dependent decrease of CFU is observed. The IC consists of two lines with $D_1 < D_2$, which can be explained by the dense microbial load. The same effect was discussed earlier for plasmas at medium pressure. The direct plasma treatment is more effective than the UV-VUV emission alone. The results show that the dose of photons produced by the plasma jet does not explain the antimicrobial effect sufficiently, although a partial loss of radiation activity must be considered in case of shielded treatment (prospective UV emitters cannot reach the immediate vicinity of the MO) [105]. Similar results were obtained with pulsed inductively coupled RF-driven discharges at low pressure [126] or atmospheric plasmas (see [105] and references therein). Comparing direct and remote exposure of DBDs, the direct treatment was found to be much more effective [127]. These results suggest an essential antimicrobial effect due to impact of charged particles and short-lived ROS, either single or in synergy with other compounds.

IC with two inactivation phases but with $D_1 > D_2$ has been investigated with DBDs at atmospheric pressure discharges, too [116]. The first (slow) phase is explained as a period of damaging alterations on outer cell structures due to the action of active species. The rapid second phase begins when the reactive species can enter the interior of MO through its damaged outer structure, causing cell death.

Direct treatment of a water reservoir with the plasma jet described earlier has led to significant acidification [128]. Water is always present in biological systems and due to reactive species (e.g., OH, NO) secondary products (e.g., HNO₃) can be formed. Similar effects have been found by treatment of water with a surface barrier discharge [111]. The enhancement of inactivation efficiency by moistening the atmosphere has already been mentioned in the literature [102] and has been observed for gliding arc discharges at atmospheric pressure, too [129]. Thus, secondary chemical processes should always be considered in realization and interpretation of experimental studies as well as in the development of new industrial applications [128].

MO can form biofilms, complex aggregation of cells marked by the excretion of a protective, and adhesive matrix (e.g., dental plaque). Cells in biofilms are more resistant to chemicals than free-floating planktonic cells. Biofilms could represent serious health hazards and cause damage, such as corrosion, to the surfaces of the materials they attach to. Attempts to evaluate the effects of nonthermal plasmas on biofilms illustrated the inherent difficulty to destroy them [130,131]. In conclusion, any organic material that covers or alliances the MO will increase the dose to achieve sterilization since slow erosion processes will be involved. Therefore, not only the initial number of MO has to be considered when comparing different conditions and plasmas. Furthermore, the sample load and density of MO per cm² as well as the properties and cleanliness of the suspension have to be taken into account.

8.2.2.4 Examples of Plasma Processes for Sterilization

8.2.2.4.1 Commercial Plasma-Assisted Sterilizers

Two sterilization systems using medium pressure plasmas were already commercialized in the 1980s: the Sterrad® system (advanced sterilization products, a Johnson & Johnson comp., Irvine, California) and the Plazlyte™ sterilization system (AbTox, Inc., Mundelein, Illinois). In both processes, the plasma appears to have no biocidal action, since the dominant role is played by a purely chemical phase of diffusion of biocidal vapors (H₂O₂ in Sterrad; peracetic acid in Plazlyte) [102,104,132]. The plasma (RF or microwave sustained, respectively) is generated in the periphery of the sterile-packed products and mainly serves as a detoxifying agent by removing noxious residues and limiting the oxidation effects of the gases. These processes are typical plasma-assisted gas sterilization processes. Sterrad is widely used, e.g., in reprocessing of medical instruments [133]. Plazlyte was stopped in 1998 because of serious eye injuries following eye surgery using instruments sterilized with Plazlyte [134].

8.2.2.4.2 Plasma-Based Processes

The first commercialized plasma-based process at atmospheric pressure is the Tip-Charger™ system (CerionX, Inc., Pennsauken, New Jersey). Based on a DBD, the system cleans and sterilizes liquid transfer devices such as pipette tips, cannulae, and pin tools. TipCharger cleaning stations can substitute traditional solvent-based wash

methods in automated liquid handlers in biopharmaceutical and diagnostic industries. Unlike washing procedures, no liquid waste is generated, and the plasma treatment does not simply dilute contaminants but removes them. This allows the reuse of disposable pipette tips [135].

Numerous developments are close to commercialization. DBDs, plasma jets, and gliding arc discharges at atmospheric pressure as well as RF and microwave-sustained plasmas at low pressure have shown the potential to sterilize heat-sensitive surfaces and goods, such as polymer foils, packaging, or medical instruments [115,121,128, 136–138]. A promising concept is the cascaded dielectric barrier discharge (CDBD), which combines UV radiation and direct plasma treatment [115]. Therefore, the discharge gap consists of two separated parts. One is filled with an excimer gas for efficient UV emission. The second gap is flushed with a discharge gas forming reactive species (e.g., air). A very effective microbial inactivation of spray-contaminated polyethylene terephthalate (PET) foils was investigated by means of CDBD [139].

8.2.2.5 Outlook

Plasmas offer the potential for innovative decontamination processes up to the level of sterility. The first plasma-assisted and plasma-based processes for surface decontamination and sterilization have already been commercialized. Even the depyrogenation and the inactivation of proteins by nonthermal plasma has been reported [140,141]. The latter gives hope to inactivation methods for prions, which are responsible for diseases in a variety of mammals (e.g., “mad cow disease” or Creutzfeldt–Jakob disease). Results from the literature are often difficult to compare with each other and thus to transfer on real products. A comprehensive knowledge on the elementary processes does not exist. This is considered as one of the reasons why the technological breakthrough of plasma-based technology in the fields mentioned at the beginning of the chapter has not been achieved yet. Interdisciplinary basic research on the interaction of plasmas with MO including its ambience is demanded to approach the potential of plasmas for life science applications.

8.2.3 SURFACE MODIFICATION

Plasma treatment of solid materials include [142] (see also Table 8.4)

- Chemical surface modification
- Cleaning and removal of contaminants
- Material erosion (plasma etching, chemical/physical sputtering)
- Thin film deposition

Generally, the surface processes listed earlier take place simultaneously, and they generate a dynamic interface layer. This means that a thin surface layer with modified chemical/physical properties is formed, and in steady state either an effective loss of surface material due to desorption of volatile products (plasma etching), adsorbate sputtering, and chemical sputtering is observed, or an effective material deposition takes place due to thin film formation. Thereby, synergetic effects between the interaction of different energetic/reactive plasma particles and the photochemical action of the plasma radiation can be observed.

This section concerns the modification of material surfaces by interactions of plasma species that change the chemical composition in a top interface layer combined with alterations of the physical properties. Surface modification depends strongly on the material's properties, the plasma composition, and the energy of the interacting plasma species. The interaction depth of plasma particles (ions, neutrals) depends on their kinetic energy. The typical kinetic energy of ions and fast neutrals in nonthermal plasmas and in the plasma sheath in front of the surface, respectively, limits the maximum interaction depth to a few monolayers only. On the other hand, the interaction depth of plasma radiation, relevant to photochemical reactions, strongly depends on the spectral absorption coefficient of the considered material and reach from the skin depth in metals of about 1 nm up to about 100 nm in polymers in the case of VUV radiation. The characteristic penetration depths of different plasma components in polymers and their interaction processes are given in Table 8.8 [143].

Plasma surface treatment processes are separated into active and passive plasma exposures [144]. Active exposures are characterized by current flow to the work piece, which acts as an electrode. Passive exposures use plasma action without electrical current to the surface. A broad spectrum of plasmas is used in surface treatment processes: from low pressure up to atmospheric pressure plasmas, excited by DC, AC, RF, and MW voltages in cw or pulsed mode operation. A brief survey on surface treatment of various materials by nonequilibrium atmospheric pressure air plasmas is presented in [145]. Plasma treatment of polymers is reviewed in [142,146,147]. The following sections are organized as follows: Firstly, the surface treatment of polymers and metals are considered; secondly, the application of plasma surface

TABLE 8.8**Efficiency of Plasma Components for Surface Treatment of Polymer Materials**

Plasma Component	Kinetic Energy	Depth of Interaction	Process
Ions, neutrals	~10 eV	Monolayer	Adsorbate sputtering, chemical reaction
	≤1 keV	≤10 ⁻⁵ m	Sputtering (implantation)
Electrons	5–10 eV	~1 nm	Surface dissociation, surface ionization
Reactive neutrals, e.g., radicals	Thermal, 0.05 eV	Monolayer	Adsorption, chemical surface reactions, formation of functional groups, low molecular (volatile) products diffusion, and chemical reactions
Photons	>5 eV (VUV)	Bulk	Photochemical processes
		10–10 ² nm depending on absorption coefficient ~μm	
	<5 eV (UV)		Secondary processes

Source: Meischner, J., Low temperature plasma for plasma surface modification, in *Low Temperature Plasmas*, Vol. 2, 2nd edn., Wiley, Wienheim, Germany, pp. 739–759, 2008.

treatment to the modification of textiles and biomedical materials is presented. One additional section deals with plasma medicine.

8.2.3.1 Polymers

Polymers are important for industrial applications as construction material and as films or foils for packaging. It is a lightweight, cheap material with advantageous bulk properties such as high stability, good electrical properties, chemical inertness, and easy processability. Surface properties such as wettability and hardness can be changed by suitable coating or by treatment procedures that modify only the chemistry of the surface. Such surface treatment is the topic of this section.

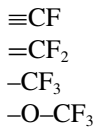
8.2.3.1.1 Manipulation of Surface Energy

Plastic foils are widely used as packing material. Some of the disadvantages concern the surface characteristics having poor adhesion properties, which need to be improved with respect to wettability, dyeability, metallization, painting, and printing features. Adhesion of the polymer surface to the coating is a crucial property. The adhesion is determined by surface energies of polymer and coating [148]. Plastic foils, e.g., are mostly characterized by nonpolar chemical inert surfaces with low surface energy (polyamide 43.0 mJ/m², polyethylene 31 mJ/m², polytetrafluoroethylene 18.5 mJ/m²). For optimum adhesion, the surface energy of a polymer has to exceed the energy of the material to be bonded with. Surface energy of common organic solvents is lower (toluene 28.4 mJ/m², carbon tetrachloride 27 mJ/m², ethanol 22.1 mJ/m²) than that of the polymers. Paintings and inks based on organic solvents are successfully applied to polymers. Environmental requirements call for a substitution by water-based paints, inks (54–56 mJ/m²), or bonding agents. Because of the high surface energy of water (72.8 mJ/m²), a treatment of polymer surfaces is necessary to enlarge their surface energy. Surface properties are determined by a thin layer of molecular dimensions and can be changed without influencing bulk properties.

Plasma processes have been developed for surface treatment to enhance adhesion, like exposure to treatments in corona and glow discharge plasmas in suitable reaction gases, without affecting the bulk properties. Treatment of polymer surfaces by oxygen- or nitrogen-containing plasmas, which enhances surface energy, leads to formation of polar functional groups at the surface [149,150]:

- ≡C-OH (alcohol)
- ≡C-O-O-H (hydroperoxide)
- H-C=O (aldehyde)
- =C=O (carbonyl)
- ≡C-O-C=O (ester)
- ≡C-O-C• (peroxy)
- OC(O)O (carbonate)
- NH₂ (amine)
- C≡N (nitrile)
- =C=N- (imine)
- CO-NH₂ (amido)

By contrast, fluorination generates hydrophobic surfaces with lowered surface energy. The fluorination of polymer surfaces is achieved by treatment in plasmas containing fluorinated compounds as fluorocarbons, e.g., CF₄, C₂F₆ . . . or NF₃ and SF₆ [146,151,152]. The formation of functional groups is observed as follows:



8.2.3.1.2 Diagnostics of Polymer Surfaces

The diagnostic methods for surface investigations are the topic of Chapter 7, (see Tables 7.1 and 7.2). FTIR spectroscopy, ellipsometry, and microgravimetry are suitable for in situ diagnostics [153], but, e.g., XPS, SIMS, and microscopic methods (TEM, SEM, AFM) are possible only ex situ. An important ex situ method of surface diagnostics of polymers concerns the determination of surface energy based on the contact angle measurement of a liquid drop on a surface [148,154].

8.2.3.1.3 Plasma Systems

Diverse plasmas are used for surface treatment of polymers. For practical applications successfully atmospheric pressure DBDs were approved without the expensive vacuum technique and suitable for continuous processing, see [155] and references therein. The surface processes of such plasmas are determined mainly by radicals and not by energetic ions.

A scheme of an arrangement for surface treatment of foils by DBD is given in Figure 8.27. Usually, this discharge operates in a filamentary mode and under special conditions in a diffuse glow mode. Such homogeneous barrier discharge at atmospheric pressure, referred as atmospheric pressure glow discharge (APGD), is very suitable for uniform surface treatment. Only a small window of operation conditions allows a stable APGD. This window is mainly determined by the properties of the feeding gas, which is very sensitive against impurities. But for surface treatment, the operation in the filamentary mode is possible if a great number of tiny microdischarges is scattered homogeneously over the dielectric surface. A homogenization of the filament mode will be enhanced by low dielectric permittivity of the dielectric barrier and small dimensions of the gas gap. High amplitude of the applied voltage and low operation frequency prefer the random migration of the filaments on the surface because of the nearly homogeneous distribution of the residual charge on the dielectric.

The effect of plasma treatment depends on the number of active particles n impinging on the treated surface; the dosage D equals n/m^2 [145]. In a first approximation, this number is determined by the energy input into the plasma. For the treatment of a moving substrate in a DBD (two small plane rectangular electrodes with a small gap), the dosage D equals

$$D = \frac{P}{s * v} \left[\frac{\text{J}}{\text{m}^2} \right]. \quad (8.55)$$

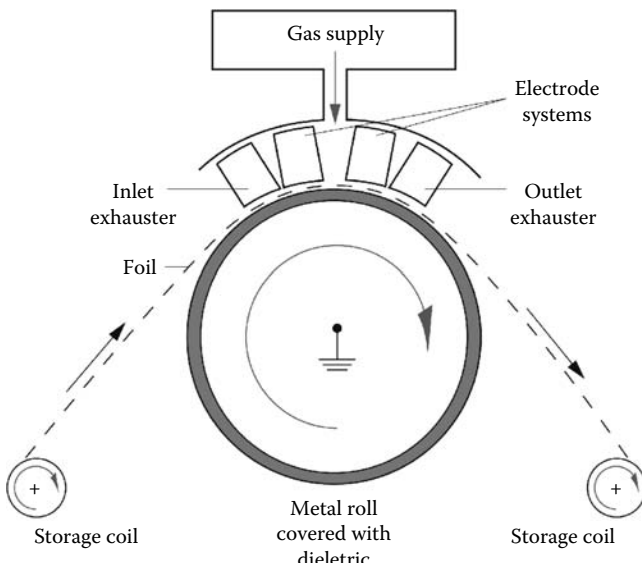


FIGURE 8.27 Scheme of plasma treatment of foils by DBD. (From Meiner, S. et al., *Surf. Coat. Technol.*, 98(1–3), 1121, 1998.)

The substrate of width s [m] moves across the electrodes of the same width with the velocity v [m/s]; P [W] is the power introduced into the discharge. The power density L in discharge volume is

$$L = E * j = \frac{P}{A * a} \left[\frac{\text{W}}{\text{m}^3} \right], \quad (8.56)$$

where

E [V/m] is the averaged voltage gradient inside the plasma

j [A/m²] is the current density

A [m²] is the electrode surface

a [m] is the gap width of the discharge

The power density O on the electrode surface is defined by

$$O = \frac{P}{A} \left[\frac{\text{W}}{\text{m}^2} \right]. \quad (8.57)$$

The product of O and the treatment time gives the dosage for a resting substrate.

The application of atmospheric pressure DBDs for plasma surface treatment is restricted to thin and flat substrates. Another type of nonthermal plasma sources are atmospheric pressure plasma jets (see Section 3.8), which are successfully applied for the treatment of large three-dimensional substrates [157].

The application of low-pressure discharges requires expensive vacuum technique. Surface treatment in such plasmas is characterized by the action of energetic ions

accelerated in the sheath between plasma bulk and surface caused by the floating potential or external applied potentials. The use of low-pressure plasma requires batch processing. The operation at low pressure facilitates the processing with cleanest gases. Application of DC, AC, MW, but mostly rf plasmas is usual. The treatment of 3D structures is promoted caused by the enlarged free path length of reactive particles.

8.2.3.1.4 Surface Treatment by Atmospheric Pressure Plasmas

The surface modification of polypropylene (PP) by treatment with oxygen-containing plasmas is studied experimentally and by modeling also. Surface energy of PP is $\approx 27 \text{ mJ/m}^2$. Plasma-treated PP in an atmospheric pressure glow (nonfilamentary) discharge in He shows surface energies up to 62 mJ/m^2 [158], 53 mJ/m^2 [161]. It should be mentioned that DBD plasma treatment of PP foils in acetylene atmosphere results in a stable improvement of surface energy of 72 mJ/m^2 , but is caused by a thin film of several nm [156].

Dorai [149] investigated in detail the processes associated with surface functionalization of an isotactic polypropylene film (0.05 mm thick) in an atmospheric pressure discharge in humid air.

The relative humidity of the air flow in the discharge region was either 2%–5% or 95%–100% at 25°C . The treated surface was analyzed to determine its chemical composition by XPS, its surface energy by contact-angle measurements, and its topology by AFM. The untreated polypropylene surface is free of oxygen. The increase of the discharge energy is associated with a decrease as well as of the advancing and receding water contact angle. This means increasing wettability. For the treatment of PP in humid air plasma, a model was developed in [149]. It includes gas phase chemistry with the formation of O, H, OH radicals and O_3 as important active species. Excited O_2^* molecules, N atoms, and HO_2 need not be taken into account because of their lower reactivity toward PP. The reactivity of radicals with the PP is different for the position of the C atom where the reaction occurs. Primary C atoms are bound with only one C atom, secondary with two, and tertiary with three C atoms inside the polymer. The reaction probability is at most for the primary C atoms, decreases for secondary, and is smallest for tertiary C atoms. The surface reactions can be classified in analogy to polymerization processes in initiation, propagation, and termination. An initiation reaction leads to formation of a radical, e.g., by abstraction of an H atom from the polypropylene surface by an O radical (see Figure 8.28).

The propagation leads, e.g., to peroxy radicals on the PP surface in a reaction of the alkyl radical with O_2 (see Figure 8.29).

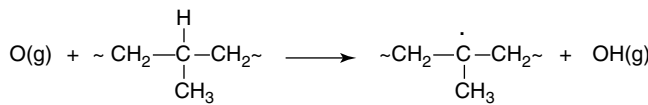


FIGURE 8.28 Radical formation, e.g., by abstraction of an H atom from the polypropylene surface by an O radical.

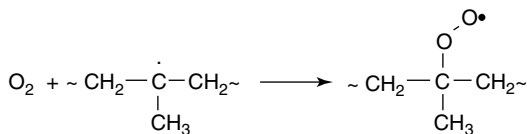


FIGURE 8.29 Peroxy radical formation on the PP surface in a reaction of the alkyl radical with O_2 .

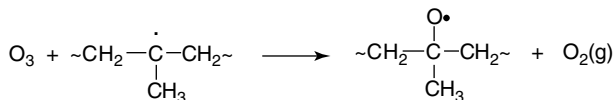


FIGURE 8.30 Alkoxy radical formation by ozone.

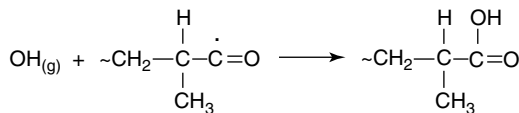


FIGURE 8.31 Termination reaction.

Reaction with ozone results in alkoxy radical formation (see Figure 8.30).

A termination reaction is, e.g., shown in Figure 8.31.

These reactions illustrate some possibilities of radical processes initiated by plasma interaction with a polypropylene surface.

An important application of polyimide caused by its outstanding properties as high tensile strength (70–150 MPa), high upper working temperature (250°C–320°C), and dielectric strength (>22 kV/mm) is the use as material for flexible chip carriers. For this purpose, a metallization with copper is necessary but is difficult because of the low adhesion between copper and polyimide. A treatment of polyimide by an atmospheric pressure DBD in N-containing gas enhances the free surface energy and leads to successful metallization. Amino-, nitrile, and imine-groups were detected on the surface [150]. Oxygen-containing polar groups were observed at a polyimide surface after air plasma treatment [160,161].

The treatment of a, e.g., low-density polyethylene (LD-PE) foil in atmospheric pressure air DBD leads to an increase of oxygen content on the surface up to 40%. Water contact angle decreases from untreated material of 102.2° down to 54.3° after plasma treatment. Similar behavior was observed for other polymers (ultrahigh density polyethylene, high-density polyethylene, polystyrene, polymethylpentene) also. Essentially smaller effects show polytetrafluoroethylene [162].

8.2.3.1.5 Surface Treatment by Low-Pressure Plasmas

The application of low-pressure plasmas for surface treatment includes the action of energetic ions, reactive neutrals, and plasma radiation. Treatment of polyamide in an inductive coupled RF oxygen plasma during 15 min change the surface energy of 40 up to 67 mJ/m². Storage in air for week nearly destroys this high value by aging. The application of additional high-voltage pulses (10 kV, duty cycle 0.5%;

treatment time 100 s) enlarges the surface energy to 110 mJ/m^2 and a reduction is observed to only $\sim 65 \text{ mJ/m}^2$ within a fortnight storage time in air environment. This combination of plasma treatment and ion bombardment reduces aging effects [163].

The treatment of thin polymer film on the powered electrode in a capacitively coupled RF discharge (13.56 MHz) leads to changes of its surface properties caused by modifications of chemical composition. Figure 8.32a represents the IR absorption spectrum, see Section 7.1 (FTIR-spectroscopy), of a thin LD-PE film with

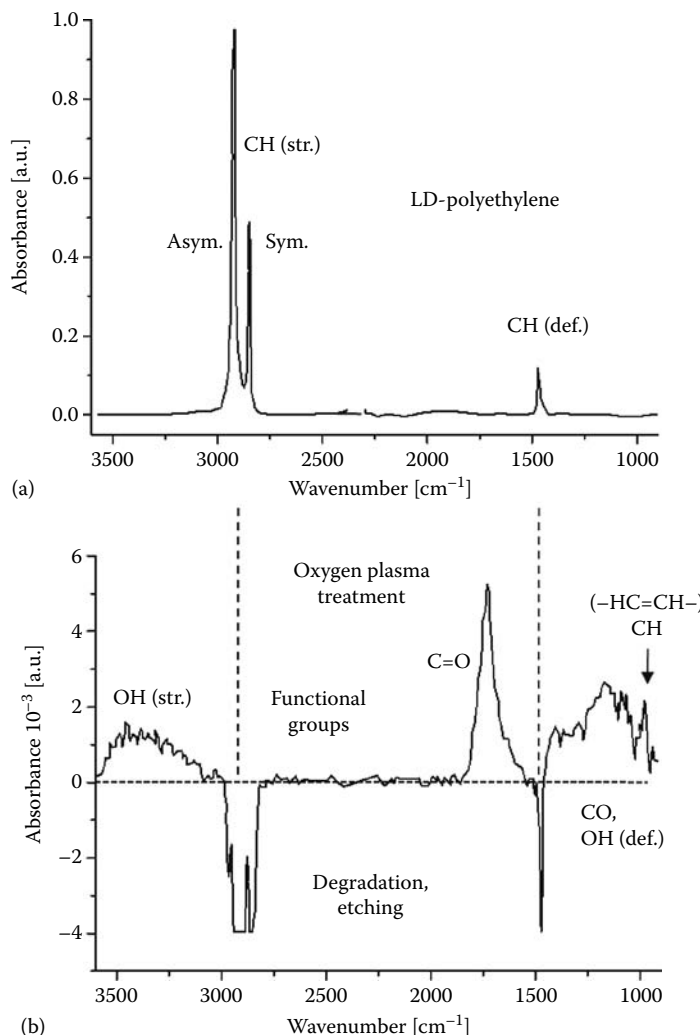


FIGURE 8.32 IR-absorption spectrum of thin polyethylene film (ca. 30 nm) taken by FTIR-(ATR)-spectroscopy (a) and the ratio spectrum of PE thin film before/after 3 s oxygen (5 Pa) RF plasma treatment, which provides both the degradation and functionalization of PE (b).

characteristic absorption bands of the asymmetric and symmetric C–H stretching vibrations ($2950\text{--}2700\text{ cm}^{-1}$) as well as the C–H deformation vibration (1460 cm^{-1}) of the $-(\text{CH}_2)_n-$ polymer. The ratio spectrum in Figure 8.32b, generated from IR spectra before and after plasma treatment, contains all the changes due to the oxygen plasma treatment. The strong polymer degradation/etching from the negative bands in the spectral range of the C–H vibrations is clearly seen. Furthermore, different oxygen-containing structures were produced in the top polymer interface. In the wave number range between 3500 and 3000 cm^{-1} , the O–H stretching vibrations of the hydroxyl groups appear broadened due to hydrogen bonds. Additionally, the carbonyl group (C=O stretching) is observed around 1750 cm^{-1} . The wide spectral range of the carbonyl group reveals a variety of C=O structures with slightly different characteristic frequencies. In the fingerprint region from 1400 to 1000 cm^{-1} , there are many overlapped bands associated with C–O stretching vibrations, O–H deformation in alcohols, as well as C–O stretching vibrations in esters and ethers. The absorption around 960 cm^{-1} can be interpreted as C–H stretching vibration from cross-linked (C=C) molecular structure. The formation of polar oxygen-containing groups causes the enhancement of surface energy.

In a similar way, the treatment of polystyrene thin films in a low pressure (5 Pa) capacitively coupled 13.56 MHz discharge in different process gases (H_2 , O_2 , CF_4) observed by *in situ* ATR leads to chemical modification of the surface [153]. H_2 plasma destroys aromatic ring structures, and new aliphatic C–H structures are formed. CO and OH functional groups are observed in O_2 plasma treated polystyrene, and CF_x groups are formed by CF_4 plasma.

8.2.3.2 Metals

Surface modification of metals include

- Cleaning of metal surfaces
- Change of the chemistry by, e.g., oxidation, nitriding
- Surface polishing

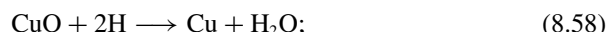
Tools for surface modification comprise not only low pressure up to atmospheric pressure plasmas, but also microplasmas in liquid ambience in plasma electrolysis.

8.2.3.2.1 *Plasma Cleaning*

Plasma cleaning of work pieces is a precision cleaning due to the low rate involved. Cleaning of metals from organic surface layers by nontoxic reaction gases as oxygen leads to an environmentally safe process with low thermal stress of the surface [164]. The application of an oxygen plasma causes the formation of CO_2 , CO, and H_2O . The mechanism includes chemical reactions of hydrocarbons with O_2 molecules, O atoms, and also ozone. Investigations of cleaning experiments using O_2/Ar mixtures show a synergistic effect of Ar ion and O_2 flux to the surface. The removal of a hydrocarbon film will be determined by ion impact-induced defects on the surface, which can easily react with the oxygen [165]. Also collisions with adsorbed O_2 molecules that react with the surface and ion-enhanced chemical erosion where ion bombardment enhances the reactivity of O_2 are discussed. The cleaning

enhancement by ion bombardment of the surface will be understood as chemical sputtering [166]. Chemical sputtering is a process in which ion bombardment induces chemical reactions, which results in the generation of volatile erosion products. Cleaning procedures in remote plasmas with the absence of energetic ion collisions indicate the effectiveness of O atoms [164].

H₂ plasmas are successfully applied to remove oxides from metal surfaces [167, 168]. The surface layer of copper exposed to clean room air contains a surface layer of CuO₂, CuO, Cu(OH)₂, and CuCO₃. For surface cleaning, a combination of thermal and plasma treatment is successful. Thermal treatment leads to decomposition of Cu carbonate and Cu hydroxide with desorption of CO₂ and H₂O. Reduction of CuO and CuO₂ occurs by hydrogen atoms, which are generated in the H₂ plasma:



The complete desorption of H₂O needs temperatures of 150°C–200°C. A broad spectrum of H₂ containing plasmas is used, from atmospheric pressure DBD [168, 169] till low pressure as 1 Pa DC discharges [170].

An interesting application is the use of hydrogen plasmas for surface cleaning of the platinum iridium prototype kilogram from hydrocarbons and metal oxides. H₂ plasmas may enable a reproducible and damage-free cleaning process of noble metal surfaces [171].

Low-pressure hydrogen plasma is successfully applied for restoration and conservation of iron artifacts. This plasma removes chlorides and prevents a fast postcorrosion of the object in humid air [172]. Increasing of surface energy is observed by plasma treatment of metals (Al, Cu) using an atmospheric pressure jet feed by N₂/O₂ mixtures [173]. Also the treatment of metal implant materials in low-pressure plasmas results in an increased surface energy [174]. This effect may be attributed to cleaning by removing contaminants and surface oxides.

8.2.3.2.2 *Ion Implantation, Nitriding*

Ion implantation is a widespread method for material treatment. The application of separate effective ion sources for the generation of high energetic (up to ~1 MeV) ion beams is a pure physical method, but application of the plasma surrounding the treated material as source of ions leads to plasma chemistry. This plasma-based ion implantation (PBII) operates with pulsed ion energies up to 100 keV [175].

Plasma nitriding and plasma immersion ion implantation (PIII) are effective methods for material treatment. Improvements of material qualities concern

- Hardening
- Frictional resistance
- Working lifespan
- Fatigue strength
- Corrosion resistance
- Biocompatibility
- Antimicrobial properties

The environment-friendly plasma activation allows low-temperature processing, but like vacuum technology, it is expensive.

Conventional plasma nitriding uses ion energies ~ 200 eV [176]. Usually low-pressure plasmas in N_2/H_2 mixtures, sometimes also with Ar admixture, are applied for this process. The metallic work piece is used as cathode. N^+ ions are accelerated to the cathode and impinge into the cathode surface. They form there nitrides in the compound layer (thickness of some tens μm); others diffuse into the bulk material (diffusion zone). The hardening of the work piece results firstly from the hard metal nitride in the compound layer and secondly from the stress generated by the nitrogen particle in the metal lattice in the diffusion zone. Besides the energetic N^+ ions according to charge transfer reactions, fast N atoms collide with the cathode surface. The Ar and H_2 admixture ensures an effective cleaning of the surface. Plasma nitriding operates in a temperature range between $\sim 300^\circ\text{C}$ and $\sim 600^\circ\text{C}$.

Various materials are suitable for nitriding: Ti, Al, and stainless steel, as well as alloy steels with elements that form nitrides such as Al, Cr, Mo, and Ti.

PIII is used also for implantation of other elements like Cu into Ti [177]. An RF discharge 13.56 MHz operates between the grounded vessel and two disk-shaped copper electrodes in an H_2O vapor atmosphere (2 Pa). Pulsed voltage (5 kV, 50 Hz) was applied to Ti samples. Cu was determined by XPS in the sample and antimicrobial properties could be demonstrated, what is important for application of this material for endoprostheses.

8.2.3.2.3 *Plasma Oxidation*

Oxidation in oxygen plasmas occurs with metals that have floating potential (plasma oxidation) or metals that are biased on a potential above floating potential (plasma anodization) [90]. Plasma anodization leads to higher rates and thicker oxide film. The development of Cu oxides by plasma oxidation in an oxygen discharge is studied in an inductive coupled O_2 discharge (13.56 MHz, 300 W, 200 Pa, O_2 flow $0.25 \text{ dm}^3 \text{ min}^{-1}$) [178]. After 5 min treatment time, Cu_xO is formed, then a mixture of Cu_2O/Cu_3O (10 min), and later CuO (20 min) is observed. The layer thickness is about 0.3 μm .

8.2.3.2.4 *Plasma Electrolysis*

Plasma electrolysis is an interesting technique of surface engineering [179]. This method is used for plasma electrolytic, e.g., oxidation, nitriding, carburizing. The work piece is immersed in a bath of liquid electrolyte and different potentials are applied between work piece and counter-electrode. A pulsed voltage higher than 200 V leads to an electrical breakdown between the metal and the electrolyte through the dielectric surface film (e.g., oxide film) or gas bubbles on the surface. The developed microplasma modifies the deposited layer or the surface, e.g., by collisions of energetic ions. Plasma electrolysis uses different electrolyte compositions for the various applications (see Table 8.9).

Thick wear resistant oxide layers on Al with maximum hardness 18–23 GPa and thickness about 500 μm have an excellent adhesion. Nitriding, carburizing, and

TABLE 8.9
Plasma Electrolysis Uses Different Electrolyte Compositions for the Various Applications

Oxidation	Na ₂ SiO ₃ /KOH
Nitriding	NaNO ₃
Carburizing	C ₃ H ₅ (OH) ₃ /Na ₂ CO ₃
Boriding	Na ₂ B ₄ O ₇ /NaOH

bording need treatment times of some minutes for formation of 200–500 µm thick compound/diffusion layers.

Plasma electrolytic procedures can also be used for plasma polishing [180]. The work piece operating as anode in the electrolyte is covered by a thin gas layer where plasma is ignited for sufficient high voltages. Polishing may be caused by

- Peaks and other roughness that are etched by chemical and plasma chemical effects
- Surface areas that are oxidized and reaction products that are dissolved

Roughness lower than 0.1 µm can be achieved. Stainless steel, Ti and Ti-alloys, and copper were successfully plasma polished.

Atmospheric pressure plasmas caused by their etching properties are also reliable for plasma polishing [181–183].

8.2.3.3 Textiles

It has long been known that the surface modification of natural substances can be achieved using plasma technologies [184]. Numerous publications to date have documented the tremendous scientific interest in the processes that take place. Now the textile industry too is showing interest in plasma technologies. The potential to save chemicals and energy as well as environmental aspects like the reduction of sewage load are strong propulsions.

The spectrum of applications of plasma technologies in the textile industry ranges from the functionalization of fiber surfaces up to the production of special layers. Surface properties like wettability, refractability, colorability, and printability or surface hardness can be influenced without changing the bulk qualities of the substrate [185].

An extensive topical overview of present plasma technologies in the textile industry including possibilities and limitations as well as further developments is given in [186,187] (see Table 8.10).

This section shows that atmospheric pressure discharges are recommended for fields of application that were reserved for low-pressure plasma methods just a few years ago.

TABLE 8.10
Nonthermal Plasma Treatment of Textiles for Details and References

Quality	Chemistry
Wettability, dyeing properties, printability, adhesion enhancing	Polar groups on surface, as C—O, C=O, O—C, C—O—O, —COOH, —OH, Si—OH, —NH ₂
Water and oil repellency	Plasma polymerization Fluorine carbon compounds Silicon compounds
Refractability	Organic phosphonate derivates
Shrink proofing	Surface oxidation
Antibacterial treatment	Metal coating, Ag in plasma polymers
Sterilization	UV, free radicals
Biocompatible textiles	Activation, graft polymerization

8.2.3.3.1 Plasma Treatment

8.2.3.3.1.1 Plasma Treatment of Wool Fibers by Dielectric Barrier Discharges

Which advantageous properties favor the DBD for technological deployment?

- The DBD can be sustained under normal pressure.
- The discharge has a positive characteristic, i.e., with rising discharge current the required voltage also increases.
- The discharge can operate at different conditions like sine voltage, rectangle voltage, pulse voltage, and pulse group. With the help of these sustaining conditions, an extensive control of the averaged discharge power is possible while also retaining the possibility to influence the single discharge.
- The DBD can operate with almost arbitrary gases and gas mixtures.
- Results from experiments performed in small discharge vessels are scalable when the discharge conditions in large arrangements and at higher powers are taken into account.

There are a lot of possible ways to manipulate the discharges. One of the possibilities is to alter the construction of the discharge configuration through the

- Choice of the dielectric, particularly with regard to the dielectric coefficient
- Thickness of the dielectric
- Thickness of the discharge gap
- Way of sustaining the discharge

In Figure 8.33, an experimental arrangement for treatment of wool fibers is given.

Figure 8.34a illustrates a typical discharge current and sustaining voltage using a sinusoidal pulse group. The energy fed in by the pulse group can be determined

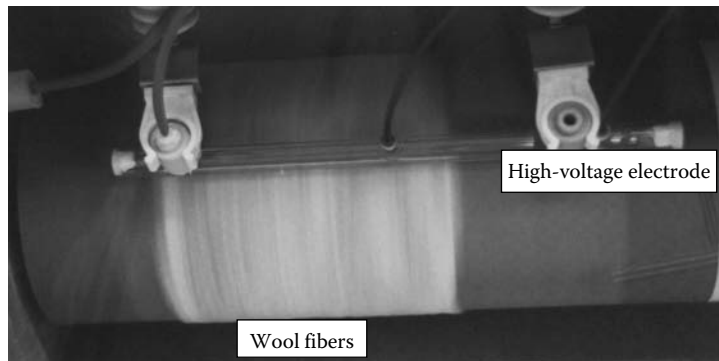


FIGURE 8.33 Experimental arrangement for treatment of wool fibers.

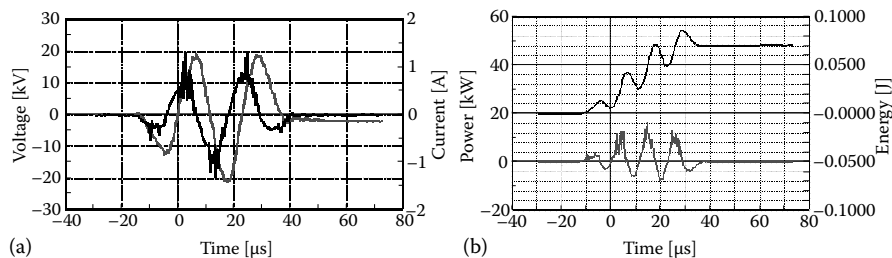


FIGURE 8.34 (a): Typical discharge current and sustaining voltage using a sinusoidal voltage pulse group. (b): Energy (up to 0.07 J) fed in and power.

by multiplication of current and voltage and following integration (Figure 8.34b). Discharge qualities and fed energy are ascertained by the height of the voltage pulses, their duration, and number of pulses. In this manner, textile fibers can be treated efficiently.

Figure 8.35 shows a thermal image during the plasma treatment of wool fibers. The picture shows the results during the treatment with a continuous sine wave voltage. The treatment is very different and the formation of single hot spots can be observed. These can locally lead to high temperatures and to the destruction of the fibers. With measures like the choice of a suitable gas space thickness (gap), streaming of the gas, and sustaining with pulse groups, a steady treatment of the wool fibers can be reached. The filaments are steadily distributed statistically. Their formation is finer; above all, however, discharges are created in the hollow cavities between the wool fibers. Such discharges in hollow cavities of insulators are known in the electric engineering as partial discharges, and there they cause aging of insulators and electrical breakdowns. Here, the discharges generate the active species directly between the wool fibers in the system of many hollow interlinked cavities, and thus they cause a very steady and effective plasma treatment.

The effect of plasma on the fiber surfaces occurs in a step-by-step process. In the first step, a quick functionalization occurs through the formation and dismantling of

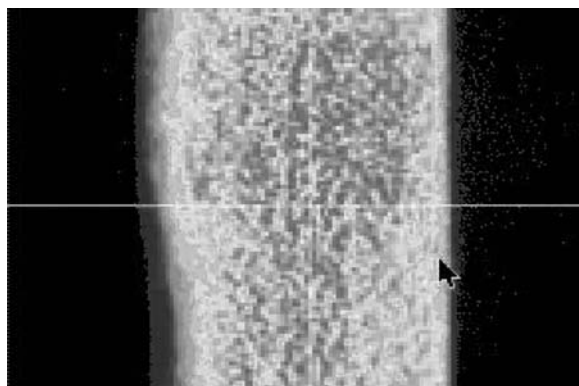


FIGURE 8.35 Thermal image during the plasma treatment of wool fibers.

functional groups. In the second step, oxygen is inserted in the solid state; in the third step, a gaseous oxidation product leaves the surface.

Other fiber qualities also change in the course of a plasma treatment in a similar way. One of these properties is the well-known felting of wool. Even a brief plasma treatment with an oxygen-containing carrier gas (e.g., air) leads to a considerable decrease of the felting. A longer plasma treatment does not automatically lead to a further decrease of the felting. On the contrary, the felting results of the treated wool fibers show a big dispersion. The felting behavior only continuously decreases again after long treatment. Now the microscopic investigation of the fiber surfaces shows a destruction of the scale structure of the wool fiber surface, which reduces the directional dependence of the fibers' frictional resistance.

Hence, in addition to the uniformity of the plasma treatment, the kind of plasma and duration of the treatment also play a determining role. With a suitable plasma treatment and a compatible resin, a wool can be obtained that is felt-free to a level comparable to that currently achieved through the use of the environmentally damaging wet-chemical chlorine Hercosett procedure.

8.2.3.3.1.2 Polymerization

Different low-pressure plasma polymerization processes applied to textile fabrics have already been applied at an industrial level [186] (see also [187]). Precursor gases determine the chemistry of the layers.

The typical thicknesses of polymer layers are 5–20 nm. The applications are permanent hydrophilic and hydrophobic layers or gas barrier layers.

De Geyter et al. examine the penetration of a DBD plasma into textile structures at medium pressure [188]. They found that the process pressure is a crucial parameter. In the pressure range 0.3–1 kPa, increasing pressure results in better treatment of all textile layers. At higher pressures, the discharge goes through the textile. The textile is in close contact with the plasma in the microchannels, resulting in a higher efficiency of the modification. However, the loss of textile-modifying particles in gas collisions at high pressures counteracts this.

Lunk [189] examined polymerization processes in a DBD under normal pressure with fluorocarbons. He could find good hydrophobicity on plasma-treated technical textiles.

8.2.3.3.1.3 *Plasma Cleaning of Textiles*

During textile manufacturing, plasma-aided processes can be used to remove sizing agents, mineral oils, or acrylate-based spin finishes, which form a film around the yarn [186].

Other applications are the purification and disinfection of textiles. In this process, the textiles are exposed to the plasma in different devices and by special methods. Different plasma reactor constructions on the basis of DBD configurations were used in the experiments, partly described in [62,190]. The different installations help to judge the impact of different effects. Figure 8.36 shows the comparison of these versions after the plasma treatment with air carrier gas.

The results show a clear degradation of the odor strength measured in odor units [ou]. Compared to the untreated sample, this outcome occurred in all three constellations. Evidently, one can reach an uncritical odor threshold.

Figure 8.37 presents the results of the microbial tests. We carried out different test series to prove that plasma procedures can be applied for the disinfection of textiles. Here we performed two different test series with different initial concentrations of *E. coli*.

The group on the left shows results of the treatment in the discharge gap of a DBD with two different frequencies: positive pulse voltages of 7.5 kV and a treatment time of 30 min.

With the treatment in the discharge gap and a frequency of 50 Hz, a reduction of the germ number in the range of about approx. 2 log 10 steps was observed. The best result, namely, more than 6 log 10 steps, was obtained by using 500 Hz.

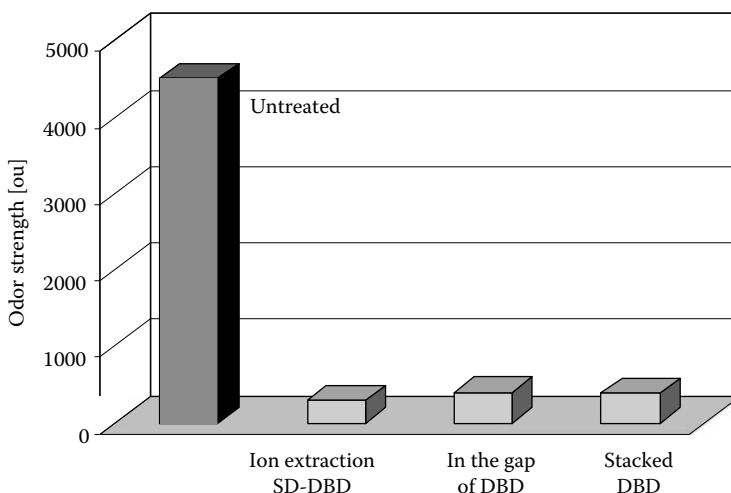


FIGURE 8.36 Odor strength after different treatment procedures.

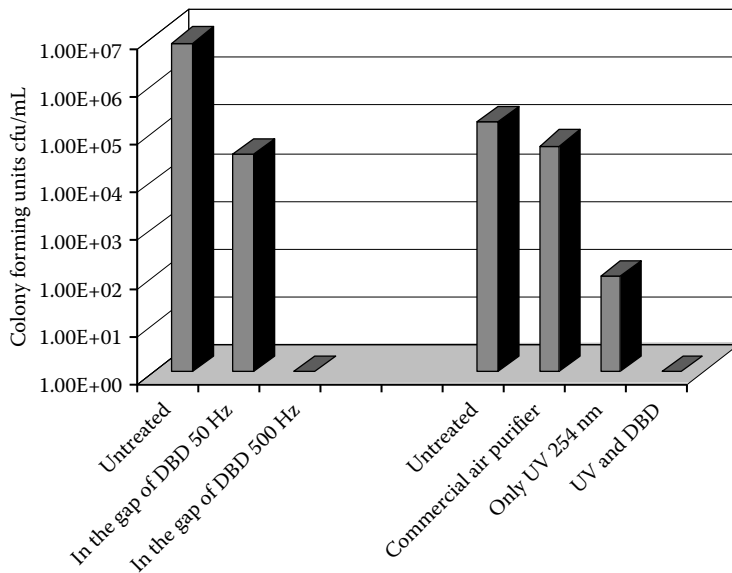


FIGURE 8.37 Results of the microbial tests by different methods.

The group on the right presents the result of the treatment beyond the discharge gaps by other methods.

The last two columns show the results when ultraviolet rays come into operation. The application of ultraviolet rays alone (254 nm) already causes a reduction of about approx. $3 \log 10$ steps. When we additionally add a DBD, a drop of more than $5 \log 10$ steps emerges.

8.2.3.3.2 Outlook

Normal pressure discharges, here in particular the DBD, have great potential for technological applications. The example of the plasma treatment of wool fibers showed that the discharge can also penetrate textile fibers and thus achieve an effective, steady result. The application of the DBD is not limited to surface modifications.

Investigations show that polymer layers on textile structures can also successfully be raised with the DBD. However, the theoretical description of the DBD with its interaction with the fiber structures is still pending. The successful implementation of plasma technologies in textile manufacture and treatment should raise the scientific interest in this issue in future.

8.2.3.4 Biomedical Applications of Plasmachemical Surface Functionalization

8.2.3.4.1 Aspired Properties of Biomaterials Surfaces

Applications of artificial materials in contact with living tissue and biomolecules pose a great challenge for surface refinement strategies. In a natural environment, cells as

the active, most essential components of living tissue receive numerous signals from their environment, which are decisive for their proper function. Even basic transformational procedures such as proliferation, cell differentiation, and programmed cell death (apoptosis) are crucially influenced by them. Typically, external signals are detected, processed, and transmitted by so-called signaling-cascades, which consist of complex networks of biomacromolecules including proteins, oligopeptides, saccharides, oligosaccharides, fatty acids, and phosphorylcholine (phospholipids).

Hereby, cells are able to respond to a large variety of environmental signals including, e.g., mechanical, thermal, electrical, and, most importantly, chemical signals. Obviously, therefore, surface properties that allow control of attachment of such macromolecules are decisive for the efficiency of medical devices and for acceptance of implants. Generally, the so-called shining through of surface properties [191] is a problem for any artificial biomaterial that was selected for a certain functional reason, e.g., mechanical strength and chemical inertness in a biological environment. A wide variety of polymers is applied as artificial biomaterials, such as polyethylene (PE), polypropylene (PP), polystyrene (PS), polycarbonate (PC), polymethyl methacrylate (PMMA), polyhydroxyethyl methacrylate (PHEMA), polyvinyl alcohol (PVA), polydimethyl silicone (PDMS), polytetrafluoroethylene (PTFE), and polyvinylidene fluoride (PVDF). These materials establish environments very different from natural environments consisting of neighboring cells or extracellular matrix components, typically. Deliberate surface modifications are needed, especially of chemical binding properties, to achieve so-called interface biocompatibility of artificial biomaterials surfaces.

Biocompatibility is defined as *the ability of a material to perform with an appropriate host response, in a specific application* [192,193]. Interfacial biocompatibility means that chemical and morphological surface properties cause a targeted or at least tolerable physiological reaction of the biological system in the context of intended application [194]. The essential absence of thrombogenicity and carcinogenic effects, minimal immunological and inflammation reactions, and required interactions with the proteins, sugars, and fatty acids to control cell adhesion are characteristics of interface biocompatibility [191,194].

The treatment of materials surfaces with nonthermal plasmas can lead to surface activation and functionalization, which creates unique surface properties, often not obtainable with conventional, solvent-based chemical methods.

The term “surface activation” refers to the creation of reactive surface sites. This type of modification can be advantageous to control biomolecule attachment in general. The term “surface functionalization” describes an intentional generation of certain surface functional groups (functionalities). Compared to surface activation, functionalization allows a more precise control of biomolecule attachment by selective chemical binding strategies such as covalent bonding. Functionalities like primary amines [195], carboxylic acids, amides [196], carbonyls [197], sulfonic acids [198], and amino sulfonic acids are reported to play a key role for the adhesion of specific polypeptides (for instance, cell adhesion molecules like fibronectin, vitronectin) and polysaccharides (like hyaluronan) [199] to polymer surfaces.

Essentially, there are three basic advantages of plasma activation and functionalization which suggest their use for such modifications of the afore mentioned materials:

1. The superior chemical reactivity of plasmas allows surface activation of inert materials, including creation of covalently bound functional groups.
2. Properly operated plasma activation and functionalization processes do neither affect bulk material characteristics nor produce toxic substances. Especially, the number of newly introduced chemical bonds or molecular substances can be limited to the absolutely necessary minimum, i.e., only a few of the topmost molecular surface layers are modified. Hence, an evocation of potentially adverse effects by the introduction of large amounts of foreign substances will be limited *a priori*. This is a significant advantage compared to alternative procedures, including plasma-assisted deposition of biocompatible plasma polymer films.
3. Properly operated nonthermal plasmas cause only minor thermal load to substrates. This is a significant advantage if heat sensitive polymeric biomaterials are treated. Many fine biomedical device structures do not tolerate substantial heating too.

Both, nonthermal plasmas at normal pressure (particularly at ambient atmosphere) and low-pressure plasmas can be applied. While normal pressure plasmas offer advantages in terms of investment cost and process integrability, low-pressure plasmas excel by their superior chemical selectivity.

The interested reader is referred to numerous reviews with direct relevance to this chapter [200–207], and reviews focusing on related applications, for instance, on plasma polymerization [208], grafting processes [209], resorbable biomaterials [210], blood compatibility [211], and the challenges to analysis [212].

Here, we will focus on examples for the application of plasma-functionalized polymer surfaces. In particular, this section will deal with chemically different surfaces applicable to control cell behavior.

8.2.3.4.2 Treatment of Polymers in Oxygen-Containing Plasmas

Surface modifications using oxygen-containing gases are easily performed by many discharge configurations. Typically, low pressure radio frequency or microwave discharges are used, but corona discharges or barrier discharges at atmospheric pressure are also often applied. At atmospheric pressure, air is the preferred working gas. Air, oxygen, or oxygen in argon carrier gas are used at low pressure. In most cases, the gases are chosen for technical reasons. Regarding chemical functionalization, the effects of all these discharges are dominated by the presence of oxygen since the atomic oxygen produced by the discharges is extremely reactive to hydrocarbons. It easily abstracts hydrogen from C–H bonds, thus producing hydrocarbon radical sites. Additional radical sites are produced by mechanisms such as UV photon absorption and ion bombardment. The radical sites in turn have a very high affinity to atomic oxygen, molecular oxygen, and OH radicals, which are often available in relevant quantities by the mere presence of residual water vapor (e.g., humidity

of air). Consequently, heterogeneous surface reactions during and after plasma processing lead to the predominant formation of different oxygen-containing functional groups like hydroxyls ($-OH$), carbonyls ($=C=O$), or carboxyls ($-C(=O)O$). This holds even for high concentrations of nitrogen in the discharges (air discharges). Examples for polymers treated in such a manner are contact lenses, artificial blood vessels, catheters, and dialyzers [200]. A further application represents the plasma functionalization of plastic disposables (typically PS or PC) used in clinical or laboratory diagnostics. Especially, cell culture consumables like dishes, titreplates, and cell culture flasks are regularly plasma treated [213,214]. Usually, the goal of such treatments is surface activation to overcome insufficient biomolecule attachment on the untreated bare materials.

Accessory prerequisite for such processes is the avoidance or at least minimization of thermal loading, etching, and degradation. High thermal loads leading to device temperatures near the glass transition point (less than 100°C for many polymers) can affect the mechanical integrity of the devices. Etching processes cause cleavage of chemical bonds thus splitting polymer molecules into smaller pieces. Both effects play a role in undesirable polymer degradation, i.e., in the formation of weak, so-called low molecular weight layers. This degradation is different for distinct polymer classes. While polyolefines show a rather small tendency for chain scission, and aromatic rings in the side chains protect polymers like polystyrene from chain scission, especially photosensitive polymers like polyacrylates, polycarbonates and polyetherketones are more susceptible to chain scission and degradation. These weak layers may reduce the adhesion strength of biomolecules and cells undesirably [215]. Additionally, such weak layers contain separate, soluble chains, so-called leachables. Such *leachables* may induce unwanted protein activation and can impede interfacial biocompatibility.

8.2.3.4.3 Polymer Treatment in Ammonia Plasmas

Next to treatments in oxygen-containing plasmas, process gas mixtures with ammonia (NH_3) are most notable. Using NH_3 plasmas, amino groups can be generated on surfaces. Despite the fact that the obtainable surface densities are low, typically between 1% and 2% of the carbon surface density [216], and although considerable concomitant nitrogen- and oxygen-related functionalization occurs, this is of interest and sufficient for many applications. Chemically, amino groups exhibit a strong basic character. This provides a potential for well-defined selective covalent coupling, e.g., of proteins. As in the case of other plasma functionalization processes, the technical requirements on processing are not very high. Considering the high toxicity and reactivity of ammonia, these processes are preferably performed under low-pressure plasma conditions. Furthermore, it is strongly recommended to ensure a low level of oxygen contamination in the gas phase since oxygen competes with amino group precursors for surface radical sites. Reduction of undesired concomitant functionalization is also principally possible by applying very short plasma activation [216,217]. However, the achieved improvement of selectivity of plasma functionalization is at the cost of amino group density.

It is noteworthy that for most applications, it seems sufficient to have a certain amount of amino groups available at all. Hence, treatment conditions are chosen

that typically result in multifunctional surfaces. Three possible explanations shall be given here. First, the aforementioned chemical selectivity of amino groups can make the existence of other functionalities irrelevant. Second, the very large molecular weight (size) of biological macromolecules does not require high surface densities of coupling groups. Third, many biomolecules are characterized by the existence of numbers of both acidic and basic functional groups, e.g., amino acids in proteins. Biomaterials with mixed surface functionalization may be better adapted for attachment of such molecules. This argumentation could serve as a (very general) explanation why so-called amino-functionalized surfaces often perform much better than standard tissue culture polystyrene, which represents one of the aforementioned oxygen functionalized surfaces.

Namely, these surfaces exhibit a mixed functionalization. An illustration of the conceivable appearance of such *amino-functionalized* surfaces is given in Figure 8.38 for the example of polystyrene. This rough imagination was developed preferentially on the basis of X-ray photoelectron spectroscopy (XPS) of polystyrene surfaces after low pressure microwave excited ammonia plasma treatment for about 10 s [216, 217]. XPS allows limited quantification of chemical bond structure. The existence of primary amino groups can be proven in conjunction with chemical derivatization techniques [218].

After longer plasma treatments, a noticeable modification of the polymer base structure takes place. In the case of polystyrene, this is visible by a marked loss of aromatic ring structures. Ring opening and hydrogen abstraction by the various active plasma species lead to numerous and different active sites. Not all of them can be occupied by amino groups or reoccupied by hydrogen atoms. A larger part of nitrogen is bound in other than primary amino groups, typically several percent of surface elemental composition. Also, the amount of oxygen, which is distributed over different functionalities, is much greater than the nitrogen amount in amino groups. It strongly depends on the time of air contact after plasma processing, indicating a preferential uptake by autoxidation reactions of atmospheric oxygen with long-lived surface alkyl radicals and their oxygen-containing derivatives [216, 219]. Other postplasma effects are oxidation reactions and surface adaptation, leading to the disappearance of amines from the surface. During and immediately after plasma processing, oxygen concentrations less than 1% of surface

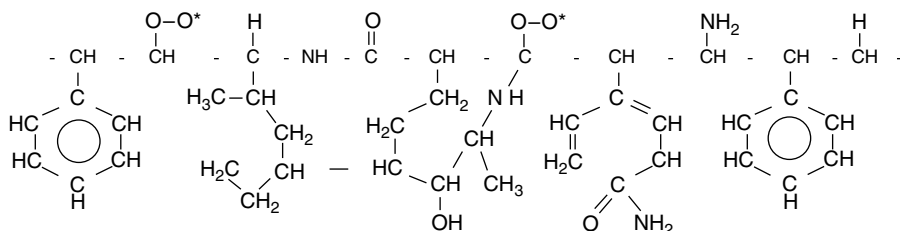


FIGURE 8.38 Schematic illustration of characteristic changes of surface composition of polymers due to ammonia plasma treatment for the example of polystyrene.

elemental composition can be found. However, after some days of exposure to air, the oxygen content reaches several percent and continues to increase for weeks and months.

Ammonia plasmas are commonly applied for polymer surface modification, and a number of research results have been published with regard to the improved understanding of the plasma processes [217] as well as on numerous biomedical applications [216]. The list of respective application examples in Table 8.11 provides just a glimpse of the width and variety of the field.

Note that ammonia plasmas can be applied not only to typical hydrocarbon polymers, but also to fluorinated polymers and to very sensitive resorbable polymers like poly(3-hydroxybutyrate (PHB)) and polylactides. Together with the improved cell culture outcome, this makes that type of surface modification an ideal candidate for demanding prospective new applications in tissue engineering, implants, devices, and consumables.

Besides direct cell culture applications, amino-functionalized polymer surfaces are frequently utilized as chemically reactive platforms for the covalent immobilization of biologically active molecules in aqueous solutions. Well established and therefore most common are carbodiimide catalyzed reactions between the surface amino groups and carboxylic groups on the molecules to be immobilized, which lead to the formation of interfacial amide bonds [207,220].

8.2.3.4.4 Carboxylated Surfaces

Another chemical functional group with relevance to biomedical applications is the carboxylic acid ($-COOH$) group. Carboxylic acid groups possess a strong nucleophilic character and hence a high chemical reactivity. They allow the generation of negatively charged surfaces and the creation of ionic or covalent chemical bonds. CO_2 plasma treatment is reported to be specially useful for functionalization with carboxylic acid groups. However, apart from producing carboxyl groups, CO_2 -containing plasmas generally create other functional groups containing C and O such as hydroxyl groups, aldehydes, ketones, esters, and (from postplasma reactions) hydroperoxides as well [207]. Also, insertion of carboxyl groups is not very high, typically in the range of some percent of surface carbon bonds. It is, therefore, not much different from oxygen plasma treatment. This can be seen as a reason why very often plasma polymerization is preferred for generation of carboxylic groups. Regardless of the complications of deposition, the outcome of plasma polymerization, e.g., of acrylic acid, can be much better in terms of density and selectivity of functional group generation.

It should be mentioned that an argumentation exists, which suggests to prefer substrates with carboxylic groups for the very popular carbodiimide-catalyzed covalent coupling procedure of proteins. Briefly, carbodiimide activates carboxylic groups on the protein that can react with amino groups on the same protein or another protein rather than with an amino group on the polymer surface, thereby causing crosslinking and oligomeric protein agglomerates. Thus, not all molecules found on the surface may be interfacially covalently linked and biological function may be compromised [207].

TABLE 8.11
Exemplified Biomedical Research Applications of Ammonia Plasma–Treated Polymer Surfaces

Field of Activity	Substrate	Interaction With	Intention	Ref.
Protein adhesion	PP	Albumin	Improved biocompatibility	[221]
Covalent protein immobilization	PET	Cysteine	Optimized grafting	[222]
Covalent protein immobilization	PS	Poly-L-lysine	Reduction of conformational changes	[223]
Covalent enzyme immobilization	PP	Glutardialdehyde	Immobilization of glucose oxidase	[224]
Covalent protein immobilization	Nitrocellulose membranes	Antibodies (IgG)	Fabrication of immunosensors	[225]
Covalent protein immobilization	PE	Glutardialdehyde	Immobilization of antibodies	[226]
Covalent enzyme immobilization	PP, PVDF, PTFE	Glutardialdehyde	Fabrication of glucose sensor	[227]
Cell adhesion	PS, PE	Cell culture medium	Artificial cornea, improved cell adhesion	[228]
Cell adhesion	PS	Cell culture medium	Improved human FL cell	[229]
Cell adhesion	PTFE	Cell culture medium	Improved endothelial cell culture	[230]
Cell adhesion	Poly(D,L-lactide)	Cell culture medium	Tissue engineering, fibroblasts	[231]
Cell adhesion	PHB	Cell culture medium	Tissue engineering	[232]
Cell adhesion	PET	Cell culture medium	Skin fibroblasts	[233]
Cell differentiation	PP, nylon-6	Cell culture medium	Tissue engineering, stem cells	[234]
Membranes	PP	Endothelial cells	Artificial lung	[235]
Prostheses		Albumin	Thromboresistance of mechanical heart valves	[236]
Prostheses	PHEMA, PMMA	Cell culture medium	Artificial cornea, epithelial cell adhesion	[237]
Prostheses	PTFE, ePTFE	Endothelial cells	Vascular graft biomaterials	[238]
Prostheses	ePTFE	Endothelial cells	Biocompatibility of vascular prostheses	[239]
Prostheses	ePTFE	Endothelial cells	Biocompatibility of vascular prostheses	[240]

Note: PE (polyethylene), PS (polystyrene), PTFE (polytetrafluoroethylene), ePTFE (expanded polytetrafluoroethylene), PP (polypropylene), PVDF (polyvinyl-lidene fluoride), PET (polyethylene terephthalate), PA (polyamide), PHEMA (polyhydroxy-ethyl methacrylate), PMMA (polymethyl methacrylate), PVA (polyvinyl alcohol), PAA (polyacrylic acid), PHB (poly(3-hydroxybutyrate)), and IgG (immunoglobulin G).

8.2.3.4.5 *Sulfonation of Polymer Surfaces*

In contrast to the large number of publications on plasma-generated amino and carboxylic acid functional surfaces, a limited number of reports on other groups is available. This is understandable considering the earlier arguments and the formidable presence of amino acids in biomolecules. But the different amino acids also contain other functional groups. This fact can serve as an argument that in special cases other functional groups than amino groups and carboxylic acid groups might be of interest for biomaterials surface functionalization. Indeed, at least a few investigations exist for all of these groups. An example is sulfonation of polymer surfaces. The treatment of polymer surfaces in SO₂ plasma facilitates the introduction of very hydrophilic oxidized sulfur species like sulfone or sulfonate groups and consequently more hydrophilic surfaces compared to carboxylic acid amino and hydroxyl groups. SO₂-plasma-treated medical grade polyvinyl chloride exhibits a particularly high fibronectin adsorption. This correlates to growth and differentiation of human endothelial cells [241]. SO₂ plasma surface modification was also employed to modify the inner surface of small diameter low-density polyethylene (LDPE) tubing with sulfonate functionalities. In this case, the SO₂-plasma-modified surface was much more thrombogenic than the untreated control [242]. Polyurethane (PU) was coated with plasma-polymerized acrylic acid and subsequently treated with SO₂ plasma to graft sulfonic acid groups on its surfaces. Sulfonic acid groups were shown to improve blood compatibility by significantly prolonging thrombin time and activated partial thromboplastin time [243]. SO₂ plasma treatment also offers the possibility to generate sulfonated surfaces of cyclic olefin copolymers (COC) and polystyrene (PS) [198]. In this case, the adhesion and proliferation of adherent cell lines was reported, which usually require coating of the substrate with extra cellular matrix molecules.

8.2.3.4.6 *Fluorination of Polymer Surfaces*

Fluorination of polymer surfaces reduces their reactivity and wettability drastically. In this way, adhesion processes are subdued. The effect is of substantial interest in cases where cell adhesion must be suppressed. Prominent examples are biomaterials in ophthalmology and for vascular grafts (hemocompatibility). For instance, intraocular lenses (IOLs) made of polymethyl methacrylate were surface modified with a tetrafluorocarbon (CF₄) plasma. The inflammatory cell response was measured after contact with human granulocytes, which showed significantly less cell activation and adhesion on the surface-modified IOLs [244]. Also, plasma polymers based on C₂F₄, C₂F₆, and C₂F₆/H₂ were found to be nonthrombogenic. Thus, interior surfaces of artificial blood tubes are nowadays coated with such plasma polymer layers and are commercially available [245]. Fluorination of polymer surfaces also plays an important role in the design of cell-based diagnostic devices [246].

8.2.3.4.7 *Patterned Surfaces*

An essential aspect of natural environments of artificial biomaterials is spatial organization of cells and extracellular matrix components in three-dimensional tissue structures. Hence, situations exist, e.g., in tissue engineering, where local control of cell adhesion on biomaterial is required. Within this topic, chemical micropatterns

consisting of cell-adhesive and cell-repulsive regions are investigated, which allow to control cell position, migration, proliferation, phenotype, membrane integrity, and finally life and death [247]. These patterns can be generated completely by plasma-based processes [248–252]. They are sometimes called *plasma lithography* [252]. Special advantages of plasma processes in this context are a good reliability and potential for facilitated integration in industrial manufacturing processes [253]. Such plasma-generated micro patterns [254] are depicted in Figure 8.39.

Topics where chemical micropatterning of biomaterial surfaces is investigated are, for instance, the development of bioartificial neuronal networks [255], advanced cell culture systems for a bioartificial liver in sandwich structure [256], for DNA- and proteinchips in high-throughput screening [257], and for high-content screening [246]. A triple chemical micropattern was described in [246] for the purpose of transverse small interfering ribonucleic acid (siRNA) transfection. This technique requires the combination of three differing types of surface adhesiveness on a chip,

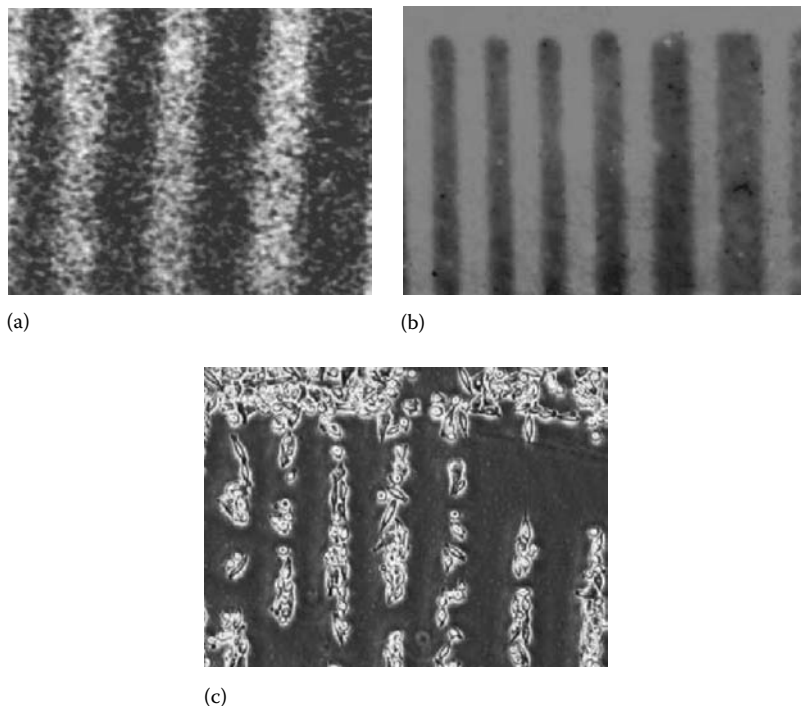


FIGURE 8.39 Plasma-generated chemical micropattern (structured width 100 µm): (a) qualitative chemical characterization by imaging O1s XPS signal. (From Schröder, K. et al., *Surf. Interface Anal.*, 36, 702, 2004.) (b) visualization by fluorescence labeling (CY3) of amino groups, and (c) pattern-guided growth of nasopharyngeal epithelial cells on lateral chemical microstructures. (From Schröder, K. and Ohl, A., Plasmamodifikationen und Proteinkopplungen für biomedizinische Anwendungen, in *Proceedings 13, Neues Dresdner Vakumtechnisches Kolloquium*, Dresden, Germany, pp. 42–49, 2005.)

which enable both good cell growth and functionality or localized spotting of a siRNA-containing gel or suppression of cell adhesion.

8.2.3.4.8 Summary and Outlook

A wide variety of plasma activation and functionalization processes, with an emphasis on creation of amino and carboxylic acid functional groups, has been developed for the purpose of improvement of interface biocompatibility of artificial biomaterials. Two main fields of applications exist: biomaterials in direct contact with living cells, e.g., implants, bioreactors, and cell culture substrates, and covalent immobilization of biomolecules, e.g., for diagnostic purposes and implants. Despite limitations concerning chemical selectivity of functionalization and obtainable densities of functional groups, this type of surface modification is frequently used, and a number of well-established applications exist. This is due to some specific advantages like ease of operation and low risk of detrimental impacts on biocompatibility. Future investigation needs to improve specifications of what is necessary for advanced interface biocompatibility. This will help to direct plasma research on critical details of the complex modification processes that are currently not yet identified precisely enough.

8.2.3.5 Plasma Medicine

Surface treatment of various materials is a wide field of plasma application. Low-pressure plasmas are successfully applied for this task. The development of nonthermal atmospheric plasma sources that generates cold plasma with gas temperatures below 50°C in the free atmosphere, allows the application of so-called tissue tolerable plasmas (TTP) for treatment of living human and animal tissues and skins, and opens the door for plasma medicine. Plasma medicine is the topic of instructive reviews [99,259,260].

Plasma medicine involves three fields, see also [262,263]:

1. Sterilization/decontamination of medical apparatus and tools [264], (see Section 8.2.1.2), including improvement of cleaning performance in medical device reprocessing by surface modification as well as inhibition of biofilm formation by surface treatment and direct action on biofilms.
2. Treatment of biorelevant surfaces for improving the biocompatibility and the incorporation of implants (e.g., stents, hip prostheses, contact lenses) into viable tissue by changing the surface characteristics (hydrophobicity, antifouling properties, cell-adhesive surfaces, application of antimicrobial active layers with drug delivery functions) [266–269].
3. Direct therapeutic applications of plasmas for prevention and treatment of diseases, e.g., for chronic wounds healing, skin and mucosal infectious diseases, localized tumors, keloid formation, promotion of angiogenesis, blood coagulation, tissue ablation, and hemostasis, dental applications [99], including promotion of improved penetration of topically applied drugs with therapeutic outcome [263].

8.2.3.5.1 Plasma Sources

Whereas for sterilization/decontamination and surface treatment, application of low-pressure plasma is possible, plasmas for direct therapeutic applications have to exist in air environments at atmospheric pressure. Such plasmas must have gas temperatures below 50°C, and the electrical stress of the investigated tissue or of the treated body must be negligible. Compilations of atmospheric plasmas for tissue processing are given in [259,271]. According to the importance of plasma jets and DBDs for plasma medical investigations, a brief description is given here of these plasma sources (see also Section 3.8).

8.2.3.5.1.1 Atmospheric Pressure Plasma Jets

Plasma jets with various mechanical constructions with different electrical excitations are presented in the literature [270]. An inert gas flow of some slm through a capillary is excited by RF voltage and the generated plasma jet (diameter ~1 mm) outside the capillary can be used for treatment of the various targets (Figure 8.40a). A pulsed operating of the plasma jet allows the decrease of the gas temperature in the jet below 30°C [271]. The UV radiation of the plasma is an order of magnitude lower than the minimal dose to produce sunburn *in vivo* [272]. These properties allow the application of this tool for medical treatment. The application of the nanosecond-pulsed negative

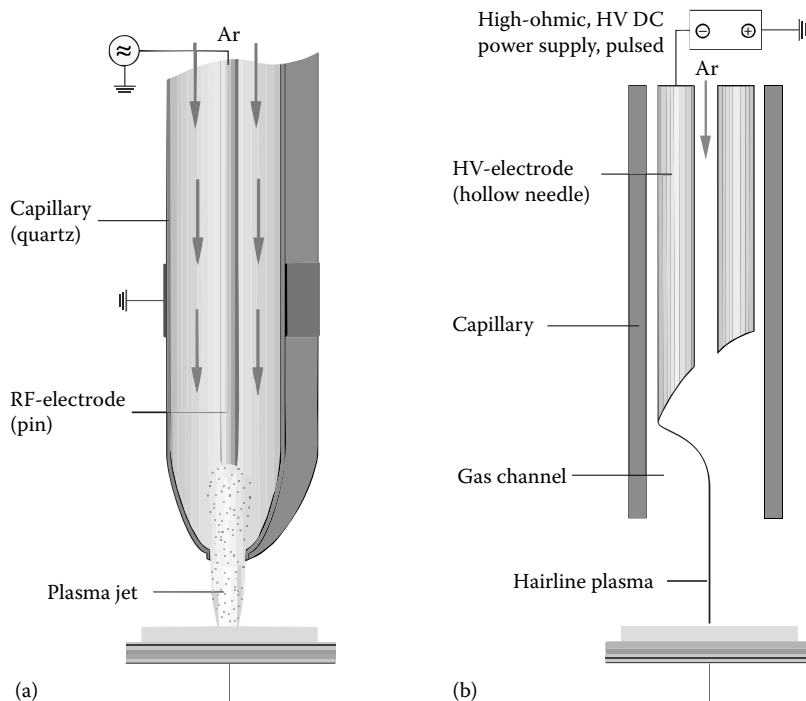


FIGURE 8.40 (a) Atmospheric pressure RF excited plasma jet and (b) hairline nanosecond pulsed negative DC corona plasma filament. (From Bussiahn, R. et al., *Appl. Phys. Lett.*, 96, 143701, 2010.)

DC corona enables the generation of a very thin ($d \sim 30 \mu\text{m}$) up to 1.5 cm long plasma filament at atmospheric pressure, which is adapted for treatment of small cavities [273] (Figure 8.40b).

The plasma jets are applied for the treatment of selected small areas but of bodily parts with complex geometries and small cavities. Furthermore, plasma jets can be arranged in arrays to adapt on special geometries.

8.2.3.5.1.2 Dielectric Barrier Discharges

The volume barrier discharge is characterized by the plasma in the gap in between two by dielectric-separated electrodes (Figure 8.41a and b). The object to treat may be used as the second electrode. Surface barrier discharge are excited by two electrodes situated on an isolating surface or embedded inside the dielectric; the plasma is generated on the dielectric surface. The subject under study is located nearby the active plasma [109] (Figure 8.41c).

In a floating electrode dielectric barrier discharge (FE-DBD) [98], the treated object serves as second active electrode in front of the dielectric-protected powered electrode. This not grounded second electrode floats, see Figure 8.41a. This discharge configuration enables charge carriers to hit directly the treated surface. Using a surface barrier discharge, the plasma is ignited on the surface of a special electrode arrangement. It can be brought close to the target to be treated, but the target is not part of the electrode configuration.

The plasma of the DBD is suitable for the treatment of more extended regions.

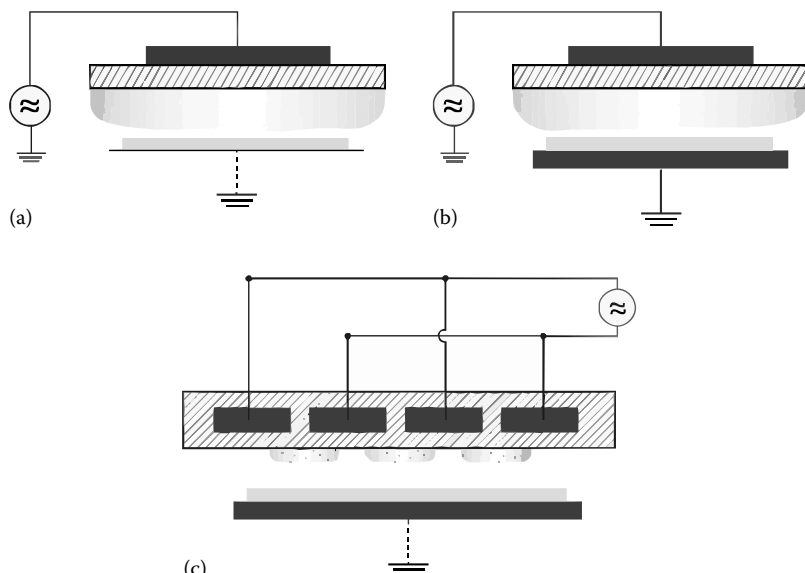


FIGURE 8.41 Dielectric barrier discharges: (a) volume barrier discharge with stray capacity, (b) volume barrier discharge with grounded electrode, and (c) surface discharge.

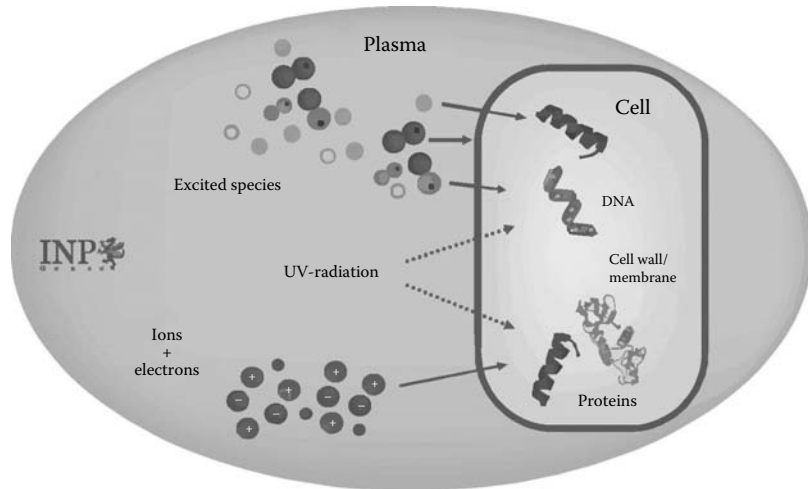


FIGURE 8.42 Scheme of plasma agencies acting with cell components.

8.2.3.5.2 Active Agencies

Active agents from the plasma that may act with treated surfaces are (Figure 8.42)

- UV radiation: In an atmospheric plasma jet are identified radiation in the UV-A (315–400 nm), UV-B (280–315 nm), UV-C (200–280 nm), and VUV range (115–200 nm) regions, but emission can be changed for selected discharge conditions [271,274,275].
- Charged particles: The interaction of active plasmas with living tissue investigated with FE-DBD is mainly determined by the action of charged species [117].
- Reactive neutral species, radicals: Examples are reactive oxygen species such as O , O_2^* , O_3 , OH , and H_2O_2 and reactive nitrogen species like NO and NO_2 [276,277]. The nature of active species generated by the plasmas in inert feed gas is influenced by the composition of the air environment, e.g., content of water vapor [278].

Thermal effects can be mostly neglected because no essential gas heating could be observed in the applied plasma sources.

8.2.3.5.3 Selected Applications

The decrease of the bacterial population on various inanimate targets by cold non-thermal atmospheric pressure plasmas is well known [264]. Because medicine knows that bacterial colonization of chronic wounds slows healing process, microorganism inactivation by plasma is also important for treatment of living tissue.

The antibacterial activity of atmospheric pressure plasma jet against wound pathogens was tested *in vitro* with various species of bacteria situated on agar plates [279].

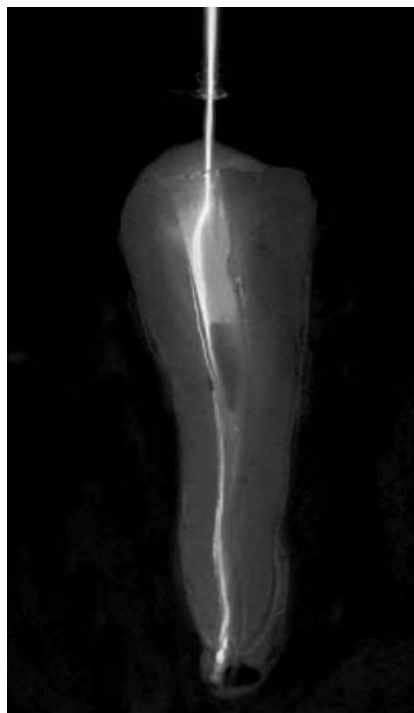


FIGURE 8.43 Hairline plasma in a prepared root canal of a human tooth. (From Bussiahn, R. et al., *Appl. Phys. Lett.*, 96, 143701, 2010.)

In a first clinical trial, for a number of patients (36) their chronic wounds were treated by nonthermal argon plasma torch. An essential decrease of the bacterial load was observed; the wound healing time was clearly reduced [280]. In another *in vivo* trial, the antitumor effect of a nonthermal atmospheric plasma treatment using a FE-DBD was studied successfully on a U87-luc glioma tumor of mice [281].

A problem of dentistry is the effective inactivation and removal of biofilms on tooth and implant surfaces as well as the treatment of the root canal after irreversible damage of the pulp by infection. This region is difficult to access for disinfection by conventional methods. The hairline plasma filament penetrates deep in the root canal and provides good chances to kill there residual bacteria [273] (Figure 8.43).

However, despite promising *in vivo* experiments and first clinical trials, a careful and comprehensive characterization of biological effects of atmospheric pressure plasma sources using a broad spectrum of cell as well as microorganism-based *in vitro* models is indispensable to guarantee safety and effectiveness of plasma applications and to explore innovative therapeutic options [262,282].

8.2.3.5.4 Conclusions

Plasma medicine in many aspects is a new field and it will take several years before it can be well established for special applications. Clear differences between plasma medicine, that is, the treatment by cold plasmas, and the conventional methods could

TABLE 8.12
Comparison of Conventional and Plasma Methods

Conventional Surgery	Plasma Treatment
Tissue is removed by excision/burning	Tissue is removed by chemical stimuli
Necrosis always occurs	Necrosis is avoided
Causes wounds	May heal wounds
Inflammation and scarring occurs	Inflammation and scarring can be avoided
Massive tissue removal is possible	Only superficial tissue removal is possible
Tissue irregularities are excised	Irregular surfaces can be treated
Depth effects are difficult to control	High precision can be reached
Conventional Medicine	Plasma Treatment
Drugs are delivered systemically	Plasma is delivered topically
The whole organism is influenced	Only diseased parts are influenced
Long-living species (drugs) are used	Short living species are used
Specific chemistry is involved	Basic physiological chemistry is involved

Source: From Stoffels, E., Atmospheric plasma: A universal tool for physicians? In R. Hippler, H. Kersten, M. Schmidt, and K. Schoenbach, eds., *Low Temperature Plasmas*, 2 edn., Wiley, Weinheim, Germany, p. 837, 2008.

be identified [283]. For some potential fields of medical applications, a comparison of conventional and plasma methods is presented in Table 8.12.

A lot of fundamental research as well as of technological development will be necessary in future, distinguished by interdisciplinary work of plasma physicists, biologists, chemist, and physicians.

8.2.4 PLASMA-ENHANCED CHEMICAL VAPOR DEPOSITION

Chemical vapor deposition [284] involves chemical reactions of reactants in the gas phase and/or on the substrate surface, which leads to the deposition of materials also as thin films. Activation processes such as thermal, photo-assisted, and, last but not least, plasma-assisted procedures are successful applied deposition technologies. Plasma-assisted chemical vapor deposition (PACVD) uses the energy content of the plasma, in nonthermal plasmas primary the energy of the hot electron gas.

Advantages of PACVD is the low temperature of the substrate, e.g., Si_3N_4 deposition required in a thermal-activated CVD process temperatures is in the range of 800°C–900°C; PACVD formation of Si_3N_4 films using a SiH_4/NH_3 operates near 350°C. Coating of temperature-sensitive substrates is possible. Disadvantages of PACVD technology are sometimes the application of low-pressure plasmas, which need expensive vacuum technique. The action of energetic ions on the deposition process has also to be taken into account.

Plasma-enhanced atomic layer deposition (PEALD) is based on a sequential use of self-terminating plasma-enhanced gas solid reactions, which leads to a coverage of the target surface by a monolayer film with good conformality. Metal-oxide films are deposited by application of metal-organic precursors and O_2 plasmas as oxidant [285].

This section first deals with organic thin films, including diamond and a-C:H films, and plasma polymers. It then inorganic films.

8.2.4.1 Organic Thin Films/Plasma Polymerization

8.2.4.1.1 Hydrocarbons: Diamond

Chemistry at surfaces is in particular interesting for industrial applications of plasmas. Due to the interaction of plasmas with surfaces, additional reaction channels compared to thermal processes are accessible. Amorphous hydrocarbon films will be used to discuss this aspect in the following. Recently, there has been growing interest in the field of amorphous hydrogenated carbon (a-C:H) films, both scientifically and technologically. This interest is due to the unusual structure of these films and the ability to control their properties over a wide range by varying the deposition conditions [286–288]. The commercial applications of amorphous hydrogenated carbon films have been reviewed in [289–292] (see Table 8.13). There is a need to understand the microscopic processes that occur during the deposition process and chemical and physical processes during plasma-surface interactions. An a-C:H film consists of a strongly cross-linked three-dimensional network in which small graphitic clusters are embedded. Tetrahedrally coordinated carbon atoms allow three-dimensional cross linking, thus leading to extraordinary hardness of a-C:H films, whereas graphite clusters composed of threefold coordinated sp^2 hybrids mainly determine the electrical and optical properties.

However, since the structure is highly disordered, no exact geometrical configuration can be given for a-C:H films and the material must be characterized in another way. Three of the most important characteristics of an a-C:H film are hydrogen content, sp^2/sp^3 bonding ratio, and density of the sample. Low density and high hydrogen concentration (~50–70 at.%) a-C:H films are generally referred to as polymer or soft a-C:H film, whereas high density, high sp^3 , and low hydrogen concentration

TABLE 8.13
Applications of Diamond-Like Carbon

Mechanical properties

Microhardness up to 4.000 Hv	Engine applications
Low friction	Die coating
Excellent wear properties	Coating tools for high-speed machining of AL and CU alloys Guides in textile processing machines Protective coating on recording discs Coating of artificial heart valves, joints, lenses, stents Bone saws
<hr/>	
<i>Optical properties</i>	
High IR transmission	Protective coating of Al mirrors
Low vis. transmission	Antireflection coating on germanium optics

Source: Lettington, A.H., *Carbon*, 36(5–6), 555, 1998.

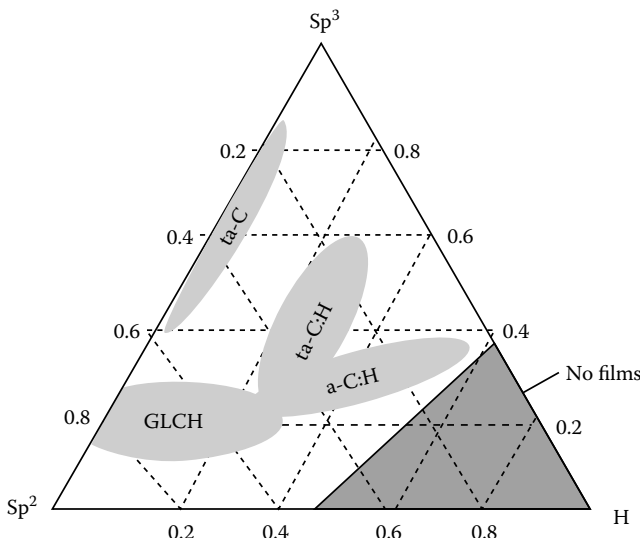


FIGURE 8.44 Ternary phase diagram of amorphous hydrocarbon films. The three corners correspond to pure diamond (sp^3), graphite (sp^2), and hydrogen films. The abbreviations used are GLCH (graphite-like hydrogenated carbon film), a-C:H (amorphous hydrogenated carbon film), ta-C (tetrahedral amorphous carbon film), and ta-C:H (tetrahedral amorphous hydrogenated carbon film). The shaded area in the corner is the region where no stable films can be deposited.

(up to 30 at.%) hydrocarbon films are usually referred to as diamond-like carbon (DLC) or hard a-C:H films [293]. The available experimental data can be most easily compared by plotting the sp^3 , sp^2 , and hydrogen contents in a ternary phase diagram as introduced by Smith [303]. Later Jacob et al. [294] used the published data and found that only within a limited region of the parameter range, a stable a-C:H films can be produced.

Figure 8.44 shows the ternary phase diagram of hydrocarbon films. The three corners of this diagram correspond to pure graphitic carbon (sp^2), diamond (sp^3), and hydrogen. The shaded area in the rightcorner is the region where no stable films can be deposited. Depending on the hydrogen content and the relative abundance of sp^2/sp^3 -bonded carbon, the films can be classified into different categories. Broadly, films which have relatively high sp^3 bonded carbon content are called DLC films and the ones with relatively high sp^2 carbon content are called graphite-like carbon (GLC) films. Amorphous carbon films that do not contain hydrogen and have sp^3 -bonded carbon content greater than 60% are called tetrahedral amorphous carbon (ta-C) films. If such a ta-C film is hydrogenated with hydrogen content ~20–40 at.%, it is called diamond-like hydrogenated carbon (DLCH) film. A ta-C:H film is amorphous and hydrogenated (H-content 25–30 at. %) with sp^3 -bonded carbon content ~70%. Similarly, a GLC film with H-content below 20 at.% and sp^3 -bonded carbon content lower than 20% is called graphite-like hydrogenated carbon (GLCH) film.

For understanding the chemical erosion of carbonaceous materials and to outline the elementary reaction steps, an experiment was performed by Horn et al. [295] where a several monolayer thick C:H film was grown and exposed to a hydrogen ion beam at a flux of $1.9 \times 10^{13} \text{ cm}^{-2}\text{s}^{-1}$. The basic atomistic processes involved in the chemical erosion process were identified, and a simple analytical model was proposed for the chemical erosion of a-C:H films. In the next section, the model to simulate the chemical erosion of porous graphite will be presented.

8.2.4.1.1.1 Analytical Description of Chemical Erosion

The chemical reaction of energetic ions with carbon atoms was found to occur after slowing down at the end of the penetration depth (range) of the ions. Three main mechanisms have been identified for the chemical erosion:

1. Thermally activated process (dominant for ion energies $\leq 1 \text{ eV}$)
2. Radiation damage (above 100 eV)
3. Kinetic hydrocarbon emission (1–100 eV)

8.2.4.1.1.2 Thermally Activated Process

The thermally activated process, which leads to a maximum of the chemical yields (Y_{therm}) at temperatures between 700 and 950 K, can be explained by the chemical mechanisms identified by Küppers and coworkers.

8.2.4.1.1.3 Küppers-Hopf Cycle for Chemical Erosion

Figure 8.45 shows various atomistic processes occurring under thermal H-atom impact on amorphous hydrogenated carbon (a-C:H) films [295]. Küppers et al. have identified the following main processes involved during the chemical erosion of the a-C:H films. The rate equation for every process is also written with the bracketed quantities as concentrations, ϕ as “H” atom flux, $\sigma_H = 1.1 \times 10^{-20} \text{ m}^2$, and $\sigma_D = 0.05 \times 10^{-20} \text{ m}^2$ as hydrogenation and dehydrogenation cross-sections, respectively.

1. Hydrogenation of the graphitic sp^2 hybridization state (state **a**), forming state **b** consisting of a radical sp^x with a neighboring hydrogen-containing carbon in the sp^3 hybridization state

$$-\frac{d[\text{CH } sp^2]}{dt} = [\text{CH } sp^2]\sigma_H\phi. \quad (8.60)$$

At higher temperatures, split-off of this hydrogen can return the two carbon atoms to their original state **b**

$$-\frac{d[\text{CH } sp^x]}{dt} = [\text{CH } sp^x]k_{-H} \exp\left(\frac{-E_{-H}}{kT}\right), \quad (8.61)$$

where

$k_{-H} = 10^{13} \text{ s}^{-1}$ is the frequency factor

$E_{-H} = 1.73 \text{ eV}$ is the activation energy for this process

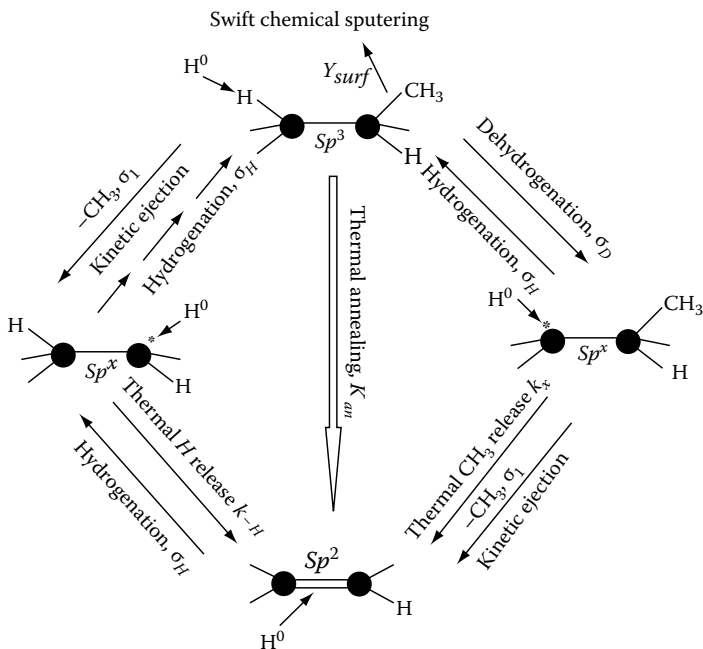


FIGURE 8.45 Schematic diagram of the reactions leading to methane production due to atomic hydrogen impact on amorphous hydrogenated carbon films, as proposed by Küppers et al. (From Horn, A. et al., *Chem. Phys. Lett.*, 231(2–3), 193, 1994; Mech, B.V. et al., *J. Appl. Phys.*, 84(3), 1655, 1998.)

2. Repetitive application of the hydrogenation to state **b** will lead to the formation of two carbons in the sp^3 hybridization state (state **c**), some fraction of which will contain a methyl group attached

$$-\frac{d[\text{CH } sp^x]}{dt} = [\text{CH } sp^x] \sigma_H \phi. \quad (8.62)$$

3. Abstraction of a singly bound hydrogen can produce state **d**, consisting of a carbon in the radical sp^x configuration with a neighboring methyl-containing carbon in the sp^3 hybridization state. The reaction proceeds directly between the bonded hydrogen atoms and the incoming hydrogen atom via an Eley-Rideal mechanism. In an Eley-Rideal mechanism, the reaction proceeds without the incident particles being thermally equilibrated prior to reaction, as opposed to the Langmuir-Hinshelwood process, which requires both the partners (incoming atom and the bonded atom) to be adsorbed and thermally equilibrated prior to reaction [298]

$$-\frac{d[\text{CH } sp^3]}{dt} = [\text{CH } sp^3] \sigma_D \phi. \quad (8.63)$$

4. Hydrogenation can return state **d** to state **c** or, for temperatures above ~ 400 K, the radical can de-excite by split-off of the neighboring methyl group and return the carbon atoms involved to their initial graphitic state **a**

$$-\frac{d[\text{CH } sp^x]}{dt} = [\text{CH } sp^x]k_x \exp\left(\frac{-E_x}{kT}\right), \quad (8.64)$$

where $k_x = 10^{13}$ s $^{-1}$ is the frequency factor and $E_x = 1.604$ eV is the activation energy for release of methyl group.

5. For graphite temperatures in excess of ~ 1100 K, thermal annealing can return state **c** to state **a** via elimination of some of the ion-induced damage accumulated in the implantation zone

$$-\frac{d[\text{CH } sp^3]}{dt} = [\text{CH } sp^3]k_{an} \exp\left(\frac{-E_{an}}{kT}\right), \quad (8.65)$$

where

$k_{an} = 10^{13}$ s $^{-1}$ is the frequency factor

$E_{an} = 2.42$ eV is the activation energy for the annealing

Thus, at low temperatures, exposure of the film to thermal hydrogen atoms results in the conversion of carbon from the sp^2 to the sp^3 hybridization state with some fraction of radical centers, determined by the ratio of σ_D/σ_H . At higher temperatures (400–650 K), an equilibrium balance between the supply of sp^x radical carbon centers from hydrogenation and abstraction and their loss through thermal decomposition due to methyl and hydrogen split-off is established, leading to measurable erosion rates. At even higher temperatures, however, the rapid decomposition of the radical states by H-atom split-off prevents significant hydrogenation to sp^3 hybridization states. This, in turn, means that there is little or no abstraction occurring, and if so, there is no significant production of carbon in the radical carbon state. Thus, chemical erosion is suppressed at higher temperatures.

The steady-state solution to the aforementioned set of differential equations leads to a very weak dependence in Y_m (maximum erosion yield) and a very strong dependence in T_m (temperature at which the yield is maximum) on the flux density ϕ . Such dependencies are not observed in experiments. Roth and García-Rosales [299] proposed that since the absolute concentration of carbon in the sp^3 hybridization state with attached methyl groups is unknown, they use k_x and k_{-H} as fitting parameters adjustable to all the available experimental data in the relevant energy and temperature ranges, taking into account the flux dependence of Y_m and T_m . The formula resulting from this fitting procedure is

$$Y_{therm} = [\text{CH } sp^3] \frac{0.033 \exp\left(\frac{-1.7 \text{ eV}}{kT}\right)}{2 \times 10^{-32} \phi + \exp\left(\frac{-1.7 \text{ eV}}{kT}\right)}. \quad (8.66)$$

8.2.4.1.1.4 Radiation Damage

In addition to Y_{therm} , a term is required, which accounts for radiation damage resulting from energetic impact. For ions with energies above the threshold for physical sputtering, energy deposition in the carbon substrate results in atomic displacement and C–C bond breaking, which creates active sites increasing the chemical erosion yield. The energy deposited that causes nuclear damage in the surface layer has a maximum between 300 and 2 keV, similar to physical sputtering. Roth and García-Rosales [299] had proposed that this enhancement can be well described by a multiplicative term that is proportional to physical sputtering such that the energetic chemical yield is given by

$$Y_{chem} = Y_{therm}(1 + DY_{phys}), \quad (8.67)$$

where

D is a constant dependent on the mass of the impinging isotope

Y_{phys} is the physical sputtering yield given by the revised Bohdansky formula [300].

8.2.4.1.1.5 Kinetic Hydrocarbon Emission

In case of low-energy hydrogen ion impact on carbon, hydrocarbon production is observed at room temperature which is not explained by the atom impact model where higher temperatures are required. The isotope effect on the yield that has been observed for this low energy impact, as well as TDS results [297], suggest that physical sputtering of weakly bound sp^3 centers with attached hydrocarbon ligands may occur at the surface. This seems reasonable since the concentration of these carbon hybridization states is high at room temperature. García-Rosales et al. argue that the dependence of this kinetic ejection process on energy should be similar to physical sputtering, but shifted toward lower threshold energies in the range of 1–2 eV, and that for hydrogenic impact at energies greater than ~ 90 eV, hydrogenation occurs at the end of range away from the surface, and so the erosion yield from this surface process is reduced. Furthermore, as the temperature of the carbon increases, the sp^3 hybridization state concentration drops, limiting the effect of this surface process to temperatures below T_m . The term proposed to describe this surface effect on erosion is

$$Y_{surf} = [\text{CH } sp^3] \frac{Y_{phys}^*}{1 + \exp\left(\frac{(E_0 - 90)}{50}\right)}, \quad (8.68)$$

where Y_{phys}^* is the yield given by modified Bohdansky equation with lower threshold energies. Note that the term in the denominator restricts the process to energies below 90 eV.

The total chemical erosion yield after incorporating all the aforementioned contributions is

$$Y_{chem} = Y_{surf} + Y_{therm}(1 + DY_{phys}). \quad (8.69)$$

Figure 8.46 shows the results of the chemical erosion of a C:H substrate. The dominant erosion product is methyl radical (not methane) and a wide spectrum

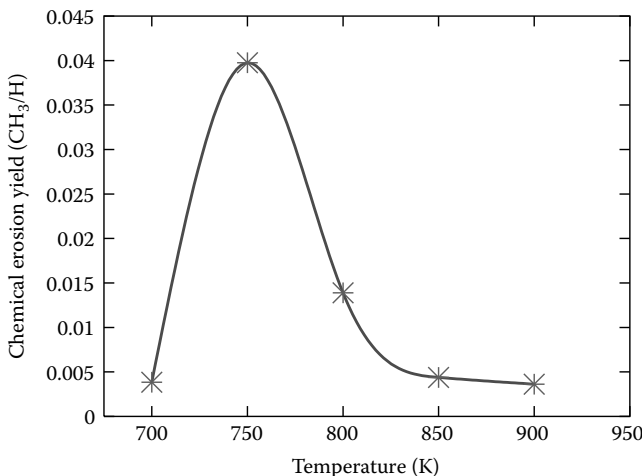


FIGURE 8.46 Chemical erosion yield as a function of temperature for incident H-flux of $10^{22} \text{ m}^{-2}\text{s}^{-1}$.

of other hydrocarbons. At low temperature, the rate of thermal decomposition of radicalic centers is small and the rather large cross section σ_H provides effective transfer of these centers back to sp^3 ; therefore one sees that at low temperatures carbon is present mainly in sp^3 hybridization state, whereas at higher temperatures, the radical centers decompose readily and therefore sp^2 carbon atoms dominate. The hydrogen split-off reaction provides a pathway to destroy erosion relevant groups. Only in an intermediate temperature range the balance between the supply of sp^x centers through dehydrogenation, their thermal decomposition via hydrogen or CH₃ split-off, and hydrogenation to sp^3 enables a noticeable chemical erosion rate.

The particular field of research of plasma surface chemistry is definitively one of the most complex problems to be understood for plasma applications. Up to now only the beginning of an understanding exists and only for selected systems. Further work is strongly needed to achieve a predictive quality of plasma chemistry techniques. This will require a joint effort of experiments and theory, bringing together different disciplines like surface science, quantum chemistry, solid state physics, plasma physics, atomic and molecular physics, material science, and even, eventually, biochemistry and biophysics (for medical applications of plasmas).

8.2.4.1.2 Plasma Polymerization

Plasma polymerization is the deposition of thin solid films (high-molecular-weight molecules) on surfaces in more or less close contact with the plasma of electrical discharges containing organic gases (low-molecular-weight molecules). The expression polymerization describes the similar properties of the deposited films to classical polymers, albeit structure and formation process being different from the known polymers. The formation of solid depositions was observed in discharges in vapors of hydrocarbons since the second half of the nineteenth century [301,302]. Plasma

polymerization is the topic of some textbooks, as [146,154,305] or, e.g., extended chapters in [147,184,306].

The plasma polymerization is a thin film formation process using organic compounds with and without double bonds; the latter cannot be polymerized in classical chemistry. This organic feed gas is called *monomer*. Therefore, activation of these molecules in the plasma is required. It is a well-proven technique for the deposition of thin films at low substrate temperature. Plasma polymerization allows the deposition of thin polymer films with a thickness of about 100 nm, which is not possible in conventional polymer chemistry [154]. The films are highly cross linked, of interesting chemical inertness against acids and bases, and have low solubility in organic solvents. They are distinguished by a high adhesive strength to substrate surface according to the activation of substrate surface by the plasma. They are pinhole free caused by the deposition mechanism without island formation. The films have a good hardness, elasticity, and thermal stability. Wettability and wear resistance can be influenced by deposition conditions. Hydrophilic films are interesting for deposition on textiles [307]. Plasma polymers are carriers of trapped radicals. Free radicals in the films may be caused by the formation process with free radicals. Generation of radicals is also possible by the reactions of plasma components (ions, UV radiation) with the thin polymer film. Concentrations of 10^{18} – 10^{20} spins/g are observed [154,308]. A high concentration of free radicals in the cross-linked film arouses aging effects concerning various properties such as dielectric losses and gas permeability [309]. The internal stress of the thin plasma polymer films can reach values up to 10^8 N/m² [309]. Plasma polymer films have a low refractive index [310], high transparency, and are amorphous. High specific resistance and good dielectric properties (dielectric permittivity, dielectric losses) are important for electronic applications. Properties of plasma polymers are summarized in Table 8.14.

Various plasma systems (DC, AF, inductively and capacitively coupled RF, MW; low pressure up to atmospheric pressure; monomer inflow inside the active plasma or downstream, substrate position in or outside the active plasma) are used for thin film deposition by plasma polymerization. DC discharges are successfully applied for fundamental research [312]. The position of the substrate in or without contact with the active plasma is essentially due to the action of the energetic ions generated by the sheath potential between substrate and active plasma. Afterglows are distinguished by low ion concentrations and energies. Pulsed plasmas allow the control of action time of active and afterglow plasma. Polymer properties such as cross linking, density of trapped radicals in the polymer film, and surface temperature depend on the exposure to charged species [154,313]. Applications of pulsed discharges with low pulsing frequency improve the deposited film homogeneity, because in the off-time the precursor gas can be distributed well in front of the substrate [310].

A modeling of the growth of plasma polymers requires consideration of activation processes of the feed gas molecules (monomer) in the volume and surface processes as adsorption and desorption of activated species [314,315]. These activated particles are responsible for polymer film formation. The surface kinetics may be influenced by the inflow of energetic components (e.g., ions) from the plasma. The generation of activated sites on the substrate surface is responsible for the good adhesion of the

TABLE 8.14
Properties of Plasma Polymers

Properties		
<i>Mechanical</i>		
Crystallinity	Amorphous	
Density	~1 g/cm ³	
Hardness		Scratch resistant coating
SiO ₂ :H	Microhardness 5–10 GPa	
a-C:H	Microhardness >20 GPa [310]	
Permeability		Semipermeable membranes
Internal stress	≤10 ⁸ N/m ² [309]	
Adhesion on substrate	Good for thin films	
Thermal stability	Good	
Pinhole density	Pinhole free	Corrosion protection
Thickness	<1 μm	
Deposition rate	~10 nm/min	
<i>Chemical</i>		
Chemical composition	Specific gas permeability for different gases	Semipermeable membranes
Cross linking	High: low solubility, chemical inertness	Corrosion protection
Radical concentration	10 ¹⁸ –10 ²⁰ spins/g: aging effects	
Surface chemistry	Surface energy, high : hydrophilic wettable, low: hydrophobic	Coating of textiles
<i>Optical properties</i>		
Transparency		
Refractive index 500 nm for various precursors [310]	1.35–1.38 C ₂ F ₄ , C ₄ F ₈ , etc.	Antireflection coating
	1.41–1.47 tetraethoxysilane	
	1.47–1.50 hexamethyldisiloxane	
	1.75 hexamethyldisilazane	
<i>Dielectric properties</i>		
Dielectric permittivity ε	2.5–5.23 [146]	Application in microelectronics
Loss angle: tang δ	5 · 10 ⁻⁴ –10 ⁻² [146]	
Electric strength [V/cm]	5–12 · 10 ⁶ [311]	
Conductivity [1/Ωcm]	3 · 10 ⁻¹⁸ –1.8 · 10 ⁻¹³ [146]	Gas sensors [146]
	Conductivity change by adsorbed gases	

deposited film. The formation of activated species in the plasma is determined directly or indirectly (formation of metastable atoms) by collisions of monomer molecules with electrons. The products are excited particles, ions, or neutral radicals generated in dissociative collisions. Reactive species with a single reactive site and also divalent reactive species are possible [305]. According to the essentially higher concentration of neutral radicals in relation to the ions, these neutral species may be accountably for

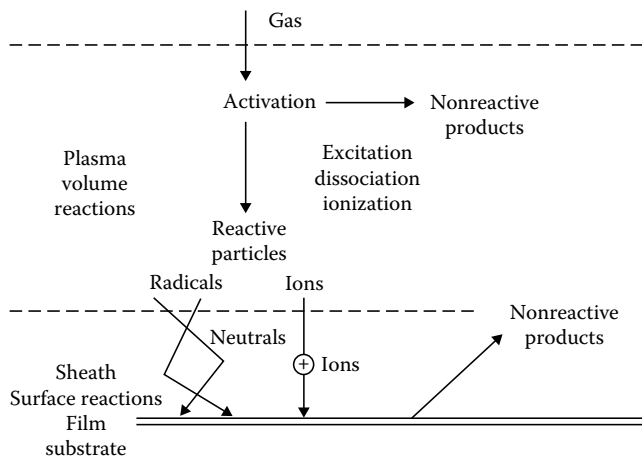


FIGURE 8.47 Reaction scheme for plasma polymerization of thin films. (From Yasuda, H., *Plasma Polymerization*, Academi Press, Orlando, FL, 1985. Poll, H.-U. et al., *Eur. Polym. J.*, 12, 505, 1976.)

the film formation. For small admixtures of monomers in inert gases, the activated species responsible for thin film deposition may be ions, as investigated for a benzene argon dc discharge [316]. Mass spectrometric investigation of a hexamethyldisiloxane (HMDSO) discharge leads to the conclusion of a film formation by ions [317,318]. The question of the generally dominant plasma component (neutral radicals or ions) in the polymerization mechanism is still open [98]. Film formation is also possible by interaction of surface adsorbed monomer molecules with energetic particles or UV radiation from the plasma. The activation reaction in the volume, as well as reactions of energetic particles with adsorbed monomer molecules or already deposited polymer film can be associated with the formation of nonreactive products, like hydrogen. A reaction schema is given in Figure 8.47.

The deposition rate depends on the operating conditions such as reactor geometry and dimensions, power input, gas pressure, nature and rate of carrier gases, flow rate, and, last but not least, of the nature of monomer gas. This complex dependence of the deposition rate and the properties of the plasma polymer on the operating conditions lead to applications of reactor parameters. The chemical reactivity of the plasma chemical system may be characterized by the dimensionless reactor parameter

$$R = \frac{\tau_0 W}{p V_A}, \quad (8.70)$$

where

τ_0 is the residence time of the monomer in the active plasma zone

W is power input into the active plasma zone

p is the gas pressure

V_A is the volume of the active plasma zone

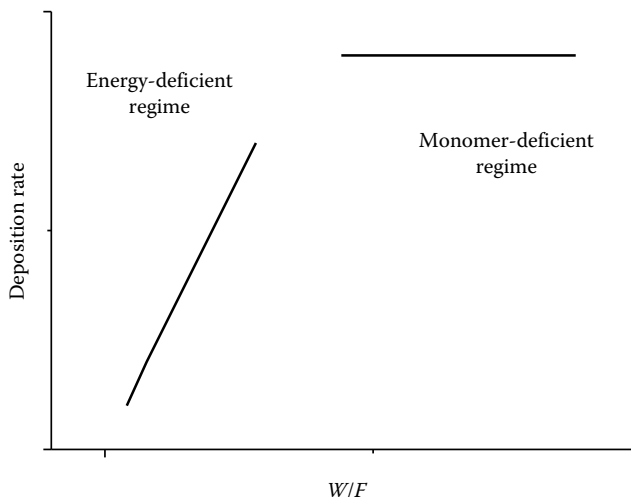


FIGURE 8.48 Deposition rate for constant monomer flow rate in relation to energy density, presents the energy- and monomer-deficient regimes.

This parameter is a measure of the energy input per particle during the flow through the active plasma zone in relation to the thermal energy kT (see Chapter 4 and [319,320]).

Yasuda introduced the composite power parameter, which includes additionally the monomer mass [305] $Cp = W/FM \cdot 1.34 \cdot 10^9$ [J/kg] with W power input [Watt] into the active plasma zone, where the polymerization occurs, F flow rate [cm^3 (STP)/min], M molecular mass of the monomer [g].

For a constant monomer flow rate, increasing power leads to linear increasing deposition rate. This is the energy-deficient regime. The following saturation of the deposition rate is caused by limited monomer concentration in this monomer-deficient regime [321] (see Figure 8.48). Increasing monomer flow rate at constant power causes a linear increase of the deposition rate up to a maximum value and beyond this region a decrease is observed due to the reduced residence time of the monomer particles in the active plasma zone.

The deposition of thin films, but also of powders and oily substances is observed [322]. Powder formation is supported by low flow rates, long residence times of the particles in the active plasma, and therefore polymerization reactions in the volume. Film formation at the substrate is assisted by shorter residence times of the active species in the plasma. Oil deposition at the substrate occurs for short residence times and therefore low cross linking [144]. The quality of the deposited material depends on the plasma parameter, in particular on electron energy and density.

8.2.4.1.2.1 Plasma Polymerization of Hydrocarbons

A broad spectrum of hydrocarbons is investigated in various plasma systems. The deposition rate depends on the chemical structure; compounds with multiple bounds and cyclic structures show in general higher deposition rates than saturated

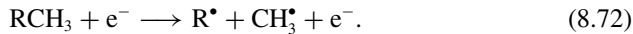
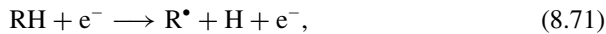
TABLE 8.15**Plasma Polymerization of Hydrocarbons, Characteristics of the Volume, and Deposition Reactions**

Type	Chemical Structure	Reaction Characteristics	Characteristic Features of Deposits
I	Aromatic, heteroaromatic triple bond	Polymerize readily with little hydrogen production	High concentration of dangling bonds and unsaturation
II	Double bond, cyclic structure	Polymerize moderate with moderate hydrogen generation	Moderate level of dangling bonds and unsaturation
III	Saturated hydrocarbons	Polymerize with lower rate and high yield of hydrogen	Low concentration of dangling bonds and unsaturation
IV	Oxygen (in aliphatic structure)	Low deposition rate, high rate of by-product gases	Very sensitive to energy input level; often oxygen containing groups are absent in polymer
V	Oxygen (in cyclic structures including epoxides)	Oxygen atom is preferentially removed; yielding diradical for polymerization	Oxygen is absent in polymer

Source: Yasuda, H., *Luminous Chemical Vapour Deposition and Interface Engineering*, Marcel Dekker, New York, 2005.

compounds. The discharge in such vapors is connected with hydrogen generation, whereas the hydrogen yield is highest for saturated compounds, lower for double bond hydrocarbons, and lowest for triple bound compounds (see Table 8.15).

Important for the activation of hydrocarbon molecules are electron collision-induced dissociation processes like



Dissociative ionization processes have also to be taken into account. The concentration of free radicals may be five or six orders of magnitude higher than that of ions [322]. The free radicals are transported by diffusion from the volume to the substrate surface and form the cross-linked polymer film. In the gas phase, propagation by recombination of two radicals and subsequent activation is possible. Bifunctionally activated species have to be taken into account as well. A high hydrogen concentration hinders the formation of higher hydrocarbons and assists the deposition of carbon-rich films. Selected plasma conditions facilitate diamond like coatings (DLC, a-C:H) or deposition of diamond films (see Section 8.2.4). Formation of clusters in the gas phase of hydro carbon plasmas is discussed in Section 8.4.

8.2.4.1.2.2 Plasma Polymerization of Fluorocarbons

Plasmas in fluorocarbon gases show special features:

- Plasmapolymerization of fluorocarbons leads to thin films with distinguished properties concerning the very low surface energy and, therefore, important properties for special applications.
- Fluorocarbon plasmas are suitable for thin film coating but also for plasma etching in dependence on the nature of admixture to the fluorocarbon feed gas.
- The discharge in fluorocarbon feed gas shows, due to the electron affinity, a high concentration of negative ions.

Monomers for coating processes are

- Perfluoralkane such as CF_4 , C_2F_6 , C_3F_8 , and C_4F_{10}
- Perfluoralkene such as C_2F_4 , C_3F_6 , and C_4F_8
- Fluorohydrocarbons such as CHF_3

A compilation of data of electron interactions (excitation, dissociation, ionization, attachment, drift and diffusion coefficients) with such plasma processing gases is given by Christophorou and Olthoff [323]. An example is presented in Figure 8.49. Here partial ionization cross sections (suggested values) for the generation of fragment ions of CF_4 and the dissociation cross section for the formation of

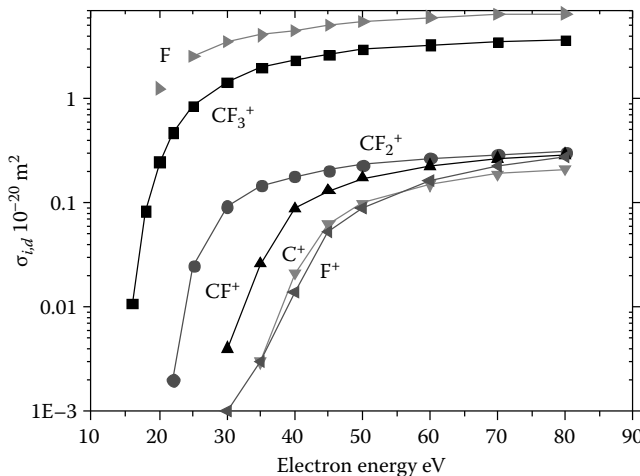


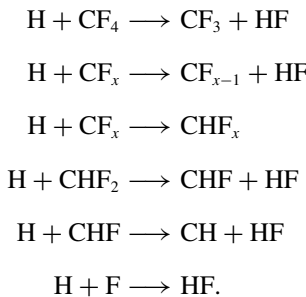
FIGURE 8.49 Partial ionization cross sections (suggested values) for the formation of fragment ions and of dissociation cross section of F atom formation by dissociative ionization and dissociation in neutral fragments [324] in dependence on electron energy. (From Christophorou, L.G. and Olthoff, J.K., *Fundamental Electron Interactions with Plasma Processing Gases*, Kluwer Academic/Plenum Publishers, New York, 2004.)

neutral F atoms by various processes (dissociation, dissociative ionization) [324] are presented.

Charge transfer reactions of Ar^+ , Ne^+ , and He^+ , as well as of O^+ and O_2^+ with CF_4 and C_2F_6 show formation of CF_3^+ , CF_2^+ , and CF^+ , and for oxygen reactions also FCO^+ and F_2CO^+ [325]. CF_3^+ ions are also products of $\text{CF}^+ + \text{CF}_4 \rightarrow \text{CF}_3^+ + \text{CF}_2$ [326]; other ion molecule reactions of perfluorocarbons are studied by [327]. The formation of high mass species (positive ions and neutrals) in the downstream region of $\text{Ar}/\text{CF}_4/\text{O}_2$ plasmas is investigated by Furuya [328].

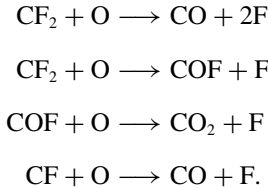
The action of the fluorocarbon plasma can be strongly influenced by admixture of hydrogen or oxygen [329].

Typical reactions of H atoms in CF_4 plasma are [330]



These reactions generate CF_x radicals, which enhance the formation of plasma polymers and reduce the fluorine content in the plasma polymer by formation of volatile HF. The reduction of F atom concentration decreases the etch probability. Thin film deposition in a CF_4/H_2 plasma is at most for a H_2 admixture of 20% [331].

The addition of oxygen generates fluorine atoms and enhances the etching rate [332]:



The plasma polymerization and etching processes in dependence on the operating time of the discharge are illustrated in Figure 8.50. A Si-substrate is positioned on the powered electrode of a 50 kHz discharge in $\text{C}_2\text{F}_6/\text{H}_2$ gas mixtures ($p_o = 28 \text{ Pa}$, $j = 0.5 \text{ mA/cm}^2$) for different H_2 admixtures in a closed system. The C_2F_4 plot shows the deposition in a discharge in pure C_2F_4 . Discharges with low H_2 admixtures are characterized by an etching of the Si-substrate, the deposition increases with growing H_2 admixture.

Applications of fluorocarbon plasma polymers are characterized by the low surface energy of these films. Coated textiles and papers are distinguished by

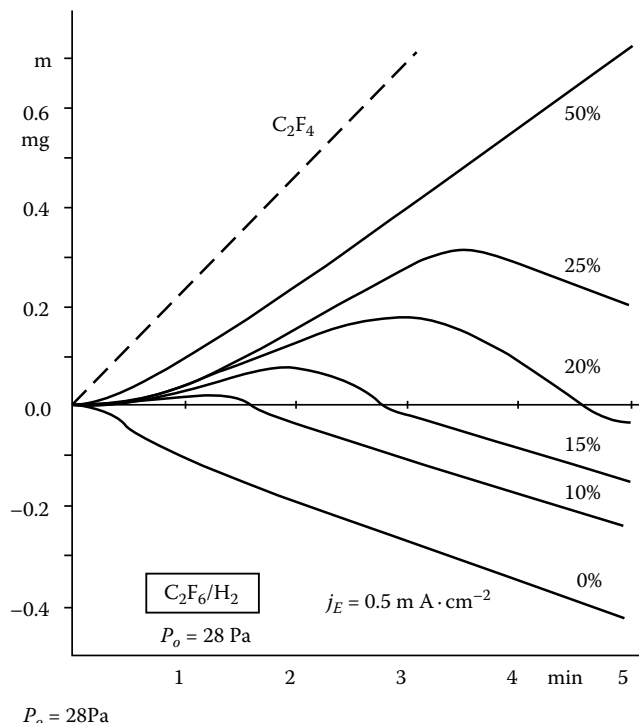


FIGURE 8.50 Polymer deposition and etching of Si measured on a Si substrate positioned on the powered electrode of a 50 kHz discharge in closed C_2F_6/H_2 discharges in relation to the discharge time for various H_2 admixtures ($P_o = 28 \text{ Pa}$, $j = 0.5 \text{ mA}$).

hydrophobicity and oleophobicity. Biomedical applications are promising due to their nonthrombogenic character, blood compatibility, and adsorption–retention properties for blood proteins [329]. See also fluorocarbons use in ASE trench etching process for sidewall protection (Section 8.2.1).

8.2.4.1.2.3 Plasma Polymerization of Siliconorganic Compounds

Siliconorganic compounds are interesting as monomers for plasma polymerization. Many monomers are sufficiently volatile, nonflammable, nontoxic, and cheap [334]. Starting with the Si–O bond and the CH components, it is possible to generate almost inorganic or organic films. Examples of monomers are shown in Table 8.16.

One of the most investigated plasma polymerization system uses hexamethyl-disiloxane (HMDSO) $(CH_3)_3Si-O-Si(CH_3)_3$ as monomer. The electron HMDSO collision processes are studied concerning the ionization processes [333,345], the formation of neutral dissociative products [346], and ion molecule reactions [345]. The ion population and neutral gas composition in discharges is investigated by [317,318,347]. CH_3 radicals as well as stable C_2H_6 , C_2H_2 , and CH_4 molecules were measured by tunable diode laser absorption spectroscopy (TDLAS) in pure HMDSO

TABLE 8.16
Examples of Monomers

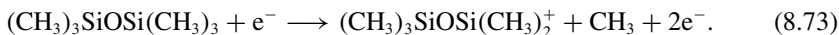
Silane	Vinyltrimethylsilane $\text{CH}_2=\text{CHSi}(\text{CH}_3)_3$ [334]
	SiH_4 [336]
	$(\text{CH}_3)_n \text{ Si } (\text{OCH}_3)_{4-n}$ [337]
	$\text{Si } (\text{OCH}_3)_4$ [338]
Siloxane	$((\text{CH}_3)_2\text{SiO})_4$ [339]
	$(\text{CH}_3)_6 \text{ Si}_2 \text{ O}$ [334,335,337,340,342]
Silazane	$(\text{CH}_3)_3 \text{ SiNHSi}(\text{CH}_3)_3$ [343,344]

TABLE 8.17
Ions Produced by Electron Impact Ionization of HMDSO, Appearance Energies and Partial Ionization Cross Section at 70 eV

m/z	Ion	AE [eV]	Cross Section at 70 eV (10^{-16} cm^2)
162	$\text{Si}_2 \text{ OC}_6 \text{ H}_{18}^+$	8.8 ± 1.3	0.017
147	$\text{Si}_2 \text{ OC}_5 \text{ H}_{15}^+$	9.6 ± 0.5	16.7
133	$\text{Si}_2 \text{ OC}_4 \text{ H}_{13}^+$	14.8 ± 0.9	0.24
131	$\text{Si}_2 \text{ OC}_4 \text{ H}_{11}^+$	15.8 ± 0.7	0.64
73	$\text{Si C}_3 \text{ H}_9^+$	16.3 ± 0.6	1.42
73	$\text{Si}_2 \text{ OH}^+$	25.3 ± 1.5	0.26
66	$\text{Si}_2 \text{ OC}_4 \text{ H}_{12}^{++}$	26.8 ± 0.6	1.49
59	$\text{Si C}_2 \text{ H}_7^+$	22.0 ± 0.6	0.96
52	$\text{Si}_2 \text{ OC}_2 \text{ H}_8^{++}$	32.6 ± 0.8	0.31
45	Si C H_5^+	21.4 ± 0.7	0.84
45	Si OH^+	21.4 ± 1.4	0.11
43	Si CH_3^+	28.4 ± 0.7	0.38
15	CH_3^+	14.7 ± 0.8	0.35
	$\text{Si}_2 \text{ O } (\text{CH}_3)_6$	Total 25.5	

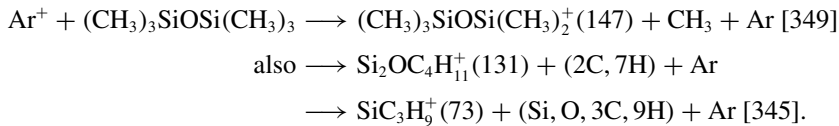
Source: Basner, R. et al., Electron impact ionization of organic silicon compounds, in B. Bederson and H. Walther, eds., *Fundamentals of Plasma Chemistry*, Vol. 43 of Advances in Atomic, Molecular, and Optical Physics, pp. 147–185, Academic Press, San Deigo, CA, 2000.

low-pressure RF plasmas [348]. The dominant electron impact ionization is the dissociative ionization

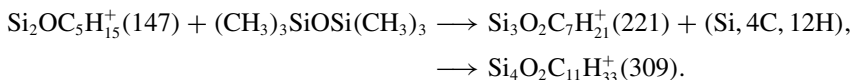


The separation of the methyl group is typical also for other silicon organic compounds [333]. Table 8.17 presents the measured appearance energies and partial ionization cross sections at 70 eV for the various ions produced by electron impact ionization of HMDSO [333].

HMDSO dissociation is reported by charge exchange reactions with Ar⁺ ions



Ion–molecule reactions between HMDSO fragment ions and HMDSO molecules could be identified, which lead to ions with higher mass (first step of formation of oligomers), e.g., [345], see also [347]



Besides the fragment ions of HMDSO, ions with mass numbers 163, 207, 221, 281, 295, 309, 353, 369, and 383 were observed in HMDSO RF discharges. ToF SIMS spectra [317,318] and pyrolysis spectra measured by a high-resolution double focusing mass spectrometer [347] of the plasma deposit show siloxane ions with mass numbers up to 295, $(\text{CH}_3)_3\text{Si}(\text{OSi}(\text{CH}_3)_2)^+$. Deposit formation will be essentially determined by ion molecule reactions.

Solubility of plasma polymers decrease with increasing energy input. Investigation using the positive column of dc glow discharge feeded by a mixture Ar/HMDSO show decreasing solubility in organic solvents of the deposit in relation to the residence time of the monomer in the active plasma (see Figure 8.51 [350]).

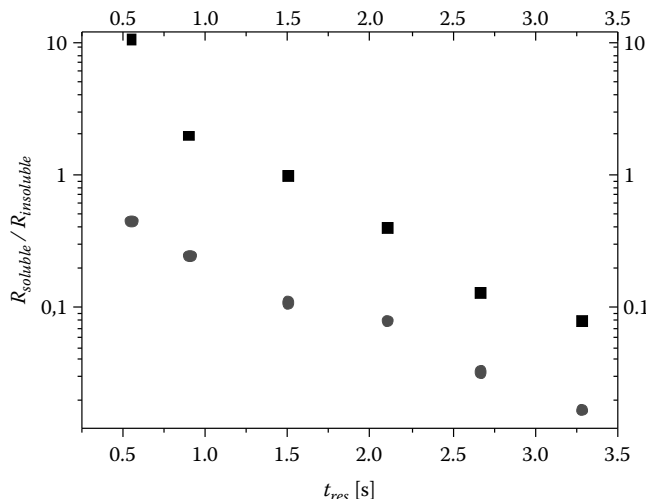


FIGURE 8.51 Relative solubility $R_{soluble}/R_{insoluble}$ of HMDSO films deposited in the positive column of an Ar HMDSO dc discharge (HMDSO-flow $0.9 \cdot 10^{-3}$ mol/h) for discharge currents of 30 mA (■) and 40 mA (●).

Plasma polymer films are proved for corrosion protection of metallic films, e.g., of Al mirrors inside head and fog lights of cars. An HMDSO plasma polymer deposit of 10 nm ($t < 30$ s) gives a good corrosion performance [351].

Si organic compounds as HMDSO and TEOS are used for plasma-assisted deposition of SiO_2 films in O_2 containing low-pressure MW- [352], RF- [353], and Helicon-plasmas [354]. Deposition of SiO_x films is possible by nonthermal atmospheric pressure plasma jet feeded by $\text{Ar}/\text{O}_2/\text{HMDSO}$ or octamethylcyclotetrasiloxane (OMTS) mixture [355,356].

Plasma polymerization is successfully used for production of gas-separating membranes because they are very thin, dense, and pinhole free. The gas separation of a membrane is based on

1. Differences of solubility and diffusion of gases inside the polymer
2. Differences of the diffusion of gases through small pores

The gas separation properties of composite membranes consisting of cellulose acetate ultrafiltration membranes or polyamide microfiltration membranes as substrates coated by hexamethyldisiloxane plasma polymer are investigated by [357].

8.2.4.1.2.4 Composite Films

Plasma polymerization allows the formation of composite materials consisting of a plasma polymer matrix and metals, or other materials as TiO_2 [358,359] (commercial nanoparticles were coated) or MoS_2 [360] (MoS_2 is sputtered). Polymers with dispersed metallic nanoparticles are of interest for optical, electrical, magnetic, and catalytic applications [361]. Biomedical applications are in discussion [362] as well as for colored decorative coatings. Film color depends on materials, particle concentration, size, and shape [310], e.g., Cu in C/F polymer: bright yellow or orange, Au in C/F polymer: blue or pink [363].

Composite metal polymer films are investigated since a long time, see [364]; they may be prepared in several ways [365]:

- Application of metal-organic compounds as monomer, e.g., tetramethyltin [366,367], see also [368]
- Evaporation of metal from independent source during the plasma polymerization process
- Sputtering of metal and polymer targets, plasma polymerization of the polymer sputter products, and embedding of metal
- Sputtering of a metal target combined with plasma polymerization
- Reactive plasma etching of metal simultaneous with plasma polymerization
- Nanocomposite deposition system consists of sputter source with nanoparticle generation by gas phase condensation, which flow into the PECVD source for matrix material deposition [369]

Various metals as Au, Ag, Ni, Cu, Al, Te, W, Bi, Ti, Mo, Ge, and fluorocarbon monomers like CF_4 , C_3F_8 , hydrocarbon monomers as C_2H_4 , C_4H_{10} , C_6H_{14} ,

organosilicon monomers like hexamethyldisiloxane were used in the deposition experiments. Ar is admixed for metal sputtering. Plasma sources as magnetrons and capacitively coupled rf discharges were applied as reactors.

Deposition of polysiloxane thin films containing Ag particles is reported by [362]. A combination of silver sputtering and plasma polymerization of HMDSO is applied. An asymmetrical rf (13.56 MHz) discharge was used with an Ag target at the powered electrode operating in an Ar ($p_{\text{Ar}} = 5.32 \text{ Pa}$) and pulsating HMDSO flow ($p_{\text{HMDSO}} = 0.27 - 1.06 \text{ Pa}$). Pulsation of the HMDSO flow varies the cathode coverage with polymer deposit. Energetic ion bombardment of the powered electrode sputters plasma polymer deposit and silver. A composite of polymer and silver is deposited on the substrate. Ag volume fraction near 50% is observed for low HMDSO flow rates; high flow rates show a disappearing Ag fraction. Small spherical metal grains (diameter between 2 and 10 nm) are observed for low-volume fractions (0.25); higher fractions show nonspherical Ag clusters of 30–100 nm separated by thin polymer domains (see Figure 8.52). Such silver-containing materials are important for biomedical applications, e.g., for prevention of biofilm formation.

The deposition of Pt-containing composite films using $\text{C}_2\text{H}_4/\text{Ar}$ mixture ($\sim 1:100$) in a asymmetric capacitively coupled 13.56 MHz discharge at 70 mTorr is investigated by Dilonardo [361]. The Pt target is positioned at the small powered electrode, the composite film growth on a polished Si-substrate on the grounded electrode. The Pt-atomic concentration increases with discharge power, but decreases with increasing C_2H_4 flow rate. The Pt-content can be continuously varied between $\sim 100\%$ and $\sim 0\%$ by the deposition conditions. The nanocrystalline clusters are embedded in the polymer matrix; their size varies with the Pt-content.

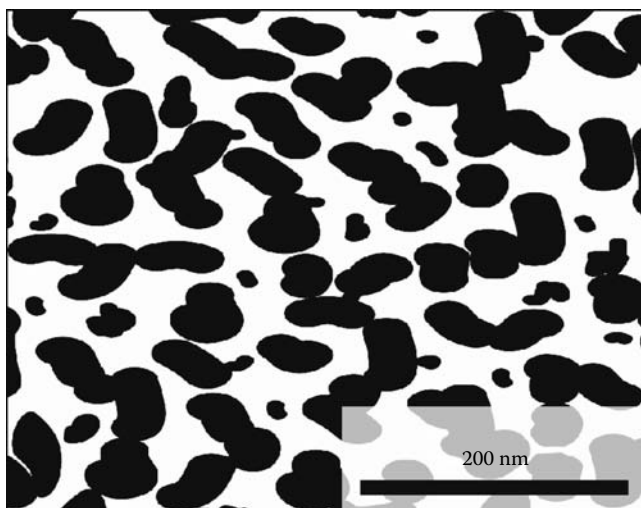


FIGURE 8.52 Large nonspherical silver clusters in an HMDSO-plasma polymer matrix. (From Despax, B. and Raynaud, P., *Plasma Process. Polym.*, 4, 127, 2007.)

8.2.4.2 Inorganic Thin Films

In the context of plasma chemistry, inorganic thin films mainly represent simple binary or ternary compounds whose ideal crystal structure and stoichiometry are known and whose thermal stability is normally better than those of organic or polymer materials. Thin films are thin material layers ranging from nanometer to micrometer scale, which can improve or totally change the material properties of substrates if one only examines the mutual effect between outermost layers and the outside world. For example, the corrosion and wear stability of bridgework can be improved by thin films of chemical inertness and abrasiveness, but the mechanical bridgework stability remains unaffected. Benefit and applicability of thin films depend on chemical, physical, and crystallographic properties of deposited material and also on the used deposition methods. The methods chemical vapor deposition (CVD) and physical vapor deposition (PVD) need thermal energy to produce films from reacting materials.

Both of these techniques can also be used if the energy necessary for producing reacting gases is supplied by plasma. These are the so-called plasma-enhanced chemical vapor deposition (PECVD) and plasma-enhanced physical vapor deposition (PEPVD).

8.2.4.2.1 Basic of Plasma-Enhanced Vapor Deposition

Figure 8.53 shows the basic principles of plasma-enhanced vapor deposition processes.

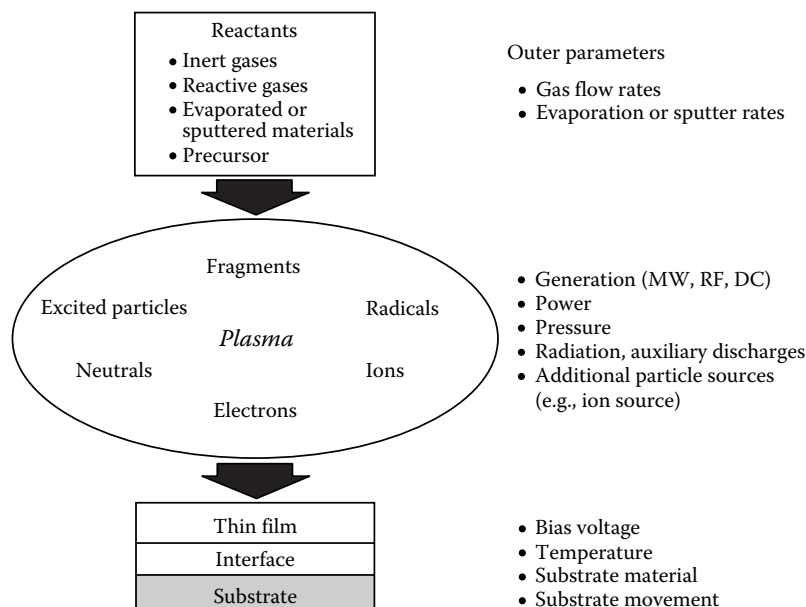


FIGURE 8.53 Basic principle and parameters in plasma-enhanced vapor deposition processes.

The reactants are gaseous. They will provide directly in the recipient as inert gas, reactive gas, precursor gas, or produced in the reaction chamber by sputtering process. The electrical source to form the plasma is an electric field (DC, MW, RF), which can act directly on the charged particles only. The plasma state can be influenced by the power of external energy source, by working pressure and auxiliary discharges, or additional ion sources. The plasma-activated material arrives at the substrate to form the films or to modify the surface layers of the substrate material.

Production and modification of thin inorganic films include PECVD and PEPVD (often used as sputtering deposition), implantation, and surface modification processes [370].

In case of PECVD, all reactants are gases or liquids. Precursor compounds or reactive species from such volatile, chemically stable feed compounds will be formed by energy transport of the electrons in the plasma, i.e., electron impact decomposition and electron impact ionization initialize the chemical reactions. The reactive chemicals can lead to deposition, which finally rules the layer growth. Because PECVD often requires reactions between gas-phase precursor components, the gas pressure in the PECVD discharge cannot be too low. Usually the working pressures in these systems are 0.1–10 mbar, which is considerably higher than the pressure in reactive sputter deposition processes. The surface temperature in PECVD is low, about 500°C, whereas the nonplasma CVD activated thermally requires usually much higher temperatures. In PECVD, typical values for plasma density are in the range of 10^9 – 10^{12} cm $^{-3}$ and the ionization degrees are 10^{-7} – 10^{-4} .

In PEPVD as well as in PVD, at least one chemical agent is solid and has to be transformed into the gas phase. This can be done by evaporation or by sputtering.

Physical sputtering implies that atoms sputtered from the target material are directly transported and deposited without chemical reactions to a substrate. In reactive sputter deposition, a feed gas is supplied to the plasma deposition system. Molecules of the feed gas form active species in the gas phase, producing chemically active species, which react with the target material during ion bombardment. The film deposited on the substrate includes not only material of the ion bombarded target but also compounds formed due to the reactive gases.

8.2.4.2.2 Types of Plasma Chemical Reactions

Chemical reactions in plasma-enhanced vapor deposition processes can take place in the plasma volume (reaction type 1), directly on the substrate surface (reaction type 2) or by complex chemical transformation reactions on the substrate surface (reaction type 3) (see Figure 8.54).

Unlike the chemical reactions of type 1 that are well described for selected plasmas [370–372], chemical reactions of type 2 are not well known yet. One reason for this is the difficulty to perform direct experimental verifications for such plasma surface processes. It is assumed that deposition material arrives at the substrate mostly in atomic or molecular form (see Figure 8.54). The atoms or molecules diffuse around the substrate with a motion determined by its binding energy to the substrate and is influenced by the nature as well as the temperature of the substrate. After a certain time, the particles will either evaporate from the surface or will join with another diffusing particle to form a doublet, which is less mobile but more stable

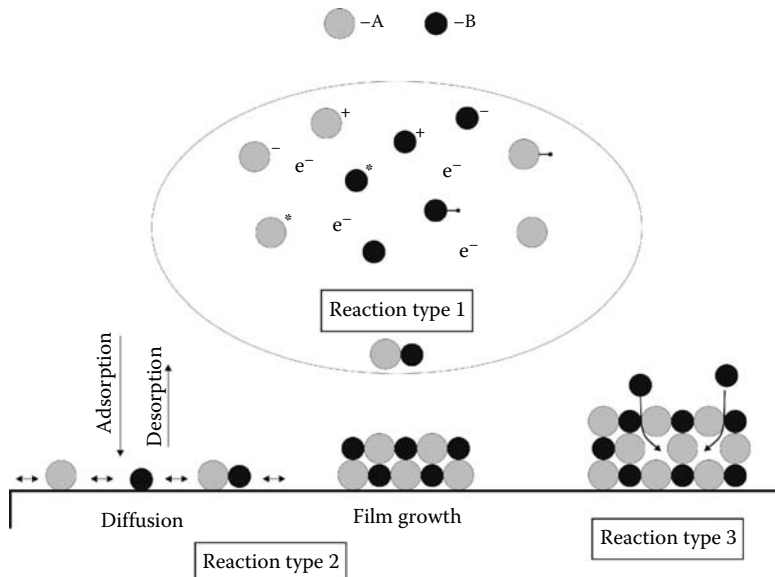


FIGURE 8.54 Chemical reactions in plasma-enhanced vapor deposition processes.

than the single particle. The doublet will be joined by other particle to form small nucleus. Via island-growing processes and coalescence of the growing nuclei, the film grows continuously [373]. In recent times, chemical reactions in solid surface layers as a response to external variable plasma parameters (reaction type 3) have been investigated [374–376].

Concerning the applications of deposited layers, there are remarkable differences between solely thermal and plasma-ruled processes. Coatings deposited with plasma-enhanced deposition processes are not limited to equilibrium compositions; they are more often the environmentally cleaner processes, and the deposition temperature is lower than in thermal stimulated film growth.

Considerable interest has been focused on deposition of inorganic layers for applications in integrated circuitry production, optics, solar energy conversation, and cutting tools. The importance of plasma technology in this field is given by the deposition of layers with superior short range order. Microcrystalline and nanocrystalline layers are a unique product of plasma processes. Two groups of applications will be discussed in more detail.

8.2.4.2.3 TCO Films

Over the past years, there has been a growing interest in both fundamental research and device applications based on transparent conductive oxides (TCOs). This unique class of fascinating materials [377] is gaining a variety of applications in the fields of solar cells, gas sensors, organic light-emitting diodes, liquid crystal, and high-definition displays, as well as for electrochromic and smart windows. A well-known TCO layer is indium tin oxide (ITO).

These products have one thing in common; they need to combine opposing material properties, namely, optical transparency and metallic conductivity, in order to produce

1. Spectral-selective characteristics
2. Transparent electrodes

Usually, transparency and metallic conductivity are mutually exclusive. There are two possibilities to overcome this contradiction. Conductive and transparent coatings can either be a multilayer arrangement based on thin metal layers or a homogeneous TCO coating [378]. In contrast to metallic multilayer, TCO films exhibit good mechanical, chemical, and thermal stability.

8.2.4.2.3.1 Physical Properties of TCO Materials

TCOs are degenerately doped wide-gap semiconductors. An important feature to characterize a TCO layer is the resistivity. To achieve a low resistivity, either the thickness of the TCO, the carrier concentration, or the electron mobility can be increased (n-type). Thickness and electron concentration have a direct effect on the optical properties of the material. The absorption in the TCO increases with increasing layer thickness (Beer's law).

The electron density influences the absorption of the TCO in two ways. The effective optical band gap of a degenerate semiconductor is widened with increasing electron concentration because of the high occupation of the lowest states in the conduction band by electrons excited from the shallow donor states, so that absorption into these conduction band states is forbidden by the Pauli principle (Burstein–Moss shift [379]). This gives a lower transparency limit, which is in the order of 350 nm.

For long wavelength light, the absorption by free carriers limits the transmittance of TCOs. The absorption and reflection of an electron gas increases, and the transmission decreases for frequencies lower than the plasma frequency ω_p

$$\omega_p^2 = \left(\frac{2\pi \cdot c}{\lambda_p} \right)^2 = \frac{n_e e^2}{\epsilon_{HF} \epsilon_0 m^*}, \quad (8.74)$$

where

ϵ_{HF} is the high-frequency dielectrically constant

m^* is the effective mass, n_e is the carrier density

Equation 8.74 describes the change from the dielectrical behavior in the visible region to the metallic characteristics in the near IR. This so-called plasma edge for TCOs usually lies in the near-infrared region (800–1 100 nm). A higher electron density allowing a higher conductivity at the same time shifts the plasma edge to shorter wavelengths.

Thus, increasing the electron mobility is the only way to achieve a higher conductivity of the TCO material without reducing its long wavelength transmittance. In general, apart from the effective mass resulting from the band structure of the material, the mobility of TCOs is limited by scattering at grain boundaries in the

polycrystalline material, at (ionized) impurities, and at phonons. The influence of grain boundary scattering decreases with increasing grain size due to the lower grain boundary density. Phonon scattering is often negligible compared to (ionized) impurity scattering [380]. Ionized impurity scattering is the dominant effect limiting the conductivity of the best highly doped TCOs reported in the literature [380]. Although the obtainable electrical properties are strongly dependent on the deposition method as well as the deposition conditions, TCO films with the low resistivity of about 10^{-4} Ωcm can only be prepared with impurity-doped binary compounds. This resistivity is still remarkably higher than the values for typical conductive materials like Ag or Cu, which is about $2 \cdot 10^{-6}$ Ωcm .

8.2.4.2.3.2 TCO Materials

Classical TCO layer systems are based on semiconducting oxides like indium-oxide (In_2O_3), tin-oxide (SnO_2), zinc-oxide (ZnO), and their compounds. These compounds exhibit high transmittance in the visible spectral range and high reflectance in the infrared. Moreover, they are convenient for a high degenerated n-type doping due to their electronic structure [381,382]. High carrier concentrations of the order of $n_e = 10^{20}\text{--}10^{21} \text{ cm}^{-3}$ can be obtained by incorporation of higher or lower valent cations or anions into the host lattice of the basic oxides. In ZnO , Zn^{2+} -ions can be substituted by Al^{3+} - or Ga^{3+} -ions. One electron of the three valent cation contributes to the conduction band. Feed materials and deposition conditions should be carefully coordinated to prevent segregation between host material and the as much as possible high concentrated doping material. The oxidation process of the doping material is thermodynamically in favor in comparison to the insertion by substitution. In case of the $\text{ZnO}:\text{Al}$ system for Al_2O_3 , the free enthalpy ($\Delta_R G = -1688 \text{ kJ/mol}$) is much lower than the free enthalpy for ZnO ($\Delta_R G = -363 \text{ kJ/mol}$) for instance.

This means that high Al concentrations as well as high partial pressures of the reaction gas oxygen cause the oxidation of Al to Al_2O_3 and form insulating material in the deposited films and must be prevented. On the other hand small reactive gas concentrations form substoichiometric film materials that act as absorbent medium. Besides the n-doping by cation substitution, an n-doping by anion substitution is possible. O^{2-} ions can be replaced by F^- ions, for instance, and therefore an additionally unbounded electron per exchanged ion is released into the conducting band. Nevertheless, TCOs with the best optical and electrical properties were manufactured by cation substitution because substoichiometric films have the tendency to form preferable dopant oxides, and halogenoid-substituted films have lower carrier concentrations.

Apart from the dopant solubility in the host lattice and the free enthalpy, the doping material should cause only small lattice distortion and the deposition procedure should form TCO films with only small amounts of imperfections (interstices, dislocations, grain boundaries) [383,384].

Figure 8.55 shows the change in minimum resistivity of typical impurity-doped basic binary compound TCO films reported in recent years [385].

The best values will be reached by doped In_2O_3 and ZnO . The obtained minimum resistivity of doped ZnO films is still decreasing, whereas those of doped SnO_2 and In_2O_3 films have essentially remained unchanged for more than 20 years. ITO is the

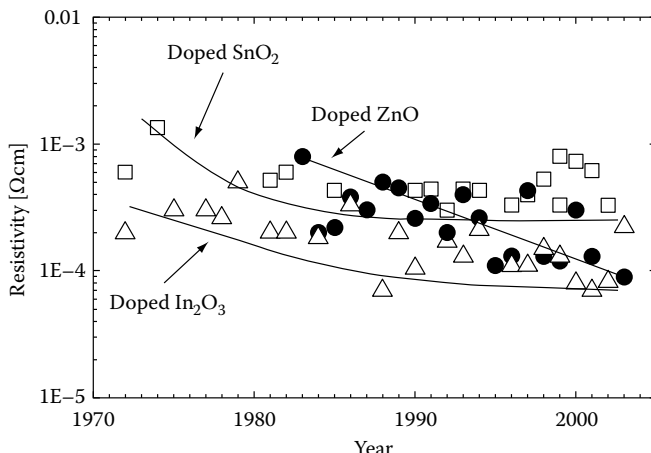


FIGURE 8.55 Reported resistivity of impurity-doped binary compound TCO films, 1972 to present. (From Minami, T., *Semicond. Sci. Tech.*, 20, S35, 2005.)

major material for TCO at present. However, it has the problem of limited resources. Indium metal is the by-product of zinc metal. At present, ZnO is a suitable material for production of large-sized devices such as flat panel displays and solar cells because the abundant sources and the low costs of Zn metal are major advantages in industrial production.

For manufacturing technology, further demands have yet to be established. So, growth methods of low costs, high throughput, and low-energy consumption are required.

8.2.4.2.3.3 Plasma-Enhanced TCO Film Deposition Techniques

Plasma methods are characterized by a set of free parameters to optimize the deposition process. Plasma power, working pressure, oxygen partial pressure, and substrate bias can influence the deposition rate and so also the film thickness [386], the film stoichiometry, the defect concentration, and, therefore, the optoelectronic properties. Target materials are either oxide ceramics or metals and metallic alloys, respectively. A further advantage of plasma-enhanced deposition techniques is the low thermal load for the substrates as mentioned before; so TCO films can be deposited on organic foils too.

An attractive technique for the deposition of TCO material is the so-called reactive sputtering. [387,388], where metallic or ceramic targets are sputtered in an atmosphere of argon admixed with the reactive gas oxygen. The gas phase chemically active species are produced by dissoziation of the feed gas ($O_2 \rightarrow O + O$) introduced into the discharge. The sputtering deposition of ZnO:Al explains the advantages of reactive sputter method. After ZnO:Al target physical sputtering, Zn, Al, and O atoms approach the substrate. Zn and Al atoms stick to the substrate surface, while O atoms partially form molecular oxygen, leaving the deposited film with a deficiency of oxygen. To restore the ZnO:Al stoichiometry of the deposited film, O_2 is added as a feed gas to the discharge, which leads to the additional formation of O atoms and

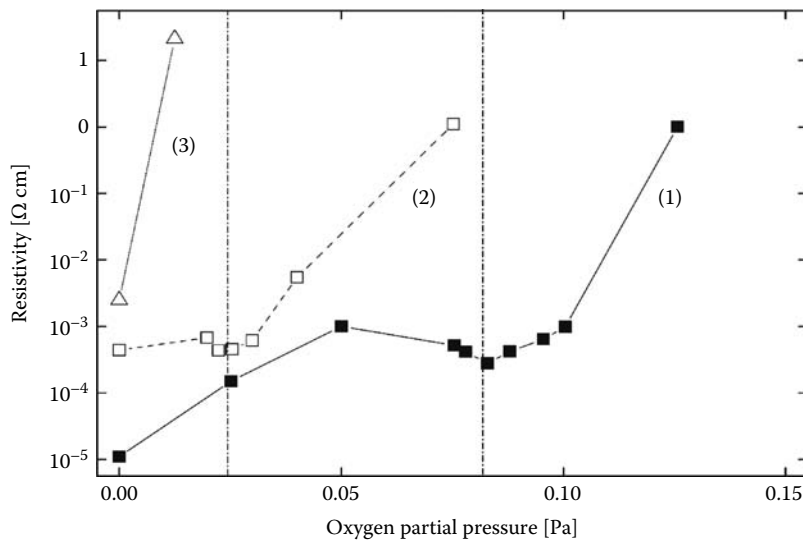


FIGURE 8.56 Resistivity vs. oxygen partial pressure for different sputtering modes, (1) dc plasma excitation from metallic target Zn:Al (2) rf plasma excitation from metallic target Zn:Al (3) rf plasma excitation from a ceramic target ZnO:Al₂O₃. (From Ellmer, K., Magnetron discharges for thin film deposition, in R. Hippler et al., eds., *Low Temperature Plasma*, Vol. 2, p. 675, Wiley-VCH, Berlin, Germany, 2008.)

their incorporation into the growing film. The feed gas is able to control oxygen concentration in the film. Therefore, even pure metallic Zn:Al targets can be used for reactive sputter deposition.

Obviously, the reactive sputtering process requires efficient tools for process control [389] since only within a narrow parameter window the desired layer properties can be obtained. In Figure 8.56 the influence of the oxygen partial pressure on the resistivity of ZnO:Al films is presented. DC and RF sputtering systems as well as metallic and ceramic targets were investigated [390]. If the oxygen partial pressure is small, the resistivity as well as the optical transparency is small too. However, increasing oxygen partial pressure causes the desired transparent ZnO:Al films with low resistivity. Further increasing oxygen flow improves the transparency of the films but produces a sharp rise in the resistivity due to the nearly complete oxidation of Zn to ZnO and Al to Al₂O₃. These films contain a mixture of insulating phases. The same experiments performed with rf-excitation show a similar behavior concerning the deposition rate and the resistivity, but the discharge voltage does not exhibit step-like curves. This is due to the fact that in the rf-discharge, the delivery of secondary electrons is nearly independent of the target material.

8.2.4.2.4 Hard Coatings

8.2.4.2.4.1 Materials and Concepts for Hard Coatings

Hard coatings have been successfully established as wear protection on cutting tools. Effectiveness and endurance of cutting tools can be improved remarkably by

protection layers with a thickness of only a few micrometers. Moreover, decorative wear protection is applied to, for example, bath armatures, spectacle frames, or other article, of daily use. Hard coatings can be deposited by CVD, PECVD, or PEPVD techniques. Applied materials, deposition parameters, and microstructure determine the properties of the coatings.

Hard materials are not a special class of chemical compounds. They are defined by properties like high hardness, high melting point, wear, and chemical resistance. Nitrides, borides, and carbides of the elements of the groups 4–6 (e.g., Ti, Cr, W, Zr) are the most interesting layer systems.

Protective coatings often require properties that are hardly realizable at the same time. The main aspects for developing hard coatings are improvements in hardness, hot hardness, strength, toughness, and resistance to crack ignition and crack propagation, adhesion, residual stress, resistance to oxidation and corrosion, and tribological behavior. These properties cannot be realized with one material. Materials showing good adhesion to substrates are highly reactive at their surfaces too. This promotes oxidation and corrosion. Hard materials often have low toughness. These considerations lead to the development of thin film concepts like multilayer and gradient layer where several materials can be combined.

The choice of the materials plays the most important role in the development of hard coatings. There are two concepts to forecast material properties, the structure–property concept and the bond classification. Both concepts cannot predict correctly desired material properties. According to the character of the chemical bindings, hard materials can be divided into three groups (see Figure 8.57). There are metallic, ionic, and covalent hard materials. Any of these groups has advantages and disadvantages. Covalent materials as C and BN are extremely hard but only in the diamond structure type. The hexagonal crystal structures of C and BN forms soft materials. Both represent the transition between covalent and metallic bonds. Ionic materials as corundum are chemically stable and therefore show low interaction with other materials. These materials are mainly suitable for surfaces.

Multilayer films are one possibility to fulfill the complex requirements of materials for hard coatings. A layer material with good adhesion will be chosen for the first layer and a material with lower adhesion for the last layer. The properties of the multilayer system usually depend on the number of layers. Film properties like toughness, hardness, and residual stress do not reach their optimum at the same layer number. For a special material combination, an optimum range exists, which gives the best protection properties [391,392]. For coating materials like TiN, TiC TiAlN, and TiB₂, the layer number is some 100 single layers for a coating with a thickness of 5 µm. Such multilayer systems can be deposited by sequential sputter techniques. Because of the low thickness of the single layers, the grain growth is reduced in multilayer systems. This has a positive influence on crack splitting, interface toughening, and stress relaxation.

In multilayer systems, usually materials with similar bonding characteristic are combined. Examples are TiN/TiAlN and TiN/AlN. These multilayer coatings have been deposited by PEPVD techniques [393,394]. The combination of hard materials with solid lubricants like C (graphite) or MoS₂ leads to coatings with very low friction coefficients [395]. The edge life of cutting tools is increased by a factor of two with

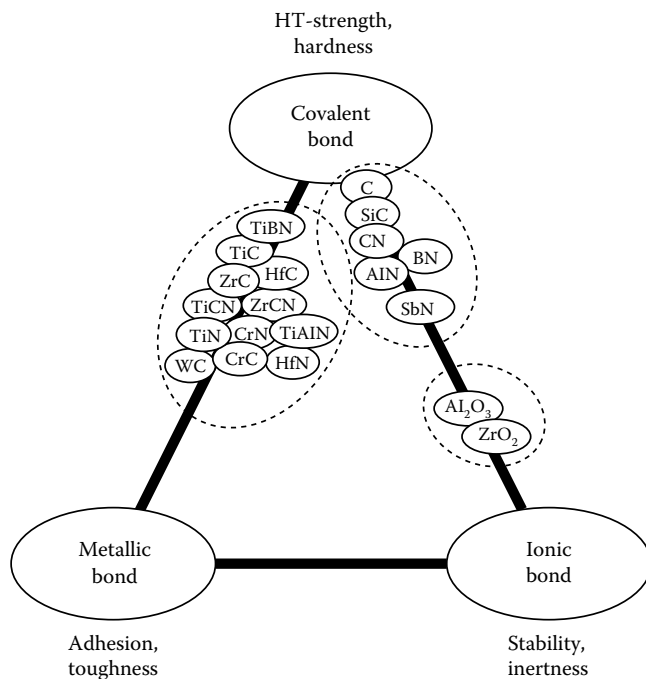


FIGURE 8.57 Hard materials in the bond triangle (HT = high temperature).

the change from single TiN or TiC layers to TiN/TiC multilayer coatings. With the introduction of the thin AlN layers between TiN and TiC, the life time will be further increased [396]. Other concepts for tribological applications are graded coatings, multiphase layers, and nanostructured coatings.

8.2.4.2.4.2 Trends in the Deposition of Hard Coatings

Today, coated hard metal tools are developed for every imaginable application of metal cutting. The market for hard metal tools is dominated by CVD-coated tools. Whereas about 60% of hard metal tools, which tolerate the high deposition temperature of 1000°C, are coated by high temperature CVD, only 10% are coated by PEPVD. The lower substrate temperature in case of PEPVD (<500°C) is well suited to high-speed steel (HSS) tools. HSS tools will be exclusively deposited by PEPVD processes (25%) [397]. Because of the diffusion of coating material into the substrate at high deposition temperature in case of CVD, the adhesion between coating and substrate is usually better than in the case of PEPVD.

Nevertheless, global industrial trends like high-speed machining, dry machining, dry forming, minimal use of lubricants, and elimination of toxic by-products are all supported by PEPVD technology. PEPVD has got some advantages when compared to CVD. The deposition temperature is remarkably lower, preserving hard metal edge toughness. This is an advantage for the deposition of edges. Cutting tips deposited with PEPVD methods can be sharp since the residual stress in this coating is compressive compared to tensile for CVD coatings. Therefore, PEPVD coatings are more suitable

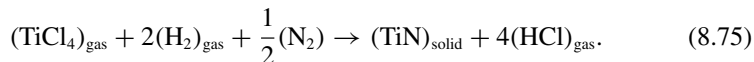
for milling and where sharp edges are needed, e.g., finishing-cut operations. The grain microstructures are finer and the microhardness is higher. Coatings deposited with PEPVD are not limited to equilibrium compositions. Innovations in the coating system process, e.g., incorporating of pulsed dc power, have evidently solved the PEPVD process difficulty to deposit insulating coating materials [398]. Isolating coatings with appropriate properties can be deposited by magnetron sputtering in a stable regime in pulsed mode only [399].

Because of the lower pressure in case of PEPVD, the deposition of three-dimensional substrates is more difficult than in the case of CVD. PEPVD processes are highly suitable for multilayer hard coatings. Unfortunately, multilayer designs are still uncommon.

8.2.4.2.4.3 Plasma-Enhanced Deposition of TiN and TiC

One of the all-purpose deposition materials for wear protection is TiN. TiN belongs to the covalent bond type, but crystallizes in the rock-salt (NaCl) structure type. However, its properties are dominated mainly by the defect structure. Lattice distortions and microcrystallinity enhance the hardness of TiN layers.

Titanium nitride can be formed by conversion of titanium chloride in plasma in the presence of hydrogen and nitrogen, or ammonia (NH_3). The formation of titanium nitride from interacting with hydrogen and nitrogen is described by



By the application of NH_3 , TiN can be deposited according to



If the deposition is supported by a plasma, the deposition temperature can be reduced to about 500°C [400] in comparison to 900°C in normal CVD. A deposition temperature of 300°C is sufficient if a metalorganic precursor like tetrakis-(dimethylamido)titanium is used in PECVD.

For PEPVD of TiN, different methods like low-voltage electron beam, cathodic arc, hollow cathode arc, and reactive magnetron sputtering can be applied. Especially magnetron sputtering has been a well-approved coating technique. The deposition of appropriate TiN coatings requires a plasma density that cannot be attained with conventional DC magnetrons. For hard TiN coatings, bias currents of about 10 mA/cm² are essential. Higher ion current density at the substrate improves the hardness of reactive-sputtered TiN layers. An increase of the ion current density on substrates in magnetron sputtering can be achieved by additional discharges, such as the usage of unbalanced magnetrons [401] or pulsed magnetron sputtering [399]. In case of unbalanced magnetrons, deposition rates of 500 nm/min were reported. Normally, an external heating of the substrate is not necessary. Nevertheless, the substrate will be heated by the plasma itself. In case of a 5 μm layer, the substrate reaches temperatures between 250°C and 300°C [402]. In case of pulsed magnetron sputtering, frequencies up to 100 kHz are used. This technique allows the deposition of TiN coatings with remarkable improved properties at 450°C.

Another typical PECVD process is the deposition of TiC. Widely used is the reaction of titanium tetrachloride with methane in a hydrogen atmosphere



Besides methane, other carbon sources like propane, heptane, and toluene are applied. The pressure varies between 1 mbar and normal pressure. Typical process times are 2–3 h. Morphology, structure, and chemical composition are estimated by the substrate, the deposition temperature, the pressure, and the precursor for C. Two independent chemical reactions take place. $TiCl_4$ will be reduced to Ti by hydrogen and reacts with C to form TiC. The reactions will be limited by the supply of reactive C species. The partial pressure ratio of the precursors $CH_4/TiCl_4$ estimates the amount of C in the gas atmosphere. It should be about one for substrates that do not contain Fe, Co, and Ni. Since these elements act as catalysts for the decomposition of methane, the ration can be increased to 3–8 if the substrate contains these elements [403]. The substrate temperature is between 850°C and 1050°C in normal CVD technique and can be reduced to about 500°C in PECVD processes [402].

8.3 PULSED ELECTRICAL DISCHARGES IN LIQUIDS

The topic of (pulsed) electrical discharges generated in water, aqueous solutions, and liquids is very broad, and it is impossible to treat this topic in its full depth and full breadth adequately in a single chapter. Therefore, this chapter makes no attempt to provide a comprehensive coverage of all aspects relating to the physics and chemistry of pulsed electrical discharges in liquids. Instead, we will give a brief overview of the basic mechanisms involved in the generation of pulsed electrical discharges in a liquid. Subsequently, we will describe some specific experiments aimed at elucidating the mechanisms that lead to the generation of reactive species (OH , O_3 , O , H_2O_2) by a pulsed discharge in water [404–411]. As an example of the technological applications of pulsed electrical discharges in liquids, we will discuss the disinfection and decontamination of the water using pulsed electrical discharges, a process that has the advantage that it does not require the transfer or disposal of chemicals, which is a necessity in conventional disinfection processes using O_3 or Cl_2 . An extended review of nonthermal plasmas in liquids and in contact with liquids is given by Bruggeman and Leys [412].

8.3.1 Background

The generation of a discharge in water requires electric field strengths of about 2 MV/cm (depending on the conductivity of the water) and proceeds through a reduction in the local density by field or heat-related mechanisms (i.e., by forming gaseous bubbles in the liquid phase), thus creating conditions favorable for the development of electron and ionization avalanches [404,413]. This process consumes a significant amount of power and converts a large fraction of the input energy into heat. Producing electrical discharges in water in the presence of externally introduced gas bubbles improves the energy balance with more energy used to produce chemically active

species [414–416]. The discharge is initiated in the gas bubble, so that no energy has to be consumed to form the bubbles in the liquid. Operating at electric field strengths of about 30 kV/cm limits the discharges to the gaseous bubbles. It is also possible to create a discharge above the water surface by placing one electrode outside the water [410,411], in which case the discharge occurs mostly in the gas phase above the water.

Different mechanisms are possible for creating an electrical discharge in the gas bubbles. Investigations using mesh and wire electrodes report discharges that initiate at points of contact between the wire, the solid insulation, air, and possibly water and proceed along the surface of the bubble [415]. Some experiments have used bubbles passing through the water relatively far from the electrodes. In other arrangements, bubbles spend long periods of time attached to the electrodes and the bubble may be in contact with one or both electrodes. In cases where the gas bubble is in direct contact with both electrodes, the discharge forms via an electron avalanche, and a transition to an arc must be prevented by the outside electrical circuit or by using short voltage pulses. If water covers one or both electrodes, the discharge current is limited, particularly for short-voltage pulses. As a consequence, DBDs or corona discharges may be expected [405,410,411,413–417]. The study of discharges in bubbled water using wire-to-plane, wire-to-wire, or mesh electrode configurations is complicated by the flow of bubbles [418,419]. The discharge can occur in various bubbles at the same time and hence the field in the bubbles is difficult to estimate and the properties of the discharge are difficult to study. Single-bubble systems allow detailed studies of the discharge process in the bubble, which is stationary and can be subjected to repeated voltage pulses.

8.3.2 Experimental Systems

Two experimental systems will be discussed here briefly. The first system allows a discharge to be created in a single stationary bubble in water [416]. The system consists of a water chamber constructed from PVC to reduce the impedance, a Blumlein pulse-forming network, a gas delivery system, and various diagnostic tools. The chamber has three ports (for the fiber-optic cable, the needle electrode with gas inlet, and the movable disk electrode) and two windows at 90° to each other (see Figure 8.58a). A gas flow controller delivers gas to a microsyringe, which is used to form a gas bubble at the tip of a hypodermic needle inserted into the water chamber. The amount of gas injected can be controlled up to a microliter, and a pressure release valve ensures that the overall pressure remains at about one atmosphere. The syringe is used to control the size of the bubble. A digital camera is used to record the size of the bubble and a UV transparent fiber is used to collect optical emissions from the bubble. Argon and oxygen bubbles have also been used in this study.

This experimental arrangement allows the study of a single stationary bubble with just the tip of the needle extending into the bubble (see Figure 8.58b). The hypodermic needle, which is mostly covered by the insulating material of the chamber with only a 0.5 mm tip protruding into the bubble, serves as the negative electrode. The second

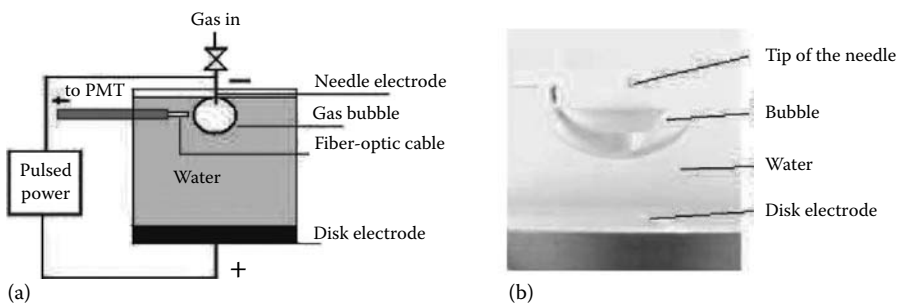


FIGURE 8.58 (a) Schematic diagram of the experimental arrangement showing the bubble around the needle electrode with the disk electrode immersed in water. Gas is fed through the needle and a stationary bubble forms around the tip of the needle. (b) A photograph of the bubble and the electrodes.

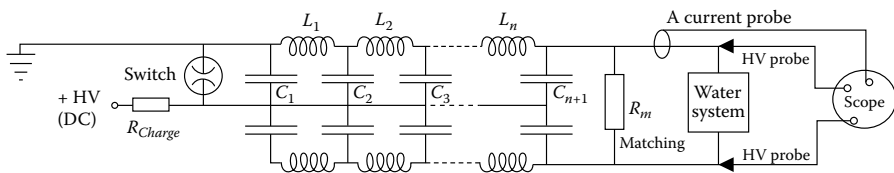


FIGURE 8.59 Electrical system: DC power supply, thyratron switch, Blumlein pulse-shaping network with 35 W matching resistor (R_m), and voltage and current probes.

electrode is a stainless steel disk. The distance between the electrodes can be varied between essentially 0 and 25 mm.

The electrical power delivery system consists of a dc high-voltage power supply and a pulse-shaping network (Figure 8.59). A 60 kV, 10 mA power supply charges the pulse generator. A thyratron switch delivers the voltage pulse. The thyratron is triggered manually delivering single pulses at intervals from 30 s to several minutes. The Blumlein pulse-shaping network delivers a 1 ms rectangular pulse in the 3–30 kV range. Optical emissions of the OH band (309 nm) and the Ar lines (765 nm) from inside the bubble are sent to a cooled photomultiplier tube (PMT) with a temporal resolution of 2 ns. All current, voltage, and PMT data are recorded by a digital oscilloscope. De-ionized water was used with a conductivity of 1.2–1.5 mS/cm, a pH of 5.0, and a temperature of 21°C. Experimental results reported here include measurements of optical emissions and the discharge current for various sizes of Ar and O₂ bubbles.

The second experimental setup shown in Figure 8.60 is a reactor that was developed for water disinfection applications. This system includes a gas flow controller and water pump. The power supply employs two rotating spark-gap switches to generate high-voltage pulses and a 40 kV DC power supply. This reactor employs a set of mesh electrodes in a plane-to-plane configuration connected sequentially either to high voltage or to ground. A forced oxygen bubble flow passes vertically through the electrode system along with the flow of contaminated water from a

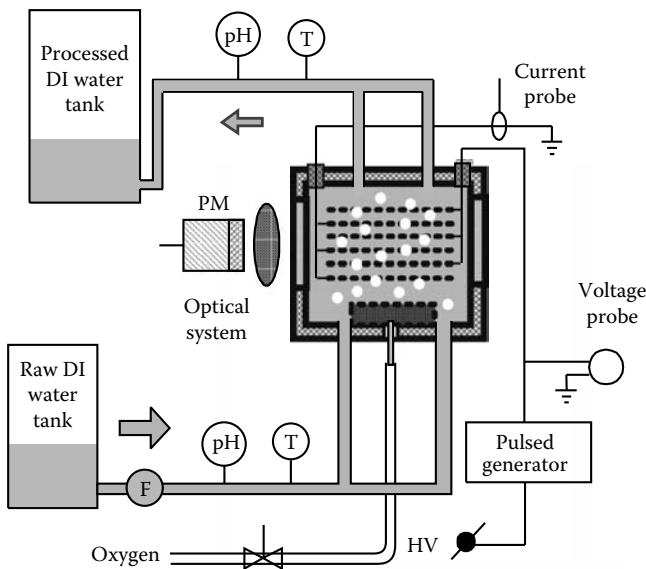


FIGURE 8.60 Schematic diagram of a water treatment system.

raw water tank. The treated water is collected in a reservoir. In addition to monitoring the current, voltage, and optical data, the system is also equipped with diagnostics that allow the measurement of radical concentrations in the water and the concentration of selected contaminants in the water prior to and after plasma treatment.

8.3.3 Selected Experimental Results

Experiments using the single-bubble system (Figure 8.58) were conducted with Ar and O₂ in bubbles of various sizes and several distances between electrodes. Saturated water vapor is an important component in all bubbles, since the gas is injected into the water and the bubble resides in the water during the entire experiment. Sharp current and light emission peaks are observed in all experiments except for those situations when a gas bubble covers the entire gap between the electrodes. In this case, the discharge occurs essentially in an atmospheric pressure gas between two metal electrodes and has the electrical signature of a spark (increasing current and decreasing voltage). All situations where the bubble does not cover the entire space between the two electrodes resemble a DBD with the needle electrode surrounded by a mixture of gases at atmospheric pressure and the disk electrode covered by a layer of water. Typical current, voltage, and optical emission pulses observed for voltages above a certain threshold, which depends on the electrode separation, the gas in the bubble (Ar or O₂), and the conductivity and pH of the water, are shown in Figure 8.61 for an Ar bubble.

Individual or series of concurrent current and light emission pulses are seen with no observable distortion of the voltage during these events. The rise and decay times

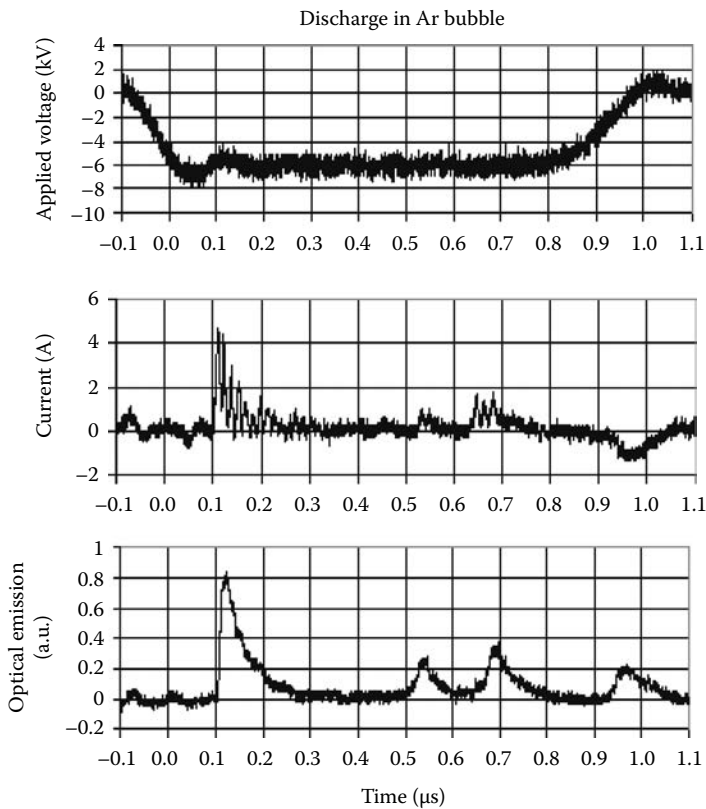


FIGURE 8.61 Typical traces for the applied voltage, the current, and the optical emission (OH band emission) for an 8 mm Ar bubble.

of these pulses are less than 10 and 50–80 ns. The optical pulses are slightly broader than the corresponding current pulses. Two sets of peaks are generally observed, a set of peaks at arbitrary times during the application of the voltage pulse and another peak in both current and optical signal during the shut-off phase of the pulse. The amplitude, the number of peaks, and the time delay for the onset of the discharge depend on the applied voltage and on the size of the bubble. The shapes of the current and the PMT traces do not change significantly from pulse to pulse for a fixed voltage. A subsequent increase in the applied voltage leads to a decrease in the time delay to the onset of the discharge. In addition, the number of peaks observed during the time the voltage is applied increases with increasing voltage. The intensity of the peak that occurs during the shut-off part of the applied pulse also increases for higher applied voltages. Experiments conducted with Ar and O₂ bubbles do not show any significant differences in the optical emission signal using the 309 nm OH filter, indicating that similar concentrations of OH radicals are produced in both Ar and O₂ bubbles.

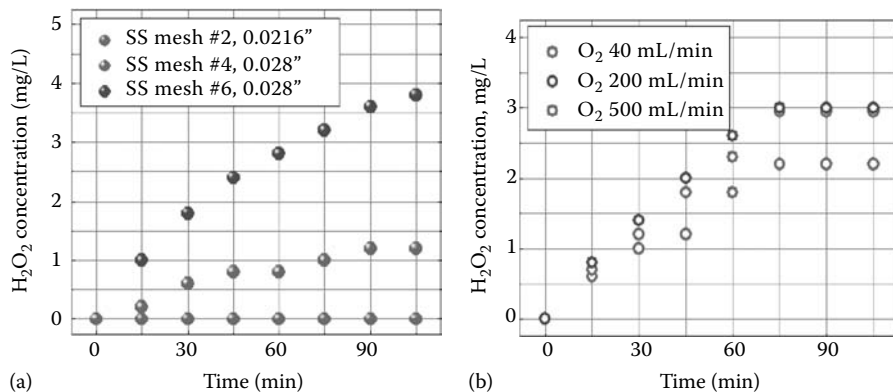


FIGURE 8.62 H₂O₂ concentration for various mesh electrode sizes at a fixed O₂ flow rate and fixed operating conditions (a) and various O₂ gas flow rates at a fixed mesh size and fixed operating conditions (b). H₂O₂ concentration increases with growing mesh width and O₂ flow rate. (From Anpilov, A.M. et al., *J. Phys. D: Appl. Phys.*, 34, 993, 2001.)

Experiments using the water treatment reactor (Figure 8.60) were carried out with the objective to

1. Ascertain the potential of pulsed electric discharges in water to generate reactive oxidants such as OH, O₃, O, and H₂O₂
2. Quantify the potential to decompose organic contaminants in the water such as phenol and rhodamine as well as energetic compounds (i.e., explosives) such as TNT, HMX, and CL20 [420]

An excellent discussion of the mechanisms for the formation of some of the oxidants can be found in the paper of Anpilov et al. [408]. Figure 8.62 shows the production of hydrogen peroxide, H₂O₂, as a function of the size of the mesh electrodes and the O₂ gas flow rate under otherwise constant operating conditions. Since the discharge produces a significant amount of hydrogen peroxide, the Fenton reaction, i.e., the reaction of H₂O₂ with Fe²⁺ to form Fe³⁺ along with OH⁻ and OH can be used to increase the decomposition rate of organic materials. Experiments were performed with the objective to assess the potential of pulsed electrical discharges in bubbled water to decompose the energetic compound HMX. This was done at a reduced pH = 3, which increases the reaction rate [421]. The reaction was initiated by adding FeSO₄ to the water to yield an Fe²⁺ concentration of 0.3 mmol/L. Roughly 50% of the energetic compound HMX is decomposed in about one hour when O₂ bubble are used. The decomposition efficiency is significantly lower when Ar bubbles are used (Figure 8.63).

8.3.4 Summary

This brief review touched on some aspects of the physical and chemical processes that are initiated by pulsed electrical discharges in bubbled water. As an example of

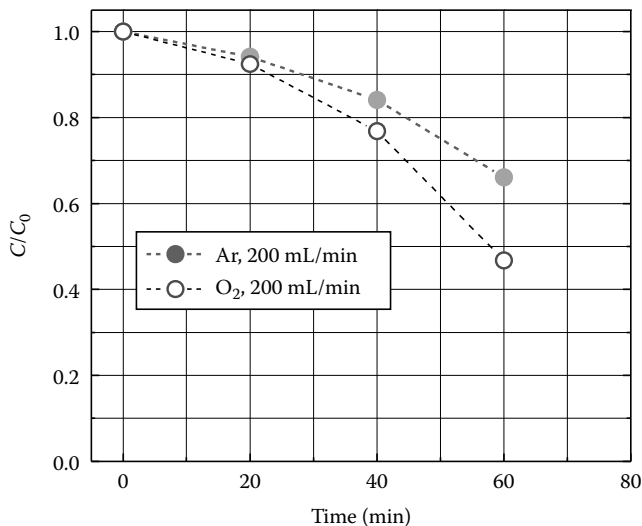


FIGURE 8.63 Decomposition of HMX by a pulsed electrical discharge in water for different gases bubbled through the reactor. The water temperature was kept at 25°C and the concentration of the added Fe^{2+} ions was 0.3 mmol/L. (From Zoh, K.-D. and Stenstrom, M.K., *Water Res.*, 36, 1331–1341, 2002.)

how water decontamination applications can benefit from a technology based on the production of reactive species by pulsed electrical discharges in water, results for the decomposition of the energetic compound HMX in an aqueous solution by pulsed discharges in water were presented.

8.4 NANO- AND MICROPARTICLES

The accents in fine particle research in plasma technology are gradually shifting from the traditional view of them as unwelcome process contaminants to new fine powder materials or to often desired elements that can essentially improve the properties of plasma-made thin films [422]. Such tailored micro- and nanoparticles in the plasma phase can be regarded as building units in nanofabrication involving doping, structural incorporation, or self-assembly processes.

Production of large amounts of powders in high-pressure thermal plasma jets (plasma spraying) is state of the art in metal and ceramic industries [423,424]. However, size distribution and uniformity of produced particles are often rather poor. A solution is the use of low-pressure plasmas for particle generation and modification. A major advantage of low-pressure nonthermal plasmas is the nonequilibrium chemistry, which provides unique possibilities for fine particle treatment without damage and thermal overload. Hence, small amounts of particles with a high added value can be fabricated using these methods. Besides the chemistry, the charge and size of the particles are crucial parameters for the explanation of the unique architectures of nano-sized objects such as nanostructured films, nanowires, and nanotubes.

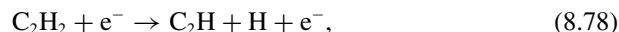
Unfortunately, particle formation in low-pressure discharges is not very efficient due to the low density of active species and due to the limited particle-trapping capacity. In addition, the injection and manipulation of particles into the vacuum system as well as collection and extraction of processed particles raise several issues. Therefore, also atmospheric pressure glow discharge systems are recently in use [425].

Particles can be generated either by nucleation and subsequent growth due to gas-phase reactions in the plasma [426] or they may originate from molecular or cluster-like species that are produced due to sputtering of electrodes [427] or peeling off of films deposited on the reactor walls [428]. Besides particle growth, incorporation of small particles into growing films [429] and coating of particles [430] are also important issues in plasma chemistry.

8.4.1 PARTICLE SYNTHESIS IN PLASMA

For particle synthesis, the growth of fine particles in reactive silane-, hydrocarbon-, and fluorocarbon-based plasmas are of interest. Despite a remarkable difference in the process kinetics and the plasma chemistry involved, the growth scenario can be very similar. Particle growth in such chemically reactive plasmas starts with the formation of sub-nanometer-sized protoparticles (clusters), which nucleate as a result of homogeneous or heterogeneous reactions. Then, agglomeration/coagulation processes result in the generation of particulates with sizes of a few tens of a nanometer which quickly acquire a negative electric charge due to collection of free electrons from the plasma [431,432]. These rapidly developing mechanisms result in a significant reorganization of the entire plasma system due to changes in the particle and charge carrier balance. As a result of the compensation of electron losses onto the dust grains, the electron temperature and, therefore, the ionization and dissociation of the precursor molecules increase. Finally, the dust particles usually proceed to sub- μm and μm size via slow mechanisms of accretion of monomer radicals. Detailed description of the particle formation processes and their modeling, in particular for silane and fluorocarbon plasmas, can be found, for example, in [433–435].

Formation of particles in a plasma has been observed often in the course of thin film deposition of hydrogenated amorphous carbon or DLC films from hydrocarbon-based precursors as methane, acetylene, etc., [431,436]. Based on numerous data from the reactive plasma, aerosol, and combustion literature, it is assumed that the carbon hydride clustering process is induced by the electron-impact abstraction of hydrogen from the acetylene monomers



followed by an efficient generation of C_xH_y radicals via chain polymerization reactions [437–439]. The measured ion mass spectrum of $\text{Ar}/\text{C}_2\text{H}_2$ plasma is displayed in Figure 8.64a; it is distinctly different from that of the Ar/CH_4 plasma where particle formation is less likely [437]. Apparently, some difficulty exists to break the carbon–carbon triple bond of acetylene. Hydrocarbon molecules in acetylene plasmas, hence, prefer to grow by addition of C_2 -containing molecules as the presence of hydrocarbon

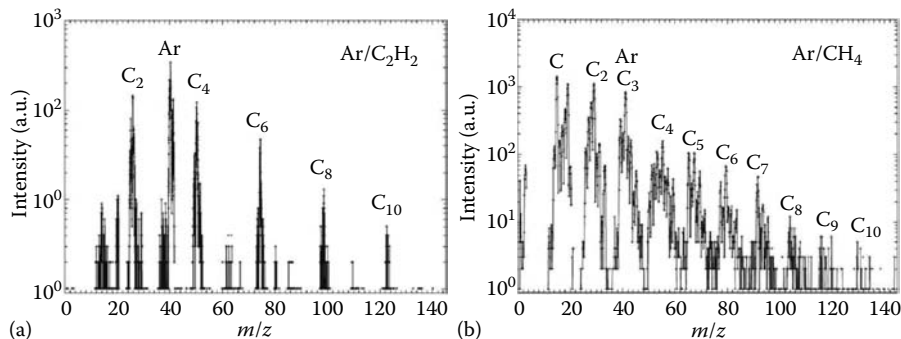
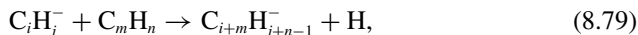


FIGURE 8.64 Ion mass spectra of Ar/C₂H₂ (a) and Ar/CH₄ (b) rf-discharges. (From Do, H.T. et al., *Contrib. Plasm. Phys.*, 45, 378, 2005.)

molecular ions with even numbers of carbon atoms is much more prominent than with odd numbers.

The observed ions are extremely hydrogen-poor, e.g., C₆H₃⁺ ($m/z = 79$) or C₈H₃⁺ ($m/z = 99$). The ion mass spectrum from Ar/CH₄ plasmas (Figure 8.64b) by contrast displays a large number of mass peaks originating from fragmentation of methane ($m/z = 14, 15$) and from formation of larger C_nH_m⁺ molecular ions, e.g., C₂H₅⁺ ($m/z = 29$) and C₃H₅⁺ ($m/z = 41$). The mass peak at $m/z = 19$ is attributed to formation of H₃O⁺ ion. Rather large molecular ions containing up to 10 carbon atoms and an odd number of hydrogen atoms are detected, e.g., C₅H₉⁺ ($m/z = 69$), C₆H₇⁺ ($m/z = 79$), C₇H₇⁺ ($m/z = 91$), C₈H₇⁺ ($m/z = 103$), and C₉H₇⁺ ($m/z = 115$). There appears to be a tendency for the larger hydrocarbon ions to become more and more hydrogen-poor. In general, the most likely clustering process is



which proceeds through the addition of anions C_iH_j⁻ to the neutrals C_mH_n accompanied by the elimination of hydrogen and the generation of higher-mass ions.

The rapid chemical nucleation stage evolves into an equilibrium which can usually be reached if the particle loss to the walls is compensated by the production of new species. In order to quantify the consumption of the precursor gas (here C₂H₂) for dust particle formation, the density of acetylene molecules can be monitored by means of absorption spectroscopy [440]. The absorption signal decreases remarkably within a short process duration, indicating fast and efficient decomposition of the precursor molecules (Figure 8.65).

Dissociated radicals (mainly C₂H) are precursors for particle formation, which starts spontaneously in Ar/C₂H₂ plasmas. The equilibrium state and, hence, the particle growth is strongly affected by the gas temperature, plasma power, discharge modulation, gas pressure, gas flow, as well as by the H₂ dilution [435,441].

Particle formation of small carbon particles after a short process time can also be observed by light transmission through the plasma region (Figure 8.66). After about 100 s, an oscillation of the transmitted laser light intensity can occur owing

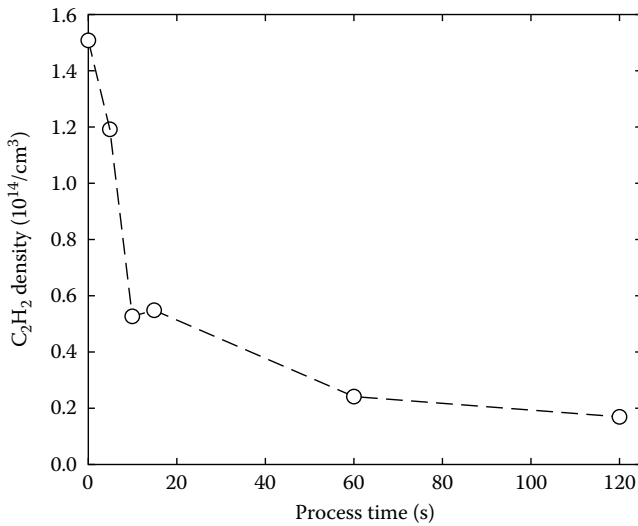


FIGURE 8.65 Decreasing C_2H_2 density vs. process time in an rf-plasma (10 W, Ar and C_2H_2 flow 2 sccm each).

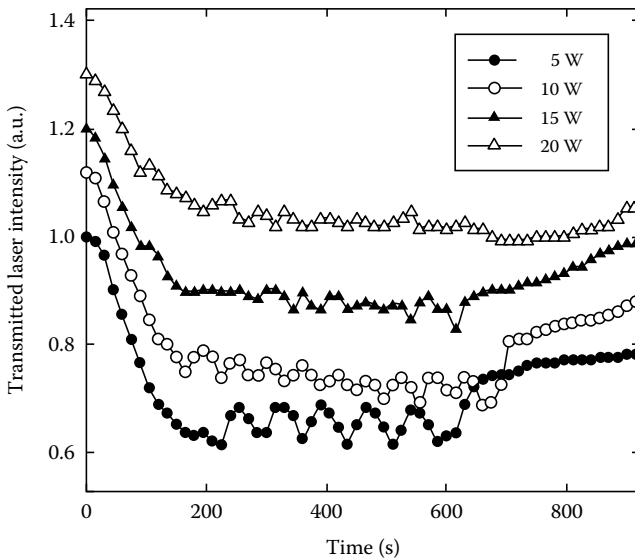


FIGURE 8.66 Transmitted laser intensity vs. time, indicating dust particle formation in Ar/ C_2H_2 rf-plasma. (From Do, H.T. et al., *Contrib. Plasma Phys.*, 45, 378, 2005.)

to the dynamics of the carbon dust formation. The growth mechanism is influenced by the combined action of various forces onto the particles (e.g., electrostatic, gravitational, neutral and ion drag, etc.) and the development of voids [431,442,443]. This behavior results in alternating dust particle-containing and dust particle-free zones. The observed periodicity in the transmission signal can be explained by noting

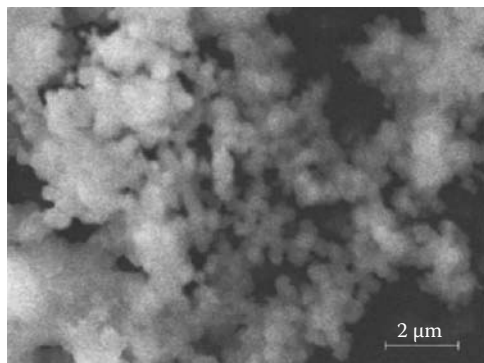


FIGURE 8.67 Synthesized fine carbon particles that form large agglomerates. (From Kersten, H. et al., *Pure Appl. Chem.*, 77, 415, 2005.)

that negatively charged particles are confined in the plasma potential as long as the forces, which scale differently with the grain radius, acting on them are balanced. If the particles reach their critical size, they are either dragged out of the plasma bulk or fall down onto the lower electrode, resulting in an increase of the transmitted signal. After switching off the acetylene supply, the light intensity increases and stabilizes again due to a decreasing particle density.

A quick change in the intensity of the signal evidences a highly monodisperse character of the powder growth process. Indeed, examination of collected carbon soot particles by scanning electron microscopy (SEM) reveals a large amount of small carbon dust particles (~ 100 nm) that are quite spherical and that are of comparable size (Figure 8.67).

Since the involvement of negative ions (8.79), which are efficiently trapped in the positive plasma potential, is an essential step in particle formation, the modulation of the discharge can influence the particle growth. On the other hand, charge fluctuation during particle formation can be observed in the discharge behavior, e.g., the generation of harmonics [444].

8.4.2 FORMATION AND DEPOSITION OF NANO-SIZED CLUSTERS IN PLASMA

Cluster formation is often the crucial intermediate stage in particle growth. On the other hand, a cluster as a system of bound atoms or molecules is a physical object between individual atoms or molecules and condensed bulk matter. Typical clusters sizes vary from two to three atoms up to nano-size clusters (particles) with more than 10^5 atoms or molecules. Clusters have due to their limited size specific optical, magnetic, and electronic properties.

Cluster deposition is also a convenient method for fabrication of thin solid films [445–447]. A typical cluster deposition setup as shown in Figure 8.68 consists of a nanocluster source inside a vacuum chamber [448]. In brief, a discharge is generated by a dc magnetron equipped with a metal (e.g., Ti, Ag, Fe) target and operated with argon as working gas. Nano-size clusters form inside a liquid nitrogen-cooled aggregation tube. After formation, clusters together with argon atoms move through an

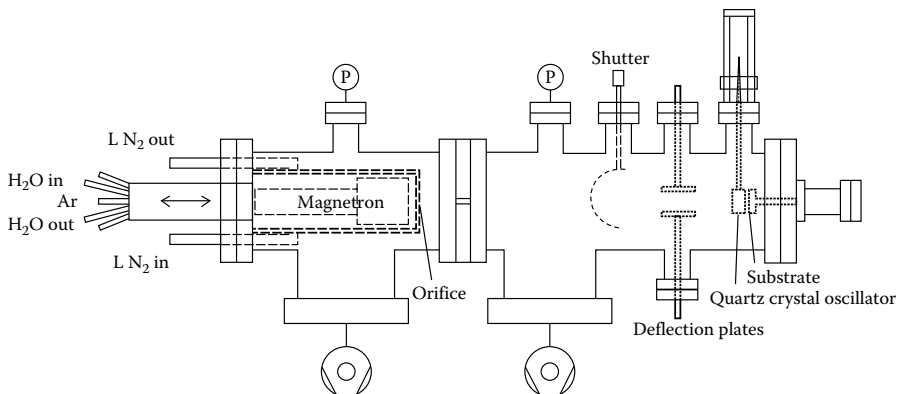


FIGURE 8.68 Experimental setup for nanosize cluster formation and deposition by a magnetron discharge. (From Shyjumon, I. et al., *Thin Solid Films*, 500, 41, 2006.)

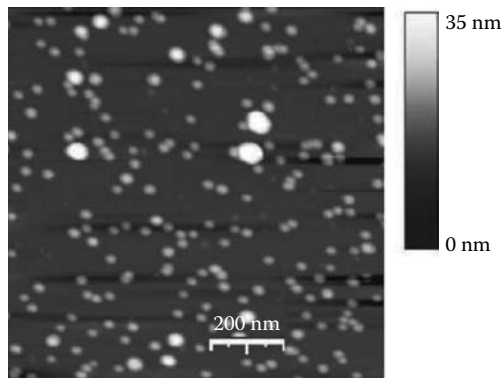


FIGURE 8.69 AFM photograph of a typical deposition pattern obtained at an aggregation chamber temperature of 148 K; deposition time was 15 s. (From Shyjumon, I. et al., *Thin Solid Films*, 500, 41, 2006.)

orifice and afterward they are deposited on a suitable, e.g., Si(100), substrate located at a distance of several cm from the exit of the magnetron chamber. Additionally, a mass-filter can be employed to select a particular cluster size [449]. The gas pressure in the magnetron discharge is low, which leads to large times of transformation of metal atoms in clusters. Therefore, only a small part of initially formed atoms are converted into clusters and many of the evaporated atoms return to the cathode. In order to increase the efficiency of cluster generation, the discharge region at low pressure where metal atoms are produced is separated from the aggregation region at higher pressure where metal atoms are transformed into clusters.

The emerging clusters are deposited on silicon substrates for fixed time intervals while the temperature inside the aggregation tube was varied from liquid nitrogen temperature (77 K) to room temperature (295 K). Figure 8.69 shows a 2D-AFM image in air of films deposited for 15 s at a temperature of 148 K. The measured atomic force

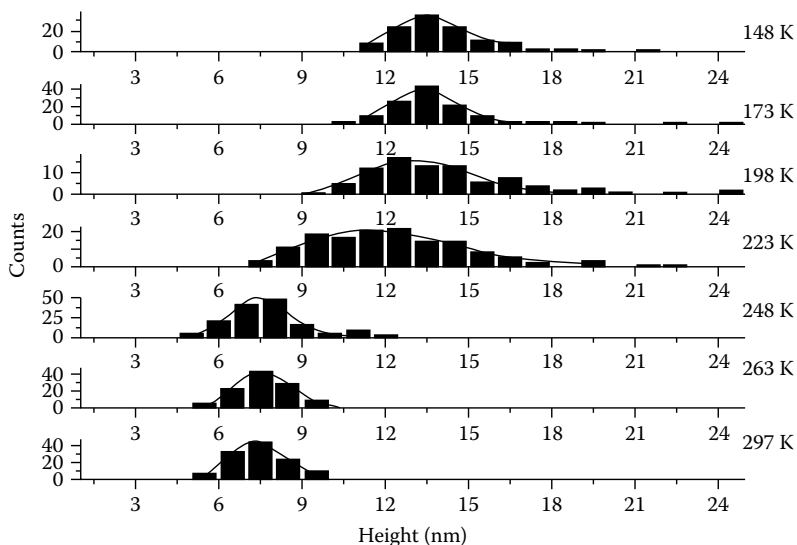


FIGURE 8.70 Height histograms with log-normal fits for the indicated wall temperatures of the chamber. (From Shyjumon, I. et al., *Thin Solid Films*, 500, 41, 2006.)

microscopy (AFM) height histograms obtained under different temperature conditions are shown in Figure 8.70. Log-normal fits reasonably reproduce the measured histograms. The mean height of clusters decreases from about 14 to 8 nm when the temperature increases from 200 to 250 K. Simultaneously, the surface coverage also decreases with increasing wall temperature.

Bombardment of the cathode by plasma ions causes emission of metal atoms. When the number density of metal atoms in the buffer gas exceeds the saturation vapor density, nucleation in the vapor can proceed. Growing clusters are located in a restricted aggregation region where they capture free metal atoms. Clusters leave the aggregation region as a result of diffusion or flow of the buffer gas (argon) and tend to spread uniformly over all the space inside the magnetron chamber. Ultimately, some clusters depart from the magnetron chamber through an orifice and are deposited on a substrate. The cluster flux onto a substratum surface as well as the cluster size can be restored from the measurement of the cluster area density on the surface at a given deposition time. This allows for an estimate of the cluster number density in the magnetron chamber.

Formation of metal clusters starts from free metal atoms. The three-body collision process [450,451]



is the bottleneck for cluster formation. Small clusters grow by atom attachment to the cluster surface:



where

A is a buffer gas atom

M is a free metal atom

Deposited nanosize clusters show unique features, for example, slightly different lattice constants and a significantly reduced melting temperature compared to bulk material [449]. An interesting example are nanosize titanium oxide clusters, which appear to have excellent photocatalytic properties.

8.4.3 MODIFICATION OF PARTICLES IN PLASMA

Generation, confinement, and processing of solid grains in a plasma can be potentially beneficial for a number of applications [422,431,452]. For example, fine particles can be efficiently incorporated into polymeric/ceramic materials to synthesize a number of advanced nanostructured materials for the applications as water repellent, protective, and wear-resistant and functional coatings [453]. By embedding nanometer-sized particles grown in silane plasmas into an amorphous silicon matrix, one can substantially improve the performance of solar cells [454]. Similarly, new classes of particle-seeded composite materials can be developed [455].

In addition, fine particles that are inadvertently injected into a process plasma can be trapped and subsequently coated to enhance their surface properties, e.g., for catalytic applications etc. Especially, unique objects like coated or layered grains with desired surface structure, color, fluorescence, etc., can be generated via plasma processing [456–458]. An approach for the coating of externally injected particles was demonstrated in [458], where a radiofrequency (rf) argon plasma was employed to charge and confine particles. Particles were coated with the help of a separate direct current (dc) magnetron sputter source. In a similar manner, deposition of different metals onto silica grains was investigated, whereas the interaction between the magnetron discharge and the trapped particles was under special investigation. Silicon oxide particles with a diameter of $18\text{ }\mu\text{m}$ were trapped in the sheath above the rf electrode. A copper ring was placed on the rf electrode in order to confine the particles in the center. The planar dc magnetron sputter source was used to deposit thin metallic films on the particles serving as microsubstrates. Al, Cu, and Ti cathodes were used as sputter targets. The distance between the sputter target and the confined particles was about 70 mm. The coated particles were examined by secondary electron microscopy (SEM); some pictures of the coated particles are shown in Figure 8.71.

Different metallic film structures were observed, depending on the target material. While Al and Cu films were deposited rather smoothly, Ti films showed a distinct island formation. This can be explained by the lower sputter yield of the titanium target and also by the different surface adhesion between the particles and the deposited material. The surface energy of titanium (1.39 J/m^2) is higher than that of aluminium (0.91 J/m^2) and copper and, therefore, the wetting of the particle surface is worse for titanium.

On most particles the deposited metal films are fully closed. A good exception is shown in Figure 8.71d where the broken layer is most likely caused by thermal tension. It was possible to estimate from this figure the thickness of the deposited

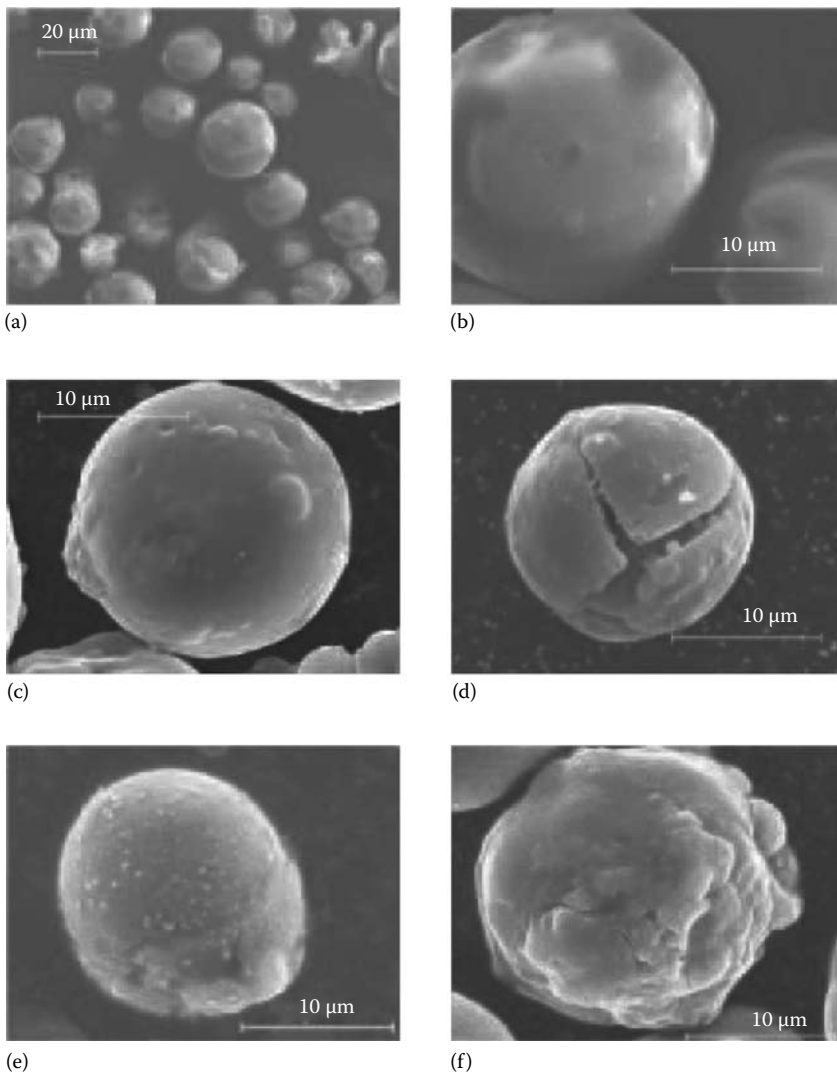


FIGURE 8.71 SEM photograph of silicon oxide particles coated by magnetron sputtering. (a and b): Uncoated silicon oxide particles, (c and d) Cu-coated silicon oxide particles, (e) Ti-coated silicon oxide particles, (f) Al-coated silicon oxide particles. (From Shyjumon, I. et al., *Thin Solid Films*, 500, 41, 2006.)

copper films amounting to about 1.5 μm. The coated particles show a rough and cauliflower-like shape, which makes them attractive, e.g., for catalytic applications. If the deposited films were thinner, the layer surrounding the particles could be smoother as well. In such cases, the surface structure of the coated particles (which was still completely closed) looked more golf ball-like, which might be of interest for optical application.

9 Modeling and Simulation

CONTENTS

9.1	Hierarchy of Plasma Models	408
9.1.1	Plasma as a Many Particle System	409
9.1.2	Kinetic Equation	410
9.1.3	Collision Integral of the Boltzmann Equation	413
9.1.4	Moments of the Kinetic Equation	414
9.1.5	Numerical Methods	418
9.1.5.1	Fluid Equations	419
9.1.5.2	Solution of the Boltzmann Equation	422
9.1.5.3	Particle Models	424
9.1.5.4	Hybrid Methods	425
9.2	Elementary Volume Processes in Gas Discharges	427
9.2.1	Fundamental Concepts	430
9.2.1.1	Collision Cross Section	430
9.2.1.2	Formal Scattering Theory	432
9.2.1.3	Adiabatic Approximation	436
9.2.1.4	Resonant Scattering	438
9.2.2	Typical Processes	441
9.2.2.1	Production of Ions	441
9.2.2.2	Destruction of Ions	445
9.2.2.3	Excitation of Internal Degrees	449
9.2.2.4	Concluding Remarks	451
9.3	Surface Processes	452
9.3.1	Basics of Plasma Material Interaction	452
9.3.1.1	Plasma-Wall Contact with an Electron Emitting Wall	454
9.3.2	Interaction of Hydrogen Plasma with Carbon-Based Materials	455
9.3.2.1	Formation of a Saturated Surface Layer	456
9.3.2.2	Diffusion	457
9.3.2.3	Codeposition	457
9.4	Example: Oxygen RF Plasma	457

Many plasmas in technological applications are ideal, weakly ionized, and nonthermal as already mentioned in Chapter 2. Hence, the following introduction into plasma modeling is restricted to this kind of plasma, which covers the large range of pressures from about 10^{-2} to 10^6 Pa at ionization degrees between about 10^{-6} and 10^{-3} . Over this range, many different mechanisms and principles of plasma generation as well as

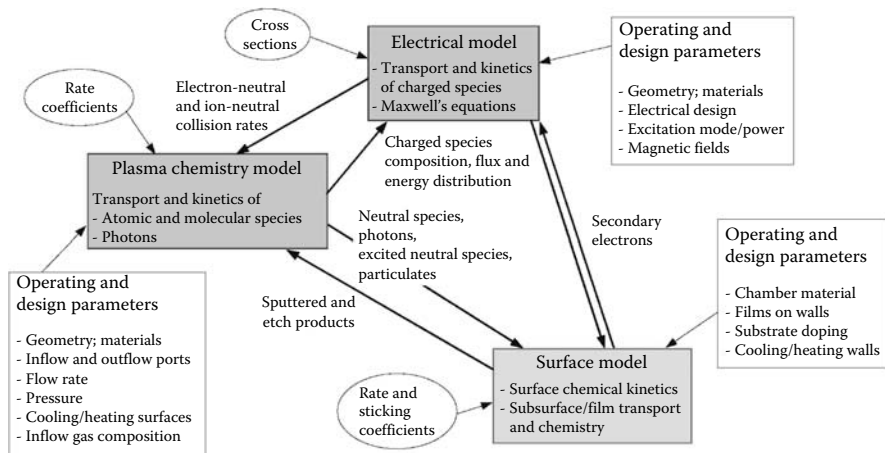


FIGURE 9.1 Components of plasma modeling. (From Graves, D.B., *IEEE Trans. Plasma Sci.*, 22, 31, 1994.)

processes at quite different temporal and spatial scales have to be taken into account in plasma modeling.

A model for the description of plasmas has to comprise of an electrical model, a plasma chemistry model, and a surface model. The different components of such models and their interrelation are shown in Figure 9.1. Each of these sub-models is coupled with the other two and includes equations that determine the temporal and spatial evolution of the relevant properties. The transport and kinetics of the charge carriers and the behavior of the electric (and magnetic) fields are described by the electrical model. The plasma chemistry model deals with the transport and reaction kinetics of the various neutral plasma components and photons. The interaction of the different species in the plasma with the surrounding walls and electrodes is treated by the surface model.

The present approach is to distinguish between the processes in the plasma volume, that is, the coupled treatment of electrical and plasma chemistry model (referred to as plasma model in the following), and the interaction of a plasma with surfaces (surface model) including the subsequent surface processes that are desired in many plasma-chemical systems. A specific requirement for models of nonthermal plasma processes is the description of states that are often far away from equilibrium states like the thermal equilibrium, chemical equilibrium, ionization-recombination equilibrium and Boltzmann distribution of excited particle states. Therefore, the section starts with the basic concept of the kinetic theory as a more general description followed by approaches of sequentially larger degrees of approximation as well as numerical methods commonly used to describe plasmas in technological applications.

9.1 HIERARCHY OF PLASMA MODELS

From a general point of view, a plasma represents a system of many particles that move and interact with each other, with boundaries and with electromagnetic fields.

Hence, an overall model has to describe the temporal behavior of all included particles of very different kinds, that is, atoms and molecules in ground and excited states, ions in ground and excited states, and electrons. Depending on the types of particles, their interaction with each other and with electromagnetic fields is also very different. In a first step, all these differences are ignored by considering more generally a many-particle system where external forces act on the particles and where interactions of the particles are possible.

9.1.1 PLASMA AS A MANY PARTICLE SYSTEM

Considering a system of N particles, a unique description of this system is given by all the coordinates \vec{x}_k and momenta \vec{p}_k of the particles $k = 1, \dots, N$. Generally, a system of $3N$ partial differential equations of second order for the coordinate components has to be solved for given initial conditions of all particles to get the complete behavior of the system—a visionary task. However, the complete information about position and momentum of every single particle is not of interest in the understanding and modeling of plasma-chemical systems. In fact, the desired information concerns the mean or thermodynamic behavior of the system. Consequently, a statistical approach is required here.

In order to deduce a statistical description, the distribution of N particles in the $6N$ -dimensional phase space is considered. In this space, a time-dependent N -particle distribution function (density function) $\rho(\vec{x}_k, \vec{p}_k, t)$ can be defined. It represents the probability to find the particle k at a given time t and at the position \vec{x}_k with the momentum \vec{p}_k and is consequently normalized to unity according to

$$\int \rho(\vec{x}_k, \vec{p}_k, t) d^{3N}x d^{3N}p = 1. \quad (9.1)$$

The average value $\langle \dots \rangle$ of a quantity $A(\vec{x}_k, \vec{p}_k)$ depending on all coordinates and momenta of the particles is given by

$$\langle A(t) \rangle = \int A(\vec{x}_k, \vec{p}_k) \rho(\vec{x}_k, \vec{p}_k, t) d^{3N}x d^{3N}p. \quad (9.2)$$

For closed systems, the density function has to be constant along the trajectory in the $6N$ -dimensional phase space according to the normalization (9.1). This requirement immediately leads to the basic equation for ρ , the continuity equation [2–5]

$$\frac{d\rho}{dt} = \frac{\partial \rho}{\partial t} + \sum_{k=1}^{3N} \left(\frac{\partial \rho}{\partial x_k} \frac{\partial x_k}{\partial t} + \frac{\partial \rho}{\partial p_k} \frac{\partial p_k}{\partial t} \right) = 0, \quad (9.3)$$

named after J. Liouville who deduced this fundamental equation in the nineteenth century.

Despite its simple structure, the Liouville equation (9.3) is a very complicated partial differential equation that cannot be solved for the large number of plasma

particles in practice. However, it provides the basis for the deduction of further average values.

In plasma chemistry, the characteristics of particles of the same kind is generally of interest. The determination of plasma properties can be described in an analogous way by the reduced one-particle distribution function $f^\alpha(\vec{x}, \vec{v}, t)$ for each particle species α . Note that the velocity $\vec{v} = \vec{p}/m_\alpha$ replaces the particle momentum without loss of generality here and in the forthcoming for a given mass m_α of the particle species α . The value of this distribution function f^α at a given position \vec{x} and velocity \vec{v} in the 6D phase space made up of three ordinary and three velocity coordinates represents the phase-space density. This means that the number dN_α of particles of species α that can be found in the volume element d^3x around the position \vec{x} and in the surrounding d^3v of velocity \vec{v} is given by $f^\alpha(\vec{x}, \vec{v}, t) d^3x d^3v$. Consequently, the integral

$$\int f^\alpha(\vec{x}, \vec{v}, t) d^3x d^3v = N_\alpha(t) \quad (9.4)$$

over the whole phase space yields the total number N_α of particles of species α . The one-particle distribution function f^α is related to the N -particle distribution function ρ by the integration over all but one volume element $d^3x_k d^3v_k$ according to

$$f^\alpha(\vec{x}, \vec{v}, t) \equiv f_1^\alpha(\vec{x}_1, \vec{v}_1, t) = N_\alpha \int \rho(\vec{x}_1, \vec{v}_1, \dots, \vec{x}_N, \vec{v}_N, t) d^3x_2 d^3v_2 \dots d^3x_N d^3v_N, \quad (9.5)$$

where α denotes the particle species to which the selected particle 1 belongs.

Now the problem is reduced to seven dimensions (including time) for each species. Before discussing the corresponding continuity equation that generates f^α , a further reduction of the problem should be mentioned. If the information about the velocity of the particles (in the sense of the average value of the velocities of all particles of species α on a microscopic scale) is no longer of interest, the distribution f^α can be averaged over the velocity. This integration over d^3v yields the particle density

$$n_\alpha(\vec{x}, t) = \int f^\alpha(\vec{x}, \vec{v}, t) d^3v \quad (9.6)$$

of species α in the configuration space. The description of densities for every species as a function of time in the plasma system corresponds to the fluid or hydrodynamic treatment that will be discussed in Section 9.1.4. The hierarchy of plasma equations is displayed in Figure 9.2.

9.1.2 KINETIC EQUATION

The following introduction focusses on the distribution function of one particle species and its determination. It is shown that distribution functions for all species finally represent the basis for the description of all interesting processes in a plasma such as transport, ionization, energy dissipation, particle conversion rates, and so on. The general concept of a classical kinetic description that yields the distribution function is based upon the separation of the particle trajectory into the movement of particles without interaction with others and the interaction process itself. At this

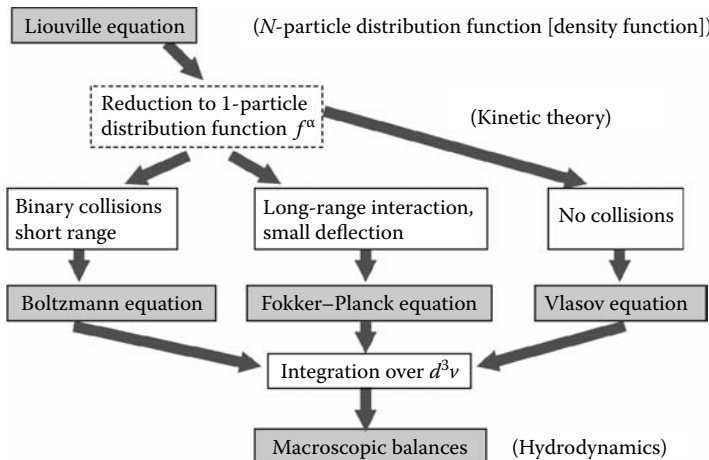


FIGURE 9.2 Hierarchy of equations in plasma physics.

point, the different interactions of the particles with each other and with particles of another kind have to be inspected in more detail. As mentioned in Section 9.2, the interaction processes have to be treated as quantum mechanical problems in principle [6].

In the framework of the classical kinetic description of gases, a large number of particles move rapidly and randomly, where interactions among the particles beyond a small distance are negligible. The velocity of a particle and its position are assumed to be uncorrelated. As soon as the impact ranges of particles overlap, a collision process occurs at which the influence of external fields is neglected in the particle interaction region. Because the interaction radius is much smaller than the mean free path of the particles and because the collision time is sufficiently small, the particle motion during the collision process and the simultaneous interaction of more than two particles can be neglected. Therefore, it is sufficient to determine the changes in velocities and states of the particles in a binary collision process. In addition, the mean free path of the particles is much smaller than the vessel dimensions, so that the influence of the wall can remain unconsidered. From a strict point of view, this approach is applicable to collision processes between neutral particles as well as between a charged and a neutral particle, while the interaction between charge carriers is long-range and collective in nature.

In order to derive the kinetic equation according to the classical kinetic theory, which yields the desired one-particle distribution function $f^\alpha(\vec{x}, \vec{v}, t)$ for the particles of species α , first the motion of the particles under the action of an external field without collisions is considered. This motion over a sufficiently small time step Δt results in a change of the space and velocity coordinates and thus the phase space element according to

$$\vec{x} \longrightarrow \hat{\vec{x}} = \vec{x} + \vec{v}\Delta t, \quad \vec{v} \longrightarrow \hat{\vec{v}} = \vec{v} + \frac{\vec{F}^a}{m_\alpha} \Delta t, \quad d^3x d^3v \longrightarrow d^3\hat{x} d^3\hat{v}, \quad (9.7)$$

where \vec{F}^a indicates the external force on the particle. Consequently, the number of particles in the small phase space volume $d^3x d^3v$ changes by

$$\begin{aligned} f^\alpha(\vec{x}, \vec{v}, t) d^3x d^3v &\longrightarrow f^\alpha(\vec{\hat{x}}, \vec{\hat{v}}, t) d^3\hat{x} d^3\hat{v} \\ &= \left[f^\alpha(\vec{x}, \vec{v}, t) + \left(\frac{\partial f^\alpha}{\partial t} + \vec{v} \cdot \nabla_{\vec{x}} f^\alpha + \frac{\vec{F}^a}{m} \cdot \nabla_{\vec{v}} f^\alpha \right) \Delta t + \dots \right] d^3\hat{x} d^3\hat{v}. \end{aligned} \quad (9.8)$$

Since the size of the phase space volume does not change during the collisionless motion of particles because of Liouville's theorem, that is, $d^3\hat{x} d^3\hat{v} = d^3x d^3v$, the total temporal change of the distribution function f^α follows in the limit of $\Delta t \rightarrow 0$:

$$\frac{d}{dt} \left[f^\alpha(\vec{x}, \vec{v}, t) d^3x d^3v \right] = \left(\frac{\partial f^\alpha}{\partial t} + \vec{v} \cdot \nabla_{\vec{x}} f^\alpha + \frac{\vec{F}^a}{m_\alpha} \cdot \nabla_{\vec{v}} f^\alpha \right) d^3x d^3v. \quad (9.9)$$

As long as the motion of particles is collisionless, the total change over time of the particle number and of the distribution function equals zero, that is, $df^\alpha/dt = 0$. On the other hand, the interaction between the particles causes alterations of momentum and kinetic energy of the particles and, depending on the type of collision, can result in changes of the particle number in the corresponding phase space volume. The consideration of this total change of the distribution function in time due to collisions leads to the basic kinetic equation [2–5,7]

$$\frac{\partial f^\alpha}{\partial t} + \vec{v} \cdot \nabla_{\vec{x}} f^\alpha + \frac{\vec{F}^a}{m_\alpha} \cdot \nabla_{\vec{v}} f^\alpha = \frac{df^\alpha}{dt} \Big|_{coll}, \quad (9.10)$$

which describes the distribution function $f^\alpha(\vec{x}, \vec{v}, t)$ for the particle species α . The right-hand side of (9.10) is referred to as the collision integral and includes all collision processes that result in a change of the distribution function. Its peculiarity specifies the type of the kinetic equation. An example for a collision integral of charge carriers in an electric potential Φ is given in Section 9.2.1.1.

Most processing plasmas are weakly ionized so that collisions between charged particles can be neglected while the short-range interaction between charged and neutral particles and of neutral particles with each other are dominant. The kinetic equation for such plasmas with predominant binary collision processes is the so-called Boltzmann equation:

$$\frac{\partial f^\alpha}{\partial t} + \vec{v} \cdot \nabla_{\vec{x}} f^\alpha + \frac{\vec{F}^a}{m_\alpha} \cdot \nabla_{\vec{v}} f^\alpha = \frac{df^\alpha}{dt} \Big|_{coll}^{bi}. \quad (9.11)$$

The explicit form of its collision integral is given in Section 9.1.3. In fully ionized plasmas, the long-range interaction between charge carriers, that is, Coulomb collisions, have to be included into the kinetic description. The corresponding kinetic equation is the Fokker–Planck equation. If collisions between particles of the plasma become unimportant, the plasma is referred to as collisionless. Then, the right-hand side in (9.10) vanishes and the so-called Vlasov equation is obtained.

9.1.3 COLLISION INTEGRAL OF THE BOLTZMANN EQUATION

For the derivation of the general form of the binary-collision integral in (9.11), the interaction of a particle α originating from a phase space volume $d^3x d^3v$ with a particle β is considered. Because the interaction range of the particles is sufficiently small, a sudden change of their velocities without change of their spatial position is assumed during the collision process. The loss and gain resulting from the interaction of particles α with particles β in the coordinate space element d^3x can be expressed by means of the transition probability W . The term $W(\vec{v}, \vec{v}'; \vec{v}_\beta, \vec{v}'_\beta) d^3v' d^3v'_\beta / d^3x$ represents the probability per unit of time and space d^3x that the colliding particles of kind α and β with the respective velocity vectors \vec{v} and \vec{v}_β before and \vec{v}' and \vec{v}'_β after the collision arrive in d^3v' and $d^3v'_\beta$ after the collision. Because $f^\alpha(\vec{x}, \vec{v}, t) d^3x d^3v$ particles α are in the element $d^3x d^3v$ and $f^\beta(\vec{x}, \vec{v}_\beta, t) d^3x d^3v_\beta$ particles β are in $d^3x d^3v_\beta$, the total number of collisions with the transition $d^3x d^3v \rightarrow d^3x d^3v'$ occurring per time unit in d^3x for all possible velocities \vec{v}_β , \vec{v}' , and \vec{v}'_β at the velocity \vec{v} is given by the integral expression

$$\left[\int \int \int f^\alpha(\vec{x}, \vec{v}, t) f^\beta(\vec{x}, \vec{v}_\beta, t) W(\vec{v}, \vec{v}'; \vec{v}_\beta, \vec{v}'_\beta) d^3v_\beta d^3v'_\beta d^3v' \right] d^3x d^3v. \quad (9.12)$$

However, that is not the only change of particles in the phase space element $d^3x d^3v$ due to collisions, and particles α can be scattered into this interval by collision processes. The corresponding total number of collisions per time unit in d^3x for the transitions $d^3x d^3v' \rightarrow d^3x d^3v$ for all possible velocities \vec{v}_β , \vec{v}' , and \vec{v}'_β at the velocity \vec{v} reads

$$\left[\int \int \int f^\alpha(\vec{x}, \vec{v}', t) f^\beta(\vec{x}, \vec{v}'_\beta, t) W(\vec{v}', \vec{v}; \vec{v}'_\beta, \vec{v}_\beta) d^3v_\beta d^3v'_\beta d^3v' \right] d^3x d^3v. \quad (9.13)$$

After subtracting the number of loss processes (9.12) from the number of gain processes (9.13) and introducing the resulting collision term into (9.11), the Boltzmann equation finally reads

$$\begin{aligned} & \frac{\partial}{\partial t} f^\alpha(\vec{x}, \vec{v}, t) + \vec{v} \cdot \nabla_{\vec{x}} f^\alpha(\vec{x}, \vec{v}, t) + \frac{\vec{F}^a}{m_\alpha} \cdot \nabla_{\vec{v}} f^\alpha(\vec{x}, \vec{v}, t) \\ &= \int \int \int [f^\alpha(\vec{x}, \vec{v}', t) f^\beta(\vec{x}, \vec{v}'_\beta, t) W(\vec{v}', \vec{v}; \vec{v}'_\beta, \vec{v}_\beta) \\ & \quad - f^\alpha(\vec{x}, \vec{v}, t) f^\beta(\vec{x}, \vec{v}_\beta, t) W(\vec{v}, \vec{v}'; \vec{v}_\beta, \vec{v}'_\beta)] d^3v_\beta d^3v'_\beta d\vec{v}'. \end{aligned} \quad (9.14)$$

Using the differential cross section σ and the fact that the energy and momentum of the system of interacting particles remains conserved, the transition probability is given by

$$W(\vec{v}', \vec{v}; \vec{v}'_\beta, \vec{v}_\beta) = \frac{v_{\text{rel}}}{(v'_{\text{rel}})^2} \sigma(v_{\text{rel}}, \theta) \delta(v'_{\text{rel}} - v_{\alpha\beta}) \delta(\vec{w}' - \vec{w}) \quad (9.15)$$

with the relative velocities $\vec{v}_{\text{rel}} = \vec{v} - \vec{v}_\beta$ and $\vec{v}'_{\text{rel}} = \vec{v}' - \vec{v}'_\beta$, their absolute values v_{rel} and v'_{rel} , the centre-of-mass velocities $\vec{w} = (m_\alpha \vec{v} + m_\beta \vec{v}_\beta) / (m_\alpha + m_\beta)$ and

$\vec{w}' = (m_\alpha \vec{v}' + m_\beta \vec{v}'_\beta) / (m_\alpha + m_\beta)$, and the scattering angle $\theta = \angle(\vec{v}_{\text{rel}}/\nu_{\text{rel}}, \vec{v}'_{\text{rel}}/\nu'_{\text{rel}})$. The absolute value of the velocity $v_{\alpha\beta} = \sqrt{\nu_{\text{rel}}^2 - 2(m_\alpha + m_\beta)\Delta E / (m_\alpha m_\beta)}$ depends on the net change in internal energy ΔE as a result of the collision process. This energy change determines the type of collision process. For elastic collisions that do not influence the internal state of the particles, ΔE is equal to zero. For inelastic collision processes, collisions of first kind, such as excitation with $\Delta E > 0$, are distinguished from collisions of second kind (de-excitation) with $\Delta E < 0$.

Collision processes that change the particle number, that is, nonconservative processes such as ionization and recombination, can be treated in a similar way. Considerable simplifications of the collision integrals can be applied for the interaction of light particles such as electrons with much heavier particles (atoms or molecules). Assumptions about the isotropy of the scattering processes and the energy sharing after the collision allow further simplifications. The collision integral, transition probability, and differential cross section for the example of electron impact ionization are explained in Section 9.2.1.1.

Equation (9.14) already yields the basis for a complete plasma description on a microscopic level. If binary collisions are the dominant processes of the relevant plasma components, then a coupled system of integro-differential equations of type (9.14) has to be solved for each species with corresponding collision integrals for every possible type of collision. Knowledge of the external forces \vec{F}^a , of initial and boundary conditions, and of the collision cross sections σ are prerequisites for the solution.

9.1.4 MOMENTS OF THE KINETIC EQUATION

The kinetic equation (9.10) and its solution, the distribution function $f^\alpha(\vec{x}, \vec{v}, t)$, yields a microscopic description of the plasma component α . Because of its complexity, it is not always possible to determine its complete solution. However, detailed information about the velocity distribution of the particles is in many cases not required. Thus, equations for the distribution function moments, that is, for macroscopic properties, can be derived from the kinetic equation and can be solved then. In general, the average value $\langle g(\vec{v}) \rangle$ of a particle property $g(\vec{v})$ relative to the velocity space with the normalization relation (9.6) is given by [2–5,7]

$$n_\alpha(\vec{x}, t) \langle g(\vec{v}) \rangle = \int g(\vec{v}) f^\alpha(\vec{x}, \vec{v}, t) d^3 v. \quad (9.16)$$

The corresponding balance equation is obtained by multiplying the kinetic equation (9.10) with $g(\vec{v})$ followed by an integration over the velocity space:

$$\int g(\vec{v}) \frac{\partial f^\alpha}{\partial t} d^3 v + \int g(\vec{v}) \vec{v} \cdot \nabla_{\vec{x}} f^\alpha d^3 v + \int g(\vec{v}) \frac{\vec{F}^a}{m} \cdot \nabla_{\vec{v}} f^\alpha d^3 v = \int g(\vec{v}) \frac{df^\alpha}{dt} \Big|_{\text{coll}} d^3 v. \quad (9.17)$$

For $g = 1$, the particle density n_α immediately results and is called zero-order moment of the distribution. The first-order moment of the particle current density \vec{j}_α and the second-order moment of the energy density $n_\alpha \epsilon_\alpha$ are defined analogously by

$$\vec{j}_\alpha(\vec{x}, t) \equiv n_\alpha(\vec{x}, t)\vec{u}^\alpha(\vec{x}, t) = \int \vec{v}f^\alpha(\vec{x}, \vec{v}, t)d^3v \quad (9.18)$$

$$n_\alpha(\vec{x}, t)\epsilon_\alpha(\vec{x}, t) = \int \frac{1}{2}m_\alpha v^2 f^\alpha(\vec{x}, \vec{v}, t)d^3v, \quad (9.19)$$

where $\vec{u}^\alpha = \langle \vec{v} \rangle$ and $\epsilon_\alpha = \langle m_\alpha v^2 / 2 \rangle$ are the average velocity and average energy of the particle, respectively. The consistent macroscopic balance equations read

$$\frac{\partial n_\alpha(\vec{x}, t)}{\partial t} + \nabla_{\vec{x}} \cdot \vec{j}_\alpha(\vec{x}, t) = G_{n_\alpha}^{coll}(\vec{x}, t) - L_{n_\alpha}^{coll}(\vec{x}, t) \quad (9.20)$$

$$m_\alpha \frac{\partial \vec{j}_\alpha(\vec{x}, t)}{\partial t} + \nabla_{\vec{x}} \cdot \check{\Pi}^\alpha(\vec{x}, t) - n_\alpha(\vec{x}, t)\vec{F}^a(\vec{x}, t) = \vec{G}_{j_\alpha}^{coll}(\vec{x}, t) - \vec{L}_{j_\alpha}^{coll}(\vec{x}, t) \quad (9.21)$$

$$\frac{\partial n_\alpha(\vec{x}, t)\epsilon_\alpha(\vec{x}, t)}{\partial t} + \nabla_{\vec{x}} \cdot \vec{Q}_\alpha(\vec{x}, t) - \vec{j}_\alpha(\vec{x}, t)\vec{F}^a(\vec{x}, t) = G_{\epsilon_\alpha}^{coll}(\vec{x}, t) - L_{\epsilon_\alpha}^{coll}(\vec{x}, t). \quad (9.22)$$

The right-hand-side terms $G_{n_\alpha}^{coll}$ and $L_{n_\alpha}^{coll}$ in the continuity equation (9.20) are the gain and loss rate, respectively, describing the particle density change because of inelastic collisions leading to generation or destruction of particles of type α in the plasma volume. In the momentum balance, the property

$$\check{\Pi}^\alpha(\vec{x}, t) \equiv m_\alpha n_\alpha(\vec{x}, t)\langle \vec{v}\vec{v} \rangle = m_\alpha \int \vec{v}\vec{v}f^\alpha(\vec{x}, \vec{v}, t)d^3v \quad (9.23)$$

denotes the tensor of the momentum flux density, which is a dyadic tensor of second rank with the components $\Pi_{kl}^\alpha = m_\alpha \int v_k v_l f^\alpha d^3v$, and the terms $\vec{G}_{j_\alpha}^{coll}$ and $\vec{L}_{j_\alpha}^{coll}$ represent the gain and loss of momentum for particles of species α as a result of elastic and inelastic collisions with all species. The energy balance equation (9.22) contains the third-order moment

$$\vec{Q}_\alpha(\vec{x}, t) \equiv \frac{1}{2}m_\alpha n_\alpha(\vec{x}, t)\langle \vec{v}v^2 \rangle = \frac{1}{2}m_\alpha \int v^2 \vec{v}f^\alpha(\vec{x}, \vec{v}, t)d^3v, \quad (9.24)$$

which is the vector of the energy flux density, and the right-hand-side terms $G_{\epsilon_\alpha}^{coll}$ and $L_{\epsilon_\alpha}^{coll}$ refer to the energy density gain and loss due to elastic and inelastic collision processes.

In order to connect (9.21) and (9.22) with common hydrodynamic equations, $\check{\Pi}^\alpha$ and \vec{Q}_α have to be expressed by macroscopic properties. Therefore, the velocity of each particle is expressed as the sum of the average velocities \vec{u}^α , that is, the directed velocity, and the random or thermal velocity \vec{w}^α , where averaging of the latter yields zero according to

$$\langle \vec{w}^\alpha \rangle \equiv \langle (\vec{v} - \vec{u}^\alpha) \rangle = \frac{1}{n_\alpha(\vec{x}, t)} \int (\vec{v} - \vec{u}^\alpha) f^\alpha(\vec{x}, \vec{v}, t) d^3v = 0. \quad (9.25)$$

Employing the summation of the particle velocity to the energy density (9.19) first, it becomes obvious that it is connected with the sum of the components that are associated with the directed and the random motion via

$$n_\alpha \epsilon_\alpha = \frac{1}{2} m_\alpha n_\alpha |\vec{u}^\alpha|^2 + \frac{1}{2} m_\alpha n_\alpha \langle (w^\alpha)^2 \rangle = \frac{1}{2} m_\alpha n_\alpha |\vec{u}^\alpha|^2 + \frac{3}{2} n_\alpha k_B T_\alpha, \quad (9.26)$$

where the mean square of the thermal velocity is given by $\langle (w^\alpha)^2 \rangle = 3k_B T_\alpha / m_\alpha$ with the temperature T_α and the Boltzmann constant k_B . The tensor (9.23) of the momentum flux density receives the set of values

$$\Pi_{kl}^\alpha = m_\alpha n_\alpha u_k^\alpha u_l^\alpha + m_\alpha n_\alpha \langle w_k^\alpha w_l^\alpha \rangle = m_\alpha n_\alpha u_k u_l + p_{kl}^\alpha \quad (9.27)$$

with the pressure tensor $\check{p}^\alpha = m_\alpha n_\alpha \langle \vec{w}^\alpha \vec{w}^\alpha \rangle$. This tensor is generally divided into the scalar pressure p^α and the so-called viscous stress tensor $\check{\pi}^\alpha$, which has the components

$$p_{kl}^\alpha = p^\alpha \delta_{kl} + \pi_{kl}^\alpha \quad \text{with} \quad \pi_{kl}^\alpha = m_\alpha n_\alpha \langle w_k^\alpha w_l^\alpha \rangle - p^\alpha \delta_{kl} \quad (9.28)$$

as is known from hydrodynamics. The scalar partial pressure p^α of the species α is determined by the average energy of the thermal motion or by the temperature according to

$$p^\alpha = \frac{1}{3} m_\alpha n_\alpha \langle (w^\alpha)^2 \rangle = n_\alpha k_B T_\alpha. \quad (9.29)$$

The tensor $\check{\pi}^\alpha$ represents the dissipative part of the pressure that arises from deviations of the distribution function f^α from spherical symmetry with respect to the thermal velocity, that is, from an isotropic distribution. Then, the combination of equations (9.20), (9.21), (9.27), and (9.28) yields the vector equation

$$\begin{aligned} & m_\alpha n_\alpha \left[\frac{\partial \vec{u}^\alpha}{\partial t} + (\vec{u}^\alpha \cdot \nabla_{\vec{x}}) \vec{u}^\alpha \right] \\ &= n_\alpha \vec{F}^\alpha - \nabla_{\vec{x}} p - \nabla_{\vec{x}} \check{\pi}^\alpha + \vec{G}_{j_\alpha}^{coll} - \vec{L}_{f_\alpha}^{coll} - m_\alpha \vec{u}^\alpha (G_{n_\alpha}^{coll} - L_{n_\alpha}^{coll}) \end{aligned} \quad (9.30)$$

for the directed velocity describing the motion of the particle of species α .

When accordingly expressing the energy flux density (9.24) in dependence on the directed and thermal velocity, the relation

$$\vec{Q}_\alpha = \vec{q}_\alpha + \left(\frac{1}{2} m_\alpha n_\alpha |\vec{u}^\alpha|^2 + \frac{1}{2} m_\alpha n_\alpha \langle (w^\alpha)^2 \rangle + p^\alpha + \check{\pi}^\alpha \right) \vec{u}^\alpha \quad (9.31)$$

is obtained, where the first term $\vec{q}_\alpha = m_\alpha n_\alpha \langle (w^\alpha)^2 \vec{w}^\alpha \rangle$ is the vector of the heat flux density characterizing the energy transfer connected exclusively with the thermal

particle motion. The further terms in (9.31) specify the flux as a result of the directed motion, that is, the energy transfer from the directed movement itself (second term) and from the thermal energy (third term) as well as the energy related to the work of the pressure forces. Then, the combination of equations (9.22), (9.26), and (9.31) finally leads to the energy balance equation

$$\frac{\partial n_\alpha \epsilon_\alpha}{\partial t} + \nabla_{\vec{x}}(n_\alpha \epsilon_\alpha \vec{u}^\alpha) = n_\alpha \vec{u}^\alpha \vec{F}^a - \nabla_{\vec{x}}(p^\alpha \vec{u}^\alpha) + \nabla_{\vec{x}}(\check{\pi}^\alpha \vec{u}^\alpha) - \nabla_{\vec{x}} \vec{q}_\alpha + G_{\epsilon_\alpha}^{coll} - L_{\epsilon_\alpha}^{coll} \quad (9.32)$$

describing the temporal change of the total (kinetic and thermal) energy density due to convection on the left-hand side as well as the action of external forces, compression/expansion, viscous stresses, heat flux, and gain and loss in collision processes on the right-hand side.

The system of moment equations (9.20) through (9.22) is not a complete description of the plasma behavior because each moment equation includes a term containing a moment of higher order. In particular, the particle flux density (first-order moment) is introduced for the solution of the particle balance (zero-order). It is determined by the momentum balance equation, where the pressure tensor (second-order moment) is inducted. The scalar pressure is connected with the average energy density and the associated energy balance calls for the vector of the energy flux density (third-order moment). Thus, a complete (infinite) set of moment equations replaces the kinetic equation in the framework of the macroscopic description. It cannot be solved in practice and some approximations, for example, concerning the symmetry or isotropy of the velocity distribution function, are needed in order to close the equation system. That way, a closed set of moment equations can be treated instead of the solution of the kinetic equation as a complex integro-differential equation.

A typical example of such a procedure is the fluid description of the species in a plasma based on the solution of the system made up by the continuity equation (9.20), the equation of motion (9.30) (or the corresponding momentum balance in conservation equation form), and the energy balance equation (9.32) determining the spatiotemporal behavior of the density $n_\alpha(\vec{x}, t)$, current density $n_\alpha(\vec{x}, t)\vec{u}^\alpha(\vec{x}, t)$, and energy density $n_\alpha(\vec{x}, t)\epsilon_\alpha(\vec{x}, t)$. Here, knowledge of the dissipative part of the pressure tensor, the heat flux density vector, and the collision terms as functions of n_α , \vec{u}^α , and ϵ_α or related properties are required, where $\check{\pi}^\alpha$ can be approximated by means of derivatives of the velocity component and viscosity coefficients and $\vec{q}_\alpha = -\kappa_\alpha \nabla_{\vec{x}} T_\alpha$ with the thermal conductivity κ_α of the species. In addition, the external forces have to be specified.

An important kind of interaction related to plasmas is the electromagnetic interaction of charged particles. The force on a particle of charge $Z_\alpha e_0$ in an electric field \vec{E} and a magnetic field (or magnetic induction) \vec{B} is given by the Lorentz force:

$$\vec{F}(\vec{x}, t) = Z_\alpha e_0 \left(\vec{E}(\vec{x}, t) + \vec{u}^\alpha(\vec{x}, t) \times \vec{B}(\vec{x}, t) \right), \quad (9.33)$$

where Z_α and e_0 are the particle charge number and elementary charge. If time-dependent electromagnetic fields are present, then Maxwell's equations

$$\nabla_{\vec{x}} \cdot \vec{D}(\vec{x}, t) = e_0 \sum_{\alpha} Z_{\alpha} n_{\alpha}(\vec{x}, t) \quad (9.34)$$

$$\nabla_{\vec{x}} \times \vec{H}(\vec{x}, t) = \vec{J}(\vec{x}, t) + \frac{\partial}{\partial t} \vec{D}(\vec{x}, t) \quad (9.35)$$

$$\nabla_{\vec{x}} \times \vec{E}(\vec{x}, t) = -\frac{\partial}{\partial t} \vec{B}(\vec{x}, t) \quad (9.36)$$

$$\nabla_{\vec{x}} \cdot \vec{B}(\vec{x}, t) = 0 \quad (9.37)$$

have to be satisfied, where \vec{D} , \vec{H} , and $\vec{J} = e_0 \sum_{\alpha} Z_{\alpha} \vec{j}_{\alpha}$ are the dielectric displacement, magnetizing field, and total current density carried by the charged particles, respectively, and the term $\partial \vec{D} / \partial t$ denotes the displacement current. In vacuum, the relations $\vec{D} = \epsilon_0 \vec{E}$ and $\vec{H} = \vec{B} / \mu_0$ hold for the external sources with the vacuum permittivity ϵ_0 and permeability of free space μ_0 . Then, the electric field satisfies Poisson's equation:

$$\Delta_{\vec{x}} \Phi(\vec{x}, t) = -\frac{e_0}{\epsilon_0} \sum_{\alpha} Z_{\alpha} n_{\alpha}(\vec{x}, t), \quad \vec{E}(\vec{x}, t) = -\nabla_{\vec{x}} \Phi(\vec{x}, t) \quad (9.38)$$

and relation (9.35) turns into

$$\nabla_{\vec{x}} \times \vec{B}(\vec{x}, t) = \mu_0 \vec{J}(\vec{x}, t) + \frac{1}{c^2} \frac{\partial}{\partial t} \vec{E}(\vec{x}, t), \quad (9.39)$$

where $c = 1/\sqrt{\epsilon_0 \mu_0}$ is the speed of light in vacuum. The set of equations has to be completed by an equation system for the external electric discharge circuit.

9.1.5 NUMERICAL METHODS

The theoretical description of transport phenomena in plasma applications can be carried out by quite different modeling approaches. As mentioned earlier, the Liouville equation (9.3) is the most general equation and it is valid in all situations. However, it is so complex from a computational point of view that it cannot be solved for real plasma applications. A fully kinetic description of the transport of charge carriers has become possible by means of particle models. Their accuracy is mainly limited by the number of particles that can be treated in the simulation. This modeling approach is computationally much more time consuming than the solution of hydrodynamic equations. The latter are the most restricted equations with respect to their range of applicability. However, fluid (or hydrodynamic) models are in principle computationally fast and have been used for many practical engineering simulations. In addition, so-called hybrid methods have been established that use the simpler hydrodynamic equations as soon as possible and employ the more complex kinetic equations only where necessary. A scheme of basic numerical modeling approaches discussed in the following text is represented in Figure 9.3.

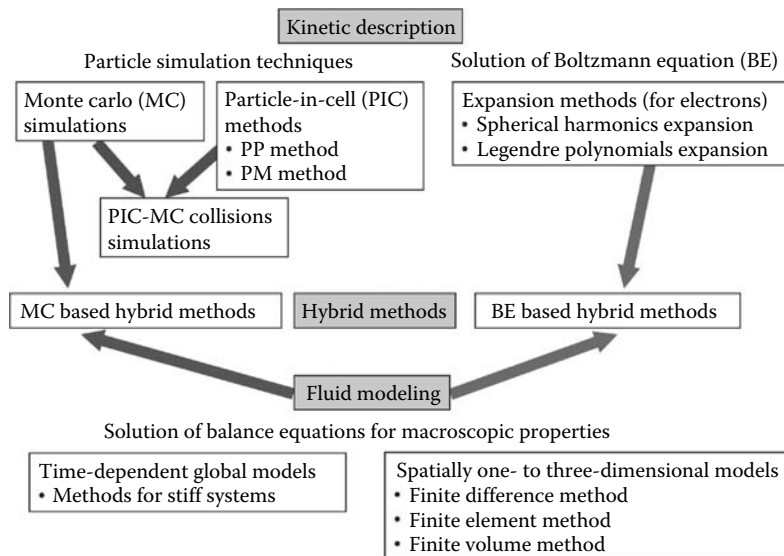


FIGURE 9.3 Basic numerical methods for modeling of plasma applications.

9.1.5.1 Fluid Equations

The system of time-dependent fluid equations discussed in Section 9.1.4 can be written in the general form

$$\frac{\partial \vec{Y}}{\partial t} = \vec{W}(\vec{Y}), \quad (9.40)$$

where $\vec{Y}(\vec{x}, t)$ represents the set of independent physical variables describing the plasma, such as the densities n_α , current densities \vec{j}_α , and energy densities $n_\alpha \epsilon_\alpha$ of the different particles in the plasma. The operator \vec{W} is generally nonlinear and includes derivatives in the spatial variable \vec{x} . The solution of the time-dependent equation (9.40) requires appropriate initial values $\vec{Y}(\vec{x}, t_0)$, for example, at time t_0 . Then, the temporal evolution of \vec{Y} is determined for all times $t_n > t_0$ in discrete time steps of size Δt where $t_n = t_0 + n\Delta t$ with $n > 0$. The discrete value \vec{Y}_n at the time t_n is obtained by solving (9.40) according to the differencing

$$\frac{\vec{Y}_n - \vec{Y}_{n-1}}{\Delta t} = \theta \vec{W}_n(\vec{Y}_n) + (1 - \theta) \vec{W}_{n-1}(\vec{Y}_{n-1}) \quad (9.41)$$

with $0 \leq \theta \leq 1$. Schemes using the approximation $\theta = 0$ are referred to as explicit and the information required to calculate the solution at time t_n depends only on the known values \vec{Y}_{n-1} at time t_{n-1} . Then, (9.41) is solved as an ordinary differential equation system. If $\theta > 0$, the right-hand side of (9.41) comprises information about \vec{Y}_n as well and a suitable inversion of the operator \vec{W} is necessary. Schemes with $\theta = 1$

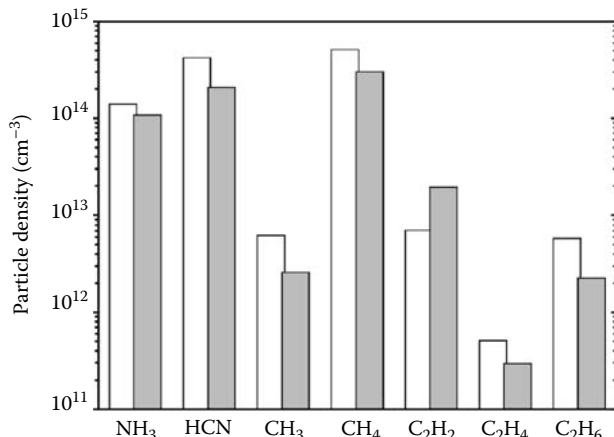


FIGURE 9.4 Calculated (gray bars) and measured (white bars) particle densities in $\text{H}_2\text{-Ar-N}_2\text{-CH}_4$ plasma.

are called fully implicit or backward time and $\theta = 0.5$ gives the Crank–Nicolson difference scheme, which is second-order accurate in time [8].

Depending on the plasma conditions considered, the operator \vec{W} can be represented in zero, one, two, or even three spatial dimensions. In the 0D case, globally averaged properties of the plasma are obtained. In particular, the plasma-chemical reaction mechanisms are often analyzed on the basis of such global models. The solution of the resulting equation system for the plasma-chemical kinetics is challenging because the different species generally evolve on very different time scales. Several software packages have been developed to integrate these stiff systems of ordinary differential equations, for example, Chemkin [9], Facsimile [10], and Odepak [11]. As an example of plasma chemistry modeling using Facsimile, Figure 9.4 shows the particle densities of several compounds in $\text{H}_2\text{-Ar-N}_2\text{-CH}_4$ microwave plasmas with a gas mixture of 73% hydrogen, 10.8% argon, 9% nitrogen, and 7.2% methane under static conditions in comparison with experimental data [12].

For the solution in one or more spatial dimensions, the methods most commonly applied to model gas discharge plasmas are the finite difference method (FDM) and the finite element method (FEM) (see, e.g., [13–15] and references therein). The finite volume method (FVM) has been applied, for example, to modeling of HID lamps and microdischarge devices [16–18] and has become very popular for the analysis of problems of computational fluid dynamics.

In the finite difference method, the solution domain is divided into a discrete set of grid points \vec{x}_i with a distance Δx_i for each coordinate of \vec{x} [19]. The first and second derivatives of \vec{W} at any grid point are approximated by suitable finite difference counterparts including function values at neighboring points. Explicit time-stepping methods are in general the easiest to implement but are restricted on the time step by the Courant–Friedrichs–Levy (CFL) condition [20].

$$\Delta t < \frac{\Delta x_i}{|v_{max}|} \quad (9.42)$$

and the von Neumann condition [21]

$$\Delta t < \frac{\Delta x_i^2}{(2D_{max})} \quad (9.43)$$

to ensure stability of the numerical scheme, where v_{max} and D_{max} are the maximum velocity and maximum diffusion coefficient, respectively, in the system of equations. Because numerical stability does not necessarily imply accuracy, the time step required for accuracy may be smaller than that needed for stability in practice.

Numerical schemes with $\theta \geq 0.5$ in (9.41) avoid the CFL and von Neumann stability conditions but are more difficult to implement than explicit schemes. Because the operator \vec{W} is nonlinear in general, an iterative procedure is usually necessary at each time step.

For partial differential equations of second order with a significant first spatial derivative term, the condition

$$|\text{Pe}| \leq 1 \quad (9.44)$$

on the local Péclet number Pe ensures non-oscillatory solutions even in regions of steep gradients and limits the spatial resolution if all neighboring points are considered for the discretization of the first derivative term [22]. The local Péclet number is a dimensionless number that relates the rate of advection of a flow to its rate of diffusion. In particular, when applying the drift-diffusion approximation

$$\vec{j}_\alpha(\vec{x}, t) = \text{sgn}(Z_\alpha)N_\alpha(\vec{x}, t)\mu_\alpha(\vec{x}, t)\vec{E}(\vec{x}, t) - \nabla_{\vec{x}}(D_\alpha(\vec{x}, t)N(\vec{x}, t)) \quad (9.45)$$

for the description of the particle flux density of charge carriers, as it is frequently done in gas discharge plasma modeling, the local Péclet number represents the ratio of the drift effect to the diffusion effect and it is given by

$$\text{Pe} = \Delta x_i \frac{\mu_\alpha E_i}{2D_\alpha}. \quad (9.46)$$

Here, μ_α and D_α are the mobility and the diffusion coefficient of species α , respectively, and E_i is the magnitude of the electric field at the grid point \vec{x}_i . An approach to avoid the requirement of very fine grids required by condition (9.44) is the application of stabilized discretization schemes such as upwind schemes and, specifically for modeling of gas discharges and semiconductor devices, the Scharfetter–Gummel discretization scheme [23].

In the finite element method, the variational formulation of the partial differential equation is considered [24]. Therefore, (9.40) is multiplied by suitable test functions for each independent physical quantity and is subsequently integrated over the solution domain of the problem. The resulting variational equation for each quantity is

discretized by dividing the solution region into a finite number of elements that are equipped with basis functions of the finite element space. When expressing the test functions and the unknown solution function as a linear combination of the basis functions and when employing the time step discretization as described earlier, a system of equations to determine the values of the solution function at the nodes for each time step is obtained. The time step constraints of the FEM are similar to the FDM. An advantage of the FEM is its high flexibility in node placement anywhere in the solution region to make optimal use of geometric and physical properties of the system. The method is used for example, in the software package COMSOL Multiphysics [25].

In the finite volume method, the function values are calculated at discrete locations on a meshed geometry similar to FDM [26]. Therefore, the solution domain is divided into nonoverlapping small control volumes surrounding each node point on the mesh and the partial differential equation is integrated over each control volume. Volume integrals in the partial differential equation that contain a divergence term are converted to surface integrals using the divergence theorem of Gauß and derivatives of higher order are replaced by difference quotients analogous to FDM. This procedure results in a system of algebraic equations for the determination of the cell averages of the unknown function values within each control volume. From a physical point of view, FVM provides the most natural scheme of discretization for conservation laws because it makes use of the integral form of the conservation law and ensures conservation of the quantities considered. Another advantage of FVM is that unstructured meshes and complex domains can easily be handled since each control volume is treated independently from its neighboring volume as in FEM. The method is used in many computational fluid dynamics packages like ANSYS CFX [27], CFD-ACE+ [28], Fluent [29], PHOENICS [30], and STAR-CD [31].

9.1.5.2 Solution of the Boltzmann Equation

With knowledge of the external force and collision cross sections, the Boltzmann equation (9.14) can be used to determine the velocity distribution function $f^\alpha(\vec{x}, \vec{v}, t)$ of species α . Depending on the complexity of the plasma physics, an equation with up to seven dimensions has to be solved for each species. For weakly ionized plasmas, the densities of the charge carriers are low in comparison with the densities of the neutral particles. Thus, collisions of charge carriers with neutral particles have marginal influence on the velocity distribution function of neutral particles, which possess a Maxwellian velocity distribution

$$f^\alpha(\vec{x}, \vec{v}, t) = n_\alpha(\vec{x}, t) \left(\frac{m_\alpha}{2\pi k_B T_\alpha} \right)^{3/2} \exp \left[- \left(\frac{m_\alpha}{2k_B T_\alpha} \right) (\vec{v} - \vec{u}^\alpha)^2 \right] \quad (9.47)$$

because of their intensive energetic contact in elastic collisions.

A standard technique for solving the Boltzmann equation of the electrons ($\alpha = e$) consists in an orthogonal expansion of the velocity distribution function

with respect to the directions \vec{v}/v of the electron velocity \vec{v} using spherical harmonics [4,32,33]

$$f^e(\vec{x}, \vec{v}, t) = \sum_{k=0}^{\infty} f_k^e(\vec{x}, v, t) \otimes \left(\frac{\vec{v}}{v} \right)^k \quad (9.48)$$

or Legendre polynomials if the direction of the force and the expected inhomogeneity are parallel to a fixed space direction. Because of the orthogonality of the spherical harmonics, this approach reduces the Boltzmann equation to a set of equations for the (tensorial) expansion coefficients f_k^e of rank k where the expansion is frequently truncated after the second term, that is, $k = 1$. Here, f_0^e is the isotropic part of the velocity distribution and the further coefficients represent contributions to the distribution anisotropy. Different FDM codes have been developed to solve the resulting set of equations for stationary discharge plasmas with zero, one, or two spatial dimensions as well as for time-dependent plasmas with zero or one spatial dimensions [15,33,34]. As an example for the solution of the spatially 1D electron Boltzmann equation by means of a multiterm method, the calculated spatial evolution of the isotropic distribution $f_0^e(z, U)$ in the cathode-fall region of an abnormal H₂-Ar-N₂ DC glow discharge in a deposition reactor is shown where the magnitude of the velocity was replaced by the kinetic energy $U = m_e v^2/2$ [35]. The solver BOLSIG+ that provides steady-state solutions of the electron Boltzmann equation is freely available [36] Figure 9.5.

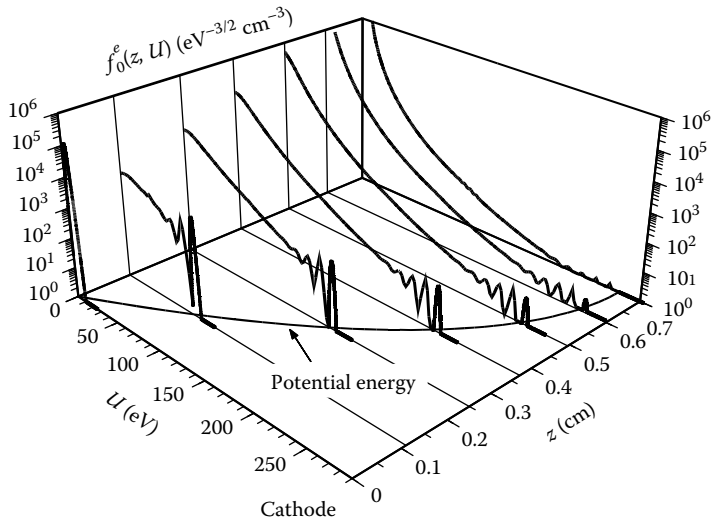


FIGURE 9.5 Spatial behavior of the isotropic distribution $f_0^e(z, U)$ in the cathode-fall region of a glow discharge in a gas mixture with 71.5% H₂, 15.3% Ar, and 13.2% N₂ obtained by a 10-term Boltzmann calculation.

9.1.5.3 Particle Models

An alternative approach for a kinetic description of the behavior of plasmas uses the techniques of particle simulation. Particle simulations of plasmas can be divided into two general categories, namely, Monte Carlo (MC) simulations and particle-in-cell (PIC) methods [37–40]. Both approaches use very similar techniques to advance particles under the action of external and interparticle forces.

In MC simulations, the trajectories of test particles (usually charged particles) between collisions with the background gas particles are obtained by the numerical integration of the equation of motion for each test particle. The dynamics during a collision process is not resolved in the MC simulation and the collisions that result from short-range forces are assumed to be binary. The time (or length) of the free flight between two collisions is calculated by generating a random number and relating it to the collision frequency (or mean free path) known in dependence on the particle energy at each position and time. Sequences of random numbers are further used to determine, for example, the type of collision process that occurred after a free flight, taking into account the cross-section values of the different collision processes at the energy of the colliding test particle, the change of the vectorial velocity during a collision process, as well as the incident of an interaction with the walls of the plasma reactor and the corresponding change of the velocity in the case of a reflection event. Monte Carlo simulations can easily be applied to multidimensional problems and complicated geometries, but this advantage is balanced by the necessity to treat a large number of test particles in any simulation to get sufficient accuracy.

PIC simulations are most commonly used to simulate fully ionized plasmas. In the PIC approach, the equations of motion for superparticles, representing a large number of real electrons and ions each, are integrated for each superparticle, taking into account the electromagnetic fields calculated on a numerical grid. Collisions are of long range because the interparticle forces are Coulomb forces between charge carriers. These forces can be included in the simulation by explicitly summing the interparticle forces and adding the net force given by the applied electromagnetic field, as it is done in the so-called particle–particle (PP) method.

An alternative procedure of including Coulomb forces between charge carriers is performed in the so-called particle-mesh (PM) method. Here, the densities and current densities of electrons and ions are summed on the numerical grid to obtain the electric charge density and total current density. Knowing these quantities, the electric and magnetic fields are then determined by solving Maxwell's equations on the same numerical grid. The PM method is computationally faster than the PP method at the cost of a resolution loss for the potential and fields.

The Newtonian equations of motion in the PIC are most commonly solved by the finite-difference Leapfrog approximation scheme according to [38]

$$\vec{x}_i^{n+1} = \vec{x}_i^n + \vec{v}_i^{n+1/2} \Delta t \quad (9.49)$$

$$\vec{v}_i^{n+1/2} = \vec{v}_i^{n-1/2} + \frac{\vec{F}(\vec{x}_i, t^n)}{m} \Delta t, \quad (9.50)$$

an explicit time-stepping scheme that is second-order accurate in both space and time.

In order to use the PIC simulation method for collisional plasma modeling and self-sustained discharges, the interaction between charge carriers and neutral particles has to be added. The inclusion of electron and ion collisions with neutral particles is carried out by use of the Monte Carlo method described earlier and the resulting simulation technique is called PIC-MCC, where MCC stands for Monte Carlo collisions. The accuracy of this kinetic simulation technique is mainly limited by the number of particles that can be treated in a simulation and the influence of velocity space diffusion leading to numerical thermalization, as discussed in [41]. PIC and PIC-MCC codes on bounded plasmas are available (freely), for example, from [42].

9.1.5.4 Hybrid Methods

Hybrid methods represent a compromise between the computationally faster fluid models and the more detailed, but computationally very extensive, kinetic treatment allowing a description of the nonequilibrium behavior of plasma species. In principle, two different approaches have been established where the main difference concerns the kinetic part of the hybrid method.

The first technique couples a fluid description of the slow species of the plasma, that is, neutrals and slow charge carriers, with MC simulations for the fast species, normally the electrons, providing the source functions of electron impact ionization (and excitation) processes that are employed in the continuity equations of the fluid module [43–45]. Concerning the transport coefficients of the charge carriers, most of these hybrid models use ion mobilities as a function of the reduced electric field $|\vec{E}|/n$ with $n = \sum_{\alpha} n_{\alpha}$ and a constant experimental value for the electron mobility at a low value of $|\vec{E}|/n$. To get the diffusion coefficients of the charge carriers, the Einstein relation [7]

$$\frac{D_{\alpha}}{\mu_{\alpha}} = \frac{k_B T_{\alpha}}{e_0} \quad (9.51)$$

is usually utilized, where for the electrons in particular, a characteristic energy $k_B T_e/e_0$ of 1 eV is normally used. This hybrid approach has so far been applied successfully to studies of DC discharge plasmas in one and two space dimensions as well as to RF and transient, spatially 1D glow discharges. It profits from its large flexibility particularly of the MC simulations.

The second hybrid approach combines a system of fluid equations for the plasma species with the solution of the Boltzmann equation of the electrons to take into account the nonequilibrium behavior of the electrons. Although the solution of the kinetic equation for the electrons can become mathematically complicated and computationally very time consuming for complex geometries, this approach has the advantage that it allows to accurately treat the nonlocal electron transport and to directly derive the transport and rate coefficients of the electrons. For instance, the rate coefficient $k_{\alpha}^{in}(\vec{x}, t)$ of an inelastic collision process of electrons with neutral heavy particles of species α gets the representation

$$k_{\alpha}^{in}(\vec{x}, t) = \frac{1}{n_e(\vec{x}, t)} 4\pi \int_0^{\infty} v Q_{\alpha}^{in}(v) f_0^e(\vec{x}, v, t) v^2 dv, \quad (9.52)$$

where the relative velocity of the two colliding particles is assumed to be equal to the electron velocity and the corresponding total collision cross section $Q_{\alpha}^{in}(v) = \int \sigma_{\alpha}^{in}(v, \theta) \sin \theta d\theta d\varphi$ is obtained by integrating the differential cross section σ_{α}^{in} over the entire solid scattering angle indicated by its element $\sin \theta d\theta d\varphi$. The rate coefficient depends on the velocity distribution function that is obtained from the solution of the electron Boltzmann equation. In plasmas at thermodynamic equilibrium, the velocity distribution becomes a Maxwellian distribution (9.47) and the rate coefficient k_{α}^{in} naturally depends on the electron temperature. The current state and recent progress of such hybrid modeling of plasmas in technological applications is reported in [15]. As an example of recent results of such time- and space-dependent Boltzmann equation-based hybrid modeling, Figure 9.6 shows the periodic behavior of the average energy $\epsilon_e(r, t)$ of the electrons in the positive column plasma of the low-pressure He-Xe lamp discharge discussed in [15].

An alternative hybrid approach is proposed in [46]. Because in various situations a hydrodynamic description is applicable in certain discharge regions while a kinetic treatment is required in other regions, such as boundary layers and regions close to electrodes and walls, this hybrid approach suggests to divide the entire discharge region into different zones using either a fluid description where and when possible, or a kinetic description where and when necessary. The main problems of this approach consist in finding the regions and conditions under which the fluid description is valid and in adapting the solutions obtained by the kinetic and fluid descriptions.

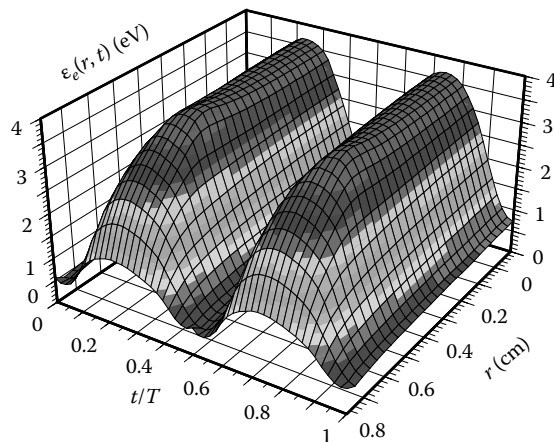


FIGURE 9.6 Periodic behavior of the average electron energy $\epsilon_e(r, t)$ in the positive column of a low-pressure lamp discharge in a gas mixture with 98% helium and 2% xenon at a pulse duration of $T = 20 \mu\text{s}$.

9.2 ELEMENTARY VOLUME PROCESSES IN GAS DISCHARGES

The plasma chemistry of reactive gas discharges strongly depends on the collision (elementary) processes operating, for given external control parameters, between the constituents of the discharge: electrons, ions, molecules, and atoms. Mathematically, these processes are encoded in the collision integrals of the Boltzmann–Poisson equations (see Section 9.1) that are classical equations describing the discharge on the macroscopic length scales defined by the mean-free paths of the various species and the screening length. The dynamics of the elementary processes, however, take place on the much shorter microscopic scale. They are thus controlled by quantum mechanical principles that will be discussed in this chapter.

From the quantum-mechanical point of view (see Figure 9.7 for an illustration), collisions proceed through temporary compound states [47] that form and fragment on the atomic length and time scales,* in contrast to the macroscopic scales on which typical plasma phenomena such as sheath formation or wave propagation occur. That the scales required to complete the momentum, energy, and particle[†] transfer (rearrangement) defining a collision are well separated from the plasma scales has two profound implications:

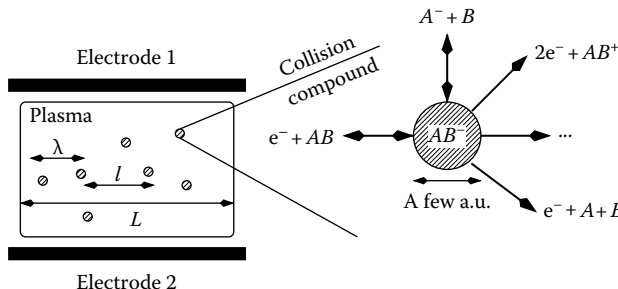


FIGURE 9.7 Schematic representation of the length scales in the bulk of a typical low-temperature gas discharge ($n_e = n_i = 10^{10} \text{ cm}^{-3}$, $T_e = 10 \text{ eV}$, $T_i = 0.03 \text{ eV}$, and $n_{\text{gas}} = 10^{16} \text{ cm}^{-3}$). The macroscopic scales on which the Boltzmann–Poisson system operates are the spatial extension of the plasma $L \sim \mathcal{O}(\text{cm})$, the mean-free-path of the species $l \sim \mathcal{O}(10^{-2} \text{ cm})$, and the plasma screening length $\lambda \sim \mathcal{O}(10^{-3} \text{ cm})$. On the right is an illustration of how the (temporary) collision compound AB^- , whose length scale is a few atomic units, that is, of the order of 10^{-7} cm , controls the first six reactions of Table 9.1. The branching of the AB^- state at a given energy determines the cross sections for the reactions. The double arrow indicates that the fragments can appear in the entrance and the exit channel of a collision.

* If not stated otherwise, in this section it is implicitly assumed that physical quantities are measured in atomic units, that is, lengths, masses, and charges are given in terms of the Bohr radius a_B , the electron mass m_e , and the elementary charge e , respectively. The unit of energy is then $2R_0$, where R_0 is the Rydberg energy.

[†] The term “particle” denotes either a single “fundamental” particle, having no internal degrees of freedom relevant for the collision process, or a collection of fundamental particles in a bound state; in the latter event the term “fragment” will be also used.

1. Cross sections measured, for instance, in crossed beam or swarm experiments, can be used without modifications as input data for plasma modeling.
2. Theoretical calculations of cross sections can neglect the plasma environment, which is a tremendous simplification.

Whereas the physics of a collision is unaffected by the plasma, the reverse is of course not true. Elementary processes determine to a large extent the properties of a plasma (see previous chapters). First of all, a gas discharge can only be maintained electrically because of electron impact ionization, and for an electro-negative gas, dissociative electron attachment produces positively and negatively charged carriers. Equally important are electron impact excitation and dissociation of molecules. They not only transform external electric energy into internal energy, but most importantly also produce the species that are eventually utilized in the technological application of the discharge: electronically excited species if the discharge is used as a light source or laser and reactive fragments (radicals) if the discharge is applied for surface processing or catalysis.

Technologically interesting gas discharges contain complex molecular gases such as CF_4 , CF_3I , C_3F_8 , CCl_2F_2 , or SF_6 with a multitude of excited and fragmented species. Even simple diatomic molecules, O_2 or N_2 for instance, give rise to a large number of species with an accordingly large number of elementary processes. Leaving aside elementary processes containing three particles in the entrance channel that are only relevant at rather high densities, the most common collisions for a generic electro-negative, diatomic gas are shown in Table 9.1, where they are also classified according to the collision compounds controlling the microphysics: AB^- , the compound illustrated on the right-hand side of Figure 9.7, A^{2-} , A_2B , A_2B^- , and AB . The branching of the compounds and thus the probabilities for the various collisions (cross sections) depend on the initial energy and properties of the compound states at the distance where they have to lock-in into the asymptotic scattering states defining the various collisions.

In view of the great technological and economical impact of reactive gas discharges, it is somewhat surprising that the number of experimental groups measuring cross sections for gases of plasma-chemical relevance is rapidly diminishing. Thus, any listing of currently available cross-section data must be necessarily incomplete. Since in addition the gases of interest change with time, cross-section data are not included at all in this chapter. As far as they exist, they can be found, for instance, in the review article by Brunger and Buckman [48], the monograph by Christophorou and Olthoff [49], and in web-based cross-section compilations sponsored by national research institutions and university groups whose activities depend on atomic and molecular collision data. The largest ones, maintained, respectively, by the International Atomic Energy Agency, the American National Institute of Standards and Technology, the Oak Ridge National Laboratory, USA, the Japanese National Institute for Fusion Science, the Weizmann Institute of Science in Israel, and the Université Paris-Sud in Orsay, France, are [50]:

TABLE 9.1
**Typical Collisions and Their Compound States for an
 Electro-Negative, Diatomic Gas**

<i>Collisions with compound state AB^-</i>	
1.	$e^- + AB_i \rightarrow AB^- \rightarrow e^- + AB_f$
2.	$e^- + AB_i \rightarrow AB^- \rightarrow 2e^- + AB_f^+$
3.	$e^- + AB_i \rightarrow AB^- \rightarrow A_f^- + B_f$
4.	$e^- + AB_i \rightarrow AB^- \rightarrow e^- + A_f + B_f$
5.	$A^- + B_i \rightarrow AB^- \rightarrow e^- + A_f + B_f$
6.	$A^- + B_i \rightarrow AB^- \rightarrow e^- + AB_f$
<i>Collisions with other compound states</i>	
7.	$e^- + A_i^- \rightarrow A^{2-} \rightarrow 2e^- + A_f$
8.	$A_i^- + AB_i^+ \rightarrow A_2B \rightarrow A_f + AB_f$
9.	$A_i^- + AB_i^+ \rightarrow A_2B \rightarrow A_f + A_f + B_f$
10.	$A_i^- + AB_i \rightarrow A_2B^- \rightarrow e^- + A_f + AB_f$
11.	$A_i^- + AB_i \rightarrow A_2B^- \rightarrow e^- + A_2B_f$
12.	$e^- + AB_i^+ \rightarrow AB \rightarrow A_f + B_f$

The indices i and f denote initial and final internal states of the molecules, atoms, and ions before and after the collision, respectively.

1. <http://www.iaea.org/programmes/amdis>
2. <http://physics.nist.gov/PhysRefData/contents.html>
3. <http://www-cfadc.phy.ornl.gov>
4. <http://dbshino.nifs.ac.jp>
5. <http://plasma-gate.weizmann.ac.il>
6. <http://gaphyor.lpgp.u-psud.fr>

Due to lack of empirical cross-section data, theoretical calculations become increasingly important. There are two major lines of attack. One, the ab initio approach, attempts to construct parameter-free eigenstates for collision compounds and to match these states to the asymptotic scattering states representing specific collision products [51], while the other tries to directly obtain parameter-free scattering matrices from a suitable variational principle [52]. Both approaches are extremely time consuming and have so far only been applied to a few selected collisions involving molecules with at most three atoms. Even when the formal problems preventing the application to complex molecules are solved in the future, it is hard to imagine a nonexpert routinely using an ab initio package to generate cross sections for as yet unstudied collision processes.

The other, perhaps more valuable approach, as far as plasma-chemical applications are concerned, is the semiempirical approach. Examples are the binary-encounter [53–55] and the Deutsch–Märk [56–58] model for electron impact ionization, the resonance model for dissociative attachment [59,60], electron-detachment

[61,62], dissociative recombination [63,64], vibrational excitation [60,65], and the Landau-Zener model for ion-ion annihilation [66,67]. Common to all these models is their attempt to encapsulate the complicated collision dynamics in a few parameters that can either be obtained from electronic structure calculations or from experiments. To some extent these models are ad hoc, but they have the great virtue of providing clear physical pictures of the collision processes, thereby helping the plasma physicist to develop an intuitive understanding of the discharge microphysics.

Despite the great diversity of elementary processes in a gas discharge, this chapter tries to give a uniform presentation of the subject within the framework of multi-channel scattering theory [68–70] focusing, in particular, on inelastic and reactive collisions. Cross-section formulae are intentionally not developed to a point where they could be applied to particular collision processes because this involves mathematical rather technical (approximate) solutions of the given equations that moreover have to be worked out case by case. The details can be found in the original literature. Additional information, in particular with regards to formal aspects of calculating cross sections, can be extracted from the review articles by Rudge [71], Bardsley and Mandl [72], Inokuti [73], Lane [74], Delos [75], Chutjian and coworkers [76], Hahn [77], and Florescu-Mitchell and Mitchell [78].

9.2.1 FUNDAMENTAL CONCEPTS

9.2.1.1 Collision Cross Section

The kinetic description of a gas discharge is based on a set of Boltzmann equations for the distribution functions $f_i(\mathbf{r}, \mathbf{v}, t)$ of the participating species $i = 1, 2, \dots, N$ and those parts of Maxwell's equations that are necessary to describe the electromagnetic driving of the discharge. For a capacitively coupled radio-frequency discharge, for instance, the equations are

$$\left[\partial_t + \mathbf{v} \cdot \nabla_r - \frac{q_i}{m_i} \nabla_r \Phi \cdot \nabla_v \right] f_i(\mathbf{r}, \mathbf{v}, t) = \sum_p I_i^p[\{f_j\}], \quad (9.53)$$

$$\Delta_r \Phi = -\frac{1}{\epsilon_0} \sum_{i=1}^N q_i \int d\mathbf{v} f_i, \quad (9.54)$$

where $I_i^p[\{f_j\}]$ is the collision integral due to process p appearing in the Boltzmann equation for species i and depending on the subset $\{f_j\}$ of the distribution functions and Φ is the electric potential.*

The external driving is in this case simply encoded in the boundary conditions for the Poisson equation; q_i and m_i are the charge and mass of species i , respectively, and ϵ_0 is the dielectric constant of the plasma.

The total number N of species required for the kinetic modeling of a generic electronegative, diatomic gas discharge can be deduced from Table 9.1. Clearly,

* In this subsection, atomic units are not used.

besides electrons and molecules of the feed-stock gas AB , atoms A and B , and ions AB^+ and A^- have to be taken into account. In general, it is also necessary to include some excited (metastable) states for the molecular and atomic constituents. Thus, in total, $N = N_{AB} + N_A + N_B + N_{AB^+} + N_{A^-} + 1$ species have to be considered, where N_σ is the number of excited states kept for the atomic or molecular constituent σ .

Each reaction shown in Table 9.1 gives rise to collision integrals in the Boltzmann equations of the respective reaction educts (species in the entrance channel) and reaction products (species in the exit channel). For elastic scattering, the structure of the collision integral is similar to the one originally derived by Boltzmann [79]. The majority of collisions, however, is inelastic and reactive; some involve even more than two reaction products. The corresponding collision integrals then have to be constructed from scratch, using elementary statistical considerations.

Take, for instance, electron impact ionization, where a primary electron scatters off a molecule and produces a secondary electron and a positively charged ion. Assuming the target molecule to be at rest, which is a very good approximation because the molecule is much heavier than the electron, the collision integral in the electron Boltzmann equation due to this process reads [80]

$$I_e[f_e] = c_{AB} \left\{ \int d\mathbf{v}_a d\mathbf{v}'' W^l(\mathbf{v}_a; \mathbf{v}, \mathbf{v}'') f_e(\mathbf{v}_a) + \int d\mathbf{v}_a d\mathbf{v}' W^l(\mathbf{v}_a; \mathbf{v}', \mathbf{v}) f_e(\mathbf{v}_a) - \int d\mathbf{v}' d\mathbf{v}'' W^l(\mathbf{v}; \mathbf{v}', \mathbf{v}'') f_e(\mathbf{v}) \right\}, \quad (9.55)$$

where momentum conservation is taken into account, the variables \mathbf{r} and t in the distribution functions are suppressed, and c_{AB} is the concentration of the molecules. The function $W^l(\mathbf{v}_a; \mathbf{v}', \mathbf{v}'')$ is the probability for an incident electron with velocity \mathbf{v}_a to produce two departing electrons with velocities \mathbf{v}' and \mathbf{v}'' , respectively. Using energy conservation, it can be related to the differential cross section for electron impact ionization

$$W^l(\mathbf{v}_a; \mathbf{v}', \mathbf{v}'') d\mathbf{v}' d\mathbf{v}'' = \frac{1}{2} v_a \sqrt{\frac{v_a^2 - v''^2 - 2E_i/m_e}{v'^2 + v''^2}} q^l(v_a, v'', \Omega'_a, \Omega''_a) \times \delta(\sqrt{v'^2 + v''^2} - \bar{u}) d\Omega'_a d\Omega''_a d\mathbf{v}' d\mathbf{v}'', \quad (9.56)$$

with the ionization energy E_i of the molecule, the electron mass m_e , $\bar{u} = \sqrt{v_a^2 - 2E_i/m_e}$, and the differential ionization cross section $q^l(v_a, v'', \Omega'_a, \Omega''_a)$ defined by the relation

$$d\sigma^l = q^l(v_a, v'', \Omega'_a, \Omega''_a) d\Omega'_a d\Omega''_a dv'' \quad (9.57)$$

with $0 \leq v'' \leq \sqrt{v_a^2 - 2E_i/m_e}$ (cf. Figure 9.8 for notational details).

The sub-nm physics of impact ionization, that is, the momentum, energy, and electron transfer during this particular electron-molecule collision, is concealed within

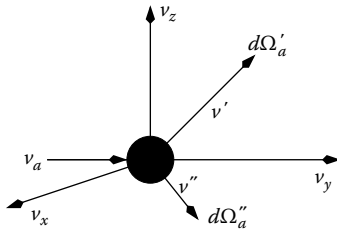


FIGURE 9.8 Velocity space kinematics of electron impact ionization. Upon impact of the incident electron with velocity vector \mathbf{v}_a , two electrons are ejected with velocity vectors \mathbf{v}' and \mathbf{v}'' , respectively. The solid angles $d\Omega'_a$ and $d\Omega''_a$ corresponding to these two velocities are defined with respect to the direction of \mathbf{v}_a . Because of the large mass difference of electrons and molecules, the molecule can be assumed to be at rest.

the function $q^l(v_a, v'', \Omega'_a, \Omega''_a)$. This statement holds for all processes. The information required about elementary processes thus reduces to a set of (differential) cross sections. Their direct measurement is tedious, expensive, and, when metastable states are involved that cannot be prepared outside the plasma, sometimes even impossible. It is at this point that theoretical calculations of cross sections—*ab initio* or otherwise—have a great impact.

A systematic solution of the electron Boltzmann equation expands the electron distribution function in terms of velocity space spherical harmonics. The angles Ω'_a and Ω''_a can then be integrated out, leading to a hierarchy of Boltzmann equations for the expansion coefficients [80]. When the anisotropy of the electron distribution is negligible, the lowest order equation suffices. The collision integral of interest is then

$$q^l(v_a, v'') = \int d\Omega'_a d\Omega''_a q^l(v_a, v'', \Omega'_a, \Omega''_a). \quad (9.58)$$

One more integration would lead to the total ionization cross section:

$$q^l(v_a) = \int dv'' q^l(v_a, v''), \quad (9.59)$$

which is usually sufficient for a particle-based simulation of the ionization process [81].

9.2.1.2 Formal Scattering Theory

Collisions affecting the charge balance and chemistry of gas discharges change the type, and sometimes even the number of scattering fragments. An example is electron impact ionization, the process used in the previous section to introduce the concept of a collision cross section. It is an inelastic, break-up collision with an electron and a molecule in the entrance and two electrons and a positive ion in the exit channel. In comparison to the entrance channel, the kinetic energy of the relative motion of the fragments in the exit channel is moreover reduced by the ionization energy of

the molecule. Thus, a microscopic description of electron-impact ionization, and likewise of many of the other processes listed in Table 9.1, cannot be based on simple potential scattering theory (elastic scattering). A generalized scattering theory is rather required, capable of accounting for changes in the internal energy (inelasticity), for rearrangement, and for breakup of the scattering fragments.

The appropriate theoretical framework is quantum-mechanical multichannel scattering theory [68–70]. To introduce its essential ingredients, two colliding fragments are considered. In the center-of-mass frame, the total Hamiltonian of the system is

$$H = T_{rel} + H_{int} + V = H_0 + V, \quad (9.60)$$

where T_{rel} is the kinetic energy of the relative motion, H_{int} controls the internal degrees of freedom of both fragments, and V is the interaction energy between the two.

The Lippmann–Schwinger equation for the scattering state with the boundary conditions shown in Figure 9.9 reads in Dirac's bra-ket notation

$$|\Psi_{k\alpha}^{(+)}\rangle = |\Phi_{k\alpha}\rangle + \frac{1}{E - H_0 + i\eta} V |\Psi_{k\alpha}^{(+)}\rangle, \quad (9.61)$$

where the first term denotes the incoming plane wave in the entrance channel. The channel state, $|\Phi_{k\alpha}\rangle = |\phi_\alpha\rangle|\mathbf{k}\rangle$, satisfies $(E - H_0)|\Phi_{k\alpha}\rangle$. Thus, $E = E_{k\alpha} = k^2/(2\mu) + \omega_\alpha$, where \mathbf{k} is the relative momentum, ω_α is the internal energy, and μ is the reduced mass of the fragments in the entrance channel.

Quite generally, the scattering amplitude, which in turn determines the differential collision cross section, is defined as the amplitude of the outgoing spherical wave emerging from the right-hand side of (9.61) for large interparticle distances. Hence, in order to find the scattering amplitude, (9.61) has to be expressed in coordinate representation, which is here specified by \mathbf{r} , the interparticle distance, and ρ , the internal coordinates of both particles; then the limit $r \rightarrow \infty$ has to be taken. Normalizing continuum states on the momentum scale then leads to [69,70]

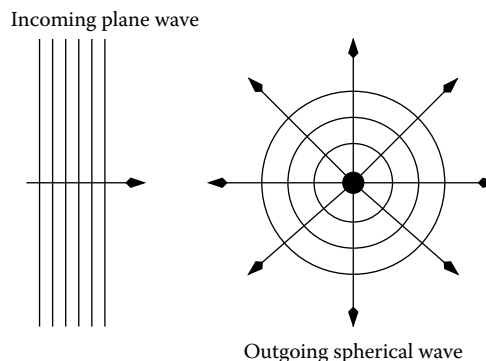


FIGURE 9.9 Schematic representation of the incoming plane wave and the diverging spherical wave as described by the Lippmann–Schwinger equation (9.61).

$$\Psi_{\mathbf{k}\alpha}^{(+)}(\mathbf{r}, \rho) \sim \sum_{\beta} \left[\exp[i\mathbf{k} \cdot \mathbf{r}] \delta_{\alpha\beta} - f(\mathbf{k}'\beta, \mathbf{k}\alpha) \frac{\exp[ik'r]}{r} \right] \phi_{\beta}(\rho) \quad (9.62)$$

$$= \sum_{\beta} \left[\exp[i\mathbf{k} \cdot \mathbf{r}] \delta_{\alpha\beta} + \tilde{\psi}_{\mathbf{k}'\beta, \mathbf{k}\alpha}^{(+)}(r) \right] \phi_{\beta}(\rho) \quad \text{for } r \rightarrow \infty, \quad (9.63)$$

where \mathbf{k}' is the relative momentum after the collision, and the factor in front of the diverging spherical wave,

$$f(\mathbf{k}'\beta, \mathbf{k}\alpha) = -\frac{\mu}{2\pi} \langle \Phi_{\mathbf{k}'\beta} | V | \Psi_{\mathbf{k}\alpha}^{(+)} \rangle, \quad (9.64)$$

is the scattering amplitude.

The differential collision cross section is microscopically defined as the ratio of the outgoing particle flux into the solid angle $d\Omega'$ originating from the diverging spherical wave $\tilde{\psi}_{\mathbf{k}'\beta, \mathbf{k}\alpha}^{(+)}(r)$ introduced in (9.63) and the incoming current density due to the plane wave. Hence,

$$d\sigma = \frac{(\mathbf{j}_{out} \cdot \mathbf{e}_r)r^2 d\Omega'}{k/\mu}, \quad (9.65)$$

where \mathbf{e}_r is the unit vector in the direction of \mathbf{r} . Inserting $\tilde{\psi}_{\mathbf{k}'\beta, \mathbf{k}\alpha}^{(+)}(r)$ into the quantum-mechanical expression for the particle flux, $\mathbf{j} = (1/(2i\mu))[\psi^* \nabla \psi - \psi \nabla \psi^*]$, yields $\mathbf{j}_{out} = k' |f(\mathbf{k}'\beta, \mathbf{k}\alpha)|^2 \mathbf{e}_r / (\mu r^2)$ and thus

$$d\sigma_{\alpha \rightarrow \beta} = \frac{k'}{k} |f(\mathbf{k}'\beta, \mathbf{k}\alpha)|^2 d\Omega' = \frac{\mu^2}{(2\pi)^2} \frac{k'}{k} |\langle \Phi_{\mathbf{k}'\beta} | V | \Psi_{\mathbf{k}\alpha}^{(+)} \rangle|^2 d\Omega', \quad (9.66)$$

or, when continuum states are normalized on the energy scale and the identity $V\Psi^{(+)} = t\Phi$ is used [69,70],

$$d\sigma_{\alpha \rightarrow \beta} = \frac{(2\pi)^4}{k^2} |\langle \Phi_{\mathbf{k}'\beta} | t | \Phi_{\mathbf{k}\alpha} \rangle|^2 d\Omega', \quad (9.67)$$

where $t = V + V[E - H_0 + i\eta]^{-1}$ t is the transition operator (T -matrix).

In the derivation of (9.64), it was implicitly assumed that \mathbf{r} is the interparticle distance in both the entrance and the exit channel. The particles therefore remain intact during the course of the collision. They may only change their internal state. Hence, the cross-section formulae (9.66) and (9.67) can be only applied to elastic ($\omega_{\beta} = \omega_{\alpha}$) and inelastic ($\omega_{\beta} \neq \omega_{\alpha}$) scattering.

To obtain the cross section for reactive scattering, the fact has to be included that the type of particles, and hence the relative and internal coordinates, change during the collision. Thus, writing the Hamiltonian in the form (9.60) is only adequate in the entrance channel. In the exit channel, it is more appropriate to partition the Hamiltonian according to the reaction products and write

$$H = T'_{rel} + H'_{int} + V' = H'_0 + V', \quad (9.68)$$

where T'_{rel} , H'_{int} , and V' are the relative kinetic energy, the internal energy, and the interaction energy in the exit channel. Then, in addition to (9.61), the scattering state $|\Psi_{\mathbf{k}\alpha}^{(+)}\rangle$ obeys also a homogeneous Lippmann–Schwinger equation,*

$$|\Psi_{\mathbf{k}\alpha}^{(+)}\rangle = \frac{1}{E - H'_0 + i\eta} V' |\Psi_{\mathbf{k}\alpha}^{(+)}\rangle, \quad (9.69)$$

from which the scattering amplitude in the exit channel (reaction amplitude) can be deduced by the same procedure as before, except that now the coordinate representation with respect to \mathbf{r}' and ρ' , the relative and internal coordinates in the exit channel, has to be chosen. In this representation, the scattering state becomes a diverging spherical wave for $r' \rightarrow \infty$. The prefactor (continuum states normalized on the momentum scale)

$$f'(\mathbf{k}'\beta, \mathbf{k}\alpha) = -\frac{\mu'}{2\pi} \langle \Phi'_{\mathbf{k}'\beta} | V' | \Psi_{\mathbf{k}\alpha}^{(+)} \rangle, \quad (9.70)$$

with the reduced mass μ' in the exit channel and an eigenstate $|\Phi'_{\mathbf{k}'\beta}\rangle$ of H'_0 can be identified with the reaction amplitude. Hence, the differential cross section for reactive scattering is given by

$$d\sigma_{\alpha \rightarrow \beta} = \frac{\mu}{\mu'} \frac{k'}{k} |f'(\mathbf{k}'\beta, \mathbf{k}\alpha)|^2 d\Omega' = \frac{\mu\mu'}{(2\pi)^2} \frac{k'}{k} |\langle \Phi'_{\mathbf{k}'\beta} | V' | \Psi_{\mathbf{k}\alpha}^{(+)} \rangle|^2 d\Omega', \quad (9.71)$$

where energy conservation now enforces $E = k'^2/(2\mu') + \omega'_{\beta} = k^2/(2\mu) + \omega_{\alpha}$. Obviously, (9.71) reduces to (9.66) for $V' = V$, which implies $H'_0 = H_0$ and thus $\mathbf{r}' = \mathbf{r}$, $\mu' = \mu$, and $\Phi' = \Phi$.

If the interaction V in the entrance channel is simpler than the interaction V' in the exit channel, it may be more convenient to use the adjoint scattering state, $\langle \Psi_{\mathbf{k}'\beta}^{(-)} |$, which describes an incoming wave in the exit channel. The reaction cross section can then be written as

$$d\sigma_{\alpha \rightarrow \beta} = \frac{\mu\mu'}{(2\pi)^2} \frac{k'}{k} |\langle \Psi_{\mathbf{k}'\beta}^{(-)} | V | \Phi_{\mathbf{k}\alpha} \rangle|^2 d\Omega', \quad (9.72)$$

which contains V instead of V' .

The formalism described so far is only applicable to binary collisions, that is, collisions containing two particles in the entrance and exit channel, respectively. The theoretical description of collisions involving three (or more) reaction products (breakup collisions) can also be based on a set of Lippmann–Schwinger equations, but the increased dimensionality of the relative motion requires a substantial extension of the formalism (see [68]) beyond the scope of this introductory presentation. Additional complications arise for identical particles in a given channel, or when the interaction is long-ranged, as is, for instance, the case for electron-impact ionization. Ionization cross sections are therefore hardly obtained from rigorous calculations. They are usually estimated from less ambitious, semiempirical models to be described in Section 9.2.2.1.

* The equation is homogeneous because the incoming wave belongs to a different Hilbert space.

9.2.1.3 Adiabatic Approximation

The formalism described in the previous subsection will be now applied to electron-molecule scattering. To be specific, a diatomic molecule with N electrons is considered. The scattering wave functions, $\Psi^{(\pm)}(\mathbf{r}', \mathbf{r}, \mathbf{R})$, from which the scattering amplitudes are obtained, then depend on the N coordinates of the target electrons, which are collectively denoted by \mathbf{r}' , the coordinate of the projectile electron \mathbf{r} , and the internuclear distance \mathbf{R} . In the interest of clarity, spin degrees of freedom are suppressed.

The Lippmann–Schwinger equation for electron-molecule scattering cannot be solved exactly. Approximation schemes, usually based on an expansion of the scattering state in an appropriate basis, are therefore necessary. When the target states, that is, the eigenfunctions of $H^{(N)} = T_R + H_{el}^{(N)}$, where T_R is the kinetic energy of the nuclei and $H_{el}^{(N)}$ is the Hamiltonian for the N target electrons at fixed \mathbf{R} , are used, the expansion leads to the close-coupling approximation. Identifying ρ with $(\mathbf{r}', \mathbf{R})$, the close-coupling approximation is basically identical to the channel state representation described in the previous section. However, this brute-force approach is not well suited. The number of channels (electronic, vibrational, and rotational) which are all coupled by the Lippmann–Schwinger equation is too large. In addition, due to the differences in the electronic and nuclear energy scales, the rate of convergence is rather poor.

An approximation scheme accounting for the difference in the energy scales, which is thus more appropriate for electron-molecule scattering, is the adiabatic approximation. It expands the scattering state in terms of eigenfunctions of $H_{el}^{(N+1)}$. These are eigenfunctions of the fixed-nuclei Hamiltonian for the $N + 1$ electrons (N target electrons and one projectile electron) of the compound state AB^- , which depend only parametrically on the internuclear distance. Since the dynamic coupling due to the perturbation T_R is usually negligible, only one term contributes to the expansion. The computational costs are thus substantially reduced. In addition, provided the conditions for the validity of the adiabatic approximation are fulfilled, the target can be also described adiabatically. Thus, the target states are Born–Oppenheimer states, which are of course also much easier to determine than the target states needed in a close-coupling calculation.

The adiabatic approximation is valid far away from excitation thresholds and when the collision time is much shorter than the period of nuclear vibration and rotation. It is thus mostly applied to nonresonant electron-molecule scattering. As shown by Shugard and Hazi [82], the differential cross section for electron impact excitation of a diatomic molecule (for continuum states normalized on the energy scale) reads

$$d\sigma_{n_i \nu_i J_i \rightarrow n_f \nu_f J_f} = \frac{(2\pi)^4}{k_i} |T_{n_f \nu_f J_f, n_i \nu_i J_i}(\Omega_f, \Omega_i)|^2 d\Omega_f, \quad (9.73)$$

with the solid angles Ω_i and Ω_f of \mathbf{k}_i and \mathbf{k}_f , the electron momenta before and after the collision, respectively. The total scattering amplitude,

$$T_{n_f \nu_f J_f, n_i \nu_i J_i}(\Omega_f, \Omega_i) = \int d\mathbf{R} F_{n_f \nu_f J_f}^*(\mathbf{R}) t_{n_f n_i}(\Omega_f, \Omega_i, \mathbf{R}) F_{n_i \nu_i J_i}(\mathbf{R}), \quad (9.74)$$

is an average of the fixed-nuclei scattering amplitude,

$$t_{n_f n_i}(\Omega_f, \Omega_i, \mathbf{R}) = \frac{k_f^{1/2}}{(2\pi)^{3/2}} \int d\mathbf{r} d\mathbf{r}' \exp[i\mathbf{k}_f \cdot \mathbf{r}] \Phi_{n_f}^*(\mathbf{r}'; \mathbf{R}) V(\mathbf{r}, \mathbf{r}'; \mathbf{R}) \Psi_{\mathcal{E}, \Omega, n_i}^{(+)}(\mathbf{r}, \mathbf{r}'; \mathbf{R}), \quad (9.75)$$

over the rovibrational states $F_{n\nu J}(\mathbf{R})$ satisfying

$$[T_R + \epsilon_n(R) - \omega_{n\nu J}] F_{n\nu J}(\mathbf{R}) = 0, \quad (9.76)$$

where $\omega_{n\nu J}$ is the rovibrational energy and $\epsilon_n(R)$ is the potential-energy-surface defined as the eigenvalue of the fixed-nuclei Schrödinger equation for the target electrons

$$[H_{el}^{(N)} - \epsilon_n(R)] \Phi_n(\mathbf{r}', \mathbf{R}) = 0. \quad (9.77)$$

In view of the discussion of the previous subsection, the structure of the formulae (9.73) through (9.75) should be clear. The physical meaning of the various energies can be deduced from Figure 9.10. Note in particular that the energy $\mathcal{E} = \epsilon_{n_i} + k_i^2/2 = \epsilon_{n_i} + E - \omega_{n_i \nu_i J_i}$ appearing in (9.75) is only the total electronic energy for the projectile electron and the N target electrons, in contrast to the total energy E that includes electronic and nuclear degrees of freedom. Rovibrational states are characterized by the quantum number n of the electronic state in which the nuclear motion takes place, the vibrational quantum number ν , and the rotational quantum number J . Energy conservation implies $E = k_i^2/2 + \omega_{n_i \nu_i J_i} = k_f^2/2 + \omega_{n_f \nu_f J_f}$.

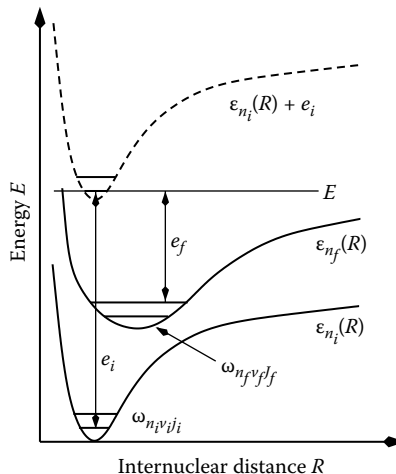


FIGURE 9.10 Potential energy surface of the initial and final state of electron-impact excitation of a diatomic molecule and the relationship of the various energies occurring in the adiabatic approximation for the scattering cross section. The kinetic energy of the electron before and after the collision is denoted by $e_i = k_i^2/2$ and $e_f = k_f^2/2$, respectively.

Within the adiabatic approximation, it is necessary to determine the fixed-nuclei scattering amplitude and the rovibrational states of the molecule, which in turn depend on the potential energy surface of the target molecule. The former can be obtained as a function of \mathbf{R} from the asymptotics of the $N + 1$ electron, fixed-nuclei Lippmann–Schwinger equation, which determines $\Psi_{\varepsilon, \Omega, n_i}^{(+)}(\mathbf{r}, \mathbf{r}'; \mathbf{R})$, while the latter requires, again as a function of \mathbf{R} , the solution of the N electron problem (9.77). In both cases, anti-symmetrized wave functions have to be used because of the indistinguishability of electrons. Thus, even when the nuclear motion is split off, the calculation of cross sections for electron-molecule scattering remains a formidable many-body problem [74].

9.2.1.4 Resonant Scattering

At electron energies of a few electron volts or less, the collision time is long compared to the period of the internuclear motion and the adiabatic approximation fails. The projectile electron is then so slow that it is captured by the molecule giving rise to a bound state of the negatively charged molecular ion, which is the collision compound for electron-molecule scattering.* This state interacts with the electron-molecule scattering continuum, acquires therefore a finite lifetime, and turns into a quasi-bound (auto-detaching) state. Auto-detaching states play a central role in (vibrational) excitation, attachment, recombination, and detachment collisions. From a theoretical point of view, all these processes can hence be analyzed within a model describing a discrete state (resonance) embedded in a continuum of scattering states.

A particularly elegant derivation of the resonance model for an electron colliding with a diatomic molecule containing N electrons has been given by Domcke [83] who uses many-particle Green functions to reduce the $N + 1$ electron scattering problem to an effective single-electron problem. The reduction is achieved by two projections: First, electronic states that are not accessible at the energy considered are eliminated by introducing an optical potential for the incoming electron. Then, in a second step, the fixed-nuclei T -matrix is split into a rapidly varying part due to the quasi-bound resonant state and a slowly varying background term. The splitting of the T -matrix can be shown to be equivalent to an effective single-electron Hamiltonian at fixed-nuclei describing a resonance coupled to a continuum of states. Finally, the kinetic energy of the nuclei is included and the electronic degrees of freedom are integrated out to obtain an effective Lippmann–Schwinger equation for the nuclear dynamics that, with appropriate boundary conditions, can then be used to calculate the collision cross sections of interest.

It is essential for the formalism that the optical potential supports a resonance and that the resonance can be extracted from the single-electron continuum such that the scattering background contains no spurious resonances. The many electron problem is then completely buried in an optical potential, which can be calculated separately using, for instance, the many-body perturbation theory [84]. In principle, the formalism can handle more than one resonance as well as electronically inelastic

* The electronic and vibrational properties of negative ions therefore play an important role in low-temperature gas discharges with $k_B T_e \sim \mathcal{O}(1 - 10 \text{ eV})$, even when the gas is not electronegative, that is, when the negative ion is unstable on the plasma time scale and therefore irrelevant at the kinetic level.

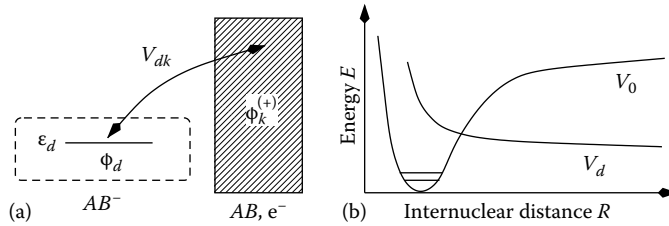


FIGURE 9.11 Illustration of the effective Hamiltonian (9.78) defining the resonance model. Panel (a) depicts for a fixed internuclear distance the coupling of the resonant state with the scattering continuum and panel (b) shows the potentials of the resonant state and the target molecule as a function of the internuclear distance.

processes [85]. So far, however, it has been only applied to electronically elastic collisions involving a single resonance and a single potential energy surface for the nuclear motion of the target.

The effective Hamiltonian, visualized in Figure 9.11, reads

$$H = H_0 + V,$$

$$H_0 = |\phi_d\rangle [T_R + V_d] \langle\phi_d| + \int kdkd\Omega_k |\phi_k^{(+)}\rangle \left[T_R + V_0 + \frac{k^2}{2} \right] \langle\phi_k^{(+)}|, \quad (9.78)$$

$$V = \int kdkd\Omega_k [|\phi_d\rangle V_{dk} \langle\phi_k^{(+)}| + \text{h.c.}],$$

where \$|\phi_d\rangle\$ is the resonant state and \$|\phi_k^{(+)}\rangle\$ are the scattering states orthogonal to \$|\phi_d\rangle\$. The coupling between the two types of states is given by \$V_{dk} = \langle\phi_d|H_{el}|\phi_k^{(+)}\rangle\$, where \$H_{el} = -\nabla^2/2 + V_{opt}\$ is the Hamiltonian for a single electron in the optical potential \$V_{opt}\$, \$V_d = \langle\phi_d|H_{el}|\phi_d\rangle + V_0\$ is an operator specifying the potential of the resonant state, and \$V_0\$ is the corresponding operator for the potential of the target molecule.

The Hamiltonian (9.78) and thus the Lippmann–Schwinger equation associated with it operate in the combined Hilbert space of the scattered electron and the two nuclei. Projecting out the electron, switching to the coordinate representation with respect to the internuclear distance, and using outgoing wave boundary conditions yields, when rotations of the molecule are ignored, a Lippmann–Schwinger equation,

$$\left[E + \frac{1}{2\mu} \frac{d^2}{dR^2} - V_d(R) \right] \Psi_{de}^{(+)}(R) - \int dR' F^{(+)}(R, R', E) \Psi_{de}^{(+)}(R') = J(R), \quad (9.79)$$

with a kernel

$$F^{(+)}(R, R', E) = \int kdkd\Omega_k V_{dk}(R) G^{(+)}(R, R', E - k^2/2) V_{dk}^*(R'), \quad (9.80)$$

where

$$G^{(+)}(R, R', E) = \langle R | \left[E + \frac{1}{2\mu} \frac{d^2}{dR^2} - V_0(R) + i\eta \right]^{-1} | R' \rangle \quad (9.81)$$

is the Green function for the nuclear motion on the potential energy surface of the target, $V_0(R) = \langle R | V_0 | R \rangle$, and μ is the reduced mass of the nuclei; $V_d(R) = \langle R | V_d | R \rangle = \epsilon_d(R) + V_0(R)$ is the potential energy surface of the resonant state and $V_{dk}(R) = \langle R | V_{dk} | R \rangle$. The inhomogeneity $J(R)$ on the right-hand side of (9.79) depends on the boundary conditions. It will be discussed in the following for particular collision processes.

Equation 9.79 is an effective Lippmann–Schwinger equation for the nuclear dynamics in the energy-dependent, nonlocal, and complex potential of the resonant state. To make this more explicit, $G_0^{(+)}(R, R'; E)$ is expressed in terms of a complete set of target nuclear wave functions $\chi_v(R)$. Employing Dirac's identity and assuming that the interaction between the resonance and the scattering continuum depends only on k (isotropic interaction) leads to

$$F^{(+)}(R, R'; E) = \Delta(R, R'; E) - \frac{i}{2} \Gamma(R, R'; E) \quad (9.82)$$

with

$$\Delta(R, R'; E) = 4\pi \sum_v P \int dE' \frac{V_{dE'}(R) \chi_v^*(R) \chi_v(R') V_{dE'}^*(R')}{E - \omega_v - E'} \quad (9.83)$$

and

$$\Gamma(R, R'; E) = 8\pi \sum_v V_{dE-\omega_v}(R) \chi_v^*(R) \chi_v(R') V_{dE-\omega_v}^*(R'), \quad (9.84)$$

where symbol “P” denotes the principal value of the integral and ω_v stands for the vibrational energies of the target molecule.

The inverse of $\Gamma(R, R'; E)$ is the lifetime of the resonance. As expected, the auto-detaching property of the resonance arises from its coupling to the scattering continuum. In principle, the resonance has a finite lifetime even in the absence of this coupling because the optical potential, V_{opt} , is complex. Its imaginary part therefore induces a lifetime. This contribution, however, is much smaller than the one due to V_{dE} . Therefore, it is usually neglected.

The nonlocality of the potential complicates the numerical solution of Equation 9.79. In the early applications of the resonance model [59–64,72], the nonlocal potential was thus replaced by a local one. The local approximation can be obtained from (9.83) to (9.84) by identifying the energy available for the scattered electron with an effective resonance energy: $E - \omega_v \approx E_{res}(R)$ [83]. The completeness of the vibrational target states can then be used to obtain $\Delta(R, R'; E) = \Delta_L(R) \delta(R - R')$ and $\Gamma(R, R'; E) = \Gamma_L(R) \delta(R - R')$ with

$$\Gamma_L(R) = 8\pi |V_{dE_{res}(R)}(R)|^2, \quad \Delta_L(R) = 4\pi P \int \frac{|V_{dE_{res}(R)}(R)|^2}{E_{res}(R) - E'}, \quad (9.85)$$

which reduces the Lippmann–Schwinger equation to an ordinary differential equation:

$$\left[E + \frac{1}{2\mu} \frac{d^2}{dR^2} - V_0(R) - \Delta_L(R) + \frac{i}{2} \Gamma_L(R) \right] \Psi_{dE}^{(+)}(R) = J(R). \quad (9.86)$$

The scattering cross sections derived from (9.79) or (9.86) are only as good as the optical potential, V_{opt} , the potential energy surfaces $V_0(R)$ and $V_d(R)$, and the coupling function $V_{dk}(R)$. These quantities have to be obtained from separate calculations, ideally using ab initio techniques of molecular structure theory, or directly from experiments. But even then, the cross sections forming the resonance model are semiempirical in the sense that a priori assumptions about the relevance or irrelevance of molecular ion and target states have to be made from the very beginning. This weakness of the model, however, also leads to its strength: Technically tractable equations with an intuitive physical interpretation, which, in the local approximation, can be even solved analytically with semiclassical techniques [86–88].

9.2.2 TYPICAL PROCESSES

Now representative elementary processes are discussed in more detail, focusing, in particular, on reactive and inelastic collisions, which change the internal energy and composition of the scattering fragments. Elastic scattering between the various species is not explicitly included although the associated cross sections are usually much larger than the cross sections for inelastic and reactive collisions combined. But they only randomize the directed motion of the electrons in the electric field. The thereby induced changes of the electron energy distribution function affects the plasma chemistry only indirectly, as far as an increase of energy in the electronic subsystem makes certain collisions more probable than others.

9.2.2.1 Production of Ions

The main production processes for ions in a molecular, electronegative gas discharge are electron impact ionization and dissociative electron attachment. Both processes share the same compound state, AB^- , but the former leads to positive molecular ions whereas the latter to negative atomic ions. Impact ionization is additionally also the main source for electrons that, depending on their energy, trigger a multitude of excitation and dissociation collisions.

Electron impact ionization is similar to electronic excitation (see the following text), except that the excited state belongs to the two-electron continuum. In the notation of the previous subsection, the differential cross section is thus proportional to the modulus of the reaction amplitude squared,

$$d\sigma_{\alpha \rightarrow \beta}^I \sim |\langle \Phi'_{\beta k_1 k_2} | V' | \Psi_{\alpha k}^{(+)} \rangle|^2 d\Omega_1 d\Omega_2 dE_2, \quad (9.87)$$

where

- Ω_1 is the solid angle associated with \mathbf{k}_1 , the momentum of the primary electron
- Ω_2 is the solid angle associated with \mathbf{k}_2 , the momentum of the secondary electron
- E_2 is the energy of the secondary electron

The exit channel state, $|\Phi'_{\beta k_1 k_2} \rangle = |\phi'^{AB^+}_{\beta} \psi'_{k_1 k_2} \rangle$, describes the internal state of the positive ion and the 6D relative motion between the two electrons and the ion, which is controlled by V' , that is, the Coulomb interaction of the primary and secondary electron with each other and with the positive ion. The entrance channel of the set

of Lippmann–Schwinger equations satisfied by the scattering state $|\Psi_{\alpha k}^{(+)}\rangle$ contains an inhomogeneity, $|\Phi_{\alpha k}\rangle = |\phi_{\alpha}^{AB}\rangle|k\rangle$, where $|\phi_{\alpha}^{AB}\rangle$ is the initial state of the molecule and $|k\rangle$ is the plane wave representing the relative motion of the initial electron and the molecule.

From a rigorous mathematical point of view, the exact two-electron scattering state in the field of a positive ion is unknown. Hence, exact calculations of electron impact ionization cross sections are not available, even for atoms, where complications due to the nuclear dynamics are absent. Perturbative treatments, based, for instance, on the distorted Born approximation, which replaces $\psi'_{k_1 k_2}$ by a plane wave for the primary electron and a Coulomb wave for the secondary electron, are possible, provided the velocity of the incident electron is much larger than the velocities of the electrons bound in the molecule. Exchange and correlation effects can then be ignored and the calculation of cross sections for electron-impact ionization essentially reduces to the calculation of photoionization cross sections. This approach, due originally to Bethe [53] and reviewed by Rudge [71] and Inokuti [73], fails at low electron energies. In that region, however, Vriens’ binary-encounter model [54] can be used. It assumes that the primary electron interacts pairwise with target electrons, leaving the remaining electrons and the nuclear dynamics undisturbed. The ionization cross section is then basically the Mott cross section for the collision of two electrons, appropriately modified by the binding and kinetic energies of the target electrons.

The semiempirical *Kim–Rudd model* for electron impact ionization [55] combines the Bethe model with the binary-encounter model. For an individual orbital, the ionization cross section is then given by

$$\sigma'(e) = \frac{S}{e + u + 1} \left\{ \frac{1}{2} Q \left(1 - \frac{1}{e^2} \right) \ln e + (2 - Q) \left[1 - \frac{1}{e} - \frac{\ln e}{e + 1} \right] \right\}, \quad (9.88)$$

with $e = E/B$ and $u = U/B$, where E is the kinetic energy of the incident electron, U is the average kinetic energy of the orbital, and B is the binding energy of the orbital. The remaining quantities are $S = 4\pi N/B^2$ and $Q = 2BM_i^2/N$, where N is the orbital occupation number and M_i is an integral over the differential oscillator strength defined in [55]. The results obtained from (9.88) are surprisingly good.

Another widely used semiempirical model for electron impact ionization is the *Deutsch–Märk model* [56–58]. It uses cross sections for the atomic constituents of the molecules and sums them up according to the atomic population of the molecular orbitals that is obtained from a Mullikan population analysis. The total ionization cross section can then be written as

$$\sigma'(E) = \sum_{n,l,i} g_{i,nl} \pi r_{i,nl}^2 N_{i,nl} f(e_{i,nl}) \quad (9.89)$$

with the mean square radius $r_{i,nl}^2$ of the n, l th sub-shell of the constituent i , the occupancy $N_{i,nl}$ of that sub-shell, weighting factors $g_{i,nl}$ that have to be determined

empirically using reliable atomic cross-section data, and a function

$$f(e_{i,nl}) = \frac{1}{e_{i,nl}} \left(\frac{e_{i,nl} - 1}{e_{i,nl} + 1} \right)^{3/2} \left\{ 1 + \frac{2}{3} \left(1 - \frac{1}{2e_{i,nl}} \right) \ln \left[2.7 + \sqrt{e_{i,nl} - 1} \right] \right\}, \quad (9.90)$$

which describes the energy dependence of the cross section. The quantity $e_{i,nl} = E/B_{i,nl}$ with $B_{i,nl}$ is the ionization energy of the considered sub-shell of the i th constituent. More elaborate versions of the Deutsch–Märk model account also for the different angular symmetries of the sub-shells [56].

The cross sections for impact ionization are fairly large because it is an optically allowed process (this can be most clearly seen when the Born approximation is applied) and the energy in the final state can be distributed among the two electrons in infinitely many ways. Hence, a gas discharge usually contains a high concentration of electrons and positive ions.

Negative ions are produced by *dissociative attachment*, which is a resonant process due to the collision of a slow electron with a (in general) vibrationally excited molecule, in which the compound state AB^- dissociates into a negative ion A^- and a neutral atom B . In principle, it would also be conceivable that the incident electron is permanently bound to the molecule and a negative molecular ion is formed. A necessary condition for this to happen would be that the relevant potential energy surface of the AB^- state is bonding and has a minimum outside the potential well corresponding to the electronic groundstate of the AB molecule. However, the electron is always captured above the re-detachment threshold, that is, the molecular ion is initially in an excited state. It can be only stabilized when it loses or disperses excess energy. The former occurs through collisions with other molecules or the wall while the latter takes place through vibrational modes of the AB^- compound. In most cases, these processes are not very efficient and the AB^- state is only a short-lived resonance not affecting the macrophysics of the discharge.

As pointed out by O’Malley [59] and others [60], dissociative attachment most likely occurs when an antibonding state of the collision compound AB^- crosses the initial potential energy surface of the AB molecule as schematically shown in Figure 9.12. This is the typical situation for the resonance model to be applicable. Thus, with the appropriate identifications and boundary conditions, the cross section for dissociative attachment can be calculated from the effective Hamiltonian (9.78).

The natural boundary conditions for dissociative attachment are an incoming plane wave for the relative electron-molecule motion and an outgoing spherical wave in the relative (A^- , B) motion. The formula for the attachment cross section, which is a reaction cross section [cp. with (9.71)], would then however contain the interaction in the exit channel, that is, the interaction between A^- and B , which is not part of the resonance model. This complication can be avoided when the adjoint scattering problem is considered, whose boundary conditions are an incoming plane wave in the (A^- , B) channel and an outgoing spherical wave in the electron-molecule channel. The cross section then contains the interaction between the resonant state and the $e - AB$ scattering continuum. Specifying (9.72) to the present case, the differential

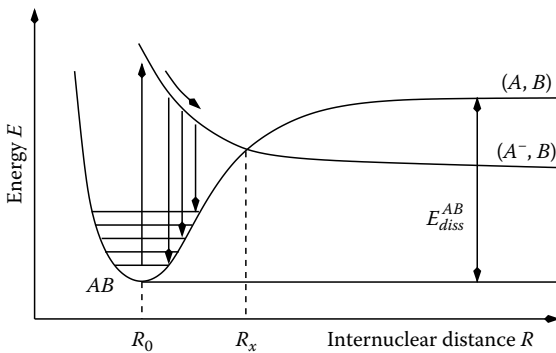


FIGURE 9.12 Schematic representation of the relevant potential energy surfaces for dissociative attachment. For simplicity, it is assumed that the molecule AB is initially in the vibrational ground state, although this is usually not the case. The electron is thus captured at $R = R_0$, where R_0 is the equilibrium distance of the two nuclei (upward vertical arrow). The thereby created AB^- compound is envisaged to be in an antibonding state whose potential energy surface crosses that of the AB state at $R = R_x$. For $R < R_x$, the compound state has thus a finite probability to decay (downward directed vertical arrows). However, provided the state survives until the nuclear distance $R > R_x$, it asymptotically reaches the (A^-, B) dissociation limit and dissociative attachment is completed.

cross section for dissociative attachment becomes

$$d\sigma_{v_i}^{\text{DA}} = \frac{mM}{(2\pi)^2} \frac{K}{k_i} \left| \int dR [\Psi_{de}^{(-)}(R)]^* V_{dk}^*(R) \chi_{v_i}(R) \right|^2 d\Omega_K, \quad (9.91)$$

where m and k are the reduced mass and the relative momentum of the (e^-, AB) system, respectively, M and K are the corresponding quantities in the (A^-, B) system, $\chi_{v_i}(R)$ is the vibrational state of the molecule, and $\Psi_{de}^{(-)}(R)$ is the scattering state satisfying the complex conjugate of (9.79) with $V_d(R) = V_{AB^-}(R)$, $V_0(R) = V_{AB}(R)$, $V_{dk}(R)$ the interaction between the antibonding AB^- state and the electron-molecule scattering continuum, and $J(R) = [V_d(\infty) - V_d(R)] \exp[iKR]$. The total energy available for the collision is $E = k^2/2 + \omega_{v_i} = K^2/(2M) + \omega_{A^-} + \omega_B$, where ω_{A^-} and ω_B denote the internal energies of the ion and atom, respectively, and ω_{v_i} is the vibrational energy of the molecule.

In order to avoid additional indices, quantum numbers for the internal state of the (A^-, B) system are suppressed and rotations of the molecule are also ignored. Because the period of rotation is much longer than the collision time, rotations could be included within the adiabatic approximation. Finally, provided the kinetic energy of the incident electron, $k^2/2$, is much larger than the vibrational energy of the target, ω_{v_i} , the local approximation could be employed, that is, (9.86) could be used instead of (9.79). Further details about the calculation of electron attachment cross sections can be found in the review article by Chutjian et al. [76].

Bardsley et al. [60] have shown that within the semiclassical approximation $d\sigma_{v_i}/d\Omega_K$ factorizes into a capture cross section, which describes the formation of the compound state, and a survival probability for that state. The semiclassical calculation

moreover shows that the capture cross section increases faster with temperature than the survival probability decreases. Thus, the attachment cross section increases with temperature. It is, however, always one or two orders of magnitude smaller than the cross section for the corresponding elastic electron-molecule scattering.

9.2.2.2 Destruction of Ions

Whereas in an electronegative gas discharge only two processes are primarily responsible for the production of ions and electrons—electron impact ionization and dissociative attachment—a large number of processes may lead to the destruction of ions and electrons (see Table 9.1). Depending on the parameters of the discharge, the loss of ions may be due primarily to recombination or detachment. Recombination may furthermore occur between positive ions and electrons or between positive and negative ions (annihilation). For molecular positive ions, the former process is usually accompanied by dissociation and is thus called dissociative recombination. Ion–ion annihilation, on the other hand, is in most cases only a charge transfer, which does not lead to a rearrangement of the nuclei. Finally, detachment of negative ions can either be initiated by electrons or by neutrals. Electron-induced detachment is similar to electron impact ionization whereas detachment due to (molecular) neutrals may lead to dissociation, as well as association, given that the neutral is in a metastable state.

Dissociative recombination is triggered by slow electrons. It is thus a resonant process, similar to dissociative attachment. Very often, it is the dominant loss process for positive ions and electrons with relatively large cross sections because at least one of the atomic fragments in the exit channel is usually in an excited state, implying that the energy in the exit channel can be distributed in many different ways [78].

The resonance model for dissociative recombination, originally proposed by Bardsley [63,64], is based on the potential energy surface diagram shown in Figure 9.13. The most favorable situation for the process to take place is when an antibonding potential energy surface of the molecule AB , which is the collision compound for this reaction, crosses the potential energy surface of the positive ion and is below the vibrational ground state of the ion for large internuclear distances. This is the case for H_2^+ , N_2^+ , and O_2^+ , for instance.

The cross section for dissociative recombination can then be cast into the form (9.91), with M and K as the reduced mass and the relative momentum of the (A, B) system, respectively, m and k as the corresponding quantities of the (e^-, AB^+) system, $\chi_{v_i}(R)$ as the initial vibrational state of AB^+ , and $\Psi_{de}^{(-)}(R)$ as the solution of the complex conjugate to (9.79) with $V_d(R) = V_{AB}(R)$, $V_0(R) = V_{AB^+}(R)$, and $V_{dk}(R)$ as the interaction between the AB state and the $e^- - AB^+$ scattering continuum. The inhomogeneity representing the boundary condition, $J(R) = [V_d(\infty) - V_d(R)]\Phi_K^C(R)$, now contains a Coulomb wave $\Phi_K^C(R)$ because the scattering continuum is for two charged particles: an electron and a positive ion. More sophisticated approaches use quantum defects to characterize the scattering states [89,90].

In electronegative gas discharges, there is an additional recombination channel: *ion–ion annihilation*. The potential energy surface diagram relevant for this process is shown in Figure 9.14. The essential point is the crossing of the potential

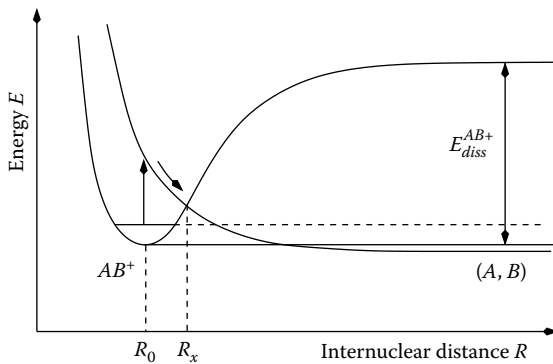


FIGURE 9.13 Dissociative recombination occurs when an antibonding potential energy surface of the (excited) molecule, $V_{AB}(R)$, crosses the potential energy surface of the positive molecular ion AB^+ . Although the states involved are different, the mechanism is similar to dissociative attachment. When the molecule, which is the collision compound in this case, survives auto-detachment for $R < R_x$, it may reach the (A, B) dissociation limit. As a result, dissociative recombination takes place.

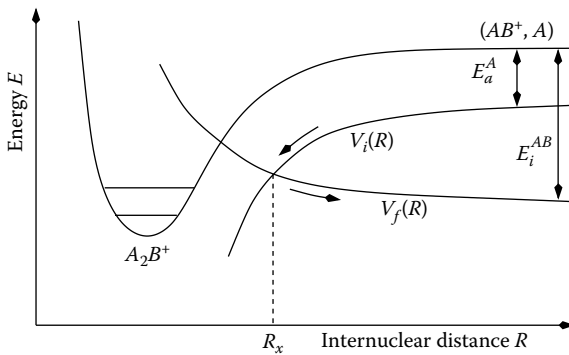


FIGURE 9.14 Relation of the potential energy surfaces typical for ion–ion annihilation. In the entrance channel, the nuclear dynamics is governed by $V_i(R)$, the potential energy surface of the (AB^+, A^-) configuration, whereas the dynamics in the exit channel is controlled by $V_f(R)$, which is the potential energy surface of the (AB, A) configuration. The strong mixing of the two configurations encoded in $V(R)$ (see (9.94)) is maximal at $R = R_x$. Both $V_i(R)$ and $V_f(R)$ belong to the collision compound A_2B . The potential energy surface for the A_2B^+ molecule is also shown. It allows us to define the relevant energies: the ionization energy of the AB molecule, E_{ion}^{AB} , and the electron affinity of the A atom, E_a^A .

energy surface for the (A^-, AB^+) configuration, which decreases with decreasing R because of the Coulomb attraction between the two ions with the antibonding potential energy surface of the A_2B collision compound at an internuclear spacing $R = R_x$. At this separation, the probability for the system to switch from the (A^-, AB^+) to the (A, AB) configuration is particularly high. Based on this observation, a semiempirical Landau–Zener model can be constructed that relates the cross section for ion–ion

annihilation to the ionization energy of the AB molecule and the electron affinity of the A atom (see Figure 9.14).

The *Landau–Zener model* illustrates quite nicely how semiempirical models encode complicated processes in a few physically intuitive parameters. In contrast to the processes discussed so far, where the relevant nuclear dynamics take place on a single potential energy surface, ion–ion annihilation forces the nuclei to switch between two potential energy surfaces of the collision compound. The minimal theoretical model is therefore based on two coupled Lippmann–Schwinger equations for the relative motion of the nuclei. The Landau–Zener model is the semiclassical approximation to this set of equations. Following Olson [66], the total ion–ion annihilation cross section is then given by

$$\sigma^{\text{IIA}}(E) = 4\pi R_x^2 \left[1 + \frac{\Delta E}{E} \right] F(\lambda), \quad (9.92)$$

with

$$F(\lambda) = \int_1^\infty dx x^3 \exp(-\lambda x) [1 - \exp(-\lambda x)] \quad (9.93)$$

and

$$\lambda = 2\pi\sqrt{\frac{M}{2}} \frac{|V(R_x)|^2}{|V_i' - V_f'| \sqrt{E + \Delta E}}, \quad (9.94)$$

where E and M are the kinetic energy and the reduced mass of the relative motion of the (A^-, AB^+) system, ΔE is the energy gain due to annihilation, $V(R_x)$ is the interaction between the (A^-, AB^+) and (A, AB) configurations at $R = R_x$, and $V_{if}' = dV_{if}(R_x)/dR$ with $V_i(R)$ and $V_f(R)$ as the potential energy surfaces of the (A^-, AB^+) and (A, AB) system, respectively.

Equation 9.92 can be developed further by recalling that $V_i(R) \sim R^{-1}$ (Coulomb interaction between A^- and AB^+) and $V_f(R) \sim r^{-n}$ with $n > 1$ (polarization interaction between A and AB). Hence, for large enough R_x , $|V_i' - V_f'| \approx R_x^{-1}$ and $\Delta E \approx -U_i(R_x) = R_x^{-1}$. Usually, $\Delta E \gg E$. Combining all this leads to $\lambda \approx \sqrt{2M\pi R_x^{5/2}} |V(R_x)|^2$ [66]. Since $F(\lambda)$ approaches its maximal value $F_{max} \approx 0.1$ at $\lambda_{max} \approx 0.424$, a rough estimate for the annihilation cross section is

$$\sigma^{\text{IIA}}(E) \approx 1.3R_x^2 \left[1 + \frac{1}{R_x E} \right] \quad (9.95)$$

with R_x determined from $\lambda_{max} = \sqrt{2M\pi R_x^{5/2}} |V(R_x)|^2$ or from empirical cross section data for high energies where $E \gg R_x^{-1}$ and $\sigma(E) \rightarrow 1.3R_x^2$. Determining $V(R_x)$ is not trivial. Ideally, it can be parametrized in terms of an effective ionization energy E_i^{AB} of the AB molecule and the electron affinity E_a^A of the A atom. Olson and coworkers [67] obtain $V(R) = 1.044\sqrt{E_i^{AB} E_a^A} \sqrt{q}\bar{R} \exp[-0.857\bar{R}]$ for large internuclear distances with $\bar{R} = 0.5(\sqrt{2E_a^A} + \sqrt{2E_i^{AB}})R$ and q the Franck–Condon factor that represents

the overlap of the vibrational states. In order to apply this formula, the ionization potential and the electron affinity have to be known. For atomic negative ions this is not a problem, whereas for molecular negative ions this can be subtle because the ion may be in an (unknown) excited state. Fortunately, molecular negative ions have a rather short lifetime, as discussed earlier. They are thus not of major concern in the commonly used gas discharges.

For molecular positive ions, *dissociative ion–ion annihilation* may also be possible. It contains two relative motions in the exit channel and is thus much harder to analyze theoretically. Experimentally, it is not always possible to discriminate between this process and the charge-transfer-type reaction discussed in the previous paragraphs. The energy dependence of the two cross sections is however essentially the same, except that they reach the constant value at different energies. Thus, when R_x is determined from the high energy asymptotics of empirical data, the annihilation cross section is in fact an effective cross section, comprising both charge-transfer-type and dissociative ion–ion annihilation.

In contrast to positive ions, negative ions can also be destroyed by slow collisions with neutral particles (detachment). To be specific, *associative detachment* of negative ions due to molecules is discussed. Microscopically, it is a resonant process similar to dissociative attachment and dissociative recombination. An auto-detaching, resonant state thus plays an important role. In Figure 9.15, the relevant potential energy surfaces are shown. The asymptotically stable configuration (A^-, AB) changes with decreasing R into a quasi-bound, resonant collision compound, A_2B^- , from which the electron auto-detaches, leaving behind a free electron and a neutral particle in an excited vibrational state [62–64].

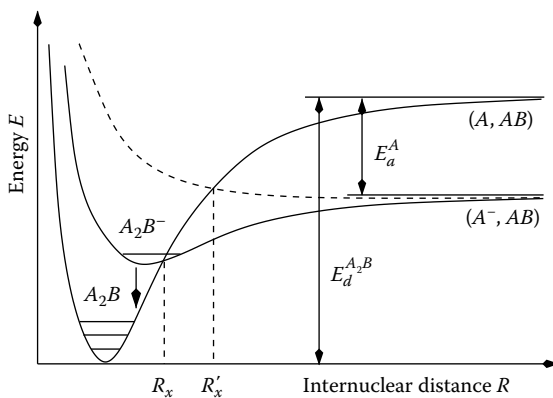


FIGURE 9.15 Illustration of associative detachment. The potential energy surface of a bonding state of the collision compound A_2B^- crosses the potential energy surface of the A_2B molecule. Auto-detachment of the compound state then produces an electron and a vibrationally excited A_2B molecule. Also shown is an antibonding A_2B^- state (dashed line). Detachment may also occur from such a state, but then the initial kinetic energy of the (A^-, AB) system has to be larger than $V_{A_2B^-}(R'_x) - V_{A_2B^-}(\infty)$.

The differential cross section for this process can be obtained from the resonance model, using an incoming plane wave in the (A^-, AB) channel and an outgoing spherical wave in the (e^-, A_2B) channel as boundary conditions. Normalizing continuum states on the energy scale and applying (9.71) leads to

$$d\sigma_{v_f}^{AD} = \frac{(2\pi)^4}{K^2} \left| \int dR \chi_{v_f}^*(R) V_{dk}^*(R) \Psi_{dE}^{(+)}(R) \right|^2 d\Omega_k, \quad (9.96)$$

where $\chi_{v_f}(R)$ is the vibrational state of the A_2B molecule and $\Psi_{dE}^{(+)}$ satisfies (9.79) with $V_d(R) = V_{A_2B^-}(R)$, $V_0(R) = V_{A_2B}(R)$, and $V_{dk}(R)$ is the interaction between the quasi-bound A_2B^- state and the $e^- - A_2B$ scattering continuum. The inhomogeneity is $J(R) = [V_d(\infty) - V_d(R)]\Phi_K(R)$, where $\Phi_K(R)$ is a plane wave for the relative motion of the (A^-, AB) system. Energy conservation enforces $E = K^2/(2M) + V_d(\infty) = k^2/(2m) + \omega_{v_f}$, where M and m are the reduced masses of the (A^-, AB) and the (e^-, A_2B) system, respectively. Note that since $d\sigma_{v_f}^{AD}$ is a differential cross section for reactive scattering, the interaction in the exit channel, V_{dk} , appears in (9.96) as it should.

The most favorable situation for associative detachment is when the potential energy surface of the neutral molecule in the exit channel supports a bound state whose dissociation energy $E_d^{A_2B}$ is larger than the electron affinity E_a^A of the A atom. This situation is shown in Figure 9.15. Provided detachment is mediated by an attractive state of the collision compound, it takes place even for vanishing initial kinetic energy in the (A^-, AB) channel. If this is the case, detachment is a very efficient loss channel for negative ions, even at low temperatures. If, on the other hand, the compound state is antibonding, associative detachment occurs only when the initial kinetic energy of the colliding particles is larger than $V_d(R'_x) - V_d(\infty)$, where R'_x is the point where the repulsive potential energy surface crosses $V_0(R)$.

9.2.2.3 Excitation of Internal Degrees

The chemistry and charge balance of a gas discharge is also affected by inelastic collisions, that is, collisions that increase the internal energy of molecules, atoms, and ions. Excited (metastable) particles are reactive and participate in basically all particle number changing collisions. In low-temperature gas discharges, vibrationally excited molecules play a particularly important role, because, for typical operating conditions, they are efficiently produced by resonant electron-molecule scattering.

The kinetic energy of electrons in a low-temperature gas discharge is typically a few electron volts. At these energies, the electron-molecule collision time is rather long, therefore favoring resonant enhancement of the collision. The cross section for *vibrational excitation* of molecules is thus given by (9.66) with the scattering state obtained from the resonance model. Specifically, for continuum states normalized on the energy scale, the cross section becomes

$$d\sigma_{v_i \rightarrow v_f}^{VE} = \frac{(2\pi)^4}{k_i^2} \left| \int dR \chi_{v_f}^*(R) V_{dk}^*(R) \Psi_{dE}^{(+)}(R) \right|^2 d\Omega_f, \quad (9.97)$$

where $\chi_{v_f}(R)$ is the vibrational state of the molecule after the collision and $\Psi_{dE}^{(+)}(R)$ is the solution of the effective Lippmann–Schwinger equation (9.79) with $V_d(R) =$

$V_{AB^-}(R)$, $V_0(R) = V_{AB}(R)$, $V_{dk}(R)$ is the interaction between the resonant AB^- state and the electron-molecule scattering continuum, and $J(R) = V_{dk}(R)\chi_{\nu_i}(R)$. Energy conservation implies $E = k_i^2/(2\mu) + \omega_{\nu_i} = k_f^2/(2\mu) + \omega_{\nu_f}$ with μ as the reduced electron-molecule mass.

The shape of the vibrational excitation cross section depends on the imaginary part of $F(R, R'; E)$, that is, on $\Gamma(R, R'; E)$ [see (9.80) and (9.82)]. When it is large compared to the inverse period of vibration in the resonant state, that is, for a short-lived resonance, the cross section is smooth. For a long-lived resonance, that is, when $\Gamma(R, R'; E)$ is much smaller than the period of vibration, the cross sections consist of a series of peaks reflecting the vibrational states of the resonant state. This dependence of the cross section on the lifetime of the resonance is illustrated in Figure 9.16.

When the energy exceeds the dissociation energy, *dissociation* may occur, either indirectly through the resonant state, or directly through a transition to the continuum of the nuclear motion of the molecule. The indirect process only contributes when the target is initially in a highly excited vibrational state [91]. Usually, the direct process dominates. For large enough energies, the adiabatic approximation applies and the dissociation cross section is given by

$$d\sigma_{\nu_i \rightarrow \nu_f}^D = \frac{(2\pi)^4}{k_i} |T_{\nu_f \nu_i}(\Omega_f, \Omega_i)|^2 d\Omega_f \quad (9.98)$$

with

$$T_{\nu_f \nu_i}(\Omega_f, \Omega_i) = \int dR F_{\nu_f}^*(R) t(\Omega_f, \Omega_i, R) F_{\nu_i}(R), \quad (9.99)$$

where $t(\Omega_f, \Omega_i, R)$ is the electronically elastic fixed-nuclei scattering amplitude and $F_{\nu_f}(R)$ is a continuum nuclear wave function of the molecule.

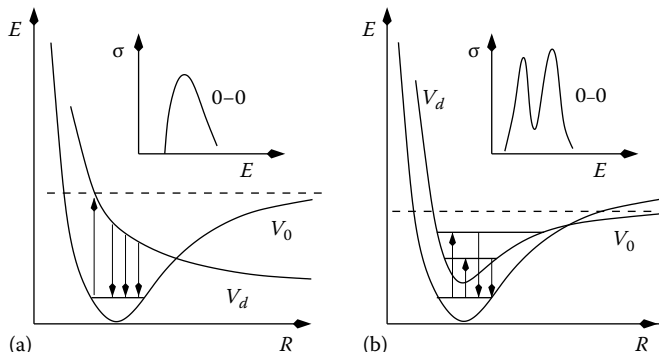


FIGURE 9.16 Illustration of resonant vibrational excitation of a molecule for a large (a) and a small (b) imaginary part of $F(R, R'; E)$. The dashed line indicates the dissociation threshold, $V_0(R)$ is the potential energy surface of the molecule, $V_d(R)$ is the potential of the auto-detaching resonant state of the negatively charged molecule, and the insets show the typical shape of the cross section for the two cases.

Electronic quantum numbers are suppressed because they are unchanged; vibrational excitation and dissociation involve only one potential energy surface of the target molecule.

Finally, the *production of electronically excited molecules* occurs due to scattering with high energy electrons. For energies far away from the dissociation threshold, the adiabatic approximation holds. Therefore, ignoring the rotational degrees of freedom, the transition amplitude can be written as

$$\begin{aligned} T_{n_f \nu_f n_i \nu_i}(\Omega_f, \Omega_i) &= \int dR F_{n_f \nu_f}^*(R) t_{n_f n_i}(\Omega_f, \Omega_i, R) F_{n_i \nu_i}(R) \\ &= t_{n_f n_i}(\Omega_f, \Omega_i, R_0) \int dR F_{n_f \nu_f}^*(R) F_{n_i \nu_i}(R). \end{aligned} \quad (9.100)$$

In the second line the fact has been utilized that $F_{n_i \nu_i}(R)$ is strongly peaked at $R = R_0$, where R_0 is the position of the minimum of the potential energy surface of the initial electronic state of the molecule. The differential cross section for electronic excitation is thus given by

$$d\sigma_{n_i \nu_i \rightarrow n_f \nu_f}^{EE} = \frac{d\sigma_{n_i \rightarrow n_f}^{R_0}}{d\Omega_f} \left| \int dR F_{n_f \nu_f}^*(R) F_{n_i \nu_i}(R) \right|^2 d\Omega_f, \quad (9.101)$$

where the first factor is the fixed-nuclei differential cross section at $R = R_0$ for the electronic transition $n_i \rightarrow n_f$ and the second is the Franck–Condon factor q already mentioned in connection with ion–ion annihilation.

9.2.2.4 Concluding Remarks

This section discussed elementary collision processes as they typically occur in molecular gas discharges, focusing in particular on inelastic and reactive collisions that change the internal energy and composition of the scattering fragments: ionization, attachment, recombination, annihilation, detachment, and excitation. These processes are the primary driving force of the plasma chemistry in these discharges. Elastic scattering, on the other hand, is not explicitly discussed because its main effect, depositing energy into the electronic subsystem, only indirectly affects the plasma chemistry.

Instead of merely listing kitchen-made cross-section formulae and unrelated cross-section data, emphasis has been placed on a unified description of elementary processes based on general principles of quantum-mechanical multichannel scattering theory. By necessity, the presentation is rather dense. Technical details left out, as well as cross-section data, can respectively be found in the original papers, review articles, monographs, and websites mentioned at the beginning of this section.

As far as the kinetic modeling of gas discharges is concerned, collision cross sections are input parameters for the collision integrals of the Boltzmann equations. They are thus always convoluted with distribution functions. Some of the quantum mechanical intricacies of particle entanglement and de-tanglement occurring during a collision are thus eventually averaged out. Calculating cross sections earmarked for plasma-chemical applications with the most sophisticated quantum-mechanical

methods is thus not only unfeasible for the (polyatomic) gases of interest, it would also be overkill. Cross sections obtained from effective (semiempirical) models containing only those microscopic degrees of freedom that, for given external control parameters, may eventually become active in the collision integrals should in fact be sufficient. A systematic effort to develop (and solve) this type of model for the various processes may significantly increase the predictability of plasma modeling. It may thus help to turn plasma processing as a whole from an art to a science [92].

9.3 SURFACE PROCESSES

9.3.1 BASICS OF PLASMA MATERIAL INTERACTION

In order to control many technical processes using plasmas, it is necessary to identify the main atomistic processes occurring during the interaction of the plasma with the wall material [93–95]. As an example, the interaction of hydrogen ions and atoms with a graphite surface is used (Figure 9.17).

When charged particles (ions or electrons) strike a solid surface, they stick to it. Ions do have a finite probability of backscattering from the surface, mainly as neutrals picking up electrons from the surface. The neutral atoms are then reemitted into the plasma where they can be re-ionized, usually by electron impact.

The incident energetic atom collides with a target surface atom and transfers its momentum; consequently, it can either be reflected from the surface (backscattering)

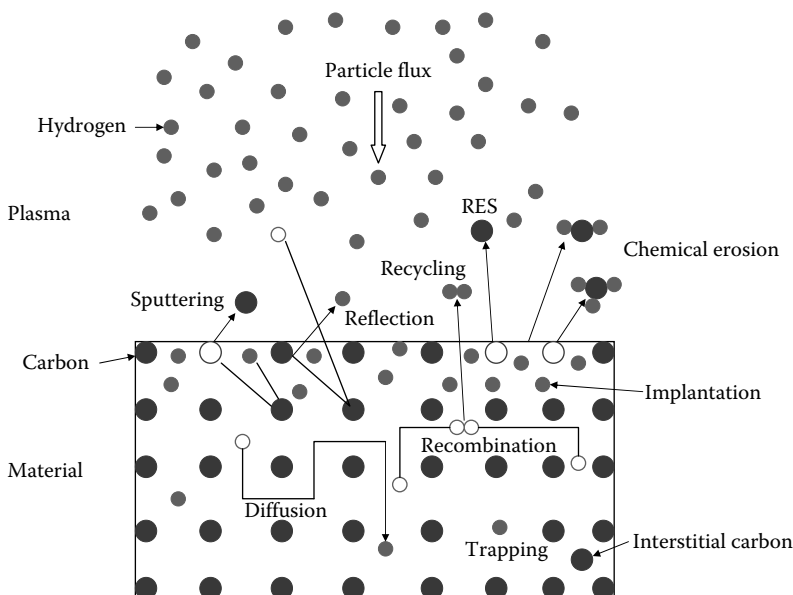


FIGURE 9.17 Overview of the atomistic processes during plasma-surface interactions relevant to particle recycling. The acronym RES stands for radiation enhanced sublimation process.

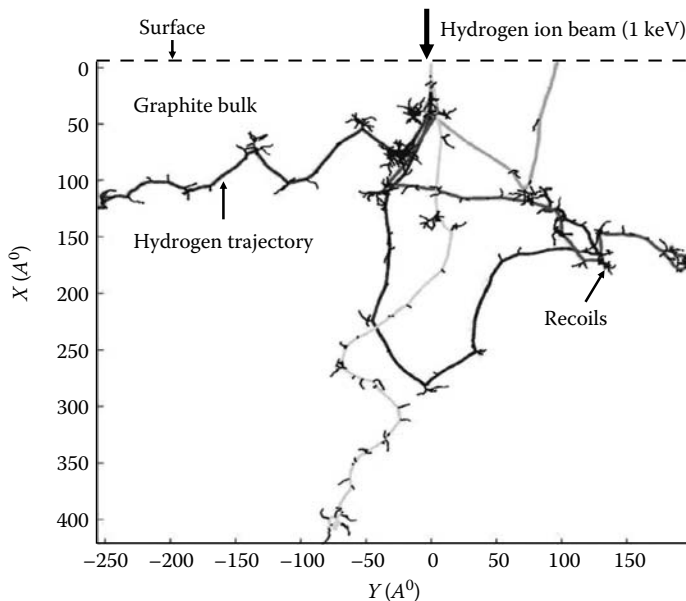


FIGURE 9.18 Collisional cascade created in graphite by 1 keV hydrogen ion beam. The simulation was done using the TRIM code.

or it penetrates into the target and, after a collision cascade, comes to rest in thermal equilibrium with the target atoms (implantation) (Figure 9.18) [96]. The target atoms that reach the surface and have more energy than the surface binding energy of the target material can be released from the surface (physical sputtering). The physical sputtering and backscattering depends on the atomic masses of the incident ion and the target as well as the energy and the angle of incidence of the incident ion. The erosion of the surface by physical sputtering and the implantation of atoms can lead to changes in the composition and structure of the material.

Incident hydrogen atoms that have equilibrated with the surface diffuse within the target and can undergo chemical reactions with the target atoms to form hydrocarbons and hydrogen molecules. Some of these molecules diffuse to the target surface and can either be desorbed by incident atoms or be released thermally from the surface, depending on the surface temperature (chemical erosion) [97]. In some cases, the incoming energetic hydrogen atom or ion breaks a covalent C–C bond on the graphite surface by pushing apart the carbon atoms due to its short range repulsive potential. This can result in the ejection of either a carbon atom or a hydrocarbon and is called swift chemical sputtering [98].

All sputtering processes are characterized by the *sputtering yield* Y , which is the number of atoms or molecules ejected per impacting particle [99–102]. For physical sputtering to occur, enough momentum must be transferred to the lattice atom to overcome the surface-binding energy; thus, a *threshold energy* E_{th} exists for physical sputtering below which no sputtering occurs. The value of E_{th} can be estimated from the surface-binding energy of the target. The physical sputtering yield can be

calculated using binary collision models like the TRIM code. Chemical sputtering [97] is dependent on

- The energy and mass of the incident particle
- The target temperature
- The incident flux of particles

No threshold kinetic energy is needed for chemical sputtering to occur, and yields even for sub-eV hydrogen ion bombardment are not negligible [103]. The strong dependence on the threshold temperature is one of the key signatures of chemical sputtering [104].

The energy deposited by the plasma on the surface determines the surface temperature, which is an important parameter in determining the diffusion of the various species and the molecule formation on the surface. At a very high incident energy flux and/or insufficient cooling of the target, the surface temperature can increase and the surface atoms can thermally evaporate. Furthermore, implanted gas atoms can accumulate in the surface layers to form bubbles. This leads to blister and flake formation and breaking of the surface layer [105].

The bombardment of energetic atoms creates damage sites (traps) and interstitials within their range of penetration in the target. This process competes with the annealing of the lattice defects by recombination of interstitials and vacancies. If the recombination rate is not high enough to anneal all the damage, a net production of damage and amorphization of the target surface arises. The porous structure of the graphite offers a large internal surface area on which the incident hydrogen atoms can diffuse and penetrate far beyond the implantation range of the ions [106].

9.3.1.1 Plasma-Wall Contact with an Electron Emitting Wall

If the wall material is emitting electrons (or ions), the plasma-wall contact is modified [107]: The potential drop is reduced, since to reach zero net current with an emitting wall with an electron emission coefficient γ , more electrons from the plasma have to reach the wall. This causes a modification of the potential at the wall [108]. Nevertheless, there is a limit for very strong emission, because with a reduced potential drop, the electric field at the wall also drops and reaches zero for a critical emission coefficient. A higher emission leads to field reversal and the creation of an electrostatic double layer at the wall, at which emitted electrons are partly reflected back to the wall and are directly re-adsorbed (space-charge limit of the emission current). Now the different emission processes will be shortly discussed. More details can be found in [109].

- *Photoelectric emission:* When a photon (with the energy $h\nu$) hits a solid surface, an electron is released with the energy $h\nu - W$, where W is the work function of the material.
- *Thermionic emission:* Electrons in a solid occupy energy levels according to the Fermi–Dirac distribution, where the Fermi-energy ϵ_F is the highest occupied energy level (at zero temperature).

The electrons from the high-energy tail of the Fermi function can leave the solid if they are able to overcome the work function (energies greater than $\epsilon_F + W$). This process is known as thermionic emission; its current is derived from the (temperature dependent) number of electrons at these energy levels. The velocity distribution of the emitted electrons is Maxwellian because they are thermalized by collision in the solid [110]. Thermionic emission is quite important in arcs and hot spots. Graphite has a work function of 4.6 eV. Therefore, about 2500 K is needed for thermionic emission to occur (which is very close to the melting temperature of carbon).

- *Field emission:* The effective work function of a solid can be reduced by the electric fields (Schottky effect) and an additional emission enhancement can be reached by the tunneling of electrons through the potential wall created by the electric field. This process is especially important for the creation of arcs in fusion plasmas. The field emission electron microscope relies on this phenomenon.
- *Secondary electron emission:* Electrons hitting a surface are either reflected elastically (usually a small amount) or ejected due to inelastic collisions with other electrons. The energy distribution of the electron-induced secondary electrons has two peaks: One at low energies and one close to the energy of the impinging electrons. Ions produce a large electric field in front of the surface and create a potential wall (as with field emission) through which the electrons can tunnel and neutralize the ions. If the difference between the energy of the electrons and the ionization energy of the ion is larger than the work function, secondary electrons can be emitted.
- *Arches:* The emission processes discussed before can locally result in strongly varying electric potential conditions at a surface [107]. For example, for field-emission at a tip, one can locally get a smaller potential drop: A positive current flows into the surface at this position. The current can melt the material and a unipolar arc is created, stabilized by thermo-electrons, for which the vessel is the cathode and the plasma the anode.

9.3.2 INTERACTION OF HYDROGEN PLASMA WITH CARBON-BASED MATERIALS

Typical high-quality graphite consists of granules (typically 1–10 μm , macroscale) separated by voids that are typically a fraction of a micrometer wide. The granules consist of graphitic micro-crystallites of 10–100 nm size separated by micro-voids that are typically 1 nm wide (mesoscale) [111,112]. These substructures, voids and micro-voids, provide a large internal surface area inside the graphite where hydrogen interstitial atoms can diffuse and react with each other. This will affect the hydrogen isotope inventory and recycling behavior and also chemical erosion. Due to the large internal surface area provided by the graphite, it acts like a sponge for hydrogen.

For carbon-based plasma-facing materials, essentially four mechanisms have been identified for the retention and uptake of hydrogen [113] (see Figure 9.19).

1. Formation of a saturated surface layer
2. Surface diffusion due to internal porosity

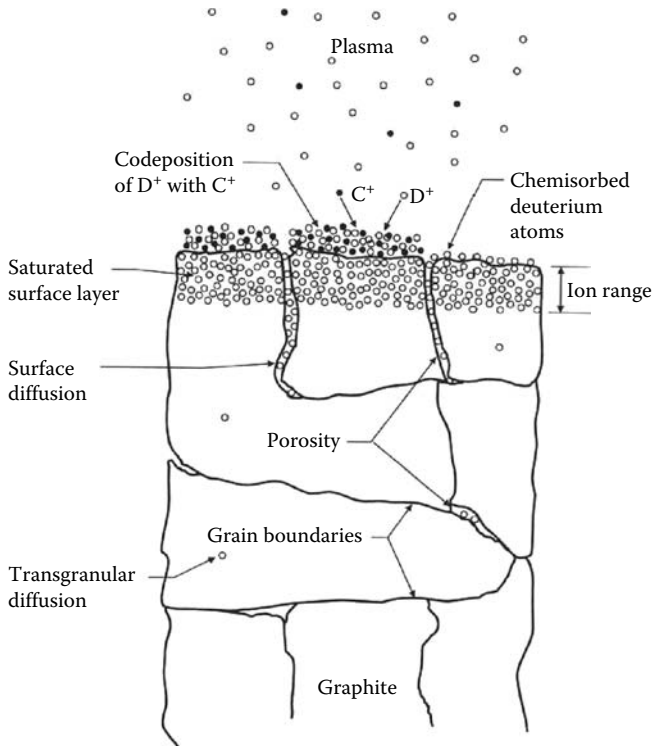


FIGURE 9.19 Schematic of the primary mechanisms for hydrogen retention and transport in graphite. (From Chiu, S. and Haasz, A.A., *J. Vac. Sci. Technol. A*, 9(3), 747, 1991.)

3. Trans-granular diffusion and bulk trapping
4. Co-deposition of hydrogen with plasma-exposed surfaces

9.3.2.1 Formation of a Saturated Surface Layer

Implantation of hydrogen into graphite creates broken carbon bonds, and due to the strong chemical reactivity of carbon with hydrogen, it can be strongly bound through the formation of C-H chemical bonds (≈ 4.5 eV). Figure 9.19 shows the primary mechanisms responsible for the retention of energetic hydrogen hitting the carbon-based materials. At low fluences and low temperatures, most of the non-reflected hydrogen is trapped and retained in the graphite. After the saturation of the implantation region has been reached, reemission sets in and most of the incident flux is reemitted. The amount of hydrogen in the implantation zone is ~ 0.4 H/C at room temperature. This hydrogen concentration level extends from the surface to the penetration depth (range) of the incident hydrogen ions. The range of the hydrogen ions depends on the energy of the incident flux and is smaller for lower energies. Thus, a smaller quantity of hydrogen is trapped for lower energy hydrogen ions.

9.3.2.2 Diffusion

As the temperature is increased (≥ 1000 K), the de-trapping of hydrogen atoms starts, leading to hydrogen release and a decreasing retention level in the implantation zone. Upon further bombardment following the saturation of the implantation zone, the hydrogen atoms and molecules start diffusing deep into the bulk (far beyond the implantation zone) along the internal porosity or the grain boundary of the granules, as shown in Figure 9.19. At temperatures above ~ 1000 K, the hydrogen atoms start entering into the granules and transgranular diffusion sets in. This provides access to the trapping sites inside the grains that are practically inaccessible at low temperatures; therefore, the retention levels start to increase again [115].

9.3.2.3 Codeposition

The carbon atoms that are sputtered from graphite or other carbon-based materials due to the impacting plasma particles can be codeposited either as neutrals or ions due to the plasma-chemistry processes in hydrocarbon plasmas, on both plasma facing and out of line-of-sight surfaces in the device. The layer that is formed is similar to the saturated implant layer described earlier. However, the saturated implant layers have a thickness of several tens of nanometers (depending on energy,) whereas the co-deposited layers seem to have no upper limit to their thickness [116] and may extend to several μm . If the layer gets too thick, one produces dust and flakes. Both kinds of layers have similar H/C ratio, namely, ~ 0.4 at room temperature.

The existence of large variations at length scales of graphite substructures coupled with the wide range of possible atomistic processes makes the study of hydrogen transport and inventory in graphite a nontrivial exercise. The key idea is to use the insights gained from the microscopic models for transport modeling at the mesoscale and further into the macroscale in order to understand the physical processes contributing to macroscopic transport. Such a multi-scale model was developed by Warrier et al. [117] to model the trace hydrogen diffusion problem. It was shown that the diffusion coefficient of the hydrogen depends on the internal structure of graphite, namely, void-size and void-fraction, which implies that molecule formation also depends on these factors.

9.4 EXAMPLE: OXYGEN RF PLASMA

PIC-MCC simulations of an oxygen capacitively coupled radio-frequency discharge combined with phase-resolved optical emission spectroscopic measurements of the plasma-induced optical emission were used to get a detailed microscopic description of the dynamic processes in rf plasmas. The PIC-MCC simulations reproduced the excitation patterns observed in experiment quite well and allowed to identify the underlying physics.

Capacitively coupled radio-frequency discharges (CCRF) are extensively applied in the area of surface treatment such as cleaning of surfaces, production of micro-electronic patterns by plasma etching or generation of functional groups on polymer surfaces. Besides, there are special applications in prospect such as a discharge oxygen-iodine laser (DOIL) [118].

CCRF plasmas between two circular plane electrodes made of stainless steel (10 cm in diameter, 2.5 cm distance) were studied in a cylindrical vacuum chamber (300 mm in diameter, 500 mm high) by phase-resolved optical emission spectroscopy (PROES) [119,144]. The plasmas were ignited in pure oxygen at pressures ranging from 20 to 100 Pa. Only one of the electrodes was powered at a frequency of 13.56 MHz (rf cycle of 74 ns), whereas the other electrode and the walls of the vacuum chamber were grounded. Thereby, a negative self-bias voltage from -70 to -550 V developed at the powered electrode corresponding to rf powers from 10 to 100 W.

Despite the wide application of capacitive rf discharges in molecular gases, combining the physics of nonequilibrium nonstationary plasmas with the complexity of reactive plasma processes, a complete description of such systems is still missing.

The phase-resolved optical emission spectroscopy provides temporal resolution to investigate the behavior of the plasma-induced optical emission within the RF cycle and therefore the dynamics of energetic electrons and other species [120,121].

The particle-in-cell (PIC) method combined with Monte-Carlo collisions (MCC) allows an accurate resolution of charged particles distribution functions and their fluxes to the electrode [81,122–124]. The model resolves one spatial but three velocity components (1d3v) and is a reduced model because out of up to 75 listed reaction and scattering processes [125], which potentially affect the properties of the discharge, only 20 are included in the model. These 20 are the ones with the largest cross sections (see Table 9.2), representing the most important atomic and molecular processes in the oxygen plasma.

The cross-section database for collisions in oxygen plasmas was critically assessed [123] and corrected cross sections for elastic scattering (O^- , O_2), recombination (O_2^+ , O^-), associative detachment (O^- , O_2), and charge exchange (O_2^+ , O_2), were implemented.

Although the simulated system is actually 3D, the discharge behavior is assumed to be 1D along the axis. This is supported by the fact that the electrode diameter is larger than the electrode spacing of $L = 4.5$ cm used in the simulation and that the radial dependence of the plasma parameters close to the symmetry axis can be neglected. Disregarding the electric asymmetry between the powered and the grounded electrode, this part of the discharge can be simulated by a planar, 1D model. This planar model retains only one spatial coordinate X , with $0 \leq X \leq L$, where L is the distance between the electrodes.

In the simulations, the initial electron density and temperature were chosen as $n_{e0} = 8 \times 10^9 \text{ cm}^{-3}$ and $T_{e0} = 10 \text{ eV}$, respectively. The computational domain length was $X_{max} = 172 \lambda_{D0} = 4.5$ cm. At the positions of the electrodes $X = 0$ and $X = X_{max}$, the absorbing wall boundary conditions were applied. Secondary electron emission was neglected. The potential at $X = 0$ was fixed at 0 V, corresponding to the grounded electrode. At the position of the powered electrode at $X = X_{max}$, the potential was assumed to oscillate according to the applied rf voltage: $\phi(X_{max}, t) = U_{RF} \sin(\omega_{RF} t)$ with $\omega_{RF}/2\pi = 13.56 \text{ MHz}$ and a rf voltage amplitude U_{RF} ranging from 75 to 1000 V. As the neutral gas density is much higher than the densities of charged species, the neutral gas was treated as a background with fixed density and temperature. The gas temperature was $T_n = 300 \text{ K}$, and pressure was varied between 20 and 60 Pa. Only the dynamics of three charged particles (electrons, O_2^+ , and O^- ions) were taken

TABLE 9.2
Collisions Included in the Model

<i>Elastic scattering</i>		
1.	$e + e \rightarrow e + e$	Coulomb scattering
2.	$O^- + O^- \rightarrow O^- + O^-$	Coulomb scattering
3.	$O_2^+ + O_2^+ \rightarrow O_2^+ + O_2^+$	Coulomb scattering
4.	$e + O_2 \rightarrow e + O_2$	Elastic scattering
5.	$O_2^+ + O_2 \rightarrow O_2^+ + O_2$	Elastic scattering
6.	$O^- + O_2 \rightarrow O^- + O_2$	Elastic scattering
7.	$O_2^+ + O_2 \rightarrow O_2 + O_2^+$	Charge exchange
<i>Electron energy loss scattering</i>		
8.	$e + O_2 \rightarrow e + O_2 (\nu = 1, \dots, 4)$	Vibrational excitation
9.	$e + O_2 \rightarrow e + O_2(\text{Ryd})$	Rydberg excitation
10.	$e + O_2 \rightarrow e + O(3P) + O(3P)$	Dissociation (6.4 eV)
11.	$e + O_2 \rightarrow e + O(3P) + O(1D)$	Dissociation (8.6 eV)
12.	$e + O_2 \rightarrow e + O_2(a^1\Delta_g)$	Metastable excitation
13.	$e + O_2 \rightarrow e + O_2(b^1\Sigma_g)$	Metastable excitation
<i>Electron and ion production and loss</i>		
14.	$e + O_2^+ \rightarrow O + O$	Dissociative recombination
15.	$O^- + O_2^+ \rightarrow O + O_2$	Neutralization
16.	$e + O_2 \rightarrow O + O^-$	Dissociative attachment
17.	$O^- + O_2 \rightarrow O + O_2 + e$	Direct detachment
18.	$O^- + O_2(a^1\Delta_g) \rightarrow O_3 + e$	Associative detachment
19.	$e + O_2 \rightarrow 2e + O_2^+$	Electron impact ionization
20.	$e + O^- \rightarrow O + 2e$	Electron impact detachment

into account. Neutral particles appearing as either educts or products in Table 9.2 are not explicitly simulated. Molecular oxygen in its ground state, O_2 (feedstock gas), is modeled as a reservoir characterized by a pressure p and a temperature T . Atomic oxygen, O , vibrationally excited oxygen molecules, $O_2(\nu)$, Rydberg states of the molecular oxygen, $O_2(\text{Ryd})$, and the molecular metastables, $O_2(a^1\Delta_g)$ and $O_2(b^1\Sigma_g)$, are included only indirectly as their production results in an energy loss for electrons.

A grid size $\Delta x = \lambda_{D0}/2 = 0.013$ cm and time step $\Delta t = 0.2/\omega_{pe0} = 3.956 \cdot 10^{-11}$ s were used to have stable free flights of charged particles (in the mean electric field given by the Poisson equation) and to resolve the electron plasma oscillation, guaranteeing numerical stability.

The number of computational particles per Debye length was chosen as $N_d = 2000$, totaling about 10^6 computational particles (“super particles”) used in the simulation. The duration of each simulation was in the order of several thousands of rf cycles (millions of time steps) in order to ensure that the system settles to dynamic equilibrium.

To distinguish different excitation mechanisms and to compare the experimental results with simulations, the excitation rates X are calculated from the measured

emission intensities. The temporal behavior of the emission intensity is also influenced by the finite lifetime of the emitting states, which is on the order of the time scale of the rf cycle (nanoseconds). To calculate the time-dependent excitation rate for each distance z from the powered electrode, the relation

$$X(t, z) \propto I(t, z) + \tau_{\text{eff}} \frac{dI(t, z)}{dt} \quad (9.102)$$

is used [126], which leads to the correct relative time behavior of the excitation rate, but does not allow to determine its absolute value. The effective lifetime τ_{eff} of the initial state of the optical transition appears as a factor in the formula. It depends on the natural lifetime τ_n of the initial state and its collisional de-excitation (quenching):

$$\frac{1}{\tau_{\text{eff}}} = \frac{1}{\tau_n} + \sum_q k_q n_q, \quad (9.103)$$

with the quenching rates k_q and the number densities n_q of the species q . The simple calculation by (9.102) and (9.103) disregards any spatial dependence of the quenching or movements of the excited atoms, which is a good assumption in most cases because of the large mass of the atoms. Another simplification is that only the most important quenching partner, the background gas oxygen, is taken into account and that its density is determined by the ideal gas law $n_q = p_q/k_B T$ at room temperature $T = 300$ K. The natural lifetime of the initial state of the 844.6 nm transition is 35.1 ns and the quenching rate with O₂ as the quenching partner is $9.3 \cdot 10^{-10}$ cm³ s⁻¹ [127].

The resulting excitation rate is shown together with the original measured intensity in Figure 9.20. It demonstrates that the calculation results in a temporal compression of the patterns and a shift of the maximum toward earlier times. This leads also to a better separation of the patterns.

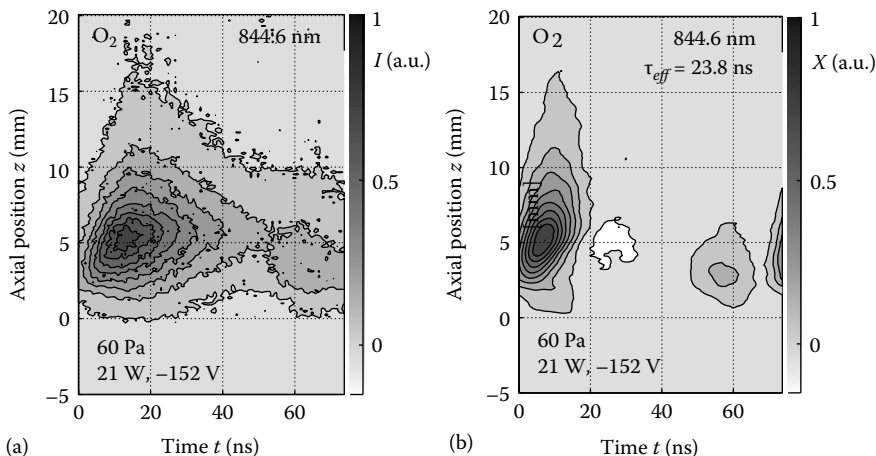


FIGURE 9.20 Measured spatial and phase-resolved optical emission (a) and the corresponding excitation rate (b) for oxygen at 60 Pa, 21 W, and 844.6 nm.

Depending on the discharge pressure and power, four excitation structures can be identified, marked from I to IV (see Figure 9.21). The first structure is always present and appears in the first half period of the rf cycle some millimeters in front of the powered electrode. The second pattern emerges at higher powers and higher pressures, following shortly after structure I at roughly the same location. At lower powers, pattern II disappears and pattern III emerges in the second part of the rf cycle closer to the electrode. In addition, a thin emission layer IV close to the electrode can be present with increasing power and pressure.

Figure 9.22 shows a comparison of the spatiotemporally resolved excitation pattern in an oxygen CCRF discharge of the corresponding transition at 844.6 nm from (a) PROES measurements and (b) PIC-MCC simulation for 60 Pa and $-350\text{ V}_{\text{Bias}}$. As one can see, aside from a small shift in time and the fact that structure IV overlays structure III in the measurement, both match very well.

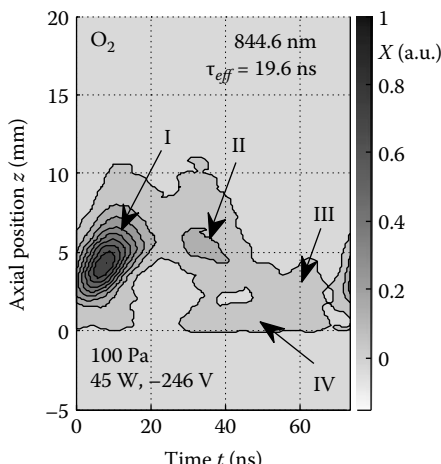


FIGURE 9.21 Spatiotemporally resolved excitation rates in an oxygen CCRF discharge of the corresponding transition at 844.6 nm (100 Pa, 45 W, -246 V self-bias).

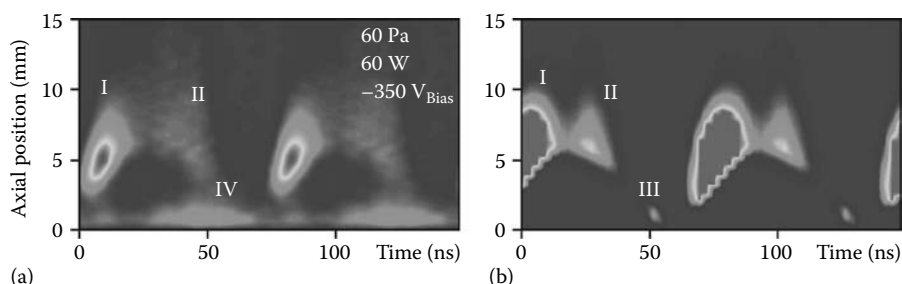


FIGURE 9.22 Phase-resolved excitation pattern in an oxygen CCRF discharge of the corresponding transition at 844.6 nm from (a) PROES measurements and (b) PIC-MCC simulation for 60 Pa and $-350\text{ V}_{\text{Bias}}$. The cross section for the excitation in the simulation is two times higher than in the original simulation to visualize pattern III.

A detailed view on the dynamics of particle densities, charge density, plasma potential, and the electron velocity distribution resulting from the PIC-MCC simulation gives a good understanding of the processes underlying the observed excitation patterns. Respectively, the axial profile of the plasma potential (a), the axial density distribution of the electrons, molecular oxygen ions, negative oxygen ions and charge density (b), the profile of the electron axial velocity component distribution (c), and the spatiotemporally resolved dissociative electron impact excitation rate profile for the corresponding emission at 844.6 nm (d) from the simulation for the oxygen rf discharge at $p = 60$ Pa and $U_{RF} = 800$ V are shown in Figures 9.23 through 9.27, corresponding to five different phases of the rf cycle. The white bar in the graph of the spatiotemporally resolved excitation rate profile indicates the actual phase position. The dissociative electron impact excitation is dominant in oxygen, because its cross sections and the density of O_2 molecules in comparison with atomic oxygen are large, even if the threshold values for dissociative excitation are about 5 eV larger than those for direct excitation [128]. An evidence for that can be found in measurements of the rise time of excited atomic oxygen, which show that the emission appears already before the ground state atomic oxygen density reaches its constant value of saturation [119,129].

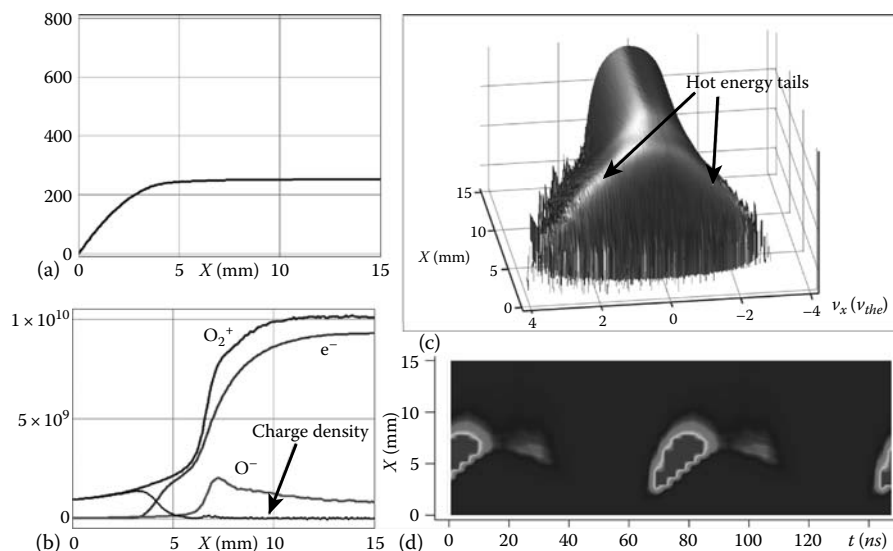


FIGURE 9.23 The axial profile of the plasma potential (a), the axial density distribution of the electrons, molecular oxygen ions, negative oxygen ions and charge density (b), the profile of the electron axial velocity component distribution (c), and the spatiotemporally resolved excitation rate profile for the corresponding emission at 844.6 nm (d) from the simulation for the oxygen rf discharge at $p = 60$ Pa and $U_{RF} = 800$ V. The white bar in the graph of the spatiotemporally resolved excitation rate profile indicates the actual phase position. The temporal position within the rf cycle is 0 ns.

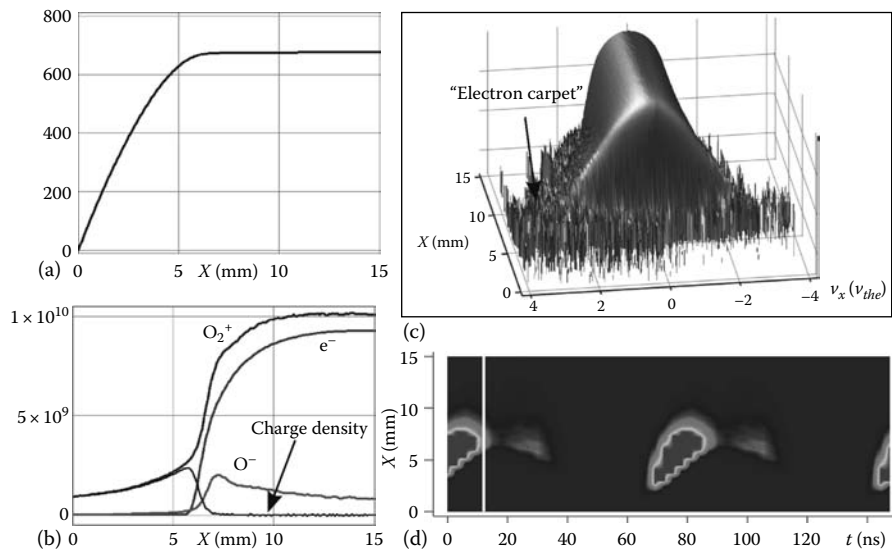


FIGURE 9.24 Same as for Figure 9.23 but the temporal position within the rf cycle is 12 ns. (a) Plasma potential (v), (b) e^- , O_2^+ , O^- and charge densities (cm^{-3}), (c) electron velocity distribution function, and (d) 844.6 mm line excitation.

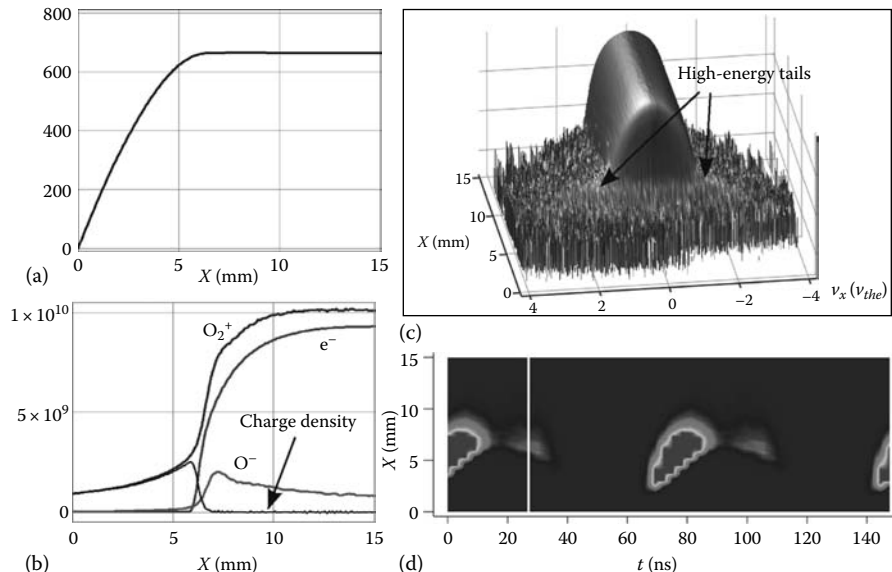


FIGURE 9.25 Same as for Figure 9.23 but the temporal position within the rf cycle is 26.5 ns. (a) Plasma potential (v), (b) e^- , O_2^+ , O^- and charge densities (cm^{-3}), (c) electron velocity distribution function, and (d) 844.6 mm line excitation.

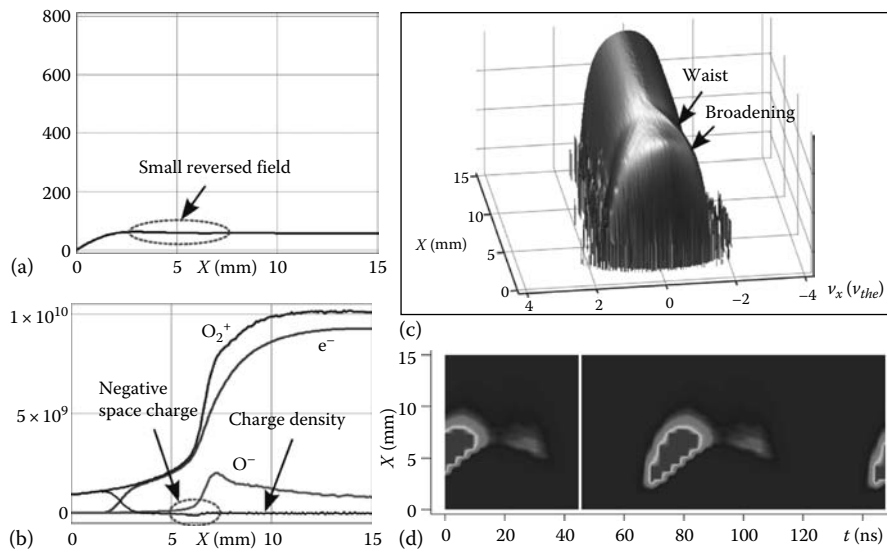


FIGURE 9.26 Same as for Figure 9.23 but the temporal position within the rf cycle is 44.3 ns. (a) Plasma potential (v), (b) e^- , O_2^+ , O^- and charge densities (cm^{-3}), (c) electron velocity distribution function, and (d) 844.6 mm line excitation.

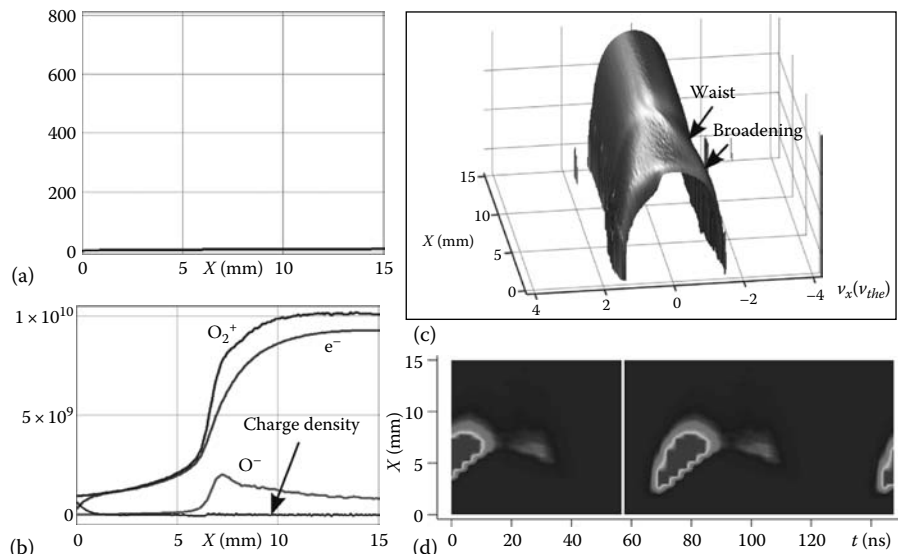


FIGURE 9.27 Same as for Figure 9.23 but the temporal position within the rf cycle is 53.1 ns. (a) Plasma potential (v), (b) e^- , O_2^+ , O^- and charge densities (cm^{-3}), (c) electron velocity distribution function, and (d) 844.6 mm line excitation.

Different plasma species respond in quite different ways to the oscillating sheath electric field, as one can see in the density plots (Figures 9.23b through 9.27b). Electrons, being extremely mobile, follow the changes of the sheath electric field, which keeps them away from the electrode for most of the rf cycle. The electrons can reach the electrode only during the short time when the sheath collapses (Figure 9.27). The positive and the negative ions, due to their much larger masses, respond only to the rf cycle averaged electric field, so their densities in the sheath are not changing significantly during the rf cycle. The average electric field in the sheath is directed toward the electrode, so the negative ions are repulsed and the positive ions are attracted to the electrode over the rf cycle. The bulk electrons that get close to the electrode during the sheath collapse (Figure 9.27) are expelled back when the sheath electric field starts to grow. These electrons gain energy from the sheath electric field as they are pushed back toward the bulk. The mean free path of electron-neutral elastic collisions for 60 Pa $\lambda_{el} \sim 1$ mm is smaller than the sheath width ~ 5 mm, so the electrons are accelerated in the sheath electric field between successive collisions with neutrals, that is, Ohmic heating occurs [130]. One can clearly see hot energy tails corresponding to the electrons heated by the expanding sheath in the plots of the electron velocity distribution function (Figures 9.23 and 9.24). These hot electrons loose their energy due to inelastic collisions with the neutral gas: ionization, dissociation, and excitation. The efficient mean free path for the inelastic collisions is about $\lambda_{in} \sim 4$ mm, this corresponds to the length scale on which the electrons from hot tails are cooled down (Figures 9.23 and 9.24). This population of energetic electrons produced by the growing sheath is responsible for the formation of the excitation pattern I, as one can see in Figures 9.23 and 9.24. Such an excitation pattern is well known from investigations of argon and hydrogen plasmas [126,131–138], among others [139–142]. As the front of the high energy electrons moves toward the bulk together with the sheath edge, one can clearly identify the sheath edge position during the first quarter of the rf cycle by the lower margin of the excitation pattern I. The width of the pattern I is comparable with the mean free path for inelastic collisions.

At the end of the first quarter of the rf cycle, when the sheath potential drop reaches its maximum (Figure 9.25), the bulk electrons are completely expelled from the sheath. This determines the end of the excitation pattern I.

The excitation pattern II, observed shortly after pattern I, during the second quarter of the rf cycle, has a different origin. The electrons can gain energy only inside the sheath, as electrons from the bulk are not able to penetrate into the sheath during this time of the rf period because of the strong repulsive electric field. Therefore, the electrons responsible for the pattern II have to originate from inside the sheath.

Such an excitation pattern is usually identified with secondary electrons produced by ion bombardment of the electrode [119,135,136]. Such secondary electrons, appearing at the electrode during the time when the sheath potential drop is maximal, get accelerated toward the bulk to energies up to several 100 eV, so they are capable of multiple ionization collisions. Thus, these electrons can trigger an electron avalanche, which is usually assumed to be responsible for the excitation pattern II.

In experiments at low rf power and self-bias voltage, the resulting low kinetic energy of impinging positive ions on the powered electrode reduces the secondary electron emission and pattern II does not appear. However, in oxygen CCRF plasmas,

pattern II appears at lower rf power as compared to discharges in hydrogen and argon [135,136]. In the PIC-MCC simulation, the secondary electron emission process was not included by purpose, but pattern II was still observed. As one can see in Figure 9.24, an “electron carpet” starts to appear in the sheath by the time the sheath potential drop reaches its maximum. In the simulation, these electrons are produced in detachment collisions of negative ions with background gas ($O^- + O_2 \rightarrow O + O_2 + e$). Although the negative ions are constantly expelled from the sheath by the sheath electric field, it takes several rf cycles for O^- ions produced in the sheath to get to the bulk, so there is always a low density background of the negative ions in the sheath. The negative ions in the sheath act as a reservoir of electrons, which get released during the collisions with neutrals. These electrons trigger an avalanche, producing the high-energy tails in the velocity distribution function (Figure 9.25). The temperature of these high-energy tails at the sheath boundary in the simulation was estimated as $T_{e_{hot}} \sim 30$ eV. These energetic electrons are responsible for the excitation pattern II observed in the simulations. As these electrons are distinctly hotter than those responsible for excitation pattern I, pattern II is further protruded into the bulk as compared with pattern I.

At lower rf power, the excitation pattern III appears in the second part of the rf cycle close to the electrode and reaches its maximum about 2–4 mm in front of the powered electrode (Figure 9.21). Dynamics of particle densities, charge density, plasma potential, and the electron velocity distribution during the sheath collapse obtained from the PIC simulations gives a good insight into this process.

Due to increase of the electron-neutral elastic collision cross section at energies of about 1 eV, the electron flow toward the electrode during the sheath collapse get inhibited. This results in a buildup of negative space charge close to the sheath edge (≈ 6 mm) causing a field reversal during the end of the sheath collapse phase (Figure 9.26). This reversed field accelerates the electrons toward the electrode, self-consistently maintaining the ion-electron current balance, which results in the excitation pattern III. The electrons heated in this reversed field are visible in the electron velocity distribution function profile in Figure 9.26 as a broadening of the distribution in front of the electrode after a clearly observable waist. The heating mechanism for these electrons is the same as for the electrons during the sheath growth—the Ohmic heating. The excitation patterns due to heating of the electrons during the sheath reversal were observed earlier in hydrogen discharges [143].

Several spatiotemporally resolved profiles of electron-impact dissociative excitation rate of the atomic oxygen $3p^3P$ level from the simulation were presented earlier. In none of them is evidence for an excitation process close to the electrode (pattern IV) as seen in the experiment. This is not really surprising, because, as one can see in Figures 9.23 through 9.27, energetic electrons can only hardly reach the electrodes. The electrons are able to reach the electrode only within a short time of the sheath collapse to balance the ion current that is permanently flowing to the electrode. For the main part of the rf cycle, there are no electrons near the electrode surface. While the energetic electrons are responsible for the rf-modulated optical emission patterns I and II located about 5 mm away from the electrode (Figure 9.28a), the emission layer closer to the electrode needs another explanation. The excitation due to heavy particle collisions must be taken into account [124]. By introducing the most

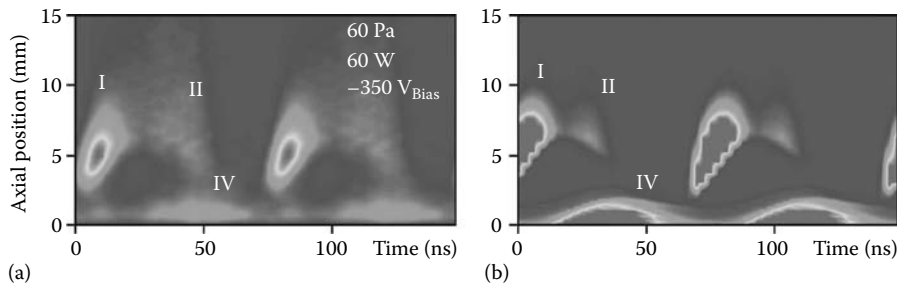


FIGURE 9.28 Phase resolved excitation pattern in an oxygen CCRF discharge of the corresponding transition at 844.6 nm from (a) PROES measurements and (b) PIC-MCC simulation for 60 Pa and $-350 \text{ V}_{\text{Bias}}$. Additional excitation process due to heavy particle impact of molecular oxygen ions with the background gas included in the simulation.

plausible process for this feature, the dissociative excitation of atomic oxygen due to collisions between energetic O_2^+ ions and neutral O_2 , the experimentally observed excitation pattern IV was reproduced close to the electrode (Figure 9.28). Pattern IV and its temporal modulation are the result of energetic ions flowing toward the powered electrode. The ion current to the powered electrode is rf modulated, which is reflected in the sine modulation of excitation pattern IV.

The PIC-MCC simulations reproduced the excitation patterns observed in the experiment quite well and made it possible to identify the underlying physics.

10 Trends and New Concepts

CONTENTS

10.1 Plasma Chemistry and Life Sciences	469
10.2 Plasma Chemistry and Nanotechnology	470
10.3 Plasma Chemistry and Environment	470
10.4 Energy Technology	470
10.5 Simulation and Modeling	470
10.6 Education and Qualification in Plasma Physics and Chemistry	471

The book *Nonthermal Plasma Chemistry and Physics* has given an introduction in basic concepts of nonthermal plasmas from the physical and chemical point of view, as well as a more detailed insight to selected chemical processes in plasma volume and at material surfaces and their specific applications. Furthermore, an overview is included about important methods of plasma and surface diagnostics, and the current state of the art in modeling of nonequilibrium plasmas.

Beside the well-known ozone generation in nonthermal atmospheric pressure plasmas for water cleaning, the nonthermal reactive plasmas have been found applications in many key technologies like the prominent example of the microelectronic technology with impressive developments over the last decades. Here, the progress was mainly achieved by innovative plasma processing in the material etching/erosion for surface patterning and the thin film deposition. In the following, it will be allowed to sketch some new trends and concepts that may be important in future developments. Beside optimization of traditional plasma technologies, new directions in applications of nonthermal reactive plasmas are strongly determined by inclusion of plasma processing in complex technologies with multidisciplinary environment. Such applications may be hybrid technologies using reactive nonthermal plasmas in connection with conventional surface treatment and thin film deposition techniques as well as nanotechnology. Furthermore, a new challenge is the application of cold reactive plasmas in life science.

10.1 PLASMA CHEMISTRY AND LIFE SCIENCES

Optimization of cold atmospheric pressure plasmas and the development of new and miniaturized plasma sources open a wide field of new applications in life sciences. In particular, microplasmas and plasma jets allow modification of surfaces of cells and tissue in their biological environment. In that case, the fundamental study of plasma–liquid interaction and plasmas in liquids is necessary to have detailed insight

in chemical and physical modification of cells or tissue. The development and specification of such plasmas may be interesting in the living tissue treatment with feasible applications in plasma medicine for therapy.

Another field is the surface treatment of implant materials or medical instrumentation by nonthermal reactive plasmas at low or atmospheric pressure. For example, the antimicrobial surface properties or the enhanced adhesion of selected human cells are of great interest in surface modification of implant materials. Furthermore, the plasma sterilization of specific medical instrumentation, for example, endoscopes with small tubes or thermal sensitive materials, is another field of interest.

10.2 PLASMA CHEMISTRY AND NANOTECHNOLOGY

Nonthermal plasma may provide further improvement in synthesis of nano- and microparticles. In particular, the preparation and/or modification of nanotubes, fullerene, graphene, or other nanostructures used as quantum dots or wire (e.g., nanoscaled columns, trenches) are interesting for fundamental studies of their physical properties (nano-electronics). The plasma-assisted thin film deposition may be also a tool for preparation of monolayers with tailored physical and chemical surface properties like specific spectral reflectance/transmittance or specific chemical reactions with surrounding molecules (grafting, self-organization) as examples. Further, nonthermal plasmas may be involved in surface finishing of chemical micro-reactors.

10.3 PLASMA CHEMISTRY AND ENVIRONMENT

The solution of environmental problems will be one of the most vital and challenging tasks in the future. In this context, nonthermal plasma chemistry can offer the improvement of techniques for remediation of air and water pollution by combination with other technologies, for example, by development of effective catalysts due to specific plasma surface treatment. Further, composite films containing nanoparticles in an organic matrix provide interesting physical and chemical properties. These composite films may be used for sensor applications or heterogeneous catalysis.

10.4 ENERGY TECHNOLOGY

Nonthermal plasmas are important for the improvement of the efficiency of solar cells, membranes for fuel cells, and flue gas cleaning of fuel burning power plants. Development of innovative multilayer coatings is of interest to improve the thermal isolation of windows as well as their surface properties for self-cleaning.

10.5 SIMULATION AND MODELING

Simulations and modeling have to be considered for two directions:

1. Modeling and simulation of basic physical and chemical processes in the volume of nonthermal reactive plasmas and the elementary surface processes due to the plasma–surface interaction. Thereby, the multispecies plasma

(electrons, positive/negative ions, excited particles, chemical reactive neutral particles) and the plasma–surface interaction represent a multi-scale problem in space and time. The challenge in modeling is the development of suitable hybrid models (2D, 3D) by combination of kinetic (e.g., Boltzmann equation, PIC-MCC) and fluid description as well as the appropriate inclusion of the surface processes, for example, by collisions models (D-TRIM) or molecular dynamic (MD) simulation.

2. Plasma process modeling by use of Computer Aided Design (CAD) tools for the design of plasma equipment. Here, 2D and 3D computer models for plasma materials processing, and plasma remediation of toxic gases, are key topics. In particular, simulations and visualizations of processes in technical plasma reactors are important for application in industry. Currently, the Hybrid Plasma Equipment Model (HPEM) is now in use by semiconductor equipment suppliers and chip manufacturers.

Nevertheless, the remaining bottleneck is still the availability and verification of atomic and molecular date of the plasma particles (collision cross sections) for the relevant systems, or the reliability of data sets is not guaranteed for all parameter, in particular at low electron temperatures large uncertainties remain. Furthermore, detailed knowledge about the microphysics of the interface between the condensed (wall, material surface) and the plasma phase is missing. The relevant data are mostly determined by macroscopic quantities (e.g., particle flux, sticking coefficient, secondary species emission coefficient). Thereby, intrinsic variations of surface data exist, for example, from micro roughness compared to “ideal surfaces” like single crystals. Moreover, chemical surface modification and adsorbate layers have to be considered.

The complexity of the system and the large number of input data needs systematic study of error propagation for coupled calculations that is often lacking. Coupling more and more codes will just amplify their individual errors and no reliable result will be possible.

10.6 EDUCATION AND QUALIFICATION IN PLASMA PHYSICS AND CHEMISTRY

Future developments in low-temperature plasma science and the application in innovative technologies need educated human resources. In nonthermal plasma physics and chemistry the colleges and universities are in the responsibility to educate and qualify the necessary experts. This book may help to promote this matter of interest.

References

CHAPTER 2

1. P.C. Cosby. Electron-impact dissociation of nitrogen. *J. Chem. Phys.*, 98:9544–9553, 1993.
2. P.C. Cosby. Electron-impact dissociation of oxygen. *J. Chem. Phys.*, 98:9560–9569, 1993.
3. L.G. Christophorou and J.K. Olthoff. Electron interactions with excited atoms and molecules. *Adv. Atom. Mol. Opt. Phys.*, 44:155–293, 2001.
4. R. Dorai and M.J. Kushner. A model for plasma modification of polypropylene using atmospheric pressure discharges. *J. Phys. D Appl. Phys.*, 36(6):666–685, 2003.
5. J.T. Herron and D.S. Green. Chemical kinetics database and predictive schemes for nonthermal humid air plasma chemistry. Part II. Neutral species reactions. *Plasma Chem. Plasma Process.*, 21:459–481, 2001.
6. K.H. Becker, M. Schmidt, A.A. Viggiano, R. Dressler, and S. Williams. Air plasma chemistry. In K.H. Becker, U. Kogelschatz, K.H. Schoenbach, and R.J. Barker, eds., *Non-Equilibrium Air Plasmas at Atmospheric Pressure*, pp. 124–182. IoP, Bristol, U.K., 2005.
7. A.Y. Starikovskii, N.B. Anikin, I.N. Kosarev, E.I. Mintoussov, S.M. Starikovskaja, and V.P. Zhukov. Plasma assisted combustion. *Pure Appl. Chem.*, 78(6):1265–1298, 2006.
8. U. Kogelschatz. Ozone generation. In K.H. Becker, U. Kogelschatz, K.-H. Schoenbach, and R.J. Barker, eds., *Non-Equilibrium Air Plasmas at Atmospheric Pressure*, p. 551. IoP, Bristol, U.K., 2005.
9. R.S. Thomas. Use of chemically reactive gaseous plasmas in preparation of specimens for microscopy. In J.R. Hollahan and A.T. Bell, eds., *Techniques and Applications of Plasma Chemistry*, p. 255. John Wiley & Sons, New York, 1974.
10. P. Adolphi and M. Stör. Glow discharge excited low temperature ashing: A new technique for separating mineral matter of coals. *Fuel*, 64(2):151–155, 1985.
11. J.F. Behnke and M. Schmidt. Surface treatment. In K.H. Becker, U. Kogelschatz, K.H. Schoenbach, and R.J. Barker, eds., *Non-Equilibrium Air Plasmas at Atmospheric Pressure*, pp. 597–621. IoP, Bristol, U.K., 2005.
12. U. Kogelschatz and J. Salge. High-pressure plasmas: Dielectric-barrier and corona discharges—Properties and technical applications. In R. Hippler, S. Pfau, M. Schmidt, and K.H. Schoenbach, eds., *Low Temperature Plasma Physics*, pp. 331–358. Wiley-VCH, Berlin, Germany, 2001.
13. L.G. Christophorou and J.K. Olthoff. *Fundamental Electron Interactions with Plasma Processing Gases*. Kluwer Academic/Plenum Publishers, New York, 2004.
14. W.L. Morgan. A critical evaluation of low-energy electron impact cross sections for plasma processing modeling. II: Cl₄, SiH₄, and CH₄. *Plasma Chem. Plasma Process.*, 12:477–493, 1992.
15. J. Röpcke, L. Mechold, X. Duten, and A. Rousseau. A time resolved laser study of hydrocarbon chemistry in H₂-CH₄ surface wave plasmas. *J. Phys. D: Appl. Phys.*, 34:2336–2345, 2001.
16. J. Ma, J.J. Henney, A. Cheesman, M.N.R. Ashfold, S. Wright, G. Duxbury, and Y.A. Mankelevich. Exploration of the gas phase chemistry in microwave activated diamond depositing plasmas by laser spectroscopy. In *ISPC 2007 Peking CD*. ISPC, Peking University, Beijing, China, 2007.

17. W. Tsang and R.F. Hampson. Chemical kinetic database for combustion chemistry. 1. Methane and related-compounds. *J. Phys. Ref. Data*, 15:1087–1279, 1986.
18. D.L. Baulch, C.J. Cobos, R.A. Cox, C. Esser, P. Frank, T. Just, J.A. Kerr, M.J. Tilling, J. Troe, R.W. Walker, and J. Warnatz. Evaluated kinetic data for combustion modeling. *J. Phys. Chem. Ref. Data*, 15:411–734, 1992.
19. M. Heintze, M. Magureanu, and M. Kettlitz. Mechanism of C₂ hydrocarbon formation from methane in a pulsed microwave plasma. *J. Appl. Phys.*, 92:7022–7031, 2002.
20. Istadi and N.A.S. Amin. Co-generation of synthesis gas and C₂₊ hydrocarbons from methane and carbon dioxide in a hybrid catalytic-plasma reactor: A review. *Fuel*, 85:577–592, 2006.
21. L.M. Zhou, B. Xue, U. Kogelschatz, and B. Eliasson. Partial oxidation of methane to methanol with oxygen or air in a nonequilibrium discharge plasma. *Plasma Chem. Plasma Process.*, 18:375–393, 1998.
22. K.V. Kozlov, P. Michel, and H.-E. Wagner. Synthesis of organic compounds from mixtures of methane with carbon dioxide in dielectric-barrier discharges at atmospheric pressure. *Plasmas Polym.*, 5(3–4):129–150, 2000.
23. C.-J. Liu, B. Xue, B. Eliasson, F. He, Y. Li, and G.-H. Xu. Methane conversion to higher hydrocarbons in the presence of carbon dioxide using dielectric-barrier discharge plasmas. *Plasma Chem. Plasma Process.*, 21:301–310, 2001.
24. J. Benedikt. *J. Phys. D: Appl. Phys.*, 43:043001, 2010.
25. P.K. Bachmann, D. Leers, and D.U. Wiechert. Diamond thin films: Preparation, characterization and selected applications progress report. *Ber. Bunsen. Phys. Chem.*, 95:1390–1400, 1991.
26. D. Das and R.N. Singh. A review of nucleation, growth and low temperature synthesis of diamond thin films. *Int. Mater. Rev.*, 52(1):29–64, 2007.
27. W.Y. Fan, P.F. Knewstubb, M. Kning, L. Mechold, J. Röpcke, and P.B. Davies. A diode laser and modeling study of mixed (CH₄-H₂-O₂) AC plasmas. *J. Phys. Chem.*, 103:4118–4128, 1999.
28. I. Schmidt and C. Benndorf. Low temperature CVD diamond deposition using halogenated precursors—Deposition on low melting materials: Al, Zn and glass. *Diamond Relat. Mater.*, 10:347–351, 2001.
29. J. Lee, R.W. Collins, R. Messier, and Y.E. Strausser. Low temperature plasma process based on CO-rich CO/H₂ mixtures for high rate diamond film deposition. *Appl. Phys. Lett.*, 70:1527–1529, 1997.
30. K. Tsugawa, M. Ishihara, J. Kim, M. Hasegawa, and Y. Koga. Large-area and low-temperature nanodiamond coating by microwave plasma chemical vapor deposition. *New Diam. Front. Carbon Technol.*, 16:337–346, 2006.
31. J. Gonzalez-Aguilar, M. Moreno, and L. Fulcheri. Carbon nanostructures production by gas-phase plasma processes at atmospheric pressure. *J. Phys. D Appl. Phys.*, 40:2361–2374, 2007.
32. M. Meyyappan, L. Delzeit, A. Cassell, and D. Hash. Carbon nanotube growth by PECVD: A review. *Plasma Sources Sci. Technol.*, 12:205–216, 2003.
33. M. Meyyappan. Plasma nanotechnology: Past, present and future. *J. Phys. D: Appl. Phys.*, 44:174002, 2011.
34. R. Vitchev, A. Malesevic, R.H. Petrov, R. Kemps, M. Mertens, and A. Vanhusel and C. Van Haesendonck. Initial stages of few-layer graphene growth by microwave plasma-enhanced chemical vapour deposition. *Nanotechnology*, 21:095602, 2010.
35. K. Ostrikov, U. Cvelbar, and A.B. Murphy. Plasma nanoscience: Setting directions, tackling grand challenges. *J. Phys. D: Appl. Phys.*, 44:174001, 2011.

36. S.L. Miller. Production of some organic compounds under possible primitive earth conditions. *J. Am. Chem. Soc.*, 77:2351–2361, 1955.
37. P.H. Abelson. Chemical events on primitive earth. *Proc. Natl. Acad. Sci. USA*, 55(6):1365–1372, 1966.
38. F. Raulin and G. Toupancre. Formation of prebiochemical compounds in models of the primitive earth’s atmosphere. *Orig. Life Evol. Biosph.*, 6:91–97, 1975.
39. A.R. Bossard, R. Kamga, and F. Raulin. Gas phase synthesis of organophosphorus compounds and the atmosphere of the giant planets. *Icarus*, 67:305–324, 1986.
40. A. Etspüler and H. Suhr. Deposition of thin rhodium films by plasma-enhanced chemical vapor deposition. *Appl. Phys. A*, 48:373–375, 1989.
41. J.P.A.M. Driessens, A.D. Kuypers, and J. Schoonman. Gas-phase chemistry in up-scaled plasma enhanced metal-organic chemical-vapor deposition of TiN and Ti(C, N) on tool steel. *J. Vac. Sci. Technol. A*, 18(4):1971–1976, 2000.
42. H.B. Profijt, S.E. Potts, M.C.M. van de Sanden, and W.M.M. Kessels. Plasma-assisted atomic layer deposition: Basics, opportunities, and challenges. *J. Vac. Sci. Technol. A*, 29(5):050801, 2011.
43. A. Matsuda. Thin-film silicon—Growth process and solar cell application. *Jpn. J. Appl. Phys.*, 43:7909–7920, 2004.
44. Y. Hamakawa, ed. *Thin-Film Solar Cells—Next Generation Photovoltaics and Its Applications*. Springer, Berlin, Germany, 2004.
45. J. Perrin, O. Leroy, and M.C. Bordage. Cross-sections, rate constants and transport coefficients in silane plasma chemistry. *Contrib. Plasma Phys.*, 36:3–49, 1996.
46. Y. Kawai, Y. Taleuchi, H. Mashima, Y. Yamauchi, and H. Takatsuka. VHF plasma production for solar cells. In R. d’Agostino, P. Favia, Y. Kawai, H. Ikegami, N. Sato, and F. Arefi-Khonsari, eds., *Advanced Plasma Technology*, pp. 211–226. Wiley-VCH, Weinheim, 2008.

CHAPTER 3

1. V.M. Lelevkin, D.K. Otorbaev, and D.C. Schram. *Physics of Non-Equilibrium Plasmas*. Elsevier Science Publishers B.V., Amsterdam, the Netherlands, 1992.
2. K. Nishikawa and M. Wakatani. *Plasma Physics*. Springer Verlag, Berlin, Germany, 1990.
3. Y.P. Raizer. *Gas Discharge Physics*. Springer-Verlag, Berlin, Germany, 1991.
4. G.L. Rogoff. Ambipolar diffusion coefficients for discharges in attaching gases. *J. Phys. D Appl. Phys.*, 18:1533–1545, 1985.
5. P.P.J.M. Schram. *Kinetic Theory of Gases and Plasmas*. Kluwer Academic Publishers, Dordrecht, the Netherlands, 1991.
6. C. Ramsauer. Über den Wirkungsquerschnitt der Gasmoleküle gegenüber langsamem Elektronen. *Ann. Phys. (Leipzig)*, 4. Folge, Band 64(6):513–540, 1921.
7. U. Fantz. Basics of plasma spectroscopy. *Plasma Sources Sci. Technol.*, 15:S137–S147, 2006.
8. A. Thorne, U. Litzen, and S. Johansson. *Spectrophysics: Principles and Applications*. Springer, Berlin, Germany, 1999.
9. G. Herzberg. *Molecular Spectra and Molecular Structure I. Spectra of Diatomic Molecules*. Krieger Publishing, Malabar, FL, 1989.
10. A.A. Radzig and B.M. Smirnov. *Reference Data on Atomic, Molecules and Ions*. Springer Series Chemical Phys. 31, Springer-Verlag, Berlin, Germany, 1985.
11. A.R. Striganov and N.S. Sventitskii. *Tables of Spectral Lines of Neutral and Ionized Atoms*. IFI/Plenum, New York, 1968.

12. H. Schmoranzer and R. Zietz. *Phys. Rev. A*, 18:1472–1475, 1978.
13. Mitsuhashi Konuma. *Deposition by Plasma Techniques, Springer Series on Atoms and Plasmas*, Vol. 10. Springer-Verlag, Berlin-Heidelberg, Germany, 1992.
14. W. Heinze. *Einführung in die Vakuumtechnik, Vol. I: Physikalische Grundlagen der Vakuumtechnik*. Verlag Technik, Berlin, Germany, 1955.
15. D.R. Lide, ed. *CRC Handbook of Chemistry and Physics*, 82nd edn. CRC Press, Boca Raton, FL, 2001.
16. L.G. Christophorou and J.K. Olthoff. *Fundamental Electron Interactions with Plasma Processing Gases*. Kluwer Academic/Plenum Publishers, New York, 2004.
17. S.M. Spyrou, I. Sauers, and L.G. Christophorou. Electron attachment to the perfluoroalkanes $n\text{C}_N\text{F}_2N+2$ ($N = 1\text{--}6$ and $i \sim \text{C}_4\text{F}_10$). *J. Chem. Phys.*, 78:7200–7216, 1983.
18. I. Iga, M.V.S. Rao, S.K. Srivastava, and J.C. Nogueira. Formation of negative ions by electron impact on SiF_4 and CF_4 . *Z. Phys. D-Atoms Mol. Clus.*, 24:111–115, 1992.
19. E.W. McDaniel. *Atomic Collisions—Electron and Photon Projectiles*. John Wiley & Sons, New York, 1989.
20. M.B. Schulman, F.A. Sharpton, S. Chung et al. Emission from oxygen atoms produced by electron-impact dissociative excitation of oxygen molecules. *Phys. Rev. A*, 32:2100–2116, 1985.
21. K. Stephan, H. Deutsch, and T.D. Märk. Absolute partial and total electron impact ionization cross sections for CF_4 from threshold up to 180 eV. *J. Chem. Phys.*, 83:5712–5720, 1985.
22. R.R. Laher and F.R. Gilmore. Updated excitation and ionization cross section for electron and impact on atomic oxygen. Technical report, R&D Associates, P.O. Box 9695, Marina Del Rey, CA, 90295, 1988.
23. F.A. Sharpton, R.M. St. John, C.C. Lin, and F.E. Fajen. Experimental and theoretical studies of electron-Impact excitation of Neon. *Phys. Rev. A*, 2:1305–1322, 1970.
24. W. Lotz. Electron binding energies in free atoms. *J. Opt. Soc. Am.*, 60:206–210, 1970.
25. M. Gryzinski. Two-particle collisions. II. Coulomb collisions in the laboratory system of coordinates. *Phys. Rev.*, 138:A322–A335, 1965.
26. H. Bethe. *Ann. Phys.*, 5:325, 1930.
27. M. Probst, H. Deutsch, K. Becker, and T.D. Märk. Technological relevance using the DM formalism, *Int. J. Mass Spectrom.*, 206:13, 2001.
28. Y.-K. Kim, W. Hwang, N.M. Weinberger, M.A. Ali, and M.E. Rudd. Electron-impact ionization cross sections of atmospheric molecules. *J. Chem. Phys.*, 106:1026, 1997.
29. W. Hwang, Y.-K. Kim, and M.E. Rudd. *J. Chem. Phys.*, 104:2956, 1996.
30. L.S. Polak and Y.A. Lebedev, eds. *Plasma Chemistry*. Cambridge International Science Publishing, Cambridge, U.K., 1998.
31. R. Winkler. In R. Hippler, S. Pfau, M. Schmidt, and K.-H. Schoenbach, eds., *Low Temperature Plasma Physics—Fundamental Aspects and Application*. Wiley-VCH, Berlin, Germany, 2001.
32. K.U. Riemann. The Bohm criterion and sheath formation. *J. Phys. D Appl. Phys.*, 24:493–518, 1991.
33. J.E. Allen. The plasma-sheath boundary: Its history and Langmuir's definition of the sheath edge. *Plasma Sources Sci. Technol.*, 18:014004, 2009.
34. R.L.F. Boyd and J.B. Thompson. The operation of Langmuir probes in electronegative plasmas. *Proc. R. Soc. A*, 252:102–119, 1959.
35. N.S.J. Braithwaite and J.E. Allen. Boundaries and probes in electronegative plasmas. *J. Phys. D Appl. Phys.*, 21:1733–1737, 1988.

36. M.A. Lieberman and A.J. Lichtenberg. *Principles of Plasma Discharges and Materials Processing*, 2nd edn. John Wiley & Sons, Inc., Hoboken, NJ, 2005.
37. W.D. Davis and T.A. Vanderslice. Ion energies at the cathode of a glow discharge. *Phys. Rev.*, 131:219–228, 1963.
38. J. Rickards. Energies of particles at the cathode of a glow discharge. *Vacuum*, 34(5):559–562, 1984.
39. M. Zeuner, H. Neumann, and J. Meichsner. Ion energy distributions in a dc biased rf discharge. *J. Appl. Phys.*, 81:2985, 1997.
40. J.R. Roth. *Industrial Plasma Engineering Volume 1, Principles*. Institute of Physics Publishing, Bristol, U.K. and Philadelphia, PA, 1995.
41. M. Kaminsky. *Atomic and Ionic Impact Phenomena on Metal Surfaces*. Springer Verlag, Berlin, Germany, 1965.
42. G.G. Raju. *Dielectrics in Electric Fields*. CRC Press, New York, 2003.
43. H. Schmoranzer and R. Zietz. Observation of selectively excited continuous vacuum ultraviolet emission in molecular hydrogen. *Phys. Rev. A*, 18:1472–1475, 1978.
44. A. Fridman and L.A. Kennedy. *Plasma Physics and Engineering*. Taylor & Francis, New York, 2004.
45. T. Bräuer, S. Gortchakov, D. Loffhagen, S. Pfau, and R. Winkler. The temporal decay of the diffusion-determined afterglow plasma of the positive column. *J. Phys. D Appl. Phys.*, 30:3223, 1997.
46. J.H. Ingold. Nonequilibrium positive column. *Phys. Rev. E*, 56:5932–5944, 1997.
47. Y.B. Golubovskii, V.A. Maiorov, V.O. Nekutchaev, J. Behnke, and J.F. Behnke. Kinetic model of ionization waves in a positive column at intermediate pressures in inert gases. *Phys. Rev. E*, 63:036409, 2001.
48. D. Uhrlandt and R. Winkler. Radially inhomogeneous electron kinetics in the dc column plasma. *J. Phys. D: Appl. Phys.*, 29:115, 1996.
49. L.L. Alves, G. Gousset, and C.M. Ferreira. Self-contained solution to the spatially inhomogeneous electron boltzmann equation in a cylindrical plasma positive column. *Phys. Rev. E*, 55:890–906, 1997.
50. S. Flügge. *Encyclopedia of Physics Vol XXII, Gas Discharges II*. Springer-Verlag, Berlin Germany, 1956.
51. H. Raether. *Electron Avalanches and Breakdown in Gases*. Butterworth Co., Washington, DC, 1964.
52. J.M. Meek, J.I. Craggs, eds. *Electrical Breakdown in Gases*. Wiley, Chichester, U.K., 1978.
53. C. Montijn, B. Meulenbroek, U. Ebert, and W. Hundsorfer. Numerical solutions and conformal analysis of growing and branching negative discharge streamers. *IEEE Trans. Plasma Sci.*, 33:260–261, 2005.
54. B. Gellert and U. Kogelschatz. Generation of excimer emission in dielectric barrier discharges. *Appl. Phys. B*, 52:14–21, 1991.
55. J.P. Boeuf. Plasma display panels: Physics, recent developments and key issues. *J. Phys. D: Appl. Phys.*, 36:R53–R79, 2003.
56. G. Janzen. *Plasmatechnik*. Hüthig Buchverlag, Heidelberg, Germany, 1992.
57. M.J. Cooke and G. Hassall. Low-pressure plasma sources for etching and deposition. *Plasma Sources Sci. Technol.*, 11:A74–A79, 2002.
58. R. Roth. *Industrial Plasma Engineering*, Vol. 1/2. IoP, Bristol, U.K., 1995.
59. J.R. Hollahan and A.T. Bell. *Techniques and Applications of Plasma Chemistry*. Wiley, New York, 1974.
60. R.J. Shul and S.J. Pearton, eds. *Handbook of Advanced Plasma Processing Techniques*. Springer, Berlin, Germany, 2000.

61. R. Hippler, H. Kersten, M. Schmidt, and K.H. Schönbach. *Low Temperature Plasmas—Fundamentals, Technologies and Techniques*, Vol. I/II, 2nd edn. Wiley-VCH, Berlin, Germany, 2008.
62. A. Lunk and M. Schmidt. Plasma processes in activated thin film deposition. *Contrib. Plasma Phys.*, 28(3):275–292, 1988.
63. Y. Ionikh, A.V. Meshchanov, J. Röpcke, and A. Rousseau. A diode laser study and modeling of NO and NO₂ formation in a pulsed DC air discharge. *Chem. Phys.*, 322:411–422, 2006.
64. F. Miethke, A. Rutscher, and H.-E. Wagner. Quasi-equilibria and plasma chemical similarity in non-isothermal reactive plasmas. *Acta Phys. Univ. Comen.*, XLI-N1: 3–32, 2000.
65. K.-H. Schoenbach, T. Tessnow, F.E. Peterkin, and W.W. Byszewski. Microhollow cathode discharges. *Appl. Phys. Lett.*, 68:13–15, 1996.
66. K.-H. Schoenbach, A. El-Habachi, W. Shi, and M. Ciocca. High-pressure hollow cathode discharges. *Plasma Sources Sci. Technol.*, 6:468–477, 1997.
67. K. Ellmer. Magnetron discharges for thin film deposition. In R. Hippler, H. Kersten, M. Schmidt, and K.-H. Schoenbach, eds., *Low Temperature Plasmas Fundamentals, Technologies, and Techniques*, Vol. 2, 2nd edn., p. 675. Wiley-VCH, Weinheim, Germany, 2008.
68. M.M. Salem, J.-F. Loiseau, and B. Held. Impedance matching for optimization of power transfer in a capacitively excited rf plasma reactor. *Eur. Phys. J. Appl. Phys.*, 3:91–95, 1998.
69. A. Grill. *Cold Plasma in Materials Fabrication from Fundamentals to Applications*. IEEE Press, New York, 1994.
70. R. Reif. Plasma enhanced chemical vapor deposition of thin films for microelectronics. In S.M. Rossnagel, J.J. Cuomo, and W.D. Westwood, eds., *Handbook of Plasma Processing Technology*. Noyes Publications, Norwich, NY, 1990.
71. P.C. Boyle, A.L. Ellingboe, and M.M. Turner. Independent control of ion current and ion impact energy onto electrodes in dual frequency plasma devices. *J. Phys. D: Appl. Phys.*, 37:697–701, 2004.
72. Y.P. Raizer, M.N. Shneider, and N.A. Yatsenko. *Radio Frequency Capacitive Discharges*. CRC Press, Boca Raton, FL, 1995.
73. Y. Kawai, Y. Taleuchi, H. Mashima, Y. Yamauchi, and H. Takatsuka. VHF plasma production for solar cells. In R. d'Agostino, P. Favia, Y. Kawai, H. Ikegami, N. Sato, and F. Arefi-Khonsari, eds., *Advanced Plasma Technology*, pp. 211–226. Wiley-VCH, Weinheim, Germany, 2008.
74. J. Hopwood. Review of inductively coupled plasmas for plasma processing. *Plasma Sources Sci. Technol.*, 1:109–116, 1992.
75. O.A. Popov. *High Density Plasma Sources Design, Physics and Performance*. Noyes Publications, Park Ridge, NJ, 1995.
76. P. Messerer, B. Boenigk, G. Keil, P. Scheubert, and P. Awakowicz. Plasma diagnostics in a double inductively coupled source (DICP) for plasma sterilisation. *Surf. Coat. Technol.*, 174–175:570–573, 2003.
77. T. Uchida and S. Hamaguchi. Magnetic neutral loop discharge (NLD) plasmas for surface processing. *J. Phys. D: Appl. Phys.*, 41:083001, 2008.
78. D. O'Connell, T. Gans, D.L. Crinetea, U. Czernetzki, and N. Sadeghi. Plasma dynamics in an inductively coupled magnetic neutral loop discharge. *Plasma Sources Sci. Technol.*, 17:024022, 2008.
79. F. Chen. Helicon plasma sources. In O. Popov, ed., *High Density Plasma Sources Design, Physics and Performance*. Noyes Publications, Park Ridge, NJ, 1995.

80. C.M. Franck, O. Grulke, A. Stark, T. Klinger, E. Scime, and G. Bonhomme. Measurements of spatial structures of different discharge modes in a helicon source. *Plasma Sources Sci. Technol.*, 14:226–235, 2005.
81. F. Werner, D. Korzec, and J. Engemann. Slot antenna 2.45 GHz microwave plasma source. *Plasma Sources Sci. Technol.*, 3:473–481, 1994.
82. M.R. Wertheimer and M. Moisan. Comparison of microwave and lower frequency plasmas for thin film deposition and etching. *J. Vac. Sci. Technol. A Vac. Surf. Films*, 3:2643–2649, 1985.
83. C.M. Ferreira and J. Loureiro. Characteristics of high-frequency and direct-current argon discharges at low-pressure—A comparative-analysis. *J. Phys. D: Appl. Phys.*, 17:1175–1188, 1984.
84. J. Marec and P. Leprince. Microwave discharges: Structures and stability. In C.M. Ferreira and M. Moisan, eds., *Microwave Discharges Fundamentals and Applications*, pp. 45–63. Plenum Press, New York, 1993.
85. R.G. Bosisio, M.R. Wertheimer, and C.F. Weissflock. Generation of large volume microwave plasmas. *J. Phys. E: Sci. Instrum.*, 6:628–630, 1973.
86. M. Moisan and Z. Zakrzewski. Plasma sources based on the propagation of electromagnetic surface waves. *J. Phys. D: Appl. Phys.*, 24:1025–1048, 1991.
87. M. Moisan, J. Margot, and Z. Zakrzewski. Surface wave plasma sources. In O. Popov, ed., *High Density Plasma Sources Design, Physics and Performance*, p. 191. Noyes Publications, Park Ridge, NJ, 1995.
88. M. Kaiser, K.-M. Baumgärtner, A. Schulz, M. Walker, and E. Räuchle. A new linearly extended bifocal microwave plasma device. *Surf. Coat. Technol.*, 142–144:939–942, 1999.
89. A. Ohl. Large area planar microwave plasmas. In C.M. Ferreira and M. Moisan, eds., *Microwave Discharges Fundamentals and Applications*, pp. 205–214. Plenum Press, New York, 1993.
90. A. Ohl. Fundamentals and limitations of large area planar microwave discharges using slotted waveguides. *J. Phys. IV*, 8(P7):83–98, 1998.
91. L. Latrasse, A. Laqcoste, J. Sirou, and J. Pelletier. High density distributed microwave plasma sources in a matrix configuration: Concept, design and performance. *Plasma Sources Sci. Technol.*, 16:7–12, 2007.
92. Z. Kissòvski, T. Tsankov, D. Korzec, S. Kytzia, and J. Engemann. Plasma parameters of an oxygen microwave discharge obtained by probe diagnostics: I. Axial distributions. *Plasma Sources Sci. Technol.*, 15:126–134, 2006.
93. Z. Kissòvski, A. Brockhaus, D. Korzec, S. Kytzia, and J. Engemann. Plasma parameters of an oxygen microwave discharge obtained by probe diagnostics: II. Radial distributions. *Plasma Sources Sci. Technol.*, 16:523–528, 2007.
94. A. Pfuch and R. Cihar. Deposition of SiO_x thin films by microwave induced plasma CVD at atmospheric pressure. *Surf. Coat. Technol.*, 183:134–140, 2004.
95. J. Ehlbeck, A. Ohl, M. Maaß, U. Krohmann, and T. Neumann. Moving atmospheric microwave plasma for surface and volume treatment. *Surf. Coat. Technol.*, 174–175:493–497, 2003.
96. S.M. Rossnagel, J.J. Cuomo, and W.D. Westwood, eds. *Handbook of Plasma Processing Technology*. Noyes Publications, Norwich, NY, 1990.
97. R. Wilhelm. Microwave plasmas for surface treatment and thin-film production. In G. Bonizzoni, W. Hooke, and E. Sindoni, eds., *Proceedings of Industrial Applications of Plasma Physics*, p. 185. Editrice Compositori, Monastero Varenna, Italy, 1993.

98. J. Pelletier. Distributed ECR plasma sources. In O. Popov, ed., *High Density Plasma Sources Design, Physics and Performance*, p. 380. Noyes Publications, Park Ridge, NJ, 1995.
99. J. Pelletier, A. Lacoste, Y. Arnal, T. Lagarde, T. Lincot, and D. Hertz. New trends in DECR plasma technology: Applications to novel duplex treatments and process combinations with extreme plasma specifications. *Surf. Coat. Technol.*, 139:222–232, 2001.
100. P. Supiot, C. Vivien, A. Granier, A. Bousquet, A. Mackova, D. Escaich, R. Clegereaux, P. Raynaud, Z. Styhal, and J. Pavlik. Growth and modification of organosilicon films in PECVD and remote afterglow reactors. *Plasma Process. Polym.*, 3:100–109, 2006.
101. R. Foest, E. Kindel, A. Ohl, M. Stieber, and K.-D. Weltmann. Non-thermal atmospheric pressure discharges for surface modification. *Plasma Phys. Contr. Fusion*, 47:B525–B536, 2005.
102. J.R. Roth, S. Nourgostar, and T.A. Bonds. The one atmosphere uniform glow discharge plasma (O AUGDP)—A platform technology for the 21st century. *IEEE Trans. Plasma Sci.*, 35:233–250, 2007.
103. A. Garscadden. Atmospheric pressure glow discharges. In R. Hippler, H. Kersten, M. Schmidt, and K.-H. Schoenbach, eds., *Low Temperature Plasmas*, Vol. 2, 2nd edn., p. 411. Wiley-VCH, Weinheim, Germany, 2008.
104. U. Kogelschatz, Y.S. Akishev, and A.P. Napartovich. History of non-equilibrium air discharges. In K.H. Becker, U. Kogelschatz, K.-H. Schoenbach, and R.J. Barker, eds., *Non-Equilibrium Air Plasmas at Atmospheric Pressure*, pp. 17–75. IoP, Bristol, U.K., 2005.
105. U. Kogelschatz and J. Salge. High pressure plasmas: Dielectric barrier and corona discharges. In R. Hippler, H. Kersten, M. Schmidt, and K.-H. Schoenbach, eds., *Low Temperature Plasmas*, Vol. 2, 2nd edn., p. 439. Wiley-VCH, Weinheim, Germany, 2008.
106. K. Becker and K.-H. Schoenbach. High-pressure microdischarges. In R. Hippler, H. Kersten, M. Schmidt, and K.-H. Schoenbach, eds., *Low Temperature Plasmas*, Vol. 2, 2nd edn., p. 463. Wiley-VCH, Weinheim, Germany, 2008.
107. R.M. Sankaran and K. Giapis. Materials applications of high-pressure microplasmas. In R. Hippler, H. Kersten, M. Schmidt, and K.-H. Schoenbach, eds., *Low Temperature Plasmas*, Vol. 2, 2nd edn., p. 495. Wiley-VCH, Weinheim, Germany, 2008.
108. E. Kunhardt. Generation of large-volume, atmospheric-pressure, nonequilibrium plasmas. *IEEE Trans. Plasma Sci.*, 28(1):189–200, 2000.
109. H.-E. Wagner, R. Brandenburg, K.V. Kozlov, A. Sonnenfeld, P. Michel, and J.F. Behnke. The barrier discharge: Basic properties and applications to surface treatment. *Vacuum*, 71:417–436, 2003.
110. S. Okazaki, M. Kogoma, M. Uehara, and Y. Kimura. Appearance of stable glow discharge in air, argon, oxygen and nitrogen at atmospheric pressure using a 50 Hz source. *J. Phys. D: Appl. Phys.*, 26:889–892, 1993.
111. U. Kogelschatz, Y.S. Akishev, K.H. Becker, E.E. Kunhardt, M. Kogoma, S. Kuo, M. Laroussi, A.P. Napartovich, S. Okazaki, and K.-H. Schoenbach. DC and low frequency air plasma sources. In K.H. Becker, U. Kogelschatz, K.-H. Schoenbach, and R.J. Barker, eds., *Non-Equilibrium Air Plasmas at Atmospheric Pressure*, pp. 276–361. IoP, Bristol, U.K., 2005.
112. J. Eden, S.-J. Park, and K.-S. Kim. Arrays of nonequilibrium plasmas confined to microcavities: An emerging frontier in plasma science and its applications. *Plasma Sources Sci. Technol.*, 15:S67–S73, 2006.

113. R. Foest, M. Schmidt, and K. Becker. Microplasmas, an emerging field of low-temperature plasma science and technology. *Int. J. Mass Spectrom.*, 248(3):87–102, 2006.
114. K. Becker, K.-H. Schoenbach, and J. Eden. Microplasmas and applications. *J. Phys. D: Appl. Phys.*, 39:R55–R70, 2006.
115. U. Kogelschatz. Applications of microplasmas and microreactor technology. *Contrib. Plasma Phys.*, 47:80–88, 2007.
116. D. Staack, B. Farouk, A. Gutsol, and A. Fridman. Characterization of a dc atmospheric pressure normal glow discharge. *Plasma Sources Sci. Technol.*, 14:700–711, 2005.
117. J.W. Frame and J.G. Eden. Planar microdischarge arrays. *Electron. Lett.*, 34:1529–1531, 1998.
118. National Research Council, ed. *Plasma Science, Advancing Knowledge in the National Interest*. The National Academic Press, Washington, DC, ISBN 978-0-309-10943-7, 2010.
119. R. Foest, E. Kindel, H. Lange, A. Ohl, M. Stieber, and K.-D. Weltmann. RF capillary jet—A tool for localized surface treatment. *Contrib. Plasma Phys.*, 47(1–2):119–128, 2007.
120. M. Laroussi and T. Akan. Arc-free atmospheric pressure cold plasma jets: A review. *Plasma Process. Polym.*, 4:777–788, 2007.
121. E. Stoffels. Tissue processing with atmospheric plasmas. *Contrib. Plasma Phys.*, 47(1–2):40–48, 2007.
122. J. Schäfer, R. Foest, A. Quade, A. Ohl, and K.-D. Weltmann. Local deposition of SiO_x plasma polymer films by a miniaturized atmospheric pressure plasma jet (APPJ). *J. Phys. D: Appl. Phys.*, 41(19):194010, 2008.
123. M. Teschke and J. Engeman. Low voltage APP-generation by piezo ceramics: A new (r)evolutionary enabling technology. In *Proceedings of the 18th International Symposium on Plasma Chemistry*, 26.–31.8.2007, Kyoto, Japan, 2007. On CD contribution: 27A-a4.
124. M. Moselhy, I. Petzenhauser, K. Frank, and K.H. Schoenbach. Excimer emission from microhollow cathode argon discharges. *J. Phys. D: Appl. Phys.*, 36:2922, 2003.
125. R. Foest, T. Bindemann, R. Brandenburg, E. Kindel, H. Lange, M. Stieber, and K.-D. Weltmann. On the vacuum ultraviolet radiation of a miniaturized non-thermal atmospheric pressure plasma jet. *Plasma Process. Polym.*, 4:S460–S464, 2007.
126. K.H. Schoenbach, A. El-Habachi, M.M. Moselhy, W. Shi, and R.H. Stark. Microhollow cathode discharge excimer lamps. *Phy. Plasmas*, 7:2186, 2000.
127. M. Moselhy and K.H. Schoenbach. Excimer emission from microhollow cathode argon discharges. *J. Appl. Phys.*, 95:1672, 2004.
128. L.E. Amorer. *Unpubl.* PhD thesis, Stevens Institute of Technology, Hoboken, NJ, 1999.
129. K. Becker, A. Koutsospyros, S.-M. Yin, C. Christodoulatos, N. Abramzon, J.C. Joaquin, and G. Brelles-Marino. Environmental and biological applications of microplasmas. *Plasma Phys. Control. Fusion*, 47:B513–B523, 2005.
130. J.G. Eden and S.J. Park. Microcavity plasma devices and arrays: A new realm of plasma physics and photonic applications. *Plasma Phys. Control. Fusion*, 47:B83–B92, 2005.
131. I.E. Kieft, B.N. van Berkel, E.R. Kieft, and E. Stoffels. *Radicals of Plasma Needle Detected with Fluorescent Probe*. In R. d'Agostino, P. Favia, C. Oehr, and M.R. Wertheimer, eds., *Plasma Processes and Polymers*, p.295. Wiley-VCH, Weinheim, Germany, 2005.

132. E. Stoffels, A.J. Flikweert, W.W. Stoffels, and G.M.W. Kroesen. Plasma needle: A non-destructive atmospheric plasma source for fine surface treatment of (bio)materials. *Plasma Sources Sci. Technol.*, 11:383–388, 2002.
133. E. Stoffels. Atmospheric plasma: A universal tool for physicians? In R. Hippler, H. Kersten, M. Schmidt, and K. Schoenbach, eds., *Low Temperature Plasmas*, Vol. 2, 2nd edn., p. 837. Wiley, Weinheim, Germany, 2008.
134. M. Schmidt, T. Föste, P. Michel, and V. Sapkin. Device for producing and investigating an electron beam plasma discharge. *Beitr. Plasma Phys.*, 22:43–441, 1982.
135. D. Leonhardt, S.G. Walton, and R.F. Fernsler. Fundamentals and applications of a plasma-processing system based on electron-beam ionization. *Phys. Plasmas*, 14:057103, 2007.
136. S.G. Walton, E.H. Lock, and R.F. Fernsler. Plasma modification of solid and porous polyethylene. *Plasma Process. Polym.*, 5:453–459, 2008.
137. K. Ostrikov and S. Xu. *Plasma-Aided Nanofabrication, from Plasma Sources to Nanoassembly*. Wiley-VCH, Weinheim, Germany, 2007.
138. K. Dittmann, K. Matyash, S. Nemschokmichal, J. Meichsner, and R. Schneider. Excitation mechanisms and sheath dynamics in capacitively coupled radio-frequency oxygen Plasmas. *Contrib. Plasma Phys.*, 50(10):942–953, 2010, doi: 10.1002/ctpp.201000038.
139. J. Schulze, A. Derzsi, K. Dittmann, T. Hemke, J. Meichsner, and Z. Donko. Ionization by drift and ambipolar electric fields in electronegative capacitive radio frequency Plasmas. *Phys. Rev. Lett.*, 107:275001, 2011, doi: 10.1103/PhysRevLett.107.275001.

CHAPTER 4

1. A. Rutscher and H.-E. Wagner. The model of macroscopic kinetics in non-equilibrium plasma chemical reactions I. General considerations and basic relations. *Contrib. Plasma Phys.*, 25:337–350, 1985.
2. A. Rutscher and H.-E. Wagner. Chemical quasi-equilibria: A new concept in the description of reactive plasmas. *Plasma Sources Sci. Technol.*, 2:279–288, 1993.
3. H.-E. Wagner. Reactive nonthermal plasmas—Chemical quasiequilibria, similarity principles, and macroscopic kinetics. In R. Hippler, H. Kersten, M. Schmidt, and K.-H. Schoenbach, eds., *Low Temperature Plasmas—Fundamentals, Technologies and Techniques*, Vol. 1, 2nd edn., pp. 385–409. Wiley-VCH, Weinheim, Germany, 2008.
4. F. Miethke, H.-E. Wagner, A. Rutscher, and S. Gundermann. Simultaneous thermal and plasma chemical activation of conversions in H_2 - I_2 -HI mixtures. *J. Phys. Chem. A*, 103:2024–2030, 1999.
5. H. Jacobs, F. Miethke, A. Rutscher, and H.-E. Wagner. Reaction kinetics and chemical quasi-equilibria of the ozone synthesis in oxygen DC discharges. *Contrib. Plasma Phys.*, 36:471–486, 1996.
6. A. Sonnenfeld, H. Strobel, and H.-E. Wagner. Kinetics, macrokinetics and dissipativity scalar of the decomposition of CO₂ in non-isothermal plasmas. *J. Non-Equilib. Thermodyn.*, 23:105–134, 1998.
7. E. Warburg. Über chemische Reaktionen, welche durch die stille Entladung in gasförmigen Körpern herbeigeführt werden. In *Jahrbuch der Radioaktivität und Elektronik*, Vol. 6, pp. 181–229. Hirzel, Leipzig, Germany, 1909.
8. H. Becker. *Wissenschaftliche Veröffentlichungen Chem.*, Vol. 7. Siemens-Konzern, 1920.

9. E.N. Eremin. *Elementy Gazovoi Elektrochimii (The Elements of Gas Electrochemistry)*. Izd. Moskov. Gos. Univ., Moscow, Russia, 1968.
10. A. Marotta. An improved low gas flow rate plasma torch. In *XI International Symposium on Plasma Chemistry (ISPC-11)*, Vol. 1. Philadelphia, PA, 1993.
11. H. Yasuda. *Plasma Polymerization*. Academic Press, Orlando, FL, 1985.
12. D. Hegemann and U. Schütz. Activation energy of an asymmetrical, radio frequency discharge with methane. *Thin Solid Films*, 491:96–103, 2005.
13. N. Hershkowitz, R. Breun, J. Ding, K. Kimse, C. Lai, J. Meyer, T. Quick et al. In J.A. Heberlein, ed., *Proceedings 12th International Symposium on Plasma Chemistry ISPC-12, 21.–25. August 1995*, Vol. 1, pp. 533–538. University of Minnesota, Minneapolis, MN, 1995.
14. S. Pfau, A. Rutscher, and K. Wojaczek. Das Ähnlichkeitsgesetz für quasineutrale, anisotherme Entladungssäulen. *Beitr. Plasmaphys.*, 9:333–358, 1969.
15. Y.P. Raizer. *Gas Discharge Physics*. Springer Verlag, Berlin, Germany, 1991.
16. S. Kattanek, R. Gröger, and C. Bode. *Ähnlichkeitstheorie*. Deutscher Verlag für Grundstoffindustrie, Leipzig, Germany, 1967.
17. F. Miethke, A. Rutscher, and H.-E. Wagner. Quasi-equilibria and plasma chemical similarity in non-isothermal reactive plasmas. *Acta Phys. Univ. Comen.*, XLI-N1: 3–32, 2000.
18. T. Ruzika, A. Rutscher, and S. Pfau. Thermodiffusion and energy-transport coefficients of electrons. *Ann. Phys.*, 24:124, 1970.
19. J. Lacina. Similarity rules in plasma physics. *Plasma Phys.*, 13:303–312, 1971.
20. K. Lackner. Figures of merit for divertor similarity. *Comments Plasma Phys. Contr. F.*, 15:359–365, 1994.
21. P.J. Catto, D.A. Knoll, S.I. Krasheninnikov, and J.W. Connor. Divertor scaling laws for tokamaks. *J. Nucl. Mater.*, 241–243:369–373, 1997.

CHAPTER 5

1. G.A. Somorjai. *Introduction to Surface Chemistry and Catalysis*. John Wiley & Sons, New York, 1994.
2. H. Doshita, K. Ohtani, and A. Namiki. *J. Vac. Sci. Technol.*, A16:265, 1998.
3. A. Zangwill. *Physics at Surfaces*. Cambridge University Press, Cambridge, U.K., 1986.
4. A. Cho. *J. Vac. Sci. Technol.*, 16:275, 1979.
5. J. Kisliuk. *J. Phys. Chem. Solids*, 3:95, 1957.
6. K. Sinniah, M. Sherman, L. Lewis, W. Weinberg, J. Yates, and K. Janda. *Phys. Rev. Lett.*, 62:567, 1989.
7. D. Koleske, S. Gates, and J. Schultz. *J. Chem. Phys.*, 99:5619, 1993.
8. D. Koleske, S. Gates, and B. Jackson. *J. Chem. Phys.*, 101:3301, 1994.
9. W. Widdra, S. Yi, R. Maboudian, G. Briggs, and W. Weinberg. *Phys. Rev. Lett.*, 74:2074, 1995.
10. M.P. Bonzel and R. Ku. *Surf. Sci.*, 33:91, 1972.
11. D.D. Eley. *Chem. Ind.*, 1:12, 1976.
12. J. Küppers. The hydrogen surface chemistry of carbon as a plasma facing material. *Surf. Sci. Rep.*, 22:249–321, 1995.
13. H.F. Winters and J.W. Coburn. *Surf. Sci. Rep.*, 14:161, 1992.
14. A. von Keudell, C. Hopf, T. Schwarz-Selinger, and W. Jacob. *Nuclear Fusion*, 39:1451, 1999.

15. C. Hopf, T. Schwarz-Selinger, W. Jacob, and A. von Keudell. *J. Appl. Phys.*, 87:2719, 2000.
16. J. Perrin, Y. Takeda, N. Hirano, Y. Takeuchi, and A. Matsuda. *Surf. Sci.*, 210:114, 1989.
17. A. Matsuda, K. Nomoto, Y. Takeuchi, A. Suzuki, Y. Yuuki, and J. Perrin. *Surf. Sci.*, 227:50, 1990.
18. D.A. Doughty, J.R. Doyle, G.H. Lin, and A. Gallagher. *J. Appl. Phys.*, 67:6220, 1990.
19. A. Nuruddin, J.R. Doyle, and J.R. Abelson. *J. Appl. Phys.*, 76:3123, 1994.
20. M. Shiratani, J. Jolly, H. Videlot, and J. Perrin. *Jpn. J. Appl. Phys.*, 36:4752, 1997.
21. P. Pecher and W. Jacob. *Appl. Phys. Lett.*, 73:31, 1998.
22. P. Pecher. PhD thesis, Universität Bayreuth, Bayreuth, Germany, 1997.
23. R. Street. *Hydrogenated Amorphous Silicon*, 1st edn. Cambridge University Press, Cambridge, U.K., 1992.
24. K. Tanaka and A. Matsuda. *Mater. Sci. Rep.*, 2:139, 1987.
25. J.R. Doyle, D.A. Doughty, and A. Gallagher. *J. Appl. Phys.*, 71:4771, 1992.
26. R. Robertson and A. Gallagher. *J. Appl. Phys.*, 59:3402, 1986.
27. J. Perrin. *J. Non-Cryst. Solids*, 137–138:639, 1991.
28. A. Gallagher. *Mat. Res. Soc. Proc.*, 70:3, 1986.
29. K. Maeda, A. Kuroe, and I. Umezawa. *Phys. Rev. B*, 51:10635, 1995.
30. Y. Toyoshima, K. Arai, A. Matsuda, and K. Tanaka. *Appl. Phys. Lett.*, 57:1028, 1990.
31. Y. Toyoshima, K. Arai, A. Matsuda, and K. Tanaka. *Appl. Phys. Lett.*, 56:1540, 1990.
32. S. Yamasaki, T. Umeda, J. Isoya, and K. Tanaka. *Appl. Phys. Lett.*, 70:1137, 1997.
33. T. Ohira, T. Adachi, Y. Takeuchi, and M. Murata. *Phys. Rev. B*, 52:8283, 1995.
34. A. von Keudell and J.R. Abelson. *Phys. Rev. B*, 59:5791, 1999.
35. E. Aydin, S. Agarwal, M. Valipa, B. Hoex, M. van de Sanden, and D. Maroudas. *Surf. Sci.*, 598:35, 2005.
36. W. Kessels, Private communication. 2006.
37. J. Abelson. *Appl. Phys. A*, 56:493, 1993.
38. J. Thornton. *J. Vac. Sci. Technol.*, 4:3059, 1986. References 127.
39. J. Thornton and A. Penfold. In J. Vossen and W. Kern, eds., *Thin Film Processes*. Academic Press, New York, 1978.
40. Y. Lifshitz, S.R. Kasi, J.W. Rabalais, and W. Eckstein. *Phys. Rev. B*, 41:10468, 1990.
41. J. Robertson. *Diam. Relat. Mater.*, 2:984, 1993.
42. A. von Keudell, W. Möller, and R. Hytry. *Appl. Phys. Lett.*, 62:937, 1993.
43. A. von Keudell and W. Möller. *J. Appl. Phys.*, 75:7718, 1994.
44. W. Möller, W. Fukarek, K. Lange, A. von Keudell, and W. Jacob. *Jpn. J. Appl. Phys.*, 34:2163, 1995.
45. W. Eckstein and J.P. Biersack. *Z. Phys.*, B63:471, 1986.
46. H. Deutsch, H. Kersten, and A. Rutscher. *Contrib. Plasma Phys.*, 29:263, 1989.
47. R.A. Haefer. *Oberflächen- und Dünnschichttechnologie*. Springer, Berlin, Germany, 1991.
48. M. Balooch, D.R. Olander, and W.J. Siekhaus. *J. Vac. Sci. Technol. B*, 4:794, 1986.
49. H. Kersten, H. Deutsch, H. Steffen, G.M.W. Kroesen, and R. Hippler. *Vacuum*, 63:385, 2001.
50. A. Durandet, O. Joubert, J. Pelletier, and M. Pichot. *J. Appl. Phys.*, 67:3862, 1990.
51. H. Kersten, H. Deutsch, and J.F. Behnke. *Vacuum*, 48:123, 1997.
52. H. Schmoranz and R. Zietz. Observation of selectively excited continuous vacuum ultraviolet emission in molecular hydrogen. *Phys. Rev. A*, 18:1472–1475, 1978.

CHAPTER 6

1. H.M. Mott-Smith and I. Langmuir. The theory of collectors in gaseous discharges. *Phys. Rev.*, 28:727–763, 1926.
2. F.F. Chen. Electric probes. In R.H. Hudlestome and S.L. Leonard, eds., *Plasma Diagnostic Techniques*. Academic Press, New York, 1965.
3. L. Schott. Electric probes. In W. Lochte-Holtgreven, ed., *Plasma Diagnostics*. North-Holland Publishing Company, Amsterdam, the Netherlands, 1968. Reprinted 1995 by the American Institute of Physics.
4. J.D. Swift and M.J.R. Schwar. *Electrical Probes for Plasma Diagnostics*. Iliffe, London, U.K., 1970.
5. P.M. Chung, L. Talbot, and K.J. Touryan. *Electric Probes in Stationary and Flowing Plasmas*. Springer-Verlag, New York, 1975.
6. B.E. Cherrington. The use of electrostatic probes for plasma diagnostics—A review. *Plasma Chem. Plasma Process.*, 2:113–140, 1982.
7. I.H. Hutchinson. *Principles of Plasma Diagnostics*. Cambridge University Press, Cambridge, U.K., 1987.
8. N. Hershkowitz. How Langmuir probes work. In O. Auciello and D.F. Flamm, eds., *Plasma Diagnostics*, Vol. 1, Academic Press, Boston, MA, 1989.
9. V.A. Godyak, R.B. Piejak, and B.M. Alexandrovich. Measurement of electron energy distribution in low-pressure rf discharges. *Plasma Sources Sci. Technol.*, 1:36–58, 1992.
10. V.I. Demidov, S.V. Ratynskaia, and K. Rypdal. Electric probes for plasmas: The link between theory and instrument. *Rev. Sci. Instrum.*, 73:3409–3439, 2002.
11. S. Pfau and M. Tichý. Langmuir probe diagnostics of low-temperature plasmas. In R. Hippler, S. Pfau, M. Schmidt, and K.H. Schoenbach, eds., *Low Temperature Plasma Physics: Fundamentals, Technologies and Techniques*, Vol. 1, 2nd edn. pp. 131–172. Wiley-VCH, Berlin, Germany, 2008.
12. V.A. Godyak and V.I. Demidov. Probe measurements of electron-energy distributions in plasmas: What can we measure and how can we achieve reliable results? *J. Phys. D Appl. Phys.*, 44:233001, 2011.
13. D. Maundrill, J. Slatter, A.I. Spiers, and C.C. Welch. Electrical measurements of rf-generated plasmas using a driven electrostatic probe technique. *J. Phys. D Appl. Phys.*, 20:815–819, 1987.
14. S. Klagge and M. Tichý. A contribution to the assessment of the influence of collisions on the measurements with Langmuir probes in the thick sheath working regime. *Czech. J. Phys.*, B35:988–1006, 1985.
15. M.S. Benilov and B.V. Rogov. Ion saturation currents to spherical and cylindrical electrostatic probes in collisional plasmas. *J. Appl. Phys.*, 70:6726–6731, 1991.
16. M.S. Benilov. Can the temperature of electrons in a high-pressure plasma be determined by means of an electrostatic probe? *J. Phys. D Appl. Phys.*, 33:1683–1698, 2000.
17. A.K. Srivastava, M.K. Garg, K.S.G. Prasad, V. Kumar, M.B. Chowdhuri, and R. Prakash. Characterization of atmospheric pressure glow discharge in helium using Langmuir probe, emission spectroscopy, and discharge resistivity. *IEEE Trans. Plasma Sci.*, 35:1135–1142, 2007.
18. Y.P. Raizer. *Gas Discharge Physics*. Springer-Verlag, Berlin, Germany, 1991.
19. S.C. Luijendijk and J. van Eck. Comparison of 3 devices for measuring second derivative of a Langmuir probe curve. *Physica*, 36:49, 1967.

20. D. Herrmann, S. Pfau, and H. Kagel. Untersuchungen zur Frage des Plasmapotentials in der positiven Säule von Niederdruckentladungen. *Beitr. Plasma Phys.*, 12:1–8, 1972.
21. D. Herrmann and S. Klagge. Untersuchungen zur Lage des Raumpotentials in der 2. Ableitung der Sondencharakteristik mit Hilfe von Glühsonden. *Beitr. Plasma Phys.*, 12:17–25, 1972.
22. J.E. Allen, R.L.F. Boyd, and P. Reynolds. The collection of positive ions by a probe immersed in a plasma. *Proc. Phys. Soc. B*, 70:297–304, 1957.
23. F.F. Chen. Numerical computations for ion probe characteristics in a collisionless plasma. *J. Nucl. Energy C*, 7:47, 1965.
24. W.L. Granowski. *Der elektrische Strom im Gas*. Akademie-Verlag, Berlin, Germany, 1955.
25. C. Steinbrüchel. A new method for analyzing Langmuir probe data and the determination of ion densities and etch yields in an etching plasma. *J. Vac. Sci. Technol. A*, 8:1663–1667, 1990.
26. M. Hannemann, P. Hardt, D. Loffhagen, M. Schmidt, and R. Winkler. The electron kinetics in the cathode region of $H_2/Ar/N_2$ discharges. *Plasma Sources Sci. Technol.*, 9:387–399, 2000.
27. M.J. Druyvesteyn. Der Niedervoltbogen. *Z. Phys.*, 64:781–798, 1930.
28. V.L. Fedorov. Definition of the electron propagation function according to their velocity in the axial-symmetric plasma. *Zh. Tekh. Fiz.*, 55:926–929, 1985. *Sov. Phys. Tech. Phys.* 30:554 (1985).
29. A.P. Mesentsev, A.S. Mustafaev, V.F. Lapshin, and V.L. Fedorov. Probe measurements of the electron collision integrals in plasmas. *J. Phys. B At. Mol. Phys.*, 20:L723–L729, 1987.
30. V.L. Fedorov and A.P. Mesentsev. Determination of the electron rate-distribution function in the axial-symmetrical plasma. *Zh. Tekh. Fiz.*, 57:595–597, 1987. *Sov. Phys. Tech. Phys.* 32:336 (1987).
31. S. Klagge and A. Lunk. Probe diagnostics of anisotropic plasma in a hollow cathode arc. *J. Appl. Phys.*, 70:99–105, 1991.
32. S. Klagge. Space- and direction-resolved Langmuir probe diagnostic in rf planar discharges. *Plasma Chem. Plasma Process.*, 12:103–128, 1992.
33. R.C. Woods and I.D. Sudit. Theory of electron retardation by Langmuir probes in anisotropic plasmas. *Phys. Rev. E*, 50:2222–2238, 1994.
34. G.R. Branner, E.M. Friar, and G. Medicus. Automatic plotting device for second derivative of Langmuir probe curves. *Rev. Sci. Instrum.*, 34:231, 1963.
35. K.F. Schoenberg. Electron-distribution function measurement by harmonically driven electrostatic probes. *Rev. Sci. Instrum.*, 51:1159–1162, 1980.
36. M. Hannemann. INP-Report VII. Institut für Niedertemperatur-Plasmaphysik Greifswald, Greifswald, Germany, 1995.
37. M. Hannemann. Determination of the electron energy distribution function from Langmuir probe characteristics using non-recursive digital filters. *Contrib. Plasma Phys.*, 52, 2012. Accepted for publication.
38. K. Wieseman. Influence of electron reemission on characteristic line of Langmuir probe. *Ann. Phys.*, 27:303, 1971.
39. M. Hannemann. Uniform description of errors in measurement and evaluation of Langmuir probe characteristics by means of apparatus functions. *Contrib. Plasma Phys.*, 48:446–452, 2008.
40. N.S.J. Braithwaite, N.M.P. Benjamin, and J.E. Allen. An electrostatic probe technique for rf plasma. *J. Phys. E Sci. Instrum.*, 20:1046–1049, 1987.

41. B.M. Annaratone and N.S.J. Braithwaite. A comparison of a passive (filtered) and an active (driven) probe for rf plasma diagnostics. *Meas. Sci. Technol.*, 2:795–800, 1991.
42. A. Dyson, P. Bryant, and J.E. Allen. Multiple harmonic compensation of Langmuir probes in rf discharges. *Meas. Sci. Technol.*, 11:554–559, 2000.
43. S. Voronin, M. Alexander, and J.W. Bradley. Time-resolved rf-driven probe measurements of the plasma parameters in a pulsed rf argon discharge. *Meas. Sci. Technol.*, 15:2375–2380, 2004.
44. P.A. Chatterton, J.A. Rees, W.L. Wu, and K. Al-Assadi. A self-compensating Langmuir probe for use in rf (13.56 MHz) plasma systems. *Vacuum*, 42:489–493, 1991.
45. M. Hopkins and P. Heynen. United States Patent US 7015703 B2, March 21, 2006.
46. U. Flender, B.H. Nguyen Thi, K. Wiesemann, N.A. Khromov, and N.B. Kolokolov. RF harmonic suppression in Langmuir probe measurements in rf discharges. *Plasma Sources Sci. Technol.*, 5:61–69, 1996.
47. P. Špatenka and V. Brunnhofer. A new simple method for suppression of influence of rf plasma oscillations during Langmuir probe measurements. *Meas. Sci. Technol.*, 7:1065–1067, 1996.
48. M. Hannemann and F. Sigeneger. Langmuir probe measurements at incomplete rf-compensation. *Czech. J. Phys.*, 56(Suppl. 2):B740–B748, 2006.
49. H. Sabadil, S. Klagge, and M. Kammeyer. Langmuir probe measurements of axial variation of plasma parameters in 27.1 MHz rf oxygen planar discharges. *Plasma Chem. Plasma Process.*, 8:425–444, 1988.
50. E. Passoth, P. Kudrna, C. Csambal, J.F. Behnke, M. Tichý, and V. Helbig. An experimental study of plasma density determination by a cylindrical Langmuir probe at different pressures and magnetic fields in a cylindrical magnetron discharge in heavy rare gases. *J. Phys. D Appl. Phys.*, 30:1763–1777, 1997.
51. H. Aikawa. The measurement of the anisotropy of electron distribution function of a magnetized plasma. *J. Phys. Soc. Jpn.*, 40:1741–1749, 1976.
52. E. Passoth, J.F. Behnke, C. Csambal, M. Tichý, P. Kudrna, Y.B. Golubovskii, and I.A. Porokhova. Radial behaviour of the electron energy distribution function in the cylindrical magnetron discharge in argon. *J. Phys. D Appl. Phys.*, 32:2655–2665, 1999.
53. R.J. D'Arcy. Dielectric impurities and surface instability in Langmuir probe plasma measurements. *J. Phys. D Appl. Phys.*, 7:1391–1401, 1974.
54. P. Špatenka and H. Suhr. Langmuir probe measurements during plasma-activated chemical vapor deposition in the system argon/oxygen/Aluminum isopropoxide. *Plasma Chem. Plasma Process.*, 13:555–566, 1993.
55. S. Klagge. Zur Anwendung der Sondendiagnostik in einem polymerisierenden plasma. *Beitr. Plasmaphys.*, 15:309–317, 1975.
56. E.R. Mosburg, R.C. Kerns, and J.R. Abelson. Use of electric probes in silane radio frequency discharges. *J. Appl. Phys.*, 54:4916–4927, 1983.
57. J. Andreu, G. Sardin, A. Lloret, J. Esteve, and J.L. Morenza. Distribution of electron energy in an electrostatically confined silane plasma. *J. Appl. Phys.*, 63:1230–1231, 1988.
58. J. Pulpytel, W. Morscheidt, and F. Arefi-Khonsari. Probe diagnostics of argon-oxygen-tetramethyltin capacitively coupled plasmas for the deposition of tin oxide thin films. *J. Appl. Phys.*, 101:073308, 2007.
59. W.E. Amatucci, M.E. Koepke, T.E. Sheridan, M.J. Alport, and J.J. Carroll. Self-cleaning Langmuir probe. *Rev. Sci. Instrum.*, 63:1253–1256, 1993.
60. C. Winkler, D. Strele, S. Tscholl, and R. Schrittweiser. On the contamination of Langmuir probe surfaces in a potassium plasma. *Plasma Phys. Contr. F.*, 42:217–223, 2000.

61. E. Stamate and K. Ohe. Influence of surface condition in Langmuir probe measurements. *J. Vac. Sci. Technol. A*, 20:661–666, 2002.
62. P. Špatenka and M. Šicha. Langmuir probe characterization of a rf discharge excited in Ar/C₂F₃Cl mixtures during plasma deposition processes. *Beitr. Plasmaphys.*, 29:57–66, 1989.
63. P. Awakowics, R. Schwefel, M. Werder, and W. Kasper. Energy-mass spectrometry and automatic Langmuir probe measurements in reactive ICP plasmas for diamond deposition. *Surf. Coat. Technol.*, 98:1020–1026, 1998.
64. I.D. Sudit and R.C. Woods. A workstation based Langmuir probe system for low-pressure dc plasmas. *Rev. Sci. Instrum.*, 64:2440–2448, 1993.
65. K. Okada, S. Komatsu, and S. Matsumoto. Langmuir probe measurements in a low pressure inductively coupled plasma used for diamond deposition. *J. Vac. Sci. Technol. A*, 17:721–725, 1999.
66. J. Kang. Radio frequency compensated emissive probe. *Rev. Sci. Instrum.*, 67:1818–1821, 1996.
67. H. Deutsch and S. Klagge. Zur Glimmentladungspolymerisation des Benzols-Vergleich gemessener mit berechneten Wachstumsraten polymerer Filme aus der Ne-Benzol-Entladung. *Beitr. Plasmaphys.*, 19:49–57, 1979.
68. J. Meichsner, H.U. Poll, and K.H. Wickleder. Negative ions in a glow discharge of tetrafluoromethane. *Beitr. Plasmaphys.*, 25:503–512, 1985.
69. M. Maass and M. Schmidt. Investigations on the electron component in an Argon-Hexamethylidisiloxane (HMDS) low pressure glow discharge by probe diagnostics. *Beitr. Plasmaphys.*, 27:187–201, 1987.
70. T. Popov and I. Petkov. Hot Langmuir probe measurements in a chemically reactive plasma and accurate evaluation of the electron energy distribution function. *Vacuum*, 51–97:89, 1998.
71. M. Dhayal and J.W. Bradley. Using heated probes in plasma polymerising discharges. *Surf. Coat. Technol.*, 184:116–122, 2004.
72. S. Klagge. Plasmadiagnostik durch Elektrostatische Sonden unter nichtidealen Bedingungen. PhD thesis, University of Greifswald, Greifswald, Germany, 1988.
73. E.O. Johnson and L. Malter. A floating double probe method for measurements in gas discharges. *Phys. Rev.*, 80:58–68, 1950.
74. B.M. Annaratone, G.F. Counsell, H. Kawano, and J.E. Allen. On the use of double probes in rf discharges. *Plasma Sources Sci. Technol.*, 1:232–241, 1992.
75. A. Brockhaus, C. Borchardt, and J. Engemann. Langmuir probe measurements in commercial plasma plants. *Plasma Sources Sci. Technol.*, 3:539–544, 1994.
76. B.A. Smith and L.J. Overzet. Improvements to floating double probe for time-resolved measurements in pulsed rf plasmas. *Rev. Sci. Instr.*, 69:1372–1377, 1998.
77. M. Čada, Z. Hubička, M. Šícha, A. Churpita, L. Jastrabík, L. Soukup, and M. Tichý. Probe diagnostics of the rf barrier-torch discharge at atmospheric pressure. *Surf. Coat. Technol.*, 174–175:530–534, 2003.
78. S.L. Chen and T. Sekiguchi. Instantaneous direct-display system of plasma parameters by means of triple probe. *J. Appl. Phys.*, 36:2363–2374, 1965.
79. P. Špatenka, H.-J. Endres, J. Krumeich, and R.W. Cook. Process control of plasma polymerization in a large industrial reactor. *Surf. Coat. Technol.*, 116–119:1228–1232, 1999.
80. M. Klick, W. Rehak, and M. Kammerer. Plasma diagnostics in rf discharges using nonlinear and resonance effects. *Jpn. J. Appl. Phys.*, 36:4625–4631, 1996.

81. M. Klick, L. Eichhorn, W. Rehak, M. Kammeyer, and H. Mischke. Influence of excitation frequency on plasma parameters and etching characteristics of radio-frequency discharges. *Surf. Coat. Technol.*, 116–119:468–471, 1999.
82. K.H. Baek, Y. Jung, G.J. Min, C. Kang, H.K. Cho, and J.T. Moon. Chamber maintenance and fault detection technique for a gate etch process via self-excited electron resonance spectroscopy. *J. Vac. Sci. Technol. B*, 23:125–129, 2005.
83. E. Stoffels, W.W. Stoffels, D. Vender, M. Haverlag, G.M.W. Kroesen, and F.J. de Hoog. Negative ions in low pressure discharges. *Contrib. Plasma Phys.*, 35:331–357, 1995.
84. M. Bacal. Plasma diagnostics in negative ion sources. *Plasma Sources Sci. Technol.*, 2:190–197, 1993.
85. N.S.J. Braithwaite and J.E. Allen. Boundaries and probes in electronegative plasmas. *J. Phys. D: Appl. Phys.*, 21:1733–1737, 1988.
86. H. Amemiya. Plasmas with negative ions-probe measurements and charge equilibrium. *J. Phys. D Appl. Phys.*, 23:999–1014, 1990.
87. H. Amemiya, B.M. Annaratone, and J.E. Allen. The collection of positive ions by spherical and cylindrical probes in an electronegative plasma. *Plasma Sources Sci. Technol.*, 8:179, 1999.
88. S. Klagge, M. Maass, and A. Serov. Investigation of the beam plasma discharge in electronegative gases using the second derivative of Langmuir probe characteristics. *Beitr. Plasmaphys.*, 25:255–262, 1985.
89. M. Shindo and Y. Kawai. Measurements of negative ion density in O₂/Ar electron cyclotron resonance plasma. *Surf. Coat. Technol.*, 142–144:355–359, 2001.
90. V. Straňák, J. Blažek, S. Wrehde, P. Adámek, Z. Hubička, M. Tichý, P. Špatenka, and R. Hippler. Study of electronegative Ar/O₂ discharge by means of Langmuir probe. *Contrib. Plasma Phys.*, 48:503–508, 2008.
91. E. Stamate, H. Sugai, O. Takai, and K. Ohe. Sheath-lens probe for negative ion detection in reactive plasmas. *J. Appl. Phys.*, 95:830–833, 2004.
92. N.C. Luhmann, H. Bindsvø, H. Park, J. Sanchez, G. Taylor, and C.X. Yu. Microwave diagnostics. *Fusion Sci. Technol.*, 53:335–396, 2008.
93. M.A. Heald and C.B. Wharton. *Plasma Diagnostics with Microwaves*. Wiley, New York, 1965.
94. I.A. Hutchinson. *Principles of Plasma Diagnostics*. Cambridge University Press, Cambridge, MA, 1987.
95. H.J. Hartfuss. RF techniques in plasma diagnostics. *Plasma Phys. Contr. F.*, 40:A231–A250, 1998.
96. A.J.H. Donne, C.J. Barth, and H. Weisen. Chapter 4: Laser-aided plasma diagnostics. *Fusion Sci. Technol.*, 53(2):397–430, 2008.
97. S. Gundermann and R. Winkler. A new method of the microwave diagnostics for determining the electron density. *Plasma Chem. Plasma Process.*, 19:111–130, 1999.
98. S. Gundermann, D. Loffhagen, H.-E. Wagner, and R. Winkler. Microwave diagnostics of the electron density in molecular mixture plasmas. *Contrib. Plasma Phys.*, 41:45–60, 2001.
99. J.A. Bittencourt. *Fundamentals of Plasma Physics*, 3rd edn. Sao Jose dos Campos, Brazil, 2003.
100. T.H. Stix. *Waves in Plasmas*. American Institute of Physics, New York, 1992.
101. S.E. Segre. Plasma polarimetry for large Cotton-Mouton and Faraday effects. *Phys. Plasmas*, 2:2908–2914, 1995.
102. C. Fuchs and H.J. Hartfuss. Cotton-Mouton effect measurement in a plasma at the W7-AS stellarator. *Phys. Rev. Lett.*, 81:1626–1629, 1998.

103. C. Lukas, M. Müller, V. Schulz-von der Gathen, and H.F. Döbele. Spatially resolved electron density distribution in an rf excited parallel plate plasma reactor by 1 mm microwave interferometry. *Plasma Sources Sci. Technol.*, 8:94–99, 1999.
104. P. Frank, G. Himmel, and H. Schlüter. Observation of low-frequency density oscillations in an rf heated magnetoplasma. *Plasma Phys. Contr. F.*, 34:1201–1210, 1992.
105. D.M. Pozar. *Microwave Engineering*, 3rd edn. Wiley, New York, 2005.
106. K.E. Greenberg and G.A. Hebner. Electron and metastable densities in parallel-plate radiofrequency discharges. *J. Appl. Phys.*, 73:8126–8133, 1993.
107. L.J. Overzet. Microwave diagnostic results from the gaseous electronics conference rf reference cell. *J. Res. Natl. Inst. Stand. Technol.*, 100:401–414, 1995.
108. G. Pretzler. Comparison of different methods of Abel inversion using computer-simulated and experimental side-on data. *Z. Naturforsch. A*, 47:955–970, 1992.
109. J. Howard and H.-P. Landgraf. Quadrature sampling phase detection. *Rev. Sci. Instrum.*, 65:2130, 1994.
110. S.A. Maas. *Microwave Mixers*. Artech House, Norwood, MA, 1986.
111. H.J. Hartfuss, T. Geist, and M. Hirsch. Heterodyne methods in millimetre wave plasma diagnostics with applications to ECE, interferometry and reflectometry. *Plasma Phys. Contr. F.*, 39:1693–1769, 1997.
112. D. Veron. Submillimeter interferometry of high-density plasmas. In K.J. Button, ed., *Infrared and Millimeter Waves*, 2nd edn., p. 67. Academic Press, New York, 1974.
113. A. Allmendinger, R. Platz, and G. Dodel. Megahertz far-infrared frequency-shifting via multiple diffraction by a rotating grating. *Rev. Sci. Instrum.*, 64:1705–1713, 1993.
114. J. Rutman. Characterization of phase and frequency instabilities in precision frequency sources 15th years of progress. *Proc. IEEE*, 66:1048–1075, 1978.
115. B. Vowinkel. Private communication.
116. Y. Kawano, A. Nagashima, T. Hatae, and S. Gunji. Dual CO₂ laser interferometer with a wavelength combination of 10.6 and 9.27 μm for electron density measurement on large tokamaks. *Rev. Sci. Instrum.*, 67:1520–1528, 1996.
117. M. Krämer, B. Clarenbach, and W. Kaiser. 1mm interferometer with high spatial and temporal resolution for electron density measurements on pulsed plasmas. In *XXVII th ICPIG*, Eindhoven, the Netherlands, 2005.
118. F.A. Hopf and M. Cervantes. Nonlinear optical interferometer. *Appl. Optics*, 21:668–677, 1982.
119. P.A. Bagryansky, A.D. Khilchenko, A.N. Kvashnin, A.A. Lizunov, R.V. Voskoboinikov, A.L. Solomakhin, and H.R. Koslowski. Dispersion interferometer based on a CO₂ laser for TEXTOR and burning plasma experiments. *Rev. Sci. Instrum.*, 77:053501, 2006.
120. R. Prentice, T. Edlington, R.T.C. Smith, D.L. Trotman, R.J. Wylde, and P. Zimmermann. A 2-color mm-wave interferometer for the JET divertor. *Rev. Sci. Instrum.*, 66:1154–1158, 1995.
121. E.E. Scime, R.F. Boivin, J.L. Kline, and M.M. Balkey. Microwave interferometer for steady-state plasmas. *Rev. Sci. Instrum.*, 72:1672–1676, 2001.
122. k. Kawahata, K. Haba, J. Fujita, and S. Okajima. Multichannel HCN laser interferometer for electron-density measurements of the JIPP T-IIU tokamak. *Rev. Sci. Instrum.*, 60:3734–3738, 1989.
123. C.A.J. Hugenholtz. Microwave interferometer and reflectometer techniques for thermonuclear plasmas. PhD thesis, Technical University Eindhoven, Eindhoven, the Netherlands, 1990.

124. N. Niemöller, V. Schulz-von der Gathen, A. Stampa, and H.F. Döbele. A quasi-optical 1 mm microwave heterodyne interferometer for plasma diagnostics using a frequency-tripled Gunn oscillator. *Plasma Sources Sci. Technol.*, 6:478–483, 1997.
125. P.F. Goldsmith. *Quasioptical Systems*. IEEE Press, Piscataway, NJ, 1998.
126. S. Svanberg. *Atomic and Molecular Spectroscopy: Basic Aspects and Practical Applications*, Vol. 6 of *Springer Series on Atoms and Plasmas*. Springer-Verlag, Berlin, Germany, 1990.
127. W. Neumann. Spektroskopische Methoden der Plasmaphysik. In R. Rompe and M. Steenbeck, eds., *Ergebnisse der Plasmaphysik und Gaselektronik*. Akademie-Verlag, Berlin, Germany, 1970.
128. W. Lochte-Holtgreven. *Plasma Diagnostics*. American Institute of Physics, New York, 1995.
129. H.R. Griem. *Plasma Spectroscopy*. McGraw-Hill Book Company, New York, 1964.
130. W. Demtröder. *Laserspektroskopie*. Springer-Verlag, Berlin, Germany, 1991.
131. U. Fantz. Basics of plasma spectroscopy. *Plasma Sources Sci. Technol.*, 15:S137–S147, 2006.
132. A. Ohl. Large area planar microwave discharges. In C.M. Ferreira, ed., *Microwave Discharges: Fundamentals and Applications*, NATO ASI series, pp. 205–214. Plenum Publishing Corporation, New York, 1993.
133. J. Röpcke, L. Mechold, M. Käning, W.Y. Fan, and P.B. Davies. Tunable diode laser diagnostic studies of H₂-Ar-O₂ microwave plasmas containing methane or methanol. *Plasma Chem. Plasma Process.*, 19:395–419, 1999.
134. F. Hempel, P.B. Davies, D. Loffhagen, L. Mechold, and J. Röpcke. Diagnostic studies of H₂-Ar-N₂ microwave plasmas containing methane or methanol using tunable infrared diode laser absorption spectroscopy. *Plasma Sources Sci. Technol.*, 12:S98–S110, 2003.
135. J. Röpcke, G. Lombardi, A. Rousseau, and P.B. Davies. Application of mid-infrared tuneable diode laser absorption spectroscopy to plasma diagnostics: A review. *Plasma Sources Sci. Technol.*, 15:S148–S168, 2006.
136. G. Duxbury. *Infrared Vibration-Rotation Spectroscopy: From Free Radicals to the Infrared Sky*. Wiley, Chichester, U.K., 2000.
137. F.K. Tittel, D. Richter, and A. Freed. Mid-infrared laser applications in spectroscopy. In I.T. Sorokina and K.L. Vodopyanov, eds., *Solid State Infrared Sources*, Vol. 89 of *Topics in Applied Physics*, p. 445. Springer, Berlin, Germany, 2003.
138. D.G. Lancaster, D. Richter, and F.K. Tittel. Portable fiber-coupled diode-laser-based sensor for multiple trace gas detection. *Appl. Phys. B.*, 69:459–465, 1999.
139. D. Rehle, D. Leleux, M. Erdely, F.K. Tittel, M. Fraser, and S. Friedfeld. Ambient formaldehyde detection with a laser spectrometer based on difference-frequency generation in PPLN. *Appl. Phys. B.*, 72:947–952, 2001.
140. G. Berden, R. Peeters, and G. Meijer. Cavity ring-down spectroscopy: Experimental schemes and applications. *Int. Rev. Phys. Chem.*, 19(4):565–607, 2000.
141. M.D. Wheeler, S.M. Newman, A.J. Orr-Ewing, and M.N.R. Ashfold. Cavity ring-down spectroscopy. *J. Chem. Soc., Faraday Trans.*, 94(3):337–351, 1998.
142. M. Mazurenka, A.J. Orr-Ewing, R. Peverall, and G.A.D. Ritchie. Cavity ring-down and cavity enhanced spectroscopy using diode lasers. *Annu. Rep. Prog. Chem., Sect. C*, 101:100–142, 2005.
143. A. Campargue, D. Romanini, and N. Sadeghi. Measurement of SiH₂ density in a discharge by intracavity laser absorption spectroscopy and CW cavity ring-down spectroscopy. *J. Phys. D Appl. Phys.*, 31:1168–1175, 1998.

144. M. Kotterer, J. Conceicao, and J.P. Maier. Cavity ringdown spectroscopy of molecular ions: $A^2\Pi_u \leftarrow X^2\sum_g^+$ (60) transition of N_2^+ . *Chem. Phys. Lett.*, 259:233–236, 1996.
145. D. Romanini, A.A. Kachanov, N. Sadeghi, and F. Stoeckel. CW cavity ring down spectroscopy. *Chem. Phys. Lett.*, 264:316–322, 1997.
146. D. Romanini, A.A. Kachanov, and F. Stoeckel. Diode laser cavity ring down spectroscopy. *Chem. Phys. Lett.*, 270:538–545, 1997.
147. P. Zalicki, Y. Ma, R.N. Zare, E.H. Wahl, T.G. Owano, and C.H. Kruger. Measurement of the methyl radical concentration profile in a hot-filament reactor. *Appl. Phys. Lett.*, 67:144–146, 1995.
148. J. Remy, M.M. Hemerik, G.M.W. Kroesen, and W.W. Stoffels. Relevance of a midinfrared cavity ring-down diagnostic in the study of a dusty SiH₄ plasma. *IEEE Trans. Plasma Sci.*, 32(2):709–715, 2004.
149. S. Welzel, L. Gatilova, P.B. Davies, R. Engeln, A. Rousseau, and J. Röpcke. New perspectives and challenges using quantum cascade lasers for plasma diagnostics. In *18th ESCAMPIG, Lecce 2006, Conference Proceedings*, Lecce, Italy, pp. 63–64, 2006. ISBN 2-914771-38-X.
150. J. Röpcke, L. Mechold, M. Käning, J. Anders, F.G. Wienhold, D. Nelson, and M. Zahniser. IRMA: A tunable infrared multicomponent acquisition system for plasma diagnostics. *Rev. Sci. Instr.*, 71:3706–3710, 2000.
151. J.B. McManus, D. Nelson, M. Zahniser, L. Mechold, M. Osiac, J. Röpcke, and A. Rousseau. TOBI: A two-laser beam infrared system for time-resolved plasma diagnostics of infrared active compounds. *Rev. Sci. Instr.*, 74:2709–2714, 2003.
152. F. Hempel, S. Glitsch, J. Röpcke, S. Saß, and H. Zimmermann. On the measurement of absolute plasma species densities using quantum cascade laser-absorption spectroscopy. In M. Mutlu, ed., *Plasma Polymers and Related Materials*, pp. 142–146. Hacettepe University Press, Ankara, Turkey, 2005. ISBN: 975-491-194-0.
153. H.-E. Wagner. Reactive nonthermal plasmas—Chemical quasiequilibria, similarity principles, and macroscopic kinetics. In *Low Temperature Plasmas—Fundamentals, Technologies and Techniques*, Vol. 1, 2 edn., pp. 385–409. WILEY-VCH Verlag GmbH & Co. KGaA, Weinheim, Germany, 2008.
154. K.V. Kozlov, H.-E. Wagner, R. Brandenburg, and P. Michel. Spatio-temporally resolved spectroscopic diagnostics of the barrier discharge in air at atmospheric pressure. *J. Phys. D Appl. Phys.*, 34:3164, 2001.
155. N.K. Bibinov, D.B. Kokh, N.B. Kolokov, V.A. Kostenko, D. Meyer, I.P. Vinogradov, and K. Wiesemann. A comparative study of the electron distribution function in the positive columns in N₂ and N₂/He dc glow discharges by optical spectroscopy and probes. *Plasma Sources Sci. Technol.*, 7:298–309, 1998.
156. T. Gans, V. Schulz-von der Gathen, and H.F. Döbele. Spectroscopic measurements of phase-resolved electron energy distribution functions in rf-excited discharges. *Europhys. Lett.*, 66:232–238, 2004.
157. J. Schäfer, F. Sigener, R. Foest, D. Loffhagen, and K.-D. Weltmann. On plasma parameters of a self-organized plasma jet at atmospheric pressure. *Eur. Phys. J. D*, 60:531–538, 2010.
158. A.A. Ovsyannikov and M.F. Zhukov. *Plasma Diagnostics*. Cambridge International Science Publishing Limited, Cambridge, U.K., 2000.
159. H.R. Griem. *Spectral Line Broadening by Plasmas*. Academic Press, Inc., New York, 1974.
160. J.W. Coburn and M. Chen. Optical emission spectroscopy of reactive plasmas: A method for correlating emission intensities to reactive particle density. *J. Appl. Phys.*, 51:3134–3136, 1980.

161. J.W. Coburn and M. Chen. Dependence of F-atom density on pressure and flow-rate in CF₄ glow-discharges as determined by emission-spectroscopy. *J. Vac. Sci. Technol.*, 18:353–356, 1981.
162. A. Gicquel, M. Chenevier, K. Hassouni, A. Tserepi, and M. Dubus. Validation of actinometry for estimating relative hydrogen atom densities and electron energy evolution in plasma assisted diamond deposition reactors. *J. Appl. Phys.*, 83(12):7504–7521, 1998.
163. M. Abdel-Rahman, V. Schulz-von der Gathen, T. Gans, K. Niemi, and H.F. Döbele. Determination of the degree of dissociation in an inductively coupled hydrogen plasma using optical emission spectroscopy and laser diagnostics. *Plasma Sources Sci. Technol.*, 15:620–626, 2006.
164. J.P. Booth, O. Joubert, and J. Pelletier. Oxygen atom actinometry reinvestigated: Comparison with absolute measurements by resonance absorption at 130 nm. *J. Appl. Phys.*, 69:618–628, 1991.
165. J.P. Booth and N. Sadeghi. Oxygen and fluorine atom kinetics in electron-cyclotron resonance plasmas by time-resolved actinometry. *J. Appl. Phys.*, 70:611–620, 1991.
166. G. Chunge, P. Chabert, and J.-P. Booth. Absolute fluorine atom concentrations in fluorocarbon plasmas determined from CF₂ loss kinetics. *J. Appl. Phys.*, 89:7750–7755, 2001.
167. M. Baeva, X. Luo, J.H. Schäfer, J. Uhlenbusch, and Z. Zhang. Experimental and theoretical studies of a pulsed microwave excited Ar/CF₄ plasma. *Plasma Chem. Plasma Process.*, 18:429–446, 1998.
168. T. Kimura and M. Noto. Experimental study and global model of inductively coupled CF₄/O₂ discharges. *J. Appl. Phys.*, 100:063303-1, 2006.
169. K. Miyata, M. Hori, and T. Goto. Infrared diode laser absorption spectroscopy measurements of CFX (X=1-3) radical densities in electron cyclotron employing C₄F₈, C₂F₆, CF₄, and CHF₃ gases. *J. Vac. Sci. Technol. A*, 14:2343–2350, 1996.
170. L.D.B. Kiss, J.-P. Nicolai, W.T. Conner, and H.H. Sawin. CF and CF₂ actinometry in a CF₄/Ar plasma. *J. Appl. Phys.*, 71:3186–3192, 1992.
171. B.P. Lavrov, M. Osiac, A.V. Pipa, and J. Röpcke. On the spectroscopic detection of neutral species in a low-pressure plasma containing boron and hydrogen. *Plasma Sources Sci. Technol.*, 12:576–589, 2003.
172. B.P. Lavrov and M.S. Ryazanov. Determination of the absolute concentration of B, Al, Ga, and Si atoms in a nonequilibrium plasma by the reabsorption-distorted intensity ratios in resonance multiplets. *Opt. Spectrosc.*, 98(2):182–189, 2005.
173. B.P. Lavrov and A.S. Mikhailov. On determination of absolute atomic densities from measured relative intensities within resonance multiplets distorted by self-absorption. In *Book of Abstracts, ECAMP IX 2007 Crete-Greece*, pp. Th2–Th19. Heraklion, Greece, 2007.
174. K.L. Menningen, M.A. Childs, H. Toyoda, Y. Ueda, L.W. Anderson, and J.E. Lawler. Absolute radical density-measurements in a CH₄-H₂ dc discharge. *Diam. Relat. Mater.*, 3:422–425, 1994.
175. J. Röpcke, M. Käning, and B.P. Lavrov. Spectroscopical diagnostics of molecular microwave plasmas. *J. Phys. IV*, 8:207–216, 1998. In *3rd International Workshop on Microwave Discharges—Fundamentals and Applications*, Fontevraud Abbey, France, April 20–25, 1997.
176. T. Lang, J. Stiegler, Y. von Kaenel, and E. Blank. Optical emission diagnostics and film growth during microwave-plasma-assisted diamond CVD. *Diam. Relat. Mater.*, 5:1171–1184, 1996.

177. S.A. Astashkevich, M. Käning, E. Käning, N.V. Kokina, B.P. Lavrov, A. Ohl, and J. Röpcke. Radiative characteristics of 3p Sigma,Pi; 3d Pi(-),Delta(-) states of H-2 and determination of gas temperature of low pressure hydrogen containing plasmas. *J. Quant. Spectr. Radiat. Transf.*, 56:725–751, 1996.
178. H.N. Chu, E.A. Den Hartog, A.R. Lefkow, J. Jacobs, L.W. Anderson, M.G. Lagally, and J.E. Lawler. Measurements of the gas kinetic temperature in a CH₄-H₂ discharge during the growth of diamond. *Phys. Rev. A*, 44:3796–3803, 1991.
179. G.M. Jellum, J.E. Daugherty, and D.B. Graves. Particle thermophoresis in low-pressure glow-discharges. *J. Appl. Phys.*, 69:6923–6934, 1991.
180. A. Gicquel, M. Chenevier, Y. Breton, M. Petiau, J.P. Booth, and K. Hassouni. Ground state and excited state H-atom temperatures in a microwave plasma diamond deposition reactor. *J. Phys. III*, 6:1167–1180, 1996.
181. A. Gicquel, K. Hassouni, Y. Breton, M. Chenevier, and J.C. Cubertafon. Gas temperature measurements by laser spectroscopic techniques and by optical emission spectroscopy. *Diam. Relat. Mater.*, 5:366–372, 1996.
182. B.P. Lavrov and J.K. Otorbaev. Relation between the rotational temperature and gas temperature in a low-pressure molecular plasma. *Sov. Tech. Phys. Lett.*, 4(12):574–575, 1978.
183. J. Laimer, F. Huber, G. Misslinger, and H. Störi. Rotational temperature measurements in hydrogen discharges. *Vacuum*, 47:183–186, 1996.
184. K.R. Stalder and R.L. Sharpless. Plasma properties of a hydrocarbon arcjet used in the plasma deposition of diamond thin-films. *J. Appl. Phys.*, 68:6187–6190, 1990.
185. L. Tomasini, A. Rousseau, G. Goussen, and P. Leprince. Spectroscopic temperature measurements in a H₂ microwave discharge. *J. Phys. D Appl. Phys.*, 29:1006–1013, 1996.
186. I.P. Vinogradov and K. Wiesemann. Classical absorption and emission spectroscopy of barrier discharges in N₂/NO and O₂/NO_x mixtures. *Plasma Sources Sci. Technol.*, 6:307–316, 1997.
187. B.P. Lavrov. Determination of the gas temperature of a low-pressure plasma from the intensities of the H₂ and D₂ molecular bands; relationship between the intensity distribution in a band and the gas temperature. *Opt. Spectrosc.*, 48:375–380, 1980.
188. B.P. Lavrov and M.V. Tyutchev. Gas temperature-measurements in non-equilibrium plasma from the intensities of H-2 molecular bands. *Acta Phys. Hung.*, 5:411–426, 1984.
189. B.P. Lavrov. Electronic-rotational spectra of diatomic molecules and diagnostics of non-equilibrium plasma. In B.M. Smirnov, ed., *Plasma Chemistry*, Vol. 45. Energoatomizdat, Moscow, Russia, 1984.
190. A.I. Drachev and B.P. Lavrov. Gas temperature determination from the intensity distribution in the rotational structure of diatomic-molecule bands excited by electron-impact. *High Temp.*, 26:129–136, 1988.
191. N.N. Sobolev, ed. *Electron-Excited Molecules in Non Equilibrium Plasma*. Nova Science Publishers, New York, 1989.
192. B.P. Lavrov, A.A. Solovev, and M.V. Tyutchev. Populations of the rotational levels of the d³ Pi_u—Levels of H₂, HD, and D₂ in an rf discharge. *J. Appl. Spectrosc.*, 32:316–320, 1980.
193. K.H. Krysmanski. Determination of gas temperature in hydrogen low-pressure gas-discharges. *Beitr. Plasmaphys.*, 23:505–510, 1983.
194. B.P. Lavrov, M. Käning, V.L. Ovtchinnikov, and J. Röpcke. In *Frontiers in Low Temperature Plasma Diagnostics II, Bad Honnef, Conference Proceedings*, p. 169, 1997.

195. J. Röpcke, B.P. Lavrov, and A. Ohl. In *Frontiers in Low Temperature Plasma Diagnostics II, Bad Honnef, Conference Proceedings*, Bad Honnef, Germany, p. 201, 1997.
196. B.P. Lavrov and V.P. Prosikhin. Distribution over the vibrational levels and brightness of the dissociation continuum of hydrogen molecules in a gas-discharge plasma. *Opt. Spectrosc.*, 58:317–320, 1985.
197. B.P. Lavrov, M.V. Tyutchev, and V.I. Ustimov. Analysis of regular perturbations in relative emission probabilities of the R and P branches of $d^3 \text{Pi}_u^+ \rightarrow a^3 \text{Sigma}_g^+$ and $e^3 \text{Sigma}_u^+ \rightarrow a^3 \text{Sigma}_g^+$ transitions of the H₂ molecule. *Opt. Spectrosc.*, 64:745–748, 1988.
198. M. Käning, N. Lang, B.P. Lavrov, V.L. Ovtchinnikov, and J. Röpcke. *Europhys. Conf. Abstr.*, 22H:396, 1998.
199. N. Lang, M. Kalatchev, M. Käning, B.P. Lavrov, and J. Röpcke. Time behaviour of various emissions in a modulated hydrogen microwave discharge. In *Frontiers in Low Temperature Plasma Diagnostics III, Saillon, Conference Proceedings*, Saillon, Switzerland, pp. 253–256, 1999.
200. A.L. Cappelli, R.A. Gottscho, and T.A. Miller. Doppler-broadened line-shapes of atomic-hydrogen in a parallel-plate radio-frequency discharge. *Plasma Chem. Plasma Process.*, 5:317–331, 1985.
201. R. Bleekrode. A study of spontaneous emission from CO₂-N₂-He-H₂ laser discharges C3PIU-B3PIG emission bands of N₂. *IEEE J. Quantum Elect.*, 5:57, 1969.
202. B.P. Lavrov, A.S. Melnikov, M. Käning, and J. Röpcke. UV continuum emission and diagnostics of hydrogen-containing nonequilibrium plasmas. *Phys. Rev. E*, 59:3526–3543, 1999.
203. M. Käning, B.P. Lavrov, A.S. Melnikov, A. Ohl, J. Röpcke, and M.A. Tchaplygin. In *Frontiers in Low Temperature Plasma Diagnostics II, Bad Honnef, Conference Proceedings*, Bad Honnef, Germany, pp. 197–200, 1997.
204. M. Pealat, J.P.E. Taran, J. Taillet, M. Bacal, and A.M. Bruneteau. Measurement of vibrational populations in low-pressure hydrogen plasma by coherent anti-stokes Raman-scattering. *J. Appl. Phys.*, 52:2687–2691, 1981.
205. M.A. Abroyan, Y.M. Kagan, N.B. Kolokolov, and B.P. Lavrov. On determination of dissociation degree of hydrogen in monoplasmatron. In *Proceedings of the XII International Conference on Phenomena in Ionized Gases*, Eindhoven, the Netherlands, p. 101, 1975.
206. B.P. Lavrov. Role of dissociative excitation in populating the atomic levels in a hydrogen plasma with a small degree of dissociation. *Opt. Spectrosc.*, 42:250–253, 1977.
207. A.M. Devyatov, A.V. Kalinin, and S.R. Miiovich. Estimate of the degree of dissociation in a low-pressure hydrogen plasma from measured intensity ratios of the H₂ line of the Fulcher α ($d^3 \text{Pi}_u \rightarrow a^3 \text{Sigma}_g$) system and the H $_{\alpha}$ line. *Opt. Spectrosc.*, 71:525–526, 1991.
208. V. Schulz-von der Gathen and H.F. Döbele. Critical comparison of emission spectroscopic determination of dissociation in hydrogen rf-discharges. *Plasma Chem. Plasma Process.*, 16:461–486, 1996.
209. B.L. Preppernau, D.A. Dolson, R.A. Gottscho, and T.A. Miller. Temporally resolved laser diagnostic measurements of atomic-hydrogen concentrations in rf plasma discharges. *Plasma Chem. Plasma Process.*, 9:157–164, 1989.
210. D. Wagner, B. Dikmen, and H.F. Döbele. Vacuum ultraviolet absorption spectroscopy in the spectral interval of Lyman-alpha of atomic hydrogen and deuterium in an ion source plasma. *Rev. Sci. Instrum.*, 67:1800–1806, 1996.

211. B.P. Lavrov and A.S. Melnikov. Excitation transfer from Ar* to H-2 in a gas-discharge plasma. *Opt. Spectrosc.*, 85:666–671, 1998.
212. G.D. Stancu, A.V. Pipa, G. Lombardi, P.B. Davies, A. Gicquel, B.P. Lavrov, and J. Röpcke. On the reaction kinetics of chemically active molecular microwave plasmas. *Contrib. Plasma Phys.*, 45:358–368, 2005.
213. B.P. Lavrov, A.V. Pipa, and J. Röpcke. On determination of the degree of dissociation of hydrogen in non-equilibrium plasmas by means of emission spectroscopy: I. The collision-radiative model and numerical experiments. *Plasma Sources Sci. Technol.*, 15:135–146, 2006.
214. B.P. Lavrov, N. Lang, A.V. Pipa, and J. Röpcke. On determination of the degree of dissociation of hydrogen in non-equilibrium plasmas by means of emission spectroscopy: II. Experimental verification. *Plasma Sources Sci. Technol.*, 15:147–155, 2006.
215. A.V. Pipa. On determination of the degree of dissociation of hydrogen in non-equilibrium plasmas by means of emission spectroscopy. PhD thesis, University of Greifswald, Greifswald, Germany, 2004. ISBN 3-8325-0645-4.
216. M. Osiac, B.P. Lavrov, and J. Röpcke. Intensity distributions in R and P branches of (0-0) band of the A(1)Pi -> X-1 Sigma(+) electronic transition of the BH molecule and determination of gas temperature in non-equilibrium plasmas. *J. Quant. Spectrosc. Radiat. Transf.*, 74:471–491, 2002.
217. G. Lombardi, G.D. Stancu, F. Hempel, A. Gicquel, and J. Röpcke. Quantitative detection of methyl radicals in non-equilibrium plasmas: A comparative study. *Plasma Sources Sci. Technol.*, 13:27–38, 2004.
218. W.Y. Fan, P.F. Knewstubb, M. Käning, L. Mechold, J. Röpcke, and P.B. Davies. A diode laser and modeling study of mixed (CH₄-H₂-O₂) AC plasmas. *J. Phys. Chem. A*, 103:4118–4128, 1999.
219. S. Welzel, A. Rousseau, P.B. Davies, and J. Röpcke. Kinetic and diagnostic studies of molecular plasmas using laser absorption techniques. *J. Phys. Conf. Ser.*, 86:012012, 2007.
220. R.A.B. Zijlmans, O. Gabriel, S. Welzel, F. Hempel, J. Röpcke, R. Engeln, and D.C. Schram. Molecule synthesis in an Ar-CH₄-O₂-N₂ microwave plasma. *Plasma Sources Sci. Technol.*, 15:564–573, 2006.
221. E.M. van Veldhuizen, ed. *Electrical Discharges for Environmental Purposes Fundamentals and Applications*. Nova Science Publishers, Huntington, NY, 2000.
222. B.M. Penetrante. Plasma chemistry and power consumption in non-thermal DeNO_x. In S. Schultheis and B. Penetrante, eds., *Non-Thermal Plasma Techniques for Pollution Control*, Vol. G34 of *NATO ASI Series*, p. 65. Springer-Verlag, Berlin, Germany, 1993.
223. T. Yamamoto. VOC decomposition by nonthermal plasma processing—A new approach. *J. Electrostat.*, 42:227–238, 1997.
224. E. Filimonova, R. Amirov, H. Kim, and I. Park. Comparative modelling of NO_x and SO₂ removal from pollutant gases using pulsed-corona and silent discharges. *J. Phys. D Appl. Phys.*, 33:1716–1727, 2000.
225. J. McAdams. Prospects for non-thermal atmospheric plasmas for pollution abatement. *J. Phys. D Appl. Phys.*, 34:2810–2821, 2001.
226. E. Filimonova, Y.-H. Kim, S. Hong, S.-Y. Han, and Y.-H. Song. Multiparametric investigation on NO_x removal from diesel-like exhaust gas with hydrocarbons by pulsed corona discharge. In *Proceedings of the 15th International Symposium Plasma Chemistry*, Orléans, France, pp. 3041–3046, 2001.

227. Y. Ionikh, A.V. Meshchanov, J. Röpcke, and A. Rousseau. A diode laser study and modeling of NO and NO₂ formation in a pulsed DC air discharge. *Chem. Phys.*, 322:411–422, 2006.
228. L.V. Gatilova, K. Allegraud, J. Guillon, Y.Z. Ionikh, G. Cartry, J. Röpcke, and A. Rousseau. NO formation mechanisms studied by infrared laser absorption in a single low-pressure plasma pulse. *Plasma Sources Sci. Technol.*, 16:S107–S114, 2007.
229. K. Namjou, S. Cai, E.A. Whittaker, J. Faist, C. Gmachl, F. Capasso, D.L. Sivco, and A.Y. Cho. Sensitive absorption spectroscopy with a room-temperature distributed-feedback quantum-cascade laser. *Opt. Lett.*, 23:219–221, 1998.
230. D.D. Nelson, J.H. Shorter, J.B. McManus, and M.S. Zahniser. Sub-part-per-billion detection of nitric oxide in air using a thermoelectrically cooled mid-infrared quantum cascade laser spectrometer. *Appl. Phys. B*, 75:343–350, 2002.
231. T. Beyer, M. Braun, and A. Lambrecht. Fast gas spectroscopy using pulsed quantum cascade lasers. *J. Appl. Phys.*, 93:3158–3160, 2003.
232. S. Welzel, L. Gatilova, J. Röpcke, and A. Rousseau. Time-resolved study of a pulsed dc discharge using quantum cascade laser absorption spectroscopy: NO and gas temperature kinetics. *Plasma Sources Sci. Technol.*, 16:822–831, 2007.
233. A. Rousseau, O. Guaitella, L. Gatilova, F. Thevenet, C. Guillard, J. Röpcke, and G.D. Stancu. Photocatalyst activation in a pulsed low pressure discharge. *Appl. Phys. Lett.*, 87:221501, 2005.
234. G.D. Stancu, N. Lang, J. Röpcke, M. Reinicke, A. Steinbach, and S. Wege. In situ monitoring of silicon plasma etching using a quantum cascade laser arrangement. *Chem. Vap. Depos.*, 13:351–360, 2007.
235. W. Demtröder. *Laser Spectroscopy: Basic Concepts and Instrumentation*, 3rd edn. Springer Verlag, Berlin, Germany, 2003.
236. J. Amorim, G. Baravian, and J. Jolly. Laser-induced resonance fluorescence as a diagnostic technique in non-thermal equilibrium plasmas. *J. Phys. D Appl. Phys.*, 33:R51–R65, 2000.
237. K. Kohse-Höinghaus. Laser techniques for the quantitative detection of reactive intermediates in combustion systems. *Prog. Energy Combust. Sci.*, 20:203–279, 1994.
238. S. Mazouffre, C. Foissac, P. Supiot, P. Vankan, R. Engeln, D.C. Schram, and N. Sadeghi. Density and temperature of n atoms in the afterglow of a microwave discharge measured by a two-photon laser-induced fluorescence technique. *Plasma Sources Sci. Technol.*, 10:168–175, 2001.
239. F. Skiff and J. Bollinger. Mini-conference on laser-induced fluorescence in plasmas. *Phys. Plasmas*, 11:2972–2975, 2004.
240. U. Czarnetzki, D. Luggenhölscher, and H.F. Döbele. Space and time resolved electric field measurements in helium and hydrogen RF-discharges. *Plasma Source. Sci. Technol.*, 8:230–248, 1999.
241. U. Czarnetzki, K. Miyazaki, and T. Kajiwara. Comparison of various two-photon excitation schemes for laser-induced fluorescence spectroscopy in atomic hydrogen. *J. Opt. Soc. Am. B*, 11:2155–2162, 1994.
242. R.B. Green, R.A. Keller, and G.G. Luther. Galvanic detection of optical absorptions in a gas discharge. *Appl. Phys. Lett.*, 29:727–729, 1976.
243. M. Ducloy. Nonlinear effects in optical pumping of atoms by a high-intensity multimode gas laser—General theory. *Phys. Rev. A*, 8:1844–1859, 1973.
244. A. Dinklage, T. Lokayczyk, and H.-J. Kunze. Measurement of the 2³S population in a ⁴He beam by means of laser-induced fluorescence. *J. Phys. B At. Mol. Phys.*, 29:1655–1665, 1996.

245. H.F. Döbele, T. Mosbach, and K. Niemi. Laser-induced fluorescence measurements of absolute atomic densities: Concepts and limitations. *Plasma Sources Sci. Technol.*, 14:S31–S41, 2005.
246. S. Franke, H. Deutsch, and A. Dinklage. Absolute calibration of laser-induced fluorescence experiments by optical depth correction. *Rev. Sci. Instrum.*, 72:2048–2051, 2001.
247. N. Omenetto, H.G.C. Human, and P. Cavalli. Laser excited atomic and ionic non-resonance fluorescence detection limits for several elements in an argon inductively coupled plasma. *Spectrochim. Acta B*, 39:115–117, 1984.
248. G.S. Selwyn. Model for bulk effects on Si interstitial diffusivity in silicon. *Appl. Phys. Lett.*, 51:115–117, 1987.
249. M.B. Leong, A.P. Dé Silva, and V.A. Fassel. Evaluation of stimulated Raman scattering of tunable dye laser radiation as a primary excitation source for exciting atomic fluorescence in an inductively coupled plasma. *Anal. Chem.*, 58:2594–2598, 1986.
250. M. Hamamoto, T. Ohgo, and K. Kondo. Coaxial laser-induced fluorescence spectroscopic system for impurity diagnostics in plasmas. *Jpn. J. Appl. Phys.*, 25:99–102, 1986.
251. N. Hata, A. Matsuda, and K. Tanaka. Spectroscopic diagnostics of plasma-chemical-vapor deposition from silane and germane. *J. Appl. Phys.*, 61:3055–3060, 1987.
252. R.M. Roth, K.G. Spears, and G. Wrong. Spatial concentrations of silicon atoms by laser-induced fluorescence in a silane glow discharge. *Appl. Phys. Lett.*, 45:28–30, 1984.
253. R.A. Gottscho and M.L. Mandish. Time-resolved optical diagnostics of radio frequency plasmas. *J. Vac. Sci. Technol. A*, 3:617–624, 1985.
254. R.A. Gottscho, R.H. Burton, and G.P. Davis. Radiative lifetime and collisional quenching of carbon monochloride ($A^2\Delta$) in an alternating current glow discharge. *J. Chem. Phys.*, 77:5298–5301, 1982.
255. S.G. Hanson, G. Luckman, and S.D. Colson. Measurements of F*, CF, and CF² formation and decay in pulsed fluorocarbon discharges. *Appl. Phys. Lett.*, 53:1588–1590, 1988.
256. V.M. Donnelly, D.L. Flamm, and G. Collins. Laser diagnostics of plasma etching: Measurement of Cl₂⁺ in a chlorine discharge. *J. Vac. Sci. Technol.*, 21:817–823, 1982.
257. W. Jacob, W. Möller, and M. Engelhard. Absolute density determination of CH radicals in a methane plasma. *Appl. Phys. Lett.*, 64:971–973, 1994.
258. F. Hummerenbrum, H. Kempkens, and A. Ruzicka. Laser-induced fluorescence measurements on the C² Sigma⁺-X²II_r transition of the CH radical produced by a microwave excited process plasma. *Plasma Sources Sci. Technol.*, 1:221–231, 1992.
259. G.P. Davis and R.A. Gottscho. Measurement of spatially resolved gas-phase plasma temperatures by optical emission and laser-induced fluorescence spectroscopy. *J. Appl. Phys.*, 54:3080–3086, 1983.
260. J. Amorim, G. Baravian, and A. Ricard. Production of N, H, and NH active species in N₂-H₂ dc flowing discharges. *Plasma Chem. Plasma Process.*, 15:721–731, 1995.
261. N.G. Adams, C.R. Herd, and D. Smith. Development of the flowing afterglow/Langmuir probe technique for studying the neutral products of dissociative recombination using spectroscopic techniques: OH production in the HCO₂⁺ + e reaction. *J. Chem. Phys.*, 91:963–973, 1989.
262. S. Singleton, K.G. Kendrick, R.A. Copeland, and J.B. Jeffries. Vibrational transition-probabilities in the B-X and B'-X systems of the SiCl radical. *J. Phys. Chem. B*, 96:9703–9709, 1992.

263. K. Tachibana, T. Mukai, and H. Harima. Measurement of absolute densities and spatial distributions of Si and SiH in an rf-discharge silane plasma for the chemical vapor deposition of a-Si:H films. *Jpn. J. Appl. Phys.*, 30:L1208–L1211, 1991.
264. A. Kono, N. Koike, K. Okuda, and T. Goto. Laser-induced-fluorescence detection of sih₂ radicals in a radio-frequency silane plasma. *Jpn. J. Appl. Phys.*, 32:L543–L546, 1991.
265. R. Walkup, P. Avouris, R.W. Dreyfus, and J.M. Jasinski. Laser detection of diatomic products of plasma sputtering and etching. *Appl. Phys. Lett.*, 45:372–374, 1984.
266. P. van der Weijer and B.H. Zwerver. Laser-induced fluorescence of OH and SiO molecules during thermal chemical vapour deposition of SiO₂ from silane-oxygen mixtures. *Chem. Phys. Lett.*, 163:48–54, 1989.
267. P. Das, G. Ongrey, N. van Veen, and R. Bersohn. 2 photon laser-induced fluorescence of carbon-atoms. *J. Chem. Phys.*, 79:724–726, 1983.
268. M. Heaven, T.A. Miller, and R.R. Freeman. Two-photon absorption, laser-induced fluorescence detection of Cl atoms. *Chem. Phys. Lett.*, 86:458–462, 1983.
269. G.S. Selwyn, L.D. Baston, and H.H. Sawin. Detection of Cl and chlorine-containing negative ions in rf plasmas by two-photon laser-induced fluorescence. *Appl. Phys. Lett.*, 51:898–900, 1987.
270. G.C. Herring, M.J. Dyer, and L.E. Jusinski. 2-photon-excited fluorescence spectroscopy of atomic fluorine at 170 nm. *Opt. Lett.*, 13:360–362, 1988.
271. J. Bokor, R.R. Freeman, and J.C. White. Two-photon excitation of the n=3 level in H and D atoms. *Phys. Rev. A*, 24:612–614, 1981.
272. W.K. Bischel, B.E. Perry, and D.R. Crosley. 2-photon laser-induced fluorescence in oxygen and nitrogen-atoms. *Chem. Phys. Lett.*, 82:85–88, 1981.
273. S.F. Adams and T.A. Miller. Two-photon absorption laser-induced fluorescence of atomic nitrogen by an alternative excitation scheme. *Chem. Phys. Lett.*, 295:305–311, 1998.
274. P. Brewer, N. van Veen, and R. Bersohn. Two-photon induced fluorescence and resonance-enhanced ionization of sulfur atoms. *Chem. Phys. Lett.*, 91:126–129, 1982.
275. P. Brewer, P. Das, G. Ondrey, and R. Bersohn. Measurement of the relative populations of I(²P_{1/2}⁰) and I(²P_{3/2}⁰) by laser induced vacuum ultraviolet fluorescence. *J. Chem. Phys.*, 79:720–723, 1983.
276. A. Goelich, T. Kawetzki, and H.F. Döbele. On absolute calibration with xenon of laser diagnostic methods based on two-photon absorption. *J. Chem. Phys.*, 108:9362–9370, 1998.
277. J.J. Thomson. *Rays of Positive Electricity and Their Application to Chemical Analyses*. Longmans, Green and Co, London, U.K., 1913.
278. F.A. White and G.M. Wood. *Mass Spectrometry, Applications in Science and Engineering*. Wiley, New York, 1986.
279. H. Budzikiewicz. *Massenspektrometrie, Eine Einführung*. VCH, Weinheim, Germany, 1992.
280. E. de Hoffmann and V. Stroobant. *Mass Spectrometry: Principles and Applications*, 2nd edn. Wiley & Sons, Ltd., Toronto, Ontario, Canada, 2003.
281. L.G. Christophorou, D.L. McCorkle, and A.A. Christodoulides. Electron attachment processes. In L.G. Christophorou, ed., *Electron-Molecule Interactions and Their Applications*, Vol. 1, p. 477. Academic Press, Orlando, FL, 1984.
282. A.G. Harrison. *Chemical Ionization Mass Spectrometry*. CRC, Boca Raton, FL, 1992.
283. H.D. Beckey. *Field Ionization Mass Spectrometry*. Akademie Verlag, Berlin, Germany, 1971.

284. H. Hayashi, H. Iwai, and F. Okuyama. Field ionization mass spectrometry of organic plasmas. *J. Phys. Colloq.*, 48(C6):247–253, 1987.
285. H. Hayashi, H. Iwai, and F. Okuyama. Diagnosis of radio-frequency silane and silane-nitrogen plasmas based on field ionization mass spectrometry. *Surf. Sci.*, 246:408–414, 1991.
286. E.W. Blauth. *Dynamische Massen Spektrometer*. Vieweg, Braunschweig, Germany, 1965.
287. P.H. Dawson, ed. *Quadrupole Mass Spectrometry and Its Applications*. Elsevier, New York, 1976.
288. S.G. Walton, D. Leonhardt, and R.F. Fernsler. Time-resolved diagnostics in a pulsed, electron beam-generated plasma. *IEEE Trans. Plasma Sci.*, 33:838–843, 2005.
289. J. Vlcek and A.D. Pajdarova, and J. Musil. Pulsed dc magnetron discharges and their utilization in plasma surface engineering. *Contrib. Plasma Phys.*, 44:426–436, 2004.
290. S.K. Karkari, H. Bäcker, D. Forder, and J.W. Bradley. A technique for obtaining time- and energy-resolved mass spectroscopic measurements on pulsed plasmas. *Meas. Sci. Technol.*, 13:1431–1436, 2002.
291. J.A.C. Broekaert. *Analytical Atomic Spectrometry with Flames and Plasmas*, 2nd edn. Wiley-VCH, Weinheim, Germany, 2005.
292. M. Zeuner. Corpuscular diagnostics of plasma polymerization processes. In H. Biedermann, ed., *Plasma Polym. Films*, pp. 85–142. Imperial College Press, London, U.K., 2004.
293. H.W. Drawin. Mass spectrometry of plasmas. In W. Lochte-Holtgreven, ed., *Plasma Diagnostics*, p. 777. North-Holland, Amsterdam, the Netherlands, 1968.
294. M. Schmidt and G. Hinzpeter. Zur Untersuchung von Teilchenströmen aus Plasmen. *Beitr. Plasmaphys.*, 10:183–198, 1970.
295. T.D. Märk and H. Helm. Mass-spectrometry as a technique for studying atomic properties of low-pressure plasmas - particle extraction and detection system. *Acta Phys. Austriaca*, 40:158–180, 1974.
296. M.J. Vasile and H.F. Dylla. Mass spectrometry in plasmas. In O. Aujiello and D.I. Flamm, eds., *Plasma Diagnostics*, Vol. 1, p. 185. Academic Press, Boston, MA, 1989.
297. J. Jolly and J. Perrin. Mass spectrometry of reactive plasmas. *Vide*, 53(286):571, 1997.
298. M. Schmidt, R. Foest, and R. Basner. Mass spectrometry in plasma physics. *J. Phys. IV*, 8(P7):231–240, 1998.
299. M. Schmidt. Mass spectrometric diagnostics. In R. Hippler, H. Kersten, M. Schmidt, and K.H. Schoenbach, eds., *Low Temperature Plasmas Fundamentals, Technologies and Techniques*, 2nd edn., p. 243. Wiley-VCH, Weinheim, Germany, 2008.
300. J.R. Woodworth, M.E. Riley, P.A. Miller, G.A. Hebner, and T.W.J. Hamilton. Ion energy and angular distributions in inductively driven radio frequency discharges in chlorine. *Appl. Phys.*, 81(9):5950–5959, 1997.
301. J. Janes. Mass-selected ion angular impact energy distributions at the powered electrode in CF_4 reactive-ion etching. *J. Appl. Phys.*, 74:659–667, 1993.
302. E. Hamers, W. van Sark, J. Bezemer, W. Goedheer, and W. van der Weg. On the transmission function of an ion-energy and mass spectrometer. *Int. J. Mass Spectrom.*, 173:91–98, 1998.
303. J. Janes, U. Bänzinger, C. Huth, P. Hoffmann, G. Neumann, H.-C. Scheer, and U. Köhler. Analysis of large-area beam attacks on surfaces and testing of etching reactions. *Rev. Sci. Instrum.*, 63:48–55, 1992.
304. J. Janes and C. Huth. Energy resolved angular distribution of argon ions at the substrate plane of a radio frequency plasma reactor. *J. Vac. Sci. Technol. A*, 10:3522–3531, 1992.

305. Y.M. Kim, Y.M. Chung, M.J. Jung, J. Vlcek, J. Musil, and J.G. Han. Optical emission spectra and ion energy distribution functions in TiN deposition process by reactive pulsed magnetron sputtering. *Surf. Coat. Technol.*, 200:835–840, 2005.
306. G. Crolly and H. Oechsner. Comparative determination of the electron temperature in Ar- and N-plasmas with electrostatic probes, optical emission spectroscopy OES and energy dispersive mass spectrometry EDMS. *Eur. Phys. J. AP*, 15:49–56, 2001.
307. R. Foest, J.K. Olthoff, R.J. Van Brunt, E.C. Benck, and J.R. Roberts. Optical and mass spectrometric investigations of ions and neutral species in SF₆ radio-frequency discharges. *Phys. Rev. E*, 54:1876–1887, 1996.
308. M. Zeuner, J. Meichsner, and J.A. Rees. High energy negative ions in a radio-frequency discharge. *J. Appl. Phys.*, 79:9379–9381, 1996.
309. J. Meichsner, M. Zeuner, B. Krames, M. Nitschke, R. Rochotski, and K. Barucki. Plasma diagnostics for surface modification of polymers. *Surf. Coat. Technol.*, 98:1565–1571, 1998.
310. F. Becker, I.W. Rangelow, and R. Kassing. Ion energy distributions in SF₆ plasmas at a radio-frequency powered electrode. *J. Appl. Phys.*, 80:56–65, 1996.
311. H.D. Beckey and H. Dreeskamp. Anreicherung isotoper Moleküle in der Gleichstrom-Glimmentladung. 3. Der Primäreffekt—Massenspektrometrische Bestimmung der relativen Ionenhäufigkeiten im Entladungsplasma. *Z. Naturforsch. A*, 9:735–740, 1954.
312. M. Pahl and U. Weimer. Zur Massenspektrometrie an Glimmentladungen. *Z. Naturforsch. A*, 13:745–753, 1958.
313. W. Walcher. Über eine Ionenquelle für massenspektroskopischen Isotopentrennung. *Z. Phys.*, 122:62–85, 1944.
314. H. Nui and R.S. Houk. Fundamental aspects of ion extraction in inductively coupled plasma mass spectrometry. *Spectrochim. Acta Part B*, 51:779–815, 1996.
315. R. Basner, M. Schmidt, K. Becker, and H. Deutsch. Electron impact ionization of organic silicon compounds. In B. Bederson and H. Walther, eds., *Fundamentals of Plasma Chemistry*, Vol. 43 of *Advances in Atomic, Molecular, and Optical Physics*, pp. 147–185. Academic Press, San Diego, CA, 2000.
316. G. Turban, Y. Catherine, and B. Grolleau. A study of the silane glow discharge deposition by isotopic labelling. *Thin Solid Films*, 77:287–300, 1981.
317. P. Benoit-Cattin and L.-C. Bernard. Anomalies of the energy of positive ions extracted from high-frequency ion sources. A theoretical study. *J. Appl. Phys.*, 39:5723–5725, 1968.
318. M. Pahl. Ambipolare Effusion aus der positiven Säule. *Z. Naturforsch. A*, 12:632–642, 1957.
319. C. Courteille, J.-L. Dorier, C. Hollenstein, L. Sansonnens, and A.A. Howling. Partial-depth modulation study of anions and neutrals in low-pressure silane plasmas. *Plasma Sources Sci. Technol.*, 5:210–215, 1996.
320. P. Awakowicz, R. Schwefel, M. Werder, and W. Kasper. Diamond deposition and plasma diagnostics in a 27 MHz inductive coupled reactor (ICP). *Diam. Relat. Mater.*, 6:1816–1823, 1997.
321. W.M.M. Kessels, M.C.M. Van de Sanden, and D.C. Schram. Hydrogen poor cationic silicon clusters in an expanding argon-hydrogen-silane plasma. *Appl. Phys. Lett.*, 72:2397–2399, 1998.
322. C. Hollenstein, W. Schwarzenbach, A.A. Howling, C. Courteille, J.L. Dorier, and L. Sansonnens. Anionic clusters in dusty hydrocarbon and silane plasmas. *J. Vac. Sci. Technol. A*, 14:535–539, 1996.

323. E. de Hoffmann and V. Stroobant. *Mass Spectrometry: Principles and Applications*, 3rd edn. Wiley & Sons, Ltd., Southern Gate, Chichester, U.K., 2007.
324. Mass Spectrometry Data Centre. *Eight Peak Index of Mass Spectra*, 2nd edn. AWRE, Aldermaston, U.K., 1974. NIST Chemistry WebBook (<http://webbook.nist.gov/chemistry>).
325. M. Bauer, T. Schwarz-Selinger, H. Kang, and A. von Keudell. Control of the plasma chemistry of a pulsed inductively coupled methane plasma. *Plasma Sources Sci. Technol.*, 14:543–548, 2005.
326. V. Dose. Bayesian inference in physics: Case studies. *Rep. Prog. Phys.*, 66:1421–1461, 2003.
327. R. Foest, F. Adler, F. Sigener, and M. Schmidt. Study of an atmospheric pressure glow discharge (APG) for thin film deposition. *Surf. Coat. Technol.*, 163:323–330, 2003.
328. Y.A. Gonvalvo, T.D. Whitemore, J.A. Rees, D.L. Seymour, and E. Stoffels. Atmospheric pressure plasma analysis by modulated molecular beam mass spectrometry. *J. Vac. Sci. Technol. A*, 24(3):550–553, 2006.
329. H. Singh, J. Coburn, and D.B. Graves. Mass spectrometric detection of reactive neutral species: Beam-to-background ratio. *J. Vac. Sci. Technol. A*, 17(5):2447–2455, 1999.
330. J. Benedikt, S. Agarwal, D. Eijkman, W. Vandamme, M. Creatore, and M.C.M. van de Sanden. Threshold ionization mass spectrometry of reactive species in remote Ar/C₂H₂ expanding thermal plasma. *J. Vac. Sci. Technol. A*, 23(5):1400–1412, 1999.
331. J. Benedikt, D. Ellerweg, and A. von Keudell. Molecular beam sampling system with very high beam-to-background ratio: The rotating skimmer concept. *Rev. Sci. Instrum.*, 80:055107, 2009.
332. J.A. Ferreira and F.L. Tabares. Cryotrapping assisted mass spectrometry for the analysis of complex gas mixtures. *J. Vac. Sci. Technol. A*, 25(2):246–251, 2007.
333. E. Stoffels, W.W. Stoffels, and K. Tachibana. Electron attachment mass spectrometry as a diagnostics for electronegative gases and plasmas. *Rev. Sci. Instrum.*, 69(1):116–122, 1997.
334. D. Rapp and D.D. Briglia. Total cross sections for ionization and attachment in gases by electron impact. II. Negative-ion formation. *J. Chem. Phys.*, 43:1480–1489, 1965.
335. A.P. Hickman. Dissociative attachment of electrons to vibrationally excited H₂. *Phys. Rev. A*, 43:3495–3502, 1991.
336. L.G. Christophorou and J.K. Olthoff. *Fundamental Electron Interactions with Plasma Processing Gases*. Kluwer Academic/ Plenum Publishers, New York, 2004.
337. A. Chutjian, A. Garscadden, and J.M. Wedehra. Electron attachment to molecules at low electron energies. *Phys. Rep.*, 264:393–470, 1996.
338. K. Teii, M. Hori, M. Ito, T. Goto, and N. Ishii. Study on polymeric neutral species in high-density fluorocarbon plasmas. *J. Vac. Sci. Technol. A*, 18(1):1–9, 2000.
339. K. Teii, M. Hori, T. Goto, and N. Ishii. Precursors of fluorocarbon film growth studied by mass spectrometry. *J. Appl. Phys.*, 87:7185–7190, 2000.
340. S. Imai and K. Tachibana. Analysis of product species in capacitively coupled C₅F₈ plasma by electron attachment mass spectroscopy. *Jpn. J. Appl. Phys.*, 38:L888–L891, 1999.
341. J. Meichsner, H.E. Wagner, V. Kroutilina, and R. Lerch. In *Abstracts XVth Europhysics Conference on Atomic and Molecular Physics of Ionized Gases*, Misolc-Lillafured, Hungary, p. 62–63, 2000.
342. M. Sablier and T. Fuji. Mass spectrometry of free radicals. *Chem. Rev.*, 102(9):2855–2924, 2002.

343. P. Kae-Nune, J. Perrin, J. Guillon, and J. Jolly. Mass spectrometry detection of radicals in SiH₄-CH₄-H₂ glow discharge plasmas. *Plasma Sources Sci. Technol.*, 4:250–259, 1995.
344. W.M.M. Kessels, F.J.H. van Assche, J. Hong, D.C. Schram, and M.C.M. van de Sanden. Plasma diagnostic study of silicon nitride film growth in a remote Ar-H₂-N₂-SiH₄ plasma: Role of N and SiH_n radicals. *J. Vac. Sci. Technol. A*, 22(1):96–106, 2004.
345. T. Fujii and K. Syouji. Mass spectrometric detection of neutral radicals in a CH₄ microwave discharge by use of Li⁺ ion attachment techniques. *J. Appl. Phys.*, 74:3009–3012, 1993.
346. Y. Shiokawa, M. Nakamura, H. Maruyama, Y. Hirano, Y. Taneda, M. Inoue, and T. Fujii. Development of ion attachment mass spectrometry and its applications. *Bunseki Kagaku*, 53(6):475–489, 2004.
347. R. Foest. Massenspektrometrische Untersuchungen der Ionen und Neutralteilchen von RF-Entladungen mit siliziumorganischen Zumischungen. PhD thesis, Ernst Moritz Arndt University, Greifswald, Germany, 1998.
348. R. Foest, R. Basner, and M. Schmidt. Identification of fragment ions by their kinetic energy gained during dissociative ionization by electron impact. *Plasmas Polym.*, 4:259–268, 1999.
349. S. Motlagh and J.H. Moore. A scheme for the specific mass-spectrometer detection of radicals. *Analyst*, 124:1065–1068, 1999.
350. I.A. Fowlis. *Gas Chromatography*. Wiley India Pvt. Ltd., India, 1995.
351. H.M. McNair and J.M. Miller. *Basic Gas Chromatography*, 2nd edn. John Wiley & Sons, Inc., Hoboken, NJ, 2009.
352. E.N. Eremin. *Elementy gazovoj Elektrochimii*. Moskva, Russia, 1968.
353. H. Drost. *Plasmachemie*. Akademieverlag, Berlin, Germany, 1978.
354. H. Deutsch, H. Sabadil, and E.-W. Görss. Untersuchungen an polymerisierenden Plasmen der Benzol-Edelgas-Glimmentladung. Teil I. Messungen des Säulengradienten bei Benzolzumischungen von weniger als 0,1%. *Beit. Plasmaphys.*, 15(4):183–190, 1975.
355. R.J. Jensen, A.T. Bell, and D.S. Soong. Plasma polymerization of ethane. I. Experimental studies of effluent gas composition and polymer deposition rates. *Plasma Chem. Plasma Process.*, 3(2):139–161, 1983.
356. K.V. Kozlov, P. Michel, and H.-E. Wagner. Synthesis of organic compounds from mixtures of methane with carbon dioxide in dielectric-barrier discharges at atmospheric pressure. *Plasmas and Polymers*, 5(3–4):129–150, 2000.
357. A. Sonnenfeld, T.M. Tun, L. Zajickova, K.V. Kozlov, H.-E. Wagner, J.F. Behnke, and R. Hippler. Deposition process based on organosilicon precursors in dielectric barrier discharges at atmospheric pressure—A comparison. *Plasmas Polym.*, 6(4):237–266, 2001.
358. G. Scarduelli, G. Guella, I. Mancini, G. Dilecce, S.D. Benedictis, and P. Tosi. Methane oligomerization in a dielectric barrier discharge at atmospheric pressure. *Plasma Process. Polym.*, 6(1):27–33, 2009.
359. A. Fridman. *Plasma Chemistry*. Cambridge University Press, Cambridge, U.K., 2008.

CHAPTER 7

1. G. Herzberg. *Molecular Spectra and Molecular Structure*. Krieger Publishing, Malabar, FL, 1989.
2. J.I. Steinfeld. *Molecules and Radiation: An Introduction to Molecular Spectroscopy*. The MIT Press, Cambridge, MA, 1985.

3. J.L. McHale. *Molecular Spectroscopy*. Prentice-Hall, Inc. Simon & Schuster/A Viacom Company, Upper Saddle River, NJ, 1999.
4. I.N. Levine. *Molecular Spectroscopy*. John Wiley & Sons, Inc., New York, 1975.
5. G. Socrates. *Infrared Characteristic Group Frequencies—Tables and Charts*, 2nd edn. John Wiley & Sons, Inc., New York, 1994.
6. P.R. Griffiths and J.A. de Haseth. *Fourier Transform Infrared Spectroscopy*. John Wiley & Sons, Inc., New York, 1986.
7. R.H. Norton and R. Beer. New apodizing functions for Fourier spectrometry. *J. Opt. Soc. Am.*, 66:259–264, 1976.
8. R.H. Norton and R. Beer. Erratum. *J. Opt. Soc. Am.*, 67:419, 1977.
9. F.M. Mirabella. *Modern Techniques in Applied Molecular Spectroscopy*. John Wiley & Sons, Inc., New York, 1998.
10. H.G. Tompkins. *Methods of Surface Analysis*. Elsevier, Amsterdam, the Netherlands, 1975.
11. R. Greenler. Infrared study of adsorbed molecules on metal surfaces by reflection techniques. *J. Chem. Phys.*, 44:310, 1966.
12. O.S. Heavens. *Optical Properties of Thin Solid Films*. Academic Press, New York, 1955.
13. S.A. Francis and A.H. Ellison. Infrared spectra of monolayers on metal mirrors. *J. Opt. Soc. Am.*, 49:131–138, 1959.
14. D.L. Allara, A. Baca, and C.A. Pryde. Distortions of band shapes in external reflection infrared spectra of thin polymer films on metal substrates. *Macromolecules*, 11:1215–1220, 1978.
15. M. Nitschke and J. Meichsner. Low-pressure plasma polymer modification from the FTIR point of view. *J. Appl. Polym. Sci.*, 65:381–390, 1997.
16. V. Danilov, H.-E. Wagner, and J. Meichsner. Modification of polydimethylsiloxane thin films in H₂ radio-frequency plasma investigated by infrared reflection absorption spectroscopy. *Plasma Process. Polym.*, 8:1059–1067, 2011.
17. N.J. Harrick. *Internal Reflection Spectroscopy*. Interscience, New York, 1975.
18. J.A. Harrington. A review of IR transmitting, hollow waveguides. *Fiber Integrated Opt.*, 19:211, 2000.
19. J.S. Sanghera and I.D. Aggarwal. *Infrared Fiber Optics*. CRC Press, Boca Raton, FL, 1998.
20. C.A. Villarruel, D.D. Dominguez, and A. Dandridge. Fiber-optic sensors II. In *SPIE Proceedings*, the Hague, the Netherlands, Vol. 798, pp. 225–229, 1987.
21. J.M. Shelly, P. Radhakrishnan, V.P.N. Nampoori, and C.P.G. Vallabhan. A fibre optic evanescent wave sensor for monitoring the rate of pulsed laser deposition of metal thin films. *Meas. Sci. Technol.*, 10:N17–N20, 1999.
22. K. Li and J. Meichsner. In situ infrared fibre evanescent wave spectroscopy as a diagnostic tool for plasma polymerization in a gas discharge. *J. Phys. D Appl. Phys.*, 34: 2001.
23. A.W. Snyder and J.D. Love. *Optical Wave Guide Theory*. Chapman & Hall Ltd, New York, 1983.
24. M.E. Lines and P. Kloczek. Optical transmission theory in infrared fiber optics. In J.S. Sanghera and I.D. Aggarwal, eds., *Infrared Fiber Optics*. CRC Press, Boca Raton, FL, 1998.
25. R.D. Driver, J.N. Downing, and G.M. Leskowitz. Infrared fiber optics III. *Proc. SPIE*, 1591:218, 1991.
26. K. Li. Investigation of plasma polymerization in rf discharge by novel fibre based FTIR diagnostic tool. PhD thesis, University of Greifswald, Greifswald, Germany, 2002.

27. B.D. Ratner. Surface modification of polymers for biomedical applications: Chemical, biological, and surface analytical challenges. In B.D. Ratner and D.G. Castner, eds., *Surface Modification of Polymeric Biomaterials*, pp. 1–10. Plenum Press, New York, 1997.
28. R.Y. Kannan, H.J. Salacinski, D.S. Vara, M. Odlyha, and A.M. Seifalian. Review paper: Principles and applications of surface analytical techniques at the vascular interface. *J. Biomater. Appl.*, 21:5–32, 2006.
29. D. Briggs and J.T. Grant. *Surface Analysis by Auger and X-Ray Photoelectron Spectroscopy*. IMP Publications and Surface Spectra Limited, Townbridge, U.K., 2003.
30. G.C. Smith. *Surface Analysis by Electron Spectroscopy*. Plenum Press, New York, 1994.
31. D. Briggs and M.P. Seah. *Practical Surface Analysis, Auger and X-ray Photoelectron Spectroscopy*, Vol. 1. John Wiley & Sons, Chichester, U.K., 1990.
32. J.F. Moulder. *Handbook of X-Ray Photoelectron Spectroscopy*. Perkin-Elmer Corporation, Eden Prairie, MN, 1992.
33. S. Tougaard. Universality classes of inelastic electron scattering cross sections. *Surf. Interface Anal.*, 25:137–155, 1997.
34. N. Fairley. XPS lineshapes and curve fitting. In D. Briggs and J.T. Grant, eds., *Surface Analysis by Auger and X-Ray Photoelectron Spectroscopy*. IMP Publications and Surface Spectra Limited, Town Bridge, U.K.
35. G. Beamson and D. Briggs. *High Resolution XPS of Organic Polymers*. John Wiley & Sons, Chichester, U.K., 1992.
36. H. Steffen, K. Schröder, B. Busse, A. Ohl, and K.D. Weltmann. Functionalization of COC surfaces by microwave plasmas. *Plasma Process. Polym.*, 4(S1):S392–S396, 2007.
37. B. Finke, K. Schröder, and A. Ohl. Surface radical detection on nh_3 -plasma treated polymer surfaces using the radical scavenger no. *Plasma Process. Polym.*, 5(4):386–396, 2008.
38. R. Wilken, A. Holländer, and J. Behnisch. Nitric oxide radical trapping analysis on vacuum-ultraviolet treated polymers. *Macromolecules*, 31:7613–7617, 1998.
39. A. Chilkoti and B.D. Ratner. Chemical derivatization methods for enhancing the analytical capabilities of X-ray photoelectron spectroscopy and static secondary ion mass spectrometry. In L. Sabbatini and P.G. Zambonin, eds., *Surface Characterization of Advanced Polymers*, pp. 221–256. Wiley-VCH, Weinheim, Germany, 1993.
40. A. Holländer, F. Pippig, M. Dubreuil, and D. Vangeneugden. Distinguishing surface OH and NH_x using TFAA derivatization and XPS. *Plasma Process. Polym.*, 5(4):345–349, 2008.
41. K. Schröder, A. Meyer-Plath, D. Keller, W. Besch, G. Babucke, and A. Ohl. Plasma-induced surface functionalization of polymeric biomaterials in ammonia plasma. *Contrib. Plasma Phys.*, 41(6):562–572, 2001.
42. S. Tougaard and H.S. Hansen. Yb growth on Ni(100) studied by XPS inelastic background analysis. *Surf. Sci.*, 236:271–281, 1990.
43. C. Perruchot, J.F. Watts, C. Lowe, R.G. White, and P.J. Cumpson. Angle-resolved XPS characterization of urea formaldehyde-epoxy systems. *Surf. Interface Anal.*, 33:869–878, 2002.
44. K. Schröder, G. Babucke, and A. Ohl. Visualization of a plasma-generated chemical micro-pattern on polystyrene by XPS. *Surf. Interface Anal.*, 36:702–705, 2004.
45. M.G. Hussein, K. Wörhoff, G. Sengo, and A. Driessens. Optimization of plasma-enhanced chemical vapor deposition silicon oxynitride layers for integrated optics applications. *Thin Solid Films*, 515:3779–3786, 2007.

46. M. Escher, N. Weber, M. Merkel, B. Krömker, D. Funnemann, S. Schmidt, F. Reinert et al. NanoESCA: Imaging UPS and XPS with high energy resolution. *J. Electr. Spectrosc. Rel. Phen.*, 144–147:1179–1182, 2006.
47. U. Vohrer, C. Blomfield, S. Page, and A. Roberts. Quantitative XPS imaging—New possibilities with the delay-line detector. *Appl. Surf. Sci.*, 252:61–65, 2005.
48. L.C. Feldman and J.W. Mayer. *Fundamentals of Surface and Thin Film Analysis*. North Holland, Amsterdam, the Netherlands, 1988.
49. J.L. Écuyer, C. Brassad, C. Cardinal, J. Chabbal, L. Deschenes, and J.P. Labrie. An accurate and sensitive method for the determination of the depth distribution of light elements in heavy materials. *J. Appl. Phys.*, 47:381–382, 1976.
50. B.L. Doyle and P.S. Peercy. Technique for profiling ^1H with 2.5-MeV Van de Graaff accelerators. *Appl. Phys. Lett.*, 34:811–813, 1979.
51. W.A. Lanford. Analysis for hydrogen by nuclear reaction and energy recoil detection. *Nucl. Instrum. Meth. B*, 66:65–82, 1992.
52. A.P. Hickman. Dissociative attachment of electrons to vibrationally excited H_2 . *Phys. Rev. A*, 43:3495–3502, 1991.
53. J.E. Klee. Mass spectrometry of step-growth polymers. *Eur. J. Mass Spectrom.*, 11:591–610, 2005.
54. E. de Hoffmann and V. Stroobant. *Mass Spectrometry Principles and Applications*, 3rd edn. Wiley, Chichester, England, 2007.
55. J. Peter-Katalinic and F. Hillenkamp. *MALDI MS: A Practical Guide to Instrumentation, Methods and Applications*. Wiley-VCH, Weinheim, Germany, 2007.
56. J. Schäfer. Komplexe Polykondensation von Ethylenglykol in einem RF-Niederdruckplasma zur Bildung funktioneller Schichten. PhD thesis, Ernst-Moritz-Arndt Universität, Greifswald, Germany, 2006.
57. J. Friedrich, W. Unger, A. Lippitz, S. Geng, I. Koprianov, G. Kühn, and S. Weidner. Modelling plasma-induced reactions on polymer surfaces using aliphatic self-assembling and LB layers. *Surf. Coat. Technol.*, 98:1132–1141, 1998.
58. S. Weidner, G. Kühn, R. Decker, D. Roessner, and J. Friedrich. Influence of plasma treatment on the molar mass of poly(ethylene terephthalate) investigated by different chromatographic and spectroscopic methods. *J. Polym. Sci. Pol. Chem.*, 36:1639–1648, 1998.
59. A. Benninghoven, G. Rüdenauer, and H.W. Werner. *Secondary Ion Mass Spectrometry: Basic Concepts, Instrumental Aspects, Applications and Trends*. Wiley, New York, 1987.
60. A.M. Belu, D.J. Graham, and D.G. Castner. Time-of-flight secondary ion mass spectrometry: Techniques and applications for the characterization of biomaterial surfaces. *Biomaterials*, 24:3635–3653, 2003.
61. E.E. Johnston and B.D. Ratner. Surface characterization of plasma deposited organic thin films. *J. Electron Spectrosc.*, 81:303–317, 1996.
62. M.S. Wagner. Towards quantitative chemical imaging with ToF-SIMS. *Appl. Surf. Sci.* 255:992–996, 2008.
63. L. Denis, D. Cossement, T. Godfroid, F. Renaux, C. Bittencourt, R. Snyders, and M. Hecq. Synthesis of allylamine plasma polymer films: Correlation between plasma diagnostic and film characteristics. *Plasma Process. Polym.*, 6:199–208, 2009.
64. F.M. Piras, R. Di Mundo, F. Fracassi, and A. Magni. Silicon nitride and oxynitride films deposited from organosilicon plasmas: ToF-SIMS characterization with multivariate analysis. *Surf. Coat. Technol.*, 202:1606–1614, 2008.

65. M. von Gradowski, B. Jacoby, H. Hilgers, J. Barz, M. Wahl, and M. Kopnarski. ToF-SIMS characterisation of ultra-thin fluorinated carbon plasma polymer films. *Surf. Coat. Technol.*, 200:334–340, 2005.
66. M. Hart, W. Parrish, and N. Masciocci. Studies of texture in thin films using synchrotron radiation and energy dispersive diffraction. *Appl. Phys. Lett.*, 50:897–899, 1987.
67. H. Oettel. Methodik der röntgenographischen Analyse von beschichteten Werkstoffen. In D. Bergner, ed., *Beiträge zur Struktur- und Gefügeanalyse von Werkstoffen*, Vol. 265, pp. 45–60. Dt. Verl. für Grundstoffindustrie, Leipzig, Germany, 1988.
68. L.G. Parratt. Surface studies of solids by total reflection of x-rays. *Phys. Rev.*, 95:359–369, 1954.
69. H. Wulff and H. Steffen. Characterization of thin films. In R. Hippler, H. Kersten, M. Schmidt, and K.-H. Schoenbach, eds., *Low Temperature Plasmas*. Vol. 1, p. 329. Wiley-VCH, Weinheim, Germany, 2008.
70. H. Yasuda. *Luminous Chemical Vapour Deposition and Interface Engineering*. Marcel Dekker, New York, 2005.
71. M. Haupt, J. Barz, and C. Oehr. Creation and recombination of free radicals in fluorocarbon plasma polymers: An electron spin resonance study. *Plasma Process. Polym.*, 5:33–43, 2008.
72. M. Kuzuya, S. Ito, N. Kondo, and A. Noguchi. Electron-spin-resonance study of the special features of plasma-induced radicals and their corresponding peroxy-radicals in polytetrafluoroethylene. *Macromolecules*, 24:6612, 1991.
73. M. Kuzuya, S. Kondo, H. Ito, and A. Noguchi. ESR study on the nature of oxygen plasma-induced surface radicals of teflon and corresponding peroxy radical reactivity. *Appl. Surf. Sci.*, 60/61:416–420, 1992.
74. M. Kuzuya, S. Kondo, M. Sugito, and T. Yamashiro. Peroxy radical formation from plasma-induced surface radicals of polyethylene as studied by electron spin resonance. *Macromolecules*, 31:3230–3234, 1998.
75. J. Janca and A. Czernichowski. Wool treatment in the gas flow from gliding discharge plasma at atmospheric pressure. *Surf. Coat. Technol.*, 98:1112–1115, 1998.
76. R. Wilken, A. Holländer, and J. Behnisch. Surface radical analysis on plasma-treated polymers. *Surf. Coat. Technol.*, 116–119:991–995, 1999.

CHAPTER 8

1. J.C. Whitehead. Plasma catalysis: A solution for environmental problems. *Pure Appl. Chem.*, 82(6):1329–1336, 2010.
2. A. Indarto, J.-W. Choi, H. Lee, and H.K. Song. Decomposition of greenhouse gases by plasma. *Environ. Chem. Lett.*, 6:215–222, 2008.
3. W. von Siemens. Über die elektrostatische Induction und die Verzeugung des Stroms in Flaschendrähten. *Ann. Phys.*, 178(9):66–122, 1857.
4. U. Kogelschatz, B. Eliasson, and W. Egli. Dielectric-barrier discharges. principle and applications. *J. Phys. IV*, 07(C4):47–66, 1997.
5. V.G. Samoilovich, V.I. Gibalov, and K.V. Kozlov. *Physical Chemistry of the Barrier Discharge*. DVS, Düsseldorf, Germany, 1997.
6. K.V. Kozlov. In *Proceedings of the 7th International Symposium on High Pressure Low Temperature Plasma Chemistry*, Greifswald, Germany, Vol. 2, pp. 292–298, 2000.

7. M.A. Bagirov, N.A. Nuraliev, and M.A. Kurbanov. Discharge in air space bounded with dielectrics—Methods for determination of partial discharge number. *Zh. Tekh. Fiz.*, 17:495–498, 1972.
8. B. Eliasson, M. Hirth, and U. Kogelschatz. Ozone synthesis from oxygen in dielectric barrier discharges. *J. Phys. D Appl. Phys.*, 20:1421–1437, 1987.
9. D. Braun, U. Küchler, and G.J. Pietsch. Microdischarges in air-fed ozonizers. *J. Phys. D Appl. Phys.*, 24:564–572, 1991.
10. V.I. Gibalov, V.G. Samoilovich, and Yu.V. Filippov. Physicochemistry of ozone electrosynthesis—The results from numerical experiments. *Zh. Fiz. Khim.*, 55:830–842, 1981.
11. B. Eliasson, U. Kogelschatz, and M. Hirth. In *Proceedings of the XVII International Conference on Phenomena in Ionized Gases*, Budapest, Hungary, pp. 590–592, 1985.
12. K. Yoshida and H. Tagashira. Computer simulation of ozone electrosynthesis in an N_2/O_2 mixture-fed ozonizer. *Mem. Kitami Inst. Technol.*, 18:11–20, 1986.
13. D. Braun, A. Hoffman, and G. Pietsch. Modelling of microdischarges in ozonizers. In *Proceedings of the 9th International Symposium on Plasma Chemistry*, Pugnochiuso, Italy, Vol. 3, pp. 751–756, 1989.
14. D. Braun. Zum Wirkungsgrad von Ozonerzeugern. PhD thesis, RWTH, Aachen, Germany, 1990.
15. D. Braun, V. Gibalov, and G. Pietsch. Two-dimensional modelling of the dielectric barrier discharge in air. *Plasma Sources Sci. Technol.*, 1:166–174, 1992.
16. Y.V. Yurgelenas and H.-E. Wagner. A computational model of a barrier discharge in air at atmospheric pressure: The role of residual surface charges in microdischarge formation. *J. Phys. D Appl. Phys.*, 39:4031–4043, 2006.
17. C. Heuser and G. Pietsch. Prebreakdown phenomena between glass-glass and glass-metal electrodes. In *Proceedings of the 6th International Conference on Gas Discharges and Their Applications*, Edinburgh, U.K., Vol. 1 of *IEE Conference Publication No. 189*, pp. 98–101, 1980.
18. C. Heuser. Zur Ozonerzeugung in Elektrischen Gasentladungen. PhD thesis, RWTH, Aachen, Germany, 1985.
19. M. Hirth, U. Kogelschatz, and B. Eliasson. The structure of the microdischarges in ozonizers and their influence on the reaction kinetics. In *Proceedings of the 6th International Symposium on Plasma Chemistry*, Montreal, Quebec, Canada, Vol. 3, pp. 663–668, 1983.
20. K. Kozlov, O. Shepeliuk, and V. Samoilovich. Spatio-temporal evolution of the dielectric barrier discharge channels in air at atmospheric pressure. In *Proceedings of the 11th International Conference on Gas Discharges and Their Applications*, Tokyo, Japan, Vol. 2, pp. 142–145, 1995.
21. K.V. Kozlov, V.V. Dobryakov, A.P. Monyakin, V.G. Samoilovich, O.S. Shepeliuk, H.-E. Wagner, R. Brandenburg, and P. Michel. Cross-correlation spectroscopy in investigations of filamentary gas discharges at atmospheric pressure. In V.N. Ochkin, ed., *Selected Research Papers on Spectroscopy of Nonequilibrium Plasma at Elevated Pressures*, Vol. 4460, pp. 165–176. Society of photo-optical Instrumentation Engineers, Bellingham, WA, 2002.
22. K.V. Kozlov, H.-E. Wagner, R. Brandenburg, and P. Michel. Spatio-temporally resolved spectroscopic diagnostics of the barrier discharge in air at atmospheric pressure. *J. Phys. D Appl. Phys.*, 34:3164–3176, 2001.
23. K.V. Kozlov and H.-E. Wagner. Progress in spectroscopic diagnostics of barrier discharges. *Contrib. Plasma Phys.*, 47:26–33, 2007.

24. B.M. Penetrante and S.E. Schultheis, eds. In *Proceedings of NATO Advanced Research Workshop on Non-Thermal Plasma Techniques for Pollution Control, Cambridge, U.K., 21–25 September 1992*, Vol. 34 of *NATO ASI Series G: Ecological Sciences*. Springer-Verlag, Berlin, New York, 1993.
25. H.H. Kim. Nonthermal plasma processing for air-pollution control: A historical review, current issues, and future prospects. *Plasma Process. Polym.*, 1:91–110, 2004.
26. K.H. Becker, U. Kogelschatz, K.H. Schoenbach, and R.J. Barker. *Non-Equilibrium Air Plasmas at Atmospheric Pressure*. Series in Plasma Physics. IOP Publishing Ltd., Bristol, U.K., 2005.
27. H.J. Hall. History of pulse energization in electrostatic precipitation. *J. Electrostat.*, 25:1–22, 1990.
28. J.D. Bapat. Application of ESP for gas cleaning in cement industry—With reference to India. *J. Hazard. Mater.*, 81:285–308, 2001.
29. G.J.J. Winands, K.P. Yan, A.J.M. Pemen, S.A. Nair, L. Zhen, and E.J.M. van Heesch. An industrial streamer corona plasma system for gas cleaning. *IEEE Trans. Plasma Sci.*, 34:2426–2433, 2006.
30. G.J.J. Winands, A.J.M. Pemen, Z. Liu, E.J.M. van Heesch, K. Ya, and E.M. van Veldhuizen. Temporal development and chemical efficiency of positive streamers in a large scale wire-plate reactor as a function of voltage waveform parameters. *J. Phys. D Appl. Phys.*, 39:3010–3017, 2006.
31. T. Ohkubo, S. Kanazawa, Y. Nomoto, M. Kocik, and J. Mizeraczyk. Characteristics of dc corona streamers induced by uv laser irradiation in non-thermal plasma. *J. Adv. Oxid. Technol.*, 8:218–225, 2005.
32. K. Urashima, S.J. Kim, and J.S. Chang. The scale-up and economic evaluation of non-thermal plasma technology for a coal fired power plant exhaust gas emission control. *J. Adv. Oxid. Technol.*, 6:123–131, 2003.
33. G. Van Oost, C. Leys, M. Joos, B. van Heesch, M. Hrabovsky, and P. Sunka. Plasma based total treatment of waste and low-grade fuels. *Czech. J. Phys.*, 52:D784–D793, 2002.
34. B.M. Penetrante, J.N. Bardsley, and M.C. Hsiao. Kinetic analysis of non-thermal plasmas used for pollution control. *Jpn. J. Appl. Phys.*, 36:5007–5017, 1997.
35. L.A. Rosocha. Chapter 11: Processing of hazardous chemicals using silent-electrical-discharge plasmas. In W. Mannheimer, L.E. Sugiyama, and T.H. Stix, eds., *Plasma Science and the Environment*, pp. 261–298. Amercian Institute of Physics, Woodbury, NY, 1997.
36. S.L. Yao, E. Suzuki, and A. Nakayama. Oxidation of activated carbon and methane using a high-frequency pulsed plasma. *J. Hazard. Mater.*, 83:237–242, 2001.
37. Z. Machala, E. Marode, M. Morvova, and Peter Lukář. DC glow discharge in atmospheric air as a source for volatile organic compounds abatement. *Plasma Process. Polym.*, 2:152–161, 2005.
38. Z. Machala, E. Marode, C.O. Laux, and C.H. Kruger. DC glow discharges in atmospheric pressure air. *J. Adv. Oxid. Technol.*, 7:133–137, 2004.
39. M.A. Wojtowicz, F.P. Miknis, R.W. Grimes, W.W. Smith, and M.A. Serio. Control of nitric oxide, nitrous oxide, and ammonia emissions using microwave plasmas. *J. Hazard. Mater.*, 74:81–89, 2000.
40. U. Kogelschatz. Applications of microplasmas and microreactor technology. *Contrib. Plasma Phys.*, 47:80–88, 2007.
41. R. Hippler, S. Pfau, M. Schmidt, and K.H. Schoenbach. *Low Temperature Plasma Physics*. Wiley-VCH-Verlag, Berlin, Germany, 2001.

42. Z.H. Wang, J.H. Zhou, J.R. Fan, and K. Cen. Direct numerical simulation of ozone injection technology for NO_x control in flue gas. *Energy Fuel.*, 20:2432–2438, 2006.
43. Y.S. Mok and H.J. Lee. Removal of sulfur dioxide and nitrogen oxides by using ozone injection and absorption-reduction technique. *Fuel Process. Technol.*, 87:591–597, 2006.
44. Y.S. Mok and E.Y. Yoon. Effect of ozone injection on the catalytic reduction of nitrogen oxides. *Ozone-Sci. Eng.*, 28(2):105–110, 2006.
45. F.G. Cottrell. The electrical precipitation of suspended particles. *J. Ind. Eng. Chem.*, 3:542–550, 1911.
46. S. Müller, J. Schwarz, and R.-J. Zahn. Spatial and temporal morphology of dielectric barrier discharges used for decomposition of no. In C.K. Wu, ed. In *13th International Symposium on Plasma Chemistry*, Beijing, China, Vol. II, pp. 731–736, 1997. Peking University Press.
47. G.J. Pietsch. Peculiarities of dielectric barrier discharges. *Contrib. Plasma. Phys.*, 41:620–628, 2001.
48. V.I. Gibalov and G. Pietsch. Properties of dielectric barrier discharges in extended coplanar electrode systems. *J. Phys. D Appl. Phys.*, 37:2093–2100, 2004.
49. J. Grundmann, S. Müller, and R.-J. Zahn. Treatment of soot by dielectric barrier discharges and ozone. *Plasma Chem. Plasma Procees.*, 25(5):455–466, 2005.
50. S. Müller, J. Conrads, and W. Best. In *Proceedings of the 7th International Symposium on High Pressure, Low Temperature Plasma Chemistry (Hakone VII)*, Greifswald, Germany, Vol. 2, pp. 340–344, 2000.
51. B. Eliasson, M. Hirth, and U. Kogelschatz. Ozone synthesis from oxygen in dielectric barrier discharges. *J. Phys. D: Appl. Phys.*, 20:1421–1437, 1986.
52. D. Braun, V. Gibalov, and G. Pietsch. Two-dimensional modelling of the dielectric barrier discharge in air. *Plasma Sources Sci. Technol.*, 1:166–174, 1992.
53. H. Kersten, D. Rhode, H. Steffen, H. Deutsch, R. Hippler, G.H.P.M. Swinkels, and G.M.W. Kroesen. On the determination of energy fluxes at plasma-surface processes. *Appl. Phys. A*, 72:531–540, 2001.
54. J. Grundmann, S. Müller, and R.-J. Zahn. Treatment of soot by dielectric barrier discharges and ozone. *Plasma Chem. Plasma Process.*, 25:455–466, 2005.
55. J. Grundmann, S. Müller, R.-J. Zahn, A. Quade, and H. Steffen. Decomposition of soot by ozone and nitrogen oxides. *Top. Catal.*, 42–43:303–305, 2007.
56. S. Kamm, O. Möhler, K.-H. Naumann, H. Saathoff, and U. Schurath. Heterogeneous interaction of ozone, NO₂ and N₂O₅ with soot aerosol. In *Transport and Chemical Transformation in the Troposphere—Proceedings of the EUROTAC Symposium 1998*, WITpress. Boston, MA, Vol. 1, pp. 644–648, 2000.
57. O. Möhler, K.-H. Naumann, H. Saathoff, and U. Schurath. The influence of soot surface reactions on the ozone and NO_x chemistry. *J. Aerosol Sci.*, 28:S309–S310, 1997.
58. A.R. Chughtai, W.F. Welch, and D.M. Smith. A spectroscopic and gravimetric study of the soot-NO₂/N₂O₄ reaction at various temperatures. *Carbon*, 28:411–421, 1990.
59. M. Berthelot. *Essai de mecanique chimique fondee sur la thermochemie*. Dunod, Paris, France, 1879.
60. G.A. Volkova, N.N. Kirillova, E.N. Pavlovskaya, and A.V. Yakovleva. Vacuum-ultraviolet lamps with a barrier discharge in inert gases. *J. Appl. Spectrosc.*, 41:1194–1197, 1984.

61. S. Müller, R.-J. Zahn, J. Grundmann, and M. Langner. Plasma treatment of aerosols and odours. In *3rd International Workshop on Microplasmas, Greifswald*, Kiebu-Druck GmbH, Germany, pp. 121, 2006.
62. S. Müller and R.-J. Zahn. Air pollution control by non-thermal plasma. *Contrib. Plasma Phys.*, 47:520–529, 2007.
63. C.K. Rhodes. *Excimer Lasers*, 2nd edn. Springer, Berlin, Germany, 1984.
64. D. Basting and U. Stamm. The development of excimer laser technology—History and future prospects. *Z. Phys. Chem.*, 215:1575–1599, 2001.
65. B. Eliasson and U. Kogelschatz. UV excimer radiation from dielectric-barrier discharges. *Appl. Phys. B*, 46:299–303, 1988.
66. B. Gellert and U. Kogelschatz. Generation of excimer emission in dielectric barrier discharges. *Appl. Phys. B*, 52:14–21, 1991.
67. U. Kogelschatz. Excimer lamps: History, discharge physics, and industrial applications. *Proc. SPIE*, 5483:272–286, 2004.
68. A. Sosnin, T. Oppenländer, and V.F. Tarasenko. Applications of capacitive and barrier discharge excilamps in photoscience. *J. Photochem. Photobiol. C Photochem. Rev.*, 7:145–163, 2006.
69. J.P. Boeuf. Plasma display panels: physics, recent developments and key issues. *J. Phys. D Appl. Phys.*, 36:R53–R79, 2003.
70. Y. Salamero, H. Asselman, A. Birot, H. Brunet, J. Galy, and P. Millet. Multiphoton excitation and frequency tripling in xenon. *J. Phys. B At. Mol. Phys.*, 16:2971–2979, 1983.
71. F. Adler and S. Müller. Formation and decay mechanisms of excimer molecules in dielectric barrier discharges. *J. Phys. D Appl. Phys.*, 33:1705–1715, 2000.
72. S. Gortchakov, D. Loffhagen, and R. Winkler. The homogeneity of a stabilized discharge-pumped XeCl* laser. *Appl. Phys. B*, 66:313–321, 1998.
73. A. Schwabedissen, D. Loffhagen, T. Hammer, and W. Bötticher. Experimental verification of a zero-dimensional model of the kinetics of XeCl* discharges by XeCl*(B)-, XeCl*(C)-, and Xe₂Cl*(C)-density measurements. *Appl. Phys. B*, 61:175–186, 1995.
74. Th. Hammer. Investigation of XeCl vibrational and quenching kinetics: Numerical simulation of gain and laser spectra in discharge-pumped oscillators. *Appl. Phys. B*, 58:505–513, 1994.
75. R. Waser, ed. *Advanced Electronic Materials and Novel Devices*, 2nd edn., Wiley-VCH, Weinheim, Germany, 2005.
76. B. Bhushan, ed. *Handbook of Nanotechnology*. Springer, Berlin, Germany, 2004.
77. W. Fahrner. *Nanotechnologie und Nanoprozesse*. Springer, Berlin, Germany, 2003.
78. H. Deutsch, H. Kersten, and A. Rutscher. Basic mechanisms in plasma etching. *Contrib. Plasma Phys.*, 29:263, 1989.
79. N. Marchack and J.P. Chang. Perspectives in nanoscale plasma etching: What are the ultimate limits? *J. Phys D: Appl. Phys.*, 44:174011, 2011.
80. J.W. Coburn. *Some Fundamental Aspects of Plasma Assisted Etching*. Springer, Berlin, Germany, 2000.
81. H. Abe, M. Yoneda, and N. Fujiwara. Developments of Plasma Etching Technology for Fabricating Semiconductor Devices. *Jpn. J. Appl. Phys.*, 47:1435–1455, 2008.
82. P. Singer. *Semicond. Int.*, 19:152, 1996.
83. T.E.F.M. Standaert, M. Schaepkens, N.R. Rueger, P.G.M. Sebel, G.S. Oehrlein, and J.M. Cook. High density fluorocarbon etching of silicon in an inductively coupled plasma: Mechanism of etching through a thick steady state fluorocarbon layer. *J. Vac. Sci. Technol.*, A16:239–249, 1998.

84. D. Zhang and J.M. Kushner. Surface kinetics and plasma equipment model for Si etching by fluorocarbon plasmas. *J. Appl. Phys.*, 87:1060–1069, 2000.
85. J.W. Coburn and H.F. Winters. Plasma etching-discussion of mechanisms. *J. Vac. Sci. Technol.*, 16:391, 1979.
86. J.W. Lee, C.R. Abernathy, S.J. Pearton, C. Constantine, R.J. Shul, W.S. Hobson. Etching of Ga-based III-V semiconductors in inductively coupled Ar and CH₄/H₂-based plasma chemistries. *Plasma Sources Sci. Technol.*, 6:499–507, 1997.
87. R.J. Shul and J.G. Fleming. Bulk Si micromachining for integrated microsystems and MEMS processing. In R.J. Shul and S.J. Pearton, eds., *Handbook of Advanced Plasma Processing Techniques*, pp. 419–458. Springer, Berlin, Germany, 2000.
88. S.J. Pearton and D.P. Norton. Dry etching of electronic oxides, polymers, and semiconductors. *Plasma Process. Polym.*, 2:16–37, 2005.
89. A. Grill. *Cold Plasma in Materials Fabrication from Fundamentals to Applications*. IEEE Press, New York, 1994.
90. H.V. Boening. *Fundamentals of Plasma Chemistry and Technology*. Technomic, Lancaster, PA, 1988.
91. H.H. Richter, S. Marschmeyer, and A. Wolff. Plasma etching in microelectronics. In R. Hippler, H. Kersten, M. Schmidt, and K.H. Schoenbach, eds., *Low Temperature Plasmas: Fundamentals, Technologies, and Techniques*, Vol. 2, 2nd edn., pp. 655–674. Wiley-VCH, Weinheim, Germany, 2008.
92. N. Hershkowitz and R.A. Breun. Diagnostics for plasma processing (etching plasmas) (invited). *Rev. Sci. Instrum.*, 68(1):880–885, 1997.
93. N. Hershkowitz, J. Ding, R.A. Breun, R.T.S. Chen, J. Meyer, and A.K. Quick. Does high density–low pressure etching depend on the type of plasma source? *Phys. Plasmas*, 3(5):2197–2202, 1996.
94. H.V. Jansen, M.J. de Boer, S. Unnikrishnan, M.C. Louwerse, and M.C. Elwenspoek. Black silicon method X: A review on high speed and selective plasma etching of silicon with profile control: An in-depth comparison between Bosch and cryostat DRIE processes as a roadmap to next generation equipment. *J. Micromech. Microeng.*, 19:033001, 2009.
95. S. Schneider and S. McClatchie. Material removing techniques-etching and chemical mechanical polishing. In R. Waser, ed., *Nanoelectronics and Information Technology*, 2nd edn., pp. 247–269. Wiley-VCH, Weinheim, Germany, 2005.
96. K.R. Ryan and I.C. Plumb. A model for the etching of silicon in SF₆/O₂ plasmas. *Plasma Chemi. Plasma Process.*, 10:207–229, 1990.
97. M.A. Lieberman and A.J. Lichtenberg. *Principles of Plasma Discharges and Materials Processing*. John Wiley & Sons, New York, 1994.
98. G. Friedman, G. Friedman, A. Gutsol, A.B. Shekhter, V.N. Vasilets, and A. Friedman. Applied plasma medicine. *Plasma Process. Polym.*, 2(6):503–533, 2008.
99. M.G. Kong, G. Kroesen, G. Morfill, T. Nosenko, T. Shimizu, J. van Dijk, and J.L. Zimmermann. Plasma medicine: An introductory review. *New J. Phys.*, 11:115012, 2009.
100. F.S. Smith, US Patent 1352699, 1920.
101. W.P. Menashi, US Patent 3383163, 1968.
102. M. Moisan, J. Barbeau, S. Moreau, J. Pelletier, M. Tabrizian, and L.H. Yahia. Low-temperature sterilization using gas plasmas: A review of the experiments and an analysis of the inactivation mechanisms. *Int. J. Pharm.*, 226(1–2):1–21, 2001.
103. M. Moisan, J. Barbeau, M.C. Crevier, J. Pelletier, N. Philip, and B. Saoudi. Plasma sterilization. Methods and mechanisms. *Pure Appl. Chem.*, 74(3):349–358, 2002.

104. S. Lerouge, M.R. Wertheimer, and L.H. Yahia. Plasma sterilization: A review of parameters, mechanisms, and limitations. *Plasmas Polym.*, 6(3):175–188, 2001.
105. M.K. Boudam, M. Moisan, B. Saoudi, C. Popovici, N. Gherardi, and F. Massines. Bacterial spore inactivation by atmospheric-pressure plasmas in the presence or absence of UV photons as obtained with the same gas mixture. *J. Phys. D Appl. Phys.*, 39(16):3494–3507, 2006.
106. J. Ehlbeck, U. Schnabel, M. Polaka, J. Winter, T. von Woedtke, R. Brandenburg, T. von dem Hagen, and K.-D. Weltmann. Low temperature atmospheric pressure plasma sources for microbial decontamination. *J. Phys. D Appl. Phys.*, 44:013002, 2011.
107. M. Laroussi. Low temperature plasma-based sterilization: Overview and state-of-the-art. *Plasma Process. Polym.*, 2(5):391–400, 2005.
108. R. Hippler, H. Kersten, M. Schmidt, and K.H. Schönbach. *Low Temperature Plasmas—Fundamentals, Technologies and Techniques*, 2 edn., Vol. 2, Wiley-VCH, Berlin, 2008.
109. K. Kelly-Wintenberg, D.M. Sherman, P.P.Y. Tsai, R.B. Gadri, F. Karakaya, C. Zhiyu, J.R. Roth, and T.C. Montie. Air filter sterilization using a one atmosphere uniform glow discharge plasma (the volfilter). *IEEE Trans. Plasma Sci.*, 28(1):64–71, 2000.
110. M.A. Malik, A. Ghaffar, and S.A. Malik. Water purification by electrical discharges. *Plasma Sources Sci. Technol.*, 10(1):82–91, 2000.
111. K. Oehmigen, M. Hähnle, R. Brandenburg, C. Wilke, K.-D. Weltmann, and Th. von Woedtke. The role of acidification for antimicrobial activity of atmospheric pressure plasma in liquid. *Plasma Process. Polym.*, 7:250–257, 2010.
112. Council of Europe. *European Pharmacopoeia*, 5th edn., EDQM, Strasbourg, France, 2005.
113. T. von Woedtke and W.-D. Jülich. Experimental data and theoretical considerations concerning the validity of the SAL concept to characterize non-thermal antimicrobial treatments. *Pharmazie*, 56(7):561–566, 2001.
114. H. Halfmann, B. Denis, N. Bibinov, J. Wunderlich, and P. Awakowicz. Identification of the most efficient VUV/UV radiation for plasma based inactivation of *Bacillus atrophaeus* spores. *J. Phys. D Appl. Phys.*, 40(19):5907–5911, 2007.
115. M. Heise, W. Neff, O. Franken, P. Muranyi, and J. Wunderlich. Sterilization of polymer foils with dielectric barrier discharges at atmospheric pressure. *Plasmas Polym.*, 9(1):23–33, 2004.
116. T.C. Montie, K. Kelly-Wintenberg, and J.R. Roth. An overview of research using the one atmosphere uniform glow discharge plasma (O AUGDP) for sterilization of surfaces and materials. *IEEE Trans. Plasma Sci.*, 28(1):41–50, 2000.
117. D. Dobrynin, G. Friedman, G. Friedman, and A. Friedman. Physical and biological mechanisms of direct plasma interaction with living tissue. *New J. Phys.*, 11:115020, 2009.
118. M. Laroussi, J.P. Richardson, and F.C. Dobbs. Effects of nonequilibrium atmospheric pressure plasmas on the heterotrophic pathways of bacteria and on their cell morphology. *Appl. Phys. Lett.*, 81(4):772–774, 2002.
119. K.H. Schoenbach, S. Katsuki, R.H. Stark, E.S. Buescher, and S.J. Beebe. Bioelectronics—New applications for pulsed power technology. *IEEE Trans. Plasma Sci.*, 30(1):293–300, 2002.
120. J. Opretzka, J. Benedikt, P. Awakowicz, J. Wunderlich, and A. von Keudell. The role of chemical sputtering during plasma sterilization of *Bacillus atrophaeus*. *J. Phys. D Appl. Phys.*, 40(9):2826–2830, 2007.

121. J. Schneider, K.M. Baumgartner, J. Feichtinger, J. Krüger, P. Muranyi, A. Schulz, M. Walker, J. Wunderlich, and U. Schumacher. Investigation of the practicability of low-pressure microwave plasmas in the sterilisation of food packaging materials at industrial level. *Surf. Coat. Technol.*, 200(1–4):962–966, 2005.
122. X.T. Deng, J.J. Shi, G. Shama, and M.G. Kong. Effects of microbial loading and sporulation temperature on atmospheric plasma inactivation of *Bacillus subtilis* spores. *Appl. Phys. Lett.*, 87(15):153901, 2005.
123. M. Laroussi and F. Leipold. Evaluation of the roles of reactive species, heat, and UV radiation in the inactivation of bacterial cells by air plasmas at atmospheric pressure. *Int. J. Mass Spectrom.*, 233(1–3):81–86, 2004.
124. R. Foest, E. Kindel, H. Lange, A. Ohl, M. Stieber, and K.-D. Weltmann. RF capillary jet—A tool for localized surface treatment. *Contrib. Plasma Phys.*, 47(1–2):119–128, 2007.
125. A.V. Pipa, T. Bindemann, R. Foest, E. Kindel, J. Röpcke, and K.-D. Weltmann. Absolute production rate measurements of nitric oxide by an atmospheric pressure plasma jet (APPJ), 2008.
126. T. Gans, M. Osiac, D. O'Connell, V.A. Kadetov, U. Czarnetzki, T. Schwarzseler, H. Halfmann, and P. Awakowicz. Characterization of stationary and pulsed inductively coupled rf discharges for plasma sterilization. *Plasma Phys. Contr. F.*, 47:A353–A360, 2005.
127. G. Fridman, A.D. Brooks, M. Balasubramanian, A. Fridman, A. Gutsol, V.N. Vasilets, H. Ayan, and G. Friedman. Comparison of direct and indirect effects of non-thermal atmospheric-pressure plasma on bacteria. *Plasma Process. Polym.*, 4(4):370–375, 2007.
128. J. Ehlbeck, R. Brandenburg, T. von Woedtke, U. Krohmann, M. Stieber, and K.D. Weltmann. PLASMOSE—Antimicrobial effects of modular atmospheric plasma sources. *GMS Krankenhaushyg. Interdiszip.*, 3(1):Doc14, 2008.
129. S. Moreau, M.G.J. Feuilloye, N. Orange, and J.-L. Brisset. Lethal effect of the gliding arc discharges on *Erwinia* spp. *J. Appl. Microbiol.*, 98(5):1039–1046, 2005.
130. K. Becker, A. Koutsospyros, S.M. Yin, C. Christodoulatos, N. Abramzon, J.C. Joaquin, and G. Brelles-Mariō. Environmental and biological applications of microplasmas. *Plasma Phys. Contr. F.*, 47:B513–B523, 2005.
131. M. Vleugels, G. Shama, X.T. Deng, E. Greenacre, T. Brocklehurst, and M.G. Kong. Atmospheric plasma inactivation of biofilm-forming bacteria for food safety control. *IEEE T. Plasma Sci.*, 33(2):824–828, 2004.
132. M.C. Krebs, P. Becasse, D. Verjat, and J.C. Darbord. Gas-plasma sterilization: Relative efficacy of the hydrogen peroxide phase compared with that of the plasma phase. *Int. J. Pharm.*, 160(1):75–81, 1998.
133. Sterrad Systems, 2007. <http://www.sterrad.com>
134. C. Werner. AbTox steamed by recall of Plazlyte sterilization system. *Health Industry Today*, June, 1998.
135. P.F. Kurunczi, US Patent 7017594, 2005.
136. F.-J. Trompeter, W.J. Neff, O. Franken, M. Heise, M. Neiger, L. Shuhai, G.J. Pietsch, and A.B. Saveljew. Reduction of *Bacillus subtilis* and *Aspergillus niger* spores using nonthermal atmospheric gas discharges. *IEEE Trans. Plasma Sci.*, 30(4):1416–1423, 2002.
137. H.W. Herrmann, I. Henins, J. Park, and G.S. Selwyn. Decontamination of chemical and biological warfare (CBW) agents using an atmospheric pressure plasma jet (APPJ). *Phys. Plasmas*, 6(5):2284–2289, 1999.

138. H. Halfmann, N. Bibinov, J. Wunderlich, and P. Awakowicz. A double inductively coupled plasma for sterilization of medical devices. *J. Phys. D Appl. Phys.*, 40(14):4145–4154, 2007.
139. P. Muranyi, J. Wunderlich, and M. Heise. Sterilization efficiency of a cascaded dielectric barrier discharge. *J. Appl. Microbiol.*, 103(5):1535–1544, 2007.
140. H.C. Baxter, G.A. Campell, A.G. Whittaker, A.C. Jones, A. Aitken, A.H. Simpson, M. Casey, L. Bountiff, L. Gibbard, and R.L. Baxter. Elimination of transmissible spongiform encephalopathy infectivity and decontamination of surgical instruments by using radio-frequency gas-plasma treatment. *J. Gen. Virol.*, 86:2393–2399, 2005.
141. X.T. Deng, J.J. Shi, H.L. Chen, and M.G. Kong. Protein destruction by atmospheric pressure glow discharges. *Appl. Phys. Lett.*, 90(1):013903, 2007.
142. J. M. Grace and L. J. Gerenser. Plasma treatment of polymers. *J. Disp. Sci. and Technol.*, 24:305–341, 2003.
143. J. Meichsner. Low temperature plasma for plasma surface modification. In R. Hippler, H. Kersten, M. Schmidt, and K.-H. Schoenbach, eds., *Low Temperature Plasmas: Fundamentals, Technologies, and Techniques*, Vol. 2, 2nd edn., pp. 739–756. Wiley Weinheim, 2008.
144. J.R. Roth. *Applications to Nonthermal Plasma Processing*, Vol. 2 of *Industrial Plasma Engineering*. IoP, Bristol, U.K., 2001.
145. J.F. Behnke and M. Schmidt. Surface treatment. In K. H. Becker, U. Kogelschatz, K. H. Schoenbach, R. J. Barker, eds., *Non-Equilibrium Air Plasmas at Atmospheric Pressure*, pp.567–621. IoP, Bristol, U.K., 2005.
146. N. Inagaki, I. Inagaki, and N. Inagaki. *Plasma Surface Modification and Plasma Polymerization*. CRC Press, Boca Raton, FL, 1996.
147. R. d'Agostino, D.L. Flamm, and O. Auciello. *Plasma Deposition, Treatment, and Etching of Polymers: The Treatment and Etching of Polymers (Plasma-Materials Interactions)*. Academic Press, Boston, MA, 1990.
148. F. Awaja, M. Gilbert, G. Kelly, B. Fox, and P.J. Pigram. Adhesion of polymers. *Prog. Polym. Sci.*, 34:948–968, 2009.
149. R. Dorai and M.J. Kushner. A model for plasma modification of polypropylene using atmospheric pressure discharges. *J. Phys. D Appl. Phys.*, 36(6):666–685, 2003.
150. J. Borris, A. Dohse, A. Hinze, M. Thomas, C.-P. Klages, A. Möbius, D. Elbick, and E.-R. Weidlich. Improvement of the adhesion of a galvanic metallization of polymers by surface functionalization using dielectric barrier discharges at atmospheric pressure. *Plasma Process. Polym.*, 6(S1):S258–S263, 2009.
151. J. Friedrich, G. Kühn, U. Schulz, K. Jansen, B. Möller, and S. Fischer. Fluorination of polymer surfaces—Fluorierung von Polymeroberflächen. *Vak. Forsch. Prax.*, 14(5):285–290, 2002.
152. F. Fanelli, F. Fracassi, and R. d'Agostino. Fluorination of polymers by means of He/CF₄-fed atmospheric pressure glow dielectric barrier discharges. *Plasma Process. Polym.*, 5(5):424–432, 2008.
153. J. Meichsner. In situ characterisation of polymer surfaces and thin organic films in plasma processing. *Contrib. Plasma Phys.*, 39(5):427–439, 1999.
154. H. Yasuda. *Luminous Chemical Vapour Deposition and Interface Engineering*. Marcel Dekker, New York, 2005.
155. H.-E. Wagner, R. Brandenburg, K.V. Kozlov, A. Sonnenfeld, P. Michel, and J.F. Behnke. The barrier discharge: Basic properties and applications to surface treatment. *Vacuum*, 71:417–436, 2003.

156. S. Meiners, J.G.H. Salge, E. Prinz, and F. Förster. Surface modification of polymer materials by transient gas discharges at atmospheric pressure. *Surf. Coat. Technol.*, 98(1–3):1121–1127, 1998.
157. U. Lommatsch, D. Pasedag, A. Baalmann, G. Ellinghorst, and H.-E. Wagner. Atmospheric pressure plasma jet treatment of polyethylene surfaces for adhesion improvement. *Plasma Process. Polym.*, 4(S1):S1041–S1045, 2007.
158. F. Massines and G. Gouda. A comparison of polypropylene-surface treatment by filamentary, homogeneous and glow discharges in helium at atmospheric pressure. *J. Phys. D Appl. Phys.*, 31(24):3411–3420, 1998.
159. S. Guimond, I. Radu, G. Czeremuszkin, D.J. Carlsson, and M.R. Wertheimer. Biaxially oriented polypropylene (BOPP) surface modification by nitrogen atmospheric pressure glow discharge (APGD) and by air corona. *Plasmas Polym.*, 7(1):71–88, 2002.
160. R. Seeböck, H. Esrom, M. Charbonnier, and M. Romand. Modification of polyimide in barrier discharge air-plasmas: Chemical and morphological effects. *Plasmas Polym.*, 5(2):103–118, 2000.
161. R. Seeböck, H. Esrom, M. Charbonnier, M. Romand, and U. Kogelschatz. Surface modification of polyimide using dielectric barrier discharge treatment. *Surf. Coat. Technol.*, 142–144:455–459, 2001.
162. G. Borcia, C.A. Anderson, and N.M.D. Brown. The surface oxidation of selected polymers using an atmospheric pressure air dielectric barrier discharge. Part I. *Appl. Surf. Sci.*, 221(1–4):203–214, 2004.
163. S. Mändl. Ionenbeschuss von Polymeren für die Medizintechnik. *Vac. Forsch. Prax.* 22(6):36–40, 2010.
164. A. Ohl, H. Strobel, J. Röpcke, H. Kammerstetter, A. Pries, and M. Schneider. Investigation of plasma surface cleaning in planar low-pressure microwave discharges—investigation of plasma surface cleaning in planar low-pressure microwave discharges. *Surf. Coat. Technol.*, 74–75:59–62, 1995.
165. J. Benedikt, C. Flötgen, G. Kussel, V. Raball, and A. von Keudell. Etching of *Bacillus atrophaeus* by oxygen atoms, molecules and argon ions. *J. Phys. Conf. Ser.*, 133:012012, 2008.
166. T. Schwarz-Selinger, U. von Toussaint, C. Hopf, M. Schlüter, and W. Jacob. Chemical sputtering of carbon films by simultaneous irradiation with argon ions and molecular oxygen. *New J. Phys.*, 10:090322, 2008.
167. M.R. Baklanov, D.G. Shamiryan, Zs. Tökei, G.P. Beyer, T. Conard, S. Vanhaelemeersch, and K. Maex. Characterization of Cu surface cleaning by hydrogen plasma. *J. Vac. Sci. Technol. B*, 19(4):1201–1211, 2001.
168. Y. Sawada, N. Taguchi, and K. Tachibana. Reduction of copper oxide thin films with hydrogen plasma generated by a dielectric-barrier glow discharge. *Jpn. J. Appl. Phys.*, 38:6506–6511, 1999.
169. D. Korzec, M. Teschke, E.G. Finatu, G. Nau, and J. Engemann. In *Conference Proceedings of the 47th Meeting of the Society of Vacuum Coaters*, Dallas, TX, pp. 455–460, 2004.
170. J.H. Hsieh, L.H. Fong, S. Yi, and G. Metha. Plasma cleaning of copper leadframe with Ar and Ar/H₂ gases. *Surf. Coat. Technol.*, 112:245–249, 1999.
171. P. Fuchs. Low-pressure plasma cleaning of Au and PtIr noble metal surfaces. *Appl. Surf. Sci.*, 256(5):1382–1390, 2009.
172. S. Veprek, J. Patscheider, and J. Elmer. Restoration and conservation of ancient artifacts: A new area of application of plasma chemistry. *Plasma Chem. Plasma Process.*, 5(2):201–209, 1985.

173. M.C. Kim, S.H. Yang, J.-H. Boo, and J.G. Han. Surface treatment of metals using an atmospheric pressure plasma jet and their surface characteristics. *Surf. Coat. Technol.*, 174–175:839–844, 2003.
174. J. Hauser, C.D. Krüger, H. Halfmann, P. Awakowicz, M. Köller, and S.A. Esenwein. Oberflächenmodifikation metallischer Implantatmaterialien durch Niederdruckplasmabehandlung/Surface modification of metal implant materials by low-pressure plasma treatment. *Biomed. Technol.*, 54(2): 98–166, 2009.
175. J. Pelletier and A. Anders. Plasma-based ion implantation and deposition: A review of physics, technology, and applications. *IEEE Trans. Plasma Sci.*, 33(6.1):1944–1955, 2005.
176. E.I. Meletis. Intensified plasma-assisted processing: Science and engineering. *Surf. Coat. Technol.*, 149:95–113, 2002.
177. M. Polak, A. Ohl, M. Quaas, G. Lukowski, F. Lüthen, K.-D. Weltmann, and K. Schröder. Oxygen and water plasma-immersion ion implantation of copper into titanium for antibacterial surfaces of medical implants. *Adv. Eng. Mater.*, 12(9):B511–B518, 2010.
178. N. Bellakhal, K. Draou, and J.L. Brisset. Electrochemical investigation of copper oxide films formed by oxygen plasma treatment. *J. Appl. Electrochem.*, 27(4):414–421, 1997.
179. A.L. Yerokhin, X. Nie, A. Leyland, A. Matthews, and S.J. Dowey. Plasma electrolysis for surface engineering. *Surf. Coat. Tech.*, 122:73–93, 1999.
180. H. Hoche, S. Groß, R. Foerster, J. Schmidt, and W. Adamitzki. Development of decorative and corrosion resistant coatings for the surface refinement of magnesium alloys by plasma-based methods. *Plasma Process. Polym.*, 6(S1):671–677, 2009.
181. B. Wang, J. Zhang, and S. Dong. New development of atmospheric pressure plasma polishing. *Chin. Opt. Lett.*, 7(6):537–538, 2009.
182. J. Zhang, B. Wang, and S. Dong. Application of atmospheric pressure plasma polishing method in machining of silicon ultra-smooth surfaces. *Front. Electr. Electron. Eng. China*, 3(4):480–487, 2008.
183. T. Arnold, G. Boehm, I.-M. Eichentopf, M. Janietz, J. Meister, and A. Schindler. Plasma jet machining: A novel technology for precision machining of optical elements. *Vak. Technol.*, 22(4):10–16, 2010.
184. H. Drost. *Plasmachemie*. Akademie-Verlag, Berlin, 1978.
185. J.Y. Kang and M. Samardi. *AATCC Rev.*, 4(10):28–32, 2004.
186. R. Shishoo. *Plasma Technologies for Textiles*. Woodhead Publishing, Cambridge, U.K., 2007.
187. R. Morent, N. De Geyter, and J. Verschuren. *Surf. Coat. Technol.*, 202:3427–3449, 2008.
188. N. De Geyter, R. Morent, and C. Leys. *Plasma Sources Sci. Technol.*, 15:78–84, 2006.
189. A. Lunk. In *Workshop Plasmaanwendungen in der Textilindustrie*, Stuttgart, Germany, pp. 27–37, 1999.
190. S. Müller, R.-J. Zahn, and J. Grundmann. *Plasma Process. Polym.*, 4:S1004–S1008, 2007.
191. P. Roach, D. Eglin, K. Rohde, and C.C. Perry. Modern biomaterials: A review-bulk properties and implications of surface modifications. *J. Mater. Sci. Mater. Med.*, 18:1263–1277, 2007.
192. D.F. Williams. Definitions in biomaterials. In D.F. Williams, ed., *Progress in Biomedical Engineering*. Elsevier Press, Amsterdam, the Netherlands, 1987.

193. H.J. Gurland and A.M. Davison. Defining terminology for biocompatibility. *Nephrol. Dial. Transplant.*, 9(Suppl. 2):3, 1994.
194. E. Wintermantel and S.-W. Ha. *Medizintechnik mit biokompatiblen Werkstoffen und Verfahren*. Springer Verlag, Heidelberg, Germany, 2002.
195. J.H. Lee, H.W. Jung, I.-K. Kang, and H.B. Lee. Cell behaviour on polymer surfaces with different functional groups. *Biomaterials*, 15:705–711, 1994.
196. H.J. Griesser, R.C. Chatelier, T.R. Gengenbach, G. Johnson, and J.G. Steele. Growth of human cells on plasma polymers: Putative role of amine and amide groups. *J. Biomat. Sci. Polym. Ed.*, 5(6):531–554, 1994.
197. S.I. Ertel, A. Chilkoti, T.A. Horbett, and B.D. Ratner. Endothelial cell growth on oxygen-containing films deposited by radio-frequency plasmas: The role of surface carbonyl groups. *J. Biomat. Sci. Polym. Ed.*, 3(2):163–183, 1991.
198. H. Steffen, K. Schröder, B. Busse, A. Ohl, and K.D. Weltmann. Functionalization of COC surfaces by microwave plasmas. *Plasma Process. Polym.*, 4(S1):S392–S396, 2007.
199. B. Finke, F. Luethen, K. Schröder, P.D. Mueller, C. Bergemann, M. Frant, A. Ohl, and B.J. Nebe. The effect of positively charged plasma polymerization on initial osteoblastic focal adhesion on titanium surfaces. *Biomaterials*, 28:4521–4534, 2007.
200. B.D. Ratner. Surface modification of polymers for biomedical applications: chemical, biological, and surface analytical challenges. In B.D. Ratner and D.G. Castner, eds., *Surface Modification of Polymeric Biomaterials*, pp. 1–9. Plenum Press, New York, 1997.
201. B.D. Ratner, D.G. Castner, T.A. Horbett, T.J. Lenk, and R.J. Rapoza. Biomolecules and surfaces. *J. Vac. Sci. Technol. A*, 8:2306–2317, 1990.
202. C.M. Chan, T.M. Ko, and H. Hiraoka. Polymer surface modification by plasmas and photons. *Surf. Sci. Rep.*, 24:1–54, 1996.
203. C.-P. Klages. Modification and coating of biomaterial surfaces by glow-discharge processes. A review. *Materialwiss. Werkstofftechn.*, 30:767–774, 1999.
204. P.K. Chu, J.Y. Chen, L.P. Wang, and N. Huang. Plasma-surface modification of biomaterials. *Mater. Sci. Eng. R Rep.*, 36:143–206, 2002.
205. C. Oehr. Plasma surface modification of polymers for biomedical use. *Nucl. Instr. Meth. Phys. Res. B*, 208:40–47, 2003.
206. R.K.Y. Fu and P.K.H. Chu. Plasma modification of materials. In G. Wnek and G.L. Bowl, eds., *Encyclopedia of Biomaterials and Biomedical Engineering*, pp. 1–12. Taylor & Francis, Boca Raton, FL, 2005.
207. K.S. Siow, L. Britcher, S. Kumar, and H.J. Griesser. Plasma methods for the generation of chemically reactive surfaces for biomolecule immobilization and cell colonization—A review. *Plasma Process. Polym.*, 3:392–418, 2006.
208. R. Förch, A.N. Chifén, A. Bousquet, H.L. Khor, and W. Knoll. Recent and expected roles of plasma-polymerized films for biomedical applications. *Chem. Vap. Depos.*, 13:280–294, 2007.
209. B. Gupta and N. Anjum. Plasma and radiation induced graft modification of polymers for biomedical applications. In H. Kausch, ed., *Radiation Effects on Polymers for Biological Use*, Vol. 162 of *Advances in Polymer Science*, pp. 35–61. Springer, Berlin, Germany, 2003.
210. Y. Ikada. Surface modification of polymers for medical applications. *Biomaterials*, 15:725–736, 2003.
211. D. Klee and H. Höcker. Polymers for biomedical applications: Improvement of the interface compatibility, 1999.

212. H.J. Mathieu. Bioengineered material surfaces for medical applications. *Surf. Interf. Anal.*, 32:3–9, 2001.
213. P. LaRocca and S. Barker. Tissue culture surface treatments. *Celline*, 6:1–2, 1996.
214. A.M.P. Pardo, M. Bryhan, H. Krasnow, N. Hardin, and D. Hoover. Corning cellbind surface: An improved surface for enhanced cell attachment. Technical note, Corning Lifescience Incorporated, Acton, MA, 2005.
215. N. Médard, J.-C. Soutif, and F. Poncin-Epaillard. CO₂, H₂O, and CO₂/H₂O plasma chemistry for polyethylene surface modification. *Langmuir*, 18:2246–2253, 2002.
216. A.A. Meyer-Plath, K. Schröder, B. Finke, and A. Ohl. Current trends in biomaterial surface functionalization-nitrogen-containing plasma assisted processes with enhanced selectivity. *Vacuum*, 71:391–406, 2003.
217. B. Finke, K. Schröder, and A. Ohl. Surface radical detection on NH₃-plasma treated polymer surfaces using the radical scavenger NO. *Plasma Process. Polym.*, 5:386–396, 2008.
218. K. Schröder, A. Meyer-Plath, D. Keller, W. Besch, G. Babucke, and A. Ohl. Plasma-induced surface functionalization of polymeric biomaterials in ammonia plasma. *Contrib. Plasma Phys.*, 41(6):562–572, 2001.
219. A.A. Meyer-Plath. Identification of surface radicals on polymers. *Vak. Forsch. Prax.*, 17(S1):40–46, 2005.
220. K. Wende, K. Schröder, U. Lindequist, and A. Ohl. Plasma-based modification of polystyrene surfaces for serum-free culture of osteoblastic cell lines. *Plasma Process. Polym.*, 3:524–531, 2006.
221. R. Sipehia and A.S. Chawla. Albuminated polymer surfaces for biomedical application. *Biomater. Med. Dev. Artif. Org.*, 10(4):229–246, 1982.
222. C. Girardeaux, N. Zammattéo, M. Art, B. Gillon, J.J. Pireaux, and R. Caudano. Amination of poly(ethylene-terephthalate) polymer surface for biochemical applications. *Plasmas Polym.*, 1(4):327–346, 1996.
223. E. Moy, F.Y.H. Lin, J.W. Vogtle, Z. Policova, and A.W. Neumann. Contact angle studies of the surface properties of covalently bonded poly-L-lysine to surfaces treated by glow-discharge. *Colloid Polym. Sci.*, 272(10):1245–1251, 1994.
224. R. Sipehia, A.S. Chawla, J. Daka, and T.M.S. Chang. Immobilization of enzymes on polypropylene bead surfaces by anhydrous ammonia gaseous plasma technique. *J. Biomed. Mater. Res.*, 22:417–422, 1988.
225. F. Arefi-Khonsari, M. Tatoulian, J. Kurdi, S. Ben-Rejeb, and J. Amouroux. Study of the surface properties and stability of polymer films treated by NH₃ plasma and its mixtures. *J. Photopolym. Sci. Technol.*, 11:277–292, 1998.
226. U. Hayat, A.M. Tinsley, M.R. Calder, and D.J. Clarke. ESCA investigation of low-temperature ammonia plasma-treated polyethylene substrate for immobilization of protein. *Biomaterials*, 13:801–806, 1992.
227. M. Kawakami, H. Koya, and S. Gondo. Immobilization of glucose oxidase on polymer membranes treated by low-temperature plasma. *Biotechnol. Bioeng.*, 32:369–373, 2004.
228. R. Sipehia, A. Garfinkle, W.B. Jackson, and T.M.S. Chang. Towards an artificial cornea: Surface modifications of optically clear, oxygen permeable soft contact lens materials by ammonia plasma modification technique for the enhanced attachment and growth of corneal epithelial cells. *Artif. Cells Blood Subst. Biotechnol.*, 18(5):643–655, 1990.
229. Y. Nakayama, T. Takahagi, F. Soeda, K. Hatada, S. Nagaoka, J. Suzuki, and A. Ishitani. XPS analysis of NH₃ plasma-treated polystyrene films utilizing gas phase chemical modification. *J. Polym. Sci. A Polym. Chem.*, 26:559–572, 1988.

230. F. Simon, G. Hermel, D. Lunkwitz, C. Werner, K. Eichhorn, and H.J. Jacobasch. Surface modification of expanded poly(tetrafluoroethylene) by means of microwave plasma treatment for improvement of adhesion and growth of human endothelial cells. *Macromol. Sympo.*, 103:243–257, 1996.
231. J. Yang, J.Z. Bei, and S.G. Wang. Improving cell affinity of poly(d,l-lactide) film modified by anhydrous ammonia plasma treatment. *Polym. Adv. Technol.*, 13(3–4):220–226, 2002.
232. M. Nitschke, G. Schmack, A. Janke, F. Simon, D. Pleul, and C. Werner. Low pressure plasma treatment of poly(3-hydroxybutyrate): Toward tailored polymer surfaces for tissue engineering scaffolds. *J. Biomed. Mater. Res. A*, 59:632–638, 2001.
233. P. Hamerli, T. Weigel, T. Groth, and D. Paul. Enhanced tissue-compatibility of polyethylenterephthalat membranes by plasma aminofunctionalisation. *Surf. Coat. Technol.*, 174–175:574–578, 2003.
234. V. Nelea, L. Luo, C.N. Demers, J. Antoniou, A. Petit, S. Lerouge, M.R. Wertheimer, and F. Mwale. Selective inhibition of type x collagen expression in human mesenchymal stem cell differentiation on polymer substrates surface-modified by glow discharge plasma. *J. Biomed. Mater. Res. A*, 75A:216–223, 2005.
235. M. Takagi, T. Haraguchi, H. Kawai, K. Shiwaku, T. Inoue, Y. Sawa, H. Matsuda, and T. Yoshida. Enhanced adhesion of endothelial cells onto a polypropylene hollow fiber membrane by plasma discharge treatment and high inoculum cell density. *J. Artif. Organs*, 4:220–225, 2001.
236. H.S. Tran, M.M. Puc, C.W. Hewitt, D.B. Soll, S.W. Marra, V.A. Simonetti, J.H. Cilley, and A.J. Delrossi. Diamond-like carbon coating and plasma or glow discharge treatment of mechanical heart valves. *J. Invest. Surg.*, 12:133–140, 1999.
237. R. Sipehia. The enhanced attachment and growth of endothelial-cells on anhydrous ammonia gaseous plasma modified surfaces of polystyrene and poly(tetrafluoroethylene). *Biomater., Artif. Cells Artif. Organs*, 18:437–446, 1990.
238. R. Sipehia, G. Martucci, M. Barbarosie, and C. Wu. Enhanced attachment and growth of human endothelial cells derived from umbilical veins on ammonia plasma modified surfaces of Ptfe and EPTFE synthetic vascular graft biomaterials. *Artif. Cells Blood Subst. Biotechnol.*, 21(4):455–468, 1993.
239. D. Mantovani, M. Castonguay, J.F. Pageau, M. Fiset, and G. Laroche. Ammonia rf-plasma treatment of tubular ePTFE vascular prostheses. *Plasmas Polym.*, 4:207–228, 1999.
240. P. Chevallier, M. Castonguay, S. Turgeon, N. Dubrulle, and G. Laroche. Ammonia rf-plasma on ptfe surfaces: Chemical characterization of the species created on the surface by vapor-phase chemical derivatization. *J. Phys. Chem. B*, 105:12490–12497, 2001.
241. D. Klee, R.V. Villari, H. Hcker, B. Dekker, and C. Mittermayer. Surface modification of a new flexible polymer with improved cell adhesion. *J. Mater. Sci. Mater. Med.*, 5(9–10):592–595, 1994.
242. J.-C. Lin and S.L. Cooper. Surface characterization and ex vivo blood compatibility study of plasmamodified small diameter tubing: Effect of sulphur dioxide and hexamethyl-disiloxane plasmas. *Biomaterials*, 16:1017–1023, 1995.
243. Q. Lv, C. Cao, and H. Zhu. Blood compatibility of polyurethane immobilized with acrylic acid and plasma grafting sulfonic acid. *J. Mater. Sci. Mat. Med.*, 15:607–611, 2004.
244. R. Eloy, D. Parrat, T.M. Duc, G. Legeay, and A. Bechettoile. Invitro evaluation of inflammatory cell response after CF4 plasma surface modification of poly (methyl methacrylate) intraocular lenses. *J. Cataract. Refract. Surg.*, 19:364–370, 1993.

245. H. Biederman and Y. Osada. Plasma chemistry of polymers. In *Polymer Physics*, Vol. 95 of *Advances in Polymer Science*, pp. 57–109. Springer, Berlin, Germany, 1990.
246. K. Schröder, B. Busse, H. Steffen, K.-D. Weltmann, and A. Ohl. *Polymer Surface Modification, Relevance to Adhesion*, Vol. 5. VSP/Birr, Leiden, the Netherlands, 2008.
247. C.S. Chen, M. Mrksich, S. Huang, G.M. Whitesides, and D.E. Ingber. Geometric control of cell life and death. *Science*, 276:1425, 1997.
248. J.B. Lhoest, E. Detrait, J.L. Dewez, P. Den Bosch de Aguilar, and P. Bertrand. A new plasma-based method to promote cell adhesion on micrometric tracks on polystyrene substrates. *J. Biomater. Sci. Polym. Ed.*, 7(12):1039, 1996.
249. A. Ohl, K. Schröder, D. Keller, A. Meyer-Plath, and G.M. Rune. Chemical micropatterning of polymeric cell culture substrates using low-pressure hydrogen gas discharge plasmas. *J. Mater. Sci. Mater. Med.*, 10:747–754, 1999.
250. P. Favia, E. Sardella, R. Gristina, and R. D'Agostino. Novel plasma processes for biomaterials: Micro-scale patterning of biomedical polymers. *Surf. Coat. Technol.*, 169–170:707–711, 2003.
251. N.A. Bullett, D.P. Bullett, F.-E. Truica-Marasescu, F. Mwale, and M.R. Wertheimer. Polymer surface micropatterning by plasma and VUV-photochemical modification for controlled cell culture. *Appl. Surf. Sci.*, 235:395, 2004.
252. A. Goessl, D.F. Bowen-Pope, and A.S. Hoffmann. Control of shape and size of vascular smooth muscle cells in vitro by plasma lithography. *J. Biomed. Mater. Res. A*, 57:15–24, 2001.
253. A. Ohl and K. Schröder. Plasma-induced chemical micropatterning for cell culturing applications: A brief review. *Surf. Coat. Technol.*, 116–119:820–830, 1999.
254. K. Schröder and A. Ohl. Plasmamodifikationen und Proteinkopplungen für biomedizinische Anwendungen. In *Proceedings 13. Neues Dresdner Vakuumtechnisches Kolloquium Dresden 13.–14.10.2005*, Dresden, Germany, pp. 42–49, 2005.
255. T. Matsuda, T. Sugawara, and K. Inoue. Two-dimensional cell manipulation technology an artificial neural circuit based on surface microphotoprocessing. *ASAIO J.*, 38(3):M243–M247, 1992.
256. S.N. Bhatia, M. Toner, R.G. Tompkins, and M.L. Yarmush. Selective adhesion of hepatocytes on patterned surfaces. *Ann. NY Acad. Sci.*, 745:187–209, 1994.
257. M. Müller, V. Sciarratta, and C. Oehr. Plasmachemische Mikrostrukturierung von polymeren Oberflächen für Pharmazie und medizinische Diagnostik—Plasmachemical microstructuring of polymeric surfaces for pharmacology and medical diagnostics. *Vak. Forsch. Prax.*, 15:19–22, 2003.
258. E. Stoffels. Medical applications of atmospheric plasmas. In K. Becker, U. Kogelschatz, K.H. Schoenbach, and R.J. Barker, eds., *Non-Equilibrium Air Plasmas at Atmospheric Pressure*, pp. 655. IOP Bristol, 2005.
259. E. Stoffels. Tissue processing with atmospheric plasmas. *Contr. Plasma Phys.*, 47(1–2):40–48, 2007.
260. R.E.J. Sladek and E. Stoffels. Deactivation of *Escherichia coli* by the plasma needle. *J. Phys. D Appl. Phys.*, 38(11):1716–1721, 2005.
261. G. Lloyd, G. Friedman, S. Jafri, G. Schultz, A. Fridman, and K. Harding. Gas plasma: Medical uses and developments in wound care. *Plasma Process. Polym.*, 7:194–211, 2010.
262. K.-D. Weltmann and T. von Woedtke. Campus PlasmaMed—From Basic Research to Clinical Proof. *IEEE Trans. Plasma Sci.*, 39:1015–1025, 2011.

263. A. Kramer, N.O. Hübner, O. Assadian, H. Below, C. Bender, H. Benkhai et al. Chancen und Perspektiven der Plasmamedizin durch Anwendung von gewebekompatiblen Atmosphärendruckplasmen (Tissue Tolerable Plasmas, TTP). *GMS Krankenhaushyg. Interdiszip.*, 4:Doc10, 2009.
264. J. Ehlbeck, U. Schnabel, M. Polak, J. Winter, T. von Woedtke, R. Brandenburg, T. von dem Hagen, and K.-D. Weltmann. Low temperature atmospheric pressure plasma sources for microbial decontamination. *J. Phys. D: Appl. Phys.*, 44:013002, 2011.
265. K. Schröder, G. Babucke, and A. Ohl. Visualization of a plasma-generated chemical micro-pattern on polystyrene by XPS. *Surf. Interface Anal.*, 36:702–705, 2004.
266. K.S. Siow, L. Britcher, S. Kumar, and H.J. Griesser. Plasma methods for the generation of chemically reactive surfaces for biomolecule immobilization and cell colonization—A review. *Plasma Process. Polym.*, 3:392–418, 2006.
267. R. Förch, A.N. Chifén, A. Bousquet, H.L. Khor, M. Jungblut, L.-Q. Chu, Z. Zhang, I. Osey-Mensah, E.-K. Sinner, and W. Knoll. Recent and expected roles of plasma-polymerized films for biomedical applications. *Chem. Vap. Depos.*, 13:280–294, 2007.
268. A. Ohl and K. Schröder. Plasma-assisted surface modification of biointerfaces. In R. Hippler, H. Kersten, M. Schmidt, and K.H. Schoenbach, eds., *Low Temperature Plasmas*, Vol. 2, pp. 803–819. Wiley-VCH, Weinheim, Germany, 2008.
269. S. Cheruthazhekatt, M. Cernak, P. Slavicek, and J. Havel. Gas plasmas and plasma modified materials in medicine. *J. Appl. Biomed.*, 8:55–66, 2010.
270. M. Laroussi and T. Akan. Arc-free atmospheric pressure cold plasma jets: A review. *Plasma Process. Polym.*, 4:777–788, 2007.
271. K.-D. Weltmann, E. Kindel, T. von Woedtke, M. Hähnel, M. Stieber, and R. Brandenburg. Atmospheric-pressure plasma sources: Prospective tools for plasma medicine. *Pure Appl. Chem.*, 82:1223–1237, 2010.
272. J. Lademann, H. Richter, A. Alborova, D. Humme, A. Patzelt, A. Kramer et al. Risk assessment of the application of a plasma jet in dermatology. *J. Biomed. Opt.*, 14:054025, 2009.
273. R. Bussiahn, R. Brandenburg, T. Gerling, E. Kindel, H. Lange, N. Lembke, K.-D. Weltmann, and T. Kocher. The hairline plasma: An intermittent negative dc-corona discharge at atmospheric pressure for plasma medical applications. *Appl. Phys. Lett.*, 96:143701, 2010.
274. R. Brandenburg, J. Ehlbeck, M. Stieber, T. von Woedtke, J. Zeymer, O. Schlüter, and K.-D. Weltmann. Antimicrobial treatment of heat sensitive materials by means of atmospheric pressure rf-driven plasma jet. *Contrib. Plasm. Phys.*, 47(1–2):72–79, 2007.
275. H. Lange, R. Foest, J. Schäfer, and K.-D. Weltmann. Vacuum uv radiation of a plasma jet operated with rare gases at atmospheric pressure. *IEEE T. Plasma Sci.*, 37:859–865, 2009.
276. M. Laroussi. Low-temperature plasmas for medicine? *IEEE T. Plasma Sci.*, 37:714–725, 2009.
277. L.F. Gaunt, C.B. Beggs, and G.E. Georghiou. Bactericidal action of the reactive species produced by gas-discharge nonthermal plasma at atmospheric pressure: A review. *IEEE T. Plasma Sci.*, 34:1257–1269, 2006.
278. M. Hähnel, T. von Woedtke, and K.-D. Weltmann. Influence of the air humidity on the reduction of bacillus spores in a defined environment at atmospheric pressure using a dielectric barrier surface discharge. *Plasma Process. Polym.*, 7:244–249, 2010.
279. G. Daeschlein, T. von Woedtke, E. Kindel, R. Brandenburg, K.-D. Weltmann, and M. Jünger. Antibacterial activity of an atmospheric pressure plasma jet against

- relevant wound pathogens *in vitro* on a simulated wound environment. *Plasma Process. Polym.*, 7:224–230, 2010.
280. G. Isbary, G. Morfill, H.U. Schmidt, M. Georgi, K. Ramrath, J. Heinlin, et al. A first prospective randomized controlled trial to decrease bacterial load using cold atmospheric argon plasma on chronic wounds in patients. *Brit. J. Dermatol.*, 163:78–82, 2010.
281. M. Vandamme, E. Robert, S. Pesnel, E. Barbosa, S. Dozias, J. Sobilo, S. Lorondel, A. Le Pape, and J.-M. Pouvesle. Antitumor effect of plasma treatment on u87 glioma xenografts: Preliminary results. *Plasma Process. Polym.*, 7:264–273, 2010.
282. K.-D. Weltmann and T. von Woedtke. Basic requirements for plasma sources in medicine. *Eur. Phys. J. Appl. Phys.*, 55:13807, 2011.
283. E. Stoffels. Atmospheric plasma: A universal tool for physicians? In R. Hippler, H. Kersten, M. Schmidt, and K. Schoenbach, eds., *Low Temperature Plasmas*, Vol. 2, 2 edn., p. 837. Wiley, Weinheim, Germany, 2008.
284. K.L. Choy. Chemical vapour deposition of coatings. *Prog. Mater. Sci.*, 48:57–170, 2003.
285. H.B. Profijt, S.E. Potts, M.C.M. van de Sanden, and W.M.M. Kessels. Plasmaassisted atomic layer deposition: Basics, opportunities, and challenges. *J. Vac. Sci. Technol. A*, 29(5):050801, 2011.
286. W. Jacob. Surface reactions during growth and erosion of hydrocarbon films. *Thin Solid Films*, 326(1–2):1–42, 1998.
287. S. Aisenberg and R. Chabot. Ion-beam deposition of thin films of diamondlike carbon. *J. Appl. Phys.*, 42:2953, 1971.
288. L. Holland and S.M. Ojha. Deposition of hard and insulating carbonaceous films on an r.f. target in a butane plasma. *Thin Solid Films*, 38:L17–L19, 1976.
289. H. Tsai and D.B. Bogy. Characterization of diamondlike carbon films and their application as overcoats on thin-film media for magnetic recording. *J. Vac. Sci. Technol. A*, 5(6):3287–3312, 1987.
290. J.A. Woolam, B.N. De, S. Orzeszko, N.J. Ianno, P.G. Snyder, S.A. Alterovitz, J.J. Pouch, R.L.C. Wu, and D.C. Ingram. Diamondlike carbon applications in infrared optics and microelectronics. *Mater. Sci. Forum*, 52–53:577–608, 1990.
291. A.H. Lettington and C. Smith. Optical properties and applications of diamond-like carbon coatings. *Diam. Relat. Mater.*, 1(7):805–809, 1992.
292. A.H. Lettington. Applications of diamond-like carbon thin films. *Carbon*, 36(5–6):555–560, 1998.
293. E. Salonen, K. Nordlund, J. Keinonen, and C.H. Wu. Swift chemical sputtering of amorphous hydrogenated carbon. *Phys. Rev. B*, 63:195415, 2001.
294. W. Jacob and W. Möller. On the structure of thin hydrocarbon films. *Appl. Phys. Lett.*, 63(13):1771–1773, 1993.
295. A. Horn, A. Schenk, J. Biener, B. Winter, C. Lutterloh, M. Wittmann, and J. Küppers. H atom impact induced chemical erosion reaction at C:H film surfaces. *Chem. Phys. Lett.*, 231(2–3):193–198, 1994.
296. M. Wittmann and J. Küppers. A model of hydrogen impact induced chemical erosion of carbon based on elementary reaction steps. *J. Nucl. Mater.*, 227:186–194, 1996.
297. B.V. Mech, A.A. Haasz, and J.W. Davis. Model for the chemical erosion of graphite due to low-energy H⁺ and D⁺ impact. *J. Appl. Phys.*, 84(3):1655–1669, 1998.
298. G.A. Somorjai. *Introduction to Surface Chemistry and Catalysis*. John Wiley & Sons, New York, 1994.
299. J. Roth and C. García-Rosales. Analytic description of the chemical erosion of graphite by hydrogen ions. *Nucl. Fusion*, 36:1647–1659, 1996.

300. C. García-Rosales, W. Eckstein, and J. Roth. Revised formulae for sputtering data. *J. Nucl. Mater.*, 218:8–17, 1994.
301. M.P. de Wilde. Vermischte Mittheilungen. *Ber. Dtsch. Chem. Ges.*, 7(1):352–357, 1874.
302. P. Thenard and A. Thenard. *C.R. Acad. Sci.*, 78:219, 1874.
303. F.W. Smith. Optical properties and local atomic bonding in hydrogenated amorphous carbon and silicon-carbon alloys. *Mater. Sci. Forum*, 52–53:323, 1990.
304. F.K. McTaggart. *Plasma Chemistry in Electrical Discharges*. Elsevier, Amsterdam, the Netherlands, 1967.
305. H. Yasuda. *Plasma Polymerization*. Academic Press, Orlando, FL, 1985.
306. J.R. Hollahan and A.T. Bell. *Techniques and Applications of Plasma Chemistry*. Wiley, New York, 1974.
307. S. Guimond, B. Hanselmann, M. Amberg, and D. Hegemann. Plasma functionalization of textiles: Specifics and possibilities. *Pure Appl. Chem.*, 82:1239–1245, 2010.
308. M. Haupt, J. Barz, and C. Oehr. Creation and recombination of free radicals in fluorocarbon plasma polymers: An electron spin resonance study. *Plasma Process. Polym.*, 5:33–43, 2008.
309. H. Yasuda, T. Hirotsu, and H.G. Olf. Polymerization of organic compounds in an electrodeless glow discharge. X. Internal stress in plasma polymers. *J. Appl. Polym. Sci.*, 21(11):3179–3184, 1977.
310. L. Martinu and D. Poltras. Plasma deposition of optical films and coatings: A review. *J. Vac. Sci. Technol. A*, 18:2619–2645, 2000.
311. A.M. Wrobel and M.R. Wertheimer. Plasma-polymerized organosilicones and organometallics. In R. d'Agostino, ed., *Plasma Deposition, Treatment, and Etching of Polymers: The Treatment and Etching of Polymers (Plasma-Materials Interactions)*, pp. 163–268. Academic Press, Boston, MA, 1990.
312. A. Lunk and M. Schmidt. Plasma processes in activated thin film deposition. *Contrib. Plasma Phys.*, 28(3):275–292, 1988.
313. E.R. Fisher, K.L. Williams, and I.T. Martin. On the importance of ions and ion-molecule reactions to plasma-surface interface reactions. *J. Am. Soc. Mass Spectrom.*, 13(5):518–529, 2002.
314. H.-U. Poll. Contribution to growth of thin polymer films in a glow discharge. *Z. Angew. Phys.*, 29:260, 1970.
315. H.-U. Poll, M. Arzt, and K.-H. Wickleder. Reaction kinetics in the polymerization of thin films on the electrodes of a glow-discharge gap. *Eur. Polym. J.*, 12:505–512, 1976.
316. H. Deutsch and S. Klagge. Zur Glimmentladungspolymerisation des Benzols-Vergleich gemessener mit berechneten Wachstumsraten polymerer Filme aus der Ne-Benzol-Entladung. *Beitr. Plasmaphys.*, 19:49–57, 1979.
317. M.R. Alexander, F.R. Jones, and R.D. Short. Mass spectral investigation of the radio-frequency plasma deposition of hexamethyldisiloxane. *J. Phys. Chem. B*, 101:3614–3619, 1997.
318. M.R. Alexander, F.R. Jones, and R.D. Short. Radio-frequency hexamethyldisiloxane plasma deposition: A comparison of plasma- and deposit-chemistry. *Plasmas Polym.*, 2(4):277–300, 1997.
319. H. Becker. In *Wissenschaftliche Veröffentlichungen Chem.*, Vol. 7. Siemens-Konzern, Germany, 1920.
320. D. Hegemann, M.M. Hossain, E. Koerner, and D.J. Balazs. Macroscopic description of plasma polymerization. *Plasma Process. Polym.*, 4:229–238, 2007.

321. M.A. Gilliam, Q. Yu, and H. Yasuda. Plasma polymerization behavior of fluorocarbon monomers in low-pressure af and rf discharges. *Plasma Process. Polym.*, 4:165–172, 2007.
322. H. Kobayashia, M. Shena, and A.T. Bella. Effects of reaction conditions on the plasma polymerization of ethylene. *J. Macromol. Sci. Chem.*, 8:373–391, 1974.
323. L.G. Christophorou and J.K. Olthoff. *Fundamental Electron Interactions with Plasma Processing Gases*. Kluwer Academic/Plenum Publishers, New York, 2004.
324. M.R. Bruce, C. Ma, and R.A. Bonham. Positive ion pair production by electron impact dissociative ionization of CF_4 . *Chem. Phys. Lett.*, 190:285–290, 1992.
325. P.B. Armentrout. Kinetic energy dependence of ion-molecule reactions related to plasma chemistry. In B. Bederson and H. Walther, eds., *Fundamentals of Plasma Chemistry*, Vol. 43 of *Advances in Atomic, Molecular, and Optical Physics*, pp. 187–229. Academic Press, San Diego, CA, 2000.
326. M.V.V.S. Rao, S.P. Sharma, and M. Meyyappan. Mass spectrometric measurements in inductively coupled CF_4/Ar plasmas. *Plasma Sources Sci. Technol.*, 11(4):397–406, 2002.
327. C.Q. Jiao, C.A. DeJoseph Jr, A. Garscadden, and S.F. Adams. Gas-phase ion chemistries in perfluoromethylcyclohexane. *Plasma Sources Sci. and Technol.*, 18:025007, 2009.
328. K. Furuya, A. Ide, H. Okumura, and A. Harata. Mass spectrometric investigation and formation mechanisms of high-mass species in the downstream region of $\text{Ar}/\text{CF}_4/\text{O}_2$ plasmas. *Phys. Chem. Chem. Phys.*, 11:934–942, 2009.
329. P. Favia. Plasma deposition of fluoropolymer films in different glow discharge regimes. In H. Biederman, ed., *Plasma Polymer Films*, pp. 25–55. Imperial College Press, London, U.K., 2004.
330. M.J. Schabel, T.W. Peterson, and A.J. Muscat. Macromolecule formation in low density CF_4 plasmas: The influence of H_2 . *J. Appl. Phys.*, 93:1389–1402, 2003.
331. F. Fanelli, F. Fracassi, and R. d'Agostino. Deposition and etching of fluorocarbon thin films in atmospheric pressure DBDs fed with $\text{Ar}-\text{CF}_4-\text{H}_2$ and $\text{AR}-\text{CF}_4 - \text{O}_2$ mixtures. *Surf. Coat. Technol.*, 204:1779–1784, 2010.
332. I.C. Plumb and K.R. Ryan. A model of the chemical processes occurring in CF_4/O_2 discharges used in plasma etching. *Plasma Chem. Plasma P.*, 6(3):205–230, 1986.
333. R. Basner, M. Schmidt, K. Becker, and H. Deutsch. Electron impact ionization of organic silicon compounds. In B. Bederson and H. Walther, eds., *Fundamentals of Plasma Chemistry*, Vol. 43 of *Advances in Atomic, Molecular, and Optical Physics*, pp. 147–185. Academic Press, San Diego, CA, 2000.
334. C. Rau and W. Kulisch. Mechanisms of plasma polymerization of various silico-organic monomers. *Thin Solid Films*, 249(1):28–37, 1994.
335. M.J. Vasile and G. Smolinsky. Organosilicon films formed by an rf plasma polymerization process. *J. Electrochem. Soc.*, 119(4):451–455, 1972.
336. Y. Catherine, G. Turban, and B. Grolleau. Reaction mechanisms in plasma deposition of $\text{Si}_x\text{C}_{1-x}:\text{H}$ films. *Thin Solid Films*, 76:23–33, 1981.
337. B.V. Tkachuk, V.V. Bushin, V.M. Kolotyrkin, and N.P. Smetankina. Polymerization of organosilicon compounds on metal surface caused by glow discharge. *Vysokomol. Soedin. A*, 9A(9):2018–2024, 1967.
338. S.P. Mukherjee and P.E. Evans. The deposition of thin films by the decomposition of tetra-ethoxy silane in a radio frequency glow discharge. *Thin Solid Films*, 14:105–118, 1972.

339. F. Dénes, C. Ungurenasu, and I. Haiduc. Plasma, polymerization in electrical discharges—III. Condensation of octamethylcyclotetrasiloxane in a silent discharge. *Eur. Polym. J.*, 6:1155–1160, 1970.
340. M. Schmidt. Zur Stabilität der Entladungsbedingungen bei der Glimmpolymerisation von Hexamethyldisiloxan. *Beitr. Plasmaphys.*, 13(6):347–353, 1973.
341. J. Marec and P. Leprince. Microwave discharges: Structures and stability. In C.M. Ferreira and M. Moisan, eds., *Microwave Discharges Fundamentals and Applications*, pp. 45–63. Plenum Press, New York, 1993.
342. Y. Segui and B. Ai. Gas discharge in hexamethyldisiloxane. *J. Appl. Polym. Sci.*, 20(6):1611–1618, 1976.
343. G. Grundmeier and M. Stratmann. Nucleation and growth of plasma-polymerised hexamethyldisilazane on iron-substrates. *Ber. Bunsen Phys. Chem.*, 99:1387–1392, 1995.
344. J. Tyczkowski and M. Kryszewski. Photoinjection into plasma-polymerised organosilicon thin films. I. Surface states. *J. Phys. D Appl. Phys.*, 14(10):1877–1888, 1981.
345. C.Q. Jiao, C.A. DeJoseph Jr., and A. Garscadden. Ion chemistries in hexamethyldisiloxane. *J. Vac. Sci. Technol. A*, 23:1295–1304, 2005.
346. P.F. Kurunczi, A. Koharian, K. Becker, and K. Martus. Dissociative excitation of tetramethylsilane (TMS) and hexamethyldisiloxane (HMDSO) by controlled electron impact. *Contrib. Plasma Phys.*, 36:723–735, 1996.
347. R. Seefeldt and M. Schmidt. Neutral-gas and polymer-film mass-spectrometry—Argon-hexamethyldisiloxane low-pressure glow-discharge. *Z. Phys. Chem. Leipzig*, 270(2):427–441, 1989.
348. J. Röpcke, G. Revalde, M. Osiac, K. Li, and J. Meichsner. Tunable diode laser absorption studies of hydrocarbons in rf plasmas containing hexamethyldisiloxane. *Plasma Chem. Plasma Process.*, 22(1):137–157, 2002.
349. M. Creatore, Y. Barrell, J. Benedikt, and M.C.M van de Sanden. On the hexamethyl-disiloxane dissociation paths in a remote Ar-fed expanding thermal plasma. *Plasma Sources Sci. Technol.*, 15:421–431, 2006.
350. W. Möller and M. Schmidt. Untersuchungen zur Löslichkeit von Hexamethyldisiloxan-Glimmpolymerschichten. *Plaste Kautsch.*, 25:635–638, 1978.
351. H. Grünwald, R. Adam, J. Bartella, M. Jung, W. Dicken, S. Kunkel, K. Nauenburg et al. Better aluminium mirrors by integrating plasma pretreatment, sputtering, and plasma polymerization for large-scale car headlight production. *Surf. Coat. Technol.*, 111:287–296, 1999.
352. E. Bapin and P.R. von Rohr. Deposition of SiO₂ films from different organosilicon/O₂ plasmas under continuous wave and pulsed modes. *Surf. Coat. Technol.*, 142–144:649–654, 2001.
353. D. Hegemann, H. Brunner, and C. Oehr. Deposition rate and three-dimensional uniformity of rf plasma deposited SiO_x films. *Surf. Coat. Technol.*, 142–144:849–855, 2001.
354. A. Granier, C. Valle, A. Goulet, K. Aumaille, and G. Turban. Experimental investigation of the respective roles of oxygen atoms and electrons in the deposition of SiO₂ in O₂/TEOS helicon plasmas. *J. Vac. Sci. Technol. A*, 17:2470–2474, 1999.
355. J. Schäfer, R. Foest, A. Quade, A. Ohl, and K.-D. Weltmann. Local deposition of SiO_x plasma polymer films by a miniaturized atmospheric pressure plasma jet (APPJ). *J. Phys. D Appl. Phys.*, 41(19):194010, 2008.
356. J. Schäfer, R. Foest, A. Quade, A. Ohl, and K.-D. Weltmann. Chemical composition of SiO_x films deposited by an atmospheric pressure plasma jet (APPJ). *Plasma Process. Polym.*, 6(S1):S519–S524, 2009.

357. K. Li and J. Meichsner. Gas-separating properties of membranes coated by HMDSO plasma polymer. *Surf. Coat. Technol.*, 116–119:841–847, 1999.
358. J.C. Shearer, M.J. Fisher, D. Hoogeland, and E.R. Fisher. Composite SiO₂/TiO₂ and amine polymer/TiO₂ nanoparticles produced using plasma-enhanced chemical vapor deposition. *Appl. Surf. Sci.*, 256:2081–2091, 2010.
359. D.P. Denis, T. Barry, and B. Gerry. Effect of titanium oxide nanoparticle incorporation into nm thick coatings deposited using an atmospheric pressure plasma. *J. Nanosci. Nanotechno.*, 10:2746–2752, 2010.
360. T. Takeno, S. Abe, K. Adachi, H. Miki, and T. Takagi. Deposition and structural analyses of molybdenum-disulfide (MoS₂)amorphous hydrogenated carbon (a-C:H) composite coatings. *Diam. Relat. Mater.*, 19(5–6):548–552, 2010.
361. E. Dilonardo, A. Milella, F. Palumbo, G. Capitani, R. d'Agostino, and F. Fracassi. One-step plasma deposition of platinum containing nanocomposite coatings. *Plasma Process. Polym.*, 7:51–58, 2010.
362. B. Despax and P. Raynaud. Deposition of “polysiloxane” thin films containing silver particles by an rf asymmetrical discharge. *Plasma Process. Polym.*, 4:127–134, 2007.
363. H. Biederman and L. Holland. Metal doped fluorocarbon polymer films prepared by plasma polymerization using an rf planar magnetron target. *Nucl. Instrum. Meth.*, 212:497–503, 1983.
364. H. Biederman. Metal doped polymer films prepared by plasma polymerization and their potential applications. *Vacuum*, 34:405–410, 1984.
365. H. Biederman, P. Kudrna, and D. Slavinskci. Hard plasma polymers, composites and plasma polymer films prepared by rf sputtering of conventional polymers. In H. Biederman, ed., *Plasma Polymer Films*, pp. 289–324. Imperial College Press, London, U.K., 2004.
366. N. Inagaki, T. Nishio, and K. Katsuura. Some optical properties of polymer films prepared by glow discharge polymerization from methane, tetramethylsilane, and tetramethyltin. *J. Polym. Sci. Polym. Lett. Ed.*, 18:765–770, 1980.
367. C. Oehr and H. Suhr. Thin films prepared from tetramethyltin. *Thin Solid Films*, 155:65–74, 1987.
368. H. Suhr. Applications and trends in plasma-enhanced organometallic chemical vapour deposition. *Surf. Coat. Technol.*, 49(1–3).
369. R. Schmittgens, M. Wolf, and E. Schultheiss. A versatile system for large area coating of nanocomposite thin films. *Plasma Process. Polym.*, 6(S1):S912–S916, 2009.
370. A. Fridman. *Plasma Chemistry*. Cambridge University Press, Cambridge, U.K., 2008.
371. H.-E. Wagner, J.F. Behnke, and H. Lange. Dissociation of titanium tetrachloride to titanium in hollow-cathode glow-discharge .2. Mechanism of dissociation. *Pol. J. Chem.*, 58:561–568, 1984.
372. J. Röpke, P.B. Davies, F. Hempel, and B.P. Lavrov. Diagnostic emission and absorption spectroscopy of nonequilibrium molecular plasmas. In R. Hippler, H. Kersten, M. Schmidt, and K.H. Schoenbach, eds., *Low Temperature Plasma*, Vol. 1, p. 215. Wiley-VCH, Berlin, Germany, 2008.
373. B. Chapman. *Glow Discharge Processes*. John Wiley & Sons, New York, 1980.
374. A. Quade, H. Wulff, H. Steffen, T.M. Tun, and R. Hippler. Investigation of the aluminium oxidation in an oxygen plasma excited by microwaves. *Thin Solid Films*, 377/278:626–630, 2000.
375. A. Quade, H. Steffen, R. Hippler, and H. Wulff. Kinetic aspects of the formation of aluminium oxide by use of a microwave-induced plasma. *Anal. Bioanal. Chem.*, 374:720–723, 2002.

376. M. Quaas, H. Wulff, O. Ivanova, and C.A. Helm. Plasma chemical reactions of thin nickel films. *Surf. Interface Anal.*, 40:552–555, 2008.
377. H.L. Hartnagel, A.W. Dawar, A.K. Jain, and C. Jagadish. *Semiconducting Transparent Thin Films*. Institute of Physics Publishing, Philadelphia, PA, 1995.
378. B. Szyska. Transparente und leitfähige Oxidschichten—Transparent and conductive oxide layers. *Vak. Forsch. Prax.*, 1:38–45, 2001.
379. E. Burstein. Anomalous optical absorption limit in InSb. *Phys. Rev.*, 93:632–633, 1954.
380. K. Ellmer. Resistivity of polycrystalline zinc oxide films: Current status and physical limit. *J. Phys. D Appl. Phys.*, 34:3097–3108, 2001.
381. K.L. Chopra, S. Major, and D.K. Pandya. Transparent conductors—Status review. *Thin Solid Films*, 102(1):1–46, 1983.
382. T. Minami. Theme article—New n-type transparent conducting oxides. *MRS Bull.*, 25(8):38–44, 2000.
383. M. Quaas, C. Eggs, and H. Wulff. Structural studies of ITO thin films with the Rietveld method. *This Solid Films*, 332:277–281, 1998.
384. M. Quaas, H. Wulff, H. Steffen, and R. Hippler. Investigation of diffusion and crystallization processes in thin ITO films by temperature and time resolved grazing incidence x-ray diffractometry. *Surf. Sci.*, 540:337–342, 2003.
385. T. Minami. Transparent conducting oxide semiconductors for transparent electrodes. *Semicond. Sci. Technol.*, 20:S35–S44, 2005.
386. W. Beyer, J. Hüpkens, and H. Stiebig. Transparent conducting oxide films for thin film silicon photovoltaics. *Thin Solid Films*, 516:147–154, 2007.
387. S.M. Rossnagel, J.J. Cuomo, and W.D. Westword, eds., *Handbook of Plasma Processing Technology*. Noyes Publications, Park Ridge, IL, 1990.
388. K. Ellmer. Magnetron discharges for thin film deposition. In R. Hippler, H. Kersten, M. Schmidt, and K.H. Schoenbach, eds., *Low Temperature Plasma*, Vol. 2, p. 675. Wiley-VCH, Berlin, Germany, 2008.
389. C. May, R. Menner, J. Strümpfel, M. Oertel, and B. Sprecher. Deposition of TCO films by reactive magnetron sputtering from metallic Zn:Al alloy targets. *Surf. Coat. Technol.*, 169–170:512–516, 2003.
390. K. Ellmer. Magnetron sputtering of transparent conductive zinc oxide: Relation between the sputtering parameters and the electronic properties. *J. Phys. D Appl. Phys.*, 33:R17–R32, 2000.
391. H. Holleck and H. Schulz. Preparation and behaviour of wear-resistant TiC/TiB₂, TiN/TiB₂ and TiC/TiN coatings with high amounts of phase boundaries. *Surf. Coat. Technol.*, 36(3–4):707–714, 1988.
392. H. Holleck, M. Lahres, and P. Woll. Multilayer coatings—Influence of fabrication parameters on constitution and properties. *Surf. Coat. Technol.*, 41:179–190, 1990.
393. O. Knotek, F. Löffler, and G. Krämer. Multicomponent and multilayer physically vapour deposited coatings for cutting tools. *Surf. Coat. Technol.*, 54/55:241–248, 1992.
394. O. Knotek, F. Löffler, and G. Krämer. Process and advantage of multicomponent and multilayer PVD coatings. *Surf. Coat. Technol.*, 59:14–20, 1993.
395. R. Ferguson, J. Rechberger, H. Curtins, and R. Dubach. Hard-soft: A new age of industrial coatings, society of vacuum coaters. In Society of Vacuum Coaters, ed., *SVC—40th Annual Technical Conference Proceedings*, Telemark. Fremont, CA, 1997.
396. H. Holleck. Design of nanostructured thin films for tribological applications. In A. Kumar, Y.-W. Chung, J.J. Moore, and J.E. Smugeresky, eds., *Surface Engineering: Science and Technology*, Vol. I. The Minerals, Metals and Materials Society, San Diego, CA, 1999.

397. D.T. Quinto. Hard coating technology update. In Society of Vacuum Coaters, ed., *SVC—42nd Annual Technical Conference Proceedings*, Denton Vacuum, LLC. Moorestown, NY, 1999.
398. D.M. Mattox and D.T. Quinto. Twenty-five years of PVD coatings at the cutting edge. In Society of Vacuum Coaters, ed., *SVC—50th Annual Technical Conference Proceedings*, Kentucky International Convention Center. Louisville, KY, 2007.
399. S. Schiller, K. Goedcke, J. Reschke, V. Kirchhoff, S. Schneider, and F. Milde. Pulsed magnetron sputter technology. *Surf. Coat. Technol.*, 61:331–337, 1993.
400. R.A. Haefer. *Oberflächen- und Dünnsschicht-Technologie, Teil I: Beschichtung von Oberflächen*. Springer-Verlag, Berlin, Germany, 1987.
401. S. Kadlec, J. Musil, W.-D. Münz, G. Hakanson, and S. Sundgren. Reactive deposition of tin films using an unbalanced magnetron. *Surf. Coat. Technol.*, 39–40:487–497, 1989.
402. W.D. Sproul, M.E. Graham, M.-S. Wong, P.J. Rudnik, and K.O. Legg. In D.A. Glockner, S.I. Shah, and W.D. Westwood, eds., *Handbook of Thin Film Technology*. IOP Publishing, Bristol, U.K., 1998.
403. I.Y. Konyashin. The influence of Fe-group metals on the CVD of titanium carbide. *Chem. Vap. Depos.*, 2(5):199–208, 1996.
404. M. Sato, T. Ohgiyama, and J.S. Clements. Formation of chemical species and their effects on microorganisms using a pulsed high-voltage discharge in water. *IEEE Trans. Ind. Appl.*, 32(1):106–112, 1996.
405. B. Sun, M. Sato, and J.S. Clements. Optical study of active species produced by a pulsed streamer corona discharge in water. *J. Electrostat.*, 39:189–202, 1997.
406. S. Ihara, T. Miichi, S. Satoh, and C. Yamabe. Ozone generation by a discharge in bubbled water. In *IEEE Proceedings of the 12th IEEE Pulsed Power Conference*, IEEE. vol. 2, pp. 1291–1294, Monterey, CA, 1999.
407. H. Akiyama. Streamer discharges in liquids and their applications. *IEEE Trans. Dielectr. Electr. Insul.*, 7:646–653, 2000.
408. A.M. Anpilov, E.M. Barkhudarov, Y.B. Bark, Y.V. Zadiraka, M. Christofi, Y.N. Kozlov, et al. Electric discharge in water as a source of UV radiation, ozone and hydrogen peroxide. *J. Phys. D Appl. Phys.*, 34:993–999, 2001.
409. A. Abou-Ghazala, S. Katsuki, K.H. Schoenbach, F.C. Dobbs, and K.R. Moreira. Bacterial decontamination of water by means of pulsed-corona discharges. *IEEE Trans. Plasma Sci.*, 30(4, Part 1):1449–1453, 2002.
410. P. Lukes, A.T. Appleton, and B. Locke. Hydrogen peroxide and ozone formation in hybrid gas-liquid electrical discharge reactors. *IEEE Trans. Ind. Appl.*, 40(1):60–67, 2004.
411. P. Lukes and B. Locke. Degradation of substituted phenols in a hybrid gas-liquid electrical discharge reactor. *Ind. Eng. Chem. Res.*, 44(9):2921–2930, 2005.
412. P. Bruggeman and C. Leys. Non-thermal plasmas in and in contact with liquids. *J. Phys. D Appl. Phys.*, 42:053001, 2009.
413. P. Sunka, V. Babický, M. Clupek, P. Lukes, M. Simek, J. Schmidt, and M. Černák. Generation of chemically active species by electrical discharges in water. *Plasma Sources Sci. Technol.*, 8:258–265, 1999.
414. T. Miichi, S. Ihara, S. Satoh, and C. Yamabe. Spectroscopic measurements of discharges inside bubbles in water. *Vacuum*, 59:236–243, 2000.
415. C. Yamabe, F. Takeshita, T. Miichi, N. Hayashi, and S. Ihara. Water treatment using discharge on the surface of a bubble in water. *Plasma Process. Polym.*, 2:246–251, 2005.

416. S. Gershman, O. Mozgina, A. Belkind, K. Becker, and E. Kunhardt. Pulsed electrical discharge in bubbled water. *Contrib. Plasma Phys.*, 47:19–25, 2007.
417. C.J. Hochanadel. Effects of cobalt gamma-radiation on water and aqueous solutions. *J. Phys. Chem.*, 56:587–594, 1952.
418. B. Sun, M. Sato, and J. Clemens. Use of a pulsed high-voltage discharge for removal of organic compounds in aqueous solution. *J. Phys. D Appl. Phys.*, 32:1908–1915, 1999.
419. Y. Wen, H. Liu, W. Liu, and X. Jiang. Degradation of organic contaminants in water by pulsed corona discharge. *Plasma Chem. Process.*, 25:137–146, 2005.
420. S. Gershman, O. Mozgina, A. Belkind, and K. Becker. Pulsed electrical discharges in water for decontamination applications. In V. Grill and T.D. Märk, eds., *15th Symposium on Atomic and Surface Physics and Related Phenomena*, pp. 136–139. University of Innsbruck Press, Innsbruck, Austria, 2006.
421. K.-D. Zoh and M.K. Stenstrom. Fenton oxidation of hexahydro-1,3,5-trinitro-1,3,5-triazine (RDX) and octahydro-1,3,5,7-tetranitro-1,3,5,7-tetrazocine (HMX). *Water Res.*, 36:1331–1341, 2002.
422. A. Bouchoule, ed. *Dusty Plasmas: Physics, Chemistry and Technological Impacts in Plasma Processing*. Wiley, New York, 1999.
423. G. Mariaux, P. Fauchais, A. Vardelle, and S. Pateyron. Modeling of the plasma spray process: From powder injection to coating formation. *High Temp. Mater. Proc.*, 5:61–85, 2001.
424. B. Dzur, H. Wilhelmi, and G. Nutsch. The deformation and cooling of ceramic particles sprayed with a thermal radio-frequency plasma under atmospheric conditions. *J. Therm. Spray Technol.*, 10:637–642, 2001.
425. M. Kogoma, K. Tanaka, and A. Takeda. Powder treatments using atmospheric pressure glow plasma. *J. Photopolym. Sci. Technol.*, 18(2):277–280, 2005.
426. C. Hollenstein, W. Schwarzenbach, A.A. Howling, and C. Courteille. Anionic clusters in dusty hydrocarbon and silane plasmas. *J. Vac. Sci. Technol. A*, 14:535–539, 1996.
427. H.H. Anderson, S. Radovanov, J.L. Mock, and P.J. Resnick. Particles in C_2F_6 -CHF₃ and CF₄-CHF₃ etching plasmas. *Plasma Sources Sci. Technol.*, 3:302–309, 1994.
428. A. Garscadden, B.N. Ganguly, P.D. Haaland, and J. Williams. Overview of growth and behaviour of clusters and particles in plasmas. *Plasma Sources Sci. Technol.*, 3:239–245, 1994.
429. P. Roca, I. Cabarocas, P. Gay, and A. Hadjadj. Experimental evidence for nanoparticle deposition in continuous argon-silane plasmas: Effects of silicon nanoparticles on film properties. *J. Vac. Sci. Technol. A*, 14:655–659, 1996.
430. H. Kersten, H. Deutsch, E. Stoffels, W.W. Stoffels, and G.M.W. Kroesen. Plasma-powder interaction: Trends in applications and diagnostics. *Int. J. Mass Spectrom.*, 223/224:313–325, 2003.
431. S.V. Vladimirov, K. Ostikov, and A.A. Samarian. *Physics and Applications of Complex Plasmas*. Imperial College Press, London, U.K., 2005.
432. L. Boufendi and A. Bouchoule. Particle nucleation and growth in a low-pressure argon-silane discharge. *Plasma Sources Sci. Technol.*, 3:262–267, 1994.
433. C. Hollenstein. The physics and chemistry of dusty plasmas. *Plasma Phys. Contr. F.*, 42:R93–R104, 2000.
434. U. Kortshagen and U. Bhandarkar. Modeling of particulate coagulation in low pressure plasmas. *Phys. Rev. E*, 60:887–898, 1999.
435. Y. Watanabe, H. Shiratani, and K. Koga. Formation kinetics and control of dust particles in capacitively-coupled reactive plasmas. *Phys. Scripta*, T89:29–32, 2001.

436. M. Schulze, A. von Keudell, and P. Awakowicz. Controlled particle generation in an inductively coupled plasma. *Appl. Phys. Lett.*, 88:141503, 2006.
437. S. Hong, J. Berndt, and J. Winter. Growth precursors and dynamics of dust particle formation in the Ar/CH₄ and Ar/C₂H₂ plasmas. *Plasma Sources Sci. Technol.*, 12:46–52, 2003.
438. E. Kovacevic, I. Stefanovic, J. Berndt, and J. Winter. Infrared fingerprints and periodic formation of nanoparticles in Ar/C₂H₂ plasmas. *J. Appl. Phys.*, 93:2924–2930, 2003.
439. H.T. Do, G. Thieme, M. Fröhlich, H. Kersten, and R. Hippler. Ion molecule and dust particle formation in Ar/CH₄, Ar/C₂H₂ and Ar/C₃H₆ radio-frequency plasmas. *Contrib. Plasma Phys.*, 45:378–384, 2005.
440. J. Röpcke, L. Mechold, M. Käning, J. Anders, F.G. Wienhold, D. Nelson, and M. Zahniser. IRMA: A tunable infrared multicomponent acquisition system for plasma diagnostics. *Rev. Sci. Instr.*, 71:3706–3710, 2000.
441. M. Shiratani, K. Sakamoto, K. Maeda, S. Koga, and Y. Watanabe. Effects of gas temperature gradient, pulse discharge modulation, and hydrogen dilution on particle growth in silane rf discharges. *Jpn. J. Appl. Phys.*, 39:287–293, 2000.
442. R.P. Dahiya, G.V. Paeva, W.W. Stoffels, E. Stoffels, G.M.W. Kroesen, K. Avinash, and A. Bhattacharjee. Evolution of a dust void in a radio-frequency plasma sheath. *Phys. Rev. Lett.*, 89:125001, 2002.
443. M. Wolter, A. Melzer, O. Arp, M. Klindworth, and A. Piel. Force measurements in dusty plasmas under microgravity by means of laser manipulation. *Phys. Plasmas*, 14:123707, 2007.
444. J.C. Schauer, S. Hong, and J. Winter. Electrical measurements in dusty plasmas as a detection method for the early phase of particle formation. *Plasma Sources Sci. Technol.*, 13:636–645, 2004.
445. H. Haberland, M. Mall, M. Moseler, Y. Qiang, T. Reiners, and Y. Thurner. Filling of micron-sized contact holes with copper by energetic cluster impact. *J. Vac. Sci. Technol. A*, 12:2925–2930, 1994.
446. K.H. Meiwes-Broer. *Metal Clusters at Surfaces*. Springer, New York, 1997.
447. P. Jensen. Growth of nanostructures by cluster deposition: Experiments and simple models. *Rev. Mod. Phys.*, 71:1695–1735, 1999.
448. I. Shyjumon, M. Gopinadhan, C.A. Helm, B.M. Smirnov, and R. Hippler. Deposition of titanium/titanium oxide clusters produced by magnetron sputtering. *Thin Solid Films*, 500:41–51, 2006.
449. I. Shyjumon, M. Gopinadhan, O. Ivanova, M. Quaas, H. Wulff, C.A. Helm, and R. Hippler. Structural deformation, melting point and lattice parameter studies of size selected silver clusters. *Eur. Phys. J. D*, 37:409–415, 2006.
450. B.M. Smirnov, I. Shyjumon, and R. Hippler. Formation of clusters through generation of free atoms. *Phys. Scripta*, 73:288–295, 2006.
451. B.M. Smirnov. Processes in expanding and condensing gases. *Sov. Phys. Uspekhi*, 37:621–657, 1994.
452. H. Kersten, H. Deutsch, E. Stoffels, W.W. Stoffels, G.M.W. Kroesen, and R. Hippler. Micro-disperse particles in plasmas: From disturbing side effects to new applications. *Contrib. Plasma Phys.*, 41:598–609, 2001.
453. M.C. Roco, S. Williams, and P. Alivisatos, eds. *Nanotechnology Research Directions: Vision for Nanotechnology Research and Development in the Next Decade*. Kluwer Academic, Amsterdam, the Netherlands, 1999.
454. A. Hadjadj, L. Boufendi, S. Huet, S. Schelz, P. Roca, I. Cabarcas, H. Estrade, and B. Rousseau. Role of the surface roughness in laser induced crystallization of nanostructured silicon films. *J. Vac. Sci. Technol. A*, 18:529–535, 2000.

455. E. Stoffels, W.W. Stoffels, H. Kersten, G.H.P.M. Swinkels, and G.M.W. Kroesen. Surface processes of dust particles in low pressure plasmas. *Phys. Scripta*, T89:168–172, 2001.
456. H. Kersten, P. Schmetz, and G.M.W. Kroesen. Surface modification of powder particles by plasma deposition of thin metallic films. *Surf. Coat. Technol.*, 108–109:507–512, 1998.
457. H. Kersten, G. Thieme, M. Fröhlich, D. Bojic, D.H. Tung, M. Quaas, H. Wulff, and R. Hippler. Complex (dusty) plasmas: Examples for applications and observation of magnetron-induced phenomena. *Pure Appl. Chem.*, 77:415–428, 2005.
458. H. Kersten, R. Wiese, G. Thieme, M. Fröhlich, A. Kopitov, D. Bojic, et al. Examples for application and diagnostics in plasma-powder interaction. *New J. Phys.*, 5:93, 2003.

CHAPTER 9

1. D.B. Graves. Plasma processing. *IEEE Trans. Plasma Sci.*, 22:31–42, 1994.
2. J.O. Hirschfelder, C.F. Curtis, and R.B. Bird. *Molecular Theory of Gases and Liquids*, 2nd edn. Wiley, New York, 1964.
3. E.A. Desloge. *Statistical Physics*. Holt, Rinehart and Winston, New York, 1966.
4. I.P. Shkarofsky, T.W. Johnston, and M.P. Bachynski. *The Particle Kinetics of Plasmas*. Addison-Wesley, London, U.K., 1966.
5. S. Chapman and T.G. Cowling. *The Mathematical Theory of Non-Uniform Gases*. Cambridge University Press, Cambridge, U.K., 1995.
6. C.J. Joachain. *Quantum Collision Theory*. North-Holland, Amsterdam, the Netherlands, 1975.
7. V.E. Golant, A.P. Zhilinsky, and I.E. Sakharov. *Fundamentals of Plasma Physics*. Wiley, New York, 1980.
8. B. Carnahan, H.A. Luther, and J.O. Wilkes. *Applied Numerical Methods*. Wiley, New York, 1969.
9. <http://www.reactiondesign.com/products/open/chemkin.html>
10. A.R. Curtis and W.P. Sweetenham. Facsimile/Chekmat users manual, Technical report. Computer Science and Systems Division. Harwell Laboratory, Oxfordshire, Great Britain, U.K., 1987.
11. https://computation.llnl.gov/casc/odepack/odepack_home.html
12. F. Hempel, P.B. Davies, D. Loffhagen, L. Mechold, and J. Röpcke. Diagnostic studies of H₂-Ar-N₂ microwave plasmas containing methane or methanol using tunable infrared diode laser absorption spectroscopy. *Plasma Sources Sci. T.*, 12:S98–S110, 2003.
13. J.P. Boeuf. Plasma display panels: physics, recent developments and key issues. *J. Phys. D Appl. Phys.*, 36:R53–R79, 2003.
14. H.C. Kim, F. Iza, S.S. Yang, M. Radmilović-Radjenović, and J.K. Lee. Particle and fluid simulations of low-temperature plasma discharges: Benchmarks and kinetic effects. *J. Phys. D Appl. Phys.*, 38:R283–R301, 2005.
15. D. Loffhagen and F. Sigenerger. Advances in Boltzmann equation based modelling of discharge plasmas. *Plasma Sources Sci. Technol.*, 18(3):034006, 2009.
16. G.M. Janssen, J. van Dijk, D.A. Benoy, M.A. Tas, K.T.A.L. Burm, W.J. Goedheer, J.A.M. van der Mullen, and D.C. Schram. PLASIMO, a general model: I. Applied to an argon cascaded arc plasma. *Plasma Sources Sci. Technol.*, 8:1–14, 1999.
17. B. Lay, R.S. Moss, S. Rauf, and M.J. Kushner. Breakdown processes in metal halide lamps. *Plasma Sources Sci. Technol.*, 12:8–21, 2003.

18. M.J. Kushner. Modelling of microdischarge devices: Plasma and gas dynamics. *J. Phys. D Appl. Phys.*, 38:1633–1643, 2005.
19. R.D. Richtmyer and K.W. Morton. *Difference Methods for Initial Value Problems*, 2nd edn. Wiley, New York, 1967.
20. R. Courant, K. Friedrichs, and H. Lewy. Über die partiellen differenzengleichungen der mathematischen physik. *Math. Ann.*, 100:32–74, 1928.
21. J. von Neumann and R.D. Richtmyer. A method for the numerical calculation of hydrodynamic shocks. *J. Appl. Phys.*, 21:232–237, 1950.
22. O.C. Zienkiewicz, R.L. Taylor, and P. Nithiarasu. *The Finite Element Method for Fluid Dynamics*, 6th edn. Elsevier Butterworth-Heinemann, Amsterdam, the Netherlands, 2005.
23. D.L. Scharfetter and H.K. Gummel. Large-signal analysis of a silicon read diode oscillator. *IEEE Trans. Electron Dev.*, 16:64–77, 1969.
24. O. Zienkiewicz, R. Taylor, and J.Z. Zhu. *The Finite Element Method—Its Basis and Fundamentals*, 6th edn. Elsevier Butterworth-Heinemann, Amsterdam, the Netherlands, 2005.
25. <http://www.femlab.de/products/multiphysics/research/tutorials/>
26. H. Verstaag and W. Malalasekra. *An Introduction to Computational Fluid Dynamics: The Finite Volume Method*, 2nd edn. Prentice Hall, NJ, 2007.
27. <http://www.ansys.com/products/cfx.asp>
28. <http://www.esi-cfd.com/content/blogcategory/90/114/>
29. <http://www.fluent.com/software/fluent/index.htm>
30. <http://www.cham.co.uk/default.php>
31. <http://www.cd-adapco.com/products/STAR-CD/index.html>
32. R. Winkler, J. Wilhelm, and V. Schüller. Legendre-Polynom-Entwicklung und allgemeine Kugelflächenfunktionsentwicklung in der Boltzmann-Gleichung des Lorentz-Plasmas. *Contrib. Plasma Phys.*, 10:51–77, 1970.
33. R. Winkler, D. Loffhagen, and F. Sigeneger. Temporal and spatial relaxation in low temperature plasmas. In T. Makabe, ed., *Advances in Low Temperature RF Plasmas: Basis for Process Design*, pp. 50–71. Elsevier, Amsterdam, the Netherlands, 2002.
34. N.R. Pinhão, Z. Donkó, D. Loffhagen, M.J. Pinheiro, and E.A. Richley. Comparison of kinetic calculation techniques for the analysis of a electron swarm transport at low and moderate E/N values. *Plasma Sources Sci. Technol.*, 13:719–728, 2004.
35. M. Hannemann, P. Hardt, D. Loffhagen, M. Schmidt, and R. Winkler. The electron kinetics in the cathode region of H₂/Ar/N₂ discharges. *Plasma Sources Sci. T.*, 9:387–399, 2000.
36. G.J.M. Hagelaar and L.C. Pitchford. Solving the Boltzmann equation to obtain electron transport coefficients and rate coefficients for fluid models. *Plasma Sources Sci. Technol.*, 14:722–733, 2005. <http://www.laplace.univ-tlse.fr/-BOLSIG-Resolution-de-l-equation-de>
37. C.K. Birdsall and A.B. Langdon. *Plasma Physics via Computer Simulation*. Adam Hilger, Bristol, U.K., 1991.
38. R.W. Hockney and J.W. Eastwood. *Computer Simulation Using Particles*. IOP, Bristol, U.K., 1994.
39. S. Longo. Monte Carlo models of electron and ion transport in non-equilibrium plasmas. *Plasma Sources Sci. Technol.*, 9:468–476, 2006.
40. D. Loffhagen, R. Winkler, and Z. Donkó. Boltzmann equation and Monte Carlo analysis of the spatiotemporal electron relaxation in nonisothermal plasmas. *Eur. Phys. J. Appl. Phys.*, 18:189–200, 2002.

41. M.M. Turner. Kinetic properties of particle-in-cell simulations compromised by Monte Carlo collisions. *Phys. Plasmas*, 13:033506, 2006.
42. ptsg.eecs.berkeley.edu
43. M. Surendra. Radio frequency discharge benchmark model comparison. *Plasma Sources Sci. Technol.*, 4:56–73, 1995.
44. A. Bogaerts and R. Gijbels. Numerical modelling of gas discharge plasmas for various applications. *Vacuum*, 69:37–52, 2003.
45. Z. Donkó, P. Hartmann, and K. Kutasi. On the reliability of low-pressure DC glow discharge modelling. *Plasma Sources Sci. Technol.*, 15:178–186, 2006.
46. V.I. Kolobov. Fokker-Planck modeling of electron kinetics in plasmas and semiconductors. *Comp. Mater. Sci.*, 28:302–320, 2003.
47. U. Fano. Unified treatment of collisions. *Phys. Rev. A*, 24:2402–2415, 1981.
48. M.J. Brunger and S.J. Buckman. Electron-molecule scattering cross sections. I. Experimental techniques and data for diatomic molecules. *Phys. Rep.*, 357:215–458, 2002.
49. L.G. Christophorou and J.K. Olthoff. *Fundamental Electron Interactions with Plasma Processing Gases*. Kluwer Academic/Plenum Publishers, New York, 2004.
50. W.L. Morgan. In M. Inokuti and K.H. Becker, eds., *Advances in Atomic, Molecular, and Optical Physics*, Vol. 43, p. 79. Academic Press, San Diego, CA, 2000.
51. P.G. Burke and J. Tennyson. R-matrix theory of electron-molecule scattering. *Mol. Phys.*, 103:2537, 2005.
52. C. Winstead and V. McKoy. Parallel computational studies of electron-molecule collisions. *Comp. Phys. Commun.*, 128:386, 2000.
53. H. Bethe. Theory of the passage of rapid corpuscular rays through matter. *Ann. Phys. (Leipzig)*, 5:325–400, 1930.
54. L. Vriens. In E.W. McDaniel and M.R.C. McDowell, eds., *Case Studies in Atomic Physics*, Vol. 1, p. 335. North-Holland, Amsterdam, the Netherlands, 1969.
55. Y.-K. Kim and M.E. Rudd. Binary-encounter-dipole model for electron-impact ionization. *Phys. Rev. A*, 50:3954–3967, 1994.
56. H. Deutsch, K. Becker, S. Matt, and T.D. Maerk. Theoretical determination of absolute electron-impact ionization cross sections of molecules. *Int. J. Mass. Spectrom.*, 197:37, 2000.
57. H. Deutsch, P. Scheier, K. Becker, and T.D. Maerk. Revised high energy behavior of the Deutsch-Maerk (DM) formula for the calculation of electron impact ionization cross sections of atoms. *Int. J. Mass. Spectrom.*, 233:13, 2004.
58. H. Deutsch, P. Scheier, S. Matt-Leubner, K. Becker, and T.D. Maerk. A detailed comparison of calculated and measured electron-impact ionization cross sections of atoms using the Deutsch-Maerk (DM) formalism. *Int. J. Mass. Spectrom.*, 243:215, 2005.
59. T.F. O’Malley. Theory of dissociative attachment. *Phys. Rev.*, 150:14–29, 1966.
60. J.N. Bardsley, A. Herzenberg, and F. Mandl. Vibrational excitation and dissociative attachment in the scattering of electrons by hydrogen molecules. *Proceedings of the Phys. Soc.*, 89:321, 1966.
61. J.N. Bardsley. Electron detachment and charge transfer in $h - h^-$ collisions. *Proc. Phys. Soc.*, 91:300, 1967.
62. A. Herzenberg. Electron-detachment in slow collisions between atoms and negative ions. *Phys. Rev.*, 160:80–94, 1967.
63. J.N. Bardsley. Configuration interaction in the continuum states of molecules. *J. Phys. B (Proc. of the Phys. Soc.)*, 1:349, 1968.
64. J.N. Bardsley. The theory of dissociative recombination. *J. Phys. B (Proceedings of the Phys. Soc.)*, 1:365, 1968.

65. L. Dube and A. Herzenberg. Absolute cross sections form the boomerang model for resonant electron-molecule scattering. *Phys. Rev. A*, 20:194–213, 1979.
66. R.E. Olson. Absorbing-sphere model for calculating ion-ion recombination total cross section. *J. Chem. Phys.*, 56:2979, 1972.
67. R.E. Olson, F.T. Smith, and E. Bauer. Estimation of the coupling matrix elements for one-electron transfer systems. *Appl. Opt.*, 10:1848, 1971.
68. E. Gerjuoy. Time-independent nonrelativistic collision theory. *Ann. Phys.*, 5:58–93, 1958.
69. R.G. Newton. *Scattering Theory of Waves and Particles*. McGraw-Hill Book Company, New York, 1966.
70. A.G. Sitenko. *Scattering Theory*. Springer-Verlag, Berlin, Germany, 1991.
71. M.R.H. Rudge. Theory of the ionization of atoms by electron impact. *Rev. Mod. Phys.*, 40:564–590, 1968.
72. J.N. Bardsley and F. Mandl. Resonant scattering of electrons by molecules. *Rep. Prog. Phys.*, 31:471–531, 1968.
73. M. Inokuti. Inelastic collisions of fast charged particles with atoms and molecules—The Bethe theory revisited. *Rev. Mod. Phys.*, 43:297–347, 1971.
74. N.F. Lane. The theory of electron-molecule collisions. *Rev. Mod. Phys.*, 52:29–119, 1980.
75. J.B. Delos. Theory of electronic transitions in slow atomic collisions. *Rev. Mod. Phys.*, 53:287–357, 1981.
76. A. Chutjian, A. Garscadden, and J.M. Wadehra. Electron attachment to molecules at low electron energies. *Phys. Rep.*, 264:393–470, 1996.
77. Y. Hahn. Electron-ion recombination processes—An overview. *Rep. Prog. Phys.*, 60:691–759, 1997.
78. A.I. Floreescu-Mitchell and J.B.A. Mitchell. Dissociative recombination. *Phys. Rep.*, 430:277–374, 2006.
79. L.W. Boltzmann. *Ber. Wien. Akad.*, 66:275, 1872.
80. J. Wilhelm and R. Winkler. Die beruecksichtigung der ionisation durch elektronenstoss in der elektronenkinetik des schwachionisierten anisothermen plasmas. *Ann. Phys.*, 36:333–351, 1979.
81. K. Matyash, R. Schneider, F. Taccogna, A. Hatayama, S. Longo, M. Capitelli, D. Tskhakaya, and F.X. Bronold. Particle in cell simulations of low temperature laboratory plasmas. *Contrib. Plasma Phys.*, 47:595–634, 2007.
82. M. Shugard and A.U. Hazi. Theory of electron-molecule scattering: Comments on the adiabatic nuclei approximation. *Phys. Rev. A*, 12:1895–1902, 1975.
83. W. Domcke. Theory of resonance and threshold effects in electron-molecule collisions: The projection-operator approach. *Phys. Rep.*, 208:97–188, 1991.
84. H.-D. Meyer. *Phys. Rev. A*, 40:5605–5613, 1989.
85. J. Brand, L.S. Cederbaum, and H.-D. Meyer. *Phys. Rev. A*, 60:2983–2999, 1999.
86. A.K. Kazansky and I.S. Yelets. The semiclassical approximation in the local theory of resonance inelastic interaction of slow electrons with molecules. *J. Phys. B At. Mol. Opt. Phys.*, 17:4767, 1984.
87. A.K. Kazansky and S.A. Kalin. Semiclassical approximation in the non-local theory of resonance processes in slow collisions of two atoms and an electron. *J. Phys. B At. Mol. Opt. Phys.*, 23:809, 1990.
88. S.A. Kalin and A.K. Kazansky. Semiclassical non-local treatment of the attachment of a slow electron in a three-body collision. *J. Phys. B At. Mol. Opt. Phys.*, 23:3017, 1990.
89. A. Giusti. A multichannel quantum defect approach to dissociative recombination. *J. Phys. B At. Mol. Phys.*, 13:3867, 1980.

90. S.A. Akhmanov, K.S. Klopovskii, and A.P. Osipov. Dissociative recombination of an electron and a molecular ion. *Sov. Phys. JETP*, 56:936, 1982.
91. D.E. Atoms and J.M. Wadehra. Resonant contribution to dissociation of h_2 by low-energy electron impact. *J. Phys. B At. Mol. Phys.*, 26:L759, 1993.
92. A. Jacob. Plasma processing. An art or science? *Solid State Technol.*, 26:151, 1983.
93. R.E.H. Clark and D.H. Reiter. *Nuclear Fusion Research: Understanding Plasma-Surface Interactions*. Chemical Physics: Springer, Berlin, Germany, 2005.
94. P.C. Stangeby. *The Plasma Boundary of Magnetic Fusion Devices*, Vol. 7 of *Plasma Physics Series*. IoP Publishing, Bristol, U.K., 2000.
95. D.E. Post and K. Lackner. Plasma models for impurity control experiments. In D.E. Post and R. Behrisch, eds., *Physics of Plasma Wall Interaction in Controlled Fusion (Proceedings of NATO Workshop ValMorin, Montreal, Quebec, Canada)*, pp. 627–693, Plenum Press, New York, 1984.
96. W. Eckstein. *Computer Simulation of Ion-Solid Interactions*, Vol. 10 of *Materials Science*. Springer, Berlin, Germany, 1991.
97. J. Roth. Chemical erosion of carbon-based materials in fusion devices. *J. Nucl. Mater.*, 266–269:51–57, 1999.
98. E. Salonen, K. Nordlund, J. Keinonen, and C.H. Wu. Swift chemical sputtering of amorphous hydrogenated carbon. *Phys. Rev. B*, 63:195415, 2001.
99. R. Behrisch and W. Eckstein. *Sputtering by Particle Bombardment I: Physical Sputtering of Single-Element Solids*, Vol. 47 of *Topics in Applied Physics*. Springer Verlag, Berlin, Germany, 1979.
100. R. Behrisch and W. Eckstein. *Sputtering by Particle Bombardment II: Sputtering of Alloys and Compounds, Electron and Neutron Sputtering, Surface Topography*, Vol. 52 of *Topics in Applied Physics*. Springer Verlag, Berlin, Germany, 1983.
101. R. Behrisch and W. Eckstein. *Sputtering by Particle Bombardment III: Characteristics of Sputtered Particles, Technical Applications*, Vol. 64 of *Topics in Applied Physics*. Springer Verlag, Berlin, Germany, 1991.
102. R. Behrisch and W. Eckstein. *Sputtering by Particle Bombardment: Experiments and Computer Calculations from Threshold to MeV Energies*, Vol. 110 of *Topics in Applied Physics*. Springer Verlag, Berlin, Germany, 2007.
103. J. Roth, E. Vietzke, and A.A. Haasz. Erosion of graphite due to particle impact. In *Atomic and Plasma-Material Interaction Data for Fusion*, Vol. 1 of *Nuclear Fusion Special Statement*, p. 63. IAEA, Vienna, Austria, 1991.
104. B.V. Mech, A.A. Haasz, and J.W. Davis. Model for the chemical erosion of graphite due to low-energy H+ and D+ impact. *J. Appl. Phys.*, 84(3):1655–1669, 1998.
105. Y. Ueda, T. Shimada, and M. Nishikawa. Impacts of carbon impurities in hydrogen plasmas on tungsten blistering. *Nucl. Fusion*, 44:62–67, 2004.
106. A. Rai. Multi-scale modeling of hydrogen isotope reactive-diffusive transport in porous graphite. PhD thesis, Ernst-Moritz-Arndt-Universität, Greifswald, Germany, 2008.
107. V.A. Rozhanskij, A.A. Ushakov, and S.P. Voskobojnikov. Electric field near an emitting surface and unipolar arc formation. *Nucl. Fusion*, 36:191–198, 1996.
108. G.D. Hobbs and J.A. Wesson. Heat flow through a Langmuir sheath in the presence of electron emission. *Plasma Phys.*, 9:85–87, 1967.
109. N.W. Ashcroft and N.D. Mermin. *Solid State Physics*. Holt, Rinehart and Winston, New York, 1976.
110. Y.P. Raizer, J.E. Allen, and V.I. Kisin. *Gas Discharge Physics*. Springer, Berlin, Germany, 1991.

111. R. Schneider, A. Rai, A. Mutzke, M. Warrier, E. Salonen, and K. Nordlund. Dynamic Monte-Carlo modeling of hydrogen isotope reactive-diffusive transport in porous graphite. *J. Nucl. Mater.*, 367–370:1238–1242, 2007.
112. M. Warrier. Subroutines for some plasma surface interaction processes: Physical sputtering, chemical erosion, radiation enhanced sublimation, backscattering and thermal evaporation. *Comp. Phys. Comm.*, 160(1):46–68, 2004.
113. K.L. Wilson and W.L. Hsu. Hydrogen recycling properties of graphite. *J. Nucl. Mater.*, 145–147:121–130, 1987.
114. S. Chiu and A.A. Haasz. Chemical release of implanted deuterium in graphite. *J. Vac. Sci. Technol. A*, 9(3):747–752, 1991.
115. R.A. Causey, M.I. Baskes, and K.L. Wilson. The retention of deuterium and tritium in POCO AXF-5Q graphite. *J. Vac. Sci. Technol. A*, 4(3):1189–1192, 1986.
116. R.A. Causey. The interaction of tritium with graphite and its impact on tokamak operations. *J. Nucl. Mater.*, 162–164:151–161, 1989.
117. M. Warrier. Multi-scale modeling of hydrogen isotope transport in porous graphite. PhD thesis, Ernst-Moritz-Arndt-Universität, Greifswald, Germany, 2004.
118. O.V. Braginsky, A.S. Kovalev, D.V. Lopaev, Yu.A. Mankelevich, O.V. Proshina, T.V. Rakhimova, A.T. Rakhimova, and A.N. Vasilieva. Discharge singlet oxygen generator for oxygen-iodine laser: I. Experiments with rf discharges at 13.56 and 81 MHz. *J. Phys. D Appl. Phys.*, 39:5183–5190, 2006.
119. K. Dittmann, D. Drozdov, B. Krames, and J. Meichsner. Radio-frequency discharges in oxygen: II. Spatio-temporally resolved optical emission pattern. *J. Phys. D Appl. Phys.*, 40:6593–6600, 2007.
120. S. Nemschokmichal, K. Dittmann, and J. Meichsner. Spatial and phase-resolved optical emission patterns in capacitively coupled radio-frequency plasmas. *IEEE Trans. Plasma Sci.*, 36:1360–1361, 2008.
121. K. Dittmann. Detailed investigations of the sheath dynamics and elementary processes in capacitively coupled rf plasmas. PhD thesis, University of Greifswald, Greifswald, Germany, 2009.
122. K. Matyash and R. Schneider. PIC-MCC modeling of a capacitive rf discharge. *Contrib. Plasma Phys.*, 44:589–593, 2004.
123. F.X. Bronold, K. Matyash, D. Tskhakaya, R. Schneider, and H. Fehske. Radio-frequency discharges in oxygen: I. Particle-based modelling. *J. Phys. D Appl. Phys.*, 40:6583–6592, 2007.
124. K. Matyash, R. Schneider, K. Dittmann, J. Meichsner, F.X. Bronold, and D. Tskhakaya. Radio-frequency discharges in oxygen: III. Comparison of modelling and experiment. *J. Phys. D Appl. Phys.*, 40:6601–6607, 2007.
125. M.W. Kiehlbauch and D.B. Graves. Inductively coupled plasmas in oxygen: Modeling and experiment. *J. Vac. Sci. Technol.*, 21:660–670, 2003.
126. C.M.O. Mahony, R. Al Wazzan, and W.G. Graham. Sheath dynamics observed in a 13.56 MHz-driven plasma. *Appl. Phys. Lett.*, 71:608–610, 1997.
127. K. Niemi, V. Schulz-von der Gathen, and H.F. Döbele. Absolute calibration of atomic density measurements by laser-induced fluorescence spectroscopy with two-photon excitation. *J. Phys. D Appl. Phys.*, 34:2330–2335, 2001.
128. H.M. Katsch, A. Tewes, E. Quandt, A. Goehlich, T. Kawetzki, and H.F. Döbele. Detection of atomic oxygen: Improvement of actinometry and comparison with laser spectroscopy. *J. Appl. Phys.*, 88:6232–6238, 2000.
129. E.J.H. Collart, J.A.G. Baggerman, and R.J. Visser. Excitation mechanisms of oxygen atoms in a low pressure O₂ radio-frequency plasma. *J. Appl. Phys.*, 70:5278–5281, 1991.

130. M.A. Lieberman and A.J. Lichtenberg. *Principles of Plasma Discharges and Materials Processing*. 2 edn., Wiley-Interscience, Hoboken, NJ, 2005.
131. T Gans, V Schulz-von der Gathen, and H F Döbele. Spectroscopic measurements of phase-resolved electron energy distribution functions in rf-excited discharges. *Europhys. Lett.*, 66:232–238, 2004.
132. N. Mutsukura, K. Kobayashi, and Y. Machi. Monitoring of radio-frequency glow-discharge plasma. *J. Appl. Phys.*, 66:4688–4695, 1989.
133. S. Djurović, J.R. Roberts, M.A. Sobolewski, and J.K. Olthoff. Absolute spatially- and temporally-resolved optical emission measurements of rf glow discharges in argon. *J. Res. Natl. Inst. Stand. Technol.*, 98:160–180, 1993.
134. Z. Lj Petrović, S. Bzenić, J. Jovanović, and S. Djurović. On spatial distribution of optical emission in radio frequency discharges. *J. Phys. D Appl. Phys.*, 28:2287–2293, 1995.
135. C.M.O. Mahony, J. McFarland, P.G. Steen, and W.G. Graham. Structure observed in measured electron energy distribution functions in capacitively coupled radio frequency hydrogen plasmas. *Appl. Phys. Lett.*, 75:331–333, 1999.
136. T. Gans, C.C. Lin, V. Schulz-von der Gathen, and H.F. Döbele. Determination of quenching coefficients in a hydrogen rf discharge by time-resolved optical emission spectroscopy. *J. Phys. D Appl. Phys.*, 34:L39–L42, 2001.
137. T. Gans. Phasenaufgelöste emissionsspektroskopische Untersuchung der Besetzungs dynamik angeregter Zustände in Wasserstoff-RF-Entladungen. PhD thesis, University of Duisburg-Essen, Duisburg and Essen, Germany, 2001.
138. T. Gans, C.C. Lin, V. Schulz-von der Gathen, and H.F. Döbele. Phase-resolved emission spectroscopy of a hydrogen rf discharge for the determination of quenching coefficients. *Phys. Rev. A*, 67:1–11, 2003.
139. F. Tochikubo, T. Kokubo, S. Kakuta, A. Suzuki, and T. Makabe. Investigation of the high-frequency glow discharge in Ar at 13.56 MHz by spatiotemporal optical emission spectroscopy. *J. Phys. D Appl. Phys.*, 23:1184–1192, 1990.
140. F. Tochikubo and T. Makabe. Absolute measurement of the excitation rate and density of the excited species in an rf discharge from optical emission spectroscopy. *Meas. Sci. Technol.*, 2:1133–1137, 1991.
141. F. Tochikubo, T. Makabe, S. Kakuta, and A. Suzuki. Study of the structure of radio frequency glow discharges in CH_4 and H_2 by spatiotemporal optical emission spectroscopy. *J. Appl. Phys.*, 71:2143–2150, 1992.
142. Z. Lj Petrović, F. Tochikubo, S. Kakuta, and T. Makabe. Spatiotemporal optical emission spectroscopy of rf discharges in SF_6 . *J. Appl. Phys.*, 73:2163–2172, 1993.
143. M.M. Turner and M.B. Hopkins. Anomalous sheath heating in a low pressure rf discharge in nitrogen. *Phys. Rev. Lett.*, 69:3511–3514, 1992.
144. K. Dittmann, K. Matyash, S. Nemischokmichal, J. Meichsner, and R. Schneider. Excitation mechanisms and sheath dynamics in capacitively coupled radio-frequency oxygen discharges. *Contrib. Plasma Phys.*, 50(10):942–953, 2010.

Nonthermal Plasma Chemistry and Physics

In addition to introducing the basics of plasma physics, **Nonthermal Plasma Chemistry and Physics** is a comprehensive presentation of recent developments in the rapidly growing field of nonthermal plasma chemistry. The book offers a detailed discussion of the fundamentals of plasma chemical reactions and modeling, nonthermal plasma sources, relevant diagnostic techniques, and selected applications.

Features

- Includes a compact introduction in the nonthermal plasma physics and plasma–surface interaction
- Classifies the plasma sources and chemical plasma reactors, and provides important similarity parameters
- Overviews experimental methods in plasma diagnostics and surface (thin film) analysis
- Presents detailed research results with modeling and applications
- Promotes strategies in plasma modeling and provides specific methods, including examples

Elucidating interconnections and trends, the book focuses on basic principles and illustrations across a broad field of applications. Expert contributors address environmental aspects of plasma chemistry. The book also includes selected plasma conditions and specific applications in volume plasma chemistry and treatment of material surfaces such as plasma etching in microelectronics, chemical modification of polymer surfaces and deposition of functional thin films. Designed for students of plasma physics, **Nonthermal Plasma Chemistry and Physics** is a concise resource also for specialists in this and related fields of research.



CRC Press
Taylor & Francis Group
an informa business

www.taylorandfrancisgroup.com

6000 Broken Sound Parkway, NW
Suite 300, Boca Raton, FL 33487
711 Third Avenue
New York, NY 10017
2 Park Square, Milton Park
Abingdon, Oxon OX14 4RN, UK

59165
ISBN: 978-1-4200-5916-8 90000
 9 781420 059168
WWW.CRCPRESS.COM